Biologically-based radiation therapy planning and adjustable robust optimization

ten Eikelder, Stefan

DOI:
10.26116/center-lis-2120

Publication date:
2021

Document Version
Publisher's PDF, also known as Version of record

Biologically-based radiation therapy planning and adjustable robust optimization

STEFAN TEN EIKELDER

TILBURG UNIVERSITY

Biologically-based radiation therapy planning and adjustable robust optimization

Proefschrift

ter verkrijging van de graad van doctor aan Tilburg University op gezag van de rector magnificus, prof. dr. W.B.H.J. van de Donk, in het openbaar te verdedigen ten overstaan van een door het college voor promoties aangewezen commissie in de aula van de Universiteit op

woensdag 20 oktober 2021 om 16.00 uur
door

Stefan Cornelis Martinus ten Eikelder

geboren op 26 januari 1994 te Eindhoven.

Promotores:	prof. dr. ir. Dick den Hertog
	prof. dr. Thomas Bortfeld
Promotiecommissie:	prof. dr. Anders Forsgren
	prof. dr. Etienne de Klerk
	prof. dr. Jan Unkelbach
	dr. Marleen Balvert
	dr. ir. Sebastiaan Breedveld

Biologically-based radiation therapy planning and adjustable robust optimization

Aan mijn ouders

Acknowledgments

This thesis marks the end of my PhD research. I am glad that there is an opportunity to put others in the spotlight, as there are many who truly deserve this.

I have been extremely fortunate to have had two advisors who are world-renowned experts in their respective fields, who have shown sincere interest in my work, and spent a lot of time and effort on our projects. First, I am very grateful for all the guidance of my advisor, Dick den Hertog. Dick, you are passionate, caring, and enthusiastic. Working under your supervision has been a wonderful experience. You involved me in many different aspects of academic life, and I felt like an equal colleague right from the start. At times, you were even more concerned about my future career than I was. I admire your passion and drive to 'make the world a little bit better' and will keep this in mind, along with many other lessons. I always left our meetings with a more positive feeling than before. Thank you for all of this!

Second, I want to express my gratitude to my second advisor, Thomas Bortfeld, for his invaluable support. Thomas, you allowed me to do research in radiation therapy planning without any prior experience, thank you for putting your trust in me. You took the time to digest my mathematical fiddling, and helped boil it down to the practically relevant insights. You taught me to look for simple examples and intuitive explanations. I admire how you can listen and ask sharp questions during discussions about virtually any topic; I have always enjoyed our discussions very much. You have always been a gracious host and made me feel welcome during my visits to Boston. I am truly thankful for all your help and support.

I also want to thank the committee members, Anders Forsgren, Etienne de Klerk, Jan Unkelbach, Marleen Balvert and Sebastiaan Breedveld, for taking the time to read my thesis. Thanks to your insightful questions, remarks and comments, the thesis is definitely in better shape.

Over the last years I have had the pleasure of working with different co-authors, who have contributed a great deal to various chapters of this thesis. Thank you for all the pleasant collaborations; you have given me new perspectives on doing research, and I learned a lot from you. In particular, I am greatly indebted to Ali Ajdari. Ali, when I started my PhD, you had just started at MGH. Nevertheless, right from the start you helped me in many ways. You have extensive knowledge of both medical physics and optimization, and I am thankful that we worked together on many research projects. You are very considerate, and your enthusiastic and open attitude made it easy for me to reach out for questions, no matter how big or small. I hope I have not exploited this too much.

Further, I wish to acknowledge the help of Zoltán Perkó. Zoltán, you took on the task of supervising my master's thesis at MGH, and patiently taught me all the basics of radiation therapy planning, at a point where I knew virtually nothing. You were an incredibly devoted supervisor, and skillfully guided me past many pitfalls. You went above and beyond in helping me write my first paper, I am very thankful for this.

I have been fortunate to visit the division of radiation biophysics at MGH on several occasions, and want to thank the group for their hospitality; the international and open environment always made me feel welcome during my visits to Boston. Even when I was on the other side of the ocean, it felt like I was a part of the group, whether it being during the optimization lab meetings or when participating in the office football betting pools. Special thanks go to Koos for embarking on our US adventure together for our master's theses, and for being a great roommate in Boston.

I want to express my gratitude to all PhD students of the OR group in Tilburg, plus those who joined us from the econometrics group. In particular, I would like to thank Andries, Daniel, Ernst, Frank, Hao, Jop, Jorgo, Lorenz, Melissa, Riley, and Valentijn for our many lunches, serious and less serious discussions, games and other activities.

My journey at Tilburg University started all the way back in 2012. During these years, I have made many great friends who have made Tilburg feel like a home. Thank you, Anouk, Coenraad, Esmee, Jeannine, Jon, Juul, Pepijn v.d.B., Pepijn W., Thijs, Thomas, Tom, Vera, and many more, for providing a steady stream of pub quizzes, board game evenings, and many more fun and crazy activities.

I also want to thank Bas for being my roommate since the second year of my studies, and Dominique for having been one for seven years. This is a ridiculously long time! You have always been constant positive factors throughout my entire studies. Thank you for this.

Dennis, Joost and Vincent, thanks for all the games, drinks, travels and other activities, and simply for being great friends ever since secondary school (and Joost even way before that). I always look forward to our next activity.

Last, and most importantly, I want to thank my loving family. Marco and Walter, you are not only brothers but also fantastic friends. I am glad and thankful we are so close. Above all, I want to thank my parents, Huub and Marijke, for their unconditional love and support in everything we do. Your encouragement of curiosity has brought us where we are now. I will always be grateful to you.

Tilburg, August 2021 Stefan ten Eikelder

Contents

List of Abbreviations

AIDP	Approximate inexact data problem
ARF	Adjustable robustly feasible
ARO	Adjustable robust optimization; adjustable robustly optimal
BAO	Beam angle optimization
BED	Biologically effective dose
CDA	Continuous dose adaptation
CQr	Conic quadratic representable
CP	Conic problem
Cr	Conic representable
CR	Conic representation
CT	Computed tomography
CTV	Clinical target volume
CVaR	Conditional value-at-risk
Cu-ATSM	copper(II)-diacetyl-bis (N4-methylthiosemicarbazone)
DAO	Direct aperture optimization
DQ	Data quality
DVH	Dose-volume histogram
EBRT	External beam radiation therapy
EDP	Exact data problem
FDG	[(18)F]-fluorodeoxyglucose
FH	Folding horizon
FLT	3'-deoxy-3'[(18)F]-fluorothymidine
FME	Fourier-Motzkin elimination
FMO	Fluence map optimization
(g)EUD	(generalized) Equivalent uniform dose
GTV	Gross tumor volume
Gy	Gray
IDP	Inexact data problem
IMPT	Intensity-modulated proton therapy
IMRT	Intensity-modulated radiation therapy
IPM	Interior-point method
LDR	Linear decision rule
LKB	Lyman-Kutcher-Burman
LP	Linear program/programming
LQ	Linear-quadratic

LQED2	LQ equivalent dose in 2 Gy fractions
LTCP	Logarithmic tumor control probability
MCO	Multicriteria optimization
MLC	Multileaf collimator
MRI	Magnetic resonance imaging
NSCLC	Non-small cell lung cancer
NTCP	Normal tissue complication probability
OAR	Organ-at-risk
OSRT	Optimal stopping in radiation therapy
PARO	Pareto adjustable robustly optimal; Pareto adjustable robust optimality
PET	Positron emission tomography
PI	Perfect information
PRO	Pareto robustly optimal; Pareto robust optimality
PTV	Planning target volume
PWL	Piecewise linear
RBE	Relative biological effectiveness
RF	Robustly feasible
RO	Robust optimization; robustly optimal
RS	Relative seriality
RT	Radiation therapy
SF	Survival fraction
TCP	Tumor control probability
TNTCR	Total number of tumor cells remaining
TPS	Treatment planning system
UDA	Uniform dose adaptation
VMAT	Volumetric modulated arc therapy

CHAPTER 1

Introduction

Cancer is one of the leading causes of death worldwide, second only to cardiovascular diseases. Globally, every one in six deaths is due to cancer (World Health Organization, 2020). According to the Global Cancer Observatory, there were 19.3 million new cancer cases in 2020 and almost 10 million deaths (Sung et al., 2021). In 2040, these numbers are expected to increase to 30.2 million new cases and 16.3 million cancer related deaths (Ferlay et al., 2020).

The three main pillars of cancer therapy[1] are surgery, chemotherapy and radiation therapy (RT, also called 'radiotherapy'). RT is especially suitable for tumors that are inaccessible by surgery. RT may also be applied in combination with surgery and/or chemotherapy, and it can be used for both curative and palliative treatments. It has been estimated that approximately half of cancer patients can benefit from RT (Delaney et al., 2005), a number that is still generally accepted today.

RT uses ionizing radiation to kill cancerous cells, by damaging their DNA. The radiation source may be positioned either inside or outside the patients' body. The former is known as brachytherapy, or internal RT. In brachytherapy, a radioactive source is (temporarily) implanted in the tumor via an invasive procedure, and the tumor is irradiated from within the patient. External beam radiation therapy (EBRT), on the other hand, uses a linear accelerator (linac) to pass beams of ionizing radiation through the patient's body. Energy is deposited in all tissues on the path of the beam. The absorbed dose is the energy deposited per unit mass, and is measured in Gray (Gy, 1 Joule per kilogram).

Inevitably, there is a trade-off between sufficiently damaging the tumor tissue, and sparing the surrounding healthy tissues. The primary goal of treatment planning for EBRT is to design a treatment plan that finds a good balance between these compet-

[1] Immunotherapy is likely to become the fourth pillar; the 2018 Nobel Prize in Physiology or Medicine has been awarded to advances in this area (Nobel Media AB, 2018).

ing objectives, i.e., a treatment plan that administers a therapeutic amount of dose to the tumor, while keeping dose to all surrounding healthy tissues within tolerable limits. To achieve this, treatment planners can decide on beam angles, beam intensities, treatment length and other degrees of freedom. Traditionally, this is done in a forward (trial-and-error) manner. A treatment plan is designed, and subsequently evaluated according to several clinically relevant performance measures. If deemed necessary, the plan is adapted and re-evaluated, until an acceptable treatment plan is found. However, contemporary treatment techniques such as intensity-modulated radiation therapy (IMRT) allow for more advanced dose modulation, leading to more complex treatment planning problems with many degrees of freedom. The forward approach is no longer practical, and is replaced by an inverse approach which employs mathematical optimization. In inverse treatment planning, the treatment goals are set a priori, and mathematical optimization is employed to find the optimal treatment plan.

This thesis deals with various topics in mathematical optimization for IMRT. The focus is on biologically-based treatment planning and the role of (adjustable) robust optimization. The remainder of this chapter deals with various preliminaries, and provides an outline of the thesis. Section 1.1 introduces the treatment planning workflow for IMRT. Section 1.2 introduces biologically-based treatment planning. After that, Section 1.3 discusses the uncertainties that play a role in treatment planning, and introduces robust optimization. In Section 1.4 the contributions of this thesis are presented, and Section 1.5 provides a disclosure.

1.1 Treatment planning for IMRT

1.1.1 Medical physics preliminaries

Medical imaging plays an essential role in treating cancer patients with radiation therapy. Without imaging, one cannot precisely locate the tumor and other relevant structures inside the patients anatomy, and designing an acceptable treatment plan is impossible. The most widely used imaging modality is computed tomography (CT), more recently also magnetic resonance imaging (MRI) is employed. A CT scan provides information on the anatomical structure of the patient. A radiation oncologist uses CT images to delineate all volumes of interest. The gross tumor volume (GTV) is the tumor volume that can be visually identified on a CT scan. To account for microscopic disease extensions that cannot be imaged, the GTV is extended by a margin to obtain the clinical target volume (CTV). The CTV is the volume that must be adequately

treated. Next to this, organs-at-risk (OARs) are delineated. OARs are critical normal tissue structures in close proximity to the tumor that are taken into account during the treatment planning. The resulting contours provide the geometrical information required for treatment planning.

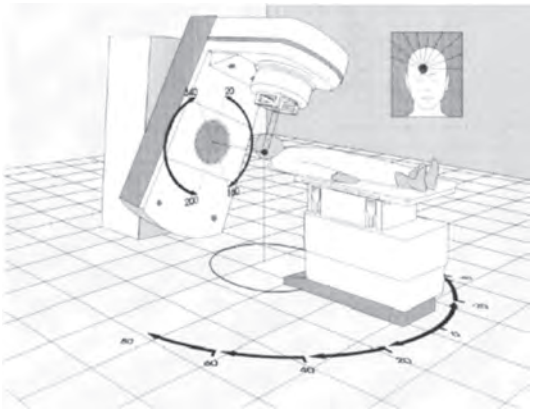

Figure 1.1: Illustration of a linac positioned in the head of a gantry. The gantry rotates around the patient to treat a brain tumor. From Küfer et al. (2005), with permission.

The treatment is typically delivered using a linac mounted on a gantry, which can rotate around the patient to direct beams at the target volume from different angles, see Figure 1.1. Moreover, the treatment couch can be moved to yield an additional degree of freedom. From a beam's eye view, the target volume is a two-dimensional shape, i.e., the three-dimensional target volume projected onto the plane orthogonal to the beam. The 2D plane can be discretized in a 2D grid, where each element is referred to as a beamlet (or bixel).

The linac aperture (in the gantry head) is equipped with a multileaf collimator (MLC), a device that modulates the beam shape. An MLC consists of a number of leaf-pairs, which can be controlled to block part of the beam, see the first part of Figure 1.2. Using the MLC, the time during which particles pass through each beamlet is modulated, and beam shapes conformal to the target volume can be created. Prior to modulation, the accelerator produces a (constant) flux (particles per unit area per unit time). By dynamically blocking beamlets with the MLC leaves during irradiation, the exposure time can differ per beamlet, leading to a (potentially) different fluence (number of crossing particles per unit area) per beamlet. The 2D grid with the fluence at each beamlet is referred to as the fluence map, see the second part of Figure 1.2 for an illustration. A fluence map is sometimes also referred to as an intensity map

or profile, although this is technically incorrect[2]. For further details on the physics of radiation oncology we refer to Gotein (2008).

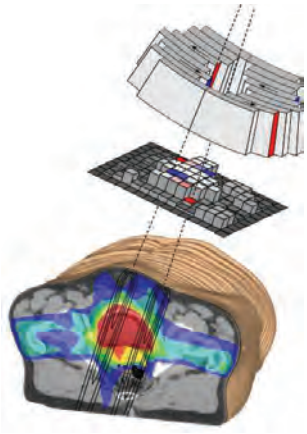

Figure 1.2: Schematic overview of dose delivery. Part 1: The multileaf collimator is dynamically controlled to modulate the fluence. Part 2: The fluence modulation results in a fluence map, which indicates the resulting fluence per beamlet. Part 3: The dose distribution, which indicates for every tissue voxel the total dose it received, is obtained by summing the contributions of all fluence maps per voxel. Image courtesy of Björn Hårdemark (Raysearch Laboratories AB, Stockholm, Sweden).

It is crucial to have accurate information on how unit fluence of an individual beamlet translates to dose deposited within the patient's body. This problem is known as dose calculation, and is typically solved using a pencil beam algorithm (Ahnesjö et al., 1992), and sometimes using Monte Carlo simulation (Seco and Verhaegen, 2013). In this way, the contribution of a single fluence map to the entire deposited dose can be determined. By directing beams from different angles, multiple fluence maps are created. To represent the total accumulated dose, all volumes of interest (the target volume and the OARs) are discretized into small cubes, called voxels. The resulting dose deposited in each voxel is referred to as the dose distribution (third part Figure 1.2).

A single non-uniform (i.e., non-constant) fluence map leads to a more heterogeneous dose distribution in the target volume distribution than a single uniform fluence

[2]The intensity at an area is the number of particles passing through that area per unit time (prior to modulation). The observant reader may also note that, despite the naming, IMRT does in fact not modulate intensity, but rather modulates fluence (Webb and Lomax, 2001).

map, which is generally not desired. However, IMRT capitalizes on the fact that superimposing multiple non-uniform beams from different angles can lead to the desired target dose distribution. Compared to 3D conformal radiation therapy (with uniform fluence maps), IMRT can achieve better target dose conformality and/or OAR sparing. There are some investigations into the required number of beams for IMRT (Bortfeld et al., 1990; Bortfeld, 2010); clinically, often approximately ten beams are used. For overviews of IMRT we refer to Bortfeld (2006) and Das et al. (2020).

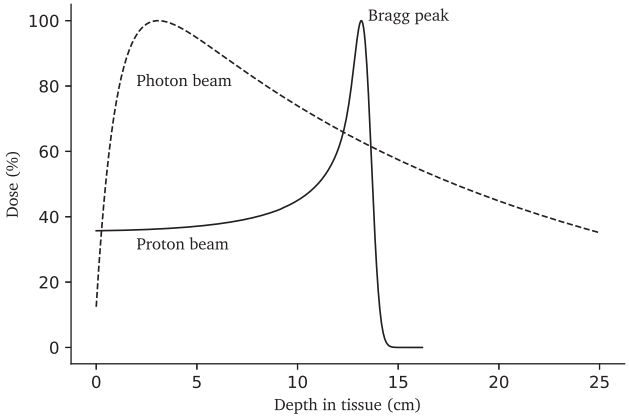

Figure 1.3: Example Bragg curves for photon and proton beams. The photon dose decreases as the beam passes through tissue. The proton beam has a pronounced peak (the Bragg peak), of which the location and width can be controlled. Image courtesy of Thomas Bortfeld (Massachusetts General Hospital and Harvard Medical School, Boston, USA).

The majority of treatment techniques, among which IMRT, make use of high-energy photons (X-rays or gamma rays). Particle therapy is an alternative, advanced form of EBRT that makes use of heavy ions such as protons or carbon ions. Proton therapy is the most common type of particle therapy. It generates proton beams, which lead to a different dose deposition than photon beams. Figure 1.3 visualizes the Bragg curves (depth-dose profiles) of a photon and a proton beam. The photon beam has a high entrance dose, and dose deposition gradually decreases along the beam's path. The proton beam, on the other hand, has a lower entrance dose and has a pronounced peak, called the Bragg peak. The Bragg peak is followed by a sharp dose falloff, thus leading to a finite range of dose deposition. The Bragg peak and width can be controlled, by changing amongst others the proton energy, which is an important advantage for OAR

sparing. The practical benefits of this theoretical advantage are highly influenced by uncertainties in treatment planning. This is discussed in more detail in Section 1.3.1. Dose modulation in proton therapy is slightly different from IMRT. The first proton therapy systems used passive scattering techniques, and more recent systems use pencil beam scanning methods, also referred to as intensity modulated proton therapy (IMPT). IMPT allows for dose modulation similar to IMRT in photon therapy, and typically uses not more than three beam angles. Further details on proton therapy physics can be found in the book by Paganetti (2019).

1.1.2 (Inverse) treatment planning for IMRT

The primary goal in treatment planning is to design a treatment plan that best satisfies the criteria set by the radiation oncologist. Predominantly, these goals will be related to the resulting dose distribution. A radiation oncologist can define hard goals (constraints) and soft goals (objectives), both for the dose in the target volume(s) and OARs. An important treatment plan evaluation tool for radiation oncologists is a (cumulative) dose-volume histogram (DVH). For any target or OAR volume, the DVH compresses the 3D dose distribution into a single line. For every dose value, the DVH line indicates the volume percentage that receives at least this dose. Figure 1.4 provides an illustration. The solid and dashed lines visualize a typical target and OAR dose distribution, respectively. The maximum point dose, the highest dose over all voxels, is around 54 Gy for both volumes. Next to this, other dose-volume metrics can be derived from the DVH. For example, the D_{30} is the minimum dose received by the 'hottest' 30% of the structure, which is approximately 30 Gy for the OAR in Figure 1.4. Conversely, V_{20} is the volume that receives at least 20 Gy. In Figure 1.4, the V_{20} of the OAR is approximately 53%. A DVH metric provides information on the dose distribution in a particular structure, and can be visualized by a single point in a DVH graph. A DVH objective or constraint essentially aims to push the DVH line above (for targets) or below (for OARs) a specific point in the DVH graph.

The types of dose criteria, i.e., objectives and constraints, that are specified will depend on the type of tissue. For serial organs such as the spinal cord, excessive damage to a small subvolume may lead to loss of functionality for the entire organ. For serial organs often maximum point dose criteria are specified. Parallel organs, on the other hand, are those where damage to small subvolumes does not restrict functionality. They continue to function as long as the spared volume is sufficiently large. For parallel organs often mean dose criteria and DVH criteria are used. For target volumes, minimum dose criteria and prescription criteria are typically used. For the latter, a

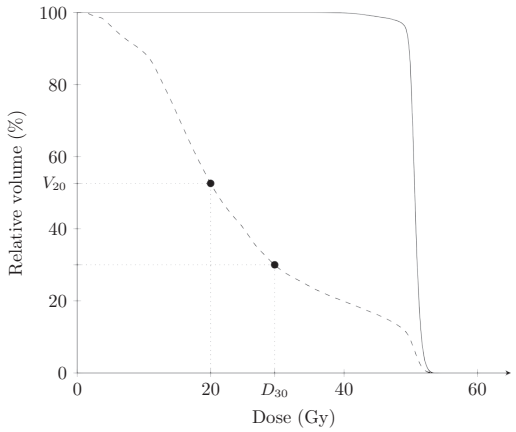

Figure 1.4: Illustration of a (cumulative) DVH. The solid and dashed lines represents the dose distribution in the target and OAR volume, respectively.

prescription dose is set for the entire volume, and underdose and/or overdose is penalized. The chosen set of objectives and constraints is for a large part based on a dose protocol, which, in turn, is based on amongst others clinical trial results and expert consensus.

Designing an IMRT treatment plan that best satisfies these criteria is the task of a medical physicist and/or dosimetrist. The process is typically split up into three parts: beam angle selection, fluence map optimization (FMO) and leaf sequencing. The first step is selecting a set of beam angles to be used for treatment planning. Then, fluence map optimization determines the optimal fluence maps for the given set of beams. Lastly, leaf sequencing is the process of determining MLC controls to efficiently and accurately replicate the desired fluence maps.

Selecting the appropriate beam angles is typically done manually (i.e., no optimization). The reason is that the number of beams is typically limited, so the forward problem is still manageable. Incorporating beam angle selection in FMO leads to the beam angle optimization (BAO) problem, which is a difficult nonconvex problem. Most BAO approaches in literature use heuristics, see, e.g., Bertsimas et al. (2013) and references therein. There are also some approaches which skip the fluence map step, and directly optimize machine parameters. This is called direct aperture optimization (DAO). Leaf sequencing and DAO are not considered in this thesis; we refer to Ehrgott et al. (2008) and Romeijn and Dempsey (2008) for reviews on these and other optimization challenges in treatment planning. The FMO problem usually has the largest

impact on the overall treatment quality (Aleman, 2018), and has received most attention from the optimization community.

When beam angles are selected and dose calculations have been performed, a dose deposition matrix (or pencil beam matrix) is obtained. This matrix maps beamlet fluences, often referred to as beamlet weights, to the deposited dose in all voxels. Consider a total of n beamlets (aggregated over all fluence maps), and let $\boldsymbol{x} \in \mathbb{R}^n$ denote the beamlet weights. Let m denote the total number of voxels (over all structures), and let $\boldsymbol{A} \in \mathbb{R}^{m \times n}$ denote the dose deposition matrix. Then the dose vector $\boldsymbol{d} \in \mathbb{R}^m$ is given by $\boldsymbol{d} = \boldsymbol{A}\boldsymbol{x}$. That is, with $\boldsymbol{a}_i$ the i-th row of matrix $\boldsymbol{A}$ (as a column vector), the dose d_i in any particular voxel i is given by $d_i = \boldsymbol{a}_i^\top \boldsymbol{x}$. Vector $\boldsymbol{a}_i$ gives for every beamlet the deposited dose in voxel i at unit fluence.

Let $f_i : \mathbb{R}^m \mapsto \mathbb{R}$, $i \in O$, denote treatment plan objectives, and let $f_j : \mathbb{R}^m \mapsto \mathbb{R}$, $j \in C$, denote treatment plan constraints. With $\boldsymbol{w} \in \mathbb{R}^{|O|}$ the vector of objective weights, a generic FMO problem can be formulated as

$$\min_{\boldsymbol{x},\boldsymbol{d}} \quad \sum_{i \in O} w_i f_i(\boldsymbol{d}), \tag{1.1a}$$

$$\text{s.t.} \quad f_j(\boldsymbol{d}) \leq 0, \quad \forall j \in C, \tag{1.1b}$$

$$\boldsymbol{d} = \boldsymbol{A}\boldsymbol{x}, \tag{1.1c}$$

$$\boldsymbol{x} \geq \boldsymbol{0}. \tag{1.1d}$$

One can also add constraints on beamlet weights $\boldsymbol{x}$ to ensure that the resulting fluence maps can actually be delivered using an MLC (i.e., can be replicated during the leaf-sequencing phase). Such smoothing constraints prevent spiked fluence maps, see, e.g., Breedveld et al. (2006).

As noted before, there is an inevitable trade-off between eradicating the tumor and sparing healthy tissues in close proximity to the tumor. Mathematically, this trade-off is captured by the weight vector $\boldsymbol{w}$, which quantifies the relative importance of the various competing objectives. A priori, it is unknown what weight vectors give desirable treatment plans, and this may differ from patient to patient. Multicriteria optimization (MCO) has been used successfully to handle these trade-offs. It makes use of the fact that only Pareto efficient (or Pareto optimal) solutions (i.e., treatment plans) are clinically relevant. A Pareto efficient solution cannot be dominated. That is, the performance in one treatment criteria can only be improved if the performance in another treatment criteria deteriorates. The set of all such solutions is called the Pareto surface, and this is the set of meaningful solutions that a physician could consider. Research focuses on accurate approximation of the Pareto surface in a time efficient manner; we refer to Breedveld et al. (2019) for a review. MCO has been implemented

in amongst others the RayStation treatment planning system (Bokrantz and Forsgren, 2013; RaySearch Laboratories AB, 2020).

During conventional IMRT delivery, the FMO problem is solved for a set of preselected beam angles, and the linac is switched off when the gantry moves from one beam position to the next. Volumetric modulated arc therapy (VMAT) is a different IMRT delivery approach that makes a single gantry arc rotation with continuous irradiation (Yu, 1995; Otto, 2008). Currently, VMAT is the most common IMRT delivery technique. It has the potential to deliver higher quality treatment plans (due to an increase in beam angles) with shorter treatment time. For adjacent beam angles the MLC leaf positions have to be coupled. Therefore, the full VMAT optimization problem is a large-scale nonconvex problem that cannot directly be decomposed in an FMO and leaf-sequencing step. However, the two-step heuristic approaches commonly used in practice do start with FMO (Craft et al., 2012).

In this section we have presented the FMO problem for IMRT treatments. The FMO problem of its proton counterpart (IMPT) has a similar mathematical formulation, although underlying physics and clinical aspects may differ.

1.2 Biologically-based treatment planning

Next to treatment planning aspects pertaining to the medical physics side of the problem, radiobiology also plays an important role in treatment planning. In this section, we discuss the use of biological information in treatment planning.

1.2.1 Fractionation

Radiation therapy treatments are typically not delivered on a single treatment day. Instead, this is spread out over multiple treatment sessions or fractions, where in each session part of the total dose is delivered. The underlying rationale is that healthy cells can (partially) recover from absorbed dose inbetween fractions, whereas tumor cells, which are primarily focused on reproduction, lack such repair mechanisms. Short treatments (i.e., few fractions) may thus unnecessarily damage the healthy tissues surrounding the target volume. On the other hand, a treatment spread out over a large number of treatment fractions may not deliver sufficient damage to the target volume, and increases the risk of tumor proliferation. The effect of fractionation differs per healthy tissue type and per tumor site. This is an important topic in radiobiology; further details can be found in the textbooks by Joiner and van der Kogel (2009) and Hall and Giaccia (2012). Hyperfractionation refers to the use of a high number of

low-dose fractions. The reverse, using a low number of high-dose fractions, is called hypofractionation. These are not precise definitions; what is considered high and low depends on amongst others the treatment site.

The linear-quadratic Poisson cell survival model, or simply LQ model, is probably the most well-known biological model (for a review, see McMahon (2019)). It provides a simple relationship between dose, fractionation and cell survival. According to the LQ model, if a voxel is homogeneously administered dose d uniformly over N fractions (i.e., with dose d/N per fraction) the surviving fraction of cells SF is given by

$$\mathrm{SF} = e^{-d(\alpha+\beta\frac{d}{N})}. \tag{1.2}$$

The α parameter is the 'intrinsic' radiation sensitivity of the tissue and determines the effect of the total dose d, and the β parameter represents the dose fractionation effect. On a lower level, SF can be interpreted as the survival probability of a cell that is administered dose d uniformly over N fractions.

The biologically effective dose (BED) model (Barendsen, 1982; Fowler, 1989, 2010) is derived from the LQ model:

$$\mathrm{BED} = -\log(\mathrm{SF})/\alpha = d + \frac{d^2}{N(\alpha/\beta)}. \tag{1.3}$$

The α/β ratio is perhaps the most well-known dose-response parameter. It captures the fractionation sensitivity of a tissue: a high α/β ratio indicates a low fractionation sensitivity and vice versa. If this parameter is known, the BED model can be used to compare the biological effect of different fractionation schemes. The BED model (1.3) can be generalized to allow for a non-uniform dose per fraction. Finding the optimal fractionation scheme is known as fractionation optimization.

In each treatment fraction, a scaled version of the dose distribution is administered. Scaling the dose distribution influences the absolute dose delivered to each voxel, but the relative dose remains unchanged. For each voxel we can define a *dose sparing factor*: the dose of this voxel as a fraction of the mean target dose. In Figure 1.5, the target volume receives a uniform dose of 45 Gy over the entire treatment course. The indicated OAR voxel receives 18 Gy and thus has a dose sparing factor of 0.4. Consequently, if in a single treatment fraction a mean target dose of 3 Gy is administered, the OAR voxel receives 1.2 Gy. Thus, with a fixed dose distribution, the sole decision in treatment fraction t is d_t, the mean tumor dose in that fraction. The corresponding dose to any voxel i with dose sparing factor s_i is $s_i d_t$. Altogether, with a fixed dose distribution, fractionation optimization problems can be described using a low number of decision variables.

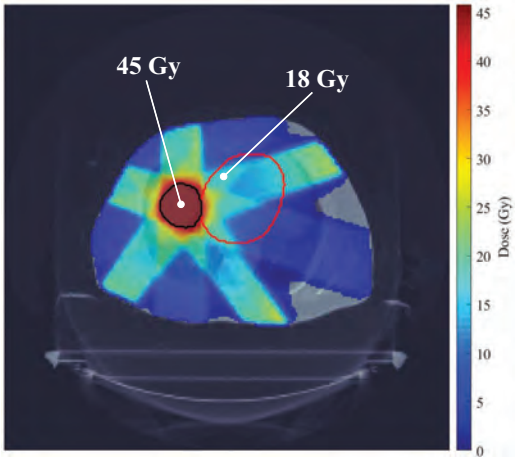

Figure 1.5: Slice of a 3D dose distribution (illustration). Target is contoured in black, OAR is contoured in red. The target volume has a mean dose of 45 Gy. The indicated OAR voxel with dose 18 Gy has a dose sparing factor of 0.4.

There is a large body of research that optimizes the number of treatment fractions for different model formulations (Mizuta et al., 2012; Unkelbach et al., 2013a; Bortfeld et al., 2015; Saberian et al., 2015). These all separate the temporal component (i.e., fractionation optimization) from the spatial component (i.e., the FMO problem), and benefit from the dimensionality reduction. Another line of research, spatiotemporal optimization, aims to solve both problems simultaneously (Unkelbach et al., 2013b; Unkelbach and Papp, 2015; Saberian et al., 2017; Gaddy, 2019).

Due to the fractionation of treatment plans, it is possible to use different treatment modalities in different treatment fractions. Treatment modalities have different physical (dosimetric) and biological advantages and disadvantages. It is thus possible that the best balance is found by combining treatment modalities. In Chapter 6 the fractionation optimization problem for combined proton-photon treatments is studied. Although proton therapy has physical advantages (Section 1.1.1), these do not always directly translate to clinical advantages over photon therapy. The price tag of proton therapy remains high, so there is value in using the available proton therapy slots as efficiently as possible.

Next to combining different radiation therapy modalities, there are also modeling studies that analyze the influence of fractionation for treatment combining radiation therapy with chemotherapy (Salari et al., 2015; Badri et al., 2018) and immunotherapy (Serre et al., 2016; Sung et al., 2020).

1.2.2 Biological response models

Despite what expressions such as 'target dose' suggest, the ultimate goal of radiation therapy is not to deliver dose to the patient. This is only a surrogate for the true goal: eradicating the tumor, with as little negative side effects as possible. Biological response models (or dose-response models) aim to quantify to what extent these goals have been achieved, by providing a relationship between delivered dose and (expected) biological effect on cells or tissue. The LQ model and the BED model are two examples of biological response models.

It is desirable to compress the biological effect of a heterogeneous spatial dose distribution delivered to a certain volume into a single number. The (generalized) equivalent uniform dose (gEUD) is the dose that, if delivered homogeneously to the volume, leads to approximately the same biological effect as the heterogeneous dose distribution. For a heterogeneous dose $\boldsymbol{d} \in \mathbb{R}^m$ delivered to m equal-sized voxels it is defined by Mohan et al. (1992) and Niemierko (1999) as

$$\mathrm{gEUD}(\boldsymbol{d}) = \Big(\frac{1}{m}\sum_{i=1}^{m} d_i^a\Big)^{\frac{1}{a}}, \tag{1.4}$$

where a is a parameter characterizing the volume effect. For parallel organs a is close to one, and for serial organs a goes to infinity. Note that, except for the factor $1/m$, the gEUD is the ℓ_a-norm.

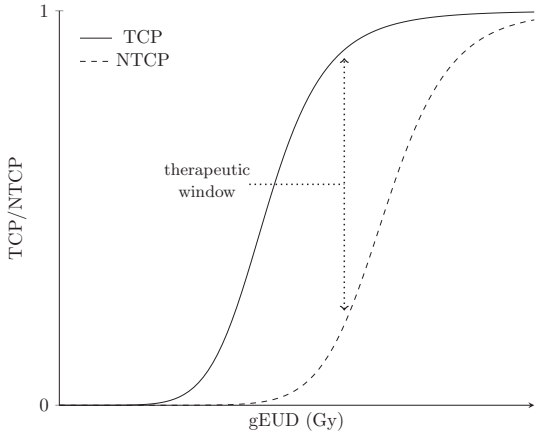

Figure 1.6: Illustration of sigmoidal TCP and NTCP functions. The gap between TCP and NTCP is referred to as the therapeutic window.

The ultimate biological response of interest is whether or not the tumor has been eradicated or controlled, and the associated normal tissue complications. The extent to which these goals are (expected to be) achieved is often quantified as the tumor control probability (TCP) and normal tissue complication probability (NTCP). One can broadly distinguish mechanistic and phenomenological TCP and NTCP models. Mechanistic models try to capture the true biological processes at play and are based on, e.g., the LQ model. On the other hand, phenomenological models try to fit to available clinical outcome data, and are often based on the gEUD model. TCP and NTCP models (and other biological response models) are functions of both dose and parameters capturing the underlying dose-response of the relevant tissue, such as the previously mentioned α, β and a. Figure 1.6 gives a schematic illustration of a (gEUD-based) TCP and NTCP curve, exhibiting a typical sigmoidal shape. The difference between TCP and NTCP for a treatment plan is referred to as the therapeutic window. Li et al. (2012) report on various considerations related to the use of biological response models in treatment planning. In recent years, there is a growing interest in using machine learning techniques for learning biological response models, we refer to Kang et al. (2015) for a review.

1.2.3 Adaptive biologically-based treatment planning

A major limitation of TCP and NTCP models is that they are typically constructed for a particular patient cohort, and not for an individual patient. Thus, they do not capture the true biological dose-response of an individual patient. Consequently, information about individual patient response collected before, during and after treatment may allow for a better assessment. Moreover, pre- and mid-treatment biological dose-response information can be used to adapt the treatment for the remainder of its course, i.e., to personalize the treatment. Baumann et al. (2016) states that "novel biological concepts for personalized treatment, including biomarker-guided prescription, combined treatment modalities and adaptation of treatment during its course" is one of two major strategies for radiation oncology in the era of precision medicine, the other being technology-driven improvement of treatment conformity.

A biomarker is a measurable indicator of the state of a particular biological process. Mid-treatment biomarkers (or changes from pre- to mid-treatment biomarkers) provide estimates of the patients' early response to the treatment. Functional imaging biomarkers, in particular positron emission tomography (PET), can provide spatial patterns of activity. Various PET tracers are being investigated as potential biomarkers for radioresistance, proliferation and hypoxia (reduced oxygen levels in tissue). Next

to imaging, biomarkers may be based on molecular biology and genetics.

Biomarker information can be used to update biological response models, and subsequently adapt the treatment plan accordingly. Depending on available biomarker information, various treatment plan parameters may be adapted. For an overview of adaptation strategies and associated optimization challenges we refer to Ajdari et al. (2019).

Chapter 2 considers a stylized model where, based on mid-treatment response parameter estimates, the length (i.e., number of treatment fractions) of the remaining treatment course is adapted. In Chapter 3, voxel-wise response parameter estimates are obtained from pre- and mid-treatment functional imaging data. The dose distribution is adapted accordingly, either using uniform dose (de)-escalation or dose redistribution via re-solving the FMO problem.

1.2.4 Conic optimization

Treatment planning with biologically-based criteria, either static or adaptive, may involve solving more difficult FMO problems. A wide variety of solution methods exist for solving FMO problems, both with and without biologically-based objectives and constraints. Section 4.1 provides an overview of commonly used optimization methods, both in literature and in commercial treatment planning systems. Many of these methods rely heavily on the convexity of the underlying optimization problem. The main advantage of convex FMO problems (and a convex optimization problems in general) is that any local optimum is a global optimum. An optimization problem is convex if the objective and all constraint functions are convex (for minimization objectives and upper bound constraints; concave for maximization objectives and lower bound constraints). Many biologically-based criteria are not convex in their natural form, see, e.g., the TCP and NTCP functions in Figure 1.6. However, as shown by Romeijn et al. (2004) and Hoffmann et al. (2008), all common biologically-based criteria can be reformulated to convex functions.

Next to convexity, there is another important characteristic of an objective or constraint function: conic representability. More specifically, is the epigraph set (for minimization objectives and upper bound constraints) or the hypograph set (for maximization objectives and lower bound constraints) of the function conic representable? If the answer is yes for each criteria, the optimization problem can be reformulated to a conic optimization problem. Conic optimization is a subfield of convex optimization. It allows for nonlinearity, thus being more general than linear optimization. Nonlinear functions are not treated in their original functional form, but are formulated by

restricting variables to belong to certain convex 'cones'. Let $\boldsymbol{c} \in \mathbb{R}^n$, $\boldsymbol{A} \in \mathbb{R}^{m \times n}$, $\boldsymbol{b} \in \mathbb{R}^m$. A conic optimization problem in standard form is of the following form:

$$\min_{\boldsymbol{x}} \ \boldsymbol{c}^\top \boldsymbol{x}, \tag{1.5a}$$

$$\text{s.t. } \boldsymbol{A}\boldsymbol{x} = \boldsymbol{b}, \tag{1.5b}$$

$$\boldsymbol{x} \in C, \tag{1.5c}$$

where $C \subseteq \mathbb{R}^n$ is a cone, i.e., a set with particular properties. If for C we choose the nonnegative orthant $\mathbb{R}^n_+$, we retain a linear optimization problem. By allowing for other cones than only the nonnegative orthant, nonlinear convex relationships can be modeled. In contrast, standard convex optimization directly uses the convex objectives and constraints in their functional form and derivative (and possibly Hessian) information is used to solve the problem.

Without restrictions on the types of cones that are allowed, conic optimization is no more restrictive than general convex optimization. In practice, C is often restrict to be (a combination of) the linear, quadratic, exponential and power cone[3]. These cones offer great modeling power, and the resulting conic optimization problems can be solved efficiently, both in theory and in practice, using interior-point methods. In Chapter 4, further details on conic optimization are provided. We apply conic optimization methodology to FMO problems, and provide conic representations of many commonly used treatment plan evaluation criteria, with an emphasis on biological response models. For a general introduction to conic optimization, we refer to Ben-Tal and Nemirovski (2001) and Nemirovski (2007).

1.3 Uncertainty and robust optimization

Thus far, we have presented an idealized version of treatment planning, where all relevant data is of perfect quality. This is not the case in practice; on the contrary, Gotein (2008) states that in radiation oncology "(almost) everything is uncertain". Dealing with uncertainties is a central topic in treatment planning. In this section, we discuss various sources of uncertainty, and introduce (adjustable) robust optimization as a methodology for optimization under uncertainty.

1.3.1 Sources of uncertainty

Many uncertainties are of geometric nature. They include, but are not limited to, imperfect imaging, delineation errors, patient positioning errors, uncertainty due to

[3]The semidefinite matrix cone is a fifth often-used cone, but it is not considered in this thesis.

breathing motion and inter-fractional anatomical changes. The traditional approach to ensure proper CTV coverage in the face of these uncertainties is to add a safety margin to the CTV, to obtain the planning target volume (PTV). By treating the PTV with a sufficiently high dose, it is ensured that the CTV is treated adequately. There is a large body of research on defining appropriate margin recipes (Van Herk, 2004). Similar safety margins may also be added to OARs. As an alternative to the PTV approach, robust and stochastic optimization methods have been proposed, see Section 1.3.2 for further details. Next to the aforementioned geometric uncertainties, these methods can also handle uncertainties in the delivered dose distribution. The latter may occur due to dose calculation uncertainty, and, in proton therapy, range uncertainty. Range uncertainty in proton therapy leads to uncertainty in the precise location of the Bragg peak (see Figure 1.3 in Section 1.1.1), which may diminish part of the theoretical benefits of proton therapy over photon therapy.

Next to designing a baseline treatment plan that ensures robustness against all uncertainties, adaptive treatment planning can be used to mitigate some of these uncertainties (Yan et al., 1997). For example, mid-treatment CT scans can be used to detect inter-fractional anatomical changes, and the treatment plan can be adapted accordingly. Mitigating and accounting for geometric and dosimetric uncertainties is beyond the scope of this thesis.

The use of biological response models gives rise to another set of uncertainties. First and foremost, biological response models are always approximations, and never describe the complex radiobiological processes perfectly. Under an assumed biological response model, the model parameters that give the best fit for an individual patient are typically unknown prior to treatment. Mid-treatment biomarker information can be used to update the biological response model (see Section 1.2.3), i.e., obtain more accurate parameter estimates. Nevertheless, uncertainty in model parameters persists, due to uncertainty in biomarker data and/or translation from biomarker data to model parameters. The adaptive treatment planning approaches in Chapters 2 and 3 account for the inexactness of parameter estimates obtained mid-treatment. Chapter 2 also discusses the fact that biomarker information quality may vary over time, and addresses the question of 'when to adapt?'.

1.3.2 Robust optimization

Robust optimization (RO) is a methodology for modeling decision-making problems under uncertainty. It gained attention in the 1990s due to the work of Ben-Tal and Nemirovski (1998, 1999) and El Ghaoui and Lebret (1997). RO was developed as a

practical alternative to stochastic programming (SP, see, e.g., the textbook by Shapiro et al. (2014)). SP assumes to have full information on the probability distribution of the uncertain parameters, and optimizes expressions involving expectations or probabilities. In contrast, RO solely assumes that a so-called uncertainty set can be described, and its solutions ensure feasibility for any realization in this uncertainty set. In many applications, full probability distribution information is not available, and deriving an uncertainty set is more manageable. Moreover, the uncertainty set approach of RO often leads to computationally tractable models, whereas SP models are generally hard to solve[4].

Let $\boldsymbol{x} \in \mathbb{R}^n$ be the decision variable, and let $\boldsymbol{z} \in \mathbb{R}^L$ denote the uncertain parameter. Let $U \subseteq \mathbb{R}^L$ denote the uncertainty set, i.e., the set of realizations of $\boldsymbol{z}$ that we want to be protected against. Then a generic robust optimization problem reads

$$\min_{\boldsymbol{x}} \max_{\boldsymbol{z} \in U} f(\boldsymbol{x}, \boldsymbol{z}), \tag{1.6a}$$

$$\text{s.t. } g_j(\boldsymbol{x}, \boldsymbol{z}) \leq 0, \quad \forall \boldsymbol{z} \in U, \ \forall j = 1, \ldots, m. \tag{1.6b}$$

In the context of (biologically-based) RT, the objective and constraints can be treatment plan evaluation criteria that depend on uncertain parameters $\boldsymbol{z}$. Any solution $\boldsymbol{x}^*$ to (1.6) is feasible for any realization $\boldsymbol{z}$ in uncertainty set U, and is optimal for the worst-case realization of $\boldsymbol{z}$ in U. Problem (1.6) is sometimes also referred to as a minimax optimization problem, as opposed to expectation optimization.

The computational tractability of (1.6) depends on the form of the objective and constraint functions. In the easiest forms, these are linear or convex in $\boldsymbol{x}$ and linear or concave in $\boldsymbol{z}$. The tractability depends additionally on the uncertainty set U. Ben-Tal and Nemirovski (1999) assume an ellipsoidal uncertainty set (for a linear RO problem). Bertsimas and Sim (2004) note that for linear RO problems, the linearity is preserved if the uncertainty set is assumed to be polyhedral (specifically, they introduce the budget uncertainty set). Additionally, they introduce the *price of robustness*, the trade-off between probability of constraint violation and the objective value of the nominal problem.

Solution approaches to (1.6) also highly depend on the functional form of objectives and constraints and the choice of uncertainty set. If U is a finite set, the scenarios for $\boldsymbol{z}$ can be enumerated and (1.6b) is tractable (if g_j is convex for all j). In RT, this approach is often taken when accounting for positioning errors (i.e., six possible shift

[4]Inbetween SP and RO is distributionally robust optimization (DRO, see, e.g., Wiesemann et al. (2014)). DRO is a methodology that attempts to use any available partial distributional information, such as the support, mean and dispersion information of the true probability distribution.

directions). If U is not a finite set, (1.6b) is a semi-infinite constraint, and a standard approach is to reformulate (1.6b) to a so-called tractable robust counterpart (Ben-Tal et al., 2015). We refer to Bertsimas et al. (2011), Gabrel et al. (2014) and Gorissen et al. (2015) for reviews of RO theory and applications. For an overview of RO (and SP) approaches in RT treatment planning, we refer to Unkelbach et al. (2018a).

In the standard paradigm, RO focuses solely on the performance in the worst-case scenario of the uncertain parameters in (1.6). For linear problems it is often the case in practice that multiple worst-case optimal solutions exist. Iancu and Trichakis (2014) note that the standard RO paradigm does not properly discriminate between these, and may select solutions that are suboptimal for non-worst case scenarios. They introduce the concept of Pareto Robustly Optimal (PRO) solutions for robust linear optimization: worst-case optimal solutions whose performance cannot be improved in one scenario, without leading to a deterioration in other scenarios. This concept closely resembles that of Pareto optimal solutions in MCO (see Section 1.1.2). Essentially, the performance in every uncertainty scenario is considered as a separate objective, and a PRO solution is a (worst-case optimal) solution that lies on the resulting (infinite dimensional) Pareto surface.

1.3.3 Adjustable robust optimization

A solution to an RO problem is feasible for *any* realization of the uncertain parameters in the uncertainty set, and this restriction is sometimes considered overly conservative, i.e., the price of robustness can be high. Part of this conservativeness can sometimes be alleviated by adaptation. In many decision-making settings, not all decisions need to be made upfront. Decisions whose implementation is only required at a later moment in time can be postponed. In particular, some decisions can be made once the values of (a part of) the uncertain parameters have been observed or measured, and it is possible to make a more informed decision.

One way to account for this temporal ordering of decision moments and flow of information is to use a folding horizon (FH, also known as a receding horizon) approach. In an FH approach, robust model (1.6) is solved for all decision variables simultaneously. However, the only decisions that are implemented are those whose implementation is required before new information (concerning uncertain parameters) is revealed. Values assigned to other decision variables (those corresponding to decisions at later moments in time) are discarded. Once (part of) the uncertainty is revealed, the model is updated and re-solved for the remaining decision horizon. The benefit of an FH approach is that the multi-stage model has the same complexity as

the static model. Section 2.1 discusses several FH approaches in adaptive RT, for both geometric and biologically-based uncertainties.

In any stage of an FH approach, the decisions are optimized as if they have to be implemented for the entire remaining decision horizon. That is, adaptability is not taken into account. Adjustable robust optimization (ARO)[5] was introduced by Ben-Tal et al. (2004) as an extension of RO to multi-stage decision-making problems under uncertainty. In a two-stage setting, it distinguishes between *here-and-now* (stage 1) decision variables and *wait-and-see* (stage 2) decision variables. In an ARO problem it is a priori taken into account that the stage-2 decision variables can depend on the uncertain parameters. Thus, they are functions of the uncertain parameters.

Similar to Section 1.3.2, let $\boldsymbol{z} \in \mathbb{R}^L$ denote the uncertain parameter and $U \subseteq \mathbb{R}^L$ the uncertainty set. Let $\boldsymbol{x} \in \mathbb{R}^{n_x}$ denote the stage-1 decision variables, and let $\boldsymbol{y} \in \mathcal{R}^{L,n_y}$ denote the stage-2 decision variables, where $\mathcal{R}^{L,n_y}$ denotes the space of all measurable functions from $\mathbb{R}^L$ to $\mathbb{R}^{n_y}$ that are bounded on compact sets. A generic two-stage adjustable robust optimization model reads

$$\min_{\boldsymbol{x},\boldsymbol{y}(\cdot)} \max_{\boldsymbol{z}\in U} f(\boldsymbol{x},\boldsymbol{y}(\boldsymbol{z}),\boldsymbol{z}), \tag{1.7a}$$

$$\text{s.t. } g_j(\boldsymbol{x},\boldsymbol{y}(\boldsymbol{z}),\boldsymbol{z}) \leq 0, \quad \forall \boldsymbol{z} \in U, \ \forall j = 1,\ldots,m. \tag{1.7b}$$

Problem (1.7) requires optimizing over functions $\boldsymbol{y}$. For that reason, ARO problems are in general NP-hard (Guslitser, 2002). A practical heuristic approach, introduced by Ben-Tal et al. (2004) is to restrict to adjustable variables $\boldsymbol{y}$ that depend affinely on the uncertain parameters; commonly referred to as linear decision rules (LDRs). Cutting plane methods are another popular solution approach, see (Zeng and Zhao, 2013). For a review of ARO we refer to Yanıkoğlu et al. (2019).

The standard ARO paradigm assumes that information obtained after the first stage yields the 'true' parameter values. In many applications, including biologically-based based radiation therapy, this assumption is not satisfied. As indicated in Section 1.3.1, biomarker information will never fully eliminate uncertainty. De Ruiter et al. (2016) provide an extension of ARO that accounts for inexact data. This methodology is used in Chapter 2.

Similar to (static) RO, ARO problems may allow for multiple worst-case optimal solutions, and the standard ARO methodology does not consider their performance in non-worst-case scenarios. In Chapters 2 and 5, the PRO concept of Iancu and Trichakis (2014) for static RO is extended to Pareto Adjustable Robust Optimality (PARO) for

[5] In recent work, the methodology is sometimes called 'adaptive robust optimization'. To distinguish from other adaptation approaches in RT treatment planning, we use 'adjustable robust optimization'.

two-stage ARO problems. Chapter 2 introduces the concept for a particular model in an RT context. Chapter 5 discusses the concept more generally, for ARO problems that are linear in both decision variables and uncertain parameters.

1.4 Contributions and outline

The remainder of this thesis consists of five self-contained chapters. The research that this thesis is based on started out with a focus on fractionation optimization problems. From there, the scope shifted to other aspects of biologically-based treatment plan optimization, particularly uncertainty and adaptive treatment planning. This led to research in both adjustable robust optimization and conic optimization. Figure 1.7 gives a high-level schematic overview of the topics covered in each chapter and their connections. Below we summarize the contributions per chapter.

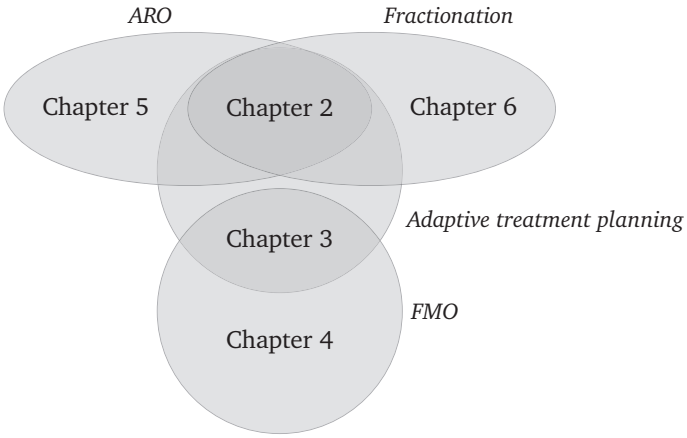

Figure 1.7: Overview of thesis chapters.

In Chapter 2, we present a two-stage ARO model for adaptive treatment-length optimization in RT based on inexact mid-treatment biomarker information. We derive optimal decision rules for the stage-2 decisions. Moreover, we note the existence of multiple worst-case optimal solutions, and introduce the PARO concept to choose among these. In numerical experiments using lung cancer data, the ARO method is benchmarked to several other static and adaptive methods, for both exact and inexact biomarker information. In the latter case, accounting for adaptability and inexactness of biomarker information is particularly beneficial when robustness (with respect to

OAR constraint violations) is of high importance. If minor OAR violations are allowed, a nominal FH approach is a good performing alternative.

Whereas Chapter 2 considers a stylized model, Chapter 3 takes a more practical approach to adaptive biologically-based treatment planning. We consider treatment plan adaptation for a data set of canine head-and-neck patients, with pre- and mid-treatment functional imaging data. Voxel-wise response parameters are estimated from imaging data, and a TCP-NTCP based model is re-optimized. Uncertainty in response parameters is accounted for, and two adaptation strategies are investigated: uniform dose (de)-escalation and continuous dose adaptation (i.e., dose painting). We find that, despite uncertainties, improvements in TCP and/or NTCP can be expected for a substantial number of patients. The chapter outlines the required components for a biologically-based treatment plan adaptation strategy, and helps to emphasize the importance of accounting for uncertainties both in the optimization process itself and in reporting results.

In Chapter 4, we take a conic optimization approach to FMO. Biologically-based approaches to RT planning, such as that of Chapter 3, can lead to challenging FMO problems with biologically-based treatment plan evaluation criteria. In this chapter, we show that for many commonly used treatment plan evaluation criteria the FMO problem can be reformulated to a conic optimization problem, using recent advances in exponential and power cone optimization. This gives theoretical efficiency and optimality guarantees, and good performance in practice. The latter is demonstrated on an open-source data set of challenging clinically-based FMO problems.

In Chapter 5, we present a theoretical investigation of the PARO concept of Chapter 2. We show that direct application of the PRO concept to ARO problems can lead to suboptimal performance in practice, and formalize PARO for two-stage linear ARO problems. We prove existence of PARO solutions, derive properties and present approaches to finding and approximating PARO solutions. Moreover, we present numerical results that demonstrate the practical value of PARO solutions. Our analysis relies on the use of Fourier-Motzkin elimination (FME) as proof technique. We also show how FME can be useful in the analysis of the (worst-case) optimality of decision rules in ARO.

In Chapter 6 we consider fractionation optimization problems, similar to Chapter 2. In particular, we investigate the potential of combined proton-photon therapy in fractionated RT. We discuss several stylized models and find conditions under which combined modality treatments can outperform single modality photon or proton treatments. Subsequently, we present a combined modality optimal fractionation model with multiple normal tissues, and test this on real patient data ($n = 17$). Results indi-

cate that for five patients combined modality treatments can outperform single modality proton treatments in terms of BED. For three other patients, combined modality treatments can yield comparable treatment quality (in terms of BED), whilst using fewer (expensive) proton fractions.

1.5 Disclosure

This thesis is based on the following five research papers:

Chapter 2 S.C.M. ten Eikelder, A. Ajdari, T. Bortfeld, D. den Hertog. Adjustable robust treatment-length optimization in radiation therapy. 2021. *Submitted to Optimization and Engineering*.

Chapter 3 S.C.M. ten Eikelder, P. Ferjančič, A. Ajdari, T. Bortfeld, D. den Hertog, and R. Jeraj. Optimal treatment plan adaptation using mid-treatment imaging biomarkers. *Physics in Medicine & Biology*. 65:245011, 2020.

Chapter 4 S.C.M. ten Eikelder, A. Ajdari, T. Bortfeld, D. den Hertog. Conic formulation of fluence map optimization problems. 2021. *Submitted to Physics in Medicine & Biology*.

Chapter 5 D. Bertsimas, S.C.M. ten Eikelder, D. den Hertog and N. Trichakis. Pareto adaptive robust optimality via a Fourier-Motzkin elimination lens. 2021. *Submitted to Mathematical Programming*.

Chapter 6 S.C.M. ten Eikelder, D. den Hertog, T. Bortfeld and Z. Perkó. Optimal combined proton-photon therapy schemes based on the standard BED model. *Physics in Medicine & Biology*. 64:065011, 2019.

The chapters cover distinct problems, and the notation may differ per chapter. Each chapter contains ideas and contributions from all its respective authors. Chapter 2 is written by me. Chapter 3 is written by me, except the introduction, parts of Section 3.2.1 and parts of the discussion (Section 3.4.2). Chapter 4 is written by me. Chapter 5 is written by me, except parts of the introduction. Chapter 6 is written by me, except parts of Sections 6.2.1, 6.4.4 and 6.4.5. All numerical experiments in all chapters are done by me. All chapters closely match their respective research papers. Figure 1.5 and its accompanying text in Chapter 1 are taken from the research paper corresponding to Chapter 2.

CHAPTER 2

Adjustable robust treatment-length optimization

2.1 Introduction

In radiation therapy (RT), the goal is to deliver a curative amount of radiation dose to the target volume(s), while keeping the dose to all organs-at-risk (OARs) within tolerable limits. As the radiation beam delivers energy to all tissues that are on its path, the OARs will (often) inevitably receive some dose as well. Treatment planning has a spatial component, where the optimal dose distribution is determined, and a temporal component, where the optimal number of treatment sessions, or fractions, is determined. Whereas the former is predominantly a geometric problem, the latter involves radiobiological effects.

Technological advances in treatment monitoring through imaging and other forms of data acquisition allow for a more accurate assessment of an individual's radiation response (Baumann et al., 2016). Biologically-based adaptive treatments aim to monitor the treatment, acquire mid-treatment biomarker information, and adapt the remainder of the treatment course accordingly. Many approaches to adaptive treatment planning have been studied in the literature. To the best of our knowledge, all existing approaches assume that all information acquired mid-treatment is exact, i.e., gives a perfect representation of the current state of treatment response. Unfortunately, the limited availability and accuracy of required biomarkers pose a primary challenge for adaptive treatments (Baumann et al., 2016). Any information from biomarker data acquired during treatment remains subject to uncertainties, stemming from both measurement errors and the inexactness in the translation of measured data to usable model parameters. Therefore, it is crucial that any adaptive treatment planning approach takes this into account. Ajdari et al. (2019) provide an overview of relevant mathematical (optimization) tools. We present an approach to optimally adapt the treatment length of RT using inexact mid-treatment biomarker information.

Specifically, we take an adjustable robust optimization (ARO, Ben-Tal et al., 2004; Yanıkoğlu et al., 2019) approach that accounts for the inexactness of biomarker information. ARO is an extension of robust optimization (RO) that takes into account the flow of information over time and exploits the fact that some decisions need to be taken only after the data has (partially) revealed itself. By using ARO, we ensure that the treatment plan delivered in the initial treatment stage (prior to obtaining biomarker information) is 'adaptation aware'. That is, it is designed with adaptation in mind, which may yield more flexibility at the time of treatment adaptation. In the standard paradigm, ARO assumes that the revealed information is exact; we employ the ARO methodology developed in De Ruiter et al. (2017) for the case when revealed information is not exact, but provides only an estimate of the true parameters.

Contributions

We consider a stylized two-stage ARO model to optimally adapt the treatment-length based on inexact biomarker information acquired mid-treatment. Although the stylized model makes several simplifying assumptions to aid the analysis, we believe it captures several important characteristics of realistic adaptive treatment planning, and it enables a precise analysis of the influence of uncertainty in biomarker information. Our main contributions are:

- We develop mathematical tools based on ARO that enable us to (i) optimally adapt the dose per fraction and treatment length after acquiring mid-treatment biomarker information, (ii) analyze the influence of biomarker information uncertainty.
- We present explicit optimal decision rules for a difficult (nonconvex, mixed-integer) yet practically relevant ARO problem.
- We show that there are multiple optimal solutions for the worst-case scenario, and that these differ in performance in non-worst-case scenarios. To handle this, we introduce the concept of Pareto Adjustable Robustly Optimal ($\mathcal{PARO}$) solutions, a generalization of Pareto Robustly Optimal ($\mathcal{PRO}$) solutions (Iancu and Trichakis, 2014) to two-stage robust optimization problems. In case the acquired biomarker information is exact, $\mathcal{PARO}$ solutions are obtained.
- We perform a computational study using real lung cancer patient data to determine the optimal timing of acquiring biomarker information in case biomarker quality improves over time. Later biomarker acquisition also limits adaptation possibilities, and the optimal balance depends on the improvement rate.

Literature review

There is a large body of adaptive treatment planning research in RT, the majority of which focuses not on biologically-based uncertainties but on geometric uncertainties and anatomical changes. Chan and Mišić (2013), Mar and Chan (2015), Böck et al. (2017), Böck et al. (2019) and Lim et al. (2020) present adaptive treatment planning approaches that start with delivery of the original treatment plan, often derived using RO methods. At given adaptation moments, the 'state' of the patient (e.g., anatomical changes, tumor shrinkage, breathing motion pattern) is observed, and the treatment is re-optimized for the remainder of the treatment plan. In RO terminology, these approaches are known as folding horizon (FH) methods. They disregard adaptation possibilities initially, and re-optimize the updated model once mid-treatment information is acquired.

Several treatment plan adaptation approaches have been proposed for adapting to biological information, differing in considered biomarker information, adapted treatment plan decisions and used methodology. Ghate (2011) and Kim et al. (2012b) propose a theoretical stochastic control framework to optimally adapt the dose distribution over a fixed number of fractions, based on hypothetically-observed tumor states. Saberian et al. (2016b) concretize this theoretical framework, using simulated hypoxia (insufficient oxygen supply at cellular level) status as biomarker. Long (2015) consider a model with a constraint on the probability of radiation-induced lung toxicity, which depends on an a priori unknown model parameter. The problem is formulated as a two-stage model (before and after parameter observation), and the optimal dose distribution is determined for each stage. They consider a finite scenario set for the parameter, and the lung toxicity constraint either has to hold in expectation or has to hold for all considered scenarios.

Nohadani and Roy (2017) consider a two-stage model to adapt to hypoxia information, where the uncertainty is time-dependent. As the hypoxia information ages the uncertainty grows, until it resets at the observation moment. In each stage the dose distribution is optimized; for the second stage a finite adaptability approach is taken. It is shown that total information degradation is minimized if the observation moment is set mid-treatment. Dabadghao and Roy (2020) consider a similar time-dependent uncertainty set, for adapting to hypoxia information in a multi-stage setting. In each stage the mean tumor dose per fraction is optimized using an FH approach. It is shown that total information degradation is minimized if the observation moments are set equidistant. They introduce a cost of observation (additional dose due to mid-treatment positron emission tomography (PET) scans), and determine the

optimal number of observations. Both papers assume that the hypoxia state varies over time, and is exactly observed at the observation moment(s). In contrast, we assume that uncertain parameters are constant in time, and consider inexact biomarker information. Moreover, they solely adapt the dose, whereas we also adapt the total number of treatment fractions itself.

Adapting the treatment length (i.e., the fractionation schedule) based on observed radiation response has been studied before in the literature. Saka et al. (2014) consider a two-stage model where after a fixed number of treatment fractions hypoxia information is acquired. Based on this information both the remaining number of treatment fractions and the dose distribution are re-optimized, in order to maximize average hypoxia-corrected tumor dose. They focus on maintaining hypoxia-corrected fraction size requirements. A similar approach is taken by Ajdari et al. (2018), where after each treatment fraction the tumor cell density in each voxel is observed, and adaptations are made after each treatment fractions instead of only once. The objective is to minimize the total number of tumor cells remaining (TNTCR) at the end of the treatment course. Both approaches can be considered FH methods. In contrast to our approach, it is assumed that any information acquired mid-treatment is exact.

Iancu et al. (2021) propose a conceptual robust monitoring and stopping model. They consider a system with a state $x(t)$, and after each observation moment the uncertainty in the system state $x(t)$ grows as t increases. At a new observation moment, the uncertainty reduces to zero, i.e., an exact observation is made. They consider multiple observation moments, and the goal is to time these optimally. At each observation moment, the (state-dependent) direct stopping reward is compared to the worst-case continuation reward, and the according action is taken. Their model does not allow for controls that influence state variables, i.e., applying their model to RT optimization problems would not allow to adjust the dose distribution or the mean dose per fraction.

Notation and organization

All variables and constants are 1-dimensional (belong to $\mathbb{R}$ or $\mathbb{N}$) unless indicated otherwise. In functions, a semicolon (;) is used to separate variables and constant arguments from uncertain parameters. Optimal solutions to optimization problems are indicated with an asterisk (*). Properties of optimal solutions to optimization problems have calligraphic font (e.g., $\mathcal{ARO}$) to distinguish them from methods with the same or similar abbreviations.

The remainder of this chapter is organized as follows. Section 2.2 introduces the used biological models, background information on biomarkers and states modeling choices. Section 2.3 introduces the adjustable treatment-length optimization problem

under the assumption of exact biomarker information and solves this using ARO techniques. Section 2.4 generalizes this to inexact biomarker information. Section 2.5 presents and discusses results of numerical experiments on a lung cancer data set. Finally, Section 2.6 concludes the chapter.

2.2 Adaptive fractionation

2.2.1 The fractionation problem

Spatial optimization exploits the fact that, by mounting the beam head on a gantry, the tumor can be targeted from various angles. It aims to find the combination of beam angles and weights that gives the best trade-off between tumor dose conformity and healthy tissue sparing. There is a large body of literature on this topic, see for example Shepard et al. (1999); Ehrgott et al. (2008) for reviews. The result of the spatial optimization problem is a dose distribution that gives the dose to each voxel (3-dimensional subvolume) of the tumor and OARs. We refer to Chapter 1 for details.

Typically, this dose is not delivered in a single treatment session, but spread out over multiple treatment fractions (fx). The underlying idea is that compared to tumor cells, healthy tissues often have better repair capabilities between fractions (Fowler, 1989; Withers, 1985). On the other hand, a treatment spread out over a large number of treatment fractions may not deliver sufficient damage to the target volume, and increases the risk of tumor proliferation. The effect of fractionation differs per healthy tissue type and per tumor site, see, e.g., Hall and Giaccia (2012) for further details. Determining the optimal number of treatment fractions is known as the fractionation problem. Treatments with a higher number of fractions and a lower dose per fraction than the conventional regimen are known as *hyperfractionated* treatments. Treatments with a lower number of fractions and a higher dose per fraction than conventional are known as *hypofractionated* treatments.

In each treatment fraction, a scaled version of the dose distribution is administered. Using dose sparing factors, the dimensionality of the fractionation optimization problem can be greatly reduced, see Section 1.2.1 for details. Typically, the target dose is homogeneous, so for simplicity we assume that each target voxel receives dose d_t (i.e., has dose sparing factor 1). Nevertheless, we emphasize that this modeling approach allows for both heterogeneous dose distributions in target and OAR volumes.

The biologically effective dose (BED) model (Fowler, 1989, 2010) states that the biological effect of an N-fraction dose sequence $\boldsymbol{d} = (d_1, \ldots, d_N)$ (in Gray (Gy)) delivered

to a tumor volume is given by

$$\mathrm{BED}_{\mathrm{T}} = \sum_{t=1}^{N} d_t + \frac{1}{\alpha/\beta} \sum_{t=1}^{N} d_t^2,$$

which is a model governed by a single parameter, the α/β ratio, which signifies the fractionation sensitivity of the tumor tissue. The BED to the OAR can be described by

$$\mathrm{BED}_{\mathrm{OAR}} = \sum_{t=1}^{N} \sigma d_t + \frac{1}{\alpha/\beta} \sum_{t=1}^{N} \sigma^2 d_t^2,$$

where σ is the generalized dose-sparing factor. For the maximum BED in the OAR volume, σ is the maximum of the individual dose sparing factors s_i. In order to describe a mean BED constraint or dose-volume BED constraint other choices for σ can be used (Saberian et al., 2016a; Perkó et al., 2018).

For notational convenience, let τ (for tumor) and ρ (for risk) denote the inverse α/β ratio of the tumor and OAR volume, respectively. Mizuta et al. (2012) consider the problem of minimizing OAR BED subject to a lower bound $\mathrm{BED}_{\mathrm{T}}^{\mathrm{pres}}$ on tumor BED. The number of fractions N is restricted to be at most $N^{\max}$. The problem reads

$$\min_{d,N} \ \sigma \sum_{t=1}^{N} d_t + \rho\sigma^2 \sum_{t=1}^{N} d_t^2, \tag{2.1a}$$

$$\text{s.t.} \ \sum_{t=1}^{N} d_t + \tau \sum_{t=1}^{N} d_t^2 \geq \mathrm{BED}_{\mathrm{T}}^{\mathrm{pres}}, \tag{2.1b}$$

$$d_1, \ldots, d_N \geq 0, N \in \{1, \ldots, N^{\max}\}. \tag{2.1c}$$

Let (d^*, N^*) denote the optimal solution to (2.1). A simple analysis in Mizuta et al. (2012) reveals the following important result:

$$N^* = \begin{cases} 1 & \text{if } \tau \geq \sigma\rho \\ N^{\max} \text{ and } d_1^* = \ldots = d_{N^{\max}}^* & \text{otherwise.} \end{cases} \tag{2.2}$$

In both cases the optimal dose d^* is such that (2.1b) is active. The same result holds if we maximize tumor BED subject to an upper bound on OAR BED (Bortfeld et al., 2015), and a similar result has been derived for the case with multiple OARs (Saberian et al., 2016a). There is a large body of research that optimizes the number of treatment fractions for different model formulations (see Saberian et al. (2017) and references therein).

In the current chapter, we restrict to one dose-limiting OAR. For many tumor sites, there is a single OAR that restricts the doses that can be delivered, and other OARs are much less restrictive. For example, for lung cancer the mean lung dose is an important indicator of toxicity. On the other hand, for head and neck cancer many OARs must be accounted for. We emphasize that other OARs are not completely disregarded. They are taken into account implicitly, because the original dose distribution was planned with all relevant OARs taken into consideration. Moreover, by restricting the minimum and maximum (mean target) dose per fraction, extreme deviations from the standard fractionation schedule are avoided, which is also designed whilst taking multiple OARs into account.

2.2.2 Adaptive fractionation using biomarkers

Most fractionation optimization methods assume the tumor and OAR fractionation sensitivity parameters τ and ρ are known exactly. There is much research on the α/β ratios for different tumor sites (Van Leeuwen et al., 2018) and OAR sites (Kehwar, 2005), but they remain subject to considerable uncertainties. We assume box uncertainty of the form:

$$Z := \big\{(\rho, \tau) : \rho_L \leq \rho \leq \rho_U, \tau_L \leq \tau \leq \tau_U\big\}, \tag{2.3}$$

with $0 < \rho_L < \rho_U$ and $0 < \tau_L < \tau_U$. It is assumed that there is a nominal scenario, e.g., parameter values $\bar{\tau}$ and $\bar{\rho}$ derived from literature. There are two reasons for assuming a box uncertainty set. First, to the best of our knowledge there is little evidence for any correlation between the α/β ratios of target volumes and normal tissues. Second, box uncertainty leads to simpler models, which allow for a more detailed analysis of optimal fractionation decisions.

Ajdari and Ghate (2016) also consider a box uncertainty set, and determine a *robustly optimal* fractionation scheme, i.e., one that is that is feasible for all possible realizations and that is optimal for the worst-case realization. If biomarker information acquired during treatment provides more accurate information on fractionation sensitivity than what was available at the start of the treatment, such a static RO approach may be overly conservative.

Somaiah et al. (2015) give an overview of various mechanisms for determining fractionation sensitivity. Using blood samples, one can quantify the involvement of non-homologous end-joining and homologous recombination in cells. For details on how to measure these, we refer to Bindra et al. (2013) and Barker and Powell (2010), respectively. Change in the expression of epidermal growth factor receptor genes can also give some hints regarding the fractionation sensitivity (Somaiah et al., 2015),

which can also be measured mid-treatment. Lastly, Somaiah et al. (2015) mention that there is a close link between proliferation index and hypoxia, both of which can be measured during RT using different PET tracers. We note that there is evidence that some of these mechanisms could be subject to change during RT, depending on, amongst others, the delivered dose, hypoxia, and immune system interaction. However, as a first study to adapting to inexact biomarker information, we make the assumption that fractionation sensitivity is static throughout treatment, i.e., there is a static 'true' (ρ, τ). In Section 2.3 we assume to observe (measure) the true (ρ, τ) exactly, and in Section 2.4 we assume to observe only an estimation/approximation $(\hat{\rho}, \hat{\tau})$.

The quality of the observed parameter estimates depends amongst others on the suitability of the biomarker itself, the measurement accuracy and when the biomarker measurement is taken during the treatment course. The relationship between the data quality and the moment of biomarker observation is complex, and it is impossible to exactly quantify this. For some biomarkers the data quality may greatly improve in the first few fractions, with a diminishing improvement in later fractions[1]. For others (e.g., functional imaging such as PET and magnetic resonance imaging (MRI)), the data quality is poor at the first couple of fractions and only increases substantially in later fractions[2]. In practice, some biomarkers, e.g., radiographic information, may also exhibit a decreasing data quality for very late observation moments (due to, for instance, interference from acute inflammation in the lung). Such behavior is rare, and as such not considered here. We impose a minimum dose per fraction, and make the assumption that biomarker data quality increases in the number of treatment fractions. In this way, the change in biomarker quality is influenced by both the dose delivered and the time passed. We will investigate several functional forms for this relationship in the numerical experiments.

2.2.3 Modeling choices

In order to establish a meaningful model for the adjustable robust optimization approach, we restrict the dose sequence $d = (d_1, \ldots, d_{N^{\max}})$ in several ways. In addition to a maximum number of fractions, we also set a minimum $N^{\min}$. Furthermore, we

[1]This is especially true in the case of certain blood biomarkers of innate immune status (such as interleukin-6 or tumor necrosis factor-α) which are also the markers of inflammation. In these biomarkers, as the biomarker acquisition is shifted towards later in the RT course, the information regarding the immune status gets mixed with the RT-induced inflammation and loses its specificity to immune system condition.

[2]This is because the effect of RT on tissue is cumulative and is morphologically manifested only after a certain amount of dose (which depends on the underlying tissue threshold) is delivered.

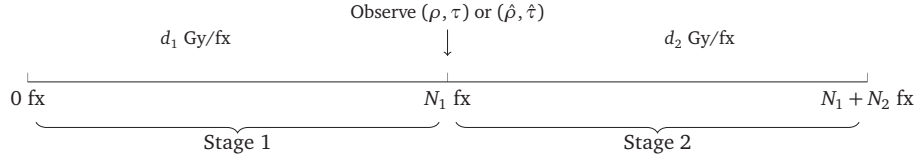

Figure 2.1: Schematic overview of the considered model. There are 3 variables: d_1, d_2 and N_2. First, we deliver N_1 fractions of dose d_1 per fraction. After this, we observe (ρ, τ) or $(\hat{\rho}, \hat{\tau})$. Subsequently, we deliver N_2 fractions of dose d_2 per fraction.

assume there is a single moment N_1 where we can adapt the treatment. Under the assumption that the uncertain parameters remain constant over time, more than one observation moment is not useful if the parameter is observed exactly. With inexact observations, there can be value in multiple observations, but given the patient burden (logistically and the delivery of additional dose) and financial cost (of for example PET scans) this is not considered here.

The dose per fraction in the first N_1 fractions is assumed to be the same, denote this by d_1. Variable N_2 denotes the number of fractions after adaptation; also these fractions have equal dose, denoted by d_2. In current clinical practice, uniform fractionated treatments are the standard. By restricting to only two different dose levels, extreme deviations from standard protocols are prevented. The above implies

$$N_2 \in \left\{N_2^{\min}, \ldots, N_2^{\max}\right\},$$

with $N_2^{\min} = \max\{1, N^{\min} - N_1\}$ and $N_2^{\max} = N^{\max} - N_1$. We additionally set the constraint that $d_1, d_2 \geq d^{\min}$, for some predetermined value $d^{\min}$. Aside of preventing an unrealistically low dose per fraction, the minimum dose serves a modeling purpose for stage 1. As noted in Section 2.2.2, the biomarker quality can depend on both dose and time. The current model implicitly makes the assumption that an early response can only be observed via biomarkers once N_1 fractions of dose at least $d_{\min}$ have been delivered. Thus, in our models, this can be interpreted as a threshold. In the numerical experiments we investigate several temporal relationships between N_1 and biomarker quality. Lastly, we set a maximum dose per fraction $d_1^{\max}$ in stage 1, to avoid delivering dose levels in stage 1 that severely restrict adaptation possibilities in stage 2. We will later impose some restrictions on the allowed combinations of $d^{\min}$, $d_1^{\max}$ and $N_2^{\max}$.

Figure 2.1 provides a schematic overview of the situation. We wish to maximize the tumor BED, subject to the constraint that the BED to the OAR is below the generalized tolerance level BED_{tol}, given by

$$\text{BED}_{\text{tol}}(\rho) = \varphi D\Big(1 + \frac{\varphi D}{T}\rho\Big),$$

i.e., the OAR is known to tolerate a total dose of D Gy if delivered in T fractions under dose shape factor φ. The dose shape factor is a parameter characterizing the spatial heterogeneity of a dose distribution, for more details see Saberian et al. (2016a) and Perkó et al. (2018). Note that $\mathrm{BED}_{\mathrm{tol}}(\rho)$ is a function of uncertain parameter ρ, the inverse α/β ratio of the OAR.

We emphasize that the model resulting from our modeling choices and assumptions does not directly represent a realistic decision-making problem in radiation therapy treatment planning. Nevertheless, it captures several important aspects of fractionation optimization. Moreover, using ARO on this stylized model, we gain insight into optimal decision rules and the role of uncertainty in adaptive fractionation optimization.

2.3 ARO: Biomarkers provide exact information

We present an adjustable robust optimization approach that optimally adjusts the remainder of the treatment once biomarker information has provided the true value of parameters τ and ρ. This serves as a stepping stone to the inexact data model.

2.3.1 Problem formulation

The Exact Data Problem (EDP) reads:

$$\max_{d_1, d_2(\rho,\tau), N_2(\rho,\tau)} \quad \min_{(\rho,\tau)\in Z} N_1 d_1 + N_2(\rho,\tau) d_2(\rho,\tau) + \tau(N_1 d_1^2 + N_2(\rho,\tau) d_2(\rho,\tau)^2), \tag{2.4a}$$

$$\text{s.t.} \quad \sigma(N_1 d_1 + N_2(\rho,\tau) d_2(\rho,\tau)) + \rho\sigma^2(N_1 d_1^2 + N_2(\rho,\tau) d_2(\rho,\tau)^2) \leq \mathrm{BED}_{\mathrm{tol}}(\rho), \quad \forall(\rho,\tau)\in Z, \tag{2.4b}$$

$$N_2(\rho,\tau) \in \{N_2^{\min}, \ldots, N_2^{\max}\}, \quad \forall(\rho,\tau)\in Z, \tag{2.4c}$$

$$d_2(\rho,\tau) \geq d^{\min}, \quad \forall(\rho,\tau)\in Z, \tag{2.4d}$$

$$d^{\min} \leq d_1 \leq d_1^{\max}. \tag{2.4e}$$

The value for the stage-1 dose d_1 has to be decided before the value of (ρ,τ) is revealed; in ARO this is also commonly referred to as a *here-and-now* variable or decision. The values for the stage-2 dose d_2 and stage-2 number of fractions N_2 need to be decided only after (ρ,τ) is revealed as they may depend on the values of these parameters. Hence, they are written as functions $d_2(\rho,\tau)$ and $N_2(\rho,\tau)$ of the uncertain parameters (ρ,τ). In ARO such variables are also commonly referred to as *wait-and-see* variables or decisions. In this chapter, we will adhere to the terms *stage 1* and *stage 2*, however.

Before we solve (2.4), we need some definitions and assumptions. The remaining BED tolerance level of the OAR, if N' fractions with dose d' have been administered, is given by

$$B(d',N';\rho) = \mathrm{BED}_{\mathrm{tol}}(\rho) - \sigma d' N' - \rho\sigma^2 (d')^2 N'. \tag{2.5}$$

Subsequently, define the function

$$g(d',N',N'';\rho) := \frac{-1+\sqrt{1+\frac{4\rho}{N''}B(d',N';\rho)}}{2\sigma\rho}. \tag{2.6}$$

The value of g can be interpreted as the maximum dose that can be delivered in N'' fractions if already N' fractions of dose d' are (scheduled to be) delivered. It is obtained by solving the equality version of (2.4b) for d_1 or d_2. Functions of this form will be used frequently throughout the remainder of this chapter.

The following assumption on the relation between $d^{\min}$, $d_1^{\max}$ and the bounds on N_2 makes sure that for a given optimal number of fractions, it is feasible to deliver that number of fractions with minimum dose.

Assumption 2.1. *It holds that*

$$d^{min} \le d_1^{max} \le \min\Big\{ g(d^{min}, N_2^{min}, N_1; \rho_L), g(d^{min}, N_2^{max}, N_1; \frac{\tau_L}{\sigma}), g(d^{min}, N_2^{max}, N_1; \rho_U) \Big\}.$$

The particular form of the upper bound on $d_1^{\max}$ will become clear later. Numerical experiments indicate that results are not very sensitive to the choices of $d^{\min}$ and $d_1^{\max}$.

We continue by formally defining several properties of solutions. Let $X(\rho,\tau)$ denote the feasible region defined by constraints (2.4b)-(2.4e) for fixed (ρ,τ).

Definition 2.2 (Adjustable robustly feasible)**.** A tuple $(d_1, d_2(\cdot), N_2(\cdot))$ is *adjustable robustly feasible* ($\mathcal{ARF}$) to (2.4) if $(d_1, d_2(\rho,\tau), N_2(\rho,\tau)) \in X(\rho,\tau)$ for all $(\rho,\tau) \in Z$. ■

Definition 2.3 (Adjustable robustly optimal)**.** A tuple $(d_1, d_2(\cdot), N_2(\cdot))$ is *adjustable robustly optimal* ($\mathcal{ARO}$) to (2.4) if it is $\mathcal{ARF}$ and there does not exist an $\mathcal{ARF}$ tuple $(\bar{d}_1, \bar{d}_2(\cdot), \bar{N}_2)$ such that

$$\begin{aligned} &\min_{(\rho,\tau)\in Z} N_1 d_1 + N_2(\rho,\tau) d_2(\rho,\tau) + \tau(N_1 d_1^2 + N_2(\rho,\tau) d_2(\rho,\tau)^2) \\ &< \min_{(\rho,\tau)\in Z} N_1 \bar{d}_1 + \bar{N}_2(\rho,\tau) \bar{d}_2(\rho,\tau) + \tau(N_1 \bar{d}_1{}^2 + \bar{N}_2(\rho,\tau) \bar{d}_2(\rho,\tau)^2). \end{aligned}$$ ■

We also define the $\mathcal{ARO}$ property for the stage-1 decisions d_1 individually.

Definition 2.4 (Adjustable robustly optimal d_1)**.** A stage-1 decision d_1 is $\mathcal{ARO}$ to (2.4) if there exist decision rules $d_2(\cdot)$ and $N_2(\cdot)$ such that $(d_1, d_2(\cdot), N_2(\cdot))$ is $\mathcal{ARO}$ to (2.4).■

Lastly, we define optimality of a decision rule.

Definition 2.5 (Optimal decision rule)**.** For a given d_1, a decision rule pair $(d_2(\cdot), N_2(\cdot))$ is *optimal* to (2.4) if $(d_1, d_2(\cdot), N_2(\cdot))$ is $\mathcal{ARF}$ and for any $(\rho, \tau) \in Z$ it holds that

$$\begin{aligned} &N_1 d_1 + N_2(\rho,\tau) d_2(\rho,\tau) + \tau(N_1 d_1^2 + N_2(\rho,\tau) d_2(\rho,\tau)^2) \\ &\geq N_1 d_1 + \bar{N}_2(\rho,\tau) \bar{d}_2(\rho,\tau) + \tau(N_1 d_1^2 + \bar{N}_2(\rho,\tau) \bar{d}_2(\rho,\tau)^2), \end{aligned}$$

for every $(\bar{d}_2(\cdot), \bar{N}_2(\cdot))$ such that $(d_1, \bar{d}_2(\cdot), \bar{N}_2(\cdot))$ is $\mathcal{ARF}$. ■

The first observation we make in (2.4) is that if $\epsilon > 0$, any fixed solution (d_1, d_2, N_2) feasible for scenario $(\rho, \tau) \in Z$ is also feasible for $(\rho, \tau + \epsilon)$ with a higher objective value. Therefore, in any worst-case realization it will hold that $\tau = \tau_L$ (see (2.3)). This observation has consequences for what uncertainty sets Z need to be considered. Due to the result (2.2), one can in general distinguish three cases for uncertainty set Z and parameter σ:

Case 1) $\sigma\rho_U \leq \tau_L$: According to (2.2), for any realization (with $\tau = \tau_L$) it is optimal to deliver the minimum number of fractions in stage 2.

Case 2) $\sigma\rho_L \geq \tau_L$: According to (2.2), for any realization (with $\tau = \tau_L$) it is optimal to deliver the maximum number of fractions in stage 2.

Case 3) $\sigma\rho_L < \tau_L < \sigma\rho_U$: In the scenario (ρ_L, τ_L), it is optimal to deliver the maximum number of fractions in stage 2 according to (2.2). In the scenario (ρ_U, τ_L), it is optimal to deliver the minimum number of fractions in stage 2 according to (2.2).

In Cases 1 and 2, (2.4) is easily solved by plugging in the (worst-case) optimal value for N_2, and solving the resulting 2-variable optimization problem. Therefore, only Case 3 is of interest and in the remainder of this chapter we make the following assumption.

Assumption 2.6. *It holds that* $\sigma\rho_L < \tau_L < \sigma\rho_U$.

In our numerical experiments, we use a lung cancer data set. Recent evidence suggests that for lung cancer Assumption 2.6 can indeed hold, i.e., the optimal number of treatment fractions is not always known prior to treatment. Further details are provided in Section 2.5.2. For other tumor sites, such as liver cancer, the tumor α/β is generally assumed to be 10 or higher, whereas the α/β of normal liver tissue is typically assumed to be 3 or 4. Thus, for such tumor sites Assumption 2.6 generally does not hold, and hyperfractionation is optimal.

2.3.2 Optimal decision rules and worst-case solution

Problem (2.4) is a 2-stage nonconvex mixed-integer ARO problem, which are generally hard to solve. Nevertheless, due to the small number of variables the problem can be solved to optimality. In order to solve (2.4), we take two steps:

Step 1) Determine optimal decision rules $d_2(\cdot)$ and $N_2(\cdot)$ for fixed d_1.

Step 2) Plug in optimal decision rules and solve for d_1.

In what follows, we give a detailed explanation of both steps. Let $(d_1^*, d_2^*(\rho,\tau), N_2^*(\rho,\tau))$ denote an $\mathcal{ARO}$ solution to (2.4).

Step 1: Determine optimal decision rules $d_2(\cdot)$ and $N_2(\cdot)$ for fixed d_1
Fix stage-1 variable d_1. Similar to the result (2.2), we will show that it is optimal to deliver either the minimum or the maximum number of fractions in stage-2. Moreover, (2.4b) is the only OAR dose-limiting constraint, so it will hold with equality if this does not violate variable bounds (2.4d) and (2.4e). We will show that the latter is not the case. The theorem below summarizes the result.

Theorem 2.7. *Let d_1 be the stage-1 decision of* (2.4)*. The decision rules*

$$N_2^*(\rho,\tau) = \begin{cases} N_2^{min} & \text{if } \tau \geq \sigma\rho \\ N_2^{max} & \text{otherwise,} \end{cases} \tag{2.7}$$

and

$$d_2^*(d_1;\rho,\tau) = \begin{cases} g(d_1, N_1, N_2^{min};\rho) & \text{if } \tau \geq \sigma\rho \\ g(d_1, N_1, N_2^{max};\rho) & \text{otherwise,} \end{cases} \tag{2.8}$$

are optimal to (2.4) *for the given d_1. These provide the unique optimal decisions unless $\tau = \sigma\rho$.*

Proof. See Appendix 2.B.1. □

Clearly, these decision rules are nonlinear, and in fact split the uncertainty region in two parts: one where it is optimal to deliver the minimum number of fractions $N_2^{\min}$ in stage 2, and one where it is optimal to deliver the maximum number of fractions $N_2^{\max}$ in stage 2. This suggests splitting the uncertainty set as follows:

$$Z^{\min} := Z \cap \{\tau \geq \sigma\rho\}, \tag{2.9a}$$
$$Z^{\max} := Z \cap \{\tau < \sigma\rho\}. \tag{2.9b}$$

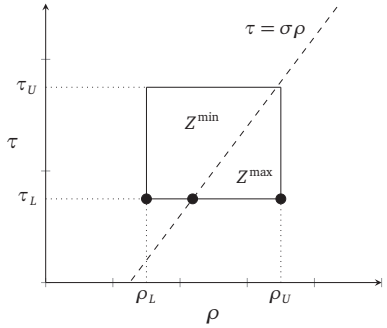

Figure 2.2: Split of uncertainty set Z according to (2.9). The circles indicate the locations of the candidate worst-case scenarios for (2.11).

An illustration is provided in Figure 2.2.

Step 2: Plug in optimal decision rules and solve for d_1
In order to find an $\mathcal{ARO}$ d_1, we introduce the following objective function for given (ρ, τ):

$$f(d_1, N_2; \rho, \tau) := \begin{cases} N_1 d_1 + N_2 g(d_1, N_1, N_2; \rho) \\ +\tau\big(N_1 d_1^2 + N_2 g(d_1, N_1, N_2; \rho)^2\big) & \text{if } d_1 \in [0, g(0,0,N_1;\rho)] \\ -\infty & \text{otherwise,} \end{cases} \tag{2.10}$$

where, for given ρ, the value $g(0,0,N_1;\rho)$ is the maximum dose that can be delivered in stage 1 due to the nonnegativity restriction on the stage-2 dose. From Assumption 2.1 it follows that $g(0,0,N_1;\rho) \geq d_1^{\max}$ for all $(\rho,\tau) \in Z$, so f is finite for all feasible d_1. According to Lemma 2.15 in Appendix 2.C, function f is either convex, concave or constant in d_1.

Plugging in (2.7) and (2.8) and using definition (2.10) allows us to rewrite (2.4) to a problem of only variable d_1:

$$\max_{d_1} \min_{(\rho,\tau)\in Z} f(d_1, N_2^*(\rho,\tau), \rho, \tau), \tag{2.11a}$$

$$\text{s.t. } d^{\min} \leq d_1 \leq d_1^{\max}. \tag{2.11b}$$

As noted in Section 2.3.1, in any worst-case realization it will hold that $\tau = \tau_L$, so it is sufficient to consider only those observations with $\tau = \tau_L$.

In order to reformulate (2.11), we make use of the properties of g and f in Lemma 2.17 in Appendix 2.C. In particular, Lemma 2.17b states that function f is either increasing or decreasing in ρ for fixed d_1. Hence, if we move (2.11a) to a constraint and

split according to (2.9), for both $Z^{\min}$ and $Z^{\max}$ it is sufficient to consider the constraint for the highest and lowest value of ρ in the uncertainty set. With $\tau = \tau_L$, this results in the scenarios (ρ_L, τ_L) and $(\frac{\tau_L}{\sigma}, \tau_L)$ for $Z^{\min}$ and $(\frac{\tau_L}{\sigma}, \tau_L)$ and (ρ_U, τ_L) for $Z^{\max}$.

Therefore, the three candidate worst-case scenarios are (ρ_L, τ_L), (ρ_U, τ_L) and $(\frac{\tau_L}{\sigma}, \tau_L)$; their locations are indicated in Figure 2.2. By Lemma 2.15, the objective value in the third scenario is equal to

$$K = \frac{1}{\sigma} B\big(0, 0, \frac{\tau_L}{\sigma}\big). \tag{2.12}$$

This is the maximum target BED that can be attained if radiation sensitivity parameters are exactly such that fractionation has no influence on the optimal objective value. It is equal to the maximum tolerable OAR BED for these radiation sensitivity parameters, divided by the generalized OAR dose sparing factor σ.

Putting everything together, we conclude that if $(d_1^*, d_2^*(\cdot), N_2^*(\cdot))$ is $\mathcal{ARO}$ to the EDP (2.4) then there exists a $q^* \in \mathbb{R}_+$ such that (d_1^*, q^*) is an optimal solution to

$$\begin{aligned}
\max_{d_1, q} \quad & q, && \text{(2.13a)}\\
\text{s.t.} \quad & q \leq f(d_1, N_2^{\min}; \rho_L, \tau_L), && \text{(2.13b)}\\
& q \leq f(d_1, N_2^{\max}; \rho_U, \tau_L), && \text{(2.13c)}\\
& q \leq K, && \text{(2.13d)}\\
& d^{\min} \leq d_1 \leq d_1^{\max}. && \text{(2.13e)}
\end{aligned}$$

Conversely, if (d_1^*, q^*) is an optimal solution to (2.13) and $N_2^*(\cdot)$ and $d_2^*(\cdot)$ are given by (2.7) and (2.8), respectively, then $(d_1^*, d_2^*(\cdot), N_2^*(\cdot))$ is $\mathcal{ARO}$ to (2.4). Hence, (2.13) and EDP (2.4) are equivalent.

According to Lemma 2.15, the RHS of (2.13b) and (2.13c) is convex and concave in d_1, respectively. Hence, (2.13) asks to find the value of d_1 that maximizes the minimum of a univariate convex (2.13b), concave (2.13c) and constant (2.13d) function on a closed interval (2.13e). Lemma 2.16 in Appendix 2.C provides information on the intersection points of the functions (2.13b)-(2.13d). Consequently, the optimal solution(s) to (2.13) is/are easily found.

Figure 2.3 illustrates a possible instance of (2.13), displaying constraints (2.13b)-(2.13d). In this case, the set of optimal solutions is the union of the two intervals for d_1 where constraint (2.13d) is active. This is indicated in red. Dose constraints (2.13e) may cut off part of these intervals. If due to constraint (2.13e) both these intervals are infeasible, the optimum is at one of the boundaries for d_1.

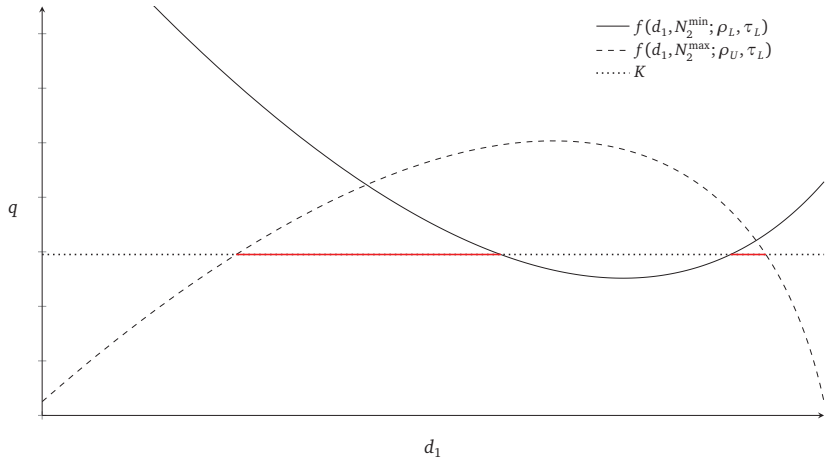

Figure 2.3: Schematic illustration of (2.13). The solid and dashed curves represent constraints (2.13b) and (2.13c), respectively, and the dotted line represent constraint (2.13d). The optimal intervals are indicated in red.

2.3.3 Pareto adjustable robustly optimal solutions

Figure 2.3 illustrates that it is possible that there are multiple optimal solutions to (2.13). These solutions are $\mathcal{ARO}$ stage-1 solutions to the EDP (2.4). In general, in case there are multiple $\mathcal{ARO}$ solutions these may perform vastly different if a non-worst-case scenario realizes (De Ruiter et al., 2016). Iancu and Trichakis (2014) study static robust optimization problems with multiple robustly optimal solutions, and introduce the concept of Pareto robustly optimal ($\mathcal{PRO}$) solutions. A robustly optimal solution is called $\mathcal{PRO}$ if there is no other robustly feasible solution that has equal or better objective value for all scenarios in the uncertainty set, while being strictly better for at least one scenario. Non-$\mathcal{PRO}$ solutions are dominated by at least one $\mathcal{PRO}$ solution and are therefore not desired[3]. The concept has previously been applied to RT planning for breast cancer by Mahmoudzadeh (2015).

Iancu and Trichakis (2014) study $\mathcal{PRO}$ solutions solely for static RO problems; we generalize the concept to 2-stage adjustable robust optimization problems.

[3]The concept of Pareto robust optimality closely resembles the concept of Pareto efficiency in multi-criteria optimization (MCO). In MCO, Pareto efficient solutions can only be improved in one criteria at the cost of a deterioration in another criteria. Only Pareto efficient solutions are of interest, and the overall goal in MCO is to compute this set of solutions (known as the Pareto surface).

Definition 2.8 (Pareto adjustable robustly optimal)**.** An $\mathcal{ARO}$ tuple $(d_1, d_2(\cdot), N_2(\cdot))$ is *Pareto adjustable robustly optimal* ($\mathcal{PARO}$) to (2.4) if there is no tuple $(\bar{d}_1, \bar{d}_2(\cdot), \bar{N}_2(\cdot))$ that is $\mathcal{ARO}$ to (2.4) and satisfies

$$\begin{aligned} &N_1 d_1 + N_2(\rho,\tau) d_2(\rho,\tau) + \tau(N_1 d_1^2 + N_2(\rho,\tau) d_2(\rho,\tau)^2) \\ &\quad \leq N_1 \bar{d}_1 + \bar{N}_2(\rho,\tau) \bar{d}_2(\rho,\tau) + \tau(N_1 \bar{d}_1{}^2 + \bar{N}_2(\rho,\tau) \bar{d}_2(\rho,\tau)^2) \ \ \forall (\rho,\tau) \in Z, \end{aligned} \tag{2.14a}$$

$$\begin{aligned} &N_1 d_1 + N_2(\bar{\rho},\bar{\tau}) d_2(\bar{\rho},\bar{\tau}) + \tau(N_1 d_1^2 + N_2(\bar{\rho},\bar{\tau}) d_2(\bar{\rho},\bar{\tau})^2) \\ &\quad < N_1 \bar{d}_1 + \bar{N}_2(\bar{\rho},\bar{\tau}) \bar{d}_2(\bar{\rho},\bar{\tau}) + \bar{\tau}(N_1 \bar{d}_1{}^2 + \bar{N}_2(\bar{\rho},\bar{\tau}) \bar{d}_2(\bar{\rho},\bar{\tau})^2) \ \text{ for some } (\bar{\rho},\bar{\tau}) \in Z. \end{aligned} \tag{2.14b}$$

■

We also define the concept $\mathcal{PARO}$ for the stage-1 decision d_1 individually.

Definition 2.9 (Pareto adjustable robustly optimal d_1)**.** A stage-1 decision d_1 is $\mathcal{PARO}$ to (2.4) if there exist decision rules $N_2(\cdot)$ and $d_2(\cdot)$ such that $(d_1, d_2(\cdot), N_2(\cdot))$ is $\mathcal{PARO}$ to (2.4). ■

If there are multiple $\mathcal{ARO}$ solutions, we wish to pick one that is $\mathcal{PARO}$. In general, finding $\mathcal{PARO}$ solutions is hard, because it requires comparing the performance of both stage-1 decisions and stage-2 decision rules on multiple scenarios simultaneously. However, for the current problem (2.7) and (2.8) are optimal decision rules. Plugging these in conditions (2.14) reduces the problem of finding a $\mathcal{PARO}$ solution to solely comparing the performance of $\mathcal{ARO}$ stage-1 decisions d_1 in non-worst-case scenarios.

In Iancu and Trichakis (2014) it is shown for linear optimization that, if we optimize over the robustly optimal solutions for a second criterion (scenario) that is in the relative interior of the uncertainty set, the resulting solution(s) are $\mathcal{PRO}$. In a similar fashion $\mathcal{PARO}$ solutions to the current problem can be found. Let X^{ARO} denote the set of $\mathcal{ARO}$ stage-1 solutions to (2.4). It turns out that consecutively optimizing over an auxiliary scenario where hyperfractionation is optimal and an auxiliary scenario where hypofractionation is optimal yields a set of $\mathcal{PARO}$ solutions. Let $(\rho^{\text{aux-min}}, \tau^{\text{aux-min}}) \in \text{int}(Z^{\min})$, where int$(\cdot)$ is the interior operator. Define the auxiliary optimization problem for the hypofractionation scenario:

$$\max_{d_1 \in X^{\text{ARO}}} f\left(d_1, N_2^{\min}; \rho^{\text{aux-min}}, \tau^{\text{aux-min}}\right). \tag{2.15}$$

Denote the set of optimal solutions to (2.15) by $X^{\text{aux-min}}$. Similarly, let $(\rho^{\text{aux-max}}, \tau^{\text{aux-max}}) \in \text{int}(Z^{\max})$. Define the auxiliary optimization problem for the hyperfractionation scenario:

$$\max_{d_1 \in X^{\text{aux-min}}} f\left(d_1, N_2^{\max}; \rho^{\text{aux-max}}, \tau^{\text{aux-max}}\right). \tag{2.16}$$

Note that it uses $X^{\text{aux-min}}$ as input, i.e., we solve the auxiliary problems consecutively. Denote the set of optimal solutions to (2.16) by X^{PARO}.

Theorem 2.10. *All solutions in X^{PARO} are $\mathcal{PARO}$ to* (2.4).

Proof. See Appendix 2.B.2. □

Solving (2.15) or (2.16) entails maximizing a strictly convex or strictly concave function over a feasible set consisting of a small number of intervals or points. Hence, these auxiliary problems are easily solved. Note that the second auxiliary problem is only relevant if the first auxiliary problem has multiple optimal solutions. Switching their order, and optimizing (2.15) over the set $X^{\text{aux-max}}$ may lead to different solutions, and these are also $\mathcal{PARO}$. Thus, in general X^{PARO} does not contain all $\mathcal{PARO}$ solutions. The two-step approach is necessary; numerical results show that optimizing over only one auxiliary scenario may indeed result in non-$\mathcal{PARO}$ solutions.

2.4 ARO: Biomarkers provide inexact information

In this section we present an adjustable robust optimization approach to solve a more realistic version of the adaptive treatment-length problem. Because in practice it is impossible to exactly determine the α/β parameters from biomarker data, any values for the α/β parameters obtained during treatment are inexact. This section presents a model that accounts for uncertainty in biomarker information.

2.4.1 Problem formulation

The setup for the ARO problem with inexact data is based on De Ruiter et al. (2017). After N_1 fractions we obtain an estimate $(\hat{\rho}, \hat{\tau})$ for (ρ, τ), the inverse α/β parameters for the OAR and the tumor. It is still assumed that Assumption 2.6 holds for uncertainty set Z. Furthermore, we assume that (ρ, τ), $(\hat{\rho}, \hat{\tau}) \in Z$ (as defined in (2.3)) and that $(\hat{\rho}, \hat{\tau}) - (\rho, \tau) \in \hat{Z}$, with

$$\hat{Z} = \{(\varepsilon^\rho, \varepsilon^\tau) \in \mathbb{R}^2 : |\varepsilon^\rho| \leq r^\rho, |\varepsilon^\tau| \leq r^\tau\}.$$

Here r^ρ and r^τ are parameters that define the accuracy of the estimate/observation $(\hat{\rho}, \hat{\tau})$. Set $\hat{Z}$ is the uncertainty set around the inexact observation. This can also be written as $(\rho, \tau) \in \{(\hat{\rho}, \hat{\tau})\} + \hat{Z}$, which is the Minkowski sum of a singleton and a set. This new set need not be contained in the original uncertainty set Z. Define

$$U := \{(\rho, \tau, \hat{\rho}, \hat{\tau}) : (\rho, \tau),\ (\hat{\rho}, \hat{\tau}) \in Z,\ (\hat{\rho}, \hat{\tau}) - (\rho, \tau) \in \hat{Z}\},$$

and

$$Z_{(\hat{\rho},\hat{\tau})} := \big(\{(\hat{\rho},\hat{\tau})\} + \hat{Z}\big) \cap Z.$$

The set U contains all possible observation-realization pairs and $Z_{(\hat{\rho},\hat{\tau})}$ contains all possible realizations after observation of $(\hat{\rho},\hat{\tau})$. For given observation $(\hat{\rho},\hat{\tau})$, the new upper and lower bounds for (ρ,τ) are given by

$$\hat{\tau}_L = \max\{\tau_L, \hat{\tau} - r^\tau\}, \;\; \hat{\tau}_U = \min\{\tau_U, \hat{\tau} + r^\tau\}, \tag{2.17a}$$
$$\hat{\rho}_L = \max\{\rho_L, \hat{\rho} - r^\rho\}, \;\; \hat{\rho}_U = \min\{\rho_U, \hat{\rho} + r^\rho\}. \tag{2.17b}$$

Compared to Section 2.3, we remove Assumption 2.1 and impose a different (slightly stricter) assumption on the relation between $d^{\min}$, $d_1^{\max}$ and the bounds on N_2.

Assumption 2.11. *It holds that* $d^{min} \leq d_1^{max}$ *and*

$$d_1^{max} \leq \min\Big\{g(d_1^{min}, N_2^{min}, N_1; \rho_L), g(d_1^{min}, N_2^{max}, N_1; \max\{\rho_L, \frac{\tau_L}{\sigma} - 2r^\rho\}), g(d_1^{min}, N_2^{max}, N_1; \rho_U)\Big\}.$$

The inexact data problem (IDP) analogous to (2.4) is given by

$$\max_{d_1, d_2(\hat{\rho},\hat{\tau}), N_2(\hat{\rho},\hat{\tau})} \;\; \min_{(\rho,\tau,\hat{\rho},\hat{\tau})\in U} N_1 d_1 + N_2(\hat{\rho},\hat{\tau}) d_2(\hat{\rho},\hat{\tau}) + \tau(N_1 d_1^2 + N_2(\hat{\rho},\hat{\tau}) d_2(\hat{\rho},\hat{\tau})^2), \tag{2.18a}$$
$$\text{s.t.} \quad \sigma(N_1 d_1 + N_2(\hat{\rho},\hat{\tau}) d_2(\hat{\rho},\hat{\tau})) + \rho\sigma^2(N_1 d_1^2 + N_2(\hat{\rho},\hat{\tau}) d_2(\hat{\rho},\hat{\tau})^2) \leq \text{BED}_{\text{tol}}(\rho), \;\; \forall(\rho,\tau,\hat{\rho},\hat{\tau}) \in U, \tag{2.18b}$$
$$N_2(\hat{\rho},\hat{\tau}) \in \{N_2^{\min}, \ldots, N_2^{\max}\}, \;\; \forall(\rho,\tau,\hat{\rho},\hat{\tau}) \in U, \tag{2.18c}$$
$$d_2(\hat{\rho},\hat{\tau}) \geq d^{\min}, \;\; \forall(\rho,\tau,\hat{\rho},\hat{\tau}) \in U, \tag{2.18d}$$
$$d^{\min} \leq d_1 \leq d_1^{\max}. \tag{2.18e}$$

For stage-2 variables $d_2(\hat{\rho},\hat{\tau})$ and $N_2(\hat{\rho},\hat{\tau})$ it is indicated that they are a function of the observations $(\hat{\rho},\hat{\tau})$ instead of the uncertain parameters (ρ,τ). Similar to Section 2.3, we formally define several properties of solutions. Let $X(\rho,\tau,\hat{\rho},\hat{\tau})$ denote the feasible region defined by constraints (2.18b)-(2.18e) for fixed $(\rho,\tau,\hat{\rho},\hat{\tau})$.

Definition 2.12 (Adjustable robust feasibility)**.** A tuple $(d_1, d_2(\cdot), N_2(\cdot))$ is *adjustable robustly feasible* ($\mathcal{ARF}$) to (2.18) if $(d_1, d_2(\hat{\rho},\hat{\tau}), N_2(\hat{\rho},\hat{\tau})) \in X(\rho,\tau,\hat{\rho},\hat{\tau})$ for all $(\rho,\tau,\hat{\rho},\hat{\tau}) \in U$. ■

Optimality of a decision rule is defined as follows.

Definition 2.13 (Optimal decision rule)**.** For a given d_1, a decision rule pair $(d_2(\cdot), N_2(\cdot))$ is *optimal* to (2.18) if $(d_1, d_2(\cdot), N_2(\cdot))$ is $\mathcal{ARTF}$ and for any $(\hat{\rho}, \hat{\tau}) \in Z$ it holds that

$$\begin{aligned}&\min_{(\rho,\tau)\in Z_{(\hat{\rho},\hat{\tau})}} N_1 d_1 + N_2(\hat{\rho},\hat{\tau}) d_2(\hat{\rho},\hat{\tau}) + \tau(N_1 d_1^2 + N_2(\hat{\rho},\hat{\tau}) d_2(\hat{\rho},\hat{\tau})^2)\\ \geq &\min_{(\rho,\tau)\in Z_{(\hat{\rho},\hat{\tau})}} N_1 d_1 + \bar{N}_2(\hat{\rho},\hat{\tau}) \bar{d}_2(\hat{\rho},\hat{\tau}) + \tau(N_1 d_1^2 + \bar{N}_2(\hat{\rho},\hat{\tau}) \bar{d}_2(\hat{\rho},\hat{\tau})^2),\end{aligned}$$

for every $(\bar{d}_2(\cdot), \bar{N}_2(\cdot))$ such that $(d_1, \bar{d}_2(\cdot), \bar{N}_2(\cdot))$ is $\mathcal{ARTF}$. ■

Note that for exact data, an optimal decision rule gives the optimal decision for any *realization* in the uncertainty set Z (given d_1). For inexact data, we call a decision rule optimal if it yields the maximum worst-case (guaranteed) objective value for any *observation* in the uncertainty set Z.

2.4.2 Optimal decision rules and conservative approximation

Depending on both the observed $(\hat{\rho}, \hat{\tau})$ and the quality of the biomarker information (i.e., r^ρ and r^τ), we may be able to immediately determine the optimal value for N_2. Therefore, we split the uncertainty set for the observations $(\hat{\rho}, \hat{\tau})$. Define

$$Z_{\text{ID}}^{\min} = \{(\hat{\rho}, \hat{\tau}) \in Z : \hat{\tau}_L \geq \sigma \hat{\rho}_U\}, \tag{2.19a}$$

$$Z_{\text{ID}}^{\text{int}} = \{(\hat{\rho}, \hat{\tau}) \in Z : \sigma \hat{\rho}_L < \hat{\tau}_L < \sigma \hat{\rho}_U\}, \tag{2.19b}$$

$$Z_{\text{ID}}^{\max} = \{(\hat{\rho}, \hat{\tau}) \in Z : \hat{\tau}_L \leq \sigma \hat{\rho}_L\}, \tag{2.19c}$$

so that $Z = Z_{\text{ID}}^{\min} \cup Z_{\text{ID}}^{\text{int}} \cup Z_{\text{ID}}^{\max}$. Figure 2.4 provides an illustration. For an observation $(\hat{\rho}, \hat{\tau})$ there are two candidate worst-case scenarios: $(\hat{\rho}_L, \hat{\tau}_L)$ and $(\hat{\rho}_U, \hat{\tau}_L)$. If both are on one side of the line $\tau = \sigma\rho$, the optimal fractionation decision is known. For an observation $(\hat{\rho}, \hat{\tau})$ near the lower boundary of Z it holds that $\hat{\tau}_L = \tau_L$, so a further decrease in $\hat{\tau}$ has no influence on $(\hat{\rho}_L, \hat{\tau}_L)$ and $(\hat{\rho}_U, \hat{\tau}_L)$ (see (2.17)), similar for the other boundaries. This leads to the non-linearity in the subset boundaries of Figure 2.4.

The split is such that if $(\hat{\rho}, \hat{\tau}) \in Z_{\text{ID}}^{\min}$ or $(\hat{\rho}, \hat{\tau}) \in Z_{\text{ID}}^{\max}$ only $N_2^{\min}$ resp. $N_2^{\max}$ fractions can be optimal in stage 2. Subset $Z_{\text{ID}}^{\text{int}}$ is the area between the dash-dotted lines. If $(\hat{\rho}, \hat{\tau}) \in Z_{\text{ID}}^{\text{int}}$ both $N_2^{\min}$ and $N_2^{\max}$ fractions in stage 2 may be optimal for the true (ρ, τ).

The following theorem states the optimal stage-2 decision rules for a given value of d_1.

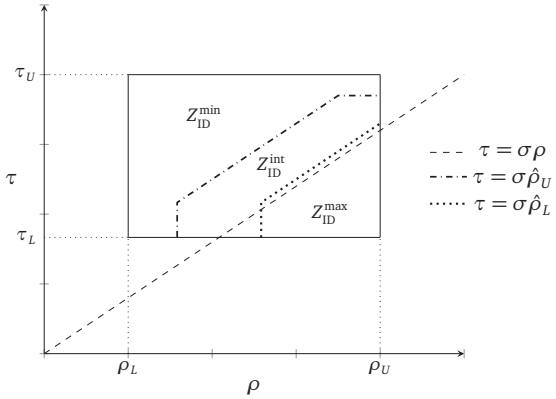

Figure 2.4: The uncertainty set Z (solid lines) for $(\hat{\rho}, \hat{\tau})$ is split into $Z_{\text{ID}}^{\min}$, $Z_{\text{ID}}^{\text{int}}$, $Z_{\text{ID}}^{\max}$, according to (2.19). Subset Z^{int} is the area between the dotted and dash-dotted curves. If $(\hat{\rho}, \hat{\tau}) \in Z_{\text{ID}}^{\text{int}}$ both $N_2^{\min}$ and $N_2^{\max}$ fractions in stage 2 may be optimal for the true (ρ, τ). If $(\hat{\rho}, \hat{\tau}) \in Z_{\text{ID}}^{\min}$ or $(\hat{\rho}, \hat{\tau}) \in Z_{\text{ID}}^{\max}$ only $N_2^{\min}$ resp. $N_2^{\max}$ fractions can be optimal in stage 2.

Theorem 2.14. *Let d_1 be the stage-1 decision of* (2.18)*. The decision rules*

$$N_2^*(d_1; \hat{\rho}, \hat{\tau}) = \begin{cases} N_2^{min} & \text{if } (\hat{\rho}, \hat{\tau}) \in Z_{ID}^{min} \\ \underset{N_2 \in \{N_2^{min}, \ldots, N_2^{max}\}}{\arg\max} \min\{f(d_1, N_2; \hat{\rho}_L, \hat{\tau}_L), f(d_1, N_2; \hat{\rho}_U, \hat{\tau}_L)\} & \text{if } (\hat{\rho}, \hat{\tau}) \in Z_{ID}^{int} \\ N_2^{max} & \text{if } (\hat{\rho}, \hat{\tau}) \in Z_{ID}^{max}, \end{cases} \tag{2.20}$$

and

$$d_2^*(d_1; \hat{\rho}, \hat{\tau}) = \min\{g(d_1, N_1, N_2^*(d_1; \hat{\rho}, \hat{\tau}); \hat{\rho}_L), g(d_1, N_1, N_2^*(d_1; \hat{\rho}, \hat{\tau}); \hat{\rho}_U)\}, \tag{2.21}$$

are optimal to (2.18) *for the given d_1.*

Proof. See Appendix 2.B.3. □

The worst-case optimal decision rule (2.20) may give a value unequal to $N_2^{\min}$ and $N_2^{\max}$ if $(\hat{\rho}, \hat{\tau}) \in Z_{\text{ID}}^{\text{int}}$. If r^ρ and r^τ are zero, i.e., we have exact data, then it holds that $\hat{\tau}_L = \tau$ and $\hat{\rho}_L = \hat{\rho}_U = \rho$. Hence, the two functions f in the RHS of (2.20) are equal, and the optimal N_2^* is the one that maximizes the resulting function. One can verify that this does not depend on d_1. Hence, in case of exact data Theorem 2.14 reduces to Theorem 2.7.

It turns out that, after plugging in (2.20) and (2.21), and splitting the uncertainty set according to (2.19), it is not apparent how to determine the optimal stage-1 decision d_1^* for (2.18). In Appendix 2.B.4 the following lower bound problem to (2.18) is derived, named the Approximate Inexact Data Problem (AIDP):

$$\max_{d_1,q} \; q, \tag{2.22a}$$
$$\text{s.t.} \; q \leq f(d_1, N_2^{\min}; \rho_L, \tau_L), \tag{2.22b}$$
$$q \leq f(d_1, N_2^{\max}; \rho_U, \tau_L), \tag{2.22c}$$
$$q \leq K, \tag{2.22d}$$
$$q \leq p(d_1), \tag{2.22e}$$
$$d^{\min} \leq d_1 \leq d_1^{\max}. \tag{2.22f}$$

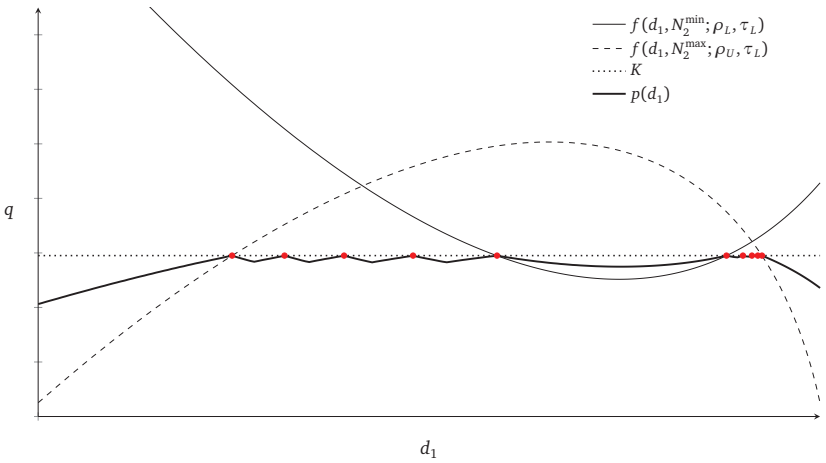

Figure 2.5: Schematic illustration of (2.22). Compared to the case with exact data (Figure 2.3), the thick black curve (constraint (2.22e)) is extra. The solid, dashed and dotted lines/curves represent constraints (2.22b), (2.22c) and (2.22d), respectively. Optimal solutions are indicated by red circles.

The AIDP is best explained using an example. Figure 2.5 illustrates a possible instance of (2.22), displaying constraints (2.22b)-(2.22e). Compared to (2.13) for exact biomarker information (see Figure 2.3), problem (2.22) has the added constraint (2.22e); a piecewise convex-concave function $p(d_1)$ defined by (2.C.19) in Lemma 2.19 (Appendix 2.C). It can be interpreted as follows. If $(\hat{\rho}, \hat{\tau}) \in Z_{\text{ID}}^{\text{int}}$, the optimal number of stage-2 fractions can be inbetween $N_2^{\min}$ and $N_2^{\max}$, as shown in Theorem 2.14. In those

cases, the optimal number of fractions also depends on the already delivered stage-1 dose d_1. The upper kinks (red circles) in the piecewise convex-concave function $p(d_1)$ in Figure 2.5 indicate values of d_1 where the worst-case scenario changes. The lower kinks indicate values where the optimal number of stage-2 fractions changes. The exact expression for $p(d_1)$ does not provide additional insight and is therefore omitted here.

In Figure 2.5, optimal solutions are locations where (2.22d) and (2.22e) are both binding, indicated by red circles. Dose constraints (2.22f) may cut off (some of) these points. If due to constraint (2.22f) none of the circles are feasible, the optimum is at one of the boundaries for d_1. Constraint (2.22e) is the only conservative constraint in (2.22). Hence, only if the feasible values for d_1 are such that none of the circles in Figure 2.5 are feasible and constraint (2.22e) is binding, it is possible that the optimal objective value of (2.22) is strictly worse than that of (2.18).

Lemmas 2.15, 2.16 and 2.19 in Appendix 2.C provide information on the shape and intersection points of constraint functions (2.22b)-(2.22e). Consequently, the optimal solution(s) of (2.18) is/are easily obtained. If (d_1^*, q^*) is optimal to AIDP (2.22), and $N_2^*(\cdot)$ and $d_2^*(\cdot)$ are given by (2.20) and (2.21) then $(d_1^*, d_2^*(\cdot), N_2^*(\cdot))$ is $\mathcal{ARF}$ to the original IDP (2.18). It is $\mathcal{ARF}$ because AIDP is a conservative approximation of IDP.

2.4.3 Pareto robustly optimal solutions to conservative approximation

Figure 2.5 also illustrates that it is possible that there are multiple optimal solutions to the AIDP (2.22). Because the AIDP provides a conservative approximation to IDP (2.18), optimizing over auxiliary scenario(s) as in Section 2.3 does not necessarily produce a stage-1 decision d_1 that is $\mathcal{PARO}$ to the original IDP. It turns out that a $\mathcal{PRO}$ solution to AIDP is obtained from the set of robustly optimal solutions to AIDP if we consecutively optimize for two auxiliary observations such that any worst-case realization is in the interior of set $Z^{\min}$ resp. $Z^{\max}$. Two important remarks are in place here. First, a $\mathcal{PRO}$ solution to AIDP need not be a $\mathcal{PARO}$ solution to IDP, even if it is $\mathcal{ARO}$ to IDP. Second, the required auxiliary scenarios need not exist; their existence depends on the values of r^ρ and r^τ. Hence, further details are omitted.

2.5 Numerical results

This section presents numerical results of the methods presented in Sections 2.3 and 2.4. First, Section 2.5.1 describes the benchmark methods against which we compare

the ARO method for EDP and IDP, and Section 2.5.2 describes the setup of the numerical experiments.

2.5.1 Benchmark static and folding horizon methods

We analyze the performance of the static and folding horizon nominal method (NOM and NOM-FH), the static and folding horizon robust optimization method (RO and RO-FH) and the adjustable robust optimization method (ARO). In the folding horizon approaches only the stage-1 decisions are implemented, and the model is re-optimized for the second stage once the biomarker information is revealed.

The static method NOM optimizes for the nominal parameter values $(\bar{\rho}, \bar{\tau})$ and disregards any uncertainty and adaptability. This method is the same for both EDP and IDP. In stage 2, NOM-FH solves the nominal problem under the assumption that the obtained biomarker estimate is exact (which is an invalid assumption for IDP). This method does not guarantee robustly feasible solution (feasible for all $(\rho, \tau) \in Z$) nor a robustly optimal solution ($\mathcal{RO}$; (static) optimal for the worst-case realization $(\rho, \tau) \in Z$). The static method RO optimizes for the worst-case realization of (ρ, τ) in the uncertainty set Z, and disregards adaptability. For EDP the method RO-FH solves the same nominal problem as NOM-FH in stage 2; for IDP it solves a static robust optimization problem in stage 2, for which the uncertainty set is determined by the accuracy of the biomarker information. RO and RO-FH both guarantee an $\mathcal{RO}$ solution.

One may add a folding horizon component to ARO (for either EDP or AIDP). This may improve the results in case a suboptimal stage-2 decision rule is used. However, as shown in Sections 2.3.2 and 2.4.2, the used stage-2 decision rules are optimal for any realized scenario (and for given stage-1 decision d_1 in case of inexact information). Hence, adding a folding horizon component will not change results.

Table 2.1 provides an overview of the guaranteed solution properties of the methods. It is important to note that in case of inexact biomarker information (IDP) the methods RO and RO-FH guarantee an $\mathcal{RO}$ solution, whereas ARO guarantees only an $\mathcal{ARF}$ solution via solving the approximate problem AIDP. Depending on the approximation quality, the $\mathcal{ARF}$ solution may be close or equal to an $\mathcal{ARO}$ solution. Next to these five methods, we also report the results for the perfect information optimum (PI). This is the attainable optimum if from the start of the first fraction the true (ρ, τ) is exactly known. It can be formulated by taking the nominal problem and replacing the nominal parameter values by their true values. While in practice not a viable strategy, PI provides information on the value of perfect information, and allows us to put the performance of and differences between the other methods in perspective.

	Method				
Problem	NOM	NOM-FH	RO	RO-FH	ARO
EDP	-	-	$\mathcal{RO}$	$\mathcal{RO}$	$\mathcal{PARO}$
IDP	-	-	$\mathcal{RO}$	$\mathcal{RO}$	$\mathcal{ARF}$

Table 2.1: Guaranteed solution properties of the five methods.

2.5.2 Study setup

We use a data set of 30 non-small cell lung cancer (NSCLC) patients, treated with either photon or proton therapy. The mathematical models in Sections 2.3 and 2.4 are based on the assumption that there is a single dose restricting OAR. We assume that the single dose restricting OAR is the normal lung itself[4]. For the models in Sections 2.3 and 2.4, an instance is defined by a tuple $(\sigma, \varphi, D, T, N_1, N^{\min}, N^{\max}, d^{\min}, d_1^{\max})$ and the relevant uncertainty sets.

Clinically, the number of treatment fractions varied between 33 and 37 fractions, with the majority of patients receiving 37 fractions. We set $N^{\min} = 30$ and $N^{\max} = 40$, to allow for slight deviations from the clinical standard. We assume the biomarker acquisition is made once $N_1 = 10$ fractions have been administered. This implies $N_2^{\min} = 20$ and $N_2^{\max} = 30$. Mean lung dose tolerance is $D = 20$ Gy, and we set $T = 37$ as that is the clinically standard regimen. The patients differ in (σ, φ), which characterize the spatial dose distribution. Using the clinically delivered dose distribution, we derive for each normal lung voxel its dose sparing factor s_i (see Section 2.2.1). The dose shape factor φ and the generalized dose sparing factor σ for mean OAR BED are given by

$$\varphi = \frac{n \sum_{i=1}^{n} s_i^2}{\left(\sum_{i=1}^{n} s_i\right)^2}, \quad \sigma = \frac{\sum_{i=1}^{n} s_i^2}{\sum_{i=1}^{n} s_i},$$

see Perkó et al. (2018) for details.

Cox (1986) estimate normal lung tissue α/β to be between 2.4 and 6.3. We set the nominal value at the midpoint 4.35. The α/β of NSCLC lung tumors has traditionally been assumed to be above 10 Gy. However, recent NSCLC hypofractionation trials show promising results, indicating that NSCLC cells are more sensitive to fraction size than previously assumed, i.e., have a lower α/β than 10. Santiago et al. (2016) find values between 2.2 and 9.0. We set the nominal value at the midpoint 5.6. Put together, we

[4]This is in line with clinical practice wherein normal lung is treated as the most important normal tissue and the treatment is designed as to minimize the radiation exposure to normal lung.

get the following uncertainty set for the inverse α/β ratios:

$$Z = \{(\rho, \tau) : 1/6.3 \leq \rho \leq 1/2.4,\ 1/9.0 \leq \tau \leq 1/2.2\},$$

and the nominal scenario is $(\bar{\rho}, \bar{\tau}) = (1/4.35, 1/5.6)$. With this uncertainty set, 20 out of 30 patient cases satisfy Assumption 2.6: these are used in the numerical experiments. For the remaining ten patients the optimal number of treatment fractions can be determined prior to treatment, so these are removed.

To discriminate between multiple $\mathcal{ARO}$ solutions, we follow the procedure detailed in Section 2.3.3 in the case of exact biomarker information. The auxiliary scenarios are sampled uniformly from $\text{int}(Z^{\min})$ and $\text{int}(Z^{\max})$. In the case of inexact biomarker information, the procedure discussed in Section 2.4.3 is followed if the required auxiliary observations exist. If such observations exist, we sample uniformly from Z until we have found two auxiliary observations for which any worst-case realization is in $\text{int}(Z^{\min})$ resp. $\text{int}(Z^{\max})$. If such observations do not exist, the robustly optimal solution to AIDP with lowest stage-1 dose is selected. The method RO (and therefore also RO-FH) may also find multiple robustly optimal solutions. For the obtained set of robustly optimal solutions we again follow the procedure detailed in Section 2.3.3. It turns out that for RO, the robustly optimal solutions often perform identical in non-worst-case scenarios. We optimize over the auxiliary scenarios consecutively; the first auxiliary scenario is the scenario corresponding to $\text{int}(Z^{\min})$.

The minimum dose per fraction is $d^{\min} = 1.5$ Gy and the maximum stage-1 dose per fraction is $d_1^{\max} = 3$ Gy. This satisfies Assumption 2.1 (for EDP) and 2.11 (for IDP). Using these parameter values, it is feasible to deliver $N_2^{\max}$ fractions with dose $d^{\min}$ in *all* scenarios in Z. This means that stage-1 decisions cannot render stage 2 infeasible for RO, NOM (and their FH counterparts) or PI. Numerical results indicate that results are not sensitive to the choice of $d^{\min}$ and $d_1^{\max}$.

First, Section 2.5.3 presents and discusses the results for the problem with exact biomarker information (EDP) of Section 2.3. After that, Section 2.5.4 presents and discusses the results for the problem with inexact biomarker information (IDP) of Section 2.4. Lastly, Section 2.5.5 again considers the inexact biomarker information case, and varies parameter N_1 in order to determine the optimal moment of biomarker acquisition.

We consider a sample of 200 scenarios for (ρ, τ) from Z. For each scenario, we compute the average tumor BED over 20 patients is computed, thus creating a tumor BED distribution for the 'average' patient. For this tumor BED distribution we report the mean, 5% quantile and worst-case value. Next to this, we report the true worst-case tumor BED over Z (averaged over 20 patients). Note that the true worst-case

scenario can differ per patient, so the true worst-case BED is typically not attained in the sample. For OAR violations, we report the percentage by which the OAR BED tolerance is exceeded (i.e., percentage overdose). The maximum violation is the maximum value found over all patients and scenarios. All reported decision variable statistics are averaged over all patients and scenarios.

2.5.3 Results exact biomarker information

	Method					
	NOM	NOM-FH	RO	RO-FH	ARO	PI
Tumor BED - sample mean (Gy)	162.75	161.44	156.57	160.14	161.40	161.49
Tumor BED - sample 5% quantile (Gy)	151.98	150.94	147.57	150.04	150.90	151.04
Tumor BED - sample wc (Gy)	145.98	146.33	142.53	145.58	146.32	146.39
Tumor BED - wc over Z (Gy)	**114.72**	**116.19**	**116.19**	**116.19**	**116.19**	**116.19**
OAR violation - mean (%)	1.25	0	0	0	0	0
OAR violation - max (%)	4.22	0	0	0	0	0
Stage-1 dose d_1 (Gy)	1.50	1.50	2.29	2.29	1.51	1.66
Stage-2 dose d_2 (Gy)	3.45	3.24	2.48	2.95	3.24	3.19
Stage-2 fractions N_2	20.0	22.2	27.2	22.2	22.2	22.2

Table 2.2: Results for experiments with exact biomarker information and uniform sampling of (ρ, τ) over Z (200 scenarios). For each scenario, results are averaged over 20 patients*. All methods optimize for worst-case tumor BED in Z, which is displayed in bold.
*: the maximum OAR violation is computed over all patients and scenarios.

Table 2.2 presents the results. Altogether, the results indicate that the value of exact information is high. NOM-FH performs very similar to ARO. This illustrates that ignoring uncertainty and adaptability in stage 1 neither compromises worst-case or mean performance, nor does it lead to OAR constraint violations if treatment can be adapted based on exact biomarker information. In fact, NOM-FH outperforms RO-FH, indicating that accounting for uncertainty in stage-1 is overly conservative.

NOM is the only method that is not worst-case optimal, but yields the highest mean tumor BED across the sample. However, it is the only method that results in OAR constraint violations. In the nominal scenario $(\bar{\rho}, \bar{\tau})$ it is optimal to hypofractionate for all patients, so the mean N_2 equals 20 for NOM. The other static method, RO, is worst-case optimal, but yields low tumor BED across the sample. This is not due to one poor (patient, scenario) pair, but consistent throughout the entire sample. It delivers significantly more fractions on average, i.e., it decides to hyperfractionate more often.

NOM-FH adds a folding horizon component to NOM, and this results in zero viola-

tions and worst-case optimality. It does have slightly lower sample mean tumor BED. RO-FH adds a folding horizon component to RO, and this results in improved performance across the entire sample. It chooses to hypofractionate more often than RO. ARO is worst-case optimal and performs very similar to NOM-FH. Excluding NOM (for OAR constraint violations) and PI (not implementable), NOM-FH, ARO, RO-FH and RO yield the (possibly joint) highest objective value in 83.4%, 76.4%, 22.1% and 0.6% of all (scenario, patient) instances, respectively.

The results of Table 2.2 show that the methods have different stage-1 decisions d_1; this indicates the existence of multiple worst-case optimal stage-1 solutions. As indicated in Section 2.5.2, RO, RO-FH and ARO optimize over auxiliary scenarios in this case. According to Theorem 2.10, ARO finds a $\mathcal{PARO}$ solution this way. Overall, methods that deliver a relatively low dose in stage-1 perform better than the methods that deliver a higher dose. This may be data set-specific. From PI we see that for the majority of patients and scenarios hypofractionation is optimal (average $N_2 = 22.2$), whereas the RO results indicate that for the majority of patients it is worst-case optimal to hyperfractionate (average $N_2 = 27.2$). We emphasize that for different data sets, where for the majority of scenarios and patients hyperfractionation is optimal, a higher stage-1 dose (which allows for $N^{\max}$ constant-dose fractions) may perform better, such as the result of RO and RO-FH.

Figure 2.6 shows the complete cumulative scenario-tumor BED graph. A point (x, y) in Figure 2.6 can be interpreted as follows: for the average patient, in y% of scenarios the tumor BED is at least x Gy. The results clearly demonstrate that RO and RO-FH are outperformed by the other methods. Both NOM-FH and ARO are visually almost indistinguishable from PI. NOM performs even better across the entire sample (except the first percent of the sample), at the cost of OAR BED violations.

To see the difference in mean performance between the multiple worst-case optimal solutions, we compare $\mathcal{PARO}$ solution found by the ARO method to the $\mathcal{ARO}$ solution that performs worst in the two auxiliary scenarios. Table 2.3 shows the results, OAR constraint violations are zero in all cases. The worst-performing $\mathcal{ARO}$ solution has a considerably higher stage-1 dose. This implies that (for the current parameter settings) delivering a high stage-1 dose does not allow as much adjustment possibilities in stage 2 as a low stage-1 dose, but it does allow for adjustments to reach the worst-case optimum. Relative to the results of Table 2.2, the difference between the best and worst ARO solution is considerable: the worst-performing ARO solution performs worse than the RO-FH solution.

Appendix 2.A reports the results of an auxiliary experiment where the (ρ, τ) sample is drawn from a superset of Z, to compare the out-of-sample performance of the

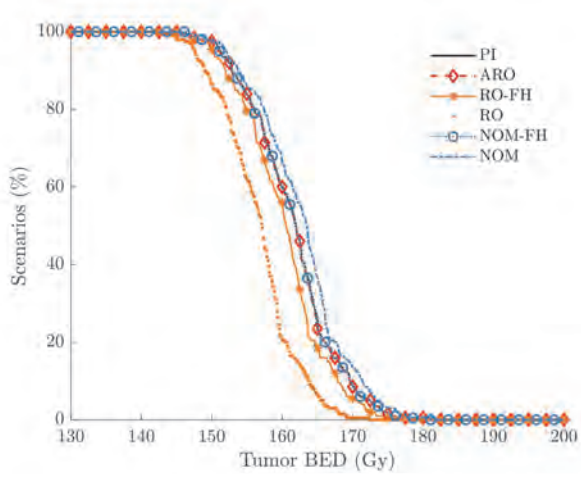

Figure 2.6: Cumulative scenario-tumor BED graph for experiments with exact biomarker information and uniform sampling of (ρ, τ) over Z (200 scenarios). A point (x, y) indicates that in y% of scenarios the tumor BED (averaged over 20 patients) is at least x Gy. ARO and NOM-FH are very close to PI.

	Method	
	$\mathcal{ARO}_{\text{worst}}$	$\mathcal{ARO}_{\text{best}}$
Tumor BED - sample mean (Gy)	159.87	161.40
Tumor BED - sample 5% quantile (Gy)	149.86	150.90
Tumor BED - sample worst-case (Gy)	145.34	146.32
Tumor BED - wc over Z (Gy)	**116.19**	**116.19**
Stage-1 dose d_1 (Gy)	2.67	1.51
Stage-2 dose d_2 (Gy)	2.79	3.24
Stage-2 fractions N_2	22.2	22.2

Table 2.3: Comparison between the best ($\mathcal{PARO}$) and worst performing $\mathcal{ARO}$ solutions, for uniform sampling of (ρ, τ) over Z (200 scenarios). For each scenario, results are averaged over 20 patients. All methods optimize for worst-case tumor BED in Z, which is displayed in bold. OAR constraint violations are zero in all cases.

methods. NOM remains the only method with OAR constraint violations. Compared to Table 2.2, static methods NOM and RO have poor performance. The relative performance of the adaptive methods remains mostly unchanged.

Altogether, the results of Section 2.5.3 demonstrate that if exact biomarker informa-

tion is available mid-treatment, most stage-1 decisions allow for sufficient adaptation space in stage 2, also with realizations outside of Z. Different stage-1 decisions yield the worst-case optimum, have good performance on the scenario sample and have no OAR BED violations. We note that all presented differences in tumor BED are of relatively small magnitude. One reason for this is that the number of stage-2 fractions is restricted to $[N_2^{\min}, N_2^{\max}] = [20, 30]$. If the minimum number of fractions represents a 'true' hypofractionation case, the dose per fraction can vary more, and the difference in performance between hypo- and hyperfractionation strategies is amplified.

2.5.4 Results inexact biomarker information

In case of in inexact biomarker information (IDP), we do not obtain the true parameter values (ρ, τ) after $N_1 = 10$ fractions, but only an estimate $(\hat{\rho}, \hat{\tau})$. As discussed in Section 2.4, we specify a new uncertainty set $\hat{Z}$ such that $(\hat{\rho}, \hat{\tau}) - (\rho, \tau) \in \hat{Z}$. Let $\mathrm{DQ} \in [0, 1]$ indicate the data quality. Then we set $\hat{Z}$ such that the width of the new uncertainty intervals for τ and ρ is $(1 - \mathrm{DQ})$ times the width of the original intervals $[\tau_L, \tau_U]$ and $[\rho_L, \rho_U]$. That is, $\mathrm{DQ} \cdot 100\%$ can be interpreted as the percentage by which the uncertainty intervals can be reduced due to the observation. The relation with the accuracy parameter r^ρ (or similarly r^τ) is given by

$$r^\rho = \frac{1}{2}(\rho_U - \rho_L)(1 - \mathrm{DQ}).$$

Note that even $\mathrm{DQ} = 0$ has some value as the new interval is centered around the observation, which already cuts off part of the original uncertainty set Z.

First, we consider the influence of DQ on the ARO decisions for an individual patient. Figure 2.7 shows the results. The worst-case tumor BED is 118.7 Gy for any DQ. Thus, an increase in data quality solely improves average tumor BED. As soon as there is some uncertainty in biomarker, the optimal stage-1 dose increases from 1.50 to 1.77 Gy. Note that there can be other stage-1 doses that are near worst-case optimal or worst-case optimal but not PARO. For the stage-2 decisions, recall (see Section 2.5.3) that for the majority of patients it is worst-case optimal to hyperfractionate. As DQ increases, we observe a linear decrease in the number of fractions N_2, and a corresponding increase in dose per fraction d_2. Thus, for higher DQ, we hypofractionate more often, deviating from the worst-case optimal decision. The bottom-left panel of Figure 2.7 shows that mean tumor BED increases linearly in DQ, with an additional jump when DQ is 1 (i.e., exact data).

In the remainder of this section we set $\mathrm{DQ} = 2/3$, so the obtained information after fraction N_1 reduces the size of the interval by 66.7% around the new observation.

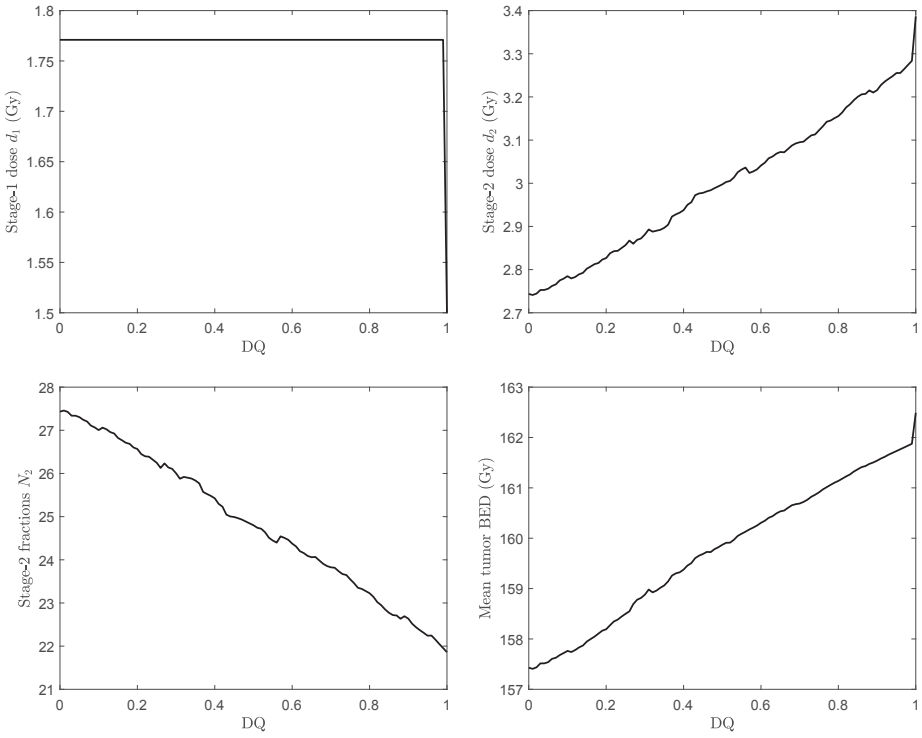

Figure 2.7: Influence of data quality (DQ) on the optimal ARO decisions and resulting mean tumor BED for an individual patient. Results are averaged over 200 (ρ, τ) scenarios, uniform sampled from Z. The worst-case tumor BED is 118.7 Gy for any DQ.

Variations for DQ are considered in Section 2.5.5. For all 20 patients the required auxiliary scenarios for the method of Section 2.4.3 can be found.

Table 2.4 shows the aggregated results. The robust methods RO, RO-FH and ARO are all worst-case optimal. This indicates that, although not theoretically guaranteed, ARO finds an ARO solution in all considered scenarios. The mean performance of RO-FH and ARO is further away from PI than in the case with exact biomarker information (Table 2.2). This is as expected, as due to inexact observations the possibility for ARO and RO-FH to make adjustments is less valuable, whereas PI is not in influenced by this. On the other hand, NOM and NOM-FH are not worst-case optimal, but have better performance on the sample of scenarios, at the cost of OAR violations.

ARO is the only method (together with PI) that has a different stage-1 decision than

	Method					
	NOM	NOM-FH	RO	RO-FH	ARO	PI
Tumor BED - sample mean (Gy)	162.52	161.03	156.38	158.76	159.46	161.16
Tumor BED - sample 5% quantile (Gy)	151.36	150.12	147.04	148.51	148.94	150.21
Tumor BED - sample wc (Gy)	147.79	146.04	144.01	145.02	145.33	146.18
Tumor BED - wc over Z (Gy)	**114.72**	**115.96**	**116.19**	**116.19**	**116.19**	**116.19**
OAR violation - mean (%)	1.25	0.16	0	0	0	0
OAR violation - max (%)	4.23	1.49	0	0	0	0
Stage-1 dose d_1 (Gy)	1.50	1.50	2.29	2.29	1.79	1.65
Stage-2 dose d_2 (Gy)	3.45	3.25	2.48	2.78	2.92	3.20
Stage-2 fractions N_2	20.0	22.0	27.2	24	24.3	22.1

Table 2.4: Results for experiments with inexact biomarker information (data quality DQ = 2/3) and uniform sampling of (ρ, τ) over Z (200 scenarios). All results are averages over a sample of 20 patients. For each scenario, results are averaged over 20 patients*. All methods optimize for worst-case tumor BED in Z, which is displayed in bold.
*: the maximum OAR violation is computed over all patients and scenarios.

in the case with exact biomarker information. This is because it is the only method that takes inexactness of biomarker information into account at the start of stage 1. The average stage-1 dose d_1 differs considerably between ARO and RO-FH, whereas their worst-case performance is equal on average (and equal to PI). This demonstrates the existence of multiple worst-case optimal solutions. Whereas optimizing worst-case optimal solutions for ARO over two auxiliary scenarios does not guarantee a PARO solution (Section 2.4.3), results in Table 2.4 indicate that it does produce solutions that perform slightly better on average than RO-FH.

For ARO, it is noteworthy that the average number of stage-2 fractions (24.3 fx) differs from that of PI (22.1 fx). Although ARO uses optimal decision rules for stage 2, these are optimal for the worst-case scenario in the new uncertainty set $Z_{(\hat{\rho},\hat{\tau})}$, and need not be optimal for the 'true' realization in this set. In fact, NOM-FH treats the inexact biomarker information as the 'true' parameter values, and administers 22.0 fractions, on average, which is closer than that of PI. Although the fractionation decision of NOM-FH is not worst-case optimal, Table 2.4 shows that it performs better on the sample of scenarios.

Figure 2.8 shows the complete cumulative scenario-tumor BED graph for the 'average patient'. Whereas in case of exact biomarker information (Figure 2.6), the ARO line was very close to PI, here a clear difference can be observed. NOM and NOM-FH outperform ARO (and RO and RO-FH) over the entire distribution.

The good performance of NOM and NOM-FH in terms of sample mean tumor BED

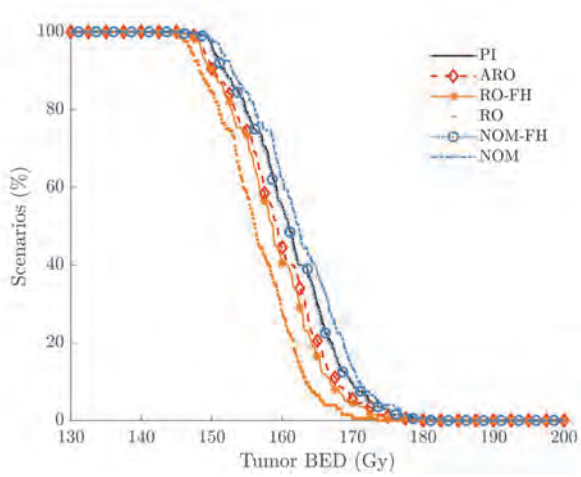

Figure 2.8: Cumulative scenario-tumor BED graph for experiments with inexact biomarker information (data quality DQ $= 2/3$) and uniform sampling of (ρ, τ) over Z (200 scenarios). A point (x, y) indicates that in y% of scenarios the tumor BED (averaged over 20 patients) is at least x Gy. NOM-FH is very close to PI.

does come at the cost of OAR violations. However, these are relatively minor. The reason for this is that the number of stage-2 fractions is relatively high (between 20 and 30fx), so any method delivers reasonably low dose per fraction in stage 2. Consequently, the quadratic term in the BED model is smaller, and so is the influence of the α/β parameters. With higher dose per fraction, the use of incorrect (e.g., nominal) α/β parameter values may result in higher OAR constraint violations. Preliminary experiments for stereotactic body radiation therapy (SBRT, an RT modality that uses around five high dose fractions) indeed result in slightly higher OAR constraint violations for NOM and NOM-FH. In any case, a trade-off can be observed between higher tumor BED attained by NOM and NOM-FH and associated OAR constraint violations.

2.5.5 Optimal moment of biomarker acquisition

The moment of biomarker observation need not be fixed. Part of the decision-making process then involves choosing this observation moment such that it maximally improves treatment quality. Late observation may result in limited possibilities for treatment adaptation, whereas with too early observation one cannot yet reliably observe the true individual patient response. Although one can incorporate N_1 as a decision variable in the mathematical model, the small decision space allows to simply vary its

value in numerical experiments. We assume a (hypothetical) mathematical relationship between information point N_1 and the data quality parameter DQ. With $N^{\max}$ the maximum number of fractions, we consider the following three data quality functions:

$$\mathrm{DQ}_1(N_1) = \left(\frac{N_1}{N^{\max}}\right)^4, \quad \mathrm{DQ}_2(N_1) = \frac{N_1}{N^{\max}}, \quad \mathrm{DQ}_3(N_1) = \left(\frac{N_1}{N^{\max}}\right)^{1/4}.$$

Hence, DQ_1, DQ_2 and DQ_3 describe a convex, linear and concave relationship between observation moment and data quality, respectively. Figure 2.9 shows the graphs of the three functions. Whether DQ_1, DQ_2 or DQ_3 is most realistic depends on the specific biomarker(s) that is/are used, see Section 2.2.2 for details.

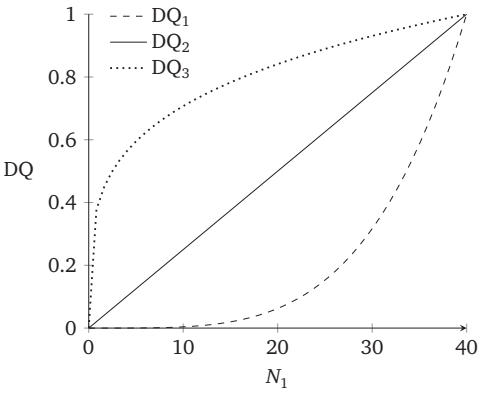

Figure 2.9: The biomarker data quality is a function of the number of treatment fractions N_1 after which it is acquired. We consider three functions $\mathrm{DQ}_i(N_1)$, $i = 1, 2, 3$.

We vary the information point N_1 from 0 to $N^{\max}-1$. Figure 2.10 shows the change in stage-1 dose d_1 (averaged over all patients and scenarios) for linear data quality function DQ_2, for methods PI, ARO, RO/RO-FH and NOM/NOM-FH. Results are very similar for DQ_1 and DQ_3. Recall from Section 2.5.3 that for the majority of (patient, scenario) pairs hypofractionation is optimal. For those cases, if N_1 is very low PI sometimes delivers a high dose boost in stage 1, and a low dose/fx in stage 2. For higher values of N_1 this is not possible anymore, leading to a lower average dose in stage 1 (and a dose boost in stage 2). For NOM/NOM-FH the same holds, because the nominal scenario is a hypofractionation scenario.

Also for ARO it is optimal to start with a higher dose per fraction in stage-1 if N_1 is very low. For slightly higher N_1, starting with a dose boost is no longer possible. For most patients it is worst-case optimal to hyperfractionate, i.e., deliver an equal

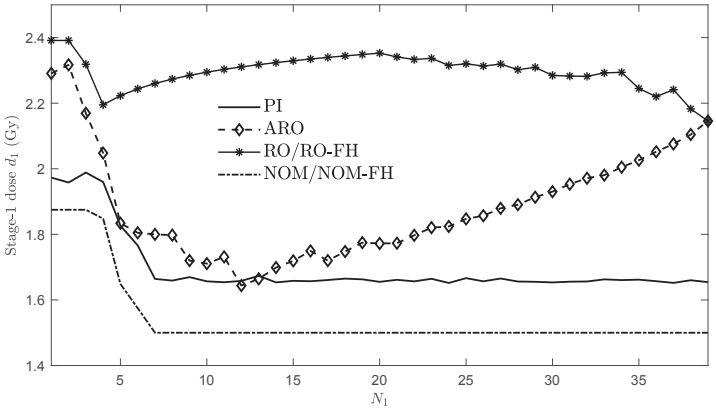

Figure 2.10: Change in stage-1 dose d_1 (averaged over all patients and scenarios) when varying the information point N_1 from 1 to $N^{\max} - 1$, for the linear data quality function $DQ_2(N_1)$.

dose per fraction for $N^{\max}$ fractions. For N_1 around $10 - 20$, worst-case optimality can be attained also with lower dose per fraction in stage 1. This tends to be the PARO solution, because it enables a higher dose boost in stage 2 for hypofractionation scenarios. For higher N_1, it is often not possible to achieve worst-case optimality (in hyperfractionation scenarios) if we deliver a low dose per fraction in stage 1. This leads to a gradual shift from low dose to medium dose per fraction in stage 1 as N_1 increases.

Figure 2.11 shows the mean tumor BED values and OAR constraint violations for varying N_1, for data quality functions $\mathrm{DQ}_i(N_1)$, $i = 1, 2, 3$. The left vertical axis indicates the mean tumor BED (averaged over all patients and scenarios), the right vertical axis indicates the maximum OAR tolerance violation for NOM and NOM-FH. It is important to note that as N_1 increases past $N^{\min} = 30$, this also increases the minimum number of fractions correspondingly. Moreover, the dose per fraction is constant per treatment stage, so the choice of N_1 also influences the types of treatments that can be delivered.

For these reasons the curve for PI is not constant, even though it does not actually use biomarker information. The optimal moment of biomarker acquisition for PI is $N_1 = 29$. This is because the minimum number of fractions is $N^{\min} = 30$. Hence, if hypofractionation is optimal we can deliver one more fraction with high dose, and deliver a low dose in stage 1. If hyperfractionation is optimal we can deliver 11 more

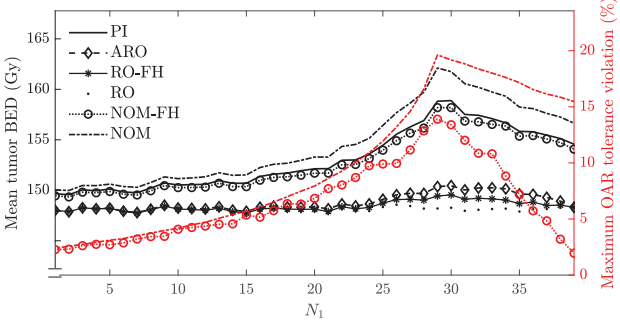

(a) DQ_1 (convex)

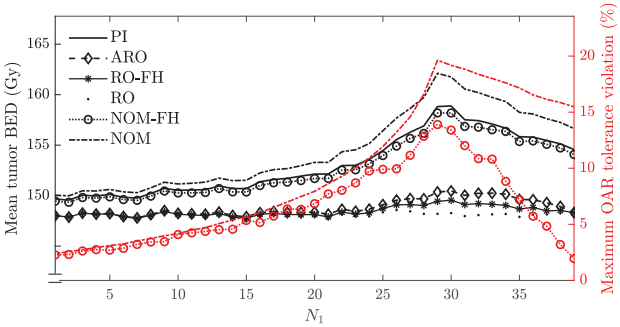

(b) DQ_2 (linear)

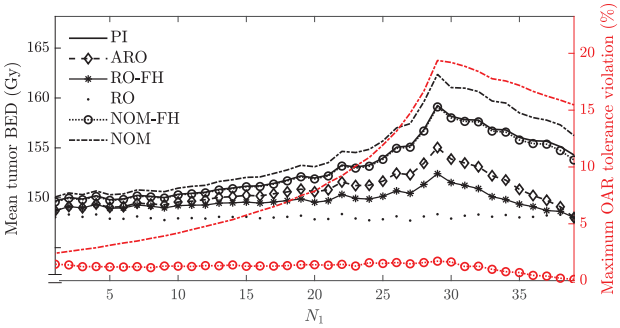

(c) DQ_3 (concave)

Figure 2.11: Change in mean tumor BED and OAR constraint violation when varying the information point N_1 from 1 to $N^{\max} - 1$, for data quality functions $DQ_i(N_1)$, $i = 1, 2, 3$. The maximum OAR BED constraint violation (%) of NOM (dash-dotted) and NOM-FH (dotted, circle marker) is measured against the right vertical axis. Note that the left vertical axis measures displays the mean tumor BED (averaged over all patients and scenarios), while the methods maximize the worst-case tumor BED per patient.

fractions (and get the total maximum of 40) with low dose. Having $N_1 > 29$ forces the use of more than $N_2^{\min} = 30$ fractions, which is disadvantageous for those (patient, scenario) cases where hypofractionation is optimal.

For the latter reason the NOM curve is also not constant. It results in a higher tumor BED than PI for any value of N_1, at the cost of OAR violations of up to 20%. NOM-FH yields a sample mean tumor BED close to PI for all three DQ functions, and the OAR violations depend on the DQ function. With poor data quality (Figure 2.11a) and an observation moment close to $N_1 = 29$, OAR violations over 10% are possible, despite the fact that NOM-FH is an adaptive method. On the other hand, with good (Figure 2.11a) data quality, the violations remain below 2%. The OAR tolerance violations are highest near $N_1 = 29$. This is because in case of hypofractionation in stage 2 the influence of the uncertain α/β parameters is highest, as was noted in Section 2.5.4.

The robust methods RO, RO-FH and ARO do not result in any OAR violations, by construction. The better the data quality, the larger the differences between RO, RO-FH and ARO. This implies that, if robustness is required, there is value in (i) adapting based on inexact information, (ii) taking adaptability into account when planning the stage-1 dose. The good performance of NOM-FH shows that this value diminishes if OAR violations are allowed. NOM-FH does not account for adaptability, and does not take inexactness of biomarker information into account. Nevertheless, it results in higher sample mean tumor BED for any N_1, and the difference increases from poor (convex) to good (concave) data quality. Thus, Figure 2.11c illustrates the trade-off between higher sample mean tumor BED and possible OAR violations that was also observed in Section 2.5.4 (for the entire sample distribution).

The shape of the data quality function influences the optimal moment of biomarker observation only slightly. For all adaptive methods, we find that the peak is more pronounced for high data quality (concave) than low data quality (convex), but it is centered around $N_1 = 29$. In case of convex data quality the peak is relatively flat, indicating a trade-off between observing at $N_1 = 29$ (giving maximum adaptation flexibility) and postponing (waiting for higher data accuracy).

2.6 Concluding remarks

In this chapter we have presented an ARO approach to optimally adapt the treatment length of radiation therapy treatments, using mid-treatment biomarker information. Using an ARO approach, adaptability is taken into account prior to treatment and it provides insight into the optimal stage-2 decisions.

In the case of exact biomarker information, there is sufficient space to adapt, and numerical results show that taking into account both robustness and adaptability is

not necessary. In the case of inexact biomarker information, adaptive strategies can use only parameter estimates instead of true parameter values, and may still result in violations if this uncertainty is not accounted for. Accounting for adaptability and inexactness of biomarker information is particularly beneficial when robustness (w.r.t. OAR violations) is of high importance. If minor OAR violations are allowed, NOM-FH is a good performing alternative, which can outperform ARO. NOM-FH and ARO thus present a trade-off between higher performance and OAR violations. Both the difference in performance and the magnitude of OAR violations of NOM-FH are highly influenced by the data quality (i.e., accuracy of parameter estimates).

The current setting can be extended in several ways. In practice the tumor and OAR α/β values would have to be estimated from actual biomarkers (e.g., imaging, blood-based biomarkers, genotyping), which can be incorporated in the model. Furthermore, the approach can be extended to heterogeneous tumor response (different α/β ratios for different tumor subvolumes), or time-dependent response parameters. Other RT applications may also benefit from ARO, such as re-optimization to account for organ motion or setup errors, optimization using the MR-linac or combining RT with chemotherapy.

2.A Results exact biomarker information: out-of-sample performance

To investigate the out-of-sample performance of the methods, we assume a uniform distribution for (ρ, τ) over a larger set than Z. We can write Z as

$$Z = \{(\rho,\tau) : \rho_L \leq \rho \leq \rho_U, \tau_L \leq \tau \leq \tau_U\} = \{(\rho,\tau) : |\bar{\rho} - \rho| \leq \varepsilon_\rho,\ |\bar{\tau} - \tau| \leq \varepsilon_\tau\},$$

where $(\varepsilon_\rho, \varepsilon_\tau)$ is the maximum deviation from the nominal scenario $(\bar{\rho}, \bar{\tau})$. This allows us to define

$$Z_c := \{(\rho,\tau) : |\bar{\rho} - \rho| \leq c\varepsilon_\rho,\ |\bar{\tau} - \tau| \leq c\varepsilon_\tau\},$$

where $c > 0$ is a parameter. We assume a uniform distribution over the new set Z_c. If $c = 1$, we have $Z_c = Z$, so we sample exactly from Z. If $c > 1$, we sample from an interval that is c^2 times as large as Z (c times larger for both ρ and τ). For $c = 2$ we obtain the results in Table 2.A.1. The stage-1 dose d_1 is the same as in Table 2.2 for all methods except PI, because PI is the only method that is aware that the sample is not taken from uncertainty set Z but from Z_2. For NOM, the maximum violation percentage has increased slightly. All other methods are able to deal with the out-of-sample realizations and do not have any OAR constraint violations.

Due to the larger sampling space (the area of Z_2 is four times the area of Z), the difference between sample mean and sample worst-case performance is much larger than in Table 2.2 for

	Method					
	NOM	NOM-FH	RO	RO-FH	ARO	PI
Tumor BED - sample mean (Gy)	156.49	158.92	151.30	156.83	158.87	159.06
Tumor BED - sample 5% quantile (Gy)	140.14	142.11	137.55	141.11	142.11	142.32
Tumor BED - sample wc (Gy)	134.06	136.80	132.56	136.09	136.79	137.12
Tumor BED - wc over Z (Gy)	**114.72**	**116.19**	**116.19**	**116.19**	**116.19**	**116.19**
OAR violation - mean (%)	1.16	0	0	0	0	0
OAR violation - max (%)	5.30	0	0	0	0	0
Stage-1 dose d_1 (Gy)	1.50	1.50	2.29	2.29	1.51	1.73
Stage-2 dose d_2 (Gy)	3.45	3.21	2.48	2.92	3.21	3.15
Stage-2 fractions N_2	20	22.9	27.2	22.9	22.9	22.9

Table 2.A.1: Results for experiments with exact biomarker information and uniform sampling of (ρ, τ) over Z_2. For each scenario, results are averaged over 20 patients*. All methods optimize for worst-case tumor BED in Z, which is displayed in bold.
*: the maximum OAR violation is computed over all patients and scenarios

all methods. The true worst-case objective value in Z is still lower than the sample worst-case in Z_2. The reason for this is that the true worst-case scenario can differ per patient.

NOM-FH and ARO are near optimal for the worst-case sample scenario, and are also close to PI in the sample 5% quantile and sample mean. The relative performance of the adaptive methods remains mostly unchanged, RO-FH performs slightly worse than NOM-FH and ARO, similar to Table 2.2. Compared to Table 2.2, NOM and RO have poor performance across the sample. This indicates bad performance of the static methods on scenarios outside of Z.

Figure 2.A.1 shows the complete cumulative scenario-tumor BED graph for the 'average patient'. Compared to Figure 2.6, the main difference is the decrease in performance of NOM. Naturally, the performance of static nominal optimization is directly related to the magnitude of possible deviations from the nominal scenario, which is higher in Z_2 than in Z.

2.B Extra analyses and proofs

For convenience, we repeat the definitions of functions B, g and f:

$$B(d', N'; \rho) := \varphi D\Big(1 + \frac{\varphi D}{T}\rho\Big) - \sigma d_1 N_1 - \sigma^2 \rho d_1^2 N_1, \tag{2.B.1a}$$

$$g(d', N', N''; \rho) := \frac{-1 + \sqrt{1 + \frac{4\rho}{N''} B(d', N'; \rho)}}{2\sigma\rho}, \tag{2.B.1b}$$

$$f(d_1, N_2; \rho, \tau) := \begin{cases} N_1 d_1 + N_2 g(d_1, N_1, N_2; \rho) & \\ +\tau\big(N_1 d_1^2 + N_2 g(d_1, N_1, N_2; \rho)^2\big) & \text{if } d_1 \in [0, g(0, 0, N_1; \rho)] \\ -\infty & \text{otherwise,} \end{cases} \tag{2.B.1c}$$

see (2.5), (2.6) and (2.10).

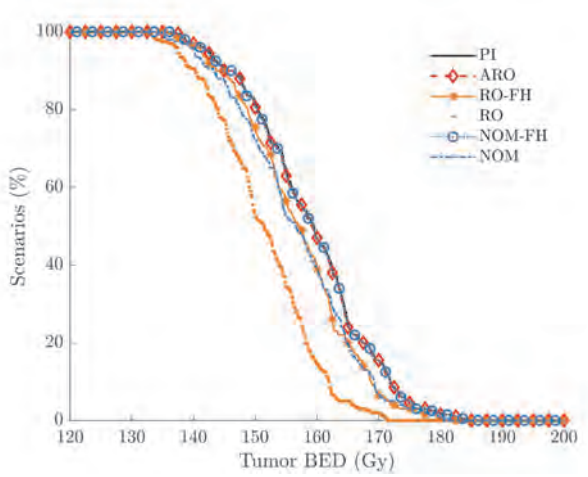

Figure 2.A.1: Cumulative scenario-tumor BED graph for experiments with exact biomarker information and uniform sampling of (ρ, τ) over Z_2 (200 scenarios). A point (x, y) indicates that in y% of scenarios the tumor BED (averaged over 20 patients) is at least x Gy. ARO and NOM-FH are very close to PI.

2.B.1 Proof Theorem 2.7

First, we show that for fixed d_1, feasible to (2.4), and given (ρ, τ), it is optimal to minimize the number of stage-2 fractions if $\tau \geq \sigma\rho$, and it is optimal to maximize the number of stage-2 fractions otherwise. After that, we show that with stage-2 dose d_2 such that (2.4b) holds with equality, $N_2(\rho, \tau) = N_2^{\min}$ is feasible if $\tau \geq \sigma\rho$ and $N_2(\rho, \tau) = N_2^{\max}$ is feasible otherwise.

Consider problem (2.4). At the start of stage 2, we have delivered N_1 fractions with dose d_1 per fraction. Let (ρ, τ) be the realization of the uncertain parameters. The stage-2 problem reads

$$N_1 d_1 + \tau N_1 d_1^2 + \max_{d_2, N_2} \; N_2 d_2 + \tau N_2 d_2^2, \tag{2.B.2a}$$

$$\text{s.t.} \;\; \sigma N_2 d_2 + \rho\sigma^2 N_2 d_2^2 \leq B(d_1, N_1, \rho), \tag{2.B.2b}$$

$$d_2 \geq d_{\min}, \tag{2.B.2c}$$

$$N_2 \in \{N_2^{\min}, \ldots, N_2^{\max}\}. \tag{2.B.2d}$$

This is a static fractionation problem. Constraint (2.B.2b) will hold with equality at the optimum, because it is the only dose-limiting constraint. This yields

$$d_2^*(d_1, N_2; \rho) = g(d_1, N_1, N_2; \rho). \tag{2.B.3}$$

Secondly, this allows us to rewrite the objective to

$$\max_{d_2,N_2} \; N_2 d_2\Big(\frac{\sigma\rho-\tau}{\sigma\rho}\Big)+\frac{\tau B(d_1,N_1,\rho)}{\sigma^2\rho},$$

which implies that if $\tau > \sigma\rho$ it is optimal to minimize d_2N_2. If $\tau < \sigma\rho$ it is optimal to maximize d_2N_2, and if $\tau = \sigma\rho$ the objective value is independent of the value of N_2. Similar results are obtained in Mizuta et al. (2012); Bortfeld et al. (2015). As given in Section 2.3, at the optimum

$$N_2 d_2^*(d_1,N_2;\rho) = N_2 g(d_1,N_1,N_2;\rho) = \frac{-N_2+\sqrt{N_2^2+4N_2\rho B(d_1,N_1;\rho)}}{2\sigma\rho},$$

and it is straightforward to show that

$$\frac{\partial N_2 g(d_1,N_1,N_2;\rho)}{\partial N_2} \geq 0.$$

Hence, if $\tau > \sigma\rho$, it is optimal to minimize the number of fractions, and if $\tau < \sigma\rho$ it is optimal to maximize the number of fractions. If $\tau = \sigma\rho$, every feasible number of fractions is optimal.

For the second part, we must show that for any $(\rho,\tau) \in Z \cap \{\tau \geq \sigma\rho\}$ resp. $(\rho,\tau) \in Z \cap \{\tau < \sigma\rho\}$, it is indeed possible to deliver $N_2^{\min}$ resp. $N_2^{\max}$ fractions with dose according to (2.B.3) in stage 2. That is, we must show

$$g(d_1,N_1,N_2^{\min};\rho) \geq d^{\min}, \quad \forall(\rho,\tau)\in Z\cap\{\tau\geq\sigma\rho\},$$
$$g(d_1,N_1,N_2^{\max};\rho) \geq d^{\min}, \quad \forall(\rho,\tau)\in Z\cap\{\tau<\sigma\rho\},$$

which is equivalent to

$$d_1 \leq g(d^{\min},N_2^{\min},N_1;\rho), \quad \forall(\rho,\tau)\in Z\cap\{\tau\geq\sigma\rho\}, \tag{2.B.4a}$$
$$d_1 \leq g(d^{\min},N_2^{\max},N_1;\rho), \quad \forall(\rho,\tau)\in Z\cap\{\tau<\sigma\rho\}. \tag{2.B.4b}$$

Lemma 2.17a states that g is increasing or decreasing in ρ for a fixed first argument. Hence, it is sufficient to consider only the largest and smallest value of ρ in either subset of Z. Therefore, (2.B.4) is equivalent to

$$d_1 \leq g(d^{\min},N_2^{\min},N_1;\rho_L), \tag{2.B.5a}$$
$$d_1 \leq g(d^{\min},N_2^{\min},N_1;\min\{\frac{\tau_U}{\sigma},\rho_U\}), \tag{2.B.5b}$$
$$d_1 \leq g(d^{\min},N_2^{\max},N_1;\frac{\tau_L}{\sigma}), \tag{2.B.5c}$$
$$d_1 \leq g(d^{\min},N_2^{\max},N_1;\rho_U). \tag{2.B.5d}$$

From (2.B.1b) we see that function g is decreasing in its second argument, so (2.B.5b) is redundant. The remaining three conditions in (2.B.5) hold true due to Assumption 2.1. Hence, an optimal decision rule for $N_2(\cdot)$ is given by

$$N_2^*(\rho,\tau) = \begin{cases} N_2^{\min} & \text{if } \tau \geq \sigma\rho \\ N_2^{\max} & \text{otherwise,} \end{cases} \tag{2.B.6}$$

and

$$d_2^*(d_1;\rho,\tau)=\begin{cases} g(d_1,N_1,N_2^{\min};\rho) & \text{if } \tau \geq \sigma\rho \\ g(d_1,N_1,N_2^{\max};\rho) & \text{otherwise.} \end{cases} \tag{2.B.7}$$

are optimal decision rules for $N_2(\cdot)$ and $d_2(\cdot)$, respectively. For $\tau \neq \sigma\rho$, these give the unique optimal decisions. For $\tau = \sigma\rho$ any $N_2 \in \{N_2^{\min},\ldots,N_2^{\max}\}$ is optimal, and the corresponding optimal d_2 follows according to (2.B.3).

2.B.2 Proof Theorem 2.10

Due to Theorem 2.7 a stage-1 decision d_1 is $\mathcal{PARO}$ according to Definition 2.9 if conditions (2.14) hold with $(d_2^*(\cdot), N_2^*(\cdot))$ plugged in. Thus, we must show that for any $d_1 \in X^{\text{PARO}}$ there is no $\mathcal{ARO}$ $\bar{d}_1$ such that

$$\begin{aligned} &f(d_1,N_2^*(\rho,\tau);\rho,\tau) \leq f(\bar{d}_1,N_2^*(\rho,\tau);\rho,\tau) \;\; \forall(\rho,\tau)\in Z, \\ &f(d_1,N_2^*(\bar{\rho},\bar{\tau});\bar{\rho},\bar{\tau}) < f(\bar{d}_1,N_2^*(\bar{\rho},\bar{\tau});\bar{\rho},\bar{\tau}) \quad \text{for some } (\bar{\rho},\bar{\tau})\in Z. \end{aligned}$$

If $|X^{\text{PARO}}| = 1$, then the single element yields a strictly better objective value than all other elements in X^{ARO} in either scenario $(\rho^{\text{aux-min}},\tau^{\text{aux-min}})$ or $(\rho^{\text{aux-max}},\tau^{\text{aux-max}})$ or both, so it is $\mathcal{PARO}$. For the remainder of this proof we assume $|X^{\text{PARO}}| \geq 2$.

Consider $X^{\text{aux-min}}$. By construction of $(\rho^{\text{aux-min}},\tau^{\text{aux-min}})$ it holds that $\tau^{\text{aux-min}} \neq \sigma\rho^{\text{aux-min}}$. Hence, according to Lemma 2.18, there can be at most two values for d_1 in $X^{\text{aux-min}}$ that yield the same objective value f in scenario $(\rho^{\text{aux-min}},\tau^{\text{aux-min}})$. Hence, $|X^{\text{aux-min}}| = |X^{\text{PARO}}| = 2$. Denote the two elements of X^{PARO} by d_1' and d_1'', let $d_1' < d_1''$. Solutions d_1' and d_1'' are both optimal to (2.15) and (2.16). Hence, according to Lemma 2.18, it holds that

$$d_1'' = t(d_1';\rho^{\text{aux-min}},\tau^{\text{aux-min}}), \tag{2.B.8a}$$
$$d_1'' = t(d_1';\rho^{\text{aux-max}},\tau^{\text{aux-max}}). \tag{2.B.8b}$$

From the definition of t (see (2.C.13)) we derive for $\sigma\rho \neq \tau$:

$$\frac{\partial\, t(d_1;\rho,\tau)}{\partial\rho} = \frac{2N_2^*(\rho,\tau)}{N_1+N_2^*(\rho,\tau)} \frac{\partial\, g(d_1,N_1,N_2^*(\rho,\tau);\rho)}{\partial\rho},$$

because $N_2^*(\rho,\tau)$ is constant in ρ unless $\sigma\rho=\tau$. According to Lemma 2.17a, if for given N_2 it holds that $d_1 \neq d_1^-(N_2)$ and $d_1 \neq d_1^+(N_2)$ (defined in (2.C.3)), then function $g(d_1,N_1,N_2,\rho)$ is strictly increasing or decreasing in ρ. By construction, it holds that $d_1^+(N_2) = t(d_1^-(N_2);\rho,\tau)$ for any ρ. According to Lemma 2.16b, we have $d_1^-(N_2^{\min}) \neq d_1^-(N_2^{\max})$, so d_1' cannot be equal to both. Additionally, it cannot hold that $d_1' = d_1^+(N_2^{\min})$ or $d_1' = d_1^+(N_2^{\max})$, because it would imply $d'' \leq d'$. Hence, either $d_1' \notin \{d_1^-(N_2^{\min}), d_1^+(N_2^{\min})\}$ or $d_1' \notin \{d_1^-(N_2^{\max}), d_1^+(N_2^{\max})\}$ holds (or both).

We show that in either case, we can construct two new scenarios where d_1' outperforms d_1'' in one scenario, and vice versa in the other. Suppose $d_1' \notin \{d_1^-(N_2^{\min}), d_1^+(N_2^{\min})\}$. In this case, it holds that

$$\frac{\partial\, t(d_1'; \rho^{\text{aux-min}}, \tau^{\text{aux-min}})}{\partial \rho} \neq 0. \tag{2.B.9}$$

We consider two new scenarios. Let $\varepsilon > 0$ be a sufficiently small number and define

$$(\rho_1, \tau_1) := (\rho^{\text{aux-min}} - \varepsilon, \tau^{\text{aux-min}}), \qquad (\in \text{int}(Z^{\min}))$$
$$(\rho_2, \tau_2) := (\rho^{\text{aux-min}} + \varepsilon, \tau^{\text{aux-min}}). \qquad (\in \text{int}(Z^{\min}))$$

This is visualized in Figure 2.B.1. Due to (2.B.9) and (2.B.8a), it holds that

$$\big(t(d_1'; \rho_1, \tau_1) > d'' \wedge t(d_1'; \rho_2, \tau_2) < d''\big) \vee \big(t(d_1'; \rho_1, \tau_1) < d'' \wedge t(d_1'; \rho_2, \tau_2) > d''\big). \tag{2.B.10}$$

If the first clause is true, we obtain

$$f(d_1', N_2^{\min}; \rho_1, \tau_1) > f(d_1'', N_2^{\min}; \rho_1, \tau_1),$$
$$f(d_1', N_2^{\min}; \rho_2, \tau_2) < f(d_1'', N_2^{\min}; \rho_2, \tau_2),$$

where we used convexity of $f(d_1, N_2^{\min}; \rho, \tau)$ for $(\rho, \tau) \in \text{int}(Z^{\min})$. Similarly, if the second clause of (2.B.10) is true, we obtain

$$f(d_1', N_2^{\min}; \rho_1, \tau_1) < f(d_1'', N_2^{\min}; \rho_1, \tau_1),$$
$$f(d_1', N_2^{\min}; \rho_2, \tau_2) > f(d_1'', N_2^{\min}; \rho_2, \tau_2).$$

In either case, there is a scenario in $Z^{\min}$ where d_1' outperforms d_1'' and a scenario in $Z^{\min}$ where d_1'' outperforms d_1'. Hence, both d_1' and d_1'' are $\mathcal{PARO}$. Using similar arguments, we can show that in case $d_1' \notin \{d_1^-(N_2^{\max}), d_1^+(N_2^{\max})\}$ also both d_1' and d_1'' are $\mathcal{PARO}$.

2.B.3 Proof Theorem 2.14

Consider problem (2.18). At the start of stage 2, we have delivered N_1 fractions with dose d_1 per fraction. Let $(\hat{\rho}, \hat{\tau})$ be the observation. The resulting stage-2 problem for (2.18) reads

$$\max_{d_2, N_2} \quad \min_{(\rho,\tau)\in Z_{(\hat{\rho},\hat{\tau})}} \quad (N_1 d_1 + N_2 d_2) + \tau(N_1 d_1^2 + N_2 d_2^2), \tag{2.B.11a}$$
$$\text{s.t.} \quad \sigma N_2 d_2 + \rho\sigma^2 N_2 d_2^2 \leq B(d_1, N_1, \rho), \quad \forall (\rho, \tau) \in Z_{\hat{\rho},\hat{\tau}}, \tag{2.B.11b}$$
$$d_2 \geq d_{\min}, \tag{2.B.11c}$$
$$N_2 \in \{N_2^{\min}, \ldots, N_2^{\max}\}. \tag{2.B.11d}$$

This is a static robust optimization problem. Constraint (2.B.11b) will hold with equality at the optimum, because it is the only dose-limiting constraint. Solving for d_2 yields the constraint

$$d_2 = g(d_1, N_1, N_2; \rho), \quad \forall (\rho, \tau) \in Z_{(\hat{\rho},\hat{\tau})},$$

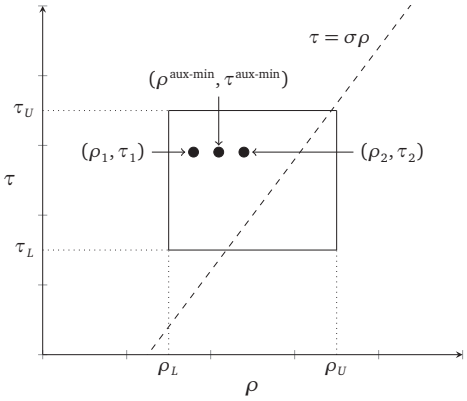

Figure 2.B.1: Case $d_1' \neq d_1^{-}(N_2^{\min})$. Construction of two new scenarios (ρ_1, τ_1) and (ρ_2, τ_2) from scenario $(\rho^{\text{aux-min}}, \tau^{\text{aux-min}})$. Solution d_1' outperforms d_1'' at one scenario, vice versa at the other.

and this is used to rewrite (2.B.11a) and (2.B.11b) in terms of functions f and g. Problem (2.B.11) is equivalent to

$$\max_{N_2} \quad \min_{(\rho,\tau)\in Z_{(\hat{\rho},\hat{\tau})}} \quad f(d_1, N_2, \rho, \tau), \tag{2.B.12a}$$

$$\text{s.t.} \quad g(d_1, N_1, N_2; \rho) \geq d^{\min}, \quad \forall (\rho, \tau) \in Z_{(\hat{\rho},\hat{\tau})}, \tag{2.B.12b}$$

$$N_2 \in \{N_2^{\min}, \ldots, N_2^{\max}\}. \tag{2.B.12c}$$

Similar to the exact case (Section 2.3), in any worst-case realization it will hold that τ is at its lowest value, so it is sufficient to consider only those observations $(\rho, \tau) \in Z_{(\hat{\rho},\hat{\tau})}$ with $\tau = \hat{\tau}_L$. Additionally, according to Lemma 2.17 functions f and g are increasing or decreasing in ρ. Hence, there are two candidate worst-case scenarios: $(\hat{\rho}_L, \hat{\tau}_L)$ and $(\hat{\rho}_U, \hat{\tau}_L)$. We can rewrite (2.B.12) to

$$\max_{N_2} \quad \min\left\{f(d_1, N_2, \hat{\rho}_L, \hat{\tau}_L),\ f(d_1, N_2, \hat{\rho}_U, \hat{\tau}_L)\right\}, \tag{2.B.13a}$$

$$\text{s.t.} \quad g(d_1, N_1, N_2; \hat{\rho}_L) \geq d^{\min}, \tag{2.B.13b}$$

$$g(d_1, N_1, N_2; \hat{\rho}_U) \geq d^{\min}, \tag{2.B.13c}$$

$$N_2 \in \{N_2^{\min}, \ldots, N_2^{\max}\}. \tag{2.B.13d}$$

We distinguish three cases:

- Case $(\hat{\rho}, \hat{\tau}) \in Z_{\text{ID}}^{\max}$: Analogous to the proof of Theorem 2.7, one can show that for any realization $(\rho, \tau) \in Z_{(\hat{\rho},\hat{\tau})}$ it is optimal to maximize the number of fractions in stage

2. We plug in $N_2^*(\rho,\tau) = N_2^{\max}$ and show that it is feasible. Constraints (2.B.13b) and (2.B.13c) reduce to

$$\min\left\{g(d_1,N_1,N_2^{\max};\hat{\rho}_L), g(d_1,N_1,N_2^{\max};\hat{\rho}_U)\right\} \geq d^{\min},$$

which is equivalent to

$$d_1 \leq \min\left\{g(d^{\min},N_2^{\max},N_1;\hat{\rho}_L), g(d^{\min},N_2^{\max},N_1;\hat{\rho}_U)\right\}. \tag{2.B.14}$$

It holds that $\hat{\rho}_L \geq \frac{\hat{\tau}_L}{\sigma} \geq \frac{\tau_L}{\sigma}$, and $\hat{\rho}_U \leq \rho_U$. According to Lemma 2.17a function g is either increasing or decreasing in ρ for other arguments fixed. Hence, by Assumption 2.11 condition (2.B.14) holds. Hence, $N_2^*(\rho,\tau) = N_2^{\max}$ is feasible and optimal. Thus, (2.B.12) equals

$$\min\left\{f(d_1,N_2^{\max},\hat{\rho}_L,\hat{\tau}_L),\ f(d_1,N_2^{\max},\hat{\rho}_U,\hat{\tau}_L)\right\}.$$

By definition of f, this implies

$$d_2 = \min\left\{g(d_1,N_1,N_2^{\max};\hat{\rho}_L), g(d_1,N_1,N_2^{\max};\hat{\rho}_U)\right\}.$$

- Case $(\hat{\rho},\hat{\tau}) \in Z_{\mathrm{ID}}^{\min}$: Similar to the previous case. Analogous to the proof of Theorem 2.7, one can show that for any realization $(\rho,\tau) \in Z_{(\hat{\rho},\hat{\tau})}$ it is optimal to minimize the number of fractions in stage 2. We plug in $N_2^*(\rho,\tau) = N_2^{\min}$ and show that it is feasible. Similar to the previous case, constraints (2.B.13b) and (2.B.13c) reduce to

$$d_1 \leq \min\left\{g(d^{\min},N_2^{\min},N_1;\hat{\rho}_L), g(d^{\min},N_2^{\min},N_1;\hat{\rho}_U)\right\}. \tag{2.B.15}$$

It holds that $\hat{\rho}_L \geq \rho_L$, and $\hat{\rho}_U \leq \rho_U$. Hence, by Assumption 2.11, Lemma 2.17a and using the fact that function g is decreasing in its second argument, condition (2.B.15) holds. Hence, $N_2^*(\rho,\tau) = N_2^{\min}$ is feasible and optimal. Similar to the previous case, we find

$$d_2 = \min\left\{g(d_1,N_1,N_2^{\min};\hat{\rho}_L), g(d_1,N_1,N_2^{\min};\hat{\rho}_U)\right\}.$$

- Case $(\hat{\rho},\hat{\tau}) \in Z_{\mathrm{ID}}^{\mathrm{int}}$: The optimal number of fractions in stage-2 is not known a priori. By definition of $Z_{\mathrm{ID}}^{\mathrm{int}}$, it holds that $\hat{\rho}_L \geq \max\{\rho_L, \frac{\tau_L}{\sigma} - 2r^{\rho})\}$ and $\hat{\rho}_U \leq \rho_U$. By Assumption 2.11 it holds that

$$d_1 \leq \min\left\{g(d^{\min},N_2^{\max},N_1;\max\{\rho_L,\frac{\tau_L}{\sigma}-2r^{\rho})\}, g(d^{\min},N_2^{\max},N_1;\rho_U)\right\}. \tag{2.B.16}$$

Lemma 2.17a, the fact that function g is decreasing in its third argument and (2.B.16) together imply that (2.B.13b) and (2.B.13c) hold for any feasible N_2. Hence, from problem (2.B.13) we derive

$$N_2^*(d_1;\hat{\rho},\hat{\tau}) = \underset{N_2\in\{N_2^{\min},\ldots,N_2^{\max}\}}{\arg\max} \min\left\{f(d_1,N_2,\hat{\rho}_L,\hat{\tau}_L),\ f(d_1,N_2,\hat{\rho}_U,\hat{\tau}_L)\right\},$$

and by definition of f the corresponding value for d_2 is

$$d_2 = \min\left\{g(d_1, N_1, N_2^*(d_1;\hat{\rho},\hat{\tau});\hat{\rho}_L), g(d_1, N_1, N_2^*(d_1;\hat{\rho},\hat{\tau});\hat{\rho}_U)\right\}.$$

Combining the above three cases, we arrive at the optimal decision rules (2.20) and (2.21) for fixed d_1.

2.B.4 Extra analysis to Section 2.4

This analysis makes use of the lemmas in Appendix 2.C. Consider problem (2.18). For given d_1, the optimal stage-2 decision rules are given by Theorem 2.14. As stated in Section 2.4, we split the uncertainty set Z into three subsets. This enables us to exploit the fact that depending on $(\hat{\rho},\hat{\tau})$ the value $N_2^*(d_1;\hat{\rho},\hat{\tau})$ may be known in advance. The split (2.19) is repeated here for convenience

$$Z_{\text{ID}}^{\min} = \{(\hat{\rho},\hat{\tau}) \in Z : \hat{\tau}_L \geq \sigma\hat{\rho}_U\}, \tag{2.B.17a}$$
$$Z_{\text{ID}}^{\text{int}} = \{(\hat{\rho},\hat{\tau}) \in Z : \sigma\hat{\rho}_L < \hat{\tau}_L < \sigma\hat{\rho}_U\}, \tag{2.B.17b}$$
$$Z_{\text{ID}}^{\max} = \{(\hat{\rho},\hat{\tau}) \in Z : \hat{\tau}_L \leq \sigma\hat{\rho}_L\}, \tag{2.B.17c}$$

so that $Z = Z_{\text{ID}}^{\min} \cup Z_{\text{ID}}^{\text{int}} \cup Z_{\text{ID}}^{\max}$. The associated sets of observation-realization pairs $(\rho,\tau,\hat{\rho},\hat{\tau})$ are given by

$$U^i = U \cap \{(\rho,\tau,\hat{\rho},\hat{\tau}) : (\hat{\rho},\hat{\tau}) \in Z_{\text{ID}}^i\}, \quad i \in \{\min, \text{int}, \max\},$$

so it holds that $U = U^{\min} \cup U^{\text{int}} \cup U^{\max}$. Set U^i can be interpreted as the set of observation-realization pairs for which the observation $(\hat{\rho},\hat{\tau})$ is in set Z_{ID}^i. Figure 2.4 illustrates the subsets Z_{ID}^i. Set $U^{\min}$ consists of those observation-realization pairs $(\rho,\tau,\hat{\rho},\hat{\tau})$ for which $N_2^*(d_1;\hat{\rho},\hat{\tau}) = N_2^{\max}$. If $(\rho,\tau,\hat{\rho},\hat{\tau}) \in U^{\text{int}}$, then based on the observation $(\hat{\rho},\hat{\tau})$ it is unclear what fractionation is worst-case optimal. Last, if $(\rho,\tau,\hat{\rho},\hat{\tau}) \in U^{\max}$ we know $N_2^*(d_1;\hat{\rho},\hat{\tau}) = N_2^{\min}$. Problem (2.18) is equivalent to

$$\max_{d_1,q} \; q, \tag{2.B.18a}$$
$$\text{s.t.} \; q \leq f(d_1, N_2^{\min};\rho,\tau), \quad \forall(\rho,\tau,\hat{\rho},\hat{\tau}) \in U^{\min}, \tag{2.B.18b}$$
$$q \leq f(d_1, N_2^*(d_1;\hat{\rho},\hat{\tau});\rho,\tau), \quad \forall(\rho,\tau,\hat{\rho},\hat{\tau}) \in U^{\text{int}}, \tag{2.B.18c}$$
$$q \leq f(d_1, N_2^{\max};\rho,\tau), \quad \forall(\rho,\tau,\hat{\rho},\hat{\tau}) \in U^{\max}, \tag{2.B.18d}$$
$$d^{\min} \leq d_1 \leq d_1^{\max}. \tag{2.B.18e}$$

Similar to the exact case (Section 2.3), in any worst-case realization it will hold that $\tau = \tau_L$. Therefore, any observation with $\hat{\tau} - r^\tau > \tau_L$ cannot yield the worst-case realization. Define

$$U_L^i = U_i \cap \{(\rho,\tau,\hat{\rho},\hat{\tau}) : \hat{\tau} - r^\tau \leq \tau_L\}, \quad i \in \{\min, \text{int}, \max\},$$

which is the subset of U^i of observation-realization pairs for which τ_L is a possible realization of τ. Constraints (2.B.18b)-(2.B.18e) can be replaced by

$$q \leq f(d_1, N_2^{\min}; \rho, \tau), \quad \forall (\rho, \tau, \hat{\rho}, \hat{\tau}) \in U_L^{\min}, \tag{2.B.19a}$$
$$q \leq f(d_1, N_2^{*}(d_1; \hat{\rho}, \hat{\tau}); \rho, \tau), \quad \forall (\rho, \tau, \hat{\rho}, \hat{\tau}) \in U_L^{\text{int}}, \tag{2.B.19b}$$
$$q \leq f(d_1, N_2^{\max}; \rho, \tau), \quad \forall (\rho, \tau, \hat{\rho}, \hat{\tau}) \in U_L^{\max}. \tag{2.B.19c}$$

For (2.B.19a) and (2.B.19c) it remains to find the worst-case realization of ρ for which the observation-realization pair is in $U_L^{\min}$ and $U_L^{\max}$, respectively. According to Lemma 2.17b, function f is increasing or decreasing in ρ for fixed d_1, so it is sufficient to check the maximum and minimum realization of ρ for which the observation-realization pair is in those sets. These are

$$\min\{\rho : (\rho, \tau, \hat{\rho}, \hat{\tau}) \in U_L^{\min}\} = \rho_L, \quad \max\{\rho : (\rho, \tau, \hat{\rho}, \hat{\tau}) \in U_L^{\min}\} = \frac{\tau_L}{\sigma},$$
$$\min\{\rho : (\rho, \tau, \hat{\rho}, \hat{\tau}) \in U_L^{\max}\} = \frac{\tau_L}{\sigma}, \quad \max\{\rho : (\rho, \tau, \hat{\rho}, \hat{\tau}) \in U_L^{\max}\} = \rho_U.$$

Plugging in $\rho = \frac{\tau_L}{\sigma}$ in (2.B.19a) and (2.B.19c) gives $q \leq K$, with K defined by (2.12). Lemma 2.19 provides a conservative approximation of constraint (2.B.19b). Putting everything together, the optimum of the following problem is a lower bound to the optimum of (2.B.18) (or, equivalently, (2.18)):

$$\max_{d_1, q} \; q, \tag{2.B.20a}$$
$$\text{s.t.} \quad q \leq f(d_1, N_2^{\min}; \rho_L, \tau_L), \tag{2.B.20b}$$
$$q \leq f(d_1, N_2^{\max}; \rho_U, \tau_L), \tag{2.B.20c}$$
$$q \leq K, \tag{2.B.20d}$$
$$q \leq p(d_1), \tag{2.B.20e}$$
$$d_{\min} \leq d_1 \leq d_1^{\max}, \tag{2.B.20f}$$

with $p(d_1)$ defined by (2.C.19) in Appendix 2.C. Constraint (2.B.20e) is the only conservative constraint, all other constraints are exact reformulations. In particular, this means that if for a solution the objective value equals K, it is certain that this is an optimal solution. It is easy to obtain other straightforward conservative approximations of (2.B.18c). For instance, a policy that delivers $N_2^{\min}$ or $N_2^{\max}$ fractions (or any number in between, for that matter) for any observation $(\hat{\rho}, \hat{\tau}) \in Z_{\text{ID}}^{\text{int}}$ is a conservative approximation. However, these perform less good and do not use all available information, as explained in the proof of Lemma 2.19.

2.C Extra lemmas

This appendix states and proves several frequently used properties of functions g and f.

Lemma 2.15 (Convexity/concavity f w.r.t. d_1)**.** *Let $\rho > 0$, $\tau > 0$ and $N_1, N_2 \in \mathbb{N}_+$. Let $d_1 \in [0, g(0,0,N_1;\rho)]$. The following properties hold for function f:*

- *Function $f(d_1, N_2; \rho, \tau)$ is strictly convex in d_1 if $\tau > \rho\sigma$, with unique minimizer $g(0,0,N_1+N_2;\rho)$;*
- *Function $f(d_1, N_2; \rho, \tau)$ is strictly concave in d_1 if $\tau < \rho\sigma$, with unique maximizer $g(0,0,N_1+N_2;\rho)$;*
- *Function $f(d_1, N_2; \rho, \tau)$ is constant in d_1 if $\tau = \rho\sigma$, with value $\frac{1}{\sigma}B(0,0,\frac{\tau}{\sigma})$.*

Proof. The partial derivative of f w.r.t. d_1 is given by

$$\frac{\partial f(d_1,N_2;\rho,\tau)}{\partial d_1} = N_1 + N_2\frac{\partial g(d_1,N_1,N_2;\rho)}{\partial d_1} + \tau\Big(2N_1d_1 + 2N_2 g(d_1,N_1,N_2;\rho)\frac{\partial g(d_1,N_1,N_2;\rho)}{\partial d_1}\Big), \quad (2.C.1)$$

where the partial derivative of g w.r.t. d_1 is given by

$$\frac{\partial g(d_1,N_1,N_2;\rho)}{\partial d_1} = -\frac{1}{N_2}(N_1 + 2N_1d_1\sigma\rho)\Big(1 + \frac{4\rho}{N_2}B(d_1,N_1;\rho)\Big)^{-\frac{1}{2}}. \quad (2.C.2)$$

Define $h(d_1,N_2;\rho) = 1 + 4\frac{\rho}{N_2}B(d_1,N_1;\rho)$. Then, plugging (2.C.2) in (2.C.1), we obtain

$$\begin{aligned}\frac{\partial f(d_1,N_2;\rho,\tau)}{\partial d_1} &= (N_1 - (N_1 + 2N_1d_1\sigma\rho)h(d_1,N_2;\rho)^{-\frac{1}{2}} \\ &\quad + \tau\Big(2N_1d_1 - \frac{2}{N_2}(N_1 + 2N_1d_1\sigma\rho)h(d_1,N_2;\rho)^{-\frac{1}{2}}N_2\frac{-1+h(d_1,N_2;\rho)^{\frac{1}{2}}}{2\sigma\rho}\Big) \\ &= \frac{N_1}{\sigma\rho}\big(h(d_1,N_2;\rho)^{-\frac{1}{2}}(2\sigma\rho d_1 + 1) - 1\big)(\tau - \rho\sigma).\end{aligned}$$

Further elementary math shows that $h(d_1,N_2;\rho)^{-\frac{1}{2}}(2\sigma\rho d_1 + 1) - 1 = 0$ if and only if $d_1 = g(0,0,N_1+N_2;\rho)$. For the second derivative of f w.r.t. d_1 we obtain:

$$\begin{aligned}\frac{\partial^2 f(d_1,N_2;\rho,\tau)}{\partial d_1^2} &= \Big(\frac{\tau-\rho\sigma}{\sigma\rho}N_1\Big)\frac{\partial}{\partial d_1}h(d_1,N_2;\rho)^{-\frac{1}{2}}(2\sigma\rho d_1 + 1) \\ &= \Big(\frac{\tau-\rho\sigma}{\sigma\rho}N_1\Big)\Big[h(d_1,N_2;\rho)^{-\frac{1}{2}}2\sigma\rho + \frac{2\rho}{N_2}(2\sigma\rho d_1 + 1)h(d_1,N_2,\rho)^{-\frac{3}{2}}(\sigma N_1 + 2\rho\sigma^2 d_1 N_1)\Big],\end{aligned}$$

and the second part of this product is positive. Hence, its sign depends only on the term $\tau - \rho\sigma$. Combining the result for the first and second derivative, we obtain

- Function $f(d_1,N_2;\rho,\tau)$ is strictly convex in d_1 if $\tau > \rho\sigma$, with unique minimizer $g(0,0,N_1+N_2;\rho)$;

- Function $f(d_1, N_2; \rho, \tau)$ is strictly concave in d_1 if $\tau < \rho\sigma$, with unique maximizer $g(0, 0, N_1 + N_2; \rho)$;
- Function $f(d_1, N_2; \rho, \tau)$ is constant in d_1 otherwise.

If $\tau = \rho\sigma$, we can rewrite $f(d_1, N_2; \frac{\tau}{\sigma}, \tau)$ to

$$\begin{aligned} f(d_1, N_2; \frac{\tau}{\sigma}, \tau) &= \max_{d_2} \left\{ d_1 N_1 + d_2 N_2 + \tau(d_1^2 N_1 + d_2^2 N_2) \mid \sigma(d_1 N_1 + d_2 N_2) + \rho\sigma^2(d_1^2 N_1 + d_2^2 N_2) \le B(0, 0; \rho) \right\} \\ &= \max_{d_2} \left\{ d_1 N_1 + d_2 N_2 + \tau(d_1^2 N_1 + d_2^2 N_2) \mid \sigma(d_1 N_1 + d_2 N_2) + \rho\sigma^2(d_1^2 N_1 + d_2^2 N_2) = B(0, 0; \rho) \right\} \\ &= \max_{d_2} \left\{ d_1 N_1 + d_2 N_2 + \tau(d_1^2 N_1 + d_2^2 N_2) \mid d_1 N_1 + d_2 N_2 + \tau(d_1^2 N_1 + d_2^2 N_2) = \frac{1}{\sigma} B(0, 0, \frac{\tau}{\sigma}) \right\} \\ &= \frac{1}{\sigma} B(0, 0, \frac{\tau}{\sigma}). \end{aligned}$$

□

Define

$$d_1^-(N_2) = \begin{cases} \dfrac{\varphi D - \varphi D\left(1 + (N_1 + N_2)\frac{N_2 - T}{N_1 T}\right)^{\frac{1}{2}}}{\sigma(N_1 + N_2)} & \text{if } N_1 + N_2 \ge T \wedge N_1 \le T \\ -\infty & \text{otherwise,} \end{cases} \tag{2.C.3a}$$

$$d_1^+(N_2) = \begin{cases} \dfrac{\varphi D + \varphi D\left(1 + (N_1 + N_2)\frac{N_2 - T}{N_1 T}\right)^{\frac{1}{2}}}{\sigma(N_1 + N_2)} & \text{if } N_1 + N_2 \ge T \wedge N_2 \le T \\ +\infty & \text{otherwise.} \end{cases} \tag{2.C.3b}$$

If two functions f with equal N_2 but different ρ intersect, d_1 takes value $d_1^-(N_2)$ or $d_1^+(N_2)$. The following lemma provides information on the existence and location of these intersection points. We consider only those values for d_1 where function $f(d_1, N_2; \rho, \tau)$ is finite for all $(\rho, \tau) \in Z$. Let

$$d_{\text{UB}} = \min_{(\rho,\tau)\in Z} g(0, 0, N_1; \rho).$$

Lemma 2.16 (Properties d_1^- and d_1^+)**.** *Let $N_1, T \in \mathbb{N}_+$.*

(a) Let $N_2 \in \mathbb{N}_+$. If $\rho_1 \neq \rho_2$, the equation

$$f(d_1, N_2; \rho_1, \tau) = f(d_1, N_2; \rho_2, \tau), \tag{2.C.4}$$

has the following real roots for d_1 on the interval $[0, d_{UB}]$:

- $d_1^-(N_2)$ *and* $d_1^+(N_2)$ — *if* $N_1 + N_2 \ge T$, $N_2 \le T$ *and* $N_1 \le T$ (2.C.5a)
- $d_1^-(N_2)$ — *if* $N_1 + N_2 \ge T$, $N_2 \le T$ *and* $N_1 > T$ (2.C.5b)
- $d_1^+(N_2)$ — *if* $N_1 + N_2 \ge T$, $N_2 > T$ *and* $N_1 \le T$ (2.C.5c)
- *no roots on interval* — *if* $N_1 + N_2 \ge T$, $N_2 > T$ *and* $N_1 > T$ (2.C.5d)
- *no real roots* — *otherwise*. (2.C.5e)

(b) Let $N_2^A, N_2^B \in \mathbb{N}_+$ such that $N_2^A < N_2^B$. It holds that

(i) If $d_1^-(N_2^A)$ and $d_1^-(N_2^B)$ are both finite, then $d_1^-(N_2^A) > d_1^-(N_2^B)$;

(ii) If $d_1^+(N_2^A)$ and $d_1^+(N_2^B)$ are both finite, then $d_1^+(N_2^A) \leq d_1^+(N_2^B)$.

Proof. Both parts of the lemma are proved individually.

Proof Lemma 2.16a

By definition of f, the equation $f(d_1, N_2; \rho_1, \tau) = f(d_1, N_2; \rho_2, \tau)$ reduces to $g(d_1, N_1, N_2; \rho_1) = g(d_1, N_1, N_2; \rho_2)$ with $d_1 \in [0, \min\{g(0,0,N_1;\rho_1), g(0,0,N_1;\rho_2)\}]$. By construction of g, this means we are interested in the pairs (d_1, d_2) that solve the system

$$\sigma(N_1 d_1 + N_2 d_2) + \rho_1 \sigma^2 (N_1 d_1^2 + N_2 d_2^2) = \varphi D(1 + \rho_1 \frac{D}{T}\varphi), \tag{2.C.6a}$$

$$\sigma(N_1 d_1 + N_2 d_2) + \rho_2 \sigma^2 (N_1 d_1^2 + N_2 d_2^2) = \varphi D(1 + \rho_2 \frac{D}{T}\varphi), \tag{2.C.6b}$$

$$d_1 \geq 0,\ d_2 \geq 0. \tag{2.C.6c}$$

We subtract $\frac{\rho_2}{\rho_1}$ times (2.C.6a) from (2.C.6b) and solve for d_1 to obtain

$$d_1 = \frac{\varphi D - \sigma N_2 d_2}{\sigma N_1}. \tag{2.C.7}$$

We know that $d_2 = g(d_1, N_1, N_2; \rho_1)$. Plugging (2.C.7) in this expression and simplifying gives the following roots for d_2:

$$r_2^-(N_2) = \frac{\varphi D + \varphi D\Big(1 + (N_1 + N_2)\big(\frac{N_1}{T} - 1\big)/N_2\Big)^{\frac{1}{2}}}{\sigma(N_1 + N_2)}, \tag{2.C.8a}$$

$$r_2^+(N_2) = \frac{\varphi D - \varphi D\Big(1 + (N_1 + N_2)\big(\frac{N_1}{T} - 1\big)/N_2\Big)^{\frac{1}{2}}}{\sigma(N_1 + N_2)}. \tag{2.C.8b}$$

Plugging (2.C.8) in (2.C.7) and simplifying gives the following roots for d_1:

$$r_1^-(N_2) = \frac{\varphi D - \varphi D\Big(1 + (N_1 + N_2)\frac{N_2 - T}{N_1 T}\Big)^{\frac{1}{2}}}{\sigma(N_1 + N_2)},$$

$$r_1^+(N_2) = \frac{\varphi D + \varphi D\Big(1 + (N_1 + N_2)\frac{N_2 - T}{N_1 T}\Big)^{\frac{1}{2}}}{\sigma(N_1 + N_2)}.$$

These roots need not be real-valued, nor in the interval $[0, \min\{g(0,0,N_1;\rho_1), g(0,0,N_1;\rho_2)\}]$. For both $r_1^-(N_2)$ and $r_1^+(N_2)$ to be real-valued, we require that

$$1 + (N_1 + N_2)\big(\frac{N_1}{T} - 1\big)/N_2 \geq 0,$$

which reduces to $N_1+N_2 \geq T$. Furthermore, for nonnegativity of $r_1^-(N_2)$ and $r_1^+(N_2)$ it suffices to check nonnegativity of the former. This is equivalent to

$$\varphi D - \sigma N_2 d_2^- \geq 0,$$

which reduces to $N_2 \leq T$. Moreover, it needs to hold that $r_1^+(N_2) \leq g(0,0,N_1;\rho_1)$ and $r_1^+(N_2) \leq g(0,0,N_1;\rho_2)$. This is equivalent to $r_2^+(N_2) \geq 0$, which can be rewritten to

$$1+(N_1+N_2)\big(\frac{N_1}{T}-1\big)/N_2 \leq 1,$$

and this reduces to $N_1 \leq T$. Parameters $d_1^-(N_2)$ resp. $d_1^+(N_2)$ (see (2.C.3)) take the values of $r_1^-(N_2)$ resp. $r_1^-(N_2)$ if they are a root of (2.C.4), and $-\infty$ resp. $+\infty$ otherwise. All together, we obtain the cases in (2.C.5).

It remains to show that the obtained roots are in the interval $[0, d_{\text{UB}}]$. It is already shown that, if they are (real-valued) roots to (2.C.4), then $d_1^-(N_2), d_1^+(N_2)$ are nonnegative. Furthermore, in that case $d_1^-(N_2) \leq d_1^+(N_2)$. It holds that

$$\frac{\partial g(0,0,N_1;\rho)}{\partial \rho} \leq 0 \Leftrightarrow N_1 \leq T.$$

Hence, if $d_1^+(N_2)$ is a real-valued root to (2.C.4) it follows that

$$d_{\text{UB}} = \min_{(\rho,\tau)\in Z} g(0,0,N_1;\rho) \geq \lim_{\rho\to+\infty} g(0,0,N_1;\rho) = \frac{\varphi D}{\sigma\sqrt{N_1 T}} \geq d_1^+(N_2),$$

where the second equality follows from the definition of g. This implies that indeed $d_1^-(N_2)$, $d_1^+(N_2) \in [0, d_{\text{UB}}]$.

Proof Lemma 2.16b
Assume $N_2^A, N_2^B \in \mathbb{N}_+$ such that $N_2^A \leq N_2^B$, and assume $N_1+N_2^A \geq T$. Statements (i) and (ii) are proved individually.

Proof part (i)
Assume $d_1^-(N_2^A)$ and $d_1^-(N_2^B)$ are both finite. The denominator of $d_1^-(N_2)$ (see (2.C.3a)) is increasing in N_2. The derivative (w.r.t. N_2) of the part within the square root in the numerator of (2.C.3a) is given by $(N_1T)^{-1}(N_1+2N_2-T) \geq 0$, because $N_1+N_2 \geq T$. Hence, the numerator is decreasing in N_2, while the denominator is increasing in N_2. This implies $d_1^-(N_2^A) > d_1^-(N_2^B)$.

Proof part (ii)
Assume $d_1^+(N_2^A)$ and $d_1^+(N_2^B)$ are both finite. One can show that

$$\frac{\partial d_1^+(N_2)}{\partial N_2} = \varphi D \frac{(N_1+N_2)(N_1+2N_2-T) - 2N_1T\sqrt{\frac{N_2(N_1+N_2-T)}{N_1T}} - 2N_2(N_1+N_2-T)}{2N_1T\sigma(N_1+N_2)^2\sqrt{\frac{N_2(N_1+N_2-T)}{N_1T}}}.$$

This implies

$$\begin{aligned}
&\frac{\partial d_1^+(N_2)}{\partial N_2} \geq 0 \\
\Leftrightarrow\ &(N_1+N_2)(N_1+2N_2-T)-2N_1T\sqrt{\frac{N_2(N_1+N_2-T)}{N_1T}}-2N_2(N_1+N_2-T)\geq 0 \\
\Leftrightarrow\ &\frac{N_1(N_1+N_2-T)+TN_2}{2N_1T}\geq\sqrt{\frac{N_2(N_1+N_2-T)}{N_1T}} \\
\Leftrightarrow\ &\frac{\big(N_1(N_1+N_2-T)+TN_2\big)^2}{4N_1^2T^2}\geq\frac{N_2(N_1+N_2-T)}{N_1T} \\
\Leftrightarrow\ &\frac{(N_1-T)^2(N_1+N_2)^2}{4N_1^2T^2}\geq 0, \qquad (2.C.9)
\end{aligned}$$

where the fourth line is obtained by using the fact that $N_1+N_2\geq T$, and squaring on both sides. The last line follows from simple algebraic manipulations. Condition (2.C.9) clearly holds, so $d_1^+(N_2^A)\leq d_1^+(N_2^B)$. □

Lemma 2.17 (Derivative f and g w.r.t. ρ)**.** *Let $(\rho,\tau)\in Z$.*

(a) Let $N',N''\in\mathbb{N}_+$. Let $d'\in[0,d_{UB}]$. If $N'+N''<T$, then

$$\frac{\partial g(d',N',N'';\rho)}{\partial\rho}<0 \quad \textit{for all } d'\in[0,d_{UB}].$$

If $N'+N''\geq T$, then

$$\frac{\partial g(d',N',N'';\rho)}{\partial\rho}\begin{cases}<0 & \textit{if } d'\in[0,d_1^-(N''))\cup(d_1^+(N''),d_{UB}]\\ =0 & \textit{if } d'\in[0,d_{UB}]\cap\{d_1^-(N''),d_1^+(N'')\}\\ >0 & \textit{if } d'\in[0,d_{UB}]\cap(d_1^-(N''),d_1^+(N'')).\end{cases} \qquad (2.C.10)$$

(b) Let $N_1,N_2\in\mathbb{N}_+$. Let $d_1\in[0,d_{UB}]$. If $N_1+N_2<T$, then

$$\frac{\partial f(d_1,N_2;\rho,\tau)}{\partial\rho}<0 \quad \textit{for all } d_1\in[0,d_{UB}].$$

If $N_1+N_2\geq T$, then

$$\frac{\partial f(d_1,N_2;\rho,\tau)}{\partial\rho}\begin{cases}<0 & \textit{if } d_1\in[0,d_1^-(N_2))\cup(d_1^+(N_2),d_{UB}]\\ =0 & \textit{if } d_1\in[0,d_{UB}]\cap\{d_1^-(N_2),d_1^+(N_2)\}\\ >0 & \textit{if } d_1\in[0,d_{UB}]\cap(d_1^-(N_2),d_1^+(N_2)).\end{cases}$$

Proof. We first prove Lemma 2.17a, after that the result of Lemma 2.17b is easily obtained.
It holds that

$$\frac{\partial g(d',N',N'';\rho)}{\partial \rho} = \frac{\sqrt{1+\frac{4\rho}{N''}B(d',N';\rho)}-1+\frac{2\rho}{N''}(d'N'\sigma-\varphi D)}{2\sigma\rho^2\sqrt{1+\frac{4\rho}{N''}B(d',N';\rho)}},$$

so

$$\frac{\partial g(d',N',N'';\rho)}{\partial \rho} \geq 0 \Leftrightarrow \sqrt{(N'')^2+4\rho N''B(d',N';\rho)} \geq N''+2\rho(\varphi D-d'N'\sigma). \tag{2.C.11}$$

We distinguish 2 cases:

- $\varphi D \geq d'N'\sigma$. In this case, squaring (2.C.11) on both sides and simplifying results in

$$-\sigma^2N'(N'+N'')d'^2+2\varphi DN'\sigma d'+\Big(\frac{N''}{T}-1\Big)\varphi^2D^2 \geq 0, \tag{2.C.12}$$

  which is a condition independent of ρ. If $N'+N'' < T$, this inequality has no roots for d', and (2.C.12) holds for all $d' \in [0, \frac{\varphi D}{N'\sigma}]$. If $N'+N'' \geq T$ one can verify that $d_1 = d_1^-(N'')$ and $d_1 = d_2^+(N'')$ are the roots of this concave parabola if they are finite. The smaller root, $d_1^-(N'')$, is finite if and only if $N'' \leq T$. The larger root, $d_1^+(N'')$ is finite if and only if $N' \leq T$.

- $\varphi D < d'N'\sigma$. In this case, $B(d',N';\rho) > 0$ only if $N' > T$. In this case, the delivered dose exceeds the dose that is used to set the BED tolerance, which is only possible if the number of fractions N' is strictly larger than the reference number of fractions T. Condition (2.C.11) clearly holds, so $g(d',N',N'';\rho)$ is increasing in ρ. Using the fact that $N' > T$ it is easily shown that $d_1^- < \frac{\varphi D}{\sigma N'} < d'$. Additionally, it can be shown that $d_{\text{UB}} < d_1^+(N'')$. Hence this case satisfies (2.C.10). Putting all of the above together yields the required result for g, i.e., Lemma 2.17a.

The partial derivative of f w.r.t. ρ is given by

$$\frac{\partial f(d_1,N_2;\rho,\tau)}{\partial \rho} = \frac{\partial g(d_1,N_1,N_2;\rho)}{\partial \rho}\Big(N_2+2\tau N_2 g(d_1,N_1,N_2;\rho)\Big).$$

Hence, the sign of the partial derivative of f w.r.t. ρ is equal to the sign of the partial derivative of g w.r.t. ρ. The result of Lemma 2.17b immediately follows. □

For given (ρ,τ) such that $\tau \neq \sigma\rho$, define the *twin point* of $d_1 \in W(\rho,\tau)$ as

$$t(d_1;\rho,\tau) := \frac{\big(N_1-N_2^*(\rho,\tau)\big)d_1+2N_2^*(\rho,\tau)g\big(d_1,N_1,N_2^*(\rho,\tau);\rho\big)}{N_1+N_2^*(\rho,\tau)}, \tag{2.C.13}$$

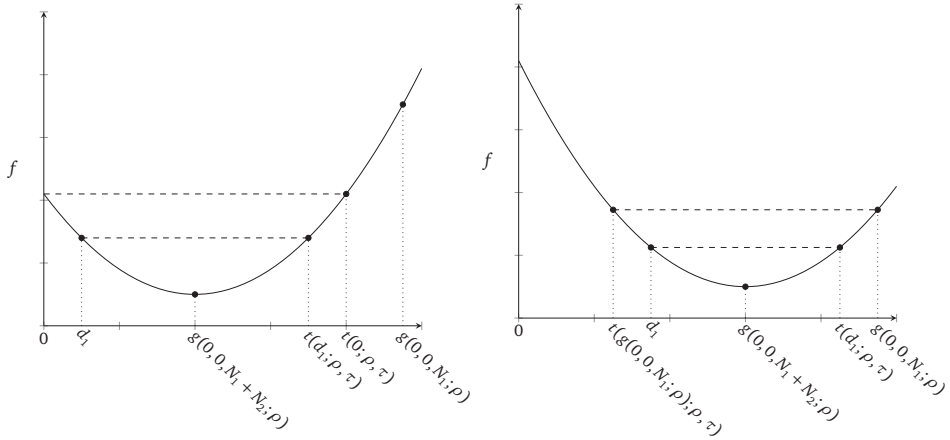

(a) Case $t(0;\rho,\tau) < g(0,0,N_1;\rho)$.

(b) Case $t(0;\rho,\tau) > g(0,0,N_1;\rho)$.

Figure 2.C.1: Illustration of d_1 and $t(d_1;\rho,\tau)$, for convex f.

where

$$W(\rho,\tau) := \Big[\max\{0, t(g(0,0,N_1;\rho);\rho,\tau)\},\ \min\{t(0;\rho,\tau), g(0,0,N_1;\rho)\}\Big] \setminus \{g(0,0,N_1+N_2;\rho)\}.$$

Figure 2.C.1 illustrates the relation between d_1 and $t(d_1;\rho,\tau)$. Set W can be interpreted as the points d_1 for which there exists another point the graph of f that has the same value, we refer to such points as twin points. The following lemma proves that for fixed (ρ,τ) any d_1 in the set $W(\rho,\tau)$ has a twin point $t(d_1;\rho,\tau)$ that is also in the set $W(\rho,\tau)$, and their objective values are equal.

Lemma 2.18. *Let $(\rho,\tau) \in Z$ such that $\tau \neq \sigma\rho$, let $N_2 = N_2^*(\rho,\tau)$ and let $d_1 \in [0, g(0,0,N_1;\rho)]$. The equation*

$$f(d_1,N_2;\rho,\tau) = f(d_1',N_2;\rho,\tau), \tag{2.C.14}$$

has a solution $d_1' \in [0, g(0,0,N_1;\rho)]$ unequal to d_1 if and only if $d_1 \in W(\rho,\tau)$. In that case, there is a unique solution $d_1' = t(d_1;\rho,\tau) \in W(\rho,\tau)$, and it holds that $d_1 = t(t(d_1;\rho,\tau);\rho,\tau)$.

Proof. Let (ρ,τ) such that $\tau \neq \sigma\rho$, let $N_2 = N_2^*(\rho,\tau)$. We first show that if there exists a solution d_1' to (2.C.14) unequal to d_1, then this solution is $d_1' = t(d_1;\rho,\tau)$ and that $d_1 = t(t(d_1;\rho,\tau);\rho,\tau)$. Subsequently, we show that this solution exists only if $d_1 \in W(\tau,\rho)$ and that in that case also $t(d_1;\rho,\tau) \in W(\rho,\tau)$.

First part:
Let $L, Q \in \mathbb{R}_+$ denote the linear and quadratic contribution of d_1 to f, i.e.,

$$L(d_1, N_2, \rho) := N_1 d_1 + N_2 g(d_1, N_1, N_2; \rho), \tag{2.C.15a}$$
$$Q(d_1, N_2, \rho) := N_1 d_1^2 + N_2 g(d_1, N_1, N_2; \rho)^2. \tag{2.C.15b}$$

We show that for any $d_1 \in [0, g(0,0,N_1;\rho)]$ unequal to $g(0,0,N_1+N_2,\rho)$ there is a unique solution d_1' such that

$$L(d_1, N_2; \rho) = L(d_1', N_2; \rho), \tag{2.C.16a}$$
$$Q(d_1, N_2; \rho) = Q(d_1', N_2; \rho). \tag{2.C.16b}$$

Any such d_1' has exactly the same objective value as d_1. Plug (2.C.15) in (2.C.16), rewrite the first equation to eliminate g, and plug this in the second equation to get

$$\begin{aligned} d_1' &= \frac{L(d_1, N_2; \rho) \pm \sqrt{\frac{N_2}{N_1}\big((N_1+N_2)Q(d_1, N_2; \rho) - L^2(d_1, N_2; \rho)\big)}}{N_1 + N_2} \\ &= \frac{N_1 d_1 + N_2 g(d_1, N_1, N_2; \rho) \pm N_2(d_1 - g(d_1, N_1, N_2; \rho))}{N_1 + N_2}. \end{aligned} \tag{2.C.17}$$

The '+' solution to (2.C.17) returns $d_1' = d_1$, and the '–' solution returns

$$d_1' = \frac{(N_1 - N_2)d_1 + 2N_2 g(d_1, N_1, N_2, \rho)}{N_1 + N_2},$$

and we denote this solution by $t(d_1; \rho, \tau)$. By construction, it holds that $d_1 = t(t(d_1;\rho,\tau);\rho,\tau)$. Because $\tau \neq \sigma\rho$, function $f(d_1, N_2; \rho, \tau)$ is a strictly convex or concave function according to Lemma 2.15, so $f(d_1, N_2; \rho, \tau) = z$ for some constant $z \in \mathbb{R}$ has either 0, 1 or 2 solutions. In particular, $d_1 = t(d_1; \rho, \tau)$ if and only if d_1 equals minimizer $g(0,0,N_1+N_2;\rho)$. Hence if there exists a solution d_1' to (2.C.14) unequal to d_1, then this solution is $d_1' = t(d_1;\rho,\tau)$.

Second part:

- Suppose $d_1 \notin W(\rho,\tau)$. We distinguish three cases. Case (i): '$d_1 = g(0,0,N_1+N_2;\rho)$'. Because this is the unique minimizer of f, there does not exist a d_1' with equal objective value. Case (ii). '$d_1 > \min\{t(0;\rho,\tau),\ g(0,0,N_1;\rho)\}$'. Because $d_1 \in [0, g(0,0,N_1;\rho)]$, this implies $d_1 > t(0,\rho,\tau)$. As shown in the first part of the proof, it holds that $d_1 = t(t(d_1;\rho,\tau);\rho,\tau)$. Hence, $d_1 > t(0;\rho,\tau)$ is equivalent to $t(t(d_1;\rho,\tau),\rho,\tau) > t(0;\rho,\tau)$. Because $t(d_1;\rho,\tau)$ is decreasing in d_1, this implies $t(d_1;\rho,\tau) < 0$, so according to (2.B.1c) it holds that $f(t(d_1;\rho,\tau),N_2;\rho,\tau) = -\infty$ and we have a contradiction. Case (iii): '$d_1 < \max\{0,\ t(g(0,0,N_1;\rho);\rho,\tau)\}$'. Similar to case (ii), one can show that $f(t(d_1;\rho,\tau),N_2;\rho,\tau) = -\infty$.

- Suppose $d_1 \in W(\rho,\tau)$. From (2.C.17) one can see that, because the term $d_1 - g(d_1, N_1, N_2, \rho)$ is increasing in d_1, the function $t(d_1;\rho,\tau)$ is decreasing in d_1. Consequently,

$$d_1 \le \min\{t(0;\rho,\tau), g(0,0,N_1;\rho)\} \Leftrightarrow d_1' \ge \max\{0, t(g(0,0,N_1;\rho);\rho,\tau)\}.$$

  Furthermore, using the same argument,

$$d_1 \ge \max\{0, t(g(0,0,N_1;\rho);\rho,\tau)\} \Leftrightarrow d_1' \le \min\{t(0;\rho,\tau), g(0,0,N_1;\rho)\}.$$

  Therefore, it holds that $d_1' \in W(\rho,\tau)$.

□

In the following lemma, let $I(\cdot|S)$ denote the indicator function for a set S:

$$I(x|S) = \begin{cases} 1 & \text{if } x \in S \\ 0 & \text{otherwise.} \end{cases}$$

Lemma 2.19. *For given $q \in \mathbb{R}_+$ and given $d_1 \in [0, d_{UB}]$,*

$$q \le f(d_1, N_2^*(d_1;\hat\rho,\hat\tau);\rho,\tau), \quad \forall(\rho,\tau,\hat\rho,\hat\tau) \in U_L^{int}, \tag{2.C.18}$$

holds if $\tau \le p(d_1)$, with

$$\begin{aligned} p(d_1) = &\sum_{\eta \in \{N_2^{min},\dots,N_2^{max}\}} \max\left\{f(d_1,\eta;\rho_L^{int},\tau_L),\ f(d_1,\eta-1;\rho_U^{int},\tau_L)\right\} I(d_1|S_\eta) \\ &+ f(d_1, N_2^{min};\rho_L^{int},\tau_L) I(d_1|S_{min}) + f(d_1, N_2^{max};\rho_U^{int},\tau_L) I(d_1|S_{max}), \end{aligned} \tag{2.C.19}$$

where sets S_{min}, S_{max} and S_η are defined in (2.C.21a), (2.C.21d) *and* (2.C.24), *respectively, and ρ_L^{int}, ρ_U^{int} are defined in* (2.C.26).

Proof. By definition of $N_2^*(d_1;\hat\rho,\hat\tau)$ and U_L^{int}, it holds that

$$q \le f(d_1, N_2^*(d_1;\hat\rho,\hat\tau);\rho,\tau), \quad \forall(\rho,\tau,\hat\rho,\hat\tau) \in U_L^{\text{int}},$$

is equivalent to

$$\begin{aligned} q \le &\max_{\tilde\eta \in \{N_2^{\min},\dots,N_2^{\max}\}} \min\{f(d_1,\tilde\eta;\hat\rho_L,\hat\tau_L), f(d_1,\tilde\eta;\hat\rho_U,\hat\tau_L)\}, \\ &\forall(\hat\rho,\hat\tau) \in Z_{\text{ID}}^{\text{int}} \cap \{(\hat\rho,\hat\tau) : \hat\tau \le \tau_L + r^\tau\}, \end{aligned} \tag{2.C.20}$$

and because function f is increasing in τ, we need to consider only those observations $(\hat\rho,\hat\tau)$ with $\hat\tau_L = \tau_L$. For the first part of the proof, we fix the observation $(\hat\rho,\hat\tau)$, plug in $\hat\tau_L = \tau_L$, and rewrite (2.C.20) for this fixed observation.

Because $(\hat{\rho}, \hat{\tau}) \in Z_{\text{ID}}^{\text{int}}$, it holds that $\sigma\hat{\rho}_L < \tau_L < \sigma\hat{\rho}_U$. Hence, by Lemma 2.15, function $f(d_1, \eta, \hat{\rho}_L, \tau_L)$ is convex and $f(d_1, \eta, \hat{\rho}_U, \tau_L)$ is concave in d_1 for any $\eta \in \mathbb{N}_+$. We make use of results of Lemma 2.16. Define

$$E^- := \{\eta : N_1 + \eta \geq T, \eta \leq T\} \cap \{N_2^{\min}, \ldots, N_2^{\max}\},$$
$$E^+ := \{\eta : N_1 + \eta \geq T, N_1 \leq T\} \cap \{N_2^{\min}, \ldots, N_2^{\max}\},$$

and let $\eta_{\min}^-$, $\eta_{\max}^-$, $\eta_{\min}^+$ and $\eta_{\max}^+$, denote the smallest and largest elements of E^- and E^+, respectively. If $\eta \in E^-$ respectively $\eta \in E^+$, then, according to Lemma 2.16a, $d_1 = d_1^-(\eta)$ respectively $d_1 = d_1^+(\eta)$ is a nonnegative real root of

$$f(d_1, \eta; \hat{\rho}_L, \tau_L) = f(d_1, \eta; \hat{\rho}_U, \tau_L),$$

and the corresponding objective value equals K. From Lemma 2.16b we know that

$$d_1^-(N_2^{\max}) < \ldots < d_1^-(N_2^{\min}) \leq d_1^+(N_2^{\min}) \leq \ldots \leq d_1^+(N_2^{\max}).$$

We use this to split the domain $[0, d_{\text{UB}}]$ as follows:

$$S_{\min} := \begin{cases} (d_1^-(\eta_{\min}^-), d_1^+(\eta_{\min}^+)) & \text{if } E^- \neq \emptyset, E^+ \neq \emptyset \\ [0, d_1^+(\eta_{\min}^+)) & \text{if } E^- = \emptyset, E^+ \neq \emptyset \\ (d_1^-(\eta_{\min}^-), d_{\text{UB}}] & \text{if } E^- \neq \emptyset, E^+ = \emptyset \\ \emptyset & \text{if } N_1 + N_2^{\max} < T \\ [0, d_{\text{UB}}] & \text{otherwise,} \end{cases} \tag{2.C.21a}$$

$$S_\eta^- := \begin{cases} [d_1^-(\eta), d_1^-(\eta-1)] & \text{if } \eta_{\min}^- \leq \eta - 1 < \eta \leq \eta_{\max}^- \\ \emptyset & \text{otherwise,} \end{cases} \tag{2.C.21b}$$
$$\forall \eta \in \{N_2^{\min} + 1, \ldots, N_2^{\max}\},$$

$$S_\eta^+ := \begin{cases} [d_1^+(\eta-1), d_1^+(\eta)] & \text{if } \eta_{\min}^+ \leq \eta - 1 < \eta \leq \eta_{\max}^+ \\ \emptyset & \text{otherwise,} \end{cases} \tag{2.C.21c}$$
$$\forall \eta \in \{N_2^{\min} + 1, \ldots, N_2^{\max}\},$$

$$S_{\max} := \begin{cases} [0, d_1^-(\eta_{\max}^-)) \cup (d_1^+(\eta_{\max}^+), d_{\text{UB}}] & \text{if } E^- \neq \emptyset, E^+ \neq \emptyset \\ (d_1^+(\eta_{\max}^+), d_{\text{UB}}] & \text{if } E^- = \emptyset, E^+ \neq \emptyset \\ [0, d_1^-(\eta_{\max}^-)) & \text{if } E^- \neq \emptyset, E^+ = \emptyset \\ [0, d_{\text{UB}}] & \text{if } N_1 + N_2^{\max} < T \\ \emptyset & \text{otherwise.} \end{cases} \tag{2.C.21d}$$

We will reformulate (2.C.20) on each interval (set) separately, assuming it is nonempty.

1. "$S_{\min}$": If $d_1 \in S_{\min}$, then $f(d_1, \eta; \hat{\rho}_L, \tau_L) < f(d_1, \eta; \hat{\rho}_U, \tau_L)$ for all $\eta \in \{N_2^{\min}, \ldots, N_2^{\max}\}$ according to Lemma 2.17b, so it is optimal to deliver $N_2^{\min}$ fractions. Hence, on this interval (2.C.20) is equivalent to

$$q \leq f(d_1, N_2^{\min}; \hat{\rho}_L, \tau_L).$$

2. "S_η^-": From Lemma 2.16a we know that $f(d_1, \eta, \hat{\rho}_L, \tau_L) = f(d_1, \eta, \hat{\rho}_U, \tau_L)$ if $d_1 = d_1^-(\eta)$ or $d_1 = d_1^+(\eta)$. In this case, the objective value equals K. Furthermore, function $f(d_1, \eta, \hat{\rho}_L, \tau_L)$ is convex and $f(d_1, \eta, \hat{\rho}_U, \tau_L)$ is concave in d_1. Consider the interval $[d_1^-(\eta), d_1^-(\eta-1)]$. It holds that

$$f(d_1, \eta; \hat{\rho}_L, \tau_L) \leq K \leq f(d_1, \eta-1; \hat{\rho}_L, \tau_L), \tag{2.C.22a}$$
$$f(d_1, \eta-1; \hat{\rho}_U, \tau_L) \leq K \leq f(d_1, \eta; \hat{\rho}_U, \tau_L). \tag{2.C.22b}$$

This implies that if $d_1 \in [d_1^-(\eta), d_1^-(\eta-1)]$, it is optimal to deliver either η or $\eta-1$ fractions. If we deliver η fractions, the restricting worst-case scenario is $(\hat{\rho}_L, \tau_L)$ and the value f is above K for the scenario $(\hat{\rho}_U, \tau_L)$. If we deliver $\eta' > \eta$ fractions, the value for the scenario $(\hat{\rho}_L, \tau_L)$ decreases, while the value for the scenario $(\hat{\rho}_U, \tau_L)$ increases even further. Hence, delivering $\eta' > \eta$ fractions cannot be optimal. Similarly, delivering less than $\eta-1$ fractions cannot be optimal. Therefore, if $d_1 \in [d_1^-(\eta), d_1^-(\eta-1)]$ it is optimal to deliver either η or $\eta-1$ fractions. This implies that on the interval S_η^- constraint (2.C.20) is equivalent to

$$q \leq \max\{f(d_1, \eta; \hat{\rho}_L, \tau_L),\ f(d_1, \eta-1; \hat{\rho}_U, \tau_L)\}. \tag{2.C.23}$$

Note that this result does not depend on the values $\hat{\rho}_L$ and $\hat{\rho}_U$, we only use that $\hat{\rho}_L < \frac{\tau_L}{\sigma} < \hat{\rho}_U$.

3. "S_η^+": Similar to the case for S_η^+, one can show that for $d_1 \in S_\eta^+$ constraint (2.C.20) is equivalent to (2.C.23).

4. "$S_{\max}$": If $d_1 \in S_{\max}$, then $f(d_1, \eta; \hat{\rho}_L, \tau_L) > f(d_1, \eta; \hat{\rho}_U, \tau_L)$ for all $\eta \in \{N_2^{\min}, \ldots, N_2^{\max}\}$ according to Lemma 2.17b, so it is optimal to deliver $N_2^{\max}$ fractions. Hence, on this interval (2.C.20) is equivalent to

$$q \leq f(d_1, N_2^{\max}; \hat{\rho}_U, \tau_L).$$

For sets S_η^- and S_η^+ the reformulation is the same. Therefore, define

$$S_\eta = S_\eta^- \cup S_\eta^+. \tag{2.C.24}$$

Putting everything together, for $d_1 \in [0, d_{\text{UB}}]$ the constraint (2.C.20) is equivalent to

$$\begin{aligned} q \leq & \sum_{\eta \in \{N_2^{\min}, \ldots, N_2^{\max}\}} \max\{f(d_1, \eta; \hat{\rho}_L, \tau_L),\ f(d_1, \eta - 1; \hat{\rho}_U, \tau_L)\} I(d_1 | S_\eta) \\ & + f(d_1, N_2^{\min}; \hat{\rho}_L, \tau_L) I(d_1 | S_{\min}) + f(d_1, N_2^{\max}; \hat{\rho}_U, \tau_L) I(d_1 | S_{\max}), \\ & \qquad \forall (\hat{\rho}, \hat{\tau}) \in Z_{\text{ID}}^{\text{int}} \cap \{(\hat{\rho}, \hat{\tau}) : \hat{\tau} \leq \tau_L + r^\tau\}. \end{aligned} \tag{2.C.25}$$

In order to find a tractable conservative robust counterpart of (2.C.25), denote

$$\rho_L^{\text{int}} = \max\{\rho_L, \frac{\tau_L}{\sigma} - 2r^\rho\}, \tag{2.C.26a}$$

$$\rho_U^{\text{int}} = \min\{\rho_U, \frac{\tau_L}{\sigma} + 2r^\rho\}, \tag{2.C.26b}$$

and note that $\rho_L^{\text{int}} \leq \hat{\rho}_L < \frac{\tau_L}{\sigma} < \hat{\rho}_U \leq \rho_U^{\text{int}}$. Only if $d_1 \in S_\eta$, the robust counterpart is conservative. By Lemma 2.17b, it holds that function f is strictly decreasing, constant or strictly increasing in ρ for fixed d_1, so

$$\begin{aligned} f(d_1, \eta; \hat{\rho}_L, \tau_L) &\geq \min\{f(d_1, \eta; \rho_L^{\text{int}}, \tau_L), f(d_1, \eta; \frac{\tau_L}{\sigma}, \tau_L)\} \\ &= \min\{f(d_1, \eta; \rho_L^{\text{int}}, \tau_L), K\} \\ &= f(d_1, \eta; \rho_L^{\text{int}}, \tau_L), \end{aligned}$$

where the second equality follows from (2.C.22). A similar result holds for $f(d_1, \eta - 1; \hat{\rho}_U, \tau_L)$. Furthermore, as shown before, f is increasing in ρ on $S_{\min}$ and decreasing in ρ on $S_{\max}$. Therefore, a conservative approximation of (2.C.18) is given by

$$\begin{aligned} q \leq & \sum_{\eta \in \{N_2^{\min}, \ldots, N_2^{\max}\}} \max\{f(d_1, \eta; \rho_L^{\text{int}}, \tau_L),\ f(d_1, \eta - 1; \rho_U^{\text{int}}, \tau_L)\} I(d_1 | S_\eta) \\ & + f(d_1, N_2^{\min}; \rho_L^{\text{int}}, \tau_L) I(d_1 | S_{\min}) + f(d_1, N_2^{\max}; \rho_U^{\text{int}}, \tau_L) I(d_1 | S_{\max}), \end{aligned}$$

and the RHS is $p(d_1)$. □

Function $p(d_1)$ is a piecewise function. On intervals defined by $S_{\min}$ and $S_{\max}$ it is convex and concave, respectively. On any interval S_η function $p(d_1)$ is the maximum of a concave and convex function.

CHAPTER 3

Optimal treatment plan adaptation using mid-treatment imaging biomarkers

3.1 Introduction

In radiation therapy (RT), the goal of personalized treatment is to tailor the RT treatment plan according to patients' biological characteristics in order to maximize the patient-specific therapeutic window; i.e., maximum tumor control and minimum RT-induced complications. This can be done either before the treatment, using baseline observations (e.g. radiological findings, gene mutation status, etc.) or during the RT course, using mid-treatment patient-specific biological information. If *appropriate* mid-treatment biomarkers[1] are available, the latter approach provides the additional opportunity to assess the *actual* (as opposed to anticipated) patients' response to RT and adjusting the treatment plan accordingly. Although in recent years some attention has been given to studying mid-treatment (mostly imaging) biomarkers of RT outcome (e.g., positron emission tomography [PET]-magnetic resonance imaging [MRI] in neoadjuvant RT of sarcoma [NCT03076333[2]], magnetic resonance elastography in RT of liver metastasis [NCT03401814[2]], diffusion-weighted MRI in glioma [NCT02186262[2]]), the question of *how* to adapt the treatment plan based on these biomarkers has not yet been properly addressed. To address this gap in the literature and provide a systematic framework for mid-treatment biomarker-based RT plan adaptation, our team recently introduced the concept of optimal stopping in radiation therapy (OSRT) (Ajdari et al., 2019). In short, OSRT views the treatment planning problem as a dynamic problem in which at each decision stage (fraction), based on the *estimated* assessment of patient's radiobiological condition, the treatment plan can

[1] For a brief discussion of the characteristics of an appropriate mid-treatment biomarker, we refer to Baumann et al. (2016) and Ajdari et al. (2019)

[2] See clinicaltrials.gov.

be optimally adapted and/or stopped, if necessary. We also provided an overview of mathematical approaches suitable for the resulting dynamic decision-making process. In order to further concretize our concept, in this chapter we set out to implement one of the aspects of OSRT, namely, the optimal mid-treatment dose adaptation, in real-world clinical cases.

Most of the research efforts in this direction can be categorized into two broad strands: clinical efforts and theoretical studies. Research in the first group generally use pre-defined dose escalation or de-escalation levels which are defined based on historical data and/or physician's judgment when the protocol is designed. A good example is an RTOG 1106 clinical trial (NCT01190527[2]), where RT plans for patients with non-small cell lung cancer (NSCLC) were adapted based on mid-treatment imaging information (Kong et al., 2017), and the treatment dose was escalated in patients who showed high focal uptake of [(18)F]-fluorodeoxyglucose (FDG) on mid-treatment PET images. Similarly, in an ongoing clinical trial (NCT02186262[2]), mid-treatment diffusion-weighted MRI is being used for escalating the dose of glioblastoma patients. Another clinical trial (NCT03416153[2]) is pursuing dose de-escalation based on mid-treatment FDG-PET scans for a select group of human papillomavirus-positive oropharyngeal cancer patients.

In the second group, researchers have proposed several theoretical methods to adapt the RT treatment plan based on (mostly) theoretical mid-treatment biomarkers. Though their method was not specifically designed for mid-treatment adaptation, Yang and Xing (2005b) proposed a theoretical framework for including radiobiological parameters (radiosensitivity parameters, proliferation rate, and clonogen cell density) — which were assumed to be known, in inverse treatment planning. South et al. (2008) then extended their work to estimate the radiobiological parameters based on "simulated" mid-treatment (hypoxia) images. Another body of literature aims to adapt treatment via direct optimization of biological criteria. Kim et al. (2009), Ghate (2011) and Kim et al. (2012b) use Markov decision processes for adaptive spatiotemporal optimization, assuming response uncertainties. Their stochastic control framework directly optimizes tumor control probability (TCP) subject to normal tissue biologically effective dose (BED) constraints. The framework has been concretized with hypoxia as a biomarker (Saberian et al., 2016b). Ajdari et al. (2018) assume temporally and spatially varying α and β parameters, and adaptively optimize the treatment-length based on (hypothetically) observed tumor density, in order maximize TCP subject to BED constraints. In Chapter 2 we take an adjustable robust optimization approach to treatment-length optimization using the BED model, assuming biomarker data provides inexact estimates of α/β parameters.

Perhaps the closest examples to our approach of blending the theoretical and clinical aspects of RT plan adaptation in this chapter are the works of Søvik et al. (2007) and Clausen et al. (2014). In Søvik et al. (2007) the RT plan of a canine sarcoma patient is retrospectively adapted using daily mid-treatment dynamic contrast-enhanced-MRI to maximize TCP by achieving a uniform clonogen cell density across the tumor volume. They also showed that the normal tissue complication probability (NTCP) is not deteriorated as the result of this adaptation. Clausen et al. (2014) performed retrospective dose escalation of tumor sub-volumes in five canine sarcoma and carcinoma patients. The sub-volumes were determined by baseline and mid-treatment functional PET scans and dose-escalation was performed based on five pre-determined dose levels (up to 150% of original dose).

What distinguishes our work from these studies is twofold: first, we present an image-guided adaptive treatment planning framework that directly optimizes patient-specific biological functions (i.e., TCP and NTCP), improving upon the indirect measures taken in the previous works. Second, the uncertainty in biomarker information, which is a significant factor in determining the quality of the adapted plans, is incorporated in our approach. In particular, the radiation response parameters are estimated from early response as measured via surrogate pre- and mid-treatment biomarkers. These are used for optimal uniform dose adaptation and continuous dose adaptation, directly optimizing TCP and NTCP criteria. The approach is demonstrated via retrospective adaptive optimization of treatment plans for a cohort of 14 canines with sinonasal tumors imaged with 3'-deoxy-3'[(18)F]-fluorothymidine (FLT) PET/computed tomography (CT) (Bradshaw et al., 2013, 2015) as the response biomarker. This work can be seen as the first step towards a clinical implementation of our OSRT framework.

The remainder of this chapter is organized as follows. Section 3.2 describes the methodology, and Section 3.3 describes the results of the retrospective adaptive optimization of a cohort of canine sinonasal patients. Subsequently, Section 3.4 discusses the results, information uncertainty and modeling limitations. Section 3.5 concludes the chapter.

3.2 Methods

In the current study, we present a methodology for optimally adapting treatment plans based on imaging biomarkers. We consider a fractionated treatment consisting of two stages. Prior to treatment, an imaging biomarker is taken, and a treatment plan is constructed. This treatment is delivered for a fixed number of fractions (stage 1),

after which a mid-treatment imaging biomarker is taken. Based on the pre- and mid-treatment scan, the treatment plan is adapted and delivered for the remainder of the treatment course (stage 2). There are four main components in this methodology (a schematic overview is provided in Figure 3.1):

1. An imaging biomarker that produces voxel-wise signals of *early* treatment response.
2. A biological response model relating absorbed dose in a tissue to a quantifiable outcome measure.
3. A method to transform the obtained imaging signals to parameter estimates for the employed biological response model.
4. An adaptive treatment plan optimization method based on the "updated" parameter estimates.

It should be noted that while the methodology presented here uses specific choices for the above components, the concept is generic enough to incorporate other choices for imaging biomarkers, biological models and parameter estimation methods.

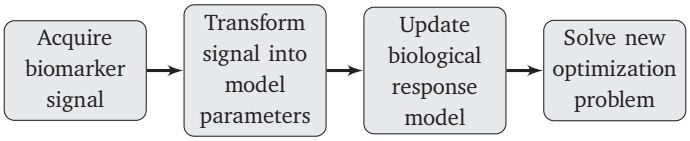

Figure 3.1: Schematic overview of adaptation framework

3.2.1 Patients, imaging and treatment

This study included 17 canine veterinary patients with sinonasal cancer, treated at the University of Wisconsin Veterinary Medical Teaching Hospital, 14 of which were selected for analysis. Two patients were excluded because not all organ-at-risk (OAR) and target volume delineations were available, one due to a missing mid-treatment FLT PET scan. Diagnosis was established using CT and analysis of histopathological samples. All patients exhibited nasal or paranasal sinus tumors without intracranial infiltration or distant metastases.

Data from multiple imaging modalities was acquired for the patients. The patients received FDG, FLT and copper(II)-diacetyl-bis(N4-methylthiosemicarbazone) (Cu-ATSM) PET/CT scans on the GE Discovery VCT scanner, using 4-10 mCi of tracer.

The FLT PET scan was acquired as a 90-minute dynamic 3D acquisition, acquired over a single 15 cm bed position. Patients fasted 12 hours before scanning and were kept in a kennel during tracer uptake to limit physical activity. During imaging, patients were anesthetized and immobilized using a custom bite block fixed to the scanner couch and a vacuum mattress.

Veterinarians contoured the gross tumor volume (GTV) as the visible anatomical changes on planning CT, and the clinical target volume (CTV) as expected extent of microscopic disease, which often included the entire nasal cavity. Mean GTV volume is 56 cm^3 (range: 3-146 cm^3, σ: 47 cm^3). A planning volume named “PTV42" was obtained by expanding the CTV by a uniform geometric expansion of 2 mm. A second planning volume named “PTV50" was obtained by directly expanding the GTV by a 2 mm margin. While this volume was primarily used in the dose boost group introduced below, the segmentation was performed for all patients in both groups, and both PTV volumes were used for dose plan evaluation. Brain and eye volumes were also contoured as relevant OARs.

Patients were prescribed intensity modulated radiation therapy (IMRT) by helical tomotherapy, with curative intent. As part of a larger study investigating dose escalation, patients were divided into two treatment groups. The first group was prescribed a clinical standard of 42 Gy radiation dose, delivered uniformly to PTV42 in ten fractions. A minimum of 98% of PTV42 volume was required to achieve the dose of 42 Gy. The second group received an additional integrated boost of 8 Gy to the PTV50, for a total of 50 Gy, also in ten fractions. A minimum of 95% of PTV50 volume was required to receive at least 50 Gy. The highest priority in dose optimization was given to achieving sufficient dose coverage in the PTV42, followed by PTV50. The remaining structures used in plan optimization, in order of importance, were: brain, eyes and normal tissues. After the first two RT fractions, amongst others “mid-treatment” FLT PET images were acquired, 7 days after the first FLT PET/CT scan. For more details on the trial we refer to Bradshaw et al. (2015).

The current study makes use of the planning CT, the pre- and mid-treatment FLT PET scans, the clinically delivered dose distribution and delineations of the PTV50, PTV42, the brain and both eyes. In the numerical experiments the target volume for the response model is the PTV50, due to the fact that the PTV42 includes anatomically invisible disease, often in the entire nasal cavity. For the current study grids of size $128 \times 128 \times 77$ with voxel size $2.3 \times 2.3 \times 3.3$ mm are used.

3.2.2 Imaging biomarker

As the first component of the adaptation framework, an imaging biomarker is required that produces voxel-wise signals of early response. Early response signals are obtained from pre- and mid-treatment scans. For any target voxel i, let F_i^p and F_i^m denote the intensity values of the pre- and mid-treatment scans, respectively. The delivered dose at the time of the mid-treatment imaging should be such that measurable signal changes can be observed, compared to the pre-treatment scan.

In the current study, FLT PET images are used as a surrogate biomarker for cell proliferation. The correlation of FLT PET uptakes with cell proliferation have been shown both in cell lines (Toyohara et al., 2002) and in in vivo experiments (Vesselle et al., 2002; Shields et al., 2005; Muzi et al., 2005; Kenny et al., 2005), and in various tumor types including breast, laryngeal, lung, and brain cancers (Been et al., 2006; Cobben et al., 2004a,b; Choi et al., 2005). Due to its applicability in assessing cell proliferation, we use change in FLT PET signals from baseline as direct indicators of cell kill, and therefore as a biomarker of early tumor RT response.

Because any imaging signal is subject to noise, low magnitude signals should be interpreted with caution. In particular, relative changes in low magnitude pre- to mid-treatment signals are subject to high uncertainty, and so are any radiation response estimates for these voxels. For this reason, voxels with pre-treatment signal below threshold value $F_{\mathrm{TH}} = 2$ are excluded from analysis; the threshold value was chosen based on expected repeatability of FLT PET scans within each voxel.

For any target voxel with a sufficiently large pre-treatment signal F_i^p, we assume that pre- to mid-treatment change in signal is positively associated with the voxels' early response to radiation. The early response of an individual target voxel i is defined as

$$r_i := \frac{F_i^p - F_i^m}{F_i^p}. \tag{3.1}$$

So, a response $r_i \in [0,1]$ means that the signal intensity in voxel i has decreased by $r_i \cdot 100\%$. Response is truncated at 0, i.e., a voxel with an increase in signal is said to have no radiation response. Similar (piecewise) linear transformations have previously been used to map scan intensity data directly to prescription doses (Alber et al., 2003; Das et al., 2004; Vanderstraeten et al., 2006).

3.2.3 Biological response models

Biological response models relate the absorbed dose in a tissue to a quantifiable outcome measure. Typically, this outcome measure is TCP or NTCP. Common TCP and

NTCP models depend on a number of parameters, and more accurate estimates of these parameters give response models that are closer to reality.

As a response model for the target volume, we use the linear-quadratic (LQ) model of cell kill (McMahon, 2019). Let n_T denote the number of voxels in the target volume. The LQ-based tumor control probability (TCP) is given by

$$\mathrm{TCP}_{\mathrm{LQ}}(\boldsymbol{d}^T; \boldsymbol{\alpha}, \boldsymbol{\nu}) = \prod_{i=1}^{n_T} \exp\Big(- \nu_i \mathrm{SF}_i(d_i^T; \alpha_i)\Big), \tag{3.2}$$

where SF_i is the survival fraction of cells in voxel i after delivery of a total dose of d_i^T Gy. Parameter ν_i is the pre-treatment number of clonogens, and α_i is the intrinsic radiation sensitivity of voxel i.

As a response model for the OARs, we use the LKB NTCP model (Lyman, 1985; Kutcher and Burman, 1989), which states that the NTCP of a homogeneous dose d_{h} is given by

$$\mathrm{NTCP}_{\mathrm{LKB}}(d_{\mathrm{h}}) = \Phi\Big(\frac{d_{\mathrm{h}} - d_{50}}{m d_{50}}\Big), \tag{3.3}$$

where $\Phi(z) = 1/\sqrt{2\pi}\int_{-\infty}^{z} e^{-\frac{1}{2}x^2} dx$ is the standard normal cumulative distribution function. Parameter d_{50} is the dose that yields a 50% complication probability if uniformly delivered to the entire organ, and m is a parameter for the slope of the NTCP curve.

In the current study, the set of OARs with NTCP criteria is $\mathcal{R} = \{\text{brain, right eye, left eye}\}$. Endpoint for brain NTCP is necrosis, endpoint for eyes NTCP is cataract. FLT PET signals are used to obtain estimates of the voxel-wise radiation response parameters $\{(\alpha_i, \nu_i)\}_{i=1}^{n_T}$ of the target volume. NTCP model parameters are not updated, but such an extension can be readily incorporated if suitable biomarkers are available. Further modeling details and parameter choices are provided in Appendix 3.A.1.

3.2.4 Estimation of radiation response parameters

As a third component of the adaptation framework, a method to transform obtained imaging signal to parameter estimates for the biological response model(s) is required.

In the current study, the early response values are used to estimate (α_i, ν_i) for each target voxel i. We assume that voxel estimates $\hat{\alpha}_i$ are obtained simultaneously for all patients in the cohort and all voxels with F_i^p at least F_{TH} via scaling of the response values. It is assumed that voxels with higher early radiation response have a higher α parameter. First, we pick a lower bound $\alpha_{\min}$ and a mean value $\bar{\alpha}$. The latter is,

e.g., a value derived from literature for the particular tumor site (Tai et al., 2008; Klement, 2017). Voxels with a response of 0 get assigned the estimate $\hat{\alpha}_i = \alpha_{\min}$. For the remaining voxels (those with a positive response), the response values are scaled such that the mean of all $\hat{\alpha}_i$ estimates is equal to $\bar{\alpha}$. That is, for a target voxel i the estimate $\hat{\alpha}_i$ is given by

$$\hat{\alpha}_i := \alpha_{\min} + c_\alpha r_i, \tag{3.4}$$

where scaling factor c_α is such that the mean α_i over all target voxels and all patients equals the pre-determined $\bar{\alpha}$. Note that for an individual patient the mean $\hat{\alpha}_i$ estimate can be either above or below $\bar{\alpha}$. This reflects that average early response differs between patients. We take reference $\bar{\alpha} = 0.35$ Gy^{-1}, a typical value for human head-and-neck tumors (Fowler et al., 2003; Fowler, 2009). We pick $\alpha_{\min} = 0.20$ Gy^{-1}, which corresponds with a deviation from $\bar{\alpha}$ of approximately 40% and covers the most probable spectrum of deviations.

In the LQ-based TCP model, the survival fraction SF_i of any voxel i is multiplied by its estimated number of clonogenic cells. Rather than assuming a uniform initial clonogen density throughout the target volume, the number of clonogens in voxel i is determined as

$$\hat{\nu}_i := c_\nu F_i^p, \tag{3.5}$$

where c_ν is a scaling factor such that the population average of $\hat{\nu}_i$ estimates equals a pre-determined $\bar{\nu}$. We assume the standard initial clonogen density of $10^7/\mathrm{cm}^3$ (Webb and Nahum, 1993; Chapman and Nahum, 2015). According to Section 3.2.1 the voxel volume is 0.0180 cm^3, so we obtain $\bar{\nu} = 1.80 \cdot 10^5$. The rationale behind (3.5) is that a higher pre-treatment signal is associated with more activity and/or more cells in a voxel, and those voxels have a higher contribution to TCP. Note that this additionally implies that the voxels with low pre-treatment signal F_i^p have less contribution to TCP, so the influence of assigning them parameter $\bar{\alpha}$ is small.

For any target voxel i, the estimates $(\hat{\alpha}_i, \hat{\nu}_i)$ are subject to uncertainty, due to inevitable biomarker measurement errors and imperfect parameter estimation from biomarker data. It has been shown that uncertainty in dose-response relationships may have considerable influence on the benefit of dose-painting strategies (Zhang et al., 2013; Barry et al., 2020; Petit et al., 2021). This issue is discussed in more detail in Section 3.4.1. To account for parameter estimation inaccuracy, we do not use the estimates $(\hat{\alpha}_i, \hat{\nu}_i)$ directly, but take a worst-case approach. Lower values of α_i correspond with lower radiation sensitivity and consequently lower TCP. On the contrary,

higher values of $\hat{\nu}_i$ correspond with higher initial clonogen numbers and lower TCP. Therefore, we optimize using worst-case radiosensitivity values

$$\hat{\alpha}_i^{\mathrm{w}} = (1 - p_\alpha)\hat{\alpha}_i, \tag{3.6a}$$

$$\hat{\nu}_i^{\mathrm{w}} = (1 + p_\nu)\hat{\nu}_i, \tag{3.6b}$$

where $p_\alpha \cdot 100\%$ and $p_\nu \cdot 100\%$ are the maximum estimation error percentages. We assume maximum error factors $p_\alpha,\ p_\nu$ of 0.1; the influence of this choice will be analyzed and discussed in Sections 3.3 and 3.4.1. The output of the method is two vectors $\hat{\boldsymbol{\alpha}}^{\mathrm{w}},\ \hat{\boldsymbol{\nu}}^{\mathrm{w}} \in \mathbb{R}_+^{n_T}$ which are to be plugged in (3.2). Note that the best-case estimates $\hat{\alpha}_i^{\mathrm{b}}$ and $\hat{\alpha}_i^{\mathrm{b}}$ are obtained by reversing the signs for p_α and p_ν in (3.6).

3.2.5 Adaptation strategies

The last component of the adaptation framework is a method to optimally adapt the treatment plan using the updated parameter estimates. Figure 3.2 gives a schematic overview of the adaptations we consider. If the original treatment plan is adapted, the dose is either uniformly or continuously adapted. Within uniform dose adaptation we can distinguish uniform dose escalation and uniform dose de-escalation, i.e., scaling the entire dose distribution up or down. Continuous dose adaptation, also known as dose painting, modulates the spatial dose pattern itself. If none of these adaptation strategies is beneficial for the treatment plan quality (e.g., in terms of TCP and/or NTCP), no adaptation is made. The original treatment plan can be continued if information acquired mid-treatment indicates the original treatment plan quality is sufficient. If neither an adapted treatment plan nor the original treatment plan yields sufficient treatment plan quality, one can stop the treatment, and possibly switch to another treatment modality. In the context of OSRT, one can also opt to optimally adapt the number of treatment fractions; in Ajdari et al. (2018) and in Chapter 2 this problem is studied from a theoretical perspective. This adaptation strategy is not considered in the current study.

Once the resulting TCP interval and NTCP values for the various considered adaptation strategies and the original treatment plan have been determined, Figure 3.2 can be used as a decision tree as well. Thresholds depending on TCP intervals, NTCP values and radiation response parameter estimates can be used as decision criteria. All of these implicitly account for uncertainty in parameter estimates. Nevertheless, clinically relevant decision criteria will likely depend on more factors than those currently presented, and precise decision criteria are likely disease site and institution specific. Formulating these is beyond the scope of this work.

Uniform dose adaptation and continuous dose adaptation are described in the next two sections.

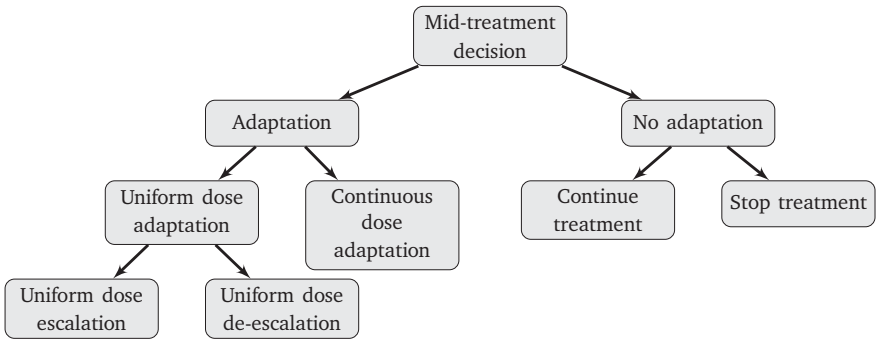

Figure 3.2: Schematic overview of adaptation strategies.

Uniform dose adaptation

The uniform dose adaptation (UDA) strategy does not involve a full beam(let) optimization step. Instead, the dose distribution that is administered in the first stage is escalated or de-escalated (i.e., scaled) for the second stage, based on the estimated radiation response parameters. Naturally, uniform dose escalation increases both TCP and NTCP, whereas uniform dose de-escalation decreases both TCP and NTCP. The decision variable is the scaling parameter s, defined by

$$s := \frac{\bar{d}^T_{\text{adapt}}}{\bar{d}^T_{\text{orig}}},$$

where $\bar{d}^T_{\text{orig}}$ and $\bar{d}^T_{\text{adapt}}$ denote the original and adapted mean target dose over both stage 1 and 2, respectively. A value $s < 1$ denotes dose de-escalation and $s > 1$ denotes dose escalation. As there is a one-to-one relationship between mean target dose in the adaptive plan and the scaling parameter s, it is more intuitive to discuss UDA policies in terms of mean target dose adaptations. The resulting worst-case and best-case TCP for an adapted mean target dose $\bar{d}^T_{\text{adapt}}$ are

$$\text{TCP}_w(\bar{d}^T_{\text{adapt}}) := \text{TCP}_{\text{LQ}}(s\boldsymbol{d}^T_{\text{orig}}; \hat{\boldsymbol{\alpha}}^{\text{w}}, \hat{\boldsymbol{\nu}}^{\text{w}}),$$
$$\text{TCP}_b(\bar{d}^T_{\text{adapt}}) := \text{TCP}_{\text{LQ}}(s\boldsymbol{d}^T_{\text{orig}}; \hat{\boldsymbol{\alpha}}^{\text{b}}, \hat{\boldsymbol{\nu}}^{\text{b}}).$$

The benefit of having a single optimization variable is that the NTCP curve and the worst- and best-case TCP curves can directly be visualized. This yields a graphical

illustration of the changes in NTCP, and worst-case and best-case TCP associated with a particular UDA policy. Thus, restrictions on the allowed adaptations in terms of physical dose, scaling factor or TCP/NTCP changes need not be set in advance.

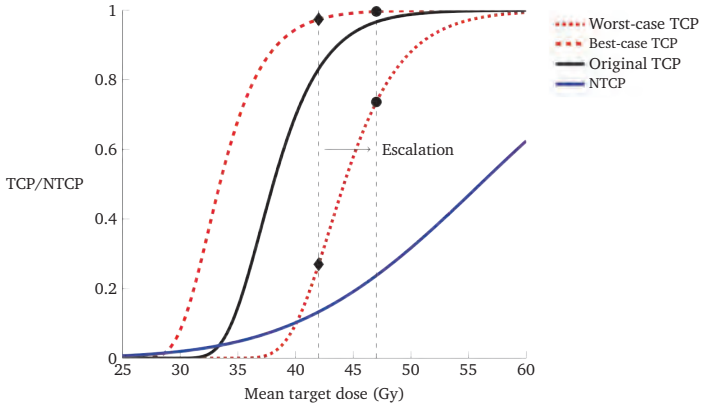

Figure 3.3: Illustrative TCP/NTCP graph from response parameter estimates. The left and right vertical lines represent the original and escalated treatment plan, respectively. The intervals contained by the diamond and circles are the TCP intervals of the original and the escalated treatment plan, respectively.

Figure 3.3 shows a toy example. The original TCP and NTCP are indicated by black and blue curves. The original treatment plan is the leftmost dashed vertical line, and yields a TCP of approximately 0.88. Mid-treatment imaging and subsequent parameter estimation allows for an update of the TCP curve, and yields the worst-case (dotted red) and best-case (dashed red) curves. This implies the original treatment plan in fact results in a TCP anywhere between 0.27 and 0.98 (interval contained by the diamonds). Uniform dose escalation by +5 Gy is visualized by the rightmost dashed vertical line. This results in a TCP interval of $[0.73, 1.00]$ (interval contained by the circles), while NTCP has increased from 0.13 to 0.25.

It is important to note that the original TCP curve need not be between the estimated best-case and worst-case TCP curves, but may also be above or below both estimated curves. Additionally, if biomarker data provides grounds for updating the NTCP curve, an updated NTCP interval can be drawn in the same figure analogous to the TCP interval.

In principle, this presents a continuum of adaptation possibilities to the clinical decision maker, with a direct visualization of resulting TCP and NTCP values. In the

current chapter, the objective is to maximize the worst-case therapeutic ratio

$$\mathrm{TR}(\bar{d}^T_{\mathrm{adapt}}) = \mathrm{TCP}_w(\bar{d}^T_{\mathrm{adapt}}) - \mathrm{NTCP}(\frac{\bar{d}^T_{\mathrm{adapt}}}{\bar{d}^T_{\mathrm{orig}}}\boldsymbol{d}^r_{\mathrm{orig}}),$$

where for NTCP structure r we use the NTCP for cataract to the eye that receives the lowest dose. Scaling the dose distribution increases or decreases $\boldsymbol{d}^T$ and $\boldsymbol{d}^r$ simultaneously.

Values of $\bar{d}^T_{\mathrm{adapt}}$ are restricted to deviate at most $d_{\mathrm{dev}} = 5$ Gy from the original mean target dose $\bar{d}^T_{\mathrm{orig}}$. Note that one could also control the adaptation by restricting the worst-case TCP or NTCP to deviate at most a certain number from the original TCP or NTCP. A drawback of this is that these measures are nonlinear, so it is less intuitive for physicians to specify the allowed deviations. For a relatively flat TCP or NTCP curve, a particular allowed deviation in terms of TCP or NTCP may result in an unexpected large dosimetric deviation. In either case, UDA finds the adaptation within the allowed deviation interval that maximizes the worst-case therapeutic ratio.

Continuous dose adaptation

Continuous dose adaptation (CDA), also known as adaptive biologically conformal treatment or dose painting, is a more complex adaptation strategy than UDA. It performs a full beam(let) optimization, in order to adapt the spatial dose distribution to spatial patterns of radiation response estimated from pre- and mid-treatment imaging data. The CDA optimization model directly optimizes the TCP and NTCP criteria. Next to this, the model imposes mean dose and voxel-wise dose restrictions on various tissues to ensure the resulting treatment plans are not too far from clinical reality. Furthermore, the mean target dose is fixed at the originally (clinically) delivered mean target dose, so that target dose is only redistributed and not added. The rationale is that redistribution of dose allows for delivering more dose to radioresistant voxels and less dose to radiosensitive voxels, thus increasing TCP while keeping mean dose equal.

Let $\boldsymbol{d} \in \mathbb{R}^n$ denote the concatenated vector of target doses $\boldsymbol{d}^T$, OAR doses $\boldsymbol{d}^r$, $r \in \mathcal{R}$, and other relevant tissue doses $\boldsymbol{d}^{\mathrm{O}}$; mean values are again indicated by a horizontal bar. Let $\boldsymbol{x} \in \mathbb{R}^m_+$ denote the (nonnegative) beamlet weight, and let $\boldsymbol{A} \in \mathbb{R}^{n\times m}$ denote the dose deposition matrix. With $\boldsymbol{a}_i^\top$ the i-th row of $\boldsymbol{A}$, the dose deposited in voxel i for beamlet weights $\boldsymbol{x}$ is given by $\boldsymbol{a}_i^\top \boldsymbol{x}$. The model maximizes the worst-case TCP subject to NTCP tolerances for all OARs in $\mathcal{R}$:

$$\max_{\boldsymbol{x},\boldsymbol{d}} \ \mathrm{TCP}_{\mathrm{LQ}}(\boldsymbol{d}^T; \hat{\boldsymbol{\alpha}}^w, \hat{\boldsymbol{v}}^w), \tag{3.7a}$$

$$\text{s.t.} \ \ \mathrm{NTCP}^r(\boldsymbol{d}^r) \le \mathrm{NTCP}^r_{\mathrm{tol}}, \ r \in \mathcal{R}, \tag{3.7b}$$

$$\bar{d}^r \leq d^r_{\text{tol}},\ r \in \mathcal{R}, \tag{3.7c}$$
$$\bar{d}^T = \bar{d}^T_{\text{orig}}, \tag{3.7d}$$
$$\boldsymbol{d}_L \leq \boldsymbol{d} \leq \boldsymbol{d}_U, \tag{3.7e}$$
$$\boldsymbol{d} = \boldsymbol{A}\boldsymbol{x}, \tag{3.7f}$$
$$\boldsymbol{x} \geq \boldsymbol{0}, \tag{3.7g}$$

where $\text{NTCP}^r(\boldsymbol{d}^r)$ is the LKB NTCP corrected for heterogeneous dose and nonuniform fractionation, see Appendix 3.A.1 for details. Constraints (3.7b) and (3.7c) ensure that for all OARs the resulting mean OAR doses and NTCP values do not exceed set tolerances. Constraint (3.7d) forces the mean target dose to equal the mean target dose of the original treatment plan, and (3.7e) prescribes minimum and maximum voxel doses. Lastly, constraint (3.7f) relates beamlet weights to voxel doses and (3.7g) ensures nonnegativity of beamlet weights. The optimization model (3.7) is convexified using the methodology of Hoffmann et al. (2008).

For the current study we add a quadratic underdose penalty to the (convexified) objective, which penalizes PTV42 dose lower than 42 Gy. This resembles the original treatment goal that a minimum of 98% of PTV42 volume was required to achieve the dose of 42 Gy. The OAR NTCP tolerance is equal to the resulting NTCP of the original treatment plan, with a minimum of 0.05. Mean OAR dose tolerance is equal to the resulting mean OAR dose of the original treatment plan. PTV50, PTV42 and OAR dose must be at most the maximum PTV50 dose of the original treatment plan plus 5 Gy. Dose to other (non-OAR) normal tissue voxels is subject to the same upper bound, see Appendix 3.A.2 for more details. By basing our NTCP upper bounds on the originally delivered dose distributions in this way, the optimized plans cannot yield a (noteworthy) worse TCP or NTCP than the originally delivered plan. Nevertheless, the obtained dose distributions may differ from the dose distribution of the original treatment plan.

Dose optimization is performed using an in-house treatment planning software WiscPlan (Flynn, 2007). Dose is calculated for 64 beamlets at 21 angles for each rotation of the gantry. Treatment pitch was set to 0.86. The WiscPlan software functionality includes classical optimization and minimax robust optimization for setup and range errors, but these are omitted for the current study. For the current study functionality was expanded to directly optimize TCP and NTCP criteria. In particular, the large-scale convex optimization problem (3.7) is solved using the open-source interior-point method IPOPT (Wächter and Biegler, 2006) in MATLAB R2018b (Math-

works, Natick, MA, US), interfaced through the MATLAB OPTI toolbox (Currie and Wilson, 2012). All computations are performed on a system with a 24-core Intel Xeon Gold 6126 (2.60GHz) CPU. Table 3.1 give an overview of the number of beamlets and the number of voxels. Further technical optimization details are provided in Appendix 3.A.2.

	Number of beamlets	Number of voxels				
		PTV50	PTV42	Brain	Right eye	Left eye
Minimum	1713	466	1385	3037	226	249
Mean	5741	4458	8892	5003	400	395
Maximum	10073	11313	17271	6091	618	509

Table 3.1: Statistics on number of beamlets and number of voxels in patient cases.

3.3 Numerical results

Section 3.3.1 presents the results of the radiation response parameter estimation. Sections 3.3.2 and 3.3.3 present the results for the UDA and CDA strategies, respectively. As indicated in Section 3.2 we make no attempt to quantify thresholds and other criteria for deciding among the various adaptation strategies. As such, we do not present individualized adaptation recommendations for each patient. Instead, we present the mathematically optimal results of UDA and CDA, and consider the influence of uncertainty. We illustrate for a few patient cases how the TCP and NTCP information available mid-treatment can be used in the decision making process.

3.3.1 Radiation response parameter estimation

Figures 3.4 and 3.5 display boxplots for the distribution of $\hat{\nu}_i$ and $\hat{\alpha}_i$ estimates, respectively, as determined from the pre- and mid-treatment FLT scans. Patients are ordered according to their mean clonogen number estimates. By construction, the minimum $\hat{\alpha}_i$ estimate is 0.20 and the mean estimate is 0.35. The resulting maximum $\hat{\alpha}_i$ estimate is approximately 0.52. By construction, the mean of the clonogen number estimates $\hat{\nu}_i$ is $1.80 \cdot 10^5$.

By construction, patients with low initial clonogen numbers (e.g., patients 11-14) have little to no variance in radiation sensitivity estimates. For these patients, the boxes in Figure 3.5 are not visible, i.e., the 25^{th} and 75^{th} percentile coincide with $\bar{\alpha}$. These are the patients with low magnitude pre-treatment voxel signals, for which pre- to mid-treatment signal changes cannot reliably be interpreted as radiation response due

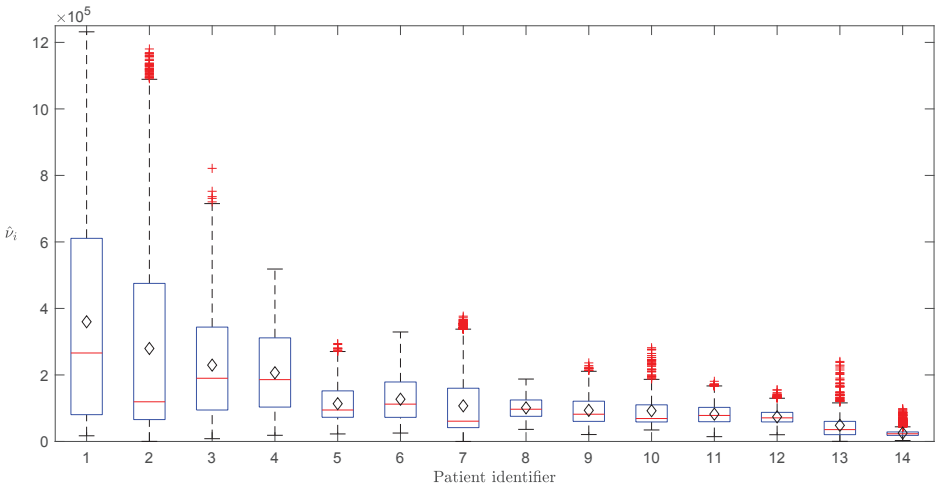

Figure 3.4: Distribution of clonogen number estimates $\hat{\nu}_i$. The bottom and top horizontal blue line indicate the 25$^{\text{th}}$ and 75$^{\text{th}}$ percentile, respectively. The horizontal red line and diamond inside the boxes indicate the median and the mean, respectively. Individual marks indicate outliers. Patients are ordered according to their mean estimates.

to influence of, e.g., noise. Although voxel-wise $\hat{\alpha}_i$ estimates are little or not available for those patients, the low estimates of initial clonogen numbers suggest that dose de-escalation may be beneficial.

For patients with higher estimated initial clonogen numbers $\hat{\nu}_i$ (e.g., patients 1-4) more heterogeneity in voxel response is observed, which translates to more heterogeneity in $\hat{\alpha}_i$ estimates. In the LQ-based TCP function (3.2), the predominant influence on TCP is due to voxels with high radioresistance. Thus, a high variation in $\hat{\alpha}_i$ estimates suggests that uniform or continuous dose adaptation may be beneficial to also ensure eradication of clonogens in those voxels with low $\hat{\alpha}_i$ estimates.

For both $\hat{\nu}_i$ and $\hat{\alpha}_i$ the median estimates (red horizontal lines in Figures 3.4 and 3.5) are unequal to the mean estimates (diamonds in Figures 3.4 and 3.5) for those patients with high intra-patient heterogeneity. Thus, for individual patients the spread of radiation sensitivity parameter estimates and initial clonogen number estimates is skewed, and cannot be described by, for instance, a normal distribution.

Figure 3.6 shows a histograms of the response estimates for a patient with an average $\hat{\alpha}_i$ higher (patient 1) and lower (patient 6) than $\bar{\alpha}$. These patients are chosen because they have sufficient heterogeneity in $\hat{\alpha}_i$ estimates but are not the extreme

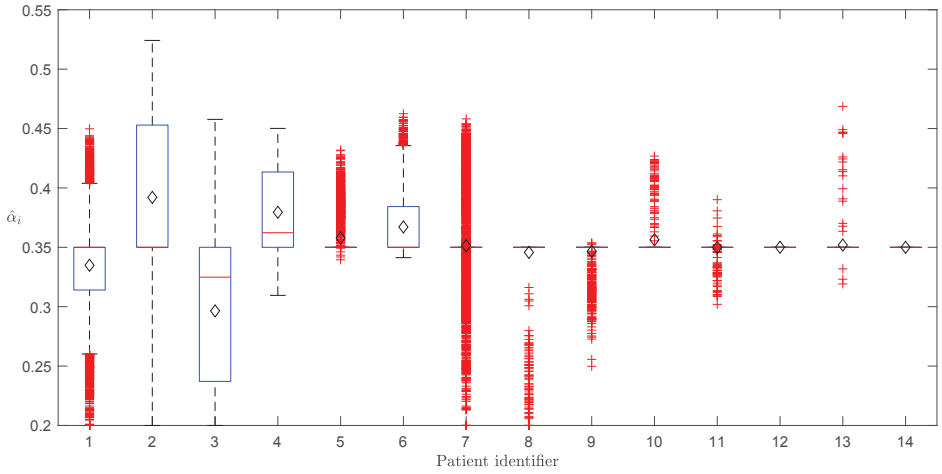

Figure 3.5: Distribution of radiation sensitivity estimates $\hat{\alpha}_i$. The bottom and top horizontal blue line indicate the 25th and 75th percentile, respectively. The horizontal red line and diamond inside the boxes indicate the median and the mean, respectively. Individual marks indicate outliers. Patients are ordered according to their mean clonogen number estimates.

cases. Figures 3.6a and 3.6c show that for both patients a large fraction of voxels receive the baseline $\bar{\alpha}$ estimate rather than an individualized estimate. This corresponds well with the clonogen number estimates; the scaling factor c_v is $8.03 \cdot 10^4$, so individual $\hat{\alpha}_i$ estimates are computed only for those voxels for which $\hat{\nu}_i \geq c_v F_{\mathrm{TH}} = 1.61 \cdot 10^5$. In Figure 3.6b and Figure 3.6d 40% resp. 69% of voxels does not pass this threshold. The worst-case, best-case and nominal (assuming no uncertainty) TCP values of the original treatment plans are obtained via (3.2). Table 3.2 reports these values along with NTCP values and dosimetric characteristics. As typical for canine sinonasal tumors (Gutiérrez et al., 2007), often one of the eyes is sacrificed to ensure proper tumor coverage. Instead of reporting results for right and left eye, results are reported for the eye with lowest and highest dose.

We observe that indeed one eye (the sacrificed) receives considerably more dose than the other (the spared). This is reflected in the mean NTCP values. Brain necrosis NTCP is close to zero on average, despite the average D_2 being substantial. The TCP of the PTV50 has a range of 0.26, for the assumed estimation error bounds $p_\alpha = p_\nu = 0.10$. This indicates that (on average) TCP is sensitive to the parameter estimates and that the original treatment plan exhibits much uncertainty regarding TCP.

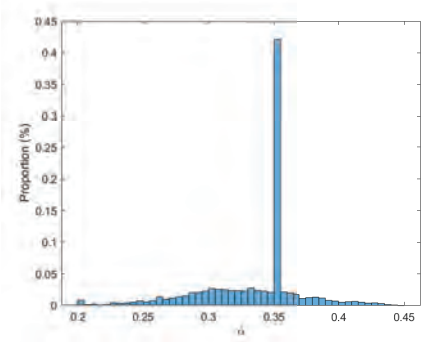

(a) $\hat{\alpha}_i$ estimates radioresistant patient

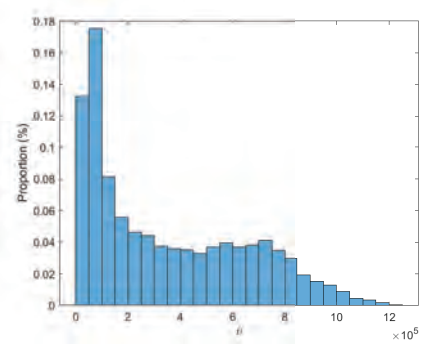

(b) $\hat{\nu}_i$ estimates radioresistant patient

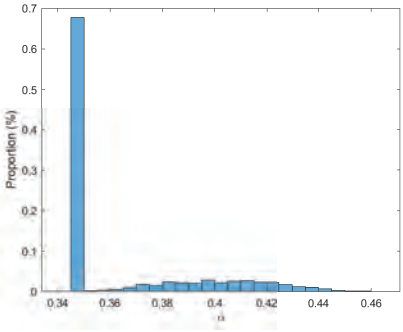

(c) $\hat{\alpha}_i$ estimates radiosensitive patient

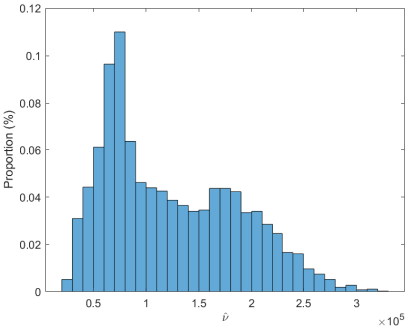

(d) $\hat{\nu}_i$ estimates radiosensitive patient

Figure 3.6: Radiation response estimates ($\hat{\alpha}_i$, $\hat{\nu}_i$) for a radioresistant (patient 1) and a radiosensitive (patient 6) patient.

	TCP_{nom} [TCP_{range}]	NTCP	d_{98} (Gy)	d_{mean} (Gy)	d_2 (Gy)
PTV50	0.64 [0.48, 0.74]		45.24	48.44	49.47
PTV42			41.02	46.63	49.45
Brain		0.03		8.14	36.63
Eye (low)		0.33		9.16	23.19
Eye (high)		0.68		15.69	33.54

Table 3.2: Results for the original treatment plan. D_{98} and D_2 are the near minimum and near maximum dose, respectively. All numbers are cohort averages.

3.3.2 Uniform dose adaptation

Patient	Original		De-escalation (-5 Gy)		Escalation (+5 Gy)	
	TCP	NTCP	TCP	NTCP	TCP	NTCP
1	[0.00, 0.50]	0.88	[0.00, 0.00]	0.69	[0.04, 0.94]	0.97
2	[0.02, 0.81]	0.96	[0.00, 0.30]	0.83	[0.44, 0.96]	1.00
3	[0.00, 0.00]	0.03	[0.00, 0.00]	0.02	[0.00, 0.20]	0.05
4	[1.00, 1.00]	0.01	[0.91, 1.00]	0.01	[1.00, 1.00]	0.02
5	[0.43, 0.99]	0.95	[0.00, 0.74]	0.77	[0.96, 1.00]	1.00
6	[0.98, 1.00]	0.17	[0.80, 1.00]	0.09	[1.00, 1.00]	0.28
7	[0.00, 0.05]	0.59	[0.00, 0.00]	0.34	[0.00, 0.74]	0.82
8	[0.00, 0.02]	0.10	[0.00, 0.00]	0.05	[0.00, 0.64]	0.19
9	[0.26, 0.98]	0.00	[0.00, 0.62]	0.00	[0.91, 1.00]	0.00
10	[1.00, 1.00]	0.09	[0.98, 1.00]	0.05	[1.00, 1.00]	0.15
11	[0.06, 0.97]	0.77	[0.00, 0.35]	0.49	[0.87, 1.00]	0.94
12	[0.99, 1.00]	0.02	[0.84, 1.00]	0.01	[1.00, 1.00]	0.03
13	[1.00, 1.00]	0.00	[0.98, 1.00]	0.00	[1.00, 1.00]	0.00
14	[0.99, 1.00]	0.01	[0.89, 1.00]	0.00	[1.00, 1.00]	0.01

Table 3.3: TCP interval and NTCP (low dose eye) for all patients, for the original treatment plan and the ± 5 Gy UDA plans. Patient numbers are the same as in Figures 3.4 and 3.5.

Before presenting the mathematically optimal UDA policies, Table 3.3 shows the TCP interval and NTCP to the low dose eye for all patients, for the original treatment plan and the maximum dose escalation and de-escalation policy. This indicates the bandwidth of adaptations for each patient. For the majority of these patients the NTCP of the high dose eye is close to one and the brain NTCP is close to zero in all three scenarios. Thus, changes in the low dose eye NTCP are most relevant for comparing adaptation strategies. For some patients, e.g., patient 13, neither maximum dose de-escalation nor dose escalation leads to noteworthy changes in TCP interval or NTCP values. Thus, the optimal UDA strategy will not differ from the original treatment plan either in terms of TCP or NTCP criteria. For other patients, e.g., patient 5, both the TCP interval and the NTCP value differ significantly between the original treatment plan and the maximum dose escalation and de-escalation plans. Thus, the optimal UDA strategy may differ substantially from the original treatment plan. For 9 out of 14 patients the worst- and best-case TCP of the original treatment plan are both near 0 or near 1. For these patients radiation response uncertainty does not lead to a wide

TCP interval, i.e., have little influence on expected outcome according to the employed TCP model. This is highly dependent on the used TCP model and is discussed in more detail in Section 3.4.2.

	TCP_{nom} [TCP_{range}]	NTCP	d_{98} (Gy)	d_{mean} (Gy)	d_2 (Gy)
PTV50	0.70 [+0.06] [0.65 [+0.17], 0.71 [-0.02]]		45.46 [+0.21]	48.67 [+0.23]	49.70 [+0.23]
PTV42			41.28 [+0.27]	46.87 [+0.25]	49.68 [+0.22]
Brain		0.07 [+0.03]		8.19 [+0.06]	36.36 [-0.27]
Eye (low)		0.30 [-0.02]		9.19 [+0.03]	23.26 [+0.07]
Eye (high)		0.65 [-0.03]		15.56 [-0.13]	33.30 [-0.23]

Table 3.4: Results for the UDA strategy. d_{98} and d_2 are the near minimum and near maximum dose, respectively. Numbers in red indicate the change compared to the original treatment plan (Table 3.2). All numbers are cohort averages.

Table 3.4 presents the results for the UDA strategy. Numbers in red indicate the change compared to the original treatment plan (Table 3.2). The average worst-case TCP has increased by approximately 0.17 (range: $[-0.02, 0.81]$, σ: 0.30) and the average best-case TCP has decreased slightly. Thus, due to an improvement (on average) in worst-case TCP, the TCP window is more than four times smaller. Nominal TCP (assuming no uncertainty) has improved from 0.64 to 0.70. The average brain necrosis NTCP has doubled, but remains low. The average NTCP values for eye cataract show only minor changes. Dosimetrically, only very minor changes can be observed on average. This indicates that the total magnitudes of dose escalation and dose de-escalation are approximately equal over the patient cohort. Recall that the objective for UDA is to maximize the worst-case TCP minus the NTCP to the low dose eye. The average therapeutic ratio has improved from 0.15 to 0.35.

In all results presented thus far the maximum radiation response errors are set at 10%. Results in Table 3.3 already indicate that this leads to rather wide TCP intervals. Figure 3.7 compares the TCP intervals of the optimal UDA treatment plans for $p_\alpha = p_\nu = 0.1$ and 0.2. The vertical bars represent the TCP interval of the original (blue) and UDA (red) treatment plan, respectively. Note that the optimal UDA treatment plan may be different for $p_\alpha = p_\nu = 0.1$ and 0.2.

Figure 3.7a shows that with $p_\alpha = p_\nu = 0.1$ UDA is able to improve the guaranteed (worst-case) TCP for a few patients, and decrease the TCP interval width at the same time. For some other patients the original best-case TCP is very low, and the therapeutic ratio can only be increased by decreasing NTCP. Thus, the worst-case and best-case TCP are both decreased to almost zero. There is only a single patient with a very uncertain

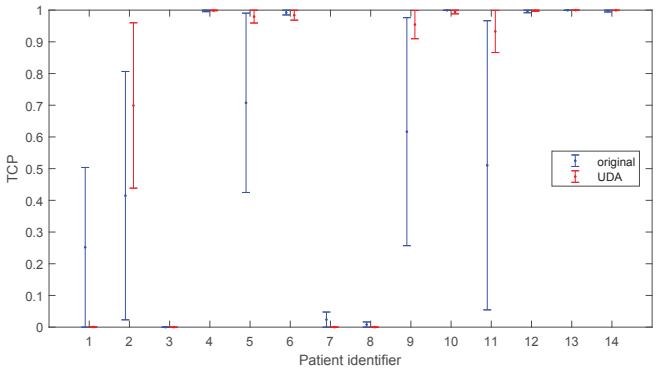

(a) $p_\alpha = p_\nu = 0.1$.

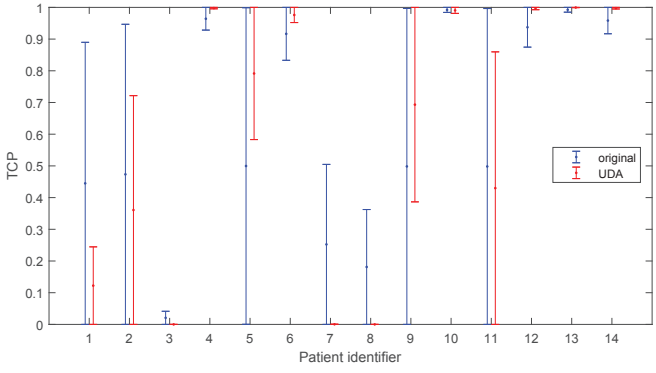

(b) $p_\alpha = p_\nu = 0.2$.

Figure 3.7: TCP intervals for the original treatment plan (blue) and the optimal UDA plan (red). Higher radiation response uncertainty (higher p_α and p_ν) increases TCP interval width. Patient numbers are the same as in previous figures.

(i.e., wide) UDA TCP interval. Note that these results are a direct consequence of optimizing for the worst-case therapeutic ratio, and the original treatment plans are optimized for different criteria. This is further discussed in Section 3.4.2.

Figure 3.7b shows that with $p_\alpha = p_\nu = 0.2$ many patients remain with a very wide TCP interval after UDA. For some patients, the resulting TCP interval has a width of over 0.7, which means data is too uncertain to draw any conclusions regarding possible benefits of uniform treatment dose adaptations. The figures demonstrate that radiation

response uncertainty can quickly decrease the benefit of UDA adaptations.

Patient-specific TCP/NTCP graphs can be created in order to visualize the continuum of adaptation possibilities, as discussed in Section 3.2.5. Figure 3.8 shows the TCP/NTCP graphs and dose-volume histogram (DVH) for four patients, again using $p_\alpha = p_\gamma = 0.1$. Next to patient 1 and 6, patients 5 and 10 are chosen to illustrate each adaptation strategy of Figure 3.2 (except CDA). For each of these patients, we illustrate how the available TCP and NTCP information can be used to make an adaptation recommendation. Note that these recommendations need not be the mathematical optimum, as presented in Table 3.4 and Figure 3.7. We emphasize that these recommendations solely serve to illustrate how the TCP and NTCP information *can* be used

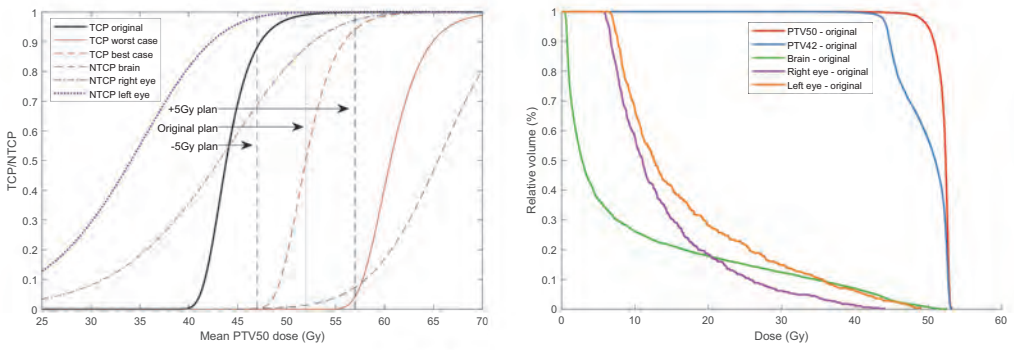

(a) Stop treatment (patient 1)

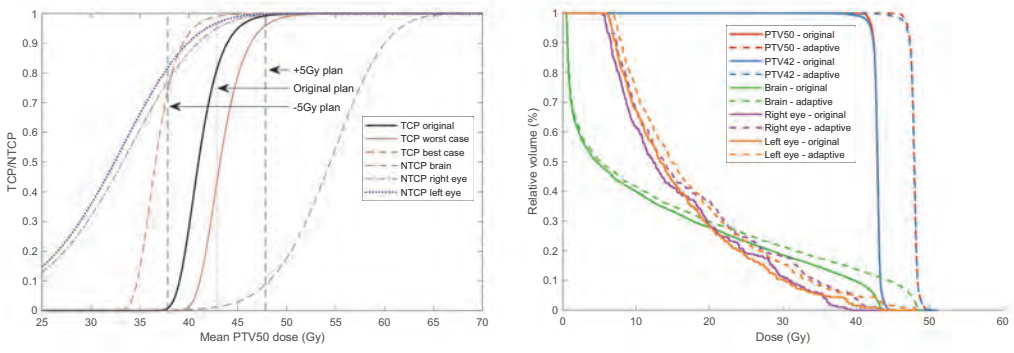

(b) Dose escalation (patient 5)

Figure 3.8 (part 1): TCP/NTCP graph showing adaptation possibilities and DVH graph of original and optimal UDA plan, for four patients. Patients 1 and 6 are the same as in Figure 3.6.

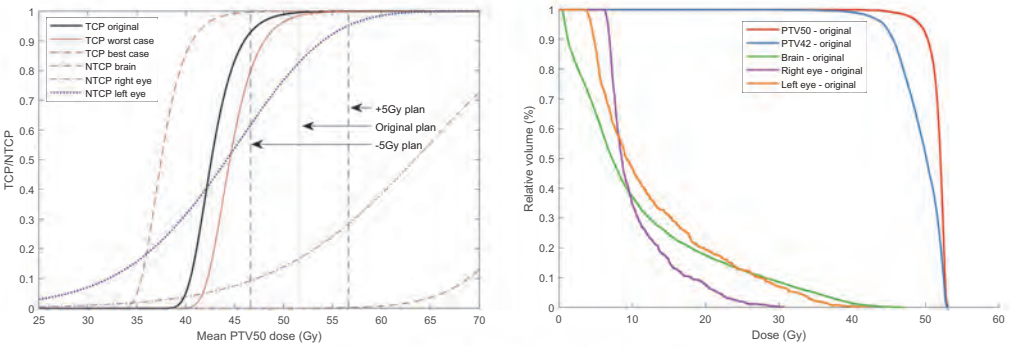

(c) Continue treatment (patient 6)

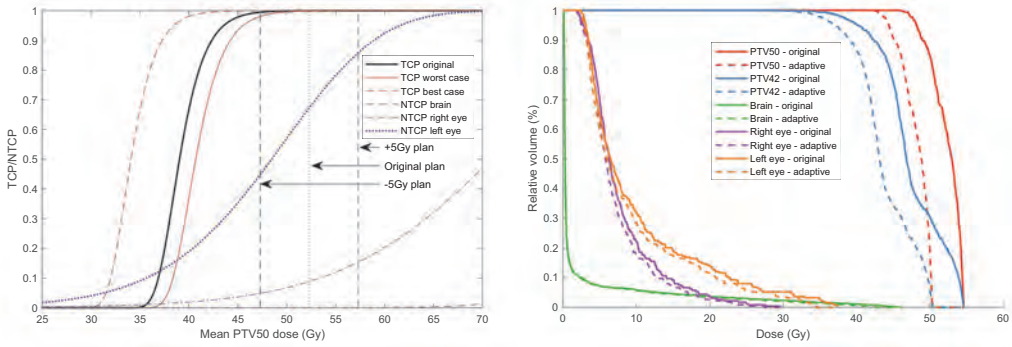

(d) Dose de-escalation (patient 10)

Figure 3.8 (part 2): TCP/NTCP graph showing adaptation possibilities and DVH graph of original and optimal UDA plan, for four patients. Patients 1 and 6 are the same as in Figure 3.6.

for a UDA strategy, and we make no attempt to specify clinical guidelines for adaptation decisions.

For each patient, the left panel in Figure 3.8 presents the TCP/NTCP graph and the right panel presents the DVH of the original plan and the recommended UDA plan. In the TCP/NTCP graphs the dotted vertical line indicates the original treatment plan, the dashed vertical lines are the maximum (de)-escalation plans. These bounds are set such that the mean target dose (on the horizontal axis) deviates by at most $d_{\text{dev}} = 5$ Gy from the original treatment plan.

In the case of Figure 3.8a, the original TCP curve is not in between the estimated

worst-case and best-case TCP curves, i.e., the estimated TCP curves are more pessimistic than the original TCP curve. The original treatment plan results in a very uncertain TCP: approximately the interval $[0, 0.51]$. The NTCP to both eyes is already extremely high, thus these complications are unavoidable. Uniform dose escalation by $+5$ Gy improves the TCP interval to $[0.05, 0.94]$, while the NTCP to the right eye and the brain increases by approximately 0.1. The TCP interval is very wide, and if worst-case TCP is the main criteria this is not a desirable adaptation. The mathematically optimal therapeutic ratio is achieved by dose de-escalation by -5 Gy, but this reduces best-case TCP to zero. Thus, continuing with any reasonably adapted treatment will not provide a satisfactorily high guaranteed TCP, and one could opt to stop radiation therapy for this patient and possibly switch to another treatment modality. The right panel of Figure 3.8a shows the DVH of the original treatment plan.

In the case of Figure 3.8b, the original treatment plan results in a very uncertain TCP, i.e., approximately the interval $[0.57, 0.99]$. The NTCP to both eyes is already extremely high, thus these complications are unavoidable. Uniform dose escalation by $+5$ Gy improves the TCP interval to $[0.95, 1.00]$, while the NTCP to the brain remains below 0.1. The optimal therapeutic ratio is achieved by dose escalation, as shown in the DVH graph.

Figure 3.8c shows a case where the original plan results in a very high TCP (both in worst- and best-case), and a high NTCP to the left eye. Any dose escalation would only marginally improve worst-case TCP, while the NTCP values for both eyes would considerably increase. Dose de-escalation would decrease worst-case TCP faster than it would decrease NTCP values. The maximum therapeutic ratio is achieved by a dose de-escalation with very small magnitude. Thus, when solely considering TCP and NTCP, (major) deviations from the original treatment plan are not recommended. The right panel gives the DVH of the original treatment plan.

Figure 3.8d shows a case where the original treatment plan has a high worst-case TCP, but the NTCP to the sacrificed (left) eye is of concern. Uniform dose de-escalation by -5 Gy results in a TCP interval of approximately $[0.97, 1.00]$, while the NTCP of the left eye is considerably decreased. Thus, uniform dose de-escalation is suitable. The right panel show the DVH graph of the original treatment plan and the plan that gives the optimal therapeutic ratio; the DVH graph shows this is indeed a uniform dose de-escalation plan.

3.3.3 Continuous dose adaptation

Compared to UDA, the CDA strategy has a much larger decision space. Thus, we cannot easily present the entire bandwidth of the adaptation possibilities analogous to

Table 3.3. Table 3.5 reports the mathematically optimal results for the CDA strategy. For the worst- and best-case TCP computation we again use error parameters $p_\alpha = p_\nu = 0.1$, and instead of reporting results for right and left eye, results are reported for the eye with lowest and highest dose. Recall that, unlike for the UDA strategy, the objective of CDA is to maximize the worst-case TCP. This is further discussed in Section 3.4.2. Compared to the original treatment plan (Table 3.2), the worst-case

	TCP_{nom} [TCP_{range}]	NTCP	d_{98} (Gy)	d_{mean} (Gy)	d_2 (Gy)
PTV50	0.77 [+0.13] [0.56 [+0.07], 0.91 [+0.17]]		43.83 [-1.41]	48.44 [-]	52.90 [+3.44]
PTV42			41.14 [+0.12]	47.79 [+1.16]	53.51 [+4.06]
Brain		0.01 [-0.03]		7.74 [-0.40]	34.64 [-1.99]
Eye (low)		0.27 [-0.06]		9.03 [-0.13]	22.32 [-0.87]
Eye (high)		0.63 [-0.06]		15.59 [-0.11]	31.39 [-2.15]

Table 3.5: Results for the CDA strategy. d_{98} and d_2 are the near minimum and near maximum dose, respectively. Numbers in red indicate the change compared to the original treatment plan (Table 3.2). All numbers are cohort averages.

TCP improved on average by 0.07 (range: $[-0.03, 0.76]$, σ: 0.21). Nominal (assuming no uncertainty) and best-case TCP increased by 0.13 and 0.17, respectively. NTCP values and d_2 have decreased slightly for all OARs, while d_{mean} remains mostly unchanged. The decrease in near-maximum OAR dose may be due to the use of slightly different dosimetric criteria for target and OAR structures in the CDA plan compared to the original treatment plan, or several post-optimization steps the original treatment plan went through to make it practically deliverable. Both PTV50 and PTV42 have a larger gap between d_{98} and d_2, on average, indicating more heterogeneous dose distributions. Summarizing, on average, the CDA dose distribution improves both TCP and NTCP criteria and does not lead to a dosimetrically worse OAR dose distribution.

The original treatment plan was optimized for physical dose criteria rather than TCP and NTCP criteria. Thus, any improvements by CDA may be partially due to inclusion of imaging biomarkers, and partially due to the direct optimization of TCP and NTCP. To investigate this, we also solve model (3.7) using reference values $(\bar{\alpha}, \bar{\nu})$ instead of $(\hat{\boldsymbol{\alpha}}^w, \hat{\boldsymbol{\nu}}^w)$ in the objective. Appendix 3.A.3 presents the results. These indicate that direct optimization of TCP using reference values $(\bar{\alpha}, \bar{\nu})$ does not produce treatment plans that are better than the original treatment plans, in terms of TCP values for estimated response parameters $(\hat{\boldsymbol{\alpha}}^w, \hat{\boldsymbol{\nu}}^w)$. Thus, the improvement is indeed due to the inclusion of imaging biomarkers, and optimizing for the updated TCP function.

Similar to Figure 3.7, we test the influence of the maximum radiation response

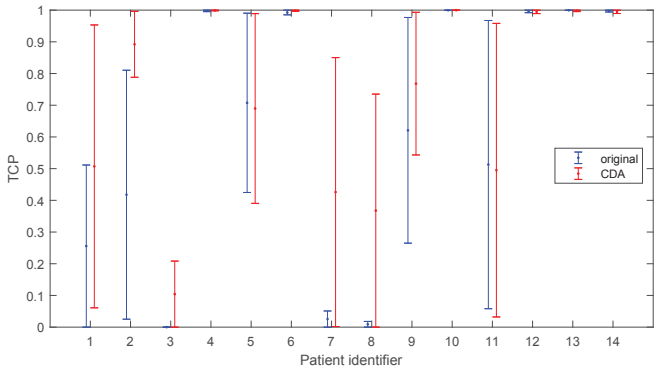

(a) $p_\alpha = p_\nu = 0.1$.

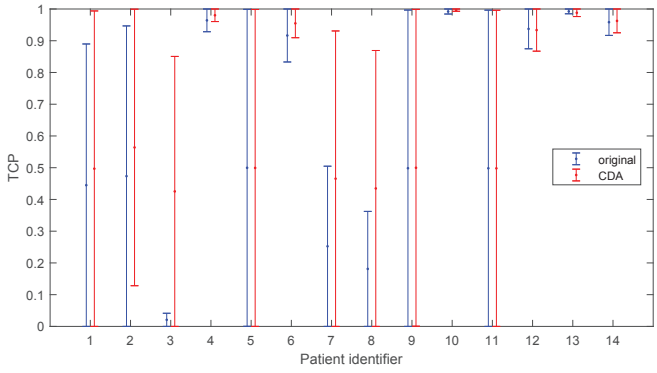

(b) $p_\alpha = p_\nu = 0.2$.

Figure 3.9: TCP intervals for the original treatment plan (blue) and the optimal CDA plan (red). Higher radiation response uncertainty (higher p_α and p_ν) increases TCP interval width. Patient numbers are the same as in previous figures.

errors on CDA results. Figure 3.9 compares the TCP intervals of the optimal CDA treatment plans for $p_\alpha = p_\nu = 0.1$ and 0.2. The vertical bars represent the TCP interval of the original (blue) and adapted (red) treatment plan, respectively. The optimal CDA treatment plan may be different for $p_\alpha = p_\nu = 0.1$ and 0.2.

If $p_\alpha = p_\nu = 0.1$, Figure 3.9a shows the worst-case TCP has improved considerably for patients 2 and 9. For patients 1, 3, 7 and 8 the worst-case TCP did not increase much, but the best-case TCP has increased, thus leading to a much wider TCP interval.

For the remaining patients, the TCP interval changes are negligible. Figure 3.9b shows that if $p_\alpha = p_\nu = 0.2$ the optimal CDA policies yield very wide TCP intervals. The uncertainty is even higher than for UDA (compare Figure 3.7b), indicating that the benefit of CDA is even more sensitive to radiation response uncertainty than UDA. The possible benefit of CDA is unclear if $p_\alpha = p_\nu = 0.2$.

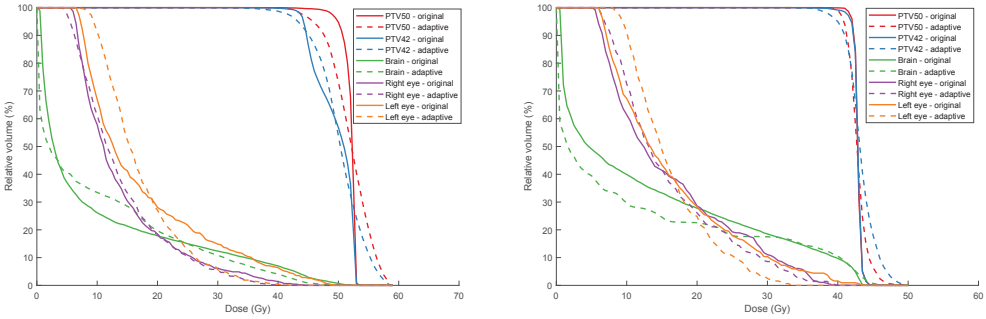

(a) patient 1 (b) patient 5

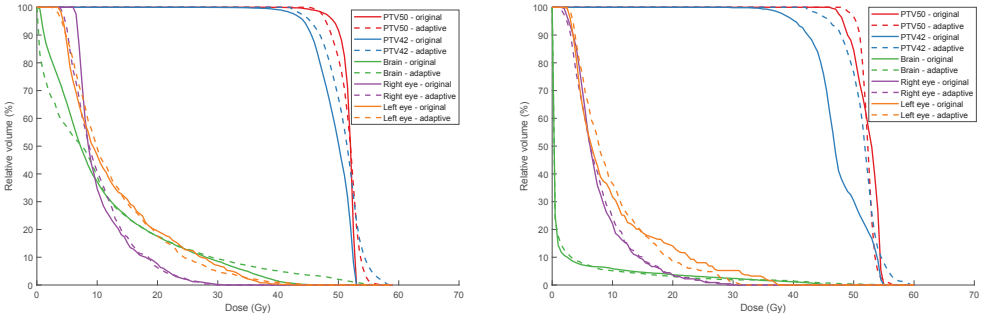

(c) patient 6 (d) patient 10

Figure 3.10: DVH of the original and optimal CDA treatment plan for patients 1, 5, 6 and 10. These are the same patients as in Figure 3.8.

Figure 3.10 gives the DVHs of the optimal CDA plans for same four patients as Figure 3.8, using $p_\alpha = p_\nu = 0.1$. As expected, the optimal CDA plans have more heterogeneous dose distributions for both the PTV50 and the PTV42. In Figure 3.10a the maximum PTV50 dose of the CDA plan is exactly 5 Gy higher than the maximum PTV50 dose of the original treatment plan, thus exactly attaining the prescribed upper bound.

In several cases OAR dose distributions differ between the original and CDA treatment plan. For example, in several cases the maximum dose to the OAR is lower, whereas the volume receiving a dose between 10 and 20 Gy has increased. As given in Table 3.A.1 in the Appendix, the generalized equivalent uniform dose (gEUD) a parameter is 3.33 for eyes and 4 for brain, which suggests that not only maximum dose but also lower doses contribute to the gEUD (i.e., contribute to NTCP). Thus, differently shaped dose distributions can yield the same LKB NTCP for eyes or brain. We present more detailed results for two patients, and again illustrate how the TCP and NTCP information and the spatial pattern of radiation sensitivity estimates *can* be used in a CDA strategy.

For patient 1, the TCP interval resulting from the original treatment plan is $[0.00, 0.51]$, and the NTCP values for brain, right and left eye are 0.01, 0.88 and 1.00, respectively. The TCP interval for the optimal CDA treatment plan is $[0.06, 0.95]$. Brain NTCP decreases to 0.00, right eye NTCP decreases to 0.75, left eye NTCP decreases to 0.87. Figures 3.11a and 3.11b show the original and optimal CDA dose distribution for patient 1, for one CT slice, focusing on the PTV50. Figure 3.11c shows there are two (small) volumes with low $\hat{\alpha}_i$, i.e., voxels with clonogenic cells that are estimated to be radioresistant. The optimal CDA treatment plan increases the dose in these volumes, and decreases the dose in other parts of the PTV50. This redistribution improves the probability of tumor control. Due to large difference between worst-case and best-case TCP, only a minor increase in guaranteed (worst-case) TCP is observed. As such, when considering only the TCP interval and NTCP values, no clear adaptation recommendation can be made.

For patient 6, the worst-case TCP improves from 0.985 in the original treatment plan to 0.996 in the CDA plan. Thus, whereas CDA is able to improve upon the original treatment plan, this does not translate to practically relevant improvements. In the original treatment plan, NTCP values for brain, right and left eye are 0.00, 0.17 and 0.83, respectively, and the CDA plan results in no noteworthy change.

Figure 3.12 presents the spatial dose distributions of $\hat{\alpha}_i$ estimates, the original plan and the CDA plan for patient 6, for one CT scan slice, focusing on the PTV50. In Figure 3.12c one can observe a volume with high $\hat{\alpha}_i$, i.e., voxels with clonogenic cells that are estimated to be radiosensitive. Figure 3.12b shows that the optimal CDA treatment plan administers slightly less dose to this area than the original plan in Figure 3.12a. Redistributing this dose to other volumes in turn improves the probability of tumor control. For patient 6 the TCP interval resulting from the original treatment plan is already sufficiently high, and a further improvement in TCP is not required. Nevertheless, the resulting heterogeneous dose distribution is more biologically conformal.

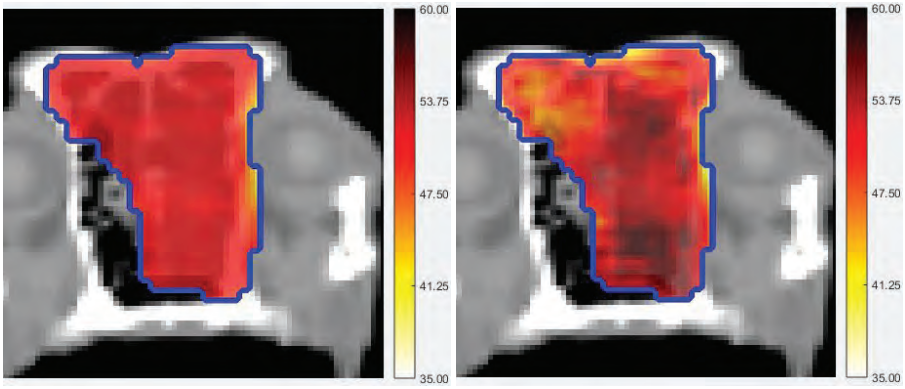

(a) Original dose distribution (Gy). (b) Optimal CDA dose distribution (Gy).

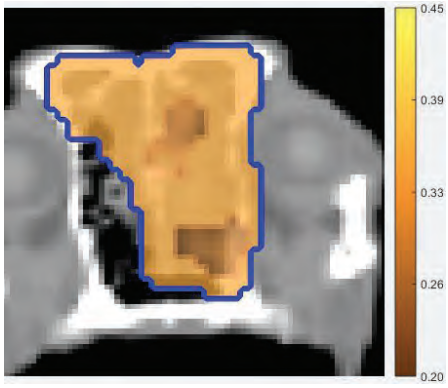

(c) Estimates $\hat{\alpha}_i$ (Gy^{-1}).

Figure 3.11: Distribution of $\hat{\alpha}_i$ estimates and dose for original and CDA plan on one CT slice for patient 1. The PTV50 is contoured in blue. Darker shades in $\hat{\alpha}_i$ spatially correlate with darker shades in CDA dose.

Compared to the original dose distributions, the CDA dose distributions in Figures 3.10 to 3.12 have changed considerably. This is a consequence of the employed optimization methodology for CDA, see Section 3.2.5, where as little additional dose-limiting structures and constraints are added as possible to focus on TCP and NTCP. More strict constraints can be imposed, and this might decrease the (worst-case) TCP gain in Table 3.5 and/or the improvement in NTCP. Nevertheless, results show that dose redistribution via optimization of TCP and NTCP criteria can improve the resulting TCP and/or NTCP, without major changes in DVH graphs.

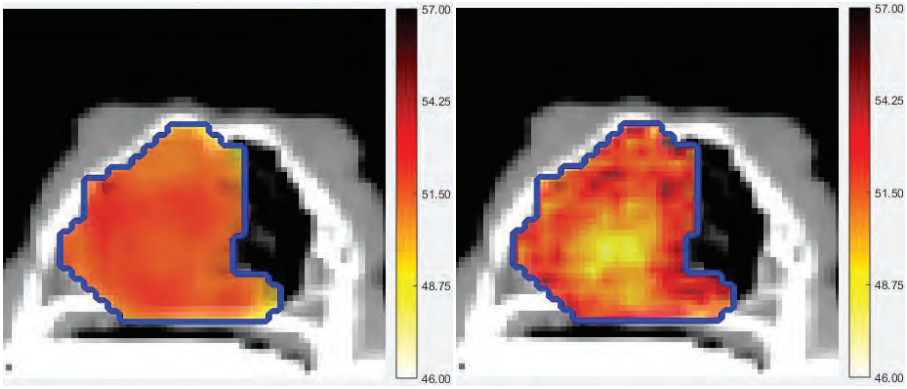

(a) Original dose distribution (Gy). (b) Optimal CDA dose distribution (Gy).

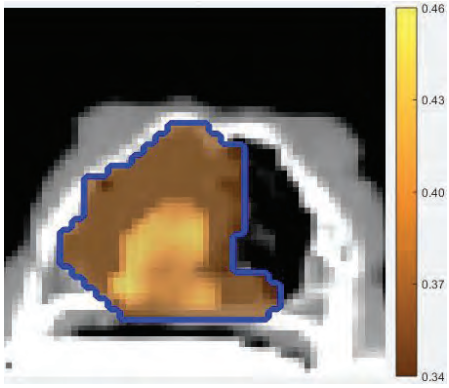

(c) Estimates $\hat{\alpha}_i$ (Gy^{-1}).

Figure 3.12: Distribution of $\hat{\alpha}_i$ estimates and dose for original and CDA plan on one CT slice for patient 6. The PTV50 is contoured in blue. Lighter shades in $\hat{\alpha}_i$ spatially correlate with lighter shades in CDA dose.

3.4 Discussion

3.4.1 Information uncertainty

Information uncertainty plays an important role in treatment plan adaptations. There is currently no generally accepted method to determine the uncertainty level of (functional) imaging data and response parameters derived from imaging data. Casares-Magaz et al. (2018) use a visual analytic tool to determine the uncertainty in TCP

values for prostate cancer cases, when initial cell density is estimated from MRI scans. Similar methods may also be used for parameters such as radiation sensitivity. In the current chapter, we have used uncertainty levels $p_\alpha = p_\nu = 0.1$ and 0.2 (i.e., 10% and 20%), and these are arbitrary to some extent. Although it is currently not clear how to determine a realistic uncertainty level (i.e., range of parameter variation), the current chapter provides insight in the reverse problem: what uncertainty level allows for useful adaptations? The results in Sections 3.3.2 and 3.3.3 show that when going from 10% to 20% uncertainty in both response parameters (α and ν), the resulting TCP interval becomes much wider. Whereas at 10% uncertainty clear benefits of treatment adaptation (either UDA or CDA) can be observed for several patients, the benefit of adaptation (in terms of TCP) is unclear if the uncertainty level is 20%. This provides information on the data accuracy required for adaptive treatments, i.e., this underlines the need for reliable imaging biomarker signals and methodology for transforming these into accurate model parameters.

The required data accuracy also depends on how uncertainty in data propagates to uncertainty in model parameters and subsequently model outcome. Uncertainty in some model parameters may have a larger influence on the uncertainty of the resulting TCP value than uncertainty in other parameters. Barry et al. (2020) have developed a tool to assess the relation between uncertainty in model parameters and the uncertainty in the calculated TCP and/or NTCP values. This allows to analyze which parameters drive the uncertainty in biological response models. In the current chapter, we did not distinguish between uncertainty levels (and their impact) for α and ν; this would be a valuable next step.

Although FLT PET imaging has been used in multiple studies and reported to be correlated with cell proliferation, its limitations should be acknowledged: first, even though FLT signals can be a rather accurate indicator of cell kill, its application as indicators of radiation response and radiosensitivity (α parameters) is perhaps less reliable; second, PET imaging quality is an important bottleneck in quantitative analysis of the image, especially for voxel-based adaptations. Nevertheless, the framework proposed here is not biomarker-specific and can in essence be used with other biomarkers such as FDG PET, contrast-enhanced CT, and dynamic contrast-enhanced MRI (Marcu et al., 2018), as long as their clinical surrogacy to favorable outcome is established. For the case of dose (de)escalation, other systemic biomarkers such as circulating tumor DNA (Cheng et al., 2016), circulating tumor cells (Perumal et al., 2019), and gene signature panels (Scott et al., 2017) can be employed to assess tumor's radiosensitivity during RT course, although these biomarker lack the spatial information necessary for dose-painting adaptation schemes. The currently proposed adaptation methodology

is applicable; next to the biomarker itself, only the method for transforming biomarker data into response model parameters would differ.

3.4.2 Modeling limitations

Currently presented absolute TCP and NTCP values depend highly on modeling assumptions and parameter choices. For instance, other NTCP models than the LKB model for brain necrosis may result in substantially higher NTCP estimates (Niyazi et al., 2020). Choices for allowed minimum and maximum dose, as well as dosimetric deviations from the original treatment plan are made for illustrative purposes only and are not necessarily according to clinical standards. Of the two presented adaptation strategies, UDA is much more in line with current clinical practice, and CDA is more speculative. The employed TCP and NTCP models are much less reliable for the resulting non-uniform dose distributions. As such, the resulting absolute TCP and NTCP numbers should mostly be considered in terms of trends rather than absolute values, especially for the CDA strategy. Nevertheless, observed differences in TCP and NTCP values between different treatment strategies may be informative for changes in tumor control and normal tissue toxicity associated with a change in strategy.

A necessary step for implementation of the presented adaptation methodology is to calibrate a biological response model (e.g., fit a sigmoidal curve (Levegrün et al., 2001)) on a sufficiently large representative data set, using a clinically relevant quantitative outcome measure. Due to limited sample size, this has not been done for the current study, and reported TCP numbers for the original treatment plan need not reflect the clinical treatment outcome.

As part of the adaptation framework, two adaptive treatment planning strategies are presented: uniform and continuous dose adaptation (abbreviated UDA and CDA, respectively). The numerical results of Sections 3.3.2 and 3.3.3 show that both strategies lead to a worst-case TCP improvement without deteriorating on NTCP, for maximum radiation response errors $p_\alpha = p_\nu = 0.1$. Naturally, for some patients the improvement is larger than for others. For several patients, clear improvements in TCP and/or NTCP can be found using either UDA or CDA. For other patients (e.g., Figure 3.8c) one might also conclude that the original treatment plan does not require any adaptations. For some patients the uncertainty in outcome (i.e., TCP criteria values) remains very large. For several of these patients, the reported optimal treatment adaptation is purely the mathematical optimum given the current model, and the preferred adaptation in clinical practice would be switching to another treatment modality or stopping treatment altogether. These adaptations are not accounted for in the current models.

There are many more adaptation possibilities than the ones currently considered. In particular, one may adapt the fractionation scheme for the remainder of the treatment. The benefit of early treatment stopping on the therapeutic ratio depends amongst others on the α/β ratio of the target volume and the relevant OARs. Other adaptation possibilities include combining dose painting (dose redistribution) with dose boosting, and adapting to anatomical and/or geometrical changes simultaneously. We refer to Baumann et al. (2016) for an overview of adaptation strategies.

An essential difference between the two presented adaptation strategies and the original treatment plan is the objective: UDA maximized the therapeutic ratio (defined as worst-case TCP minus the cataract NTCP to the spared eye), CDA maximized worst-case TCP, and the original treatment plan did not take TCP and/or NTCP into account at all. The current objective for CDA is not suitable for UDA, because if the maximum NTCP is fixed and the dose distribution can only be uniformly scaled, there are no degrees of freedom left to optimize. Differences between CDA and UDA can for a large part be attributed to the set boundary conditions. CDA is restricted to dose redistribution whereas UDA can add or remove dose. Moreover, UDA can increase NTCP if this yields an improvement in therapeutic ratio, whereas CDA cannot increase NTCP. Thus, results in Tables 3.4 and 3.5 are consistent with the imposed boundary conditions. We did not attempt to make a direct comparison between the results of UDA and CDA. Moreover, in cases where therapeutic ratio is maximized for a worst-case TCP and NTCP both close to zero, the clinically preferred adaptation might not be captured by either model (see previous paragraph). The results show the importance of deciding what outcome measure is to be optimized under what boundary conditions, and the influence of this component of the adaptation framework.

In the current study a linear transformation is used to acquire radiation response parameter estimates from imaging signals. For an individual voxel the relative remaining signal $1-r_i$ can be interpreted analogous to the survival fraction in equation (3.A.1). Alternative to our approach, one could substitute $1-r_i$ for SF_i, plug in the delivered voxel dose and directly obtain α_i for each voxel i. However, in order to obtain estimates α_i that are in the order of magnitude of a reference (literature) value of 0.35 Gy^{-1}, response estimates need to be approximately 0.95, i.e., approximately 5% of original signal should be remaining in the mid-treatment signal. Preliminary numerical experiments using standardized uptake values acquired via FLT PET imaging as signals show that the relative remaining signal is typically much higher. As such, $\hat{\alpha}_i$ estimates obtained this way are typically too low for use in adaptive optimization methods. The current estimation method is not directly based on biological models, and is based on a few simple assumptions regarding early response.

Radiation response values found for α via fitting the TCP curve to clinical data may be substantially lower than the employed minimum of 0.20 Gy^{-1} (Van Leeuwen et al., 2018), but the fitted TCP model parameters depend largely on the employed methodology. Many studies see parameters α_i and v_i as fitting parameters, and decouple the biological interpretation. This has considerable influence on obtained parameter values (Chapman and Nahum, 2015).

The currently proposed methodology takes a cohort-based approach in the radiation response parameter estimation. It is assumed that the average radiation response parameters of the entire patient cohort are equal to parameter estimates taken from literature. A large-scale study would be needed to establish average imaging and radiation response parameters in a representative population, to serve as a reference baseline. While this would be a necessary step before practical implementation, it is outside the scope of this work.

Finally, we note that the proposed framework solely adapts to biological response and does not consider adaptations to anatomical and/or geometric changes or delivered dose. Such adaptations have been studied for decades, see, e.g., Lim-Reinders et al. (2017) for a review. Whereas methodology can readily applied to both approaches, one should be aware of significant differences. For example, biological changes occur much faster than anatomical changes (e.g., FLT PET signal often drops beyond detectability limit, when CT changes are still largely negligible), which significantly affects potential for adaptation. In addition they are driven by different factors (e.g., anatomical changes follow biological changes and are affected by other physiological changes, such as inflammation, infiltration), so direct comparisons should be very carefully considered.

3.5 Conclusion

This chapter presents a framework for mid-treatment imaging-based adaptive treatment plan optimization. By directly taking into account both the baseline and early response information, more information than typically considered in a re-optimization workflow, it allows for 'smarter' adaptations. The generic concept requires the availability of reliable biomarkers, biological response models and a way of transforming imaging data into model parameters. These components remain subject to research. The possibilities of the proposed adaptation framework crucially depend on the level on uncertainty associated with the above mentioned components. The current results, based on real patient data, account for these uncertainties and show the possibilities of the proposed framework. Under the current modeling choices and a 10% uncertainty level, both the UDA and CDA strategy result in a noteworthy average improvement

in guaranteed (worst-case) TCP. If the required components are sufficiently reliable, the presented framework enables a first step towards individualized adaptive radiation therapy.

Acknowledgments

The authors would like to thank the referees for the useful comments that helped to improve the paper on which this chapter is based.

3.A Modeling details

3.A.1 Modeling choices

To account for non-standard fractionation schemes, we make use of the biologically effective dose (BED) model (Fowler, 1989, 2010). The BED to voxel i is

$$\mathrm{BED}_i(d_i) = (d_i - d_i^{(1)})\Big(1 + \frac{1}{\alpha/\beta}\frac{d_i - d_i^{(1)}}{N^{(2)}}\Big) + d_i^{(1)}\Big(1 + \frac{1}{\alpha/\beta}\frac{d_i^{(1)}}{N^{(1)}}\Big),$$

where $d_i^{(1)}$ is the dose already delivered to voxel i in the first $N^{(1)}$ treatment fractions (stage 1), and $N^{(2)}$ is the remaining number of treatment fractions after mid-treatment biomarker acquisition (stage 2). Parameter α/β is the (fixed) fractionation sensitivity parameter of the tissue to which the voxel belongs.

For the TCP model, we assume a assume a fixed $(\alpha/\beta)_T = 10$, typical for human head-and-neck tumors (Fowler et al., 2003; Fowler, 2009). For any target voxel $i = 1, \ldots, n_T$, the surviving fraction of cells after delivery of a total dose of d_i^T Gy is

$$\mathrm{SF}_i(d_i^T; \alpha_i) = \exp\Big(-\alpha_i \mathrm{BED}_i(d_i^T)\Big). \tag{3.A.1}$$

Plugging this in the TCP function (3.2) completely specifies the model.

The NTCP model (3.3) takes as input a homogeneous dose d_h. Additionally, for correct application of the NTCP model, the parameters and the dose used for evaluation should be normalized to the same fraction dose (Li et al., 2012). Burman et al. (1991) give LKB-NTCP parameters for a 2 Gy per fraction scheme.

An OAR often does not receive a homogeneous dose distribution. The generalized equivalent uniform dose (gEUD) (Niemierko, 1999) is the dose that, if delivered uniformly to the OAR tissue, yields the same biological effect as the original heterogeneous dose distribution. For an OAR r with a_r a tissue specific parameter indicating the volume effect and n_r the number of voxels in the OAR, the gEUD of a heterogeneous dose distribution $\boldsymbol{d}^r$ is given by

$$\mathrm{gEUD}(\boldsymbol{d}^r) = \Big(\frac{1}{n_r}\sum_{i=1}^{n_r}(d_i)^{a_r}\Big)^{\frac{1}{a_r}}.$$

To account for non-standard fractionation schemes, we do not directly use the physical dose but convert this into the equivalent dose delivered in 2 Gy fractions:

$$\mathrm{LQED2}(d_i^r) = \frac{\mathrm{BED}_i^r(d_i^r)}{1 + \frac{2}{(\alpha/\beta)_r}},$$

where $(\alpha/\beta)_r$ is the fractionation sensitivity parameter of tissue r. The resulting $\mathrm{gEUD}(\mathrm{LQED2}(d_i^r))$ is also known in literature as the modified equivalent uniform dose (Park et al., 2005). AAPM Report 166 (Li et al., 2012) recommends that NTCP computations are done using this fractionation-corrected uniform dose. Hence, in the current methodology the normal tissue complication probability for OAR r, resulting from a heterogeneous OAR dose distribution $\boldsymbol{d}^r$, is calculated as

$$\mathrm{NTCP}^r(\boldsymbol{d}^r) := \mathrm{NTCP}^r_{\mathrm{LKB}}(\mathrm{gEUD}(\mathrm{LQED2}(\boldsymbol{d}^r))).$$

LKB-NTCP parameters (a, TD_{50} and m) for the OARs are taken from human head-and-neck data for a 2 Gy per fraction scheme (Burman et al., 1991), and OAR α/β parameters are taken from an earlier canine sinonasal tumor study (Gutiérrez et al., 2007). Table 3.A.1 gives the parameter values.

Endpoint	α/β (Gy)	a	TD_{50} (Gy)	m
Brain (necrosis)	2	4	60	0.15
Eyes (cataract)	3	3.33	18	0.27

Table 3.A.1: Parameter settings for LKB NTCP model. Parameter α/β taken from Gutiérrez et al. (2007), parameters a, TD_{50} and m taken from Burman et al. (1991).

3.A.2 Optimization method

In order to reduce the total number of variables, the optimization problem (3.7) is first solved with only voxels belonging to the PTV50, PTV42 and the three OARs. Subsequently, the set of normal tissue voxels i for which the resulting dose exceeds $d_U^i + \varepsilon$ is determined, with $\varepsilon > 0$ a tolerance parameter. If this set is nonempty, these voxels are added to the model (constraints (3.7e)-(3.7f) are updated) and the model is re-solved. This is continued until no voxels exceed the dose tolerance with more than ε and the total number of voxel violations is at most n^ε. For our implementation we choose $\varepsilon = 1$ (Gy) and $n^\varepsilon = 10$. This typically requires no more than 3 iterations. An iteration is terminated once feasible and near-optimal results are obtained, which takes between 30 minutes and 2 hours.

The intent of this procedure is to avoid hot-spots without requiring the delineation of artificial dose-limiting ring structures. Whereas the latter procedure will be more successful in

avoiding hot spots, the intent of the current study is to let the TCP and NTCP criteria have the dominant influence on the final dose distribution.

3.A.3 TCP and NTCP optimization with reference response parameters

The original treatment plan did not optimize directly for TCP and NTCP. Thus, the improvements of CDA over the original treatment plan that are reported in Section 3.3.3 may be partially due to inclusion of imaging biomarkers, and partially due to the direct optimization of TCP and NTCP. We solve model (3.7) using reference values $(\bar{\alpha}, \bar{\nu})$ instead of $(\hat{\boldsymbol{\alpha}}^w, \hat{\boldsymbol{\nu}}^w)$ in the objective.

	TCP_{nom} [TCP_{range}]	NTCP	d_{98} (Gy)	d_{mean} (Gy)	d_2 (Gy)
PTV50	0.64 [-] [0.47 [-0.01], 0.73 [-0.01]]		44.61 [-0.64]	48.44 [-]	52.73 [+3.27]
PTV42			42.65 [+1.63]	48.11 [+1.48]	53.67 [+4.22]
Brain		0.01 [-0.02]		7.71 [-0.43]	35.44 [-1.19]
Eye (low)		0.29 [-0.04]		8.98 [-0.17]	23.28 [+0.09]
Eye (high)		0.63 [-0.05]		15.57 [-0.12]	32.18 [-1.36]

Table 3.A.2: Results for the CDA strategy with reference $(\bar{\alpha}, \bar{\nu})$. d_{98} and d_2 are the near minimum and near maximum dose, respectively. Numbers in red indicate the change compared to the original treatment plan (Table 3.2). All numbers are cohort averages.

Table 3.A.2 presents the results. Numbers in red indicate changes compared to the original treatment plan (Table 3.2). Both the worst-case and best-case TCP decreased by one percentage point, on average. The CDA strategy with the estimated $(\hat{\boldsymbol{\alpha}}^w, \hat{\boldsymbol{\nu}}^w)$ (Table 3.5) yields improvements in worst-case and best-case TCP of 0.07 and 0.17, on average. Thus, direct optimization of TCP using reference values $(\bar{\alpha}, \bar{\nu})$ does not produce treatment plans that are better than the original treatment plans in terms of TCP values for estimated response parameters $(\hat{\boldsymbol{\alpha}}^w, \hat{\boldsymbol{\nu}}^w)$. The reported dosimetric statistics are comparable to those of the CDA strategy with the estimated response parameters (Table 3.5).

CHAPTER 4

Conic formulation of fluence map optimization problems

4.1 Introduction

Fluence map optimization (FMO) is one of the core elements of inverse treatment planning for intensity-modulated radiation therapy (IMRT) and an essential part of any treatment planning system (TPS). It aims to find the combination of fluences (beamlet intensities) that yields the optimal trade-off between various treatment plan evaluation criteria. For an overview of fluence map optimization and other optimization challenges in the IMRT planning phase, we refer to Shepard et al. (1999) and Ehrgott et al. (2008). In general, determining the optimal fluence map is a large-scale optimization problem. In the current chapter, we formulate this as a conic optimization problem and propose to solve these using state-of-the art algorithms from the conic optimization field.

The types of employed evaluation criteria determine whether the FMO problem is linear, quadratic, otherwise convex or nonconvex. For example, minimum, mean and maximum dose criteria lead to linear functions and quadratic errors from a prescription dose lead to quadratic functions. Dose-volume based constraints are known to be nonconvex, but convex approximations exist (Romeijn et al., 2003; Saberian et al., 2016b; Liu et al., 2018; Fu et al., 2019); several of these papers solve multiple convex sub-problems.

Next to dose and dose-volume criteria, one can also optimize biologically-based evaluation criteria, such as tumor control probability (TCP) and normal tissue complication probability (NTCP) criteria. The potential of biological-based models over surrogate dose-based criteria has long been recognized (Ling et al., 2005; Niemierko, 2006), and their importance can be expected to increase with the advance of personalized treatment planning (Baumann et al., 2016). In Ajdari et al. (2019) and Chapter 3

it is proposed to optimally adapt treatment plans based on direct optimization of TCP and/or NTCP criteria. Although practical implementation presents many challenges, the attention of commercial treatment planning systems in biological-based models is increasing (Li et al., 2012).

Biologically-based evaluation criteria often have more complicated structures involving exponentials, logarithms and power functions. However, many commonly used dose-based and biologically-based treatment planning criteria can be (re)formulated as convex objectives and constraints (Romeijn et al., 2004; Hoffmann et al., 2008). In these approaches, a strictly increasing or decreasing function is applied to the evaluation criterion such that the new composite function is convex. For constraints, this immediately gives a convex constraint. For an objective, optimizing the new composite function is equivalent to optimizing the original objective function, and in a multicriteria optimization (MCO) setting the Pareto surface remains unchanged. Hence, most FMO problems, both physical dose-based and/or biologically-based, can be formulated as convex optimization problems. The main advantage of convex optimization problems is that any local optimum is a global optimum.

TPS	Algorithm	Supported biological models
RayStation	Sequential quadratic programming	TCP Poisson-LQ, NTCP Poisson-LQ, NTCP LKB, min/max gEUD
Eclipse	conjugate gradient method*	TCP Poisson-LQ, NTCP Poisson-LQ, NTCP Lyman, min/max gEUD
Pinnacle	L-BFGS	Min/target/max gEUD
Monaco	barrier method	Poisson TCP, serial and parallel complication model

Table 4.1: Used algorithm and supported biological models for treatment plan optimization in commercial treatment planning systems. Supported biological models are according to the report of AAPM Task Group 166 (Li et al., 2012) for Monaco® V1.0, Pinnacle® V8.0h and Eclipse V10.0, and according to RaySearch Laboratories AB (2017a) for RayStation. LQ = linear quadratic, LKB = Lyman-Kutcher-Burman, gEUD = generalized equivalent uniform dose. *: If biological optimization is selected, Eclipse uses a separate plug-in (by RaySearch), instead of its own FMO solver.

In order to solve these problems, commercial TPSs use a variety of solution methods. RayStation (RaySearch Laboratories AB, Stockholm, Sweden) uses sequential

quadratic programming (RaySearch Laboratories AB, 2017b), Eclipse (Varian Medical Systems, Palo Alto, CA) uses conjugate gradient methods (Doolan et al., 2014), Pinnacle (Philips Medical Systems, Andover, MA) uses a limited memory Broyden—Fletcher—Goldfarb-–Shanno (L-BFGS) algorithm adapted to account for constraints (Philips, 2019), and Monaco (CMS/Elekta, Maryland Heights, MO) uses a (interior-point) barrier method (Alber and Reemtsen, 2007). Table 4.1 provides an overview of the algorithms implemented by commercial TPSs, and the supported biologically-based evaluation criteria (next to physical dose and dose-volume criteria).

Next to these, several open-source research-oriented TPSs exist. The CERR toolbox (Deasy et al., 2003) requires a user pre-installed solver, and the matRad toolbox (Wieser et al., 2017) calls the open-source general convex optimization solver IPOPT (Wächter and Biegler, 2006). Many different solution approaches have been considered to improve speed and/or solution quality for specific problem formulations. FMO problems formulated as penalty-based problems (without hard constraints, except beamlet nonnegativity) are often solved using first-order methods such as gradient descent and conjugate gradient methods, and (quasi-)Newton methods (e.g., L-BFGS), see amongst others Bortfeld et al. (1990), Wu and Mohan (2000), Zhang et al. (2004) and Pflugfelder et al. (2008). To allow for constraints, a different line of research uses linear FMO formulations and employs projection algorithms, which have been shown to be very fast (Censor et al., 2006; Chen et al., 2010; Gorissen, 2019).

Proximal operators can be seen as generalizations of projections, and they are the basis for the class of proximal algorithms, which can solve non-smooth and constrained problems. These include proximal gradient descent and alternating direction method of multipliers (ADMM). Constraints are handled via proximal operators, and proximal algorithms work particularly well when the proximal operators can be efficiently evaluated, e.g., for linear constraints. ADMM has been applied to FMO problems with linear constraints (Gao, 2016; Liu et al., 2017).

Interior-point methods (IPMs) are general purpose algorithms for constrained convex optimization, and have successfully been implemented in a wide variety of applications. Especially primal-dual IPMs are regarded as the state-of-the art algorithms in the optimization community. IPMs have been used in fluence map optimization with linear evaluation criteria by Romeijn et al. (2003), Romeijn et al. (2006), Aleman et al. (2010) and Gorissen (2021). The in-house solver of Erasmus MC (Rotterdam, The Netherlands), iCycle (Breedveld et al., 2012, 2017), allows for several nonlinear evaluation criteria. It is the state-of-the-art (functional form) primal-dual IPM implementation in radiation therapy, and it is specially tuned for FMO problems with particular treatment plan evaluation criteria. Each of the above approaches solves FMO

problems in functional form. These algorithms may attain the global optimum, but in general do not guarantee to do so efficiently (i.e., do not guarantee to converge in polynomial time). For the latter, one needs to prove that the feasible region described by the evaluation criteria allows for a so-called self-concordant barrier function (Nesterov and Nemirovski, 1994), which is a non-trivial task.

In this chapter, we take a conic optimization approach to FMO. Conic optimization is a subfield of convex optimization. It allows for nonlinear evaluation criteria, thus being more general than linear optimization. Nonlinear evaluation criteria are not treated in their original functional form, but are formulated by restricting variables to belong to certain convex 'cones'. By restricting the types of allowed cones to the quadratic, exponential and power cone, it is more structured than convex optimization in functional form. The main advantages of formulating an optimization problem in conic form using these three cones are:

- Implementing the model is more structured and less error prone. For example, it is not necessary to specify derivatives and Hessians.
- By formulating an optimization problem in conic form using these three cones, we know there exist IPM algorithms that can solve the problem in polynomial time. To the best of our knowledge, all other currently used approaches for FMO lack this theoretical backing.
- General purpose primal-dual IPM solvers exist for these conic optimization problems, with very good practical performance. It is not necessary to develop and maintain a solver for FMO problems of a specific form.
- It is flexible regarding extensions. For example, it can be shown that for problems in conic form the robust counterpart can also be written in conic form. Moreover, the dual problem of any conic problem is easy to set up.

We present a conic optimization methodology for FMO, with a focus on biological-based evaluation criteria. We emphasize that we do not develop a new dedicated algorithm for these problems. Instead, we model FMO problems as conic optimization problems, and use general purpose conic solvers. Specifically, our contributions are:

- We provide (approximate) conic representations of all common biological-based treatment plan evaluation criteria, e.g., TCP and NTCP criteria, making use of the quadratic, exponential and power cone. Any new treatment plan evaluation criteria can be incorporated in a similar, straightforward manner, if conic representable. Whereas for some individual criteria results exist, to the best of our

knowledge this is the first proof that FMO problems with any combination of the analyzed biological criteria can be solved in polynomial time.

- We provide numerical results using a general purpose conic primal-dual IPM solver on the TROTS data set (Breedveld and Heijmen, 2017), demonstrating that conic form problems can be solved to optimality in practice, with promising speed.

We note that conic optimization has been used before in FMO. Chu et al. (2005) rewrites the robust counterpart of a linear FMO problem with uncertain data to conic quadratic form. Kim et al. (2012a) uses a first-order conic method to solve FMO problems with a total-variation regularization term, containing ℓ_1- and ℓ_2-norms. Both studies use conic optimization only for a particular problem formulation, and do not use the modeling capabilities of quadratic, exponential and power cones to set up a general framework.

The remainder of this chapter is organized as follows. First, Section 4.2.1 introduces the conic optimization methodology. To emphasize its general applicability and improve readability, conic optimization will first be introduced in a general setting. After that, Section 4.2.2 shows that all common biological-based treatment plan criteria can be reformulated to conic form. Section 4.2.3 describes the setup of our numerical experiments on the TROTS data set. Section 4.3 presents numerical results. Section 4.4 discusses the methodology and results and Section 4.5 concludes the chapter.

4.2 Methods

In a generic FMO problem, the goal is to minimize particular treatment plan evaluation criterion f_0, subject to constraints on evaluation criteria $f_1, \ldots, f_p$, evaluated in dose vector $\boldsymbol{d}$. In a typical FMO setup, functions $f_0, \ldots, f_p$ are convex, or can be reformulated to or approximated by convex functions. The FMO problem can be written as

$$\min_{\boldsymbol{x},\boldsymbol{d}} \; f_0(\boldsymbol{d}), \tag{4.1a}$$

$$\text{s.t.} \; f_j(\boldsymbol{d}) \leq 0, \; j = 1, \ldots, p, \tag{4.1b}$$

$$\boldsymbol{d} = \boldsymbol{A}\boldsymbol{x}, \tag{4.1c}$$

$$\boldsymbol{x} \geq \boldsymbol{0}. \tag{4.1d}$$

Constraint (4.1c) relates $\boldsymbol{d}$ to the pencil beam weights $\boldsymbol{x}$ according to pencil beam (or dose deposition) matrix $\boldsymbol{A}$. Constraint (4.1d) ensures (elementwise) nonnegativity of pencil beam weights. In solving an FMO, we can in general distinguish two steps:

1. Formulate an FMO problem in such a way that it is algorithm readable.

2. Solve the FMO problem formulation using a suitable algorithm.

Many implementations use formulations of form (4.1). This is what we refer to as *functional form*, i.e., the functions $f_0, \ldots, f_p$ describing the treatment plan evaluation criteria are directly used as input for the algorithm. In the current chapter, we introduce an alternative form, known as the *conic form*. This allows us to use conic optimization algorithms in the second step of the FMO procedure.

4.2.1 Conic optimization methodology

Introduction to conic optimization

We provide a brief introduction to conic optimization (not restricted to FMO problems), starting from linear optimization. For details we refer to Ben-Tal and Nemirovski (2001) and Nemirovski (2007). Let $\boldsymbol{c} \in \mathbb{R}^n$, $\boldsymbol{A} \in \mathbb{R}^{m \times n}$, $\boldsymbol{b} \in \mathbb{R}^m$. A linear optimization problem in standard form is given by

$$\min_{\boldsymbol{x}} \ \boldsymbol{c}^\top \boldsymbol{x}, \tag{4.2a}$$

$$\text{s.t.} \ \boldsymbol{A}\boldsymbol{x} = \boldsymbol{b}, \tag{4.2b}$$

$$\boldsymbol{x} \in \mathbb{R}^n_+, \tag{4.2c}$$

where the set $\mathbb{R}^n_+$ is the nonnegative orthant. When moving from linear to convex optimization, the common approach is to replace the objective by a convex function $f_0(\boldsymbol{x})$ and replace the constraints by convex constraints $f_j(\boldsymbol{x}) \leq 0, \ j = 1, \ldots, p$, where $\boldsymbol{u} \in \mathbb{R}^p$ is an upper bound vector. A general convex optimization problem reads

$$\min_{\boldsymbol{x}} \ f_0(\boldsymbol{x}), \tag{4.3a}$$

$$\text{s.t.} \ f_j(\boldsymbol{x}) \leq 0, \ j = 1, \ldots, p. \tag{4.3b}$$

Conic optimization takes an alternative approach and solely changes (4.2c) by replacing it with a proper cone. A set C is a cone if $\boldsymbol{x} \in C$ implies that $\lambda \boldsymbol{x} \in C$ for all scalars $\lambda \geq 0$. A proper cone is defined as follows.

Definition 4.1 (Ben-Tal and Nemirovski (2001))**.** A cone $C \subseteq \mathbb{R}^n$ is a *proper* (or regular) cone if it is closed, has a nonempty interior and

- $\boldsymbol{x} \in C, -\boldsymbol{x} \in C \Rightarrow \boldsymbol{x} = \boldsymbol{0}$ (Pointed),

- $\boldsymbol{x}, \boldsymbol{y} \in C \Rightarrow \boldsymbol{x} + \boldsymbol{y} \in C$ (Convex). ■

The standard form of a conic optimization problem, introduced by Nesterov and Nemirovski (1994, Chapter 4) is

$$\min_{\boldsymbol{x}} \ \boldsymbol{c}^\top \boldsymbol{x}, \tag{4.4a}$$

$$\text{s.t.} \ \boldsymbol{A}\boldsymbol{x} = \boldsymbol{b}, \tag{4.4b}$$

$$\boldsymbol{x} \in C, \tag{4.4c}$$

with C a proper cone. It is straightforward to see that the nonnegative orthant $\mathbb{R}^n_+$ is a proper cone. Another way of moving from linear optimization to conic optimization is by considering the inequality associated with $\mathbb{R}^n_+$. The element-wise inequality $\boldsymbol{x} \geq \boldsymbol{y}$ is equivalent to $x_i - y_i \geq 0$, $i = 1, \ldots, n$, which can also be written as $\boldsymbol{x} - \boldsymbol{y} \in \mathbb{R}^n_+$. Similarly, for a proper cone C the generalized inequality $\boldsymbol{x} \geq_C \boldsymbol{y}$ is equivalent to $\boldsymbol{x} - \boldsymbol{y} \geq_C \boldsymbol{0}$, which is again equivalent to $\boldsymbol{x} - \boldsymbol{y} \in C$. For more details we refer to Ben-Tal and Nemirovski (2001). Instead of the standard form (4.4) we consider the general conic optimization form

$$\min_{\boldsymbol{x}} \ \boldsymbol{c}^\top \boldsymbol{x}, \tag{4.5a}$$

$$\text{s.t.} \ \boldsymbol{l}^c \leq A\boldsymbol{x} \leq \boldsymbol{u}^c, \tag{4.5b}$$

$$\boldsymbol{l}^x \leq \boldsymbol{x} \leq \boldsymbol{u}^x, \tag{4.5c}$$

$$\boldsymbol{x} \in C, \tag{4.5d}$$

with $\boldsymbol{l}^c, \boldsymbol{u}^c$ bounds on the linear constraints and $\boldsymbol{l}^x, \boldsymbol{u}^x$ bounds on variable $\boldsymbol{x}$. Additionally, we assume there exists a partitioning $\boldsymbol{x} = (\boldsymbol{x}^1, \ldots, \boldsymbol{x}^p)$, such that $\boldsymbol{x}^k \in C_k$, i.e., each subvector $\boldsymbol{x}^k$ belongs to a smaller cone C_k. The following property allows models involving a mix of various different proper cones to be represented in form (4.5)[1].

Proposition 4.2 (Ben-Tal and Nemirovski (2001))**.** *If $C_1, \ldots, C_p$ are proper cones, their Cartesian product $C = C_1 \times \ldots \times C_p$ is a proper cone.*

Practically useful cones

The simplest useful cone is the n-dimensional nonnegative orthant

$$\mathbb{R}^n_+ = \left\{ \boldsymbol{x} \in \mathbb{R}^n : x_1, \ldots, x_n \geq 0 \right\}.$$

[1]Form (4.5) implies that any subvector $\boldsymbol{x}^k$ belongs to exactly one cone. However, this is not a restriction because duplicates of variables can be introduced via linear equality constraints. For conciseness, we will not explicitly state these extra constraints in the remainder of the chapter.

Note that in form (4.5) the nonnegative orthant is redundant because all linear components are captured by (4.5b) and (4.5c). The n-dimensional quadratic cone is given by

$$\mathcal{Q}^n = \left\{ \boldsymbol{x} \in \mathbb{R}^n : x_1 \geq \sqrt{x_2^2 + x_3^2 + \ldots + x_n^2} \right\},$$

which is also known as the second-order, Lorentz or ice-cream cone. Sometimes it is more convenient to use the n-dimensional rotated quadratic cone representation, which is given by

$$\mathcal{Q}_r^n = \left\{ \boldsymbol{x} \in \mathbb{R}^n : 2x_1 x_2 \geq x_3^2 + \ldots + x_n^2,\ x_1, x_2 \geq 0 \right\}.$$

There is an easy transformation from quadratic cones to rotated quadratic cones (MOSEK ApS, 2018). The nonnegative orthant and quadratic cone are so-called symmetric cones[2] (Nemirovski, 2007), and offer great modeling flexibility. However, they do not admit the modeling of expressions involving amongst others exponentials and logarithms. Also, many power functions can in theory be represented using quadratic cones, but these functions are more naturally represented using different cones.

Two particularly useful non-symmetric cones are the exponential cone and the power cone. The 3-dimensional exponential cone is given by

$$K_{\text{exp}} = \left\{ (x_1, x_2, x_3) : x_1 \geq x_2 \exp(x_3/x_2), x_2 > 0 \right\} \cup \left\{ (x_1, 0, x_3) : x_1 \geq 0, x_3 \leq 0 \right\}.$$

Various representations of the power cone exist. With $0 < \alpha < 1$, the most common form of the n-dimensional power cone is given by

$$\mathcal{P}_n^{\alpha,1-\alpha} = \left\{ \boldsymbol{x} \in \mathbb{R}^n : x_1^{\alpha} x_2^{1-\alpha} \geq \sqrt{x_3^2 + \ldots + x_n^2},\ x_1, x_2 \geq 0 \right\},$$

but one may also define a more general version where the left hand side consists of arbitrarily many terms (MOSEK ApS, 2018). It is widely accepted in the optimization community that the quadratic, exponential and power cone, together with the semidefinite cone, can model almost all convex functions arising in practice. Lubin et al. (2016) showed that all (mixed-integer) convex problems in the MINLPLIB2 benchmark library (Vigerske, 2021) can be modeled using the quadratic, exponential and power cone. The MOSEK modeling cookbook (MOSEK ApS, 2018) provides an overview of (simple) functions and sets that can be represented using these cones. Modeling using these conic representable expressions is called extremely disciplined convex optimization/modeling by MOSEK. For clarity, we will simply use *conic optimization* and *conic modeling*.

[2]The semidefinite cone is a third often used symmetric cone, but we omit it here because it is irrelevant for modeling radiation therapy functions and it clutters notation.

Lastly, we note there are generalizations of Farkas' lemma (Farkas, 1902) from linear optimization to conic optimization, see, e.g., Renegar (2001). Thus, formulating a problem in conic form (using the quadratic, exponential and power cone) immediately presents a feasibility check. Farkas' lemma has previously been used in FMO by Gorissen (2019).

Conic reformulations

Reformulating a convex optimization problem P of form (4.3) to an equivalent problem Q of form (4.5) typically requires the introduction of auxiliary variables. Let $\boldsymbol{x} \in \mathbb{R}^n$ denote the variable vector of problem P, and let $(\boldsymbol{x}, \boldsymbol{y}) \in \mathbb{R}^{n+q}$ denote the variable vector of problem Q. That is, in Q we distinguish between original variables $\boldsymbol{x}$ that already exist in the original problem P and auxiliary variables $\boldsymbol{y} \in \mathbb{R}^q$. Equivalence of P and Q is defined as follows.

Definition 4.3. Optimization problems P and Q are *equivalent* if $\boldsymbol{x}^*$ is optimal to P if and only if there exists a $\boldsymbol{y}^* \in \mathbb{R}^q$ such that $(\boldsymbol{x}^*, \boldsymbol{y}^*)$ is optimal to Q. ■

The idea is that after the reformulation the new problem Q can be represented using only the cones introduced in Section 4.2.1. A conic problem is defined as follows[3]:

Definition 4.4. An optimization problem Q of form (4.5) is named a *conic problem* (CP) if all cones C_k, $k = 1, \ldots, p$, are quadratic, rotated quadratic, exponential or power cones. ■

We are now equipped to reformulate problems to equivalent CPs. We start with the functional form (4.3), as many optimization problems arising in practice come in this form. We rewrite (4.3) to

$$\min_{\boldsymbol{x}, t} \quad t, \tag{4.6a}$$

$$\text{s.t.} \quad f_0(\boldsymbol{x}) \leq t, \tag{4.6b}$$

$$f_j(\boldsymbol{x}) \leq 0, \; j = 1, \ldots, p, \tag{4.6c}$$

where in the FMO setting functions f_j could be TCP or NTCP functions. This form suggests the analysis of epigraph sets

$$\text{epi}(f) = \left\{(\boldsymbol{x}, t) \; : \; \boldsymbol{x} \in \mathbb{R}^n, t \in \mathbb{R}, f(\boldsymbol{x}) \leq t\right\},$$

for f_0 and f_j for all j. We make use of the following definitions[3]:

[3] In the definitions of a *conic problem* and *conic constraint* we restrict to a certain family of cones. These are not the standard definitions of conic problems and constraints, but these are more suitable for practical purposes.

Definition 4.5. A constraint is a *conic constraint* if it is a linear constraint or a constraint of the form $\boldsymbol{x} \in C$, with C a quadratic, rotated quadratic, exponential or power cone. ■

Definition 4.6. A set $S \subseteq \mathbb{R}^n$ is *conic representable* (Cr) if (i) there exists a set $T \subseteq \mathbb{R}^{n+q}$ such that T can be described by finitely many conic constraints, and (ii) $\boldsymbol{x} \in S$ if and only if there exists an $\boldsymbol{u} \in \mathbb{R}^q$ such that $(\boldsymbol{x}, \boldsymbol{u}) \in T$. The conic constraints describing set T are the conic representation (CR) of S. ■

If, via the introduction of auxiliary variables and constraints, we find CRs for the epigraphs of f_0 and f_j, $j = 1, \ldots, p$, the resulting optimization problem is a CP that is equivalent to (4.6) (or (4.3)). While sufficient, it turns out that this is not necessary.

Proposition 4.7. *Let $g_0 : \mathbb{R} \mapsto \mathbb{R}$ and $g_j : \mathbb{R} \mapsto \mathbb{R}$, $j = 1 \ldots, p$ be strictly increasing functions. Solution $\boldsymbol{x}$ is optimal to* (4.3) *if and only if there exists a $\tau \in \mathbb{R}$ such that $(\boldsymbol{x}, \tau)$ is optimal to*

$$\min_{\boldsymbol{x},\tau} \ \tau, \tag{4.7a}$$

$$s.t. \ \ g_0(f_0(\boldsymbol{x})) \leq \tau, \tag{4.7b}$$

$$g_j(f_j(\boldsymbol{x})) \leq g_j(0), \ j = 1, \ldots, p. \tag{4.7c}$$

Proof. Consider the strictly increasing functions $g_0 : \mathbb{R} \mapsto \mathbb{R}$ and $g_j : \mathbb{R} \mapsto \mathbb{R}$, $j = 1 \ldots, p$. Applying g_0 to (4.6b) is equivalent to

$$g_0(f_0(\boldsymbol{x})) \leq \tau, \tag{4.8a}$$

$$\tau \leq g_0(t), \tag{4.8b}$$

where $\tau \in \mathbb{R}$ is a new variable. The objective of (4.6) is to minimize t, which is equivalent to minimizing $g_0(t)$ because g_0 is strictly increasing. Variable t occurs only in constraint (4.8b), so we can equivalently minimize τ and remove variable t altogether. Stated differently, when applying g_0 to both sides of the inequality $f_0(\boldsymbol{x}) \leq t$, we can replace right-hand side $g_0(t)$ by new variable τ. This results in (4.7a) and (4.7b). Lastly, applying functions g_j to (4.6c) gives (4.7c). □

Note that $g_j(0)$ is a constant for all $j = 1, \ldots, p$. This shows that, in order to find a CP equivalent to (4.3), it suffices to find for every $j = 0, \ldots, p$ a strictly increasing function g_j for which we can find a CR of the set $\text{epi}(g_j \circ f_j)$. In particular, any function f is suitable for conic optimization if we can find a strictly increasing function g such that $\text{epi}(g \circ f)$ is Cr.

Note that in the above we impose an upper bound or minimize function f. In case of a lower bound or maximization, we instead consider the hypograph

$$\text{hypo}(f) = \left\{(\boldsymbol{x}, t) \,:\, \boldsymbol{x} \in \mathbb{R}^n, t \in \mathbb{R}, f(\boldsymbol{x}) \geq t\right\},$$

and function f is suitable for conic optimization if we can find a strictly increasing function g such that hypo$(g \circ f)$ is Cr.

An optimization problem that can be transformed to a CP using only the aforementioned cones can be solved to optimality using (amongst others) primal-dual IPMs. More details on solving conic optimization problems, IPMs and complexity theory are provided in Appendix 4.A. In Appendix 4.B it is shown that reformulating an FMO problem to a CP (using the presented reformulation methodology) guarantees that the original FMO problem can be solved in polynomial time. There are two (mild) technical conditions: (i) the number of additional variables introduced by the conic reformulation is polynomial in the original number of variables, and (ii) the strictly increasing function g is differentiable.

Lastly, we emphasize that formulating an FMO problem in conic form does not restrict the solution method to IPMs. This point is further discussed in Section 4.4.

4.2.2 Conic representations of common evaluation criteria

The methodology of Section 4.2.1 describes how to reformulate a generic FMO problem of form (4.1) (functional form) to conic form. In this section, we show that many commonly used objectives and constraints in radiation therapy treatment optimization can be reformulated to conic form via this methodology. As mentioned in Section 4.2.1, FMO problems consisting only of functions that can be reformulated using the proposed methodology can be solved in polynomial time. This has an important theoretical consequence: to the best of our knowledge, this is the first proof that FMO problems with any combination of such functions can be solved in polynomial time.

Observation: *Any FMO problem consisting only of evaluation criteria described in the current section can be solved in polynomial time.*

According to the methodology of Section 4.2.1, for each function f that is to be minimized or has an upper bound, we find a strictly increasing function g and a CR of epi$(g \circ f)$. Alternatively, if f is to be maximized or has a lower bound, we find a strictly increasing function g and a CR of hypo$(g \circ f)$. We mainly consider the library of TCP and NTCP functions that are analyzed in Romeijn et al. (2004). Conic reformulations

and/or conic approximations of the fractionation-corrected models analyzed by Hoffmann et al. (2008) are derived in Appendix 4.C. These results are summarized at the end of this section.

Notation: We consider a set of n voxels indexed by i. Let $\boldsymbol{d} \in \mathbb{R}^n_+$ denote the voxel doses. Let $v_i > 0$ denote the relative volume of voxel i, i.e., $\sum_{i=1}^n v_i = 1$. For every voxel i dose d_i is delivered uniformly over N fractions. Let $\alpha > 0$ denote the tissue radiation sensitivity parameter and let $\alpha/\beta > 0$ denote the tissue fractionation sensitivity parameter.

Linear Poisson survival function

The linear Poisson survival function (McMahon, 2019) describes the cell survival fraction after delivery of dose d_i in a voxel i as

$$\mathrm{SF_L}(d_i) = \exp\Big\{-\alpha d_i\Big\}.$$

It is also known as the single-hit model. The inequality $\mathrm{SF_L}(d_i) \leq t$ is equivalent to the following conic constraint:

$$(t, 1, -\alpha d_i) \in K_{\exp}.$$

We did not require a strictly increasing function g for the reformulation, so we can pick $g(t) = t$. Then $\mathrm{epi}(g \circ \mathrm{SF_L})$ is Cr. The linear-quadratic Poisson survival function is discussed in Appendix 4.C.

Linear Poisson TCP function

The linear Poisson TCP (see, e.g., Brahme and Argren (1987)) is given by

$$\mathrm{TCP_L}(\boldsymbol{d}) = \exp\Big(-N_0 \sum_{i=1}^n v_i \mathrm{SF_L}(d_i)\Big), \tag{4.9}$$

where N_0 is the total initial number of clonogenic cells. The total number of tumor cells remaining (TNTCR) is given by $-\log(\mathrm{TCP_L})$, which gives

$$\mathrm{TNTCR_L}(\boldsymbol{d}) = N_0 \sum_{i=1}^n v_i \mathrm{SF_L}(d_i).$$

Generally the goal is to maximize TCP, so we aim to find a CR of $\mathrm{hypo}(g \circ \mathrm{TCP_L})$ and consider the inequality $\mathrm{TCP_L}(\boldsymbol{d}) \geq t$, for some $t \in [0, 1)$. Consider the strictly

increasing function $g(t) = \log(t)$, and let τ denote either the new objective variable or the constant term (see Section 4.2.1) that replaces $g(t)$. Then, with $\boldsymbol{y} \in \mathbb{R}^n$ an auxiliary variable, $\mathrm{TCP}_{\mathrm{L}}(\boldsymbol{d}) \geq t$ is equivalent to

$$\begin{cases} -N_0 \sum_{i=1}^{n} v_i y_i \geq \tau, & \text{(4.10a)} \\ y_i \geq \mathrm{SF}_{\mathrm{L}}(d_i), \quad \forall i. & \text{(4.10b)} \end{cases}$$

The second inequality is shown to be Cr in the reformulation of the linear Poisson survival fraction model.

Alternatively, with $p \in \mathbb{R}$ an auxiliary variable, $\mathrm{TNTCR}_{\mathrm{L}}(\boldsymbol{d}) \leq t$ can be reformulated to

$$\begin{cases} N_0 \sum_{i=1}^{n} v_i \exp\{-\alpha d_i - p\} \leq 1, \\ p \leq \log(t). \end{cases}$$

With the introduction of auxiliary variable $\boldsymbol{y} \in \mathbb{R}^n$, this is equivalent to

$$\begin{cases} N_0 \sum_{i=1}^{n} v_i y_i \leq 1, \\ (t, 1, p) \in K_{\exp}, \\ (y_i, 1, -\alpha d_i - p) \in K_{\exp}, \quad \forall i. \end{cases}$$

The benefit of this reformulation is that the exponents $-\alpha d_i - p$ have (much) smaller absolute values than $-\alpha d_i$ itself if $p < 0$ (i.e., upper bound $t \leq 1$), thus improving numerical stability.

Alber and Reemtsen (2007) uses the logarithmic tumor control probability (LTCP), which is a variation on the linear TCP and is given by

$$\mathrm{LTCP}(\boldsymbol{d}) = \frac{1}{n} \sum_{i=1}^{n} \exp\{-\alpha(d_i - d_p)\},$$

with α the radiation sensitivity parameter and d_p the prescribed dose. The inequality $\mathrm{LTCP}(\boldsymbol{d}) \leq t$ is equivalent to

$$\begin{cases} \frac{1}{n} \sum_{i=1}^{n} y_i \leq t, \\ (y_i, 1, -\alpha(d_i - d_p)) \in K_{\exp}, \end{cases}$$

where $\boldsymbol{y} \in \mathbb{R}^n$ is an auxiliary variable. For the reformulation methodology, we pick $g(t) = t$ and we find that $\mathrm{epi}(g \circ \mathrm{LTCP})$ is Cr.

Equivalent uniform dose (EUD)

The EUD (Niemierko, 1997) of a nonuniform dose to the tumor is the dose that, if delivered homogeneously to the tumor, yields the same TCP. With the linear Poisson survival model the EUD is given by

$$\mathrm{EUD}_{\mathrm{L}}(\boldsymbol{d}) = -\frac{1}{\alpha}\log\Big(\frac{1}{n}\sum_{i=1}^{n}\mathrm{SF}_{\mathrm{L}}(d_i)\Big). \tag{4.11}$$

As we generally wish to maximize tumor EUD, we consider the inequality $\mathrm{EUD}_{\mathrm{L}}(\boldsymbol{d}) \geq t$. With strictly increasing function $g(t) = -\exp\{-\alpha t\}$ and $g(t)$ replaced by new variable τ, $\mathrm{hypo}(g \circ \mathrm{EUD}_{\mathrm{L}})$ is equivalent to

$$\begin{cases} \dfrac{1}{n}\displaystyle\sum_{i=1}^{n} y_i \leq -\tau, \\ y_i \geq \mathrm{SF}_{\mathrm{L}}(d_i), \quad \forall i, \end{cases}$$

and the latter inequality is Cr (see the reformulation of the linear Poisson survival fraction model).

Generalized equivalent uniform dose (gEUD)

The gEUD of a heterogeneous dose distribution (Niemierko, 1999) is given by

$$\mathrm{gEUD}(\boldsymbol{d}; a) = \Big(\frac{1}{n}\sum_{i=1}^{n} d_i^a\Big)^{\frac{1}{a}}, \tag{4.12}$$

where a is a tissue specific parameter. The analysis depends on the value of parameter a, see also Choi and Deasy (2002). As $a \to +\infty$, the gEUD approaches the maximum dose; as $a \to -\infty$, the gEUD approaches the minimum dose. Furthermore, $a = 1$ is the mean dose and as $a \to 0$ the gEUD approaches the geometric mean. For an organ-at-risk (OAR), it is assumed that $a \geq 1$ and for a target volume it is assumed that $a < 0$. For the analysis we rewrite (4.12) to

$$\mathrm{gEUD}(\boldsymbol{d}; a) = n^{-\frac{1}{a}}\Big(\sum_{i=1}^{n} d_i^a\Big)^{\frac{1}{a}} = n^{-\frac{1}{a}}\|\boldsymbol{d}\|_a,$$

where $\|\cdot\|_a$ is the generalized a-norm (slight abuse of notation: not in fact a norm if $a < 0$). We consider the cases $a < 0$ and $a \geq 1$ separately.

Case 1 ($a < 0$):
For a target volume, we consider the inequality $\|\boldsymbol{d}\|_a \geq t$. This is equivalent to $t \geq \sum_i d_i^a t^{1-a}$, which, on its part, is equivalent to

$$\begin{cases} \sum_{i=1}^{n} y_i \leq t, & \text{(4.13a)} \\ y_i^{\frac{1}{1-a}} d_i^{\frac{-a}{1-a}} \geq t, \ \forall i, & \text{(4.13b)} \\ d_i \geq 0, \ \forall i. & \text{(4.13c)} \end{cases}$$

It is straightforward to note that (4.13b) is equivalent to

$$(y_i, d_i, t) \in \mathcal{P}_3^{\frac{1}{1-a}, \frac{-a}{1-a}}, \ \forall i,$$

so the hypograph of the gEUD function with $a < 0$ can be modeled using a power cone. Alternatively, Ben-Tal and Nemirovski (2001, Chapter 3) show that (4.13b) is conic quadratic representable[4] (CQr) if we restrict $a < 0$ to be a rational number, although the reformulation is complicated and impractical. As the explicit description of (4.13b) in conic quadratic inequalities is cumbersome, we omit it here. The CQr representation of gEUD has previously been discussed by Zinchenko et al. (2008). For the reformulation methodology, we pick $g(t) = t$ and the above result shows that hypo($g \circ$ gEUD) is Cr for $a < 0$.

Case 2 ($a \geq 1$):
For an OAR, we consider the inequality $\|\boldsymbol{d}\|_a \leq t$. This can be rewritten to $\sum_i d_i^a t^{1-a} \leq t$. Compared to the case $a < 0$ the inequality sign is reversed, but (due to the value of a) also this inequality can be rewritten to $\sum_i d_i^a t^{1-a} \leq t$. Subsequently, this is equivalent to

$$\begin{cases} \sum_{i=1}^{n} y_i \leq t, & \text{(4.14a)} \\ d_i \leq y_i^{\frac{1}{a}} t^{\frac{a-1}{a}}, \ \forall i, & \text{(4.14b)} \\ d_i \geq 0, \ \forall i. & \text{(4.14c)} \end{cases}$$

The inequality (4.14b) is equivalent to

$$(y_i, t, d_i) \in \mathcal{P}_3^{\frac{1}{a}, \frac{a-1}{a}}, \ \forall i,$$

[4]Optimization using only the linear and quadratic cone is known as conic quadratic programming or second-order cone programming, see, e.g., Ben-Tal and Nemirovski (2001).

so the epigraph of the gEUD function with $a \geq 1$ can be modeled using a power cone. Similar to the previous case, if we restrict $a \geq 1$ to be a rational number, (4.14b) can again be shown to be CQr. For the reformulation methodology, we pick $g(t) = t$ and the above result shows that epi($g \circ$ gEUD) is Cr for $a \geq 1$.

NTCP functions

The LKB function (Lyman, 1985; Kutcher and Burman, 1989) for NTCP is given by

$$\text{NTCP}_{\text{LKB}}(d) = \Phi\Big(\frac{d - d_{50}}{m d_{50}}\Big),$$

where d is a homogeneous dose and $\Phi(z) = 1/\sqrt{2\pi}\int_{-\infty}^{z} e^{-\frac{1}{2}x^2} dx$ is the standard normal cumulative distribution function (CDF). Parameter d_{50} is the dose that yields a 50% complication probability and $m > 0$ is a parameter for the slope of the NTCP curve. The inequality $\text{NTCP}_{\text{LKB}}(\boldsymbol{d}) \leq t$ can be rewritten as

$$\frac{d - d_{50}}{m d_{50}} \leq \Phi^{-1}(t) \Leftrightarrow d \leq d_{50}\big(1 + m\Phi^{-1}(t)\big),$$

which constitutes a linear constraint. Function Φ^{-1} is a strictly increasing function, and so is $g(t) = d_{50}\big(1 + m\Phi^{-1}(t)\big)$. Therefore, with τ a new variable taking the value $g(t)$, epi($g \circ \text{NTCP}_{\text{LKB}}$) is equivalent to $d \leq \tau$. The inequality is linear, so Cr.

Stavrev et al. (2003) apply the NTCP LKB function to the gEUD of a heterogeneous dose $\boldsymbol{d}$. With the same strictly increasing function g, the epigraph epi($g \circ \text{NTCP}_{\text{LKB}}$) is equivalent to $\text{gEUD}(\boldsymbol{d}; a) \leq \tau$, where τ again replaces $g(t)$. As shown in the previous section, gEUD constraints are Cr.

Alber and Nüsslin (2001) uses mechanistic concepts to derive a phenomenological NTCP model. They propose the following expression:

$$\text{NTCP}_{\text{A\&N}}(\boldsymbol{d}; a) = 1 - \exp\Big\{-\Big(\frac{\text{gEUD}(\boldsymbol{d}; a)}{\Delta}\Big)^a\Big\},$$

where $a \geq 1$ is the gEUD parameter and Δ is the dose that yields a $1 - \text{e}^{-1}$ complication probability. The inequality $\text{NTCP}_{\text{A\&N}}(\boldsymbol{d}; a) \leq t$ can be rewritten as

$$\text{gEUD}(\boldsymbol{d}; a) \leq \Delta\Big[\log\Big(\frac{1}{1-t}\Big)\Big]^{\frac{1}{a}}.$$

Hence, with strictly increasing function $g(t) = \Delta \log\Big(\frac{1}{1-t}\Big)^{\frac{1}{a}}$, the epigraph epi($g \circ \text{NTCP}_{\text{A\&N}}$) is equivalent to $\text{gEUD}(\boldsymbol{d}; a) \leq \tau$, where τ replaces $g(t)$. This is again Cr.

Sigmoidal criteria based on gEUD

Wu et al. (2002) propose to maximize a sigmoidal-shaped function based on the gEUD for both target volume and OARs. With a the gEUD parameter, their logistic function based criteria reads

$$w(\boldsymbol{d};a)=\begin{cases}\dfrac{1}{1+\left(\frac{\mathrm{gEUD}_0}{\mathrm{gEUD}(\boldsymbol{d};a)}\right)^k} & \text{if } a<0\\[2ex] \dfrac{1}{1+\left(\frac{\mathrm{gEUD}(\boldsymbol{d};a)}{\mathrm{gEUD}_0}\right)^k} & \text{if } a\geq 1,\end{cases}$$

where for the target volume gEUD_0 is the gEUD of the prescription dose. For OARs gEUD_0 is the gEUD of the tolerable uniform dose, e.g., d_{50}. Parameter $k>0$ determines the steepness of the function at gEUD_0. As we wish to maximize function w, we are interested in the inequality $w(\boldsymbol{d};a)\geq t$, with $t\in(0,1)$. If $a<0$, this reduces to

$$\mathrm{gEUD}(\boldsymbol{d};a)\geq \mathrm{gEUD}_0\Big(\frac{t}{1-t}\Big)^{\frac{1}{k}}, \tag{4.15}$$

and the RHS is strictly increasing in t for $t\in(0,1)$. Denote the RHS by $g(t)$ and replace this by a new variable τ. Then the hypograph $\mathrm{hypo}(g\circ w)$ is equivalent to $\mathrm{gEUD}(\boldsymbol{d})\geq\tau$. This is Cr (see gEUD reformulation). If $a\geq 1$, we obtain

$$-\mathrm{gEUD}(\boldsymbol{d};a)\geq -\mathrm{gEUD}_0\Big(\frac{1-t}{t}\Big)^{\frac{1}{k}},$$

and the RHS is strictly increasing in t for $t\in(0,1)$. Denote the RHS by $g(t)$ and replace this by a new variable τ. The hypograph $\mathrm{hypo}(g\circ w)$ is equivalent to $\mathrm{gEUD}(\boldsymbol{d})\leq-\tau$. This is Cr.

Romeijn et al. (2004) indicate that one could also maximize a sigmoidal-shaped function based on the CDF of the normal distribution. The following criteria is obtained:

$$\breve{w}(\boldsymbol{d};a)=\begin{cases}1-\Phi\Big(\dfrac{\mathrm{gEUD}_0-\mathrm{gEUD}(\boldsymbol{d};a)}{\sigma\mathrm{gEUD}_0}\Big) & \text{if } a<0\\[2ex] 1-\Phi\Big(\dfrac{\mathrm{gEUD}(\boldsymbol{d};a)-\mathrm{gEUD}_0}{\sigma\mathrm{gEUD}_0}\Big) & \text{if } a\geq 1,\end{cases}$$

where σ determines the steepness at gEUD_0. We are interested in the inequality $\breve{w}(\boldsymbol{d};a)\geq t$, $t\in(0,1)$. In case $a<0$, the inequality reduces to

$$\mathrm{gEUD}(\boldsymbol{d};a)\geq \mathrm{gEUD}_0\big(1-\sigma\Phi^{-1}(1-t)\big),$$

and the RHS is increasing in t for $t \in (0,1)$. Denote the RHS by $g(t)$ and replace this by a new variable τ. The hypograph hypo$(g \circ w)$ is equivalent to gEUD$(\boldsymbol{d}; a) \geq \tau$ which is Cr for $a < 0$. Similarly, for $a \geq 1$ and strictly increasing function $g(t) = -\text{gEUD}_0\big(1+\sigma\Phi^{-1}(1-t)\big)$, the hypograph hypo$(g \circ w)$ is equivalent to gEUD$(\boldsymbol{d}; a) \leq -\tau$.

Over- and underdose penalty functions

A general underdose penalty function for tumors reads

$$f_{\text{T}}(\boldsymbol{d}) = \sum_{i=1}^{n} v_i \max\{0, p_i - d_i\}^{\gamma},$$

where p_i is the prescription dose to voxel i, $\gamma \geq 1$ is the shape parameter of the error and v_i is the relative volume of voxel i. Common choices $\gamma = 1$ and $\gamma = 2$ correspond to absolute errors and squared errors, respectively. The goal is to minimize this error, and as such we consider the inequality $f_{\text{T}}(\boldsymbol{d}) \leq t$. By extracting the max operator this can be rewritten to

$$\begin{cases} \displaystyle\sum_{i=1}^{n} v_i y_i^{\gamma} \leq t, \\ y_i \geq \max\{0, p_i - d_i\}, \ \forall i, \end{cases}$$

which is equivalent to

$$\begin{cases} \displaystyle\sum_{i=1}^{n} v_i z_i \leq t, & \text{(4.16a)} \\ z_i \geq y_i^{\gamma}, \ \forall i, & \text{(4.16b)} \\ y_i \geq p_i - d_i, \ \forall i, & \text{(4.16c)} \\ y_i \geq 0, \ \forall i. & \text{(4.16d)} \end{cases}$$

In the special case $\gamma = 1$, then the second inequality is linear. In case $\gamma = 2$ the second inequality is CQr. If γ is any other value larger than one, because $y_i \geq 0$, the second inequality is equivalent to $z_i^{\frac{1}{\gamma_i}} \geq y_i$, which can be written as $(z_i, 1, y_i) \in \mathcal{P}_3^{1/\gamma, 1-1/\gamma}$. Therefore, all inequalities in (4.16) are conic constraints. Hence, with $g(t) = t$ the epigraph epi$(g \circ f_{\text{T}})$ is Cr.

The overdose penalty function for OARs reads

$$f_{\text{OAR}}(\boldsymbol{d}) = \sum_{i=1}^{n} v_i \max\{0, d_i - p_i\}^{\gamma}.$$

For OARs it is common that $p_i = 0$ for all voxels. The reformulation of f_{OAR} is analogous to that of f_{T}.

Quadratic smoothing constraints

Smoothing constraints prevent spiked beamlet profiles, and generate smoother fluence maps that are more easily deliverable in practice using multileaf collimators, and are less sensitive to patient movement. Webb et al. (1998) propose to use the second derivative of the fluence as an indication of smoothness. Breedveld et al. (2006) discretize this and define the quadratic smoothness term

$$s_q(\boldsymbol{x}) = \frac{1}{2}\boldsymbol{x}^\top \boldsymbol{S}_q \boldsymbol{x},$$

with $\boldsymbol{S}_q \in \mathbb{R}^{n\times n}$ a symmetric positive definite matrix. Let matrix $\boldsymbol{F} \in \mathbb{R}^{p\times n}$ be such that $\boldsymbol{S}_q = \boldsymbol{F}^\top \boldsymbol{F}$, e.g., $\boldsymbol{F}$ can be the Cholesky factor of $\boldsymbol{S}_q$. Then $s_q(\boldsymbol{x}) \leq t$ is equivalent to

$$(\boldsymbol{F}\boldsymbol{x})^\top(\boldsymbol{F}\boldsymbol{x}) \leq 2t, \tag{4.17}$$

which is equivalent to $(t, 1, \boldsymbol{F}\boldsymbol{x}) \in \mathcal{Q}_r^{n+2}$. Thus, with strictly increasing function $g(t) = t$, $\operatorname{epi}(g \circ s_q)$ is Cr. If upper bound t is a constant, (4.17) can also be rewritten to $(\sqrt{2t}, \boldsymbol{F}\boldsymbol{x}) \in \mathcal{Q}^{n+1}$.

An alternative linear form is proposed by Saberian et al. (2017), who consider the linear term $s_l(\boldsymbol{x}) = \boldsymbol{S}_l\boldsymbol{x}$, with $\boldsymbol{S}_l$ a block diagonal matrix with entries $-(1-\epsilon), (1-\epsilon), -1, 0, +1$, positioned such that adjacent beamlet intensity variation is at most ϵ. Naturally, this is Cr with $g(t) = t$.

Dose-volume criteria

Dose-volume criteria are common in current clinical treatment planning. They impose dose restrictions on partial volumes. For example, a dose-volume constraint can state "at least 95% of the target volume must receive the prescription dose" or "at most 5cc of a particular OAR may receive a dose higher than 15 Gy". They can also be included in the objective. A major advantage of dose-volume criteria is that clinical experience can be translated to dose-volume criteria (Deasy, 1997; Bortfeld et al., 1997). Moreover, they can be visualized directly on a dose-volume histogram (DVH), which aids interpretation. Unfortunately, dose-volume criteria are nonconvex (Deasy, 1997) and many different approaches have been proposed to incorporate them.

Romeijn et al. (2003), Romeijn et al. (2006) and Engberg et al. (2017) propose to approximate dose-volume constraints using conditional value-at-risk (CVaR) constraints, which can be reformulated to linear constraints. Kishimoto and Yamashita (2018) propose to solve a sequence of CVaR constrained problems for an improved approximation. Saberian et al. (2016b), Liu et al. (2018) and Fu et al. (2019) propose approaches that solve several convex subproblems, which can be reformulated

to CPs. Zinchenko et al. (2008) prove that a dose-volume constraint is equivalent to an infinite sequence of gEUD constraints, and use this to construct a tractable approximation. Thus, dose-volume constraints can be approximated by solving a sequence of CPs. Presenting conic reformulations of these convex approximations is beyond the scope of this chapter.

Criterion		Parameter range	Type	$g(t)$	Cones*
Survival fraction	$\mathrm{SF}_{\mathrm{L}}(d)$	-	min	t	$K_{\exp}$
Tumor control probability	$\mathrm{TCP}_{\mathrm{L}}(\boldsymbol{d})$	-	max	$\log(t)$	$K_{\exp}$
Logarithmic tumor control probability	$\mathrm{LTCP}(\boldsymbol{d})$	-	min	t	$K_{\exp}$
Equivalent uniform dose	$\mathrm{EUD}_{\mathrm{L}}(\boldsymbol{d})$	-	max	$-\exp(-at)$	$K_{\exp}$
	$\mathrm{gEUD}(\boldsymbol{d};a)$	$a<0$	max	t	$\mathcal{P}_3$
		$a\geq 1$	min	t	$\mathcal{P}_3$
NTCP models	$\mathrm{NTCP}_{\mathrm{LKB}}(d)$	-	min	$d_{50}(1+m\Phi^{-1}(t))$	linear
	$\mathrm{NTCP}_{\mathrm{LKB}}(\mathrm{gEUD}(\boldsymbol{d};a))$	$a\geq 1$	min	$d_{50}(1+m\Phi^{-1}(t))$	$\mathcal{P}_3$
	$\mathrm{NTCP}_{\mathrm{A\&N}}(\boldsymbol{d};a)$	$a\geq 1$	min	$\Delta\log(\frac{1}{1-t})^{\frac{1}{a}}$	$\mathcal{P}_3$
Sigmoidal criteria	$w(\boldsymbol{d};a)$	$a<0$	max	$\mathrm{gEUD}_0(\frac{t}{1-t})^{\frac{1}{k}}$	$\mathcal{P}_3$
		$a\geq 1$	max	$-\mathrm{gEUD}_0(\frac{1-t}{t})^{\frac{1}{k}}$	$\mathcal{P}_3$
	$\breve{w}(\boldsymbol{d};a)$	$a<0$	max	$\mathrm{gEUD}_0(1-\sigma\Phi^{-1}(1-t))$	$\mathcal{P}_3$
		$a\geq 1$	max	$-\mathrm{gEUD}_0(1+\sigma\Phi^{-1}(1-t))$	$\mathcal{P}_3$
Over- and underdose penalty	$f_{\mathrm{T}}(\boldsymbol{d})$	-	min	t	$\mathcal{P}_3$
	$f_{\mathrm{OAR}}(\boldsymbol{d})$	-	min	t	$\mathcal{P}_3$
Smoothing constraints	$s_q(\boldsymbol{x})$	-	min	t	$\mathcal{Q}_r^{n+2}$
	$s_l(\boldsymbol{x})$	-	min	t	linear

Table 4.2: Overview of results without fractionation correction. The column 'type' indicates min if the epigraph is Cr, and max if the hypograph is Cr (i.e., it can be used for minimization resp. maximization).
*: Next to the nonnegative orthant.

Table 4.2 provides an overview of the cones (next to the nonnegative orthant) necessary to describe the radiation therapy criteria in a single-hit case (excluding fractionation). For each criterion the strictly increasing function $g(t)$ used in the reformulation is also provided. Column 3 indicates the criterion type; for minimization criteria the epigraph of epi$(g\circ f)$ is Cr, for maximization criteria the hypograph hypo$(g\circ f)$ is Cr. For cases where the conic reformulation depends on gEUD parameter a, its range is indicated. Table 4.3 gives an overview of the results for fractionation-corrected mod-

els. Several of these results are not exact conic reformulations but approximations. For details on these models and proofs of the results we refer to Appendix 4.C.

Criterion		Parameter range	Type	$g(t)$	Cones*
Survival fraction	$\widehat{\mathrm{SF}}_{\mathrm{LQ}}(d)$	-	min	t	$K_{\exp}$, $\mathcal{Q}_r^3$
Tumor control probability	$\mathrm{TCP}_{\mathrm{LQ}}(\boldsymbol{d})$	-	max	$\log(t)$	$K_{\exp}$, $\mathcal{Q}_r^3$
Equivalent uniform dose	$\mathrm{EUD}_{\mathrm{LQ}}(\boldsymbol{d})$	-	max	$-\exp(-\alpha N(t+\frac{t^2}{\alpha/\beta}))$	$K_{\exp}$, $\mathcal{Q}_r^3$
	$\mathrm{gEUD}(\mathrm{BED}(\boldsymbol{d});a)$	$a \geq 1$	min	t	$\mathcal{P}_3$, $\mathcal{Q}^3$
NTCP models	$\mathrm{NTCP}_{\mathrm{LKB}}(\mathrm{BED}(d))$	-	min	$d_{50}(1+m\Phi^{-1}(t))$	$\mathcal{Q}^3$
	$\mathrm{NTCP}_{\mathrm{LKB}}(\mathrm{gEUD}(\mathrm{BED}(\boldsymbol{d});a))$	$a \geq 1$	min	$d_{50}(1+m\Phi^{-1}(t))$	$\mathcal{P}_3$, $\mathcal{Q}^3$
	$\mathrm{NTCP}_{\mathrm{A\&N}}(\mathrm{BED}(\boldsymbol{d}))$	$a \geq 1$	min	$\Delta\log(\frac{1}{1-t})^{\frac{1}{a}}$	$\mathcal{P}_3$, $\mathcal{Q}^3$
	$\widehat{\mathrm{NTCP}}_{\mathrm{RS}}(\boldsymbol{d})$	-	min	$-\log(1-t^s)$	$\mathcal{Q}_r^3$

Table 4.3: Overview of results with fractionation correction. The column 'type' indicates min if the epigraph is Cr, and max if the hypograph is Cr (i.e., it can be used for minimization resp. maximization). RS = relative seriality s-model. For details see Appendix 4.C.
*: Next to the nonnegative orthant.

Generalization to multicriteria optimization

The optimal trade-off between various treatment plan evaluation criteria in FMO depends on the relative importance of these criteria. As often these criteria are conflicting, e.g., an increase in dose might increase both TCP and NTCP, an important element in FMO is balancing several conflicting objectives. Multicriteria optimization (MCO) (Miettinen, 1999; Ehrgott, 2005) is the predominant method for handling such trade-offs (Küfer et al., 2003; Breedveld et al., 2019), and aims to compute a set of solutions known as the Pareto surface (or frontier). Loosely speaking, it is the set of all solutions for which the objective value of one objective function cannot be strictly decreased without strictly increasing the objective value of another objective function. It is regarded as the set of all meaningful candidate solutions that could be considered in decision making.

There are many methods for generation of the Pareto surface (Craft et al., 2006), a common family of methods are scalarization methods (Ehrgott, 2005). One such method, the ε-constraint method, introduces a vector $\boldsymbol{\varepsilon} \in \mathbb{R}^p$ and solves for each $k = 1, \ldots, p$ the problem

$$\min_{\boldsymbol{d} \in S} \; f_k(\boldsymbol{d}), \tag{4.18a}$$

$$\text{s.t.} \; f_j(\boldsymbol{d}) \leq \varepsilon_j, \; j = 1 \ldots, p, \; j \neq k. \tag{4.18b}$$

By varying the $\boldsymbol{\varepsilon}$ in (4.18), the Pareto surface can be computed. The ε-constraint method solves problems with a single objective function, so if CRs of the epigraphs of the individual treatment criteria are found, the ε-constraint method can be used in the conic reformulation methodology to obtain the Pareto surface.

4.2.3 Experiment setup

The Radiotherapy Optimisation Test Set (TROTS) is an extensive data set of FMO problems originating from patients treated at Erasmus MC in the Netherlands (Breedveld and Heijmen, 2017). For various treatment sites/protocols, it contains patient data, pencil beam matrices and the FMO problem descriptions. Beam angles (and related planning aspects) are fixed, and clinical deliverability (i.e., leaf-sequencing) is not taken into account. The multicriteria FMO problems are converted to single-objective problems by a priori selection of objective weights. For all instances, the results obtained by the Erasmus MC in-house TPS iCycle are available[5]. The pencil beam matrices in the TROTS data set are generated by iCycle using a pencil beam algorithm (Breedveld et al., 2012).

TROTS contains instances from six treatment sites/protocols, Table 4.4 gives an overview of the considered treatment sites/protocols. The TROTS liver cases, with (nonconvex) dose-volume constraints, are not considered here, although convexified approximations exist (see Section 4.2.2). TROTS also contains brachytherapy cases, which are beyond the scope of this study. We note that, despite the naming, the `Prostate_VMAT` cases are in fact 23-beam IMRT FMO problems. In Voet et al. (2014), the iCycle solution for these problems is used as a starting point to generate a single-arc volumetric modulated arc therapy (VMAT) plan. The proton cases contain only linear minimum and maximum dose constraints. All other cases contain several nonlinear treatment criteria. Conic reformulations of gEUD, LTCP and quadratic smoothing criteria are presented in Section 4.2.2. Thus, the FMO problems in Table 4.4 can be solved as conic problems and results can be compared to those obtained by other solvers. For further details on the protocols we refer to Breedveld and Heijmen (2017) and references therein.

The considered TROTS instances are convex optimization problems, and different algorithms for such problems find globally optimal solutions in theory. However, this does not always translate to good performance in practice, due to amongst others numerical issues. We test the performance of several solvers, both solvers for optimization problems in conic form and functional form. All methods use the same pencil beam ma-

[5] TROTS data and iCycle results are available at `https://sebastiaanbreedveld.nl/trots/`.

Site/ protocol	# Cases	# Beamlets*	# Voxels*	Min/max dose	Linear smoothing	Quadratic smoothing	gEUD	LTCP
Protons	20	1803	350,428	✓	✗	✗	✗	✗
Prostate CK	30	2937	153,151	✓	✓	✓	✗	✓
Prostate VMAT	30	2697	155,787	✓	✓	✓	✓	✓
Head & Neck	15	8302	283,137	✓	✓	✓	✓	✓

Table 4.4: TROTS data set overview.
*: Averaged over all patients.

trices. In sparse matrix format, these range in size between 350 MB for the `Protons` cases to 1.9 GB for the `Prostate_VMAT` cases (on average). The tested solvers are

- iCycle: A (non-conic) primal-dual IPM developed by Erasmus MC and optimized for the TROTS data set (Breedveld et al., 2017). It uses a Mehrotra predictor-corrector method[6]. Using problem-specific information an initial feasible solution is constructed to the FMO problem, and subsequently extended to a feasible primal-dual solution. By efficient handling of the pencil beam matrices, the computational efficiency of solving the normal equation of the IPM is improved. The solver is not open-source, but results obtained for the TROTS data set are available online[5]. Thus, the iCycle objective values (and convergence aspects) can be compared to those obtained by other solvers.

- matRad (version 3.0.0): The TPS system matRad makes use of IPOPT (version 3.11.8), an open-source (non-conic) primal-dual solver (Wächter and Biegler, 2006) developed for general purpose convex optimization problems. It uses a limited memory implementation, approximating the Hessian of the Lagrangian by a limited-memory quasi-Newton method (L-BFGS) and approximating maximum dose constraints via a log-sum-exp function. Changing this to exact Hessian computations resp. exact maximum dose constraints leads to memory issues. We extended the matRad capabilities to include all evaluation criteria in Table 4.4.

- MOSEK (version 9.2): A commercial primal-dual conic optimization solver supporting the quadratic, exponential and power cone (MOSEK ApS, 2020).

- ECOS (version 2.0.7): An open-source primal-dual conic optimization solver supporting the quadratic and exponential cone, but not the power cone (Domahidi et al., 2013; Serrano, 2015).

[6]They also propose a combined Mehrotra-Gondzio approach, where first a full Mehrotra step is taken before using the Gondzio update scheme. This approach did not yield better results than the Mehrotra method.

- SCS (version 2.1.2): An open-source (first-order) splitting conic solver (O'Donoghue et al., 2019) which uses an algorithm based on ADMM.

TROTS contains challenging problems, and preliminary results indicate that not all solvers are able to solve the instances. ECOS encounters numerical issues on several problems, preventing convergence. Additionally, ECOS is designed for small and medium sized problems and does not scale well to larger problems. SCS is not fast enough to allow for comparison, and (due it being a first order method) it lacks solution accuracy.

For many instances, matRad has difficulties dealing with the hard maximum dose constraints on OARs (even using the log-sum-exp approximation). For most of those instances, replacing the constraint with a quadratic overdose penalty leads to significant better results (denote this approach by matRad-p). Only for the Prostate CK cases, the original matRad approach produced reasonable results. For these cases we report results for both matRad and matRad-p, for other treatment sites/protocols we report solely the result of matRad-p. Note that, to ensure a fair comparison, when comparing the final objective values of different solvers, the value of the penalty term for matRad-p is omitted.

In Section 4.3, we report results for iCycle, MOSEK, matRad (only for Prostate CK) and matRad-p. All results of iCycle are obtained using a dual CPU system with two octocore Intel Xeon E5-2690 CPUs (2.90GHz) (Breedveld et al., 2017). The results of MOSEK, matRad and matRad-p are obtained on a system with a 24-core Intel Xeon Gold 6126 (2.60GHz) CPU, restricted to using 16 cores. For MOSEK, all instances are solved in primal form, and all solver options are left at their default values. For matRad and matRad-p, the maximum computation time is set at 3000s and the maximum number of iterations at 20000. The relative convergence tolerance parameter is set at 10^{-8} (both desired and acceptable). Other IPOPT options are left at their default values.

4.3 Results

The results obtained by iCycle, MOSEK, matRad and matRad-p are compared on objective value, constraint violations, time and number of iterations. The objective for instance in the TROTS data set is a weighted sum of various criteria, both dose-based and biological. For constraint violations the number of constraints with a violation above 5% is reported. This includes dose-based and biological constraints, as well as smoothing constraints. Thus, both the reported objective value and constraint violations do not have a direct clinical interpretation. However, lower objective value and

lower constraint violations do imply better results in general, and this allows us to compare the performance of the tested solvers.

4.3.1 Quality of solutions

Figure 4.1 presents the constraint violations of the solution found by each solver for each instance. Results are grouped by treatment site/protocol. Individual instances are ordered on the horizontal axis, so vertically stacked symbols correspond to the objective values obtained by the different solvers for the same instance. Figure 4.2 presents the objective values; note the logarithmic vertical axis.

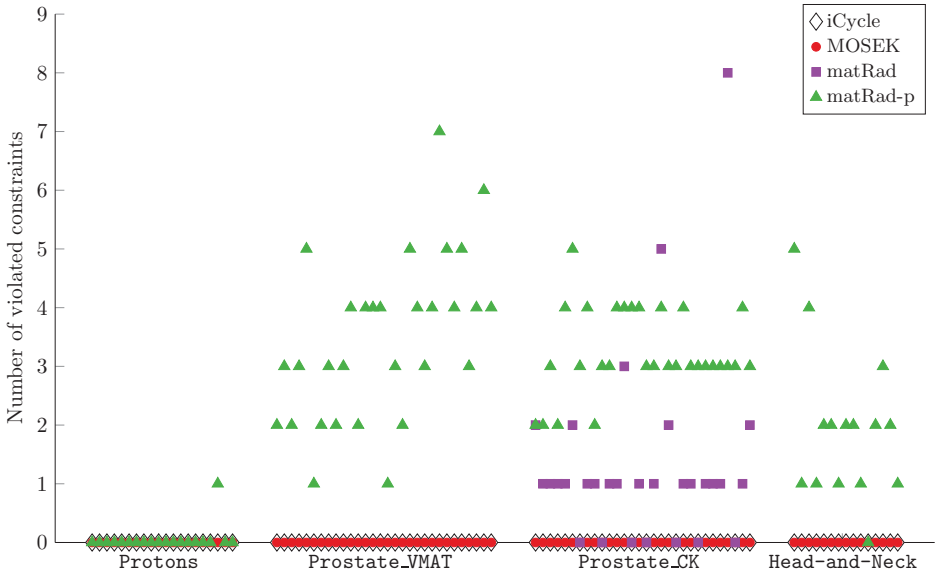

Figure 4.1: Number of violated constraints. Each symbol represents the result of one solver for one instance of the TROTS data set. The violations for iCycle and MOSEK are zero for all instances.

Both iCycle and MOSEK find a solution that does not violate any constraint (above 5%) for each instance in every protocol/treatment site. In fact, violations are less than 0.01% for all constraints for these solvers. This means that hard constraints on dose, gEUD and LTCP are satisfied, as well as the dose smoothing constraints. For Protons, matRad-p achieves constraint violations smaller than 5% for all instances except one. Solutions with a single constraint violation may still be useful. For example, they may

occur due to the fact that maximum dose constraints are handled using an approximation. A higher number of violated constraints may indicate that the solver was not able to properly handle the imposed constraints. For some instances of Prostate CK, matRad produced solutions that handled the constraints better than matRad-p. For the other treatment sites/protocols, matRad did not produce meaningful results; these are omitted in all figures to improve clarity.

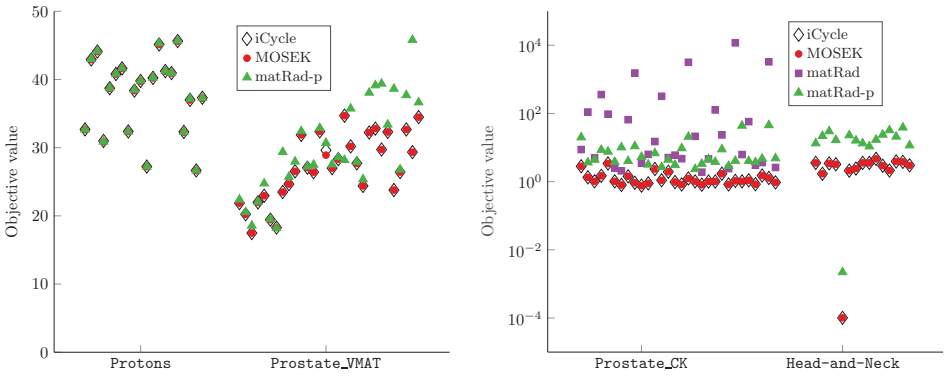

(a) Protocols `Protons` and `Prostate_VMAT`.

(b) Protocols `Prostate_CK` and `Head-and-Neck`.

Figure 4.2: Obtained objective values. Each symbol represents the result of one solver for one instance of the TROTS data set. Note the different scaling on the y-axes.

Figure 4.2 reports the objective values. Both iCycle and MOSEK find the optimal objective value for each instance in every protocol/treatment site. The relative difference in objective value is smaller than 0.005 for all instances except for an outlier of 0.03. In Figure 4.2, the markers for iCycle and MOSEK coincide for all instances. Not only the objective values coincide but also the corresponding solutions are the same. The beamlet weight vectors have a cosine similarity of above 0.99 in almost all instances (with a few outliers in $[0.95, 0.99]$). Hence, the dose distributions of MOSEK and iCycle are indistinguishable in almost all instances.

For Protons and Prostate VMAT, matRad-p is able to find solutions with optimal or near-optimal objective value, although we know from Figure 4.1 that for Prostate VMAT these come with constraint violations. For Prostate CK, matRad and matRad-p find solutions with higher objective values and for Head-and-Neck matRad-p finds solutions with higher objective values. Some of these suboptimal solutions may still translate to dose distributions that are clinically reasonable, this would have to be

checked on a case-by-case basis. For cases with objective values of several orders of magnitudes higher, or high constraint violations, matRad and matRad-p do not offer a reasonable alternative to iCycle and MOSEK.

4.3.2 Computation time and convergence

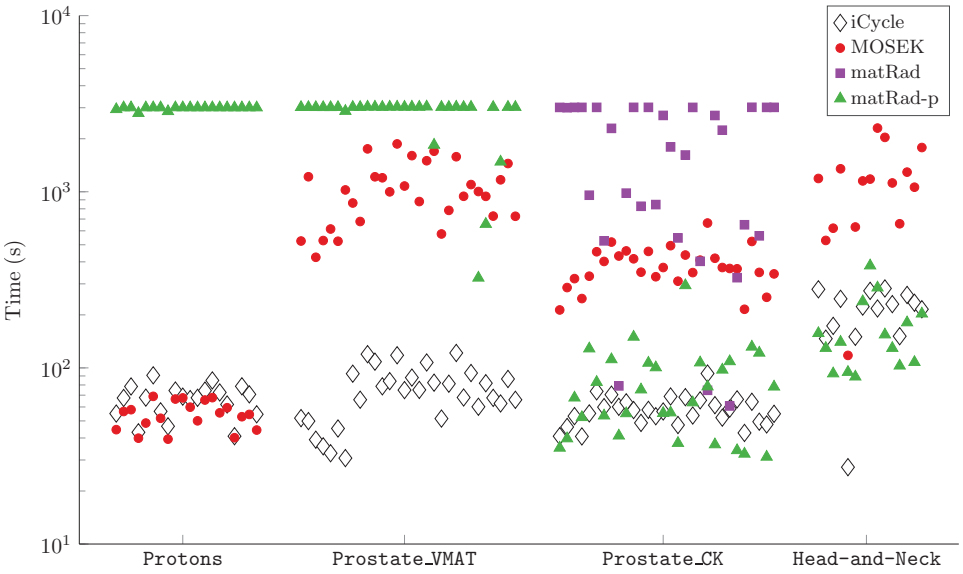

Figure 4.3: Required computation time. Each symbol represents the result of one solver for one instance of the TROTS data set.

Figures 4.3 and 4.4 presents the computation time and required number of iterations for all instances, respectively, similar to Figures 4.1 and 4.2. For Protons and Prostate VMAT matRad-p reached the time limit of 3000 seconds. Together with results of Section 4.3.1, this implies that whereas the objective value was near optimum, matRad-p was not able to further reduce constraint violations within the set time limit. This is also reflected in the high number of iterations for these cases. One possible reason for this slow convergence is that it uses only approximate Hessian information, whereas iCycle and MOSEK use exact Hessians. For Prostate CK and Head-and-Neck, the computation times of matRad-p are comparable to those of iCycle and the required number of iterations is relatively low. Thus, it was able to obtain a solution very fast, but the solution did not reach the optimal objective value and/or violated constraints.

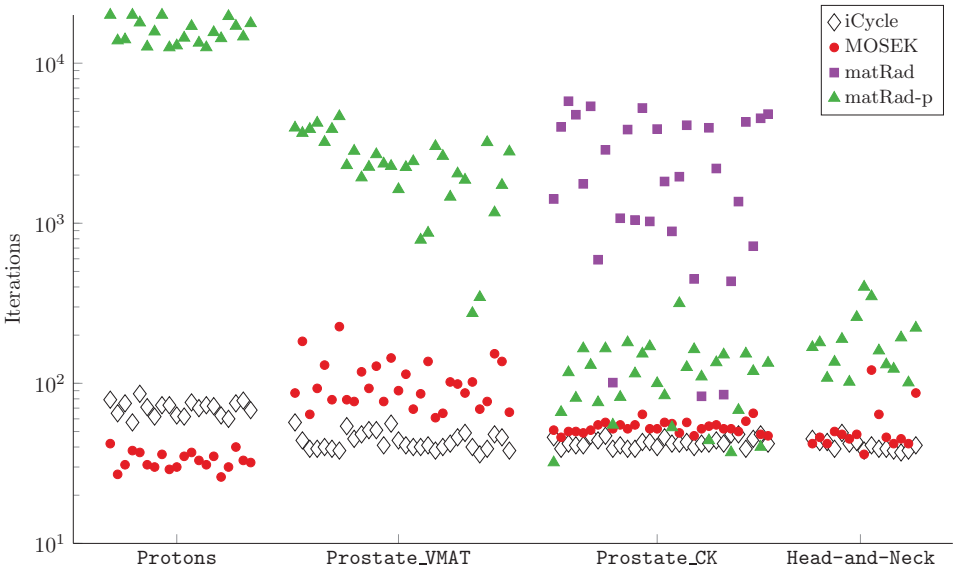

Figure 4.4: Number of iterations required. Each symbol represents the result of one solver for one instance of the TROTS data set.

For Prostate CK, matRad requires considerably more computation time and iterations than matRad-p, but often has better objective values and/or lower constraint violations. These results indicate that matRad and matRad-p are not very numerically stable: sometimes it converges very fast to a suboptimal or infeasible solution and sometimes it converges towards the optimal solution, but does so very slowly.

MOSEK requires slightly less time than iCycle for the Protons cases, but requires significantly more time for the other treatment sites/protocols. The CPU used for iCycle is worse than the one used for MOSEK (see Section 4.2.3), so iCycle outperforms MOSEK in terms of speed for those treatment sites. The required number of iterations is consistently low for both iCycle and MOSEK, indicating stable numerical performance. The results demonstrate that the theoretical guarantee of polynomial-time convergence for conic optimization indeed translates to fast convergence in practice.

Figure 4.5 displays detailed convergence results of MOSEK for two test cases, `Prostate_CK_01` and `Head-and-Neck_02`. For each iteration, the primal and dual objective values are plotted w.r.t. the left vertical axis. The corresponding primal and dual infeasibility are plotted w.r.t. the right vertical axis (note the logarithmic scale). The infeasibility measure is the infinity norm of the linear constraint violations. The

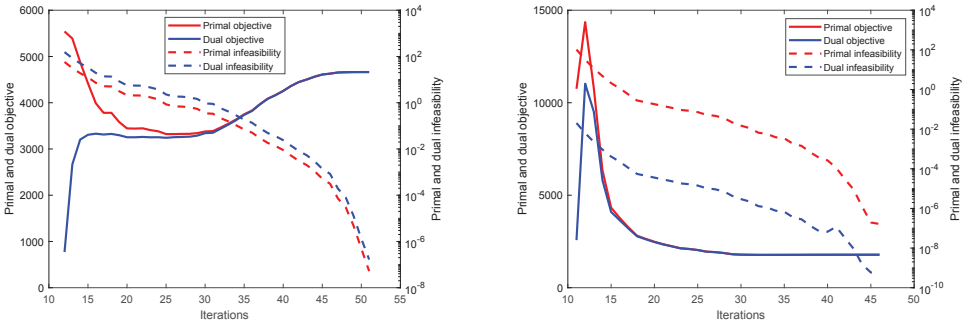

(a) Convergence for `Prostate_CK_01`.

(b) Convergence for `Head-and-Neck_02`.

Figure 4.5: Convergence results for MOSEK on two test cases. Optimality and infeasibility (both primal and dual) are plotted w.r.t. the left and right vertical axis, respectively. The infeasibility measure is the infinity norm of the linear constraint violations. Notice the logarithmic scale of the right vertical axis.

first few iterations are not very informative and distort scaling, and are hence removed. Primal-dual IPMs start from an infeasible point, and in each iteration attempt to improve the primal and dual objective value and reduce primal and dual infeasibilities. A decrease in infeasibilities may lead to an increase in objective value, so the objective value curves are not guaranteed to be decreasing. The MOSEK algorithm terminates after 51 and 46 iterations for the two test cases.

As noted in Appendix 4.A, one may terminate the algorithm early to get an approximate solution. If both the primal and dual solution are feasible, the duality gap is a measure for suboptimality of the current primal solution. In both Figure 4.5a and Figure 4.5b, the duality gap is closed before the primal and dual solutions have a sufficiently low infeasibility measure (i.e., low linear constraint violations). Therefore, early termination results in an infeasible solution. In other instances similar convergence results are obtained. Thus, although early termination of primal-dual IPMs for FMO problems in conic form is possible in theory, no such opportunity presents itself in the current numerical experiments.

4.3.3 Illustrative example

To illustrate the practical implications of differences in objective value, we study the results for `Head-and-Neck_02` in more detail. The dose distributions of MOSEK and iCycle are indistinguishable (see Section 4.3.1), so we display only one for clarity.

Figures 4.6a and 4.6b show a slice of the dose distribution obtained by MOSEK/iCycle and matRad-p, respectively. Note that the dosimetric criteria set for these cases (which are based on TROTS' specifications) are not necessarily meant to result in clinically-acceptable dose distributions.

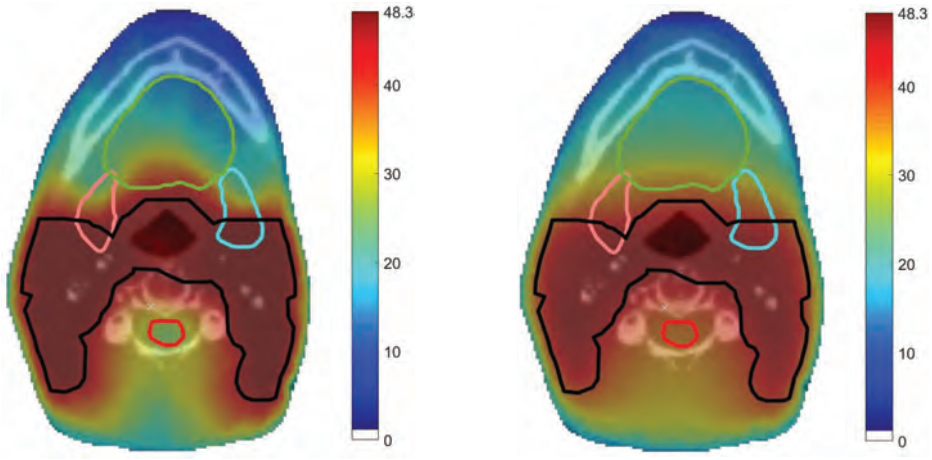

(a) Dose distribution MOSEK/iCycle.

(b) Dose distribution matRad-p

Figure 4.6: Results for `Head-and-Neck_02`. SMG = submandibular gland.

The MOSEK/iCycle solution achieves an objective value of 1.7 and matRad-p achieves 21.8, i.e., the matRad-p solution is suboptimal. MOSEK obtained the optimal solution in 46 iterations (529s) and iCycle in 43 iterations (147s). After 180 iterations (107s) matRad-p reported solution status 'solved', which indicates that the solution satisfies all imposed feasibility and optimality tolerances. However, the matRad-p solution violates a maximum dose constraint on an auxiliary planning target volume (PTV) shell by 0.50 Gy. This is a consequence of the approximation of maximum dose constraints (see Section 4.2.3).

The aggregate objective score (lower is better) contains amongst others an LTCP objective on the PTV, gEUD objectives on other auxiliary PTV structures and mean dose

objectives on various OARs. The MOSEK/iCycle solution results in an LTCP of 0.40, versus 21.3 for matRad-p. The dose distributions in Figure 4.6 show that the lower LTCP of the MOSEK/iCycle solution indeed translates to a higher and more conformal PTV dose than the matRad-p solution. Moreover, the MOSEK/iCycle solution yields a maximum spinal cord dose of 29.0 Gy versus 37.9 Gy for the matRad-p solution.

We emphasize that the resulting dose distributions are a direct consequence of the FMO problem formulations in the TROTS data set. Different objective weights may result in different dose distributions; for the current set of weights, MOSEK/iCycle found a lower objective value than matRad-p. This does not necessarily mean that MOSEK/iCycle perform better than matRad-p for all individual objectives. If the clinical decision maker does not find the MOSEK/iCycle dose distribution more desirable (while it has a lower aggregate objective value), one can adjust the weights or reformulate the FMO problem to better reflect the clinical goals and priorities. In the current study, the FMO problems are taken from the TROTS data set with fixed weights; we do not study the clinical relevance of the problem formulations and the solutions.

4.4 Discussion

We have presented a methodology for formulating FMO problems as conic optimization problems. FMO problems with many commonly used treatment plan evaluation criteria (including biological models) can be formulated as conic optimization problems using the quadratic, exponential and power cone. Implementing the conic form is more structured and less error prone than implementing a convex optimization model in functional form. For example, one need not specify derivatives and Hessians. Nevertheless, for FMO problems in functional form work has been done to make implementation of derivatives easier (Van Haveren and Breedveld, 2019).

The conic reformulation methodology can be seen as a next step in the work of Romeijn et al. (2004) and Hoffmann et al. (2008). Whereas they solely prove convexity of treatment plan evaluation criteria, we provide conic reformulations. This is not only a stronger result from a theoretical point of view, but also more useful in practice. After formulating FMO problems in conic form, one can directly use an existing conic optimization solver. Thus, it is directly implementable in the FMO module of both commercial and research treatment planning systems. Dose-volume criteria are nonconvex and cannot be transformed to conic form like many other evaluation criteria. Nevertheless, all common convex approximation procedures for handling dose-volume criteria can be formulated as conic optimization problems. For fractionation-corrected criteria, conic reformulations or approximations are presented in Appendix 4.C.

The methodology enables the use of advanced primal-dual IPM algorithms from the field of conic optimization, which guarantee polynomial-time convergence to an optimal solution. To the best of our knowledge, this is the first proof that FMO problems with (any combination of) evaluation criteria in Table 4.2 can be solved in polynomial time. We note that the algorithms implemented in software packages are not necessarily the ones with the best theoretical guarantees. In particular, the MOSEK algorithm does not guarantee polynomial-time convergence, but this has been shown for a related variant. For more details, see Appendix 4.A.

Conic optimization using exponential and power cones is a recent development in the mathematical optimization community. Several solvers have been developed in recent years, both commercial and open-source, but it remains ongoing research. Whereas in our exposition we have primarily focused on primal-dual IPMs as solvers for FMO problems, writing an FMO problem in conic form is not tied to the use of IPMs. In particular, there are also developments in proximal algorithms (Parikh and Boyd, 2014). These are typically first-order methods, i.e., they may scale to higher dimensions than second-order methods such as IPMs, at the cost of reduced accuracy. Proximal algorithms rely on the efficient computation of proximal operators. For hard constraints, the proximal operators reduce to the projection operators for the set defined by the constraints. Whereas for a constrained convex optimization problem in functional form these projections are often non-trivial, for the commonly used cones this is a relatively easy operation (Parikh and Boyd, 2014; Khanh Hien, 2015). The tested solver SCS uses a method based on ADMM, with projections onto these cones (O'Donoghue et al., 2016). Although the solver did not produce competitive results, developments in this area may be interesting for solving FMO problems in conic form.

We have evaluated several conic and non-conic solvers on the TROTS data set, and the results are promising. Whereas two conic optimization solvers were not able to solve the problems properly, the conic solver MOSEK already outperforms the matRad TPS, in terms of speed and/or solution quality. Both the iCycle TPS and MOSEK obtain the optimal solution, indicating that the theoretical optimality guarantee of conic optimization indeed translates to optimal solutions in practice. Nevertheless, the iCycle TPS outperforms MOSEK in terms of speed for most treatment sites. We note that iCycle is an in-house TPS and is not available to the larger research and clinical community; our proposed methodology has the potential to be readily incorporated in RT research. Commercial solvers often offer free academic licenses, and open-source solvers can readily be used. We have also attempted to compare our methodology with the solutions of commercial TPSs, but did not succeed, because they typically do not directly provide the pencil beam matrices necessary for formulating the FMO problem.

The currently observed speed difference between iCycle and MOSEK is likely due to the fact that iCycle is specifically tailored to FMO problems of the form encountered in the TROTS data set. Breedveld et al. (2017) also note that using application specific properties to improve efficiency of sparse matrix operations can yield significant speedups. This is also noted by Engberg et al. (2017), who implement a custom primal-dual IPM and use the FMO structure to eliminate voxel variables in the linear system of the IPM. In principle, one could also tailor a conic optimization solver to exploit the particular structure of FMO problems. However, there is a trade-off between tailoring the solver to the current type of FMO problems and preserving the flexibility of general purpose solvers. One benefit of the latter is that adding new treatment criteria will likely have less negative impact on performance. Another benefit is that improvements in general purpose conic solvers will directly translate to improvements in the FMO module. The latter is not unlikely, given that conic optimization is a hot topic in the mathematical optimization community. For example, a recent minor update of MOSEK reduced the total number of iterations by 3.7%.

On a higher level, solvers can often be tuned by the user, by setting various parameters such as termination criteria. Solvers typically allow the specification of, amongst others, an optimality tolerance, to strike the right balance between optimality and speed. In our numerical experiments, we have decreased such a parameter for IPOPT to focus on optimality. For FMO problems, one typically aims to find a near-optimal solutions whilst preventing spending many iterations on improvements with irrelevant magnitude. Further tuning of parameters may improve computation time of both MOSEK and matRad for the current data set, and possibly for FMO problems in general. In Appendix 4.A it is noted that primal-dual IPMs for conic optimization may be used to obtain approximate solutions to FMO problems, and the duality gap provides a bound on the suboptimality. A prerequisite for this is that the primal and dual solutions are both feasible. Results in Section 4.3.2 indicate that primal and dual feasibility is not always achieved early on, so this theoretical result is not directly applicable in practice. Adapting the solver or tuning solver parameters to initially focus on primal and dual feasibility instead of closing the duality gap may be necessary for early solver termination in practice. This requires further research.

Solution methods for FMO cannot directly be applied to the planning of VMAT treatments. During VMAT, the gantry makes a single arc rotation with continuous irradiation (Otto, 2008). If delivery time is taken into account, the FMO problem for each beam angle cannot be separated from the multi-leaf collimator leaves. Thus, the currently presented conic optimization approach to FMO is not directly applicable to VMAT planning. However, this is not a disadvantage particular to conic optimization,

other FMO approaches also face this limitation. Moreover, a common two-step heuristic for VMAT planning does solve FMO problems, and subsequently merges neighboring fluence maps (Craft et al., 2012). Lastly, we note that for IMRT we have applied conic optimization solely to the FMO component of the entire treatment planning process, which also consists of beam angle optimization and leaf sequencing. However, of these three components usually FMO has the largest impact on the overall quality of the treatment (Aleman, 2018). Therefore, improvements in quality and speed of the FMO component might translate into treatment plans with better quality and save valuable clinical time.

4.5 Conclusion

We have presented a methodology for reformulating FMO problems to conic optimization problems, which has both theoretical and practical advantages. We have shown that many commonly used treatment plan evaluation criteria are conic representable, and for others accurate conic approximations can be obtained, thus making the methodology generally applicable. Numerical results using a general purpose conic solver on the TROTS data set show that the theoretical advantages of conic optimization indeed translate to good practical performance in terms of speed and solution quality.

4.A Solving conic optimization problems

In complexity theory, one distinguishes optimization problems for which there exists an algorithm that solves the problem to optimality in polynomial time from problems for which such an algorithm does not exist. In the former case, the algorithm is said to be *efficient* for the considered problem. It the latter case, any algorithm that produces the optimal solution has exponential time convergence. Such algorithms may perform well on small-scale problems, but the required number of iterations (and time) often grows prohibitively fast to be of practical use for large-scale problems. For an introduction to complexity theory, focused at primal-dual IPMs, we refer to Wright (1997).

Traditionally, IPMs for conic optimization were restricted to the symmetric cones (nonnegative orthant, quadratic and semidefinite matrix cone). More recent developments extend capabilities to exponential and power cones. Several different IPM approaches exist for solving conic optimization problems with these five cones. By proving the existence of self-concordant barrier functions for these cones, Nesterov and Nemirovski (1994); Nesterov (2006) have shown that the barrier method converges in polynomial time for such conic optimization problems.

That is, it guarantees an objective value that is within a factor ε of the global optimum, within a number of iterations that is polynomial in n (the number of decision variables) and $\log(1/\varepsilon)$.

The above guarantees hold for the *conic form* of the FMO problem, and it must be verified that they translate to guarantees for the original FMO problem. This is confirmed in Appendix 4.B under mild technical conditions. Therefore, formulating an FMO problem (or any other optimization problem) in conic form (using these five cones) automatically gives the guarantee that the problem can be solved in polynomial time. In contrast, directly proving that specific FMO problems can be solved in polynomial time is difficult. This requires proving the existence of a self-concordant barrier function for the feasible region described by the set of treatment plan evaluation criteria. To the best of our knowledge, such attempts have been unsuccessful.

As an alternative to the (primal) barrier methods, primal-dual IPMs for the symmetric cones were introduced by Nesterov and Todd (1997, 1998). They are also proven to converge in polynomial time (for the symmetric cones) and outperformed the barrier methods in practice. Recently, progress in primal-dual methods for the exponential and power cone has found its way to software packages. The second-order cone solver ECOS (Domahidi et al., 2013) has been extended to incorporate exponential cones (Serrano, 2015). Coey et al. (2021) describes the development of a solver (Hypatia) with a large number of predefined cones, to stay as close to the natural formulation of the problem as possible. Recently the primal-dual method of the commercial solver MOSEK was extended to support the exponential cone and the power cone. Its algorithm for the exponential cone is described in Dahl and Andersen (2021). Recently, Badenbroek and Dahl (2021) proved polynomial time convergence of a stylized version of MOSEK's implementation for the exponential and power cone. Specifically, they proved it requires at most $\mathcal{O}(\nu \log(1/\varepsilon))$ iterations, with ν a parameter depending on the dimension of cone C in problem (4.5).

As noted in Section 4.1, primal-dual IPMs are a general class of algorithms. They are not solely restricted to optimization problems in conic form, but can also be used to solve convex optimization problems in functional form, by solving the KKT optimality conditions. Understanding the intricacies of the various methods requires a high level of expertise. Part of the good practical performance of primal-dual IPMs for symmetric cones can be attributed to the existence of a unique so-called scaling point for these cones, which relates primal and dual variables. Dahl and Andersen (2021) and Badenbroek and Dahl (2021) use a 'scaling matrix' to mimic this behavior in non-symmetric cones.

Lastly, we note that primal-dual IPMs may also be used to find an approximate solution to the conic reformulation of the FMO problem. In each iteration, the algorithm produces a solution to the primal problem and a solution to the dual problem. If both solutions are feasible for their respective problems, the corresponding difference in primal and dual objective values, known as the duality gap, provides useful convergence information. In particular, it is an upper bound on the suboptimality of the currently found (primal) solution. The algorithm

can be terminated once primal an dual feasibility is achieved and the duality gap is deemed low enough, i.e., a sufficiently accurate solution has been obtained. Appendix 4.B relates the desired accuracy of the FMO objective to the termination criteria of the conic form problem. In general, early termination of other optimization algorithms does not give bounds on the suboptimality of the current solution. The primal-dual IPM of iCycle (Breedveld et al., 2017) provides an estimation of the duality gap in each iteration, but this is not exact.

4.B Convergence

IPMs guarantee an objective value that is within ε of the global optimum, within a number of iterations that is polynomial in the number of decision variables and $\log(1/\varepsilon)$. However, these guarantees are for the conic reformulation of the FMO problem. It must be verified that this indeed translates to convergence guarantees for the original FMO problem. Note that is not just the case for FMO problems. This must be verified for any optimization problem which is reformulated to conic form, before statements on polynomial time convergence of the original problem can be made.

Consider an FMO problem with objective $f : \mathbb{R}^n \mapsto \mathbb{R}$ and feasible region $X \subseteq \mathbb{R}^n$:

$$\min_{\boldsymbol{x} \in X} f(\boldsymbol{x}). \tag{4.B.1}$$

Let OPT denote the optimal objective value. Let $g : \mathbb{R} \mapsto \mathbb{R}$ be a strictly increasing function, such that the set defined by $g(f(\boldsymbol{x})) \leq \tau$ is conic representable. Then, according to our conic reformulation methodology, (4.B.1) is equivalent to the following problem in epigraph form:

$$\min_{\boldsymbol{x} \in X, \tau} \quad \tau, \tag{4.B.2a}$$

$$\text{s.t.} \quad g(f(\boldsymbol{x})) \leq \tau. \tag{4.B.2b}$$

The optimal objective value to (4.B.2) (and its conic reformulation) is $g(\text{OPT})$. Let n_c denote the number of variables in the conic reformulation of (4.B.2). We assume that n_c is polynomial in n, i.e., the conic reformulation leads to a polynomial increase in number of variables. For all treatment plan evaluation criteria discussed in Section 4.2.2 this is satisfied; in fact, they all yield a linear increase in number of variables.

Moreover, the following assumption asserts that the conic form problem can be solved efficiently.

Assumption 4.8. *Let $\varepsilon \in (0, 1)$. There exists an algorithm that produces a solution $\boldsymbol{x}^*$ to the conic reformulation of* (4.B.2) *such that $g(f(\boldsymbol{x}^*)) \leq g(OPT) + \varepsilon$ in $\mathcal{O}(n_c \log(1/\varepsilon))$ iterations.*

Suppose we use the algorithm of Assumption 4.8 to solve the conic reformulation of (4.B.2), and terminate once we find a solution $(\bar{\boldsymbol{x}}, \bar{\tau})$ with an objective value that is at most $\varepsilon > 0$ higher

than $g(\text{OPT})$. Then it holds that

$$g(f(\boldsymbol{x}^*)) = \bar{\tau} \leq g(\text{OPT}) + \varepsilon.$$

Because $g^{-1}(\cdot)$ is also strictly increasing we know

$$f(\boldsymbol{x}^*) \leq g^{-1}(g(\text{OPT}) + \varepsilon).$$

The value ε must be set such that $f(\boldsymbol{x}^*) - \text{OPT} \leq \theta$. A sufficient condition is

$$g^{-1}(g(\text{OPT}) + \varepsilon) \leq \text{OPT} + \theta,$$

or

$$\varepsilon \leq g(\text{OPT} + \theta) - g(\text{OPT}).$$

The value of OPT is not known prior to the optimization. A conservative choice is

$$\varepsilon^* = \min_{z \in \text{range}(f)} g(z + \theta) - g(z). \tag{4.B.3}$$

Denote the minimizer by z^*. Function g is univariate and strictly increasing, so z^* is easily obtained. For Assumption 4.8, we require $\varepsilon^* \in (0, 1)$, so the tolerance θ must be set (by the user) such that

$$g(z^* + \theta) - g(z^*) \in (0, 1).$$

Additionally, θ must also be such that $z^* + \theta \in \text{dom}(g)$. For any function g, we can determine this implicit upper bound on θ, call this u. Thus, if $\theta \in (0, u)$, the desired accuracy of the original FMO problem (4.B.1) is ensured if tolerance (4.B.3) is used for the conic reformulation of problem (4.B.2).

The following proposition provides the required complexity result.

Proposition 4.9. *Let $\theta \in (0, u)$ and suppose that $g(\cdot)$ is differentiable and n_c is polynomial in n. There exists an algorithm that produces a solution $\boldsymbol{x}^*$ to* (4.B.1) *such that $f(\boldsymbol{x}^*) \leq OPT + \theta$ in $\mathcal{O}(n \log(1/\theta))$ iterations.*

Proof. Assumption 4.8 guarantees that the solution $\boldsymbol{x}^*$ is produced in a number of iterations that is polynomial in $n_c \log(1/\varepsilon^*)$. By assumption, n_c is polynomial in n, so the number of iterations is clearly polynomial in the problem size n of (4.B.1). We proceed by bounding a polynomial of $\log(1/\varepsilon^*)$ by a polynomial of $\log(1/\theta)$. Let $q : \mathbb{R} \mapsto \mathbb{R}$ be a polynomial such that the number of iterations to find a solution to the conic reformulation of (4.B.1) within ε^* of $g(\text{OPT})$ is bounded by $q(\log(1/\varepsilon^*))$. Function g is differentiable, so we can define

$$\theta_l = \arg\min_{\theta \in (0,u)} \frac{\partial g(z^* + \theta)}{\partial \theta},$$

i.e., the point with lowest slope on the interval $(0, u)$. Define linear function $l : \mathbb{R} \mapsto \mathbb{R}$ by $l(\theta) = g'(z^* + \theta_l)\theta$. We have

$$0 < l(\theta) \leq g(z^* + \theta) - g(z^*), \quad \forall \theta \in (0, u).$$

Consequently, using the definition of ε^* and $l(\theta)$, for any $\theta \in (0, u)$ it holds that

$$\begin{aligned} q(\log(1/\varepsilon^*)) &= q\left(\log\Big(\frac{1}{g(z^* + \theta) - g(z^*)}\Big)\right) \\ &\leq q\Big(\log\big(1/l(\theta)\big)\Big) \\ &= q\Big(\log\big(1/g'(z^* + \theta_l)\big) + \log\big(1/\theta\big)\Big), \end{aligned} \tag{4.B.4}$$

and in (4.B.4), the first term of the argument of q is a finite real constant ($g'(\cdot) > 0$). Thus, (4.B.4) is a polynomial in $\log(1/\theta)$. This completes the proof. □

If (4.B.1) is a maximization problem, the term $g(z+\theta)-g(z)$ is replaced by $g(z)-g(z-\theta)$ everywhere, e.g., ε^* is now

$$\varepsilon^* = \min_{z \in \text{range}(f)} g(z) - g(z - \theta), \tag{4.B.5}$$

and the linear function $l : \mathbb{R} \mapsto \mathbb{R}$ is instead defined by $l(\theta) = g'(z^* - \theta_l)\theta$. The remainder of the analysis remains unchanged.

Example 4.10. Let f be the linear TCP function (4.9), then we have $g(t) = \log(t)$. Using (4.B.5), we find that $z^* = 1$, and we can derive $u = 1 - e^{-1} \approx 0.6321$. Thus, as long as accuracy parameter θ for the original TCP maximization problem is chosen from the interval $(0, 0.6321)$, the corresponding accuracy parameter ε^* for the conic reformulation can be chosen. Given that the TCP is between (0.1), the maximum allowed deviation will not likely exceed 0.6321, so the condition on θ is mild.

Note that ε^* is chosen conservatively. Suppose we set accuracy parameter $\theta = 0.01$ and suppose the true optimal attainable TCP is OPT $= 0.6$. The conic reformulation maximizes log(TCP), i.e., it minimizes the total number of tumor cells remaining (TNTCR) according to the Poisson model. We have $\log(\text{TCP}) = -0.511$, i.e., the TNTCR is 0.511. According to (4.B.5), $\varepsilon^* = 0.010$, so the algorithm terminates once the TNTCR is lower than 0.521. However, if instead of using the conservative $z^* = 1$ we use $z^* = \text{OPT}$ we get $\varepsilon^* = 0.017$. Thus, the algorithm can in fact already terminate once the TNTCR is lower than 0.528. ▲

4.C Fractionation-corrected models

Radiation treatments are typically delivered over multiple fractions. Several of the previously discussed treatment criteria can be corrected to account for the dose-per-fraction effects. The

Poisson LQ survival model (McMahon, 2019) is the predominant model for expressing the cell survival fraction of fractionated treatments. According to the LQ model, the surviving fraction of cells in voxel i after receiving a dose of d_i in N fractions is given by

$$\mathrm{SF}_{\mathrm{LQ}}(d_i) = \exp\Big\{-\alpha d_i\big(1+\frac{1}{\alpha/\beta}\frac{d_i}{N}\big)\Big\}. \tag{4.C.1}$$

In Hoffmann et al. (2008) it is shown that (4.C.1) is convex, as long as the voxel dose satisfies

$$d_i \geq \sqrt{\frac{1}{2}\frac{(\alpha/\beta)N}{\alpha}} - \frac{1}{2}(\alpha/\beta)N.$$

Let

$$L = \max\Big\{0,\ \sqrt{\frac{1}{2}\frac{(\alpha/\beta)N}{\alpha}} - \frac{1}{2}(\alpha/\beta)N\Big\}.$$

We restrict ourselves to $d_i \geq L$. This bound is not very restrictive, see e.g. Hoffmann et al. (2008). The LQ survival function is only convex on a subset (i.e., $d_i \geq L$) of its natural domain. Such functions are typically not Cr. Indeed, it is not apparent to find an exact CR, and we provide an approximation. Let $\bar{d}_i \geq L$ and let

$$\widehat{\mathrm{SF}}_{\mathrm{LQ}}(d_i;\bar{d}_i) = \max\big\{0, a_1(\bar{d}_i)d_i + a_2(\bar{d}_i)\big\}\exp\Big\{a_3(\bar{d}_i)d_i + a_4(\bar{d}_i)\Big\}, \tag{4.C.2}$$

with fitting parameters $a_1(\bar{d}_i), a_3(\bar{d}_i) < 0$, $a_2(\bar{d}_i) > 0$, $a_4(\bar{d}_i)$. Function $\widehat{\mathrm{SF}}_{\mathrm{LQ}}(d_i;\bar{d}_i)$ is a lower bound to $\mathrm{SF}_{\mathrm{LQ}}(d_i)$ for all $d_i \geq L$ that is tangent at the point $d_i = \bar{d}_i$. The precise definitions of the fitting parameters that result in this behavior are rather complicated; these are given in Appendix 4.E.1. They do not have a direct physical interpretation. The result is formalized in the following lemma.

Lemma 4.11. *For all $d_i \geq L$ it holds that $\widehat{SF}_{LQ}(d_i;\bar{d}_i) \leq SF_{LQ}(d_i)$ and $\widehat{SF}_{LQ}(d_i;\bar{d}_i)$ is tangent to $SF_{LQ}(d_i)$ at $d_i = \bar{d}_i$.*

Proof. See Appendix 4.E.1. □

The provided approximation is not conservative, i.e., if (d_i, t) satisfies $\widehat{\mathrm{SF}}_{\mathrm{LQ}}(d_i;\bar{d}_i) \leq t$ it need not satisfy $\mathrm{SF}_{\mathrm{LQ}}(d_i) \leq t$. By taking the pointwise maximum over $\widehat{\mathrm{SF}}_{\mathrm{LQ}}(d_i;\bar{d}_i)$ for various values of $\bar{d}_i$, improved approximations are obtained. Already for a few values of $\bar{d}_i$, the obtained approximation is very accurate. Numerical results demonstrating the approximation quality can be found in Appendix 4.D.1.

We proceed by showing that the epigraph of (4.C.2) is Cr. Consider the inequality $\widehat{\mathrm{SF}}_{\mathrm{LQ}}(d_i;\bar{d}_i) \leq t$. We introduce an auxiliary variable $z \in \mathbb{R}$ to eliminate the max operator

multiplied by $a_3(\bar{d}_i)/a_1(\bar{d}_i)$. Then the inequality is equivalent to

$$\begin{cases} \dfrac{a_1(\bar{d}_i)}{a_3(\bar{d}_i)} z \exp\left\{ z - \dfrac{a_2(\bar{d}_i)a_3(\bar{d}_i)}{a_1(\bar{d}_i)} + a_4(\bar{d}_i) \right\} \le t, & \text{(4.C.3a)} \\ z \ge a_3(\bar{d}_i) d_i + \dfrac{a_2(\bar{d}_i)a_3(\bar{d}_i)}{a_1(\bar{d}_i)}, & \text{(4.C.3b)} \\ z \ge 0. & \text{(4.C.3c)} \end{cases}$$

Inequality (4.C.3a) is of the form $cz\exp\{z\} \le t$ for some constant $c > 0$. As shown in MOSEK ApS (2018), because $z \ge 0$ the inequality (4.C.3a) can be written as

$$z\exp(z^2/z) \le t/c \iff \begin{cases} z\exp(w/z) \le t/c \\ z^2 \le w \end{cases} \iff \begin{cases} (t/c, z, w) \in K_{\exp} \\ (1/2, w, z) \in \mathcal{Q}_r^3. \end{cases}$$

Putting everything together, $\widehat{\mathrm{SF}}_{\mathrm{LQ}}(d_i; \bar{d}_i) \le t$ holds if and only if there exist scalar variables z, w such that

$$\begin{cases} (t/c, z, w) \in K_{\exp}, \\ (1/2, w, z) \in \mathcal{Q}_r^3, \\ z \ge a_3(\bar{d}_i) d_i + \dfrac{a_2(\bar{d}_i)a_3(\bar{d}_i)}{a_1(\bar{d}_i)}, \\ z \ge 0. \end{cases}$$

We did not require a strictly increasing function g for the reformulation; pick $g(t) = t$. Then $\mathrm{epi}(g \circ \widehat{\mathrm{SF}}_{\mathrm{LQ}})$ is Cr on $d_i \ge L$. We will proceed by analyzing several composite treatment criteria based on the LQ survival fraction function. These will assume either form (4.C.1) or (4.C.2).

As a first example, we consider the fractionation-corrected analogue of the TCP function (4.9) in Section 4.2.2:

$$\mathrm{TCP}_{\mathrm{LQ}}(\boldsymbol{d}) = \exp\Big(-N_0 \sum_{i=1}^{n} v_i \widehat{\mathrm{SF}}_{\mathrm{LQ}}(d_i) \Big). \tag{4.C.4}$$

The reformulation is analogous to that of function (4.9), only with SF_{L} replaced by $\widehat{\mathrm{SF}}_{\mathrm{LQ}}$ in (4.10b).

The single-hit EUD model (4.11) is discussed in Section 4.2.2. Using $\widehat{\mathrm{SF}}_{\mathrm{LQ}}$, the LQ-based EUD model is given by

$$\mathrm{EUD}_{\mathrm{LQ}}(\boldsymbol{d}) = -\frac{1}{2}\frac{\alpha}{\beta} \left[1 - \sqrt{1 - \frac{4\beta}{\alpha^2 N} \log\Big(\frac{1}{n} \sum_{i=1}^{n} \widehat{\mathrm{SF}}_{\mathrm{LQ}}(d_i) \Big)} \right], \tag{4.C.5}$$

see also McGary et al. (2000). We consider the inequality $\mathrm{EUD}_{\mathrm{LQ}}(\boldsymbol{d}) \geq t$. By extracting the survival fraction functions and rewriting, this is equivalent to

$$\begin{cases} -\frac{1}{n}\sum_{i=1}^{n} y_i \geq -\exp\left\{-\alpha N\left(t + \frac{1}{\alpha/\beta}t^2\right)\right\}, \\ y_i \geq \widehat{\mathrm{SF}}_{\mathrm{LQ}}(d_i), \quad \forall i. \end{cases}$$

Hence, with strictly increasing function $g(t) = -\exp\left\{-\alpha N\left(t + \frac{1}{\alpha/\beta}t^2\right)\right\}$ and $g(t)$ replaced by the new variable τ, $\mathrm{hypo}(g \circ \mathrm{EUD}_{\mathrm{LQ}})$ is equivalent to the following Cr inequalities:

$$\begin{cases} -\frac{1}{n}\sum_{i=1}^{n} y_i \geq \tau, \\ y_i \geq \widehat{\mathrm{SF}}_{\mathrm{LQ}}(d_i), \quad \forall i. \end{cases}$$

Using the LQ model, the dose to each voxel can be converted to its biologically effective dose (BED) (Fowler, 1989, 2010). If voxel i receives a dose d_i, its BED is given by

$$\mathrm{BED}(d_i) = d_i\left(1 + \frac{d_i}{(\alpha/\beta)N}\right).$$

Let $\mathrm{BED}(\boldsymbol{d})$ denote the BED vector associated with dose vector $\boldsymbol{d}$. The BED model enables the construction of fractionation-corrected gEUD constraints. For OARs (gEUD parameter $a \geq 1$), the inequality of interest is $\|\mathrm{BED}(\boldsymbol{d})\|_a \leq t$ (see Section 4.2.2). We can extract the BED term to obtain

$$\begin{cases} \|\boldsymbol{y}\|_a \leq t, \\ \mathrm{BED}(d_i) \leq y_i, \ \forall i, \end{cases}$$

and for any i the latter constraint is equivalent to

$$\begin{aligned} d_i + \frac{d_i^2}{(\alpha/\beta)N} \leq y_i \ &\Leftrightarrow d_i^2 \leq \frac{1}{4}\left[(\alpha/\beta)N(y_i - d_i) + 1\right]^2 - \frac{1}{4}\left[(\alpha/\beta)N(y_i - d_i) - 1\right]^2 \\ &\Leftrightarrow \left\| \left(d_i, \ \frac{1}{2}\left[(\alpha/\beta)N(y_i - d_i) + 1\right]\right) \right\|_2 \leq \left[(\alpha/\beta)N(y_i - d_i) - 1\right] \\ &\Leftrightarrow \left(\left[(\alpha/\beta)N(y_i - d_i) - 1\right], \ d_i, \ \frac{1}{2}\left[(\alpha/\beta)N(y_i - d_i) + 1\right]\right) \in \mathcal{Q}^3. \end{aligned} \tag{4.C.6}$$

For tumor volumes (gEUD parameter $a < 0$), the inequality of interest is $\|\mathrm{BED}(\boldsymbol{d})\|_a \geq t$, which is not convex, because the BED model is convex quadratic. As such, it is not Cr.

Similar to the gEUD models, the BED model can also be used as a fractionation-correction to the NTCP models of Section 4.2.2. For any of the NTCP models, the inequality $\mathrm{NTCP}(\mathrm{BED}(\boldsymbol{d})) \leq t$ is equivalent to

$$\begin{cases} \mathrm{NTCP}(\boldsymbol{z}) \leq t, \\ \mathrm{BED}(d_i) \leq z_i, \ \forall i, \end{cases}$$

and the latter is Cr according to (4.C.6). Note that model parameters should be replaced by their BED equivalents, i.e., BED_{50} instead of D_{50} for the LKB NTCP model.

Lastly, we consider the relative-seriality s-model, proposed by Källman et al. (1992):

$$\text{NTCP}_{\text{RS}}(\boldsymbol{d}) = \left(1 - \prod_{i=1}^{n} \left(1 - \exp\{-N_0 \text{SF}_{\text{LQ}}(d_i)\}^s\right)^{v_i}\right)^{\frac{1}{s}}. \tag{4.C.7}$$

Parameter $s \in (0,1]$ is the relative seriality parameter. It is not apparent to find an exact CR of the epigraph of $\text{NTCP}_{\text{RS}}(\boldsymbol{d})$. We provide an approximation. We consider the function $f(y) = \log\left(1 - \exp\left\{-N_0 s \exp(-y)\right\}\right)$, which is concave for $d \geq 0$ (Hoffmann et al., 2008). Let $Y = \{y^1, \ldots, y^K\} \subset \text{dom}(f)$ denote a finite set of K points with $y^1 < \ldots < y^K$. The line segment between $(y^k, f(y^k))$ and $(y^{k+1}, f(y^{k+1}))$ is a lower bound of $f(y)$ on the interval $[y^k, y^{k+1}]$, $k = 1, \ldots, K-1$. Denote the linear function corresponding to this line segment by $h_k(y)$.

For the approximation of (4.C.7), let $\boldsymbol{d} \in \mathbb{R}^n$ such that $0 \leq d_i \leq U$, $i = 1, \ldots, n$. Choose set $Y_d = \{d^1, \ldots, d^K\}$ such that $0 = d^1 < \ldots < d^K = U$, and set $y^k = \alpha\text{BED}(d^k)$ for $k = 1, \ldots, K$. Define

$$\widehat{\text{NTCP}}_{\text{RS}}(\boldsymbol{d}) = \left(1 - \prod_{i=1}^{n} \exp\left\{v_i \min_{k-1,\ldots,K} h_k(\alpha\text{BED}(d_i))\right\}\right)^{\frac{1}{s}}. \tag{4.C.8}$$

Lemma 4.12. *Let $\boldsymbol{d} \in \mathbb{R}^n$ such that $0 \leq d_i \leq U$, $i = 1, \ldots, n$. It holds that $\text{NTCP}_{RS}(\boldsymbol{d}) \leq \widehat{\text{NTCP}}_{RS}(\boldsymbol{d})$.*

Proof. The inequality $\text{NTCP}_{\text{RS}}(\boldsymbol{d}) \leq \widehat{\text{NTCP}}_{\text{RS}}(\boldsymbol{d})$ is equivalent to

$$\prod_{i=1}^{n} \exp\left\{v_i \min_{k=1,\ldots,K} h_k\big(\alpha\text{BED}(d_i)\big)\right\} \leq \prod_{i=1}^{n} \left(1 - \exp\{-N_0 \text{SF}_{\text{LQ}}(\mathbf{d}_i)\}^s\right)^{v_i}.$$

Take the logarithm on both sides and plug in the definition of $\text{SF}_{\text{LQ}}(\mathbf{d}_i)$ to obtain

$$\sum_{i=1}^{n} v_i \min_{k=1,\ldots,K} h_k\big(\alpha\text{BED}(d_i)\big) \leq \sum_{i=1}^{n} v_i \log\left(1 - \exp\left\{-N_0 s \exp\big(-\alpha\text{BED}(d_i)\big)\right\}\right).$$

By construction of h_k, it holds that $\min_{k=1,\ldots,K} h_k(y) \leq f(y)$. Therefore,

$$\min_{k=1,\ldots,K} h_k(\alpha\text{BED}(d)) \leq f(\alpha\text{BED}(d)), \ \forall\ 0 \leq d \leq U. \tag{4.C.9}$$

Consequently, $\text{NTCP}_{\text{RS}}(\boldsymbol{d}) \leq \widehat{\text{NTCP}}_{\text{RS}}(\boldsymbol{d})$ for all $\boldsymbol{d} \in \mathbb{R}^n$ such that $0 \leq d_i \leq U$, $i = 1, \ldots, n$. □

Lemma 4.12 provides a conservative approximation to the relative seriality NTCP model. The minimum over functions h_k constitutes a piecewise linear approximation. Similar to the approximation for the survival fraction function (Lemma 4.11), adding more points to set K improves the approximation. Numerical results demonstrating the good approximation quality can be found in Appendix 4.D.2.

We proceed by showing that the epigraph of (4.C.8) is Cr. Consider the inequality $\widehat{\text{NTCP}}_{\text{RS}}(\boldsymbol{d}) \leq t$. Apply the strictly increasing function $g(t) = -\log(1-t^s)$ on both sides to obtain

$$-\sum_{i=1}^{n} v_i \min_{k=1,\ldots,K} h_k(\alpha\text{BED}(d_i)) \leq -\log(1-t^s).$$

Introduce the auxiliary variable τ and substitute $\tau = g(t)$. Subsequently, we multiply both sides by -1 and introduce an auxiliary variable $\boldsymbol{y} \in \mathbb{R}^n$ to obtain

$$\begin{cases} \sum_{i=1}^{n} v_i y_i \geq -\tau, \\ \qquad y_i \leq h_k(\alpha\text{BED}(d_i)), \quad \forall k, i. \end{cases}$$

Lastly, we introduce a new variable $\boldsymbol{z} \in \mathbb{R}^n$ to extract the CQr BED term and find

$$\begin{cases} \sum_{i=1}^{n} v_i y_i \geq -\tau, & \text{(4.C.10a)} \\ \qquad y_i \leq h_k(z_i), \quad \forall k, i, & \text{(4.C.10b)} \\ \qquad z_i \geq \alpha\text{BED}(d_i), \quad \forall i. & \text{(4.C.10c)} \end{cases}$$

Because the functions h_k, $k = 1, \ldots, K$, are linear, (4.C.10) is a CR of $\text{epi}(g \circ \widehat{\text{NTCP}}_{\text{RS}})$.

Table 4.C.1 provides an overview of the results incorporating fractionation via the linear-quadratic model. For the LQ survival fraction model (4.C.1) and the relative seriality NTCP model (4.C.7) the conic reformulations are approximate. The survival fraction model is also used for the LQ TCP model (4.C.4) and the LQ EUD model (4.C.5). Table 4.C.1 is identical to Table 4.3.

4.D Approximation quality

4.D.1 Survival fraction approximation

Figure 4.D.1 shows the true survival fraction function SF and the approximation $\widehat{\text{SF}}$, for parameters $\alpha = 0.3$, $\alpha/\beta = 10$, $N = 30$. Figure 4.D.1a shows both $\text{SF}(d)$ and $\widehat{\text{SF}}(d, \bar{d})$, using tangent point $\bar{d} = 30$. Figure 4.D.1b shows the difference function. The maximum difference is attained at $d = 5$.

Criterion		Parameter range	Type	$g(t)$	Cones*
Survival fraction	$\widehat{\text{SF}}_{\text{LQ}}(d)$	-	min	t	K_{exp}, $\mathcal{Q}_r^3$
Tumor control probability	$\text{TCP}_{\text{LQ}}(\boldsymbol{d})$	-	max	$\log(t)$	K_{exp}, $\mathcal{Q}_r^3$
Equivalent uniform dose	$\text{EUD}_{\text{LQ}}(\boldsymbol{d})$	-	max	$-\exp(-\alpha N(t+\frac{t^2}{\alpha/\beta}))$	K_{exp}, $\mathcal{Q}_r^3$
	$\text{gEUD}(\text{BED}(\boldsymbol{d});a)$	$a \geq 1$	min	t	$\mathcal{P}_3$, $\mathcal{Q}^3$
NTCP models	$\text{NTCP}_{\text{LKB}}(\text{BED}(d))$	-	min	$d_{50}(1+m\Phi^{-1}(t))$	$\mathcal{Q}^3$
	$\text{NTCP}_{\text{LKB}}(\text{gEUD}(\text{BED}(\boldsymbol{d});a))$	$a \geq 1$	min	$d_{50}(1+m\Phi^{-1}(t))$	$\mathcal{P}_3$, $\mathcal{Q}^3$
	$\text{NTCP}_{\text{A\&N}}(\text{BED}(\boldsymbol{d}))$	$a \geq 1$	min	$\Delta\log(\frac{1}{1-t})^{\frac{1}{a}}$	$\mathcal{P}_3$, $\mathcal{Q}^3$
	$\widehat{\text{NTCP}}_{\text{RS}}(\boldsymbol{d})$	-	min	$-\log(1-t^s)$	$\mathcal{Q}_r^3$

Table 4.C.1: Overview of results with fractionation correction. The column 'type' indicates min if the epigraph is Cr, and max if the hypograph is Cr (i.e., it can be used for minimization resp. maximization).
*: Next to the nonnegative orthant.

An improved approximation can be obtained by adding $\bar{d} = 5$ as a second tangent point. The approximation function is the pointwise maximum of $\widehat{\text{SF}}(d, 5)$ and $\widehat{\text{SF}}(d, 5)$. Figure 4.D.1c and Figure 4.D.1d show the results. The results show that using two tangent points yields a very accurate approximation.

As an alternative approximation error measure, one could look at the relative difference in survival fraction:

$$\text{rel-diff}(d) = \frac{\text{SF}(d) - \widehat{\text{SF}}(d, \bar{d})}{\text{SF}(d)}.$$

However, unless one of the tangent points is the upper bound for d (this is 50 in the example), the approximate survival fraction equals zero for high values of d. This results in a relative difference of one and is not very informative.

4.D.2 Relative seriality NTCP approximation

Unlike the survival fraction function (4.C.1), the relative seriality NTCP function (4.C.7) is multivariate. We uniformly sample a dose vector $\boldsymbol{d} \in [30, 40]^n$, with $n = 100{,}000$ voxel, $v_i = 1/n$ for $i = 1, \ldots, n$. Let $L = 0$, $U = 50$, $\alpha = 0.3$, $\alpha/\beta = 3$, $N_0 = 10^6$ and $s = 0.2$. By scaling dose vector $\boldsymbol{d}$ to a given mean dose d, the NTCP curve can be visualized. Figure 4.D.2 shows NTCP_{RS} and the approximation $\widehat{\text{NTCP}}_{\text{RS}}$ with the dose vector $\boldsymbol{d}$ scaled according to the horizontal axis. In order to have scaled voxel doses in the interval $[0, 50]$, mean dose is restricted to $[0, 43.75]$.

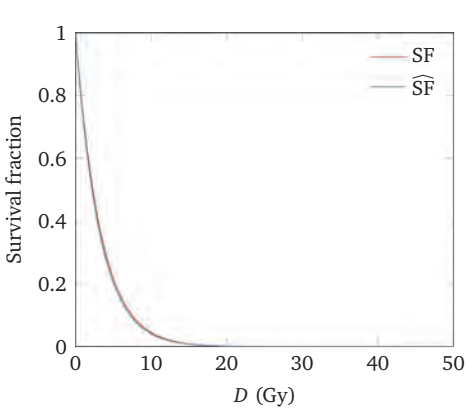

(a) $\text{SF}(d)$ (red) and $\widehat{\text{SF}}(d, 30)$ (blue)

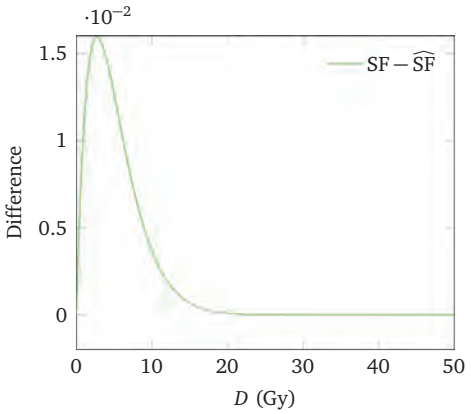

(b) Difference $\text{SF}(d) - \widehat{\text{SF}}(d, 30)$

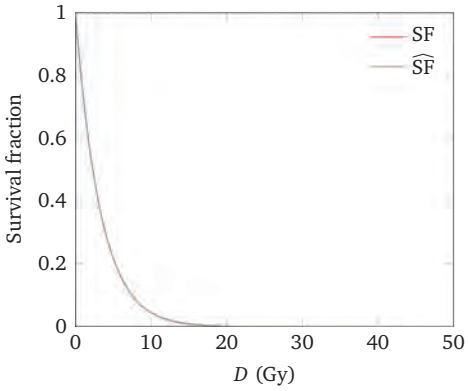

(c) $\text{SF}(d)$ (red) and $\max_{\tilde{d} \in \{5,30\}} \widehat{\text{SF}}(d, \tilde{d})$ (blue)

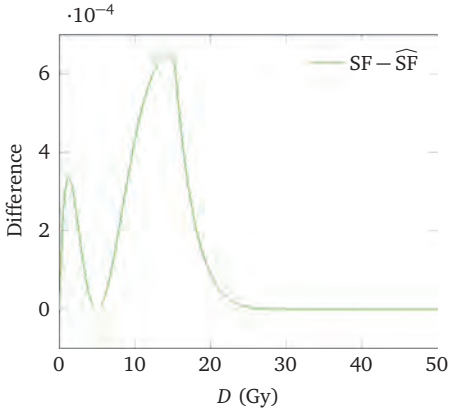

(d) Difference $\text{SF}(d) - \max_{\tilde{d} \in \{5,30\}} \widehat{\text{SF}}(d, \tilde{d})$

Figure 4.D.1: Comparison of survival fraction function $\text{SF}(d)$ and approximation $\widehat{\text{SF}}(d, 30)$, with $\alpha = 0.3$, $\alpha/\beta = 10$, $N = 30$.

Figure 4.D.2a displays NTCP_{RS} and the approximation $\widehat{\text{NTCP}}_{\text{RS}}$ using 3 line segments. Figure 4.D.2b shows the corresponding difference function. It is important to note that even if $d \in Y$, the approximation function does not equal the true NTCP function, unless the dose vector $\boldsymbol{d}$ is homogeneous. Figure 4.D.2c displays NTCP_{RS} and the approximation $\widehat{\text{NTCP}}_{\text{RS}}$ using 6 line segments. Figure 4.D.2d shows the corresponding difference function. The figures show that an accurate approximation can be obtained using 6 line segments.

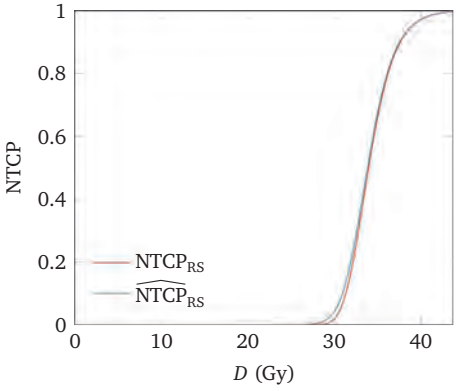

(a) $\mathrm{NTCP}_{\mathrm{RS}}(d)$ (red) and the approximation $\widehat{\mathrm{NTCP}}_{\mathrm{RS}}(d)$ (blue) using $Y_d = \{0, 30, 34, 50\}$.

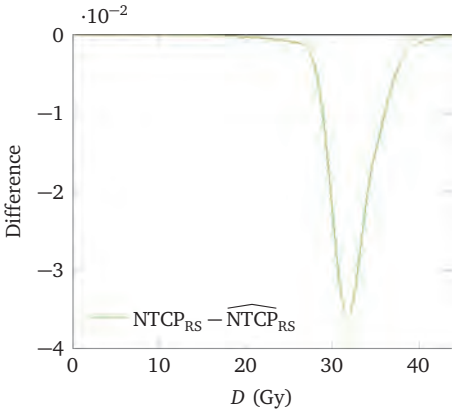

(b) Difference $\mathrm{NTCP}_{\mathrm{RS}}(d) - \widehat{\mathrm{NTCP}}_{\mathrm{RS}}(d)$ using $Y_d = \{0, 30, 34, 50\}$.

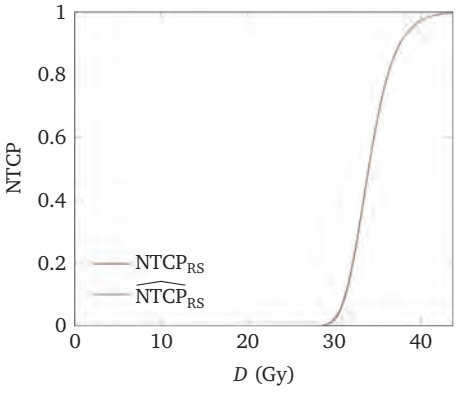

(c) $\mathrm{NTCP}_{\mathrm{RS}}(d)$ (red) and the approximation $\widehat{\mathrm{NTCP}}_{\mathrm{RS}}(d)$ (blue) using $Y_d = \{0, 28, 30, 32, 34, 36, 50\}$.

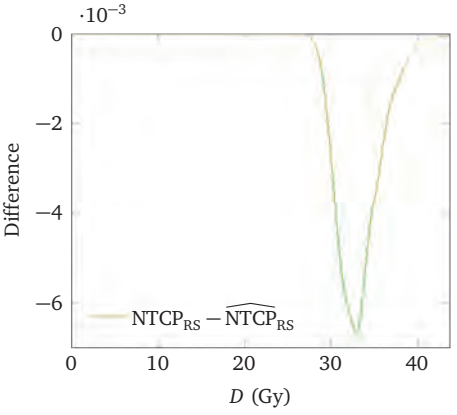

(d) Difference $\mathrm{NTCP}_{\mathrm{RS}}(d) - \widehat{\mathrm{NTCP}}_{\mathrm{RS}}(d)$ using $Y_d = \{0, 28, 30, 32, 34, 36, 50\}$.

Figure 4.D.2: Comparison of relative seriality function $\mathrm{NTCP}_{\mathrm{RS}}(\boldsymbol{d})$ and approximation $\widehat{\mathrm{NTCP}}_{\mathrm{RS}}(\boldsymbol{d})$, with $\alpha = 0.3$, $\alpha/\beta = 3$, $N = 30$, $N_0 = 10^6$ and $s = 0.2$. For a given value of d (horizontal axis), dose vector $\boldsymbol{d}$ is scaled by c such that $\frac{1}{n}\sum_1^n c d_i = d$.

4.E Proofs

4.E.1 Proof Lemma 4.11

We can rewrite (4.C.1) to

$$\mathrm{SF}_{\mathrm{LQ}}(d_i) = \exp\Big\{-ad_i^2 - bd_i - c\Big\},$$

with parameters

$$\begin{aligned} a &= \frac{\alpha}{(\alpha/\beta)N} \ (>0), \\ b &= \alpha\Big(1 + \frac{2L}{(\alpha/\beta)N}\Big) \ (>0), \\ c &= \alpha L\Big(1 + \frac{L}{(\alpha/\beta)N}\Big) \ (>0). \end{aligned}$$

It is straightforward to show that this implies $b^2 \geq 2a$, a result which will be used later on. Define the function $f : \mathbb{R}_+ \mapsto (0,1]$ as

$$f(x) := \exp\big\{-ax^2 - bx\big\}.$$

Parameters a and b are chosen such that function $f(x)$ is convex for all $x \geq 0$. Note that $\mathrm{SF}(d_i) = f(d_i - L)\exp(-c)$. Therefore, we can restrict to function $f(x)$. Specifically, we will find parameters $p < 0, q > 0$ and $r < 0$ such that

$$\phi(x) = \max\{0, px + q\}\exp\{rx\}, \tag{4.E.1}$$

satisfies for $y = \bar{d}_i - L$ the conditions

$$\phi(y) = f(y), \tag{4.E.2a}$$
$$\phi'(y) = f'(y), \tag{4.E.2b}$$
$$\phi(x) \leq f(x), \quad \forall x \geq 0. \tag{4.E.2c}$$

First, we note that $f'(y) = (-2ay - b)f(y)$. If $y < \frac{q}{r}$, conditions (4.E.2a) and (4.E.2b) reduce to

$$(py + q)\exp\{ry\} = f(y), \tag{4.E.3a}$$
$$\big(p + (py + q)r\big)\exp\{ry\} = (-2ay - b)f(y). \tag{4.E.3b}$$

Rewriting (4.E.3a) in terms of $py + q$ and plugging this in (4.E.3b) yields:

$$p = -\exp\{-ry\}f(y)(r + 2ay + b). \tag{4.E.4}$$

Condition $p < 0$ holds if $r > -2ay - b$. Rewriting (4.E.3a) in terms of $\exp\{ry\}$ and plugging this in (4.E.3b) yields:

$$p = \frac{-q(r + 2ay + b)}{1 + y(r + 2ay + b)}. \tag{4.E.5}$$

Equating (4.E.4) and (4.E.5) allows us to derive an expression for q in terms of the unknown parameter r:

$$q = \exp\{-ry\} f(y)(1 + y(r + 2ay + b)). \tag{4.E.6}$$

Clearly, if $p < 0$ then $q > 0$. Also note that $q/p = y + (r + 2ay + b)^{-1}$, so $y < q/p$ if $r > -2ay - b$. Hence, it holds that $\phi(y) > 0$, which should indeed hold because $f(x) > 0$ for all $x \geq 0$. Plugging (4.E.4) and (4.E.6) in (4.E.1) results in

$$\phi(x) = \max\Big\{0, 1 + (x - y)(-r - 2ay - b)\Big\} f(y) \exp\big\{r(x - y)\big\}.$$

It remains to find a $r \in (-2ay - b, 0)$ such that

$$\max\Big\{0, 1 + (x - y)(-r - 2ay - b)\Big\} f(y) \exp\big\{r(x - y)\big\} \leq f(x), \quad \forall x \geq 0. \tag{4.E.7}$$

First, we note that we need to consider only the case where $1 + (x - y)(-r - 2ay - b) > 0$, otherwise the constraint is clearly satisfied. Define $\kappa := r + 2ay + b$, so $\kappa \in (0, 2ay + b)$. Plugging in the definition of κ and removing the $\max\{0, \cdot\}$ operator, (4.E.7) reduces to

$$(1 - \kappa(x - y)) \leq \exp\{-\kappa(x - y) - a(x - y)^2\}, \quad \forall x \geq 0.$$

Define

$$H(x) = \big(1 - \kappa(x - y)\big) - \exp\Big\{-\kappa(x - y) - a(x - y)^2\Big\}, \quad x \geq 0.$$

We must find an expression for $\kappa \in (0, 2ay + b)$ such that

$$H(x) \leq 0, \ \forall x \geq 0. \tag{4.E.8}$$

We make use of the following result:

Lemma 4.13. *Inequality* (4.E.8) *holds if and only if* $\kappa \geq \sqrt{2a}$ *and* $H(0) \leq 0$.

Proof. See Appendix 4.E.2. □

Denote $h(\kappa) = (1 + \kappa y) - \exp\{\kappa y - ay^2\}$, then condition $H(0) \leq 0$ is equivalent to $h(\kappa) \leq 0$. The best lower bound is found by picking $\kappa \in [\sqrt{2a}, 2ay + b)$ such that $h(\kappa) = 0$, if feasible. Note that the interval is nonempty because $b^2 \geq 2a$ and we consider only $y > 0$.

Function $h(\kappa)$ is concave in κ with maximizer $\kappa = ay$ and a positive value at $\kappa = 0$. We check the signs at the bounds of the intervals. The lower bound $\kappa = \sqrt{2a}$ satisfies $h(\sqrt{2a}) \geq 0$ if $\sqrt{2a} \leq ay$, because both $h(0)$ and $h(ay)$ are larger than zero. If $\sqrt{2a} > ay$, the inequality $h(\sqrt{2a}) \geq 0$ can be shown to hold by computing the first and second derivative w.r.t. y. For the upper bound, $h(2ay + b) < 0$ reduces to

$$\exp\{ay^2 + by\} > 2ay^2 + by + 1,$$

which can be shown to hold via the 2nd order Taylor series expansion of the LHS, and making use of the fact that $b^2 \geq 2a$ and $y > 0$.

Thus, a positive solution to $h(\kappa) = 0$ satisfies $\kappa \in [\sqrt{2a}, 2ay + b)$. To find the solution we make use of the substitution $\eta = -\kappa y - 1$, so it must hold that $\eta \in \big(-2ay^2 - by - 1, -\sqrt{2a}y - 1\big]$. We obtain:

$$\begin{aligned} &-\eta = \exp\{-\eta - 1 - ay^2\}, \\ \Leftrightarrow\ &\eta \exp\{\eta\} = -\exp\{-1 - ay^2\}, \\ \Leftrightarrow\ &\eta = W\Big(-\exp\{-1 - ay^2\}\Big), \end{aligned}$$

where W is the Lambert W function, see, e.g., Corless et al. (1996). First, we note that $-\exp\{-1 - ay^2\} \in (-\frac{1}{e}, 0)$ for $y > 0$. Hence, both branches W_0 and W_{-1} are defined on the input argument. We seek a solution $\eta \leq -\sqrt{2a}y - 1$ which restricts us to the branch W_{-1} with range $(-\infty, -1]$.

Because $\eta = -\kappa y - 1$ and $r = \kappa - 2ay - b$ we obtain the following expression for the original parameters p, q and r:

$$\begin{aligned} p^* &= -\exp\{-r^* y\} f(y)(r^* + 2ay + b), \\ q^* &= \exp\{-r^* y\} f(y)(1 + y(r^* + 2ay + b)), \\ r^* &= \frac{1}{y}\Big(-1 - W_{-1}\Big(-\exp\{-1 - ay^2\}\Big)\Big) - 2ay - b. \end{aligned}$$

Finally, with $d_i = x + L$ and $\bar{d}_i = y + L$, we obtain as lower bound to $\mathrm{SF}_{\mathrm{LQ}}(d_i)$:

$$\begin{aligned} \widehat{\mathrm{SF}}_{\mathrm{LQ}}(d_i, \bar{d}_i) &= \phi(d_i - L)\exp(-c) \\ &= \max\{0, p^*(d_i - L) + q^*\}\exp\{r^*(d_i - L) - c\} \\ &= \max\{0, a_1(\bar{d}_i)d_i + a_2(\bar{d}_i)\}\exp\{a_3(\bar{d}_i)d_i + a_4(\bar{d}_i)\}, \end{aligned}$$

with $a_1(\bar{d}_i) = p^*$ (< 0), $a_2(\bar{d}_i) = q^* - p^* L$ (> 0), $a_3(\bar{d}_i) = r^*$ (< 0), $a_4(\bar{d}_i) = -r^* L - c$. This concludes the proof.

4.E.2 Proof Lemma 4.13

First, we show that if $\kappa < \sqrt{2a}$ then (4.E.8) cannot hold. Afterwards, we show that function $H(x)$ is decreasing in x if $x \geq y$ and quasiconvex in x on $[0, y]$. We make use of the following:

$$H'(x) = -\kappa - \exp\left\{-\kappa(x-y) - a(x-y)^2\right\}(-\kappa - 2a(x-y)), \tag{4.E.9a}$$
$$H''(x) = -\exp\left\{-\kappa(x-y) - a(x-y)^2\right\}\left(4a^2(x-y)^2 + 4\kappa a(x-y) + \kappa^2 - 2a\right). \tag{4.E.9b}$$

1. At $x = y$ we have $H(y) = 0$, $H'(y) = 0$ and $H''(y) = 2a - \kappa^2$. Hence, if $\kappa < \sqrt{2a}$ we have $H(y+\epsilon) > 0$ for sufficiently small $\epsilon > 0$. Therefore, condition (4.E.8) does not hold if $\kappa < \sqrt{2a}$. In the remainder of the proof we assume $\kappa \geq \sqrt{2a}$.

2. Second, let $x \geq y$. We show that $H(x)$ is decreasing. From (4.E.9a) we find that $H'(y) = 0$. Because $\kappa \geq \sqrt{2a}$, the second derivative (4.E.9b) is nonpositive for all $x \geq y$. Hence, $H(x)$ is decreasing in x for $x \geq y$.

3. Third, let $x \in [0, y]$. We show that $H(x)$ is quasiconvex. Because $H(x)$ is twice differentiable on $[0, y]$, it is quasiconvex if for all interior points with zero slope the second derivative is nonnegative, i.e., for all $x \in (0, y)$ it holds that $H'(x) = 0 \Rightarrow H''(x) \geq 0$ (Boyd and Vandenberghe, 2004). The condition $H''(x) \geq 0$ holds if and only if

   $$x \leq y + \frac{\sqrt{2a} - \kappa}{2a}.$$

   Hence, it remains to show there is no $x \in \left(y + \frac{\sqrt{2a}-\kappa}{2a}, y\right)$ with $H'(x) = 0$. First, we note that

   $$H'\left(y + \frac{\sqrt{2a} - \kappa}{2a}\right) = -\kappa + \sqrt{2a}\exp\left\{\frac{\kappa^2}{4a} - \frac{1}{2}\right\}.$$

   Hence, $H'(y + \frac{\sqrt{2a}-\kappa}{2a}) > 0$ is equivalent to

   $$\exp\left\{\frac{\kappa^2}{2a} - 1\right\} > \frac{\kappa^2}{2a},$$

   which can be shown to hold via the 1st order Taylor series expansion of the LHS. Moreover, at $x = y$ it holds that $H(y) = 0$ and $H''(y) < 0$. Hence, $x = y$ is a local (boundary) maximum. Thus, $H(x)$ has a positive derivative at $x = y + \frac{\sqrt{2a}-\kappa}{2a}$, which diminishes on the entire interval $[y + \frac{\sqrt{2a}-\kappa}{2a}, y]$, whilst $x = y$ is a boundary maximum. Thus, function $H(x)$ must be strictly increasing on the interior of the interval, and there is no x in the interior such that $H'(x) = 0$. Therefore, $H(x)$ is quasiconvex on $[0, y]$.

On the interval $[0, y]$ function $H(x)$ is maximized either at $x = 0$ or $x = y$ due to quasiconvexity. On the interval $[y, +\infty)$ the function $H(x)$ is maximized at $x = y$ because it is decreasing. By construction, it holds that $H(y) = 0$. Hence, condition (4.E.8) holds if and only if $H(0) \leq 0$.

CHAPTER 5

Pareto adjustable robust optimality via a Fourier-Motzkin elimination lens

5.1 Introduction

Robust optimization (RO) is a widespread methodology for modeling decision-making problems under uncertainty that seeks to optimize worst-case performance (Bertsimas et al., 2011; Gabrel et al., 2014; Gorissen et al., 2015). In practice, RO problems usually admit multiple worst-case optimal solutions, the performance of which may differ substantially under non-worst-case uncertainty scenarios. Consequently, the choice of an optimal solution often has material impact on performance under real-world implementations. This important consideration, which was first brought forth by Iancu and Trichakis (2014), has been successfully tackled for static, single-stage (linear) RO problems. For the increasingly popular and broad class of dynamic, multi-stage adjustable robust optimization (ARO) problems (Ben-Tal et al., 2004), however, there is no successful approach for choosing an optimal solution, and the purpose of this chapter is to bridge this gap.

In particular, for static RO problems, Iancu and Trichakis (2014) proposed the choice of so-called Pareto robustly optimal (PRO) solutions. In general, PRO solutions unarguably dominate non-PRO solutions, because, by definition, the former guarantee that there do not exist other worst-case optimal solutions that perform at least as good as the current solution for all scenarios in the uncertainty set, while performing strictly better for at least one scenario.

Going beyond static RO problems, it is well understood that the choice of an optimal solution remains crucial for the broader class of multi-stage ARO problems. Similar to RO solutions, by following a worst-case philosophy and not considering performance across the entire spectrum of possible scenarios, ARO optimal solutions could lead to substantial performance losses. For example, see the work by De Ruiter et al. (2016),

who numerically demonstrate existence of multiple worst-case optimal solutions for the classical multi-stage inventory-production model that was considered in Ben-Tal et al. (2004), and find them to differ considerably from each other in their non-worst-case performance.

For ARO problems, however, a solution approach that unarguably chooses "good solutions," similar to PRO solutions for static RO problems, has proved to be elusive thus far. Extant approaches have all attempted to simply apply the concept of PRO to ARO problems. Specifically, they advocate restricting attention to adjustable variables that depend affinely on the uncertain parameters; commonly referred to as linear decision rules (LDRs). Restricting to LDRs reduces the problem to static RO, and enables the search for associated PRO solutions (Iancu and Trichakis, 2014; Bertsimas et al., 2015; De Ruiter et al., 2016). As we shall show, however, this indirect application of the PRO concept fails to produce solutions that cannot be dominated.

In this chapter, we introduce and study the concept of *Pareto adjustable robustly optimal (PARO)* solutions for linear ARO problems. Similar to PRO solutions for static RO problems, PARO solutions yield worst-case optimal performance and are not dominated by any other such solutions in non-worst-case scenarios. In other words, PARO solutions unarguably dominate non-PARO solutions, leading to improved performance in non-worst-case scenarios, while maintaining worst-case optimality. From a practical standpoint, this means that implementing PARO solutions can only yield performance benefits, without any associated drawbacks.

To introduce the PARO concept and highlight its practical importance, we provide an illustrative toy example. The example also serves two additional important purposes. First, it enables us to show in a simple setting how PARO solutions can dominate PRO solutions, as remarked above. Second, the example motivates the need for new analysis techniques for studying PARO.

Example 5.1. In treatment planning for radiation therapy, the goal is to deliver a curative amount of dose to the target volume (tumor tissue), while minimizing the dose to healthy tissues. Consider a simplified case with two target subvolumes. For subvolume $i \in \{1,2\}$, the required dose level d_i depends on the radiation sensitivity of the tissue, which is unknown. Assume that, prior to treatment, the doses lie in

$$U = \{(d_1, d_2) \mid 50 \leq d_i \leq 60,\ i = 1,2\}.$$

Mid-treatment, the required doses are ascertained via biomarker measurements.

Treatment doses are administered in two stages. The dose administered in the first stage, denoted by x, needs to be decided prior to treatment. The dose administered in the second stage, denoted by y, can be decided after the required doses have been ascertained, i.e., it can

be adapted to uncertainty revelation. Both treatment doses are delivered homogeneously over both volumes in each stage. Dose in each stage is limited to the interval $[20, 40]$. The total dose administered is $x + y$, and the healthy tissue receives a fraction $\delta > 0$ of it. The stage-1 dose x, and a decision rule $y(\cdot)$ for the adjustable stage-2 dose can be chosen by solving:

$$\min_{x, y(\cdot)} \max_{(d_1,d_2)\in U} \delta(x + y(d_1, d_2)) \tag{5.1a}$$

$$\text{s.t. } x + y(d_1, d_2) \geq d_1, \quad \forall (d_1, d_2) \in U, \tag{5.1b}$$

$$x + y(d_1, d_2) \geq d_2, \quad \forall (d_1, d_2) \in U, \tag{5.1c}$$

$$20 \leq x \leq 40, \tag{5.1d}$$

$$20 \leq y(d_1, d_2) \leq 40, \quad \forall (d_1, d_2) \in U. \tag{5.1e}$$

Problem (5.1) is an ARO problem with constraintwise uncertainty, for which static decision rules are worst-case optimal (Ben-Tal et al., 2004). Plugging in $y(d_1, d_2) = \hat{y}$ and solving the resulting static RO model yields a worst-case optimal objective value of 60δ, achieved by all $(x, \hat{y})$ such that $x + \hat{y} = 60$. For any such solution, the objective value remains 60δ in not only the worst-case scenario but in all scenarios. Hence, all these solutions are PRO, according to the definition of Iancu and Trichakis (2014). Consequently, the stage-1 decisions that are PRO lie in the set:

$$X^{\text{PRO}} = \{x \mid 20 \leq x \leq 40\}.$$

Consider now the decision rule $y^*(d_1, d_2) = \max\{20, d_1 - x, d_2 - x\}$, which is feasible for all feasible x. Furthermore, this rule minimizes the objective for any fixed x, d_1 and d_2. Plugging this in gives

$$\min_{20\leq x\leq 40} \max_{(d_1,d_2)\in U} \delta \max\{20 + x, d_1, d_2\}.$$

For given (d_1, d_2) the objective value is at least $\delta \max\{d_1, d_2\}$, and this is achieved by all $x \leq 30$. Thus, it should be preferable to implement one of these solutions for the stage-1 decision. In fact, these solutions, which we call PARO, cannot be dominated by other solutions. Notably, the set of PARO solutions

$$X^{\text{PARO}} = \{x \mid 20 \leq x \leq 30\},$$

is a strict subset of X^{PRO}. This implies that PARO solutions could dominate PRO solutions that are non-PARO. To exemplify, compare the following three solutions: (i) PARO solution $x^* = 25$ with optimal decision rule $y^*(d_1, d_2)$, (ii) PRO (non-PARO) solution $\hat{x}^* = 25$ with optimal decision rule $y^*(d_1, d_2)$, (iii) PRO solution $\hat{x}^* = 25$ with static decision rule $\hat{y} = 35$. Table 5.1 shows the performance for three scenarios. For worst-case scenario $(60, 60)$ all solutions perform equal. For scenario $(50, 55)$ the solution (iii) is outperformed by the other two solutions, for scenario $(50, 50)$ both solutions (ii) and (iii)) are outperformed by PARO solution (i). There is no scenario where $\hat{x}$ results in a strictly better objective value than x^*, irrespective of the used decision rule. Thus, the PRO solution $\hat{x}$ is dominated by the PARO solution x^*. ▲

Scenario (d_1, d_2)	(x^*, y^*)	$(\hat{x}, y^*)$	$(\hat{x}, \hat{y})$
$(60, 60)$	60δ	60δ	60δ
$(50, 55)$	55δ	55δ	60δ
$(50, 50)$	50δ	55δ	60δ

Table 5.1: Differences in objective values for PARO and PRO solutions for Example 5.1.

Besides showing that PRO solutions could be dominated in ARO problems, Example 5.1 also provides intuition into how. In particular, what unlocks extra performance in ARO problems is the application of decision rules that are not merely worst-case optimal, but rather "Pareto optimal," i.e., they optimize performance over non-worst-case scenarios as well. Note, however, that although for worst-case optimality linear decision rules might suffice under special circumstances, for Pareto optimality nonlinear rules appear to be more often necessary, as illustrated by the example.

The application of nonlinear decision rules to study PARO solutions invalidates the techniques used in the analysis of Pareto efficiency in RO in the extant literature, which is solely focused on linear formulations. In other words, analysis of Pareto efficiency in ARO calls for a new line of attack, which brings us to another contribution we make. Specifically, to study PARO solutions, we rely heavily on Fourier-Motzkin elimination (FME) as a proof technique. Through the lens of FME we consider optimality of decision rule structures, which then enables us to study PARO. Furthermore, we illustrate how this proof technique can be applied in ARO more generally, by providing more general and more insightful proofs of known results (not related to Pareto efficiency).

Findings and contributions

Before we begin our analysis, we summarize the findings and the contributions of this chapter. The treatment presented is restricted to two-stage ARO models that are linear in both decision variables and uncertain parameters.

1. *Concept of PARO solutions.* In the context of linear ARO problems, we introduce the concept of Pareto Adjustable Robustly Optimal (PARO) solutions. PARO solutions have the property that no other solution and associated adjustable decision rule exist that dominate them, i.e., perform at least as good under any scenario, and perform strictly better under at least some scenario. As Example 5.1 above has already shown, in the context of ARO problems, PARO solutions can dominate other Pareto optimal solution concepts already proposed in the literature

(Iancu and Trichakis, 2014). In practice, PARO solutions can only yield performance benefits compared with non-PARO solutions, as the latter lead to efficiency losses.

2. *Properties of PARO solutions.* We derive several properties of PARO solutions. Among them, we show that first-stage PARO solutions exist for any two-stage ARO problem with a compact feasible region. Furthermore, we prove that for any two-stage ARO problem there exists a piecewise linear (PWL) decision rule that is PARO. To arrive at these results, our analysis relies on FME.

3. *Finding PARO solutions and their practical value.* We present several approaches to find and/or approximate PARO solutions in practice, amongst others using techniques based on FME. We also conduct a numerical study for a facility location example. The results reveal that (approximate) PARO solutions can yield substantially better performance in non-worst-case scenarios than worst-case optimal and PRO solutions, thus demonstrating the practical value of the proposed methodology.

4. *FME as a proof technique for PARO.* Zhen et al. (2018) introduce FME as both a solution and proof technique for ARO. We apply and extend the latter idea, and use FME to prove worst-case and Pareto optimality of various decision rule structures. We extend and/or generalize known results in ARO, not related to Pareto optimality, and provide more insightful proofs; for example, one that uses FME to establish the results by Bertsimas and Goyal (2012) and Zhen et al. (2018) on optimality of LDRs under simplex uncertainty sets.

Finally, we note that PARO solutions have already been discussed for a nonlinear ARO problem arising in radiation therapy treatment planning in Chapter 2, but no general treatment of the topic was included. In this chapter we formalize the concept, derive properties, such as existence of PARO solutions, and also discuss constructive approaches towards finding them. With regards to FME, Zhen et al. (2018) were the first to recognize its applicability to linear ARO problems, owing to its ability to eliminate adjustable variables. They use FME as both a solution and proof technique; for the latter the main obstacle is the exponential increase in number of constraints after variable elimination. In the current chapter, we apply and extend the ideas of Zhen et al. (2018), and use FME as a proof technique. Through the lens of FME we first consider (worst-case) optimality of decision rule structures, and provide more general and more insightful proofs of known results. Subsequently, we investigate Pareto opti-

mality using FME and present numerical results which demonstrate the value of PARO solutions.

Notation and organization

Boldface characters represent matrices and vectors. All vectors are column vectors and the vector $\boldsymbol{a}_i$ is the i-th row of matrix $\boldsymbol{A}$. The space of all measurable functions from $\mathbb{R}^n$ to $\mathbb{R}^m$ that are bounded on compact sets is denoted by $\mathcal{R}^{n,m}$. The vectors $\boldsymbol{e}_i$, $\mathbf{1}$ and $\mathbf{0}$ are the standard unit basis vector, the vector of all-ones and the vector of all-zeros, respectively. Matrix $\boldsymbol{I}$ is the identity matrix. The relative interior of a set S is denoted by $\text{ri}(S)$; its set of extreme points is denoted by $\text{ext}(S)$.

The chapter is organized as follows. First, Section 5.2 introduces the ARO setting and the notion of PARO. Section 5.3 introduces FME and uses it to establish (worst-case) optimality of decision rule structures. Section 5.4 investigates the existence of PARO solutions, and Section 5.5 presents some practical approaches for the construction of PARO solutions. In Section 5.6 we present the results of our numerical experiments.

5.2 Pareto optimality in (adjustable) robust optimization

We first generalize the definition of PRO of Iancu and Trichakis (2014) to nonlinear static RO problems. The reason for this is that there turns out to be a relation between Pareto efficiency for nonlinear static RO problems and linear ARO problems. Let $\boldsymbol{x} \in \mathcal{X} \subseteq \mathbb{R}^{n_x}$ denote the decision variables and let $\boldsymbol{z} \in U \subseteq \mathbb{R}^L$ denote the uncertain parameters. Let $f : \mathbb{R}^{n_x} \times \mathbb{R}^L \mapsto \mathbb{R}$ and consider the static RO problem

$$\min_{\boldsymbol{x}\in\mathcal{X}} \max_{\boldsymbol{z}\in U} f(\boldsymbol{x}, \boldsymbol{z}). \tag{5.2}$$

Let $\mathcal{X}^{\text{RO}}$ denote the set of robustly optimal (i.e., worst-case optimal) solutions. A robustly optimal solution $\boldsymbol{x}$ is PRO if there does not exist another robustly optimal solution $\bar{\boldsymbol{x}}$ that performs at least as good as $\boldsymbol{x}$ for all scenarios in the uncertainty set, while performing strictly better for at least one scenario. If such a solution $\bar{\boldsymbol{x}}$ does exist, it is said to *dominate* $\boldsymbol{x}$. In practice, solution $\bar{\boldsymbol{x}}$ will always be preferred over $\boldsymbol{x}$. If all uncertainty in the objective is moved to constraints using an epigraph formulation, Pareto robust optimality may also be defined in terms of slack variables (Iancu and Trichakis, 2014, Section 4.1), but we do not use that definition here. We use the following formal definition:

Definition 5.2 (Pareto robustly optimal)**.** A solution $\boldsymbol{x} \in \mathcal{X}^{\mathrm{RO}}$ is PRO to (5.2) if there does not exist another $\bar{\boldsymbol{x}} \in \mathcal{X}^{\mathrm{RO}}$ such that

$$f(\bar{\boldsymbol{x}}, \boldsymbol{z}) \leq f(\boldsymbol{x}, \boldsymbol{z}), \quad \forall \boldsymbol{z} \in U,$$
$$f(\bar{\boldsymbol{x}}, \bar{\boldsymbol{z}}) < f(\boldsymbol{x}, \bar{\boldsymbol{z}}), \quad \text{for some } \bar{\boldsymbol{z}} \in U. \qquad \blacksquare$$

We aim to extend the concept of PRO to ARO problems. In particular, we consider the following adjustable linear optimization problem:

$$\min_{\boldsymbol{x}, \boldsymbol{y}(\cdot)} \max_{\boldsymbol{z} \in U} \boldsymbol{c}(\boldsymbol{z})^\top \boldsymbol{x} + \boldsymbol{d}^\top \boldsymbol{y}(\boldsymbol{z}), \tag{5.3a}$$
$$\text{s.t. } \boldsymbol{A}(\boldsymbol{z})\boldsymbol{x} + \boldsymbol{B}\boldsymbol{y}(\boldsymbol{z}) \leq \boldsymbol{r}(\boldsymbol{z}), \quad \forall \boldsymbol{z} \in U, \tag{5.3b}$$

where $\boldsymbol{z} \in U \subseteq \mathbb{R}^L$ is an uncertain parameter, with U a compact, convex uncertainty set with nonempty relative interior. Variables $\boldsymbol{x} \in \mathbb{R}^{n_x}$ are the stage-1 (*here-and-now*) decisions. Usually we will assume $\boldsymbol{x}$ to be continuous variables, but we emphasize that all results in the chapter also hold if (part of) $\boldsymbol{x}$ is restricted to be integer-valued. Variables $\boldsymbol{y} \in \mathcal{R}^{L, n_y}$ are also continuous and capture the stage-2 (*wait-and-see*) decisions, i.e., they are functions of $\boldsymbol{z}$. The matrix $\boldsymbol{B} \in \mathbb{R}^{m \times n_y}$ and vector $\boldsymbol{d} \in \mathbb{R}^{n_y}$ are assumed to be constant (fixed recourse), and $\boldsymbol{A}(\boldsymbol{z})$, $\boldsymbol{r}(\boldsymbol{z})$ and $\boldsymbol{c}(\boldsymbol{z})$ depend affinely on $\boldsymbol{z}$:

$$\boldsymbol{A}(\boldsymbol{z}) := \boldsymbol{A}^0 + \sum_{k=1}^{L} \boldsymbol{A}^k z_k, \quad \boldsymbol{r}(\boldsymbol{z}) := \boldsymbol{r}^0 + \sum_{k=1}^{L} \boldsymbol{r}^k z_k, \quad \boldsymbol{c}(\boldsymbol{z}) := \boldsymbol{c}^0 + \sum_{k=1}^{L} \boldsymbol{c}^k z_k,$$

with $\boldsymbol{A}^0, \ldots, \boldsymbol{A}^L \in \mathbb{R}^{m \times n_x}$, $\boldsymbol{r}^0, \ldots, \boldsymbol{r}^L \in \mathbb{R}^m$ and $\boldsymbol{c}^0, \ldots, \boldsymbol{c}^L \in \mathbb{R}^{n_x}$. Uncertainty in the objective (5.3a) can be moved to the constraint using an epigraph formulation. Nevertheless, it is explicitly stated in the objective to facilitate a convenient definition of PARO. Let OPT denote the optimal (worst-case) objective value of (5.3). We continue by stating several assumptions and definitions regarding adjustable robust feasibility and optimality.

Definition 5.3 (Adjustable robustly feasible)**.** A pair $(\boldsymbol{x}, \boldsymbol{y}(\cdot))$ is *adjustable robustly feasible* (ARF) to (5.3) if $\boldsymbol{A}(\boldsymbol{z})\boldsymbol{x} + \boldsymbol{B}\boldsymbol{y}(\boldsymbol{z}) \leq \boldsymbol{r}(\boldsymbol{z}), \quad \forall \boldsymbol{z} \in U.$ $\blacksquare$

Sometimes it is useful to consider properties of the first- and second-stage decisions separately. Therefore, we also define adjustable robust feasibility for stage-1 and stage-2 decisions individually.

Definition 5.4 (Adjustable robustly feasible $\boldsymbol{x}$ and/or $\boldsymbol{y}(\cdot)$)**.**

(i) A stage-1 decision $\boldsymbol{x}$ is ARF to (5.3) if there exists a $\boldsymbol{y}(\cdot)$ such that $(\boldsymbol{x}, \boldsymbol{y}(\cdot))$ is ARF to (5.3).

(ii) A stage-2 decision $\boldsymbol{y}(\cdot)$ is ARF to (5.3) if there exists a $\boldsymbol{x}$ such that $(\boldsymbol{x}, \boldsymbol{y}(\cdot))$ is ARF to (5.3). ■

The set of all ARF solutions $\boldsymbol{x}$ is given by

$$\mathcal{X} = \{\boldsymbol{x} \in \mathbb{R}^{n_x} \mid \exists \boldsymbol{y} \in \mathcal{R}^{L,n_y} : \boldsymbol{A}(\boldsymbol{z})\boldsymbol{x} + \boldsymbol{B}\boldsymbol{y}(\boldsymbol{z}) \leq \boldsymbol{r}(\boldsymbol{z}), \quad \forall \boldsymbol{z} \in U\}.$$

We assume set $\mathcal{X}$ is nonempty, i.e., there exists an $\boldsymbol{x}$ that is ARF, and we assume (5.3) has a finite optimal objective value, i.e., OPT is a finite number. After feasibility, the natural next step is to formally define optimality.

Definition 5.5 (Adjustable robustly optimal)**.** A pair $(\boldsymbol{x}, \boldsymbol{y}(\cdot))$ is *adjustable robustly optimal* (ARO)[1] to (5.3) if it is ARF and $\boldsymbol{c}(\boldsymbol{z})^\top \boldsymbol{x} + \boldsymbol{d}^\top \boldsymbol{y}(\boldsymbol{z}) \leq \text{OPT}, \quad \forall \boldsymbol{z} \in U$. ■

We also define adjustable robust optimality for stage-1 and stage-2 decisions individually.

Definition 5.6 (Adjustable robustly optimal $\boldsymbol{x}$ and/or $\boldsymbol{y}(\cdot)$)**.**

(i) A stage-1 decision $\boldsymbol{x}$ is ARO to (5.3) if there exists a $\boldsymbol{y}(\cdot)$ such that $(\boldsymbol{x}, \boldsymbol{y}(\cdot))$ is ARO to (5.3).
(ii) A stage-2 decision $\boldsymbol{y}(\cdot)$ is ARO to (5.3) if there exists a $\boldsymbol{x}$ such that $(\boldsymbol{x}, \boldsymbol{y}(\cdot))$ is ARO to (5.3). ■

We are now in position to define Pareto adjustable robust optimality for two-stage ARO problems.

Definition 5.7 (Pareto adjustable robustly optimal)**.** A pair $(\boldsymbol{x}, \boldsymbol{y}(\cdot))$ is *Pareto adjustable robustly optimal* (PARO) to (5.3) if it is ARO and there does not exist a pair $(\bar{\boldsymbol{x}}, \bar{\boldsymbol{y}}(\cdot))$ that is ARO and

$$\begin{aligned} &\boldsymbol{c}(\boldsymbol{z})^\top \bar{\boldsymbol{x}} + \boldsymbol{d}^\top \bar{\boldsymbol{y}}(\boldsymbol{z}) \leq \boldsymbol{c}(\boldsymbol{z})^\top \boldsymbol{x} + \boldsymbol{d}^\top \boldsymbol{y}(\boldsymbol{z}), \quad \forall \boldsymbol{z} \in U, \\ &\boldsymbol{c}(\bar{\boldsymbol{z}})^\top \bar{\boldsymbol{x}} + \boldsymbol{d}^\top \bar{\boldsymbol{y}}(\bar{\boldsymbol{z}}) < \boldsymbol{c}(\bar{\boldsymbol{z}})^\top \boldsymbol{x} + \boldsymbol{d}^\top \boldsymbol{y}(\bar{\boldsymbol{z}}), \quad \text{for some } \bar{\boldsymbol{z}} \in U. \end{aligned}$$ ■

As before, the definitions can be extended to stage-1 and stage-2 decisions individually.

Definition 5.8 (Pareto adjustable robustly optimal $\boldsymbol{x}$ and/or $\boldsymbol{y}(\cdot)$)**.**

[1] To ease exposition, we overload and reuse certain acronyms, such as ARO for "adjustable robust optimization" and "adjustable robustly optimal", as long as they can be readily disambiguated from the context.

(i) A stage-1 decision $\boldsymbol{x}$ is PARO to (5.3) if there exists a $\boldsymbol{y}(\cdot)$ such that $(\boldsymbol{x}, \boldsymbol{y}(\cdot))$ is PARO to (5.3).
(ii) A stage-2 decision $\boldsymbol{y}(\cdot)$ is PARO to (5.3) if there exists a $\boldsymbol{x}$ such that $(\boldsymbol{x}, \boldsymbol{y}(\cdot))$ is PARO to (5.3). ■

Our main interest is in Definition 5.8(i). The reason for this is that the here-and-now decision $\boldsymbol{x}$ is usually the only one that the decision maker has to commit to. In contrast, instead of using decision rule $\boldsymbol{y}(\cdot)$, one can often resort to re-solving the optimization problem for the second stage once the value of the uncertain parameter has been revealed. This is known as the folding horizon approach, and it is applicable as long as there is time to re-solve between observing $\boldsymbol{z}$ and having to implement $\boldsymbol{y}(\boldsymbol{z})$. There is no such alternative for $\boldsymbol{x}$, however, and different decisions in stage 1 may lead to different adaptation possibilities in stage 2.

Lastly, Pareto optimality can also be investigated for stage-2 decisions if the stage-1 decision $\boldsymbol{x}$ is fixed.

Definition 5.9 (Pareto adjustable robustly optimal extension $\boldsymbol{y}(\cdot)$)**.** A stage-2 decision $\boldsymbol{y}(\cdot)$ is a *PARO extension* to $\boldsymbol{x}$ for (5.3) if $(\boldsymbol{x}, \boldsymbol{y}(\cdot))$ is ARO to (5.3) and there does not exist another $\bar{\boldsymbol{y}}(\cdot)$ such that $(\boldsymbol{x}, \bar{\boldsymbol{y}}(\cdot))$ is ARO to (5.3) and

$$\begin{aligned} &\boldsymbol{c}(\boldsymbol{z})^\top \boldsymbol{x} + \boldsymbol{d}^\top \bar{\boldsymbol{y}}(\boldsymbol{z}) \leq \boldsymbol{c}(\boldsymbol{z})^\top \boldsymbol{x} + \boldsymbol{d}^\top \boldsymbol{y}(\boldsymbol{z}), \quad \forall \boldsymbol{z} \in U, \\ &\boldsymbol{c}(\bar{\boldsymbol{z}})^\top \boldsymbol{x} + \boldsymbol{d}^\top \bar{\boldsymbol{y}}(\bar{\boldsymbol{z}}) < \boldsymbol{c}(\bar{\boldsymbol{z}})^\top \boldsymbol{x} + \boldsymbol{d}^\top \boldsymbol{y}(\bar{\boldsymbol{z}}), \quad \text{for some } \bar{\boldsymbol{z}} \in U. \end{aligned}$$ ■

Figure 5.1 illustrates the PARO concept for a single uncertain parameter. Each graph represents the objective value of (5.3) for a given pair $(\boldsymbol{x}, \boldsymbol{y}(\boldsymbol{z}))$ as a function of uncertain parameter $\boldsymbol{z}$. The solution pair $(\hat{\boldsymbol{x}}, \hat{\boldsymbol{y}}(\boldsymbol{z}))$ (solid line) is dominated by $(\hat{\boldsymbol{x}}, \bar{\boldsymbol{y}}(\boldsymbol{z}))$ (solid-dotted line), which has the same here-and-now decision $\hat{\boldsymbol{x}}$ but a different decision rule. Thus, according to Definition 5.9, decision rule $\hat{\boldsymbol{y}}(\cdot)$ cannot be a PARO extension of $\hat{\boldsymbol{x}}$, but decision rule $\bar{\boldsymbol{y}}(\cdot)$ may be. Further, the graph of solution $(\boldsymbol{x}^*, \boldsymbol{y}^*(\boldsymbol{z}))$ is below the graphs of the other two solution pairs, so neither of those pairs can be PARO according to Definition 5.7. However, care must be exercised. It may be the case that there is yet another decision rule $\tilde{\boldsymbol{y}}(\boldsymbol{z})$ so that $(\hat{\boldsymbol{x}}, \tilde{\boldsymbol{y}}(\boldsymbol{z}))$ is not dominated by $(\boldsymbol{x}^*, \boldsymbol{y}^*(\boldsymbol{z}))$. Hence, we cannot conclude that $\hat{\boldsymbol{x}}$ is not PARO. Lastly, $(\boldsymbol{x}^*, \boldsymbol{y}^*(\boldsymbol{z}))$ can be PARO, but that cannot be concluded from the figure either.

We conclude this section by mentioning three ways that the PARO concept can be generalized and relaxed, although we do not consider these any further. First, Bertsimas et al. (2015) define Pareto optimal adaptive solutions for general (nonlinear) two-stage ARO problems, which for linear problems is equivalent to our definition of PARO. They subsequently define Pareto optimal affine adaptive solutions, which is

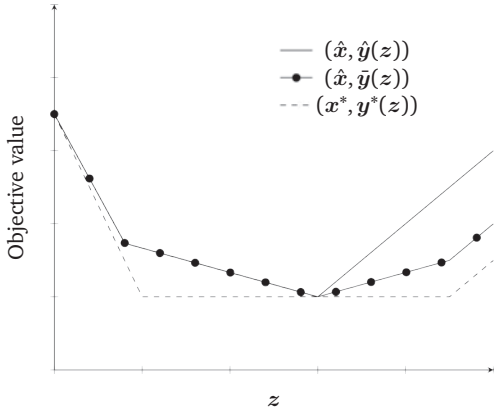

Figure 5.1: Illustration of PARO concept. Each graph represents the objective value of (5.3) for a given pair $(x, y(z))$ as a function of uncertain parameter z. Solution $(\hat{x}, \hat{y}(z))$ is dominated by $(\hat{x}, \bar{y}(z))$. Decision rule $\bar{y}(z)$ may be a PARO extension of $\hat{x}$, decision rule $\hat{y}(z)$ is not. Solution $(x^*, y^*(z))$ dominates both $(\hat{x}, \hat{y}(z))$ and $(\hat{x}, \bar{y}(z))$ and may be PARO. Solution $\hat{x}$ may also be a PARO stage-1 solution.

equivalent to the definition of PRO after using LDRs, and focus on finding the latter type of solutions. In their numerical studies, Iancu and Trichakis (2014) also consider two-stage problems and find PRO solutions after plugging in LDRs.

Secondly, we can also solely relax the requirement that the solution is ARO. For example, often LDRs do not guarantee an ARO solution but do exhibit good practical performance (Kuhn et al., 2009). Suppose these yield a worst-case objective value p ($>$ OPT). Then we can define p-PARO solutions as those solutions $(x, y(\cdot))$ that yield an objective value of at most p in each scenario, and are not dominated by another solution $(\bar{x}, \bar{y}(\cdot))$ that yields an objective value of at most p in each scenario.

Thirdly, PARO may also be defined in terms of slack variables, analogous to the extension of PRO to constraint slacks in Iancu and Trichakis (2014, Section 4.1). In that paper, a slack value vector is introduced that quantifies the relative importance of slack in each constraint. This scalarization allows the computation of the total slack value of a solution in any scenario. Subsequently PRO (and also PARO) can be defined on this total slack value instead of the objective value. This may be useful in applications where ARO is mainly used for maintaining feasibility, such as immunizing against uncertain renewable energy source output (Jabr, 2013) and adjusting to disturbances in railway timetabling (Polinder et al., 2019).

5.3 Optimality of decision rule structures via an FME lens

In this section, we introduce FME as a proof technique for ARO, and we analyze various decision rule structures. This FME lens enables us to prove that an ARF decision rule with the particular structure exists for *every* ARF $\boldsymbol{x}$, instead of solely proving it is optimal for an ARO $\boldsymbol{x}$. These results are crucial for one of our main results in Section 5.5. Moreover, the results in this section show that FME not only provides more general results, but also leads to more concise (and perhaps more intuitive) proofs to known results on optimal decision structures.

5.3.1 Eliminating adjustable variables using Fourier-Motzkin elimination

FME (Fourier, 1827; Motzkin, 1936) is an algorithm for solving systems of linear inequalities. We refer to Bertsimas and Tsitsiklis (1997) for an introduction to FME in linear optimization. Its usefulness in ARO is due to the fact that it can be used to eliminate adjustable variables, as proposed by Zhen et al. (2018). FME leads to an exponential increase in number of constraints. Zhen et al. (2018) introduce a redundant constraint identification scheme, which helps to reduce the number of redundant constraints, although the number of constraints remains exponential. Zhen et al. (2018) also propose to use FME to eliminate only part of the variables and using LDRs for remaining adjustable variables. Next to this, they use FME to prove (worst-case) optimality of PWL decision rules. Furthermore, they consider optimal decision rules for the adjustable variable in the dual problem: they prove (worst-case) optimality of LDRs in case of simplex uncertainty and (two-)piecewise linear decision rules in case of box uncertainty. Zhen and den Hertog (2018) use a combination of FME and ARO techniques to compute the maximum volume inscribed ellipsoid of a polytopic projection. The following example illustrates the use of FME to eliminate an adjustable variable.

Example 5.10. We use FME to eliminate adjustable variable y from (5.1) in Example 5.1. We move the uncertain objective to the constraints using an epigraph variable $t \in \mathbb{R}$, and rewrite the constraints to obtain:

$$\min_{x,t,y(d_1,d_2)} \quad t, \tag{5.4a}$$

$$\text{s.t.} \quad 20 \leq x \leq 40, \tag{5.4b}$$

$$y(d_1,d_2) \leq t/\delta - x, \quad \forall (d_1,d_2) \in U, \tag{5.4c}$$

$$d_1 - x \le y(d_1, d_2), \qquad \forall (d_1, d_2) \in U, \tag{5.4d}$$
$$d_2 - x \le y(d_1, d_2), \qquad \forall (d_1, d_2) \in U, \tag{5.4e}$$
$$20 \le y(d_1, d_2) \le 40, \qquad \forall (d_1, d_2) \in U. \tag{5.4f}$$

For fixed (d_1, d_2), Constraints (5.4c)-(5.4f) specify lower and/or upper bounds on y. By combining each pair of lower and upper bounds on y into a new constraint, we find the following problem in terms of (x, t):

$$\min_{x,t} \ t, \tag{5.5a}$$
$$\text{s.t. } 20 \le x \le 40, \tag{5.5b}$$
$$d_1 \le t/\delta, \ \ \forall (d_1, d_2) \in U, \tag{5.5c}$$
$$d_2 \le t/\delta, \ \ \forall (d_1, d_2) \in U, \tag{5.5d}$$
$$20 \le t/\delta - x, \ \ \forall (d_1, d_2) \in U, \tag{5.5e}$$
$$d_1 - x \le 40, \ \ \forall (d_1, d_2) \in U, \tag{5.5f}$$
$$d_2 - x \le 40, \ \ \forall (d_1, d_2) \in U, \tag{5.5g}$$

where we have removed the trivial new constraint $20 \le 40$. Any solution (x, t) sets the following bounds on y:

$$\max\{d_1 - x, d_2 - x, 20\} \le y(d_1, d_2) \le \min\{t/\delta - x, 40\}, \ \ \forall (d_1, d_2) \in U,$$

and any decision rule satisfying these inequalities is ARO to (5.1). Thus, two-stage problem (5.1) has been reduced to static linear RO problem (5.5). Auxiliary variable t can be eliminated, but this transforms (5.5) to an RO problem with a PWL objective. ▲

We focus on applying FME as a proof technique. Through the "lens" of FME we first consider (worst-case) optimality of decision rule structures, and subsequently consider Pareto optimality. In the remainder of the chapter, if FME is applied, w.l.o.g. it is applied on the adjustable variables in the order $y_1(\boldsymbol{z}), \ldots, y_{n_y}(\boldsymbol{z})$, i.e., according to their index. We first state some frequently used definitions. If FME is performed on $\mathcal{X}$ until all adjustable variables are eliminated, the feasible region can be written as

$$\mathcal{X}_{\text{FME}} = \{\boldsymbol{x} \in \mathbb{R}^{n_x} \mid \boldsymbol{G}(\boldsymbol{z})\boldsymbol{x} \le \boldsymbol{f}(\boldsymbol{z}), \ \ \forall \boldsymbol{z} \in U\},$$

for some matrix $\boldsymbol{G}(\boldsymbol{z})$ and vector $\boldsymbol{f}(\boldsymbol{z})$ depending affinely on $\boldsymbol{z}$. Zhen et al. (2018) show that $\mathcal{X} = \mathcal{X}_{\text{FME}}$. For the analysis of particular decision rule structures, it is crucial to keep track of the original constraints during the FME procedure. A frequently used technical result on this is provided in Lemma 5.36 in Appendix 5.A.1.

5.3.2 Optimality of decision rule structures

In this section, we consider several special cases of problem (5.3) for which particular decision rule structures are known to be optimal. We use FME to prove generalizations of these results for linear two-stage ARO problems. In particular, using FME as a proof technique enables us to show that the particular decision rule structure is not only ARO (i.e., worst-case optimal), but is ARF for each ARF stage-1 decision $\boldsymbol{x}$. These results will later be used in analyzing PARO in Section 5.5.

We consider the cases where uncertainty appears (i) constraintwise, (ii) in a hybrid structure (part constraintwise, part non-constraintwise), (iii) in a block structure, and we consider (iv) the case with a simplex uncertainty set and the case with only one uncertain parameter.

(i) Constraintwise uncertainty

Ben-Tal et al. (2004) show that for constraintwise uncertainty the objective values of the static and adjustable problem are equal, i.e., there exists an optimal static decision rule. Using FME, a generalization of their result can be easily proved. We first provide an example.

Example 5.11. Consider the following ARO problem with constraintwise uncertainty:

$$\begin{aligned}
\min_{x,\boldsymbol{y}(\cdot)}\ & x, \\
\text{s.t.}\ & x - y_2(\boldsymbol{z}) \le -\frac{1}{2}z_1, \quad \forall z_1 \in [0,1], \\
& -x + y_1(\boldsymbol{z}) + y_2(\boldsymbol{z}) \le \frac{1}{2}z_2 + \frac{1}{2}z_3 + 2, \quad \forall (z_2, z_3) \in [0,1]^2, \\
& 1 \le y_1(\boldsymbol{z}), \quad \forall \boldsymbol{z} \in U, \\
& \frac{3}{2} \le y_2(\boldsymbol{z}) \le 2, \quad \forall \boldsymbol{z} \in U
\end{aligned}$$

with $U = [0,1]^3$. Uncertain parameter z_1 occurs only in the first constraint and (z_2, z_3) occur only in the second constraint. Using FME, we first eliminate $y_1(\boldsymbol{z})$ and subsequently eliminate $y_2(\boldsymbol{z})$.

$$\begin{aligned}
1 \le y_1(\boldsymbol{z}) &\le -y_2(\boldsymbol{z}) + x + 2 + \frac{1}{2}z_2 + \frac{1}{2}z_3, \quad \forall \boldsymbol{z} \in U, \\
\max\{\frac{3}{2}, x + \frac{1}{2}z_1\} \le y_2(\boldsymbol{z}) &\le \min\{2, x + 1 + \frac{1}{2}z_2 + \frac{1}{2}z_3\}, \quad \forall \boldsymbol{z} \in U.
\end{aligned}$$

From the bounds on $y_2(\boldsymbol{z})$ four linear constraints for x can be derived. One can verify that the (unique) ARO solution is $x^* = \frac{1}{2}$. Additionally, note that the term $\frac{1}{2}z_2 + \frac{1}{2}z_3$ appears in

both upper bounds with a positive sign. As this is the only term that depends on (z_2, z_3), it can be replaced by its worst-case value 0. Similarly, the term $-\frac{1}{2}z_1$ appears in the lower bound on $y_2(\boldsymbol{z})$ with a negative sign, and can be replaced by its worst-case value $-\frac{1}{2}$. This gives the following bounds on $y_1(\boldsymbol{z})$ and $y_2(\boldsymbol{z})$:

$$\begin{aligned} 1 \leq & y_1(\boldsymbol{z}) \leq -y_2(\boldsymbol{z}) + \frac{5}{2}, \quad \forall \boldsymbol{z} \in U, \\ \max\{\frac{3}{2}, 1\} \leq & y_2(\boldsymbol{z}) \leq \min\{2, \frac{3}{2}\}, \quad \forall \boldsymbol{z} \in U. \end{aligned}$$

For $y_2(\boldsymbol{z})$, the only feasible (and hence ARO) decision rule is $y_2(\boldsymbol{z}) = \frac{3}{2}$. This implies $y_1(\boldsymbol{z}) = 1$, and we find that for both adjustable variables the optimal decision rule is static. ▲

According to Lemma 5.36, any term such as $\frac{1}{2}z_2 + \frac{1}{2}z_3$ in Example 5.13 appears in all upper bounds with a positive sign and all lower bounds with a negative sign, or vice versa. Hence, if this is the only term depending on z_2 and z_3, these uncertain parameters can be eliminated by replacing them with their worst-case value. The resulting bounds on adjustable variables are independent of uncertain parameters. Constraintwise uncertainty is formally defined as follows.

Definition 5.12. ARO problem (5.3) has *constraintwise uncertainty* if there is a partition

$$\boldsymbol{z} = (\boldsymbol{z}_{(0)}, \boldsymbol{z}_{(1)}, \ldots, \boldsymbol{z}_{(m)}),$$

such that $\boldsymbol{z}_{(0)}, \ldots, \boldsymbol{z}_{(m)}$ are disjoint, the objective depends only on $\boldsymbol{z}_{(0)}$ and constraint i depends only on $\boldsymbol{z}_{(i)}$, $i = 1, \ldots, m$. Additionally, $U = \{(\boldsymbol{z}_{(0)}, \ldots, \boldsymbol{z}_{(m)}) \mid \boldsymbol{z}_{(i)} \in U^i, i = 0, \ldots, m\}$, with $U^i \subseteq \mathbb{R}^{|\boldsymbol{z}_{(i)}|}$ for all $i = 0, \ldots, m$. ■

Instead of directly providing a formal proof of the result for constraintwise uncertainty, it follows as a corollary from our analysis of hybrid uncertainty, which is considered next.

(ii) Hybrid uncertainty

Hybrid uncertainty is a generalization of constraintwise uncertainty, where part of the uncertain parameters appear constraintwise, and part does not appear constraintwise. This uncertainty structure has previously been considered in Marandi and den Hertog (2018).

In case of hybrid uncertainty, there exist ARO decision rules that do not depend on the constraintwise uncertain parameters. We illustrate this with a toy example.

Example 5.13. We extend Example 5.11 to a problem with hybrid uncertainty by introducing a non-constraintwise uncertain parameter $\hat{z}$:

$$\min_{x,\boldsymbol{y}(\cdot)} \; x, \tag{5.6a}$$

$$\text{s.t.} \; x - y_2(\boldsymbol{z}) \leq -\hat{z} - \frac{1}{2}z_1, \quad \forall (\hat{z}, z_1) \in [0,1]^2, \tag{5.6b}$$

$$-x + y_1(\boldsymbol{z}) + y_2(\boldsymbol{z}) \leq \hat{z} + \frac{1}{2}z_2 + \frac{1}{2}z_3 + 2, \quad \forall (\hat{z}, z_2, z_3) \in [0,1]^3, \tag{5.6c}$$

$$1 \leq y_1(\boldsymbol{z}), \quad \forall \boldsymbol{z} \in U, \tag{5.6d}$$

$$\frac{3}{2} \leq y_2(\boldsymbol{z}) \leq 2, \quad \forall \boldsymbol{z} \in U, \tag{5.6e}$$

with $U = [0,1]^4$. Uncertain parameter $\hat{z}$ occurs in both constraints, z_1 occurs only in the first constraint and (z_2, z_3) occur only in the second constraint. Using FME, we again first eliminate $y_1(\boldsymbol{z})$ and subsequently eliminate $y_2(\boldsymbol{z})$.

$$\begin{aligned} 1 \leq & y_1(\boldsymbol{z}) \leq \hat{z} - y_2(\boldsymbol{z}) + x + 2 + \frac{1}{2}z_2 + \frac{1}{2}z_3, \quad \forall \boldsymbol{z} \in U, \\ \max\{\frac{3}{2}, x + \hat{z} + \frac{1}{2}z_1\} \leq & y_2(\boldsymbol{z}) \leq \min\{2, x + 1 + \hat{z} + \frac{1}{2}z_2 + \frac{1}{2}z_3\}, \quad \forall \boldsymbol{z} \in U. \end{aligned}$$

From the bounds on $y_2(\boldsymbol{z})$ again four linear constraints for x can be derived. The new parameter $\hat{z}$ does not break robustness of solution $x^* = \frac{1}{2}$, so this is still the unique ARO solution. The unique ARO solution is still $x^* = \frac{1}{2}$. Similar to Example 5.11, we can replace both occurrences of the term $\frac{1}{2}z_2 + \frac{1}{2}z_3$ by its worst-case value 0, and $-\frac{1}{2}z_1$ can be replaced by its worst-case value $-\frac{1}{2}$. This yields the following bounds on $y_1(\boldsymbol{z})$ and $y_2(\boldsymbol{z})$:

$$\begin{aligned} 1 \leq & y_1(\boldsymbol{z}) \leq \hat{z} - y_2(\boldsymbol{z}) + \frac{5}{2}, \quad \forall \boldsymbol{z} \in U, \\ \max\{\frac{3}{2}, 1 + \hat{z}\} \leq & y_2(\boldsymbol{z}) \leq \min\{2, \frac{3}{2} + \hat{z}\}, \quad \forall \boldsymbol{z} \in U. \end{aligned}$$

For $y_2(\boldsymbol{z})$, the only feasible (and hence ARO) LDR is $y_2(\hat{z}) = \frac{3}{2} + \frac{1}{2}\hat{z}$. This implies $1 \leq y_1(\boldsymbol{z}) \leq 1 + \frac{1}{2}\hat{z}$, and any decision rule that satisfies these bounds is ARO. Note that both decision rules do not depend on the constraintwise uncertain parameters. One can also pick a PWL decision rule for $y_2(\boldsymbol{z})$, such as its lower or upper bound. Also in this case the decision rules for y_1 and y_2 do not depend on z_1, z_2 or z_3. ▲

Hybrid uncertainty is defined as follows.

Definition 5.14. ARO problem (5.3) has *hybrid uncertainty* if there is a partition

$$\boldsymbol{z} = (\hat{\boldsymbol{z}}, \boldsymbol{z}_{(0)}, \boldsymbol{z}_{(1)}, \ldots, \boldsymbol{z}_{(m)}),$$

such that $\hat{\boldsymbol{z}}, \boldsymbol{z}_{(0)}, \ldots, \boldsymbol{z}_{(m)}$ are disjoint, the objective depends only on $\hat{\boldsymbol{z}}$ and $\boldsymbol{z}_{(0)}$ and constraint i depends only on $\hat{\boldsymbol{z}}$ and $\boldsymbol{z}_{(i)}$, $i = 1, \ldots, m$. Additionally,

$$U = \{(\hat{\boldsymbol{z}}, \boldsymbol{z}_{(0)}, \ldots, \boldsymbol{z}_{(m)}) \mid \hat{\boldsymbol{z}} \in \hat{U}, \boldsymbol{z}_{(i)} \in U^i, i = 0, \ldots, m\},$$

with $\hat{U} \subseteq \mathbb{R}^{|\hat{\boldsymbol{z}}|}$ and $U^i \subseteq \mathbb{R}^{|\boldsymbol{z}_{(i)}|}$ for all $i = 0, \ldots, m$. ■

To formally prove our claim that there exist ARO decision rules that do not depend on the constraintwise uncertain parameters, we first need a result on feasibility.

Lemma 5.15. *Let P_{hybrid} denote an ARO problem of form* (5.3) *with hybrid uncertainty and let $\boldsymbol{x}$ be ARF to P_{hybrid}. Then, there exists a decision rule $\boldsymbol{y}(\cdot)$ that depends only on $\hat{\boldsymbol{z}}$ such that $(\boldsymbol{x}, \boldsymbol{y}(\cdot))$ is ARF to P_{hybrid}.*

Proof. See Appendix 5.A.2. □

The following result is an immediate consequence of Lemma 5.15 for ARO decisions.

Corollary 5.16. *Let P_{hybrid} denote an ARO problem of form* (5.3) *with hybrid uncertainty. For each $\boldsymbol{x}$ that is ARO to P_{hybrid} there exists a decision rule $\boldsymbol{y}(\cdot)$ depending only on $\hat{\boldsymbol{z}}$ such that the pair $(\boldsymbol{x}, \boldsymbol{y}(\cdot))$ is ARO to P_{hybrid}.*

Proof. See Appendix 5.A.3. □

In case of pure constraintwise uncertainty ($U^0 = \emptyset$) Lemma 5.15 shows that for each ARF $\boldsymbol{x}$ there exists a static $\boldsymbol{y}$ such that $(\boldsymbol{x}, \boldsymbol{y})$ is ARF. Additionally, Corollary 5.16 shows that for each ARO $\boldsymbol{x}$ there exists a static $\boldsymbol{y}$ such that $(\boldsymbol{x}, \boldsymbol{y})$ is ARO.

Marandi and den Hertog (2018) prove a similar result to Corollary 5.16 for nonlinear problems. More precisely, they prove that for problems with hybrid uncertainty there exists an optimal decision rule that is a function of only the non-constraintwise uncertain parameters if the problem is convex in the decision variables, concave in uncertain parameters, has a convex compact uncertainty set and a convex compact feasible region for the adjustable variables.

(iii) Block uncertainty

Suppose we can split the constraints into blocks, where each block has its own uncertain parameters and adjustable variables, and the uncertainty set is a Cartesian product of the block-wise uncertainty sets, then there exists an optimal decision rule for each adjustable variable that depends only on the uncertain parameters in its own block. We first provide an example to develop some intuition for block uncertainty.

Example 5.17. Consider again Example 5.13. Add the following constraints to (5.6):

$$y_3(\boldsymbol{z}) + x \leq -\frac{1}{2}z_4 + \frac{3}{2}, \quad \forall z_4 \in [0,1], \tag{5.7a}$$

$$y_3(\boldsymbol{z}) + 2x \geq \frac{1}{2}z_5 + 1, \quad \forall z_5 \in [0,1], \tag{5.7b}$$

and let $U = [0,1]^6$ denote the new uncertainty set. Then the first block consists of constraints (5.6b)-(5.6e), adjustable variables $y_1(\boldsymbol{z}), y_2(\boldsymbol{z})$ and uncertain parameters $z_0, \ldots, z_3$. The second block consists of constraints (5.7), adjustable variable $y_3(\boldsymbol{z})$ and uncertain parameters z_4 and z_5. One can verify that the unique ARO solution remains $x^* = \frac{1}{2}$. The following bounds on $y_3(\boldsymbol{z})$ are obtained:

$$\frac{1}{2}z_5 \leq y_3(\boldsymbol{z}) \leq 1 - \frac{1}{2}z_4, \quad \forall \boldsymbol{z} \in U.$$

One feasible (and hence ARO) decision rule is $y_3(z_4, z_5) = \frac{1}{2}(1 + z_5 - z_4)$. The decision rules for y_1 and y_2 remain unchanged. It follows that for each adjustable variable the optimal decision rule is a function of only the uncertain parameters in its own block. ▲

The formal definition of block uncertainty is as follows. Recall that constraints are indexed $1, \ldots, m$. Let index 0 refer to the objective.

Definition 5.18. ARO problem (5.3) has *block uncertainty* if there exist partitions $\boldsymbol{z} = (\boldsymbol{z}_{(1)}, \ldots, \boldsymbol{z}_{(V)})$, $\boldsymbol{y}(\cdot) = (\boldsymbol{y}_{(1)}(\cdot), \ldots, \boldsymbol{y}_{(V)}(\cdot))$ and $\{0, \ldots, m\} = \{K_{(1)}, \ldots, K_{(V)}\}$ such that

- $U = \{(\boldsymbol{z}_{(1)}, \ldots, \boldsymbol{z}_{(V)}) \mid \boldsymbol{z}_{(v)} \in U^v, v = 1, \ldots, V\}$, with $U^v \subseteq \mathbb{R}^{|\boldsymbol{z}_{(v)}|}$ for all blocks $v = 1, \ldots, V$.
- A constraint or objective with index in set $K_{(v)}$ is independent of uncertain parameters $\boldsymbol{z}_{(w)}$ and adjustable variables $\boldsymbol{y}_{(w)}$ if block $w \neq v$. ■

In order to prove the claim that there exists an optimal decision rule for each adjustable variable that depends only on the uncertain parameters in its own block, we again first consider feasibility.

Lemma 5.19. *Let P_{block} denote an ARO problem of form* (5.3) *with block uncertainty and let $\boldsymbol{x}$ be ARF to P_{block}. Then there exists a decision rule $\boldsymbol{y}(\cdot)$ with $\boldsymbol{y}_{(v)}(\cdot)$ depending only on $\boldsymbol{z}_{(v)}$, for all $v = 1, \ldots, V$, such that $(\boldsymbol{x}, \boldsymbol{y}(\cdot))$ is ARF to P_{block}.*

Proof. See Appendix 5.A.4. □

Corollary 5.20. *Let P_{block} denote an ARO problem of form* (5.3) *with block uncertainty. For each $\boldsymbol{x}$ that is ARO to P_{block} there exists a decision rule $\boldsymbol{y}(\cdot)$ with $\boldsymbol{y}_{(v)}(\cdot)$ depending only on $\boldsymbol{z}_{(v)}$, for all $v = 1, \ldots, V$, such that the pair $(\boldsymbol{x}, \boldsymbol{y}(\cdot))$ is ARO to P_{block}.*

Proof. Follows from Lemma 5.19 analogous to the proof of Corollary 5.16. □

(iv) Simplex uncertainty or one uncertain parameter

Bertsimas and Goyal (2012) prove optimality of LDRs for right-hand side uncertainty and a simplex uncertainty set. Zhen et al. (2018) generalize this to both left- and right-hand side uncertainty, their proof uses FME on the dual problem. We use FME on the primal problem, which leads to a more intuitive proof; the following example illustrates the main idea. We note that the case with one uncertain parameter is a special case of simplex uncertainty, so the results of this section also hold for that case.

Example 5.21. Consider the problem

$$\begin{aligned}
\min\ & x, \\
\text{s.t. }& x - y_2 \le -z_1 - \frac{1}{2}z_2 - \frac{1}{2}, \quad \forall \boldsymbol{z} \in U, \\
& -x + y_1 + y_2 \le z_1 + z_3 + 2, \quad \forall \boldsymbol{z} \in U, \\
& 0 \le y_1(\boldsymbol{z}), \quad \forall \boldsymbol{z} \in U, \\
& \frac{3}{2} \le y_2(\boldsymbol{z}) \le 2, \quad \forall \boldsymbol{z} \in U,
\end{aligned}$$

with standard simplex uncertainty set $U = \{(z_1, z_2, z_3) : z_1 + z_2 + z_3 \le 1, z_1, z_2, z_3 \ge 0\}$. Similar to Example 5.13, we first eliminate y_1 and then y_2. This results in the following bounds on the adjustable variables:

$$0 \le y_1(\boldsymbol{z}) \le z_1 + z_3 + 2 + x - y_2(\boldsymbol{z}), \quad \forall \boldsymbol{z} \in U, \tag{5.8a}$$

$$\max\{\frac{3}{2}, \frac{1}{2} + x + z_1 + \frac{1}{2}z_2\} \le y_2(\boldsymbol{z}) \le \min\{2, z_1 + z_3 + 1 + x\}, \quad \forall \boldsymbol{z} \in U. \tag{5.8b}$$

Equivalently, these bounds have to be satisfied for each point in $\text{ext}(U)$. One can verify that $x^* = \frac{1}{2}$ is an ARO solution. Plugging this in (5.8), we get the following bounds for each extreme point:

$$\begin{aligned}
&(0,0,0): && 0 \le y_1 \le \frac{5}{2} - y_2, && \frac{3}{2} \le y_2 \le \frac{3}{2}, \\
&(1,0,0): && 0 \le y_1 \le \frac{7}{2} - y_2, && 2 \le y_2 \le 2, \\
&(0,1,0): && 0 \le y_1 \le \frac{5}{2} - y_2, && \frac{3}{2} \le y_2 \le \frac{3}{2}, \\
&(0,0,1): && 0 \le y_1 \le \frac{7}{2} - y_2, && \frac{3}{2} \le y_2 \le 2.
\end{aligned} \tag{5.9}$$

Because U is a simplex, the four extreme points are affinely independent. Therefore, there is a unique LDR such that the upper bound on $y_2(\cdot)$ holds with equality for each extreme point. This is also the case for the lower bound, and any convex combination of both decision

rules also satisfies the bounds for y_2 in (5.9). The LDR corresponding with the upper bounds is $y_2(z_1, z_3) = \frac{1}{2}(3 + z_1 + z_3)$, and plugging this in the bounds on y_1 yields a similar system as (5.9) for y_1. This guarantees existence of an LDR for y_1; for the upper bound we find $y_1(z_1, z_3) = \frac{1}{2}(2 + z_1 + z_3)$. Note that this does not generalize to uncertainty sets described by more than $L + 1$ extreme points. ▲

Similar to the cases for hybrid and block uncertainty, we first prove feasibility for each ARF $\boldsymbol{x}$, and subsequently prove optimality.

Lemma 5.22. *Let $P_{simplex}$ denote an ARO problem of form* (5.3) *with a simplex uncertainty set, i.e., $U = Conv(\boldsymbol{z}^1, \ldots, \boldsymbol{z}^{L+1})$, with $\boldsymbol{z}^j \in \mathbb{R}^L$ such that $\boldsymbol{z}^1, \ldots, \boldsymbol{z}^{L+1}$ are affinely independent. Let $\boldsymbol{x}$ be ARF to $P_{simplex}$. Then there exists an LDR $\boldsymbol{y}(\cdot)$ such that $(\boldsymbol{x}, \boldsymbol{y})$ is ARF to $P_{simplex}$.*

Proof. See Appendix 5.A.5. □

Similar to Corollary 5.16, we have the following result for ARO decisions.

Corollary 5.23. *Let $P_{simplex}$ denote an ARO problem of form* (5.3) *with a simplex uncertainty set, i.e., $U = Conv(\boldsymbol{z}^1, \ldots, \boldsymbol{z}^{L+1})$, with $\boldsymbol{z}^j \in \mathbb{R}^L$ such that $\boldsymbol{z}^1, \ldots, \boldsymbol{z}^{L+1}$ are affinely independent. For each $\boldsymbol{x}$ that is ARO to $P_{simplex}$ there exists an LDR $\boldsymbol{y}(\cdot)$ such that the pair $(\boldsymbol{x}, \boldsymbol{y}(\cdot))$ is ARO to $P_{simplex}$.*

Proof. Follows from Lemma 5.22 analogous to the proof of Corollary 5.16. □

Because the case with one uncertain parameter is a special case of simplex uncertainty, the results of Lemma 5.22 and Corollary 5.23 also hold for that case.

The results on PARO in the next sections make use of the fact that an ARF decision rule with the particular structure exist for *every* ARF $\boldsymbol{x}$, i.e., Lemmas 5.15, 5.19 and 5.22.

5.4 Properties of PARO solutions

In this section, we prove existence of PARO solutions for two-stage ARO problems of form (5.3). First, we use FME to prove that a PARO stage-1 (here-and-now) solution is equivalent to a PRO solution of a PWL convex static RO problem, and use that to prove the existence of a PARO stage-1 solution. Subsequently, we prove that there exists a PWL decision rule that is PARO to (5.3).

5.4.1 Existence of a PARO stage-1 solution

We prove existence of PARO stage-1 solutions in two steps. First, we prove that a PARO solution to (5.3) is equivalent to a PRO solution to a static RO problem with a convex PWL objective. Subsequently, we prove that PRO solutions to such problems always exist.

Lemma 5.24. *A solution $\boldsymbol{x}^*$ is PARO to* (5.3) *if and only if it is PRO to*

$$\min_{\boldsymbol{x}\in\mathcal{X}_{FME}} \max_{\boldsymbol{z}\in U} \boldsymbol{c}(\boldsymbol{z})^\top \boldsymbol{x} + \max_{(S,T)\in M} \{h_{S,T}(\boldsymbol{x},\boldsymbol{z})\}, \tag{5.10}$$

where each element (S,T) of set M is a pair of sets of original constraints of (5.3) *and each function $h_{S,T}(\boldsymbol{x},\boldsymbol{z})$ is bilinear in $\boldsymbol{x}$ and $\boldsymbol{z}$.*

Proof. See Appendix 5.A.6. □

Thus, existence of a PARO solution to (5.3) is now reduced to existence of a PRO solution to a static RO problem with a convex PWL objective in both $\boldsymbol{x}$ and $\boldsymbol{z}$. For problems without adjustable variables in the objective the following result immediately follows.

Corollary 5.25. *If $\boldsymbol{d} = \boldsymbol{0}$, a solution $\boldsymbol{x}^*$ is PARO to* (5.3) *if and only if it is PRO to*

$$\min_{\boldsymbol{x}\in\mathcal{X}_{FME}} \max_{\boldsymbol{z}\in U} \boldsymbol{c}(\boldsymbol{z})^\top \boldsymbol{x}.$$

Proof. This directly follows from plugging in $\boldsymbol{d} = \boldsymbol{0}$ in the proof of Lemma 5.24. □

We can now prove one of our main results: existence of a PARO $\boldsymbol{x}$ for any ARO problem of form (5.3) with compact feasible region. Our proof uses Lemma 5.24 and essentially proves existence of a PRO solution to (5.10).

Theorem 5.26. *If $\mathcal{X}$ is compact, there exists a PARO $\boldsymbol{x}$ to* (5.3).

Proof. See Appendix 5.A.7. □

Note that the theorem also holds if $\mathcal{X}$ restricts (some elements of) $\boldsymbol{x}$ to be integer-valued. The boundedness assumption on $\mathcal{X}$ cannot be relaxed, because in that case a PRO solution to (5.10) need not exist. For example, consider the static RO problem $\max_{x\geq 0} \min_{z\in[0,1]} xz$. The worst-case scenario is $z = 0$, and any $x \geq 0$ is worst-case optimal. In any other scenario $z > 0$, higher x is better. Any x is dominated by $x + \epsilon$ with $\epsilon > 0$, and there is no PRO solution.

5.4.2 Existence of a PARO piecewise linear decision rule

Now that existence of a PARO $\boldsymbol{x}$ is established, we investigate the structure of decision rule $\boldsymbol{y}(\cdot)$. We illustrate via an example that for any ARF $\boldsymbol{x}$ there exists a PWL PARO extension $\boldsymbol{y}(\cdot)$.

Example 5.27. Consider the following ARO problem, a slight adaptation of Example 5.13:

$$\min_{x,\boldsymbol{y}(\cdot)} \max_{\boldsymbol{z}\in[0,1]^4} x - y_1(\boldsymbol{z}) + y_2(\boldsymbol{z}), \tag{5.11a}$$

$$\text{s.t. } x - y_2(\boldsymbol{z}) \le -z_0 - \frac{1}{2}z_1, \quad \forall (z_0, z_1) \in [0,1]^2, \tag{5.11b}$$

$$-x + y_1(\boldsymbol{z}) + y_2(\boldsymbol{z}) \le z_0 + \frac{1}{2}z_2 + \frac{1}{2}z_3 + 2, \quad \forall (z_0, z_2, z_3) \in [0,1]^3, \tag{5.11c}$$

$$1 \le y_1(\boldsymbol{z}) \le 2, \quad \forall \boldsymbol{z} \in U, \tag{5.11d}$$

$$\frac{3}{2} \le y_2(\boldsymbol{z}) \le 2, \quad \forall \boldsymbol{z} \in U. \tag{5.11e}$$

We eliminate $y_1(\boldsymbol{z})$ and $y_2(\boldsymbol{z})$ in constraints (5.11b)-(5.11e) analogous to Example 5.13, and find the ARF solution $x^* = \frac{1}{2}$ and the following bounds on $y_1(\boldsymbol{z})$ and $y_2(\boldsymbol{z})$:

$$1 \le y_1(\boldsymbol{z}) \le \min\{2, z_0 - y_2(\boldsymbol{z}) + \frac{5}{2}\}, \tag{5.12a}$$

$$\max\{\frac{3}{2}, 1 + z_0\} \le y_2(\boldsymbol{z}) \le \min\{2, \frac{3}{2} + z_0\}. \tag{5.12b}$$

Variables $y_1(\boldsymbol{z})$ and $y_2(\boldsymbol{z})$ have not been eliminated in the objective. Therefore, any decision rule satisfying (5.12) is ARF to (5.11) but need not be ARO or PARO.

Variable $y_1(\boldsymbol{z})$ does not appear in the bounds of $y_2(\boldsymbol{z})$, so we can consider its individual contribution to the objective value. The objective coefficient of $y_1(\boldsymbol{z})$ is negative, so for any $\boldsymbol{z}$ (including the worst-case) the best possible contribution of $y_1(\boldsymbol{z})$ to the objective value is achieved if we set $y_1(\boldsymbol{z})$ equal to its upper bound. Therefore, for the given x^*, we have the following PWL PARO extension as a function of $y_2(\boldsymbol{z})$:

$$y_1^*(\boldsymbol{z}) = \min\{2, z_0 - y_2(\boldsymbol{z}) + \frac{5}{2}\}.$$

Now that $y_1(\boldsymbol{z})$ is eliminated in the objective value, it remains to find the optimal decision rule for $y_2(\boldsymbol{z})$. Variable $y_2(\boldsymbol{z})$ now appears directly in the objective (5.11a) and through its occurrence in the decision rule $y_1^*(\boldsymbol{z})$. For fixed $\boldsymbol{z}$, the optimal $y_2(\boldsymbol{z})$ is determined by solving

$$\begin{aligned}
&\min_{y_2(\boldsymbol{z})} -\min\{2, z_0 - y_2(\boldsymbol{z}) + \frac{5}{2}\} + y_2(\boldsymbol{z}),\\
&\text{s.t. } \max\{\frac{3}{2}, 1 + z_0\} \le y_2(\boldsymbol{z}) \le \min\{2, \frac{3}{2} + z_0\}.
\end{aligned}$$

One can easily see that the objective is increasing in $y_2(\boldsymbol{z})$, so for any $\boldsymbol{z}$ the best possible contribution of $y_2(\boldsymbol{z})$ to the objective value is achieved if we set $y_2(\boldsymbol{z})$ equal to its lower bound. Thus, for the given x^*, we have the following PWL PARO extension:

$$y_2^*(\boldsymbol{z}) = \max\{\frac{3}{2}, 1 + z_0\}.$$

Note that plugging in a PWL argument in a PWL function retains the piecewise linear structure. Therefore, we also obtain the following PWL PARO extension for $y_1^*(\boldsymbol{z})$:

$$y_1^*(\boldsymbol{z}) = \min\{2, z_0 - \max\{\frac{3}{2}, 1 + z_0\} + \frac{5}{2}\}.$$

Note that we did not move adjustable variables in the objective to the constraints using an epigraph variable, as was done in Example 5.10. Using an epigraph variable for the objective ensures that each decision rule satisfying the bounds is worst-case optimal, but prevents from comparing performance in other scenarios. Naturally, computationally it has the major advantage that it remains a linear program. ▲

Bemporad et al. (2003) show worst-case optimality of PWL decision rules for right-hand polyhedral uncertainty, i.e., ARO PWL decision rules in our terminology. Zhen et al. (2018, Theorem 3) generalize this to problems of form (5.3) with particular assumptions on the uncertainty set. These decision rules are general PWL in $\boldsymbol{z}$ for all variables y_j, $j \neq l$, where y_l is the last eliminated variable in the FME procedure. The decision rule is convex or concave PWL in y_l. These results solely consider the performance of PWL decision rules in the worst-case. Example 5.27 illustrates that for any ARF $\boldsymbol{x}$ there exists a PWL PARO extension $\boldsymbol{y}(\cdot)$. The lemma below formalizes this claim.

Lemma 5.28. *For any $\boldsymbol{x}$ that is ARF to* (5.3) *there exists a PARO extension $\boldsymbol{y}(\boldsymbol{z})$ that is PWL in $\boldsymbol{z}$.*

We present two proofs to Lemma 5.28; one via FME using the idea of Example 5.27, and one via basic solutions in linear optimization.

Proof of Lemma 5.28 via FME. See Appendix 5.A.8. □

Proof of Lemma 5.28 via linear optimization. See Appendix 5.A.9. □

In both proofs the constructed decision rule is in fact optimal for *all* scenarios in the uncertainty set. As long as $\boldsymbol{x}$ is fixed, this is necessary for PARO solutions. The following theorem establishes the existence of PARO PWL decision rules.

Theorem 5.29. *If $\mathcal{X}$ is compact, there exists a PARO $\boldsymbol{y}(\cdot)$ for* (5.3) *such that $\boldsymbol{y}(\boldsymbol{z})$ is PWL in $\boldsymbol{z}$.*

Proof. According to Theorem 5.26 there exists a PARO $\boldsymbol{x}$, and according to Lemma 5.28 there exists a PARO extension $\boldsymbol{y}(\cdot)$ for this $\boldsymbol{x}$ that is PWL in $\boldsymbol{z}$. It immediately follows that $\boldsymbol{y}(\cdot)$ is PARO. □

5.5 Constructing PARO solutions

Adjustable robust optimization problems of form (5.3) are in general NP-hard (Guslitser, 2002), and finding ARO solutions is still the focus of ongoing research (Yanıkoğlu et al., 2019). Thus, finding a method that, given an ARO solution to (5.3), can produce a PARO solution is not an easy task either. The methods used in the existence proofs of Section 5.4 are not computationally tractable, i.e., they provide little guidance for finding PARO solutions in practice. In this section we present several practical methods for finding and approximating PARO solutions for particular problems.

First, we consider the problems with known ARO decision rules of Section 5.3, and show how to obtain PARO solutions in case stage-2 variables do not appear in the objective. Subsequently, we show how for fixed $\boldsymbol{x}$ we can check whether $\boldsymbol{y}(\cdot)$ is a PARO extension. After that, we consider an application of the finite subset approach of Hadjiyiannis et al. (2011). Lastly, we consider two practical approaches for finding (approximate) PARO solutions if a convex hull description of the uncertainty set is available.

5.5.1 Known worst-case optimal decision rules

In Section 5.3, we have shown that for particular ARO problems there exist decision rule structures such that for any ARF stage-1 decision there exists an ARF decision rule with that structure. For example, for ARO problems with hybrid uncertainty, for any ARF stage-1 decision there exists an ARF decision rule that depends only on the non-constraintwise uncertain parameter. It turns out that, in case there are no adjustable variables in the objective, PRO solutions to the static problem obtained after plugging in that decision rule structure are PARO solutions to the original ARO problem. To formalize this, let $\boldsymbol{y}(\boldsymbol{z}) = f_{\boldsymbol{w}}(\boldsymbol{z})$ be a decision rule with known form f (e.g., linear or quadratic) and finite number of parameters $\boldsymbol{w} \in \mathbb{R}^p$, such that $f_{\boldsymbol{w}}(\boldsymbol{z}) \in \mathcal{R}^{L,n_y}$ for any $\boldsymbol{w}$.

Theorem 5.30. *Let P denote an ARO problem of form* (5.3) *with $\boldsymbol{d} = \boldsymbol{0}$ and where for any ARF $\boldsymbol{x}$ there exists an ARF decision rule of form $\boldsymbol{y}^*(\boldsymbol{z}) = f_{\boldsymbol{w}}(\boldsymbol{z})$ for some $\boldsymbol{w}$. Then*

any $\boldsymbol{x}^*$ that is PRO to the static robust optimization problem obtained after plugging in decision rule structure $f_{\boldsymbol{w}}(\boldsymbol{z})$ is PARO to P.

Proof. See Appendix 5.A.10. □

Due to Lemmas 5.15, 5.19 and 5.22, the following result immediately follows for hybrid, block and simplex uncertainty.

Corollary 5.31.

(i) Let P_{hybrid} denote an ARO problem of form (5.3) *with $\boldsymbol{d} = \boldsymbol{0}$ and hybrid uncertainty. Let Q denote the static robust optimization problem obtained from P_{hybrid} by plugging in a decision rule structure that depends only on the non-constraintwise parameter. Any $\boldsymbol{x}^*$ that is PRO to Q is PARO to P_{hybrid}.*

(ii) Let P_{block} denote an ARO problem of form (5.3) *with $\boldsymbol{d} = \boldsymbol{0}$ and block uncertainty. Let Q denote the static robust optimization problem obtained from P_{block} by plugging in a decision rule structure where adjustable variable $\boldsymbol{y}^*_{(v)}(\cdot)$ depend only on $\boldsymbol{z}_{(v)}$ for all $v = 1, \ldots, V$. Then any $\boldsymbol{x}^*$ that is PRO to Q is PARO to P_{block}.*

(iii) Let $P_{simplex}$ denote an ARO problem of form (5.3) *with $\boldsymbol{d} = \boldsymbol{0}$ and a simplex uncertainty set, i.e., $U = Conv(\boldsymbol{z}^1, \ldots, \boldsymbol{z}^{L+1})$, with $\boldsymbol{z}^j \in \mathbb{R}^L$ such that $\boldsymbol{z}^1, \ldots, \boldsymbol{z}^{L+1}$ are affinely independent. Let Q denote the static robust optimization problem obtained from $P_{simplex}$ by plugging in an LDR structure. Then any $\boldsymbol{x}^*$ that is PRO to Q is PARO to $P_{simplex}$.*

Proof. See Appendix 5.A.11. □

Similar to Section 5.3, the case with constraintwise uncertainty is again a special case of Corollary 5.31(i). The case with one uncertain parameter is again a special case of Corollary 5.31(iii). Note that, unlike for worst-case optimization, it is necessary that $\boldsymbol{d} = \boldsymbol{0}$, because our definition of PRO involves the term $\boldsymbol{d}$. If $\boldsymbol{d} \neq \boldsymbol{0}$, the results above do not hold. This is also illustrated in Example 5.1 in Section 5.1.

The results of Corollary 5.31 can be combined. For example, for problems with both simplex uncertainty and hybrid uncertainty, Corollary 5.31(i) and Corollary 5.31(iii) together imply that one needs to consider only decision rules that are affine in the non-constraintwise parameter, if there are no adjustable variables in the objective. Simplex uncertainty sets arise in a variety of applications and can be used to approximate other uncertainty sets (Ben-Tal et al., 2020).

5.5.2 Check whether a decision rule is a PARO extension

If the stage-1 decision $\boldsymbol{x}$ is fixed, one can verify whether the decision rule $\boldsymbol{y}$ is a PARO extension (Definition 5.9) as follows.

Lemma 5.32. *Let* $(\tilde{\boldsymbol{x}}, \tilde{\boldsymbol{y}}(\cdot))$ *be an ARO solution to* (5.3)*. Consider the problem*

$$\max_{\boldsymbol{z},\boldsymbol{y}} \ \boldsymbol{d}^\top(\tilde{\boldsymbol{y}}(\boldsymbol{z}) - \boldsymbol{y}), \tag{5.13a}$$

$$s.t. \ \ \boldsymbol{A}(\boldsymbol{z})\tilde{\boldsymbol{x}} + \boldsymbol{B}\boldsymbol{y} \leq \boldsymbol{r}(\boldsymbol{z}), \tag{5.13b}$$

$$\boldsymbol{z} \in U. \tag{5.13c}$$

If the optimal objective value is zero, $\tilde{\boldsymbol{y}}(\cdot)$ *is a PARO extension of* $\tilde{\boldsymbol{x}}$*. If the objective value is positive, then* $\tilde{\boldsymbol{y}}(\cdot)$ *is not a PARO extension of* $\tilde{\boldsymbol{x}}$ *and the suboptimality of* $\tilde{\boldsymbol{y}}(\cdot)$ *is bounded by the optimal objective value.*

Proof. See Appendix 5.A.12. □

If the optimal value is positive and $(\boldsymbol{z}^*, \boldsymbol{y}^*)$ denotes an optimal solution to (5.13), then $\boldsymbol{z}^*$ is a scenario where the suboptimality bound is attained, and $\boldsymbol{y}^*$ is an optimal decision for this scenario. Also, note that if the optimal value of (5.13) equals zero, the pair $(\tilde{\boldsymbol{x}}, \tilde{\boldsymbol{y}}(\cdot))$ need not be PARO; there may be a different pair $(\hat{\boldsymbol{x}}, \hat{\boldsymbol{y}}(\cdot))$ that dominates the current pair.

5.5.3 Unique ARO solution on finite subset of scenarios is PARO

The finite subset approach of Hadjiyiannis et al. (2011) can be used in a PARO setting as well. If the lower bound problem has a unique solution and this solution is feasible to the original problem, it is a PARO solution to the original problem. This is formalized in Lemma 5.33.

Lemma 5.33. *Let* $S = \{\boldsymbol{z}^1, \ldots, \boldsymbol{z}^N\}$ *denote a finite set of scenarios,* $S \subseteq U$*. Let* $\boldsymbol{x}$ *be the unique ARO here-and-now decision for which there exist* $\boldsymbol{y}^1, \ldots, \boldsymbol{y}^N$ *such that* $(\boldsymbol{x}, \boldsymbol{y}^1, \ldots, \boldsymbol{y}^N)$ *are an optimal solution to*

$$\min_{\boldsymbol{x},\boldsymbol{y}^1,\ldots,\boldsymbol{y}^N} \ \max_{i=1,\ldots,N} \{\boldsymbol{c}(\boldsymbol{z}^i)^\top \boldsymbol{x} + \boldsymbol{d}^\top \boldsymbol{y}^i\}, \tag{5.14a}$$

$$s.t. \ \ \boldsymbol{A}(\boldsymbol{z}^i)\boldsymbol{x} + \boldsymbol{B}\boldsymbol{y}^i \leq \boldsymbol{r}(\boldsymbol{z}^i), \ \forall i = 1, \ldots, N. \tag{5.14b}$$

Then $\boldsymbol{x}$ *is PARO to* (5.3).

Proof. Let $(\bar{\boldsymbol{x}}, \bar{\boldsymbol{y}}(\cdot))$ be ARO to (5.3) with $\bar{\boldsymbol{x}}$ unequal to $\boldsymbol{x}$. Then the solution $(\bar{\boldsymbol{x}}, \bar{\boldsymbol{y}}(\boldsymbol{z}^1), \ldots, \bar{\boldsymbol{y}}(\boldsymbol{z}^N))$ is feasible to (5.14). Because $\boldsymbol{x}$ is the unique here-and-now ARO decision that can be extended to an optimal solution of (5.14), it holds that

$$\boldsymbol{c}(\boldsymbol{z}^i)^\top \boldsymbol{x} + \boldsymbol{d}^\top \boldsymbol{y}^i < \boldsymbol{c}(\boldsymbol{z}^i)^\top \bar{\boldsymbol{x}} + \boldsymbol{d}^\top \bar{\boldsymbol{y}}(\boldsymbol{z}^i) \text{ for some } \boldsymbol{z}^i \in S.$$

That is, for each $\bar{\boldsymbol{x}}$ that is ARO to (5.3) and unequal to $\boldsymbol{x}$ there is at least one scenario $\boldsymbol{z}^i$ in U for which $\boldsymbol{x}$ outperforms $\bar{\boldsymbol{x}}$. This implies that $\boldsymbol{x}$ is PARO to (5.3). □

It should be noted that requiring $\boldsymbol{x}$ to be both ARO to (5.3) and a unique optimal solution to (5.14) is quite restrictive.

5.5.4 Convex hull description of scenario set

Next, consider the case where the uncertainty set is given by the convex hull of a finite set of points, i.e., $U = \text{Conv}(\boldsymbol{z}^1, \ldots, \boldsymbol{z}^N)$. Then (5.3) is equivalent to

$$\min_{\boldsymbol{x}, \boldsymbol{y}^1, \ldots, \boldsymbol{y}^N} \quad \max_{i=1,\ldots,N} \boldsymbol{c}(\boldsymbol{z}^i)^\top \boldsymbol{x} + \boldsymbol{d}^\top \boldsymbol{y}^i, \tag{5.15a}$$

$$\text{s.t.} \quad \boldsymbol{A}(\boldsymbol{z}^i)\boldsymbol{x} + \boldsymbol{B}\boldsymbol{y}^i \leq \boldsymbol{r}(\boldsymbol{z}^i), \ \forall i = 1, \ldots, N. \tag{5.15b}$$

Let $(\tilde{\boldsymbol{x}}, \tilde{\boldsymbol{y}}^1, \ldots, \tilde{\boldsymbol{y}}^N)$ denote the optimal solution. Note that $\tilde{\boldsymbol{x}}$ is ARO to (5.3). Analogous to Iancu and Trichakis (2014), we can perform an additional step by optimizing the set of ARO solutions over a scenario in the relative interior (denoted ri$(\cdot)$) of the convex hull of our finite set of scenarios. If the objective does not contain adjustable variables, this produces a PARO here-and-now solution to (5.3).

Lemma 5.34. *Let $\boldsymbol{d} = \boldsymbol{0}$. Let $U = \text{Conv}(\boldsymbol{z}^1, \ldots, \boldsymbol{z}^N)$, $\bar{\boldsymbol{z}} \in \text{ri}(U)$ and let $(\bar{\boldsymbol{x}}, \bar{\boldsymbol{y}}^1, \ldots, \bar{\boldsymbol{y}}^N)$ denote an optimal solution to*

$$\min_{\boldsymbol{x}, \boldsymbol{y}^1, \ldots, \boldsymbol{y}^N} \quad \boldsymbol{c}(\bar{\boldsymbol{z}})^\top \boldsymbol{x}, \tag{5.16a}$$

$$s.t. \quad \boldsymbol{A}(\boldsymbol{z}^i)\boldsymbol{x} + \boldsymbol{B}\boldsymbol{y}^i \leq \boldsymbol{r}(\boldsymbol{z}^i), \ \forall i = 1, \ldots, N, \tag{5.16b}$$

$$\boldsymbol{c}(\boldsymbol{z}^i)^\top \boldsymbol{x} + \boldsymbol{d}^\top \boldsymbol{y}^i \leq OPT, \ \forall i = 1, \ldots, N, \tag{5.16c}$$

where OPT denotes the optimal objective value of (5.15). *Then $\bar{\boldsymbol{x}}$ is PARO to* (5.3).

Proof. See Appendix 5.A.13. □

For the general case with $\boldsymbol{d} \neq \boldsymbol{0}$, we restrict ourselves to problems with right-hand side uncertainty. Let $\hat{\boldsymbol{x}}$ denote an ARO (worst-case optimal) solution. Let V denote a set where each element is a pair of a scenario in U and a required objective value

for that scenario. We initialize $V = \{(\boldsymbol{z}^1, \text{OPT}), \ldots, (\boldsymbol{z}^N, \text{OPT})\}$; the proposed solution method will later add additional elements to this set. The following optimization problem produces a scenario $\bar{\boldsymbol{z}}$ where $\hat{\boldsymbol{x}}$ is most suboptimal, and provides the ARO stage-1 decision $\bar{\boldsymbol{x}}$ that allows for the largest improvement:

$$p(\hat{\boldsymbol{x}}, V) = \min_{\substack{\bar{\boldsymbol{z}}, \bar{\boldsymbol{x}}, \bar{\boldsymbol{y}}, \\ \bar{\boldsymbol{y}}^1, \ldots, \bar{\boldsymbol{y}}^{|V|}}} \quad \max_{\hat{\boldsymbol{y}}: \boldsymbol{A}\hat{\boldsymbol{x}} + \boldsymbol{B}\hat{\boldsymbol{y}} \leq \boldsymbol{r}(\bar{\boldsymbol{z}})} (\boldsymbol{c}^\top \bar{\boldsymbol{x}} + \boldsymbol{d}^\top \bar{\boldsymbol{y}}) - (\boldsymbol{c}^\top \hat{\boldsymbol{x}} + \boldsymbol{d}^\top \hat{\boldsymbol{y}}), \tag{5.17a}$$

$$\text{s.t. } \boldsymbol{A}\bar{\boldsymbol{x}} + \boldsymbol{B}\bar{\boldsymbol{y}} \leq \boldsymbol{r}(\bar{\boldsymbol{z}}), \tag{5.17b}$$

$$\boldsymbol{A}\bar{\boldsymbol{x}} + \boldsymbol{B}\bar{\boldsymbol{y}}^i \leq \boldsymbol{r}(\boldsymbol{z}^i), \quad \forall i = 1, \ldots, |V|, \tag{5.17c}$$

$$\boldsymbol{c}^\top \bar{\boldsymbol{x}} + \boldsymbol{d}^\top \bar{\boldsymbol{y}}^i \leq v^i, \quad \forall i = 1, \ldots, |V|, \tag{5.17d}$$

$$\bar{\boldsymbol{z}} \in U. \tag{5.17e}$$

Constraint (5.17b) ensures that the stage-1 decision $\bar{\boldsymbol{x}}$ and the decision $\bar{\boldsymbol{y}}$ for scenario $\bar{\boldsymbol{z}}$ are feasible for that scenario. Due to the current choice of set V, constraint (5.17c) ensures robust feasibility of $\bar{\boldsymbol{x}}$ and constraint (5.17d) ensures robust optimality of $\bar{\boldsymbol{x}}$. Hence, $\bar{\boldsymbol{x}}$ is ARO and performs strictly better than $\hat{\boldsymbol{x}}$ on the scenario $\bar{\boldsymbol{z}}$, if the optimal objective value of (5.17) is strictly negative.

One may note that solving (5.17) is non-trivial. We first describe how problem (5.17) can be incorporated in an algorithm that guarantees a PARO solution. Subsequently, we describe an approach to approximately solve (5.17).

Solution $\bar{\boldsymbol{x}}$ need not be PARO; further improvements may be possible. We propose an algorithm that solves problem (5.17) multiple times. In each iteration the starting stage-1 solution is the optimal stage-1 solution of the previous iteration. Additionally, the scenario where the maximum difference is attained is added to the scenario set V, together with the attained objective value in that scenario. Algorithm 5.1 describes the algorithm and Lemma 5.35 proves that it yields a PARO stage-1 solution.

Lemma 5.35. *A solution $\bar{\boldsymbol{x}}$ obtained from Algorithm 5.1 is PARO to* (5.3).

Proof. See Appendix 5.A.14. □

Algorithm 5.1 requires solving (5.17) multiple times, but unfortunately it is intractable in general. The reason is that for the original stage-1 decision $\hat{\boldsymbol{x}}$, the optimal recourse decision $\hat{\boldsymbol{y}}$ for scenario $\bar{\boldsymbol{z}}$ needs to be chosen adversely. However, the set of feasible recourse decisions depends on the scenario $\bar{\boldsymbol{z}}$. We propose to use a simple alternating direction heuristic, also known as mountain climbing, which guarantees a local optimum (Konno, 1976). For some initial $\bar{\boldsymbol{z}}$ one can determine the optimal $\{\bar{\boldsymbol{x}}, \bar{\boldsymbol{y}}, \bar{\boldsymbol{y}}^1, \ldots, \bar{\boldsymbol{y}}^{|V|}\}$ by solving an LP. Subsequently, we alternate between optimizing

Algorithm 5.1: Iterative improvement algorithm

begin
  Set $k = 0$, $p_0 = -\infty$ and $V_0 = \{(\boldsymbol{z}^1, \text{OPT}), \ldots, (\boldsymbol{z}^N, \text{OPT})\}$;
  Compute ARO solution $\boldsymbol{x}^0$;
  while $p_k < 0$ **do**
    Set $k = k + 1$;
    if $k > 1$ **then**
      Set $V_k \leftarrow V_{k-1} \cup \{(\boldsymbol{z}^{k-1}, \boldsymbol{c}^\top \boldsymbol{x}^{k-1} + \boldsymbol{d}^\top \boldsymbol{y}^{k-1})\}$;
    end
    Compute $p_k := p(\boldsymbol{x}^{k-1}, V_k)$ and denote the solution by $(\boldsymbol{z}^k, \boldsymbol{x}^k, \boldsymbol{y}^k, \boldsymbol{y}^{1,k}, \ldots, \boldsymbol{y}^{N,k})$;
  end
  Set $\bar{\boldsymbol{x}} = \boldsymbol{x}^k$;
end

for $\hat{\boldsymbol{y}}$ and $\{\bar{\boldsymbol{z}}, \bar{\boldsymbol{x}}, \bar{\boldsymbol{y}}, \bar{\boldsymbol{y}}^1, \ldots, \bar{\boldsymbol{y}}^{|V|}\}$ while keeping the other set of variables at their current value. For either set of variables, the problem is an LP. This is continued until two consecutive LP problems yield the same objective value.

By using a heuristic approach to solving (5.17), it possible that at a certain iteration k in Algorithm 5.1 we obtain an estimate $\hat{p}_k \geq 0$, while the true $p_k < 0$, so the algorithm terminates without finding a PARO solution. Nevertheless, also solutions obtained this way that are not proven to be PARO can improve upon the original ARO solution.

The solution quality of Algorithm 5.1 depends on the starting $\bar{\boldsymbol{z}}$. One option is to simply pick the nominal scenario, if it is defined. An alternative starting solution can be obtained by plugging in an LDR for $\hat{\boldsymbol{y}}$ in (5.17), i.e., solving

$$\max_{\boldsymbol{w}, \boldsymbol{W}} \min_{\substack{\bar{\boldsymbol{z}}, \bar{\boldsymbol{x}}, \bar{\boldsymbol{y}}, \\ \bar{\boldsymbol{y}}^1, \ldots, \bar{\boldsymbol{y}}^{|V|}}} \Big\{ (\boldsymbol{c}^\top \bar{\boldsymbol{x}} + \boldsymbol{d}^\top \bar{\boldsymbol{y}}) - (\boldsymbol{c}^\top \hat{\boldsymbol{x}} + \boldsymbol{d}^\top (\boldsymbol{w} + \boldsymbol{W} \bar{\boldsymbol{z}})) \mid \boldsymbol{A}\hat{\boldsymbol{x}} + \boldsymbol{B}(\boldsymbol{w} + \boldsymbol{W}\bar{\boldsymbol{z}}) \leq \boldsymbol{r}(\bar{\boldsymbol{z}}) \Big\},$$

additionally subject to (5.17b)-(5.17e). This is a static linear robust optimization problem.

An alternative approach gives an exact solution to (5.17). The inner minimization problem is an LP for which we can write down the optimality conditions. Subsequently, the complementary slackness conditions can be linearized using big-M constraints and auxiliary binary variables. This results in an exact reformulation to a mixed binary convex reformulation (mixed binary linear if U is polyhedral). This reformulation was previously used in the column-and-constraint generation method of Zeng and Zhao (2013) for ARO problems with a polyhedral uncertainty set, and to solve bilinear op-

timization problems with a disjoint uncertainty set (Zhen et al., 2021). By dualizing the inner maximization problem, we obtain

$$\min_{\substack{\bar{\boldsymbol{z}},\bar{\boldsymbol{x}},\bar{\boldsymbol{y}},\boldsymbol{\lambda} \\ \bar{\boldsymbol{y}}^1,\ldots,\bar{\boldsymbol{y}}^{|V|}}} \quad (\boldsymbol{c}^\top \bar{\boldsymbol{x}} + \boldsymbol{d}^\top \bar{\boldsymbol{y}}) - (\boldsymbol{c}^\top \hat{\boldsymbol{x}} + \boldsymbol{\lambda}^\top (\boldsymbol{r}(\bar{\boldsymbol{z}}) - \boldsymbol{A}\hat{\boldsymbol{x}})), \tag{5.18a}$$

$$\text{s.t.} \quad \boldsymbol{A}\bar{\boldsymbol{x}} + \boldsymbol{B}\bar{\boldsymbol{y}} \leq \boldsymbol{r}(\bar{\boldsymbol{z}}), \tag{5.18b}$$

$$\boldsymbol{A}\bar{\boldsymbol{x}} + \boldsymbol{B}\bar{\boldsymbol{y}}^i \leq \boldsymbol{r}(\boldsymbol{z}^i), \quad \forall i = 1,\ldots,|V|, \tag{5.18c}$$

$$\boldsymbol{c}^\top \bar{\boldsymbol{x}} + \boldsymbol{d}^\top \bar{\boldsymbol{y}}^i \leq v^i, \quad \forall i = 1,\ldots,|V|, \tag{5.18d}$$

$$\bar{\boldsymbol{z}} \in U, \tag{5.18e}$$

$$\boldsymbol{B}^\top \boldsymbol{\lambda} = \boldsymbol{d}, \quad \boldsymbol{\lambda} \leq \boldsymbol{0}. \tag{5.18f}$$

The feasible sets for $\boldsymbol{\lambda}$ and $\{\bar{\boldsymbol{z}}, \bar{\boldsymbol{x}}, \bar{\boldsymbol{y}}, \bar{\boldsymbol{y}}^1, \ldots, \bar{\boldsymbol{y}}^{|V|}\}$ are disjoint, so this is indeed a disjoint bilinear optimization problem. Problem (5.18) can be solved using a variety of methods, we refer to Konno (1976), Nahapetyan (2009) and Zhen et al. (2021) for details. The mountain climbing heuristic can also be used for solving (5.18), possibly with different partitions of the set of variables than in (5.17). The partition for (5.17) with $\hat{\boldsymbol{y}}$ separate works best in our numerical experiments.

Lastly, the presented approach can also be applied to problems with uncertain $\boldsymbol{A}(\boldsymbol{z})$ and/or $\boldsymbol{c}(\boldsymbol{z})$. It would be interesting to investigate the numerical performance of the mountain climbing heuristic for those cases.

5.6 Numerical experiments

To demonstrate the value of PARO solutions in practice, we focus on one example problem in which (adaptive) robust optimization has been successfully applied: a facility location problem.

5.6.1 Setup

We will study a problem formulation with right-hand side uncertainty, and consider instances that are small enough so that the vertices of the uncertainty set can be enumerated. Thus, we can obtain an ARO solution $\boldsymbol{x}_{\text{ARO}}$ by defining a separate recourse variable for each vertex of the uncertainty set. Moreover, Algorithm 5.1 of Section 5.5.4 can be used; denote the approximate PARO solution by $\boldsymbol{x}_{\text{PARO}}$.

For comparison purposes, we also compute a PRO solution to (5.3) using the methodology of Iancu and Trichakis (2014, Theorem 1), which we repeat for convenience. Specifically, we plug in LDR $\boldsymbol{y}(\boldsymbol{z}) = \boldsymbol{w} + \boldsymbol{W}\boldsymbol{z}$, and obtain solution $(\boldsymbol{x}_1, \boldsymbol{w}_1, \boldsymbol{W}_1)$. Subsequently, we optimize for the nominal scenario $\bar{\boldsymbol{z}}$ whilst ensuring that performance in

other scenarios does not deteriorate, and feasibility is maintained:

$$\min_{\substack{x,w,W\\ x_2,w_2,W_2}} \quad c(\bar{z})^\top x_2 + d^\top (w_2 + W_2 \bar{z}), \tag{5.19a}$$

$$\text{s.t.} \quad c(z)^\top x_2 + d^\top (w_2 + W_2 z) \leq 0, \quad \forall z \in U, \tag{5.19b}$$

$$A(z)x + B(w + Wz) \leq r(z), \quad \forall z \in U, \tag{5.19c}$$

$$x = x_1 + x_2, w = w_1 + w_2, W = W_1 + W_2. \tag{5.19d}$$

Constraint (5.19d) states that the new solution equals the original solution (variables with subscript 1) plus an adaptation (variables with subscript 2). Constraint (5.19b) ensures that the adaptation does not deteriorate performance in any scenario, and the objective is to optimize performance in scenario $\bar{z}$. According to Iancu and Trichakis (2014, Theorem 1), the optimal solution for (x, w, W) is PRO to (5.3). Let x_{PRO} denote the optimal solution for x.

We compare the performance of the stage-1 (here-and-now) solutions x_{PARO}, x_{ARO} and x_{PRO}. For solutions x_{PARO} and x_{ARO} we use the optimal recourse decision. For x_{PRO} we report the results for two decision rules: (i) the optimal recourse decision, (ii) the LDR. We refer to the four objective values as *PARO*, *ARO*, *PRO* and *PRO(LDR)*. We compute the relative improvement (in %) of *PARO* over the other three objective values for three different cases:

Nominal: Relative improvement in nominal scenario $\bar{z}$.

Average: Average relative improvement over 10 uniform randomly sampled scenarios.

Maximum: Relative improvement in the scenario with the maximum performance difference between x_{ARO} and x_{PARO}. This scenario, which we denote z^*, is found by solving (5.17) with fixed $\hat{x} = x_{\text{ARO}}$ and $\bar{x} = x_{\text{PARO}}$.

All optimization problems are solved using Gurobi 9.0 (Gurobi Optimization LLC, 2020) with the dual simplex algorithm selected. We note that the influence of different solvers may also be investigated, but this is beyond the scope of this work.

During our numerical studies we found examples where Algorithm 5.1 was not able to improve upon the initial stage-1 solution x_{ARO}. This could occur if the initial x_{ARO} happens to be PARO. Or, it could occur if there is a unique ARO solution - after all, not every ARO instance has multiple worst-case optimal stage-1 solutions. The latter has been reported before in literature. De Ruiter et al. (2016) show that the multi-stage production-inventory model of Ben-Tal et al. (2004) has unique here-and-now decisions in almost all time periods, if LDRs are used. In that example, the reported

multiplicity of solutions is mainly due to non-PRO decision rule coefficients. We find that multiplicity of stage-1 solutions appears in particular when problem data is integer.

5.6.2 Problem description

Consider a strategic decision-making problem where a number of facilities are to be opened, in order to satisfy the demand of a number of customers. The goal is to choose the locations for opening a facility such that the cost for opening the facilities plus the transportation cost for satisfying demand is minimized. We consider this problem in a two-stage setting with uncertain demand. Thus, facility opening decisions need to be made in stage 1, before stage-2 demand is known.

Suppose there are n locations where a facility can be opened, and m demand locations. Let $\boldsymbol{x} \in \{0,1\}^n$ be a binary stage-1 decision variable denoting the facility opening decisions. Opening facility costs f_i and yields a capacity s_i, $i = 1,\dots,n$. Let $\boldsymbol{y} \in \mathcal{R}^{m,m\times n}$ be the stage-2 decision variable denoting transport from facility i to demand location j; let c_{ij} denote the associated costs, $i = 1,\dots,n$, $j = 1,\dots,m$. Let z_j denote the uncertain demand in location j. The two-stage facility location model reads

$$\min_{\boldsymbol{x},\boldsymbol{y}(\cdot)} \ \max_{\boldsymbol{z}\in U} \sum_{i=1}^{n}\sum_{j=1}^{m} c_{ij}y_{ij}(\boldsymbol{z}) + \sum_{i=1}^{n} f_i x_i, \tag{5.20a}$$

$$\text{s.t.} \ \sum_{i=1}^{n} y_{ij}(\boldsymbol{z}) \geq z_j, \ \ \forall \boldsymbol{z} \in U, \ \forall j = 1,\dots,m, \tag{5.20b}$$

$$\sum_{j=1}^{m} y_{ij}(\boldsymbol{z}) \leq s_i x_i, \ \ \forall \boldsymbol{z} \in U, \ \forall i = 1,\dots,m, \tag{5.20c}$$

$$y_{ij}(\boldsymbol{z}) \geq 0, \ \forall \boldsymbol{z} \in U, \ \ \forall i = 1,\dots,n, \ j = 1,\dots,m, \tag{5.20d}$$

$$\boldsymbol{x} \in \{0,1\}^n, \tag{5.20e}$$

with uncertainty set

$$U = \{\boldsymbol{z} : \sum_{j=1}^{m} z_j \leq \Gamma, \ l_j \leq z_j \leq u_j, \ \forall j = 1,\dots,m\}.$$

5.6.3 Data

We consider 1000 instances with $m = 8$ demand locations and $n = 20$ possible facility locations. Facility capacity s_i is set at 15 for each i. Other parameters are independently drawn from a discrete uniform distribution. Construction costs $\boldsymbol{f} \in \mathbb{R}^n$ are

drawn between 4 and 22. Entries of transportation cost matrix $\boldsymbol{C} \in \mathbb{R}^{n\times m}$ are drawn between 2 and 12.

We set lower and upper bound $l_j = 8$ and $u_j = 12$ for each demand location $j = 1,\dots,m$, and set maximum total demand $\Gamma = 90$. The nominal demand scenario is $\bar{z}_j = 10$ for all j. Note that $\bar{\boldsymbol{z}} \in \mathrm{ri}(U)$.

5.6.4 Results

Computing an ARO solution takes on average 10 seconds. Subsequently, Algorithm 5.1 performs 1 or 2 iterations (average 51 seconds) to find a (approximate) PARO solution.

For the worst-case scenario, *PRO(LDR)* and *PRO* are both within 0.72% of the optimum for all instances. In 28% of the instances the stage-1 solution $\boldsymbol{x}_{\mathrm{PARO}}$ differs from $\boldsymbol{x}_{\mathrm{ARO}}$ and/or $\boldsymbol{x}_{\mathrm{PRO}}$. Table 5.2 reports the median and maximum difference in ℓ_1-norm for these instances. This represents the number of different facilities that are opened. For example, an ℓ_1-norm of 2 indicates that one solution opened facility i and another solution opened facility j, or one solution opened both facilities i and j and the other solution opened neither. The total number of considered facility locations is $n = 20$, so the differences reported in Table 5.2 are substantial.

	$\|\boldsymbol{x}_{\mathrm{PARO}} - \boldsymbol{x}_{\mathrm{ARO}}\|_1$	$\|\boldsymbol{x}_{\mathrm{PARO}} - \boldsymbol{x}_{\mathrm{PRO}}\|_1$	$\|\boldsymbol{x}_{\mathrm{ARO}} - \boldsymbol{x}_{\mathrm{PRO}}\|_1$
median	0	1	1
max	7	8	9

Table 5.2: Total differences in stage-1 facility openings.

Figure 5.2 shows histograms of the relative objective value improvement of *PARO* over *ARO*, *PRO* and *PRO(LDR)* for the 28% of instances with different stage-1 decisions. Figure 5.2a show the improvement for maximum difference scenario $\boldsymbol{z}^*$, Figure 5.2b show the improvement for nominal scenario $\bar{\boldsymbol{z}}$ and Figure 5.2c show the improvement for 10 random scenarios in the uncertainty set. Table 5.3 details the minimum, median and maximum relative improvement.

The magnitude of differences is larger for scenario $\boldsymbol{z}^*$ than for the other two measures. In all cases the maximum relative improvement is substantial, but the median relative improvement is only minor in most cases. However, if the stage-1 solution represents a decision that is to be implemented in practice, even the possibility to get an improvement of a few percentage points warrants the extra effort to obtain a (approximate) PARO solution. We note that for *ARO* we use the first found ARO solution $\boldsymbol{x}_{\mathrm{ARO}}$; it is possible that there exists yet another ARO solution, for which the improve-

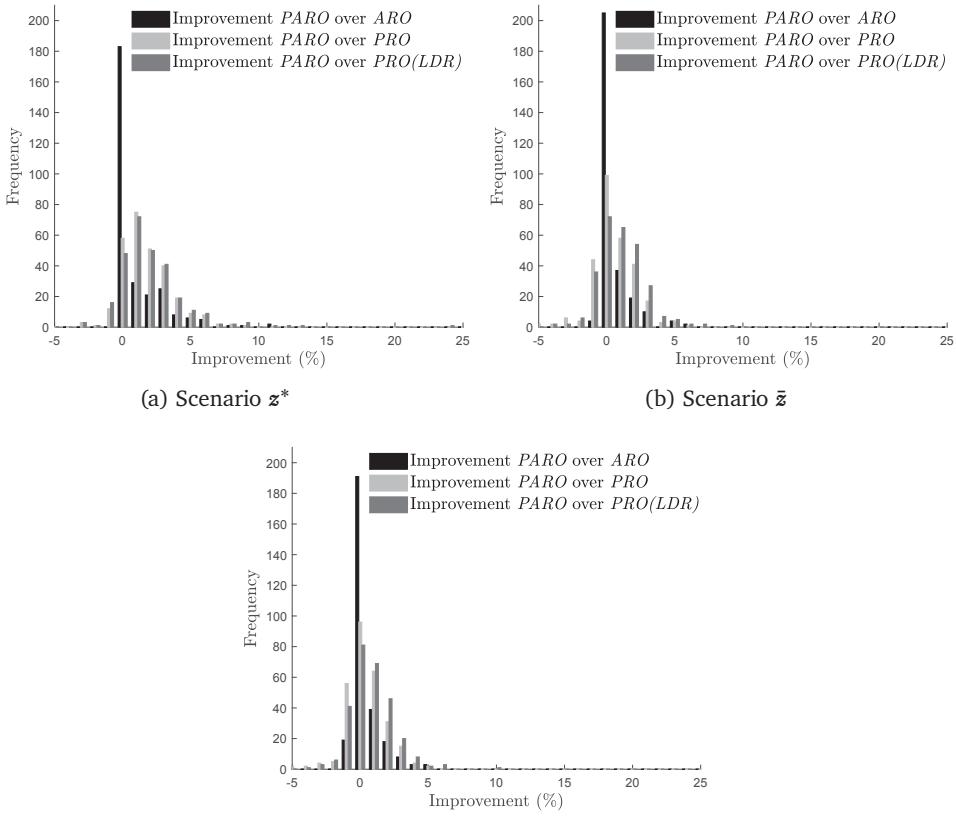

(a) Scenario $\boldsymbol{z}^*$

(b) Scenario $\bar{\boldsymbol{z}}$

(c) 10 Random scenarios

Figure 5.2: Histograms with relative improvement of PARO solution over alternative solutions for the facility location example.

ment percentages of *PARO* over *ARO* are larger than those reported in Table 5.3 and Figure 5.2.

The relative improvement of *PARO* over *PRO* is similar to that of *PARO* over *PRO(LDR)*, although the latter has slightly higher magnitude. Thus, reported differences are for a large part due to the different stage-1 decision, and for a small part due to the stage-2 decision rule. In some scenarios the relative improvement is negative (i.e., *PARO* has a worse objective value), although Figure 5.2 shows that for the large majority of instances the relative improvement is positive. For many instances

		Relative improvement (%)		
		PARO over *ARO*	*PARO* over *PRO*	*PARO* over *PRO(LDR)*
Scenario $\boldsymbol{z}^*$	minimum	0	-2.62	-2.62
	median	0	1.89	2.00
	maximum	11.2	9.48	24.2
Scenario $\bar{\boldsymbol{z}}$	minimum	-0.39	-4.89	-3.51
	median	0	0.77	1.35
	maximum	6.37	6.37	9.97
10 Random scenarios	minimum	-0.58	-4.65	-3.58
	median	0	0.71	1.15
	maximum	5.48	5.35	10.9

Table 5.3: Relative improvement of PARO solution over alternative solutions for the facility location example.

the relative difference between *PARO* and *ARO* is zero, i.e., a different stage-1 solution $\boldsymbol{x}$ does not always translate to a different performance on the three reported measures. Nevertheless, also compared to *ARO*, the maximum relative improvement of *PARO* can be substantial. Lastly, the results indicate a larger spread in objective value for *PRO* and *PRO(LDR)* than for *ARO*.

5.7 Conclusion

In this chapter, we dealt with Pareto efficiency in two-stage adjustable robust optimization problems. Similar to static robust optimization, the large majority of solution techniques focus only on worst-case optimality, and may yield solutions that are not Pareto efficient. To alleviate this, we introduced the concept of Pareto adjustable robustly optimal (PARO) solutions.[2]

Using FME as the predominant technique, we have analyzed the relation between PRO and PARO and investigated optimality of various decision rule structures in both worst-case and non-worst-case scenarios. We have shown the existence of PARO here-and-now decisions and shown that there exists a PWL decision rule that is PARO.

Moreover, we have provided several practical approaches to generate or approximate PARO solutions. Numerical experiments on a facility location example demon-

[2]For ARO problems, every non-PARO solution is dominated by a PARO solution, even if the former is Pareto robustly optimal (PRO), as defined by Iancu and Trichakis (2014).

strate that PARO solutions can significantly improve performance in non-worst-case scenarios over ARO and PRO solutions.

A potential direction for future research would be to further investigate constructive approaches to find or approximate PARO solutions. In particular, it would be valuable to have tractable algorithms for larger instances and/or more general classes of problems than the ones that can be tackled using the currently presented approaches.

5.A Technical lemmas and proofs

5.A.1 Bounds on eliminated adjustable variables

Lemma 5.36. *Let $\boldsymbol{x}$ be ARF to* (5.3)*. Let $\varphi_i(\boldsymbol{x},\boldsymbol{z}) = \boldsymbol{r}_i(\boldsymbol{z}) - \boldsymbol{a}_i(\boldsymbol{z})^\top \boldsymbol{x}$ for each constraint $i = 1,\dots,m$ of* (5.3b)*. Consider the system of inequalities $\boldsymbol{b}_i^\top \boldsymbol{y}(\boldsymbol{z}) \le \varphi_i(\boldsymbol{x},\boldsymbol{z})$, $i = 1,\dots,m$ and use FME to eliminate all variables. For all $k = 1,\dots,n_y$ we can write the bounds after elimination of variable $y_k(\boldsymbol{z})$ as*

$$\begin{aligned}\max_{S_k \in C_k^-} \Big\{ \sum_{p\in S_k} \alpha(S_k,p)\varphi_p(\boldsymbol{x},\boldsymbol{z}) - \sum_{l=k+1}^{n_y} \beta(S_k,l) y_l(\boldsymbol{z}) \Big\} \le y_k(\boldsymbol{z}) \\ \le \min_{T_k \in C_k^+} \Big\{ \sum_{q\in T} \alpha(T_k,q)\varphi_q(\boldsymbol{x},\boldsymbol{z}) - \sum_{l=k+1}^{n_y} \beta(T_k,l) y_l(\boldsymbol{z}) \Big\}, \quad \forall \boldsymbol{z} \in U,\end{aligned} \tag{5.A.1}$$

for some coefficients α and β independent of $\boldsymbol{z}$, and $C_k^-, C_k^+ \subseteq P(\{1,\dots,m\})$, with $P(\{1,\dots,m\})$ the power set of $\{1,\dots,m\}$. Additionally, if $S_k \in C_k^-$ for some k, then $\alpha(S_k,p) < 0$ for all $p \in S_k$. If $T_k \in C_k^+$ for some k, then $\alpha(T_k,q) > 0$ for all $q \in T_k$.

Proof. Proof by induction.

Base case:
Elimination of variable $y_1(\boldsymbol{z})$ yields

$$\max_{\{p:b_{p,1}<0\}} \Big\{ \frac{\varphi_p(\boldsymbol{x},\boldsymbol{z})}{b_{p,1}} - \frac{\sum_{l=2}^{n_y} b_{p,l} y_l(\boldsymbol{z})}{b_{p,1}} \Big\} \le y_1(\boldsymbol{z}) \le \min_{\{q:b_{q,1}>0\}} \Big\{ \frac{\varphi_q(\boldsymbol{x},\boldsymbol{z})}{b_{q,1}} - \frac{\sum_{l=2}^{n_y} b_{q,l} y_l(\boldsymbol{z})}{b_{q,1}} \Big\}. \tag{5.A.2}$$

Define

$$C_1^- = \{p \mid b_{p,1} < 0\}, \quad C_1^+ = \{q \mid b_{q,1} > 0\},$$

then each constraint in C_1^- defines a lower bound on $y_1(\boldsymbol{z})$ and each constraint in C_1^+ defines an upper bound on $y_1(\boldsymbol{z})$. Each element of C_1^- and C_1^+ is an individual 'original' constraint index and not a set of constraints indices. For all $S_1 = \{p\} \in C_1^-$ set $\alpha(S,p) = b_{p,1}^{-1}$, and for all

$T_1 = \{q\} \in C_1^+$ set $\alpha(T,q) = b_{q,1}^{-1}$. Furthermore, set $\beta(S_1,l) = b_{p,l}B_{p,1}^{-1}$ for all $S_1 = \{p\} \in C_1^- \cup C_1^+$ and all $l = 2,\dots,n_y$. With these definitions, (5.A.2) is reformulated in form (5.A.1). Additionally, by construction, $\alpha(S_1,p) < 0$ if $p \in S_1$, $S_1 \in C_1^-$ and $\alpha(T_1,q) > 0$ if $q \in T_1$, $T_1 \in C_1^+$.

Induction step:
Suppose the result holds for some $k-1$ (i.e., after elimination of variable $y_{k-1}(\boldsymbol{z})$). Variable $y_k(\boldsymbol{z})$ can occur in two types of constraints: (i) original constraints $i = 1,\dots,m$ that do not depend on $y_1(\boldsymbol{z}),\dots,y_{k-1}(\boldsymbol{z})$) and (ii) the new constraints acquired after elimination of $y_1(\boldsymbol{z}),\dots,y_{k-1}(\boldsymbol{z})$). For case (i), define

$$I_k^- = \{p \mid b_{p,k} < 0,\ b_{p,l} = 0,\ \forall l = 1,\dots,k-1\},$$
$$I_k^+ = \{p \mid b_{p,k} > 0,\ b_{p,l} = 0,\ \forall l = 1,\dots,k-1\},$$

then each constraint in I_k^- defines a lower bound on $y_k(\boldsymbol{z})$ and each constraint in I_k^+ provides an upper bound on $y_k(\boldsymbol{z})$. Reformulation to form (5.A.1) is similar to the case $k = 1$. Thus, $\alpha(S_k,p) < 0$ if $p \in S_k$, $S_k \in I_k^-$ and $\alpha(T_k,p) > 0$ if $p \in T_k$, $T_k \in I_k^+$.

For case (ii), $y_k(\boldsymbol{z})$ can occur in constraints resulting from picking linear lower and upper bounds on $y_l(\boldsymbol{z})$ from (5.A.1). If these bounds are independent of $y_{l+1}(\boldsymbol{z}),\dots,y_{k-1}(\boldsymbol{z})$, for $l = 1,\dots,k-1$, they are used directly to eliminate $y_k(\boldsymbol{z})$. For any such pair of constraints $S_l \in C_l^-$ and $T_l \in C_l^+$, FME yields the following bound on $y_k(\boldsymbol{z})$ (due to the induction assumption):

$$\sum_{p\in S_l} \alpha(S_l,p)\varphi_p(\boldsymbol{x},\boldsymbol{z}) - \sum_{q\in T_l} \alpha(T_l,q)\varphi_q(\boldsymbol{x},\boldsymbol{z}) - \sum_{l=k+1}^{n_y} y_l(\boldsymbol{z})\big(\beta(S_l,l) - \beta(T_l,l)\big) \le y_k(\boldsymbol{z})\big(\beta(S_l,k) - \beta(T_l,k)\big). \tag{5.A.3}$$

We proceed by dividing by the coefficient of $y_k(\boldsymbol{z})$. If $\beta(S_l,k) > \beta(T_l,k)$, inequality (5.A.3) defines a lower bound for $y_k(\boldsymbol{z})$; if $\beta(S_l,k) < \beta(T_l,k)$, inequality (5.A.3) defines an upper bound for $y_k(\boldsymbol{z})$. Define

$$J_k^- = \{S_k \mid \exists l = 1,\dots,k-1 \text{ s.t. } S_k = S_l \cup T_l,\ S_l \in C_l^-,\ T_l \in C_l^+,\ \beta(S_l,j) = \beta(T_l,j),\ \forall j < l,\ \beta(S_l,k) > \beta(T_l,k)\},$$
$$J_k^+ = \{T_k \mid \exists l = 1,\dots,k-1 \text{ s.t. } T_k = S_l \cup T_l,\ S_l \in C_l^-,\ T_l \in C_l^+,\ \beta(S_l,j) = \beta(T_l,j),\ \forall j < l,\ \beta(S_l,k) < \beta(T_l,k)\},$$

so each element S_k in J_k^- (or T_k in J_k^+) is a union of the indices of a lower bound constraint (set S_l) and an upper bound constraint (set T_l) on $y_l(\boldsymbol{z})$. The condition $\beta(S_l,j) = \beta(T_l,j),\ \forall j < l$ on the second line ensures that these lower and upper bound constraints on $y_l(\boldsymbol{z})$ do not specify a constraint on $y_{l+1}(\boldsymbol{z}),\dots,y_{k-1}(\boldsymbol{z})$.

Set the coefficients for the not yet eliminated variables $y_{k+1}(\boldsymbol{z}),\dots,y_{n_y}(\boldsymbol{z})$ for form (5.A.1) as

$$\beta(S_k,j) = \frac{\beta(S_l,j) - \beta(T_l,j)}{\beta(S_l,k) - \beta(T_l,k)},\ \forall j = k+1,\dots,n_y.$$

If $S_k \in J_k^-$, with $S_k = S_l \cup T_l$ for some $S_l \in C_l^-$ and $T_l \in C_l^+$, $l = 1, \ldots, k-1$, then set

$$\alpha(S_k, p) = \begin{cases} \dfrac{\alpha(S_l, p)}{\beta(S_l, k) - \beta(T_l, k)} & \text{if } p \in S_l,\ p \notin T_l, \\ \dfrac{\alpha(S_l, p) - \alpha(T_l, p)}{\beta(S_l, k) - \beta(T_l, k)} & \text{if } p \in S_l \cap T_l, \\ \dfrac{-\alpha(T_l, p)}{\beta(S_l, k) - \beta(T_l, k)} & \text{if } p \notin S_l,\ p \in T_l. \end{cases} \tag{5.A.4}$$

Similarly, if $T_k \in J_k^+$, with $T_k = S_l \cup T_l$ for some $S_l \in C_l^-$ and $T_l \in C_l^+$ for some $l = 1, \ldots, k-1$, then set

$$\alpha(T_k, p) = \begin{cases} \dfrac{\alpha(S_l, p)}{\beta(S_l, k) - \beta(T_l, k)} & \text{if } p \in S_l,\ p \notin T_l, \\ \dfrac{\alpha(S_l, p) - \alpha(T_l, p)}{\beta(S_l, k) - \beta(T_l, k)} & \text{if } p \in S_l, \cap T_l \\ \dfrac{-\alpha(T_l, p)}{\beta(S_l, k) - \beta(T_l, k)} & \text{if } p \notin S_l,\ p \in T_l. \end{cases} \tag{5.A.5}$$

Due to the induction hypothesis, $\alpha(S_l, p) < 0$ if $S_l \in C_l^-$ and $\alpha(T_l, p) > 0$ if $T_l \in C_l^+$ for $l < k$. The denominator in both lines of (5.A.4) is positive, so in that case $\alpha(S_k, p) < 0$. The denominator in both lines of (5.A.5) is negative, so in that case $\alpha(T_k, p) > 0$. With the new coefficients chosen as above, (5.A.3) provides a lower or upper bound on $y_{\hat{k}}(\boldsymbol{z})$ of the form inside the maximum or minimum operator in (5.A.1), respectively.

Finally, define $C_k^- = I_k^- \cup J_k^-$ and $C_k^+ = I_k^+ \cup J_k^+$. Each constraint in C_k^- defines a lower bound on $y_k(\boldsymbol{z})$ and each constraint in C_k^+ defines an upper bound on $y_k(\boldsymbol{z})$. Moreover, set $C_k = C_k^- \cup C_k^+$ contains all constraints after elimination of $y_1(\boldsymbol{z}), \ldots, y_{k-1}(\boldsymbol{z})$ that have $y_k(\boldsymbol{z})$ as lowest indexed adjustable variable. This completes the induction step. □

5.A.2 Proof Lemma 5.15

We consider only adjustable robust feasibility and not optimality, so the objective of P_{hybrid} can be ignored. According to Lemma 5.36, each adjustable variable $y_k(\boldsymbol{z})$, $k = 1, \ldots, n_y$ must satisfy bounds (5.A.1). For P_{hybrid} term $\varphi_i(\hat{\boldsymbol{z}}, \boldsymbol{z}_{(i)}) = r_i(\hat{\boldsymbol{z}}, \boldsymbol{z}_{(i)}) - \boldsymbol{a}_i(\hat{\boldsymbol{z}}, \boldsymbol{z}_{(i)})^\top \boldsymbol{x}$ depends only on $\hat{\boldsymbol{z}}$ and $\boldsymbol{z}_{(i)}$, for each $i = 1, \ldots, m$. Sets $\hat{U}$ and U^i are disjoint for each $i = 1, \ldots, m$ so this is equivalent to

$$\begin{aligned} \max_{S \in C_k^-} \Big\{ \sum_{p \in S} \max_{\boldsymbol{z}_{(p)} \in U^p} \big(\alpha(S, p) \varphi_p(\hat{\boldsymbol{z}}, \boldsymbol{z}_{(p)}) - \sum_{l=k+1}^{n_y} \beta(S, l) y_l(\boldsymbol{z}) \big) \Big\} &\le y_k(\boldsymbol{z}) \\ \le \min_{T \in C_k^+} \Big\{ \sum_{q \in T} \min_{\boldsymbol{z}_{(q)} \in U^q} \big(\alpha(T, q) \varphi_q(\hat{\boldsymbol{z}}, \boldsymbol{z}_{(q)}) - \sum_{l=k+1}^{n_y} \beta(T, l) y_l(\boldsymbol{z}) \big) \Big\}, &\quad \forall \hat{\boldsymbol{z}} \in \hat{U}. \end{aligned} \tag{5.A.6}$$

We proceed by backward induction. For $k = n_y$, i.e., the last eliminated variable, bounds (5.A.6) depend only on $\boldsymbol{z}$ and not on other adjustable variables. According to Lemma 5.36, each term $\varphi_i(\boldsymbol{z}_{(i)})$, $i = 1, \ldots, m$, appears in upper bounds with a positive coefficient and in lower bounds with a negative coefficient for all variables $y_1(\boldsymbol{z}), \ldots, y_{n_y}(\boldsymbol{z})$ (if it appears), or vice versa. Hence, the worst-case scenario for $\boldsymbol{z}_{(i)} \in U^i$ (in terms of feasibility) is equal for all linear terms in the lower and the upper bound for all $i = 1, \ldots, m$. Plugging in this worst-case scenario yields lower and upper bounds on $y_{n_y}(\boldsymbol{z})$ depending only on $\hat{\boldsymbol{z}}$. Thus, there exists a decision rule for $y_{n_y}(\cdot)$ that is a function of only the non-constraintwise uncertain parameters $\hat{\boldsymbol{z}}$.

Suppose that for some k the lower and upper bounds (5.A.6) for $y_k(\boldsymbol{z})$ depend only on $\hat{\boldsymbol{z}}$. Thus, there exists a decision rule for $y_k(\cdot)$ that is a function of only $\hat{\boldsymbol{z}}$. Plug this decision rule in the lower and upper bounds (5.A.6) for $y_{k-1}(\boldsymbol{z})$. Then, according to Lemma 5.36, each term $\varphi_i(\boldsymbol{z}_{(i)})$, $i = 1, \ldots, m$, appears in upper bounds with a positive coefficient and in lower bounds with a negative coefficient (if it appears), or vice versa. Hence, the worst-case scenario for $\boldsymbol{z}_{(i)} \in U^i$ (in terms of feasibility) is equal for all linear terms in the lower and the upper bound, for all $i = 1, \ldots, m$. Plugging in this worst-case scenario yields lower and upper bounds on $y_{k-1}(\boldsymbol{z})$ depending only on $\hat{\boldsymbol{z}}$. This completes the induction.

Let $\boldsymbol{y}(\hat{\boldsymbol{z}})$ be the decision rule resulting from the above procedure. Because $\boldsymbol{x}$ is ARF to P_{hybrid}, the resulting pair $(\boldsymbol{x}, \boldsymbol{y}(\hat{\boldsymbol{z}}))$ is ARF to P_{hybrid}.

5.A.3 Proof Corollary 5.16

We note that if (5.3) has hybrid uncertainty and the objective (5.3a) contains adjustable variables, it can equivalently be written as

$$\min_{t, \boldsymbol{x}, \boldsymbol{y}(\cdot)} \quad t, \tag{5.A.7a}$$

$$\text{s.t.} \quad \boldsymbol{c}(\hat{\boldsymbol{z}}, \boldsymbol{z}_{(0)})^\top \boldsymbol{x} + \boldsymbol{d}^\top \boldsymbol{y}(\boldsymbol{z}) \leq t \quad \forall (\hat{\boldsymbol{z}}, \boldsymbol{z}_{(0)}) \in \hat{U} \times U^0, \tag{5.A.7b}$$

$$\boldsymbol{a}_i(\hat{\boldsymbol{z}}, \boldsymbol{z}_{(i)})^\top \boldsymbol{x} + \boldsymbol{b}_i^\top \boldsymbol{y}(\boldsymbol{z}) \leq r_i(\hat{\boldsymbol{z}}, \boldsymbol{z}_{(i)}), \quad \forall (\hat{\boldsymbol{z}}, \boldsymbol{z}_{(i)}) \in \hat{U} \times U^i, \quad \forall i = 1, \ldots, m, \tag{5.A.7c}$$

where $t \in \mathbb{R}$ is an auxiliary here-and-now decision variable. Problem (5.A.7) also has hybrid uncertainty, and a pair $(\boldsymbol{x}, \boldsymbol{y}(\cdot))$ is ARO to (5.3) if and only if there exists a $t \in \mathbb{R}$ such that $(\boldsymbol{x}, \boldsymbol{y}(\cdot), t)$ is ARO to (5.A.7). Thus, in the remainder of the proof we can assume $\boldsymbol{d} = \boldsymbol{0}$, i.e., the objective is independent of adjustable variables.

According to Lemma 5.15, for any ARF $\boldsymbol{x}$ there exists a decision rule $\boldsymbol{y}(\cdot)$ that depends only on $\hat{\boldsymbol{z}}$ such that $(\boldsymbol{x}, \boldsymbol{y}(\cdot))$ is ARF to P_{hybrid}. Any $\boldsymbol{x}^*$ that is ARO to P_{hybrid} is also ARF to P_{hybrid}, so also for each ARO $\boldsymbol{x}^*$ there exists such a decision rule $\boldsymbol{y}^*(\cdot)$. The objective is independent of adjustable variables, so $(\boldsymbol{x}^*, \boldsymbol{y}(\cdot))$ is ARO for any ARF $\boldsymbol{y}(\cdot)$. Hence, $(\boldsymbol{x}^*, \boldsymbol{y}^*(\cdot))$ is ARO to P_{hybrid}.

5.A.4 Proof Lemma 5.19

We consider only adjustable robust feasibility and not optimality, so the objective of P_{block} can be ignored. Remove index 0 from its constraint set $K(v)$ (for some v). The set of constraints can be written as

$$\boldsymbol{a}_i(\boldsymbol{z}_{(v)})^\top \boldsymbol{x} + \boldsymbol{b}_i^\top \boldsymbol{y}_{(v)}(\boldsymbol{z}) \leq r_i(\boldsymbol{z}_{(v)}), \quad \forall \boldsymbol{z} \in U,\ \forall i \in K(v),\ \forall v = 1,\ldots,V.$$

Due to the block uncertainty structure, all adjustable variables can be eliminated by performing FME on each block v separately. According to Lemma 5.36, bounds on each adjustable variable $y_k(\boldsymbol{z})$ can be represented by (5.A.1). If for some $k = 1,\ldots,n_y$, variable $y_k(\boldsymbol{z})$ is an element of $\boldsymbol{y}_{(v)}(\boldsymbol{z})$ for some block v, any $S \in C_k^-$ or $T \in C_k^+$ is a subset of $K_{(v)}$, the original set of constraints for block v. The following two observations immediately follow for the given block v:

- For each $l = 1,\ldots,n_y$ the coefficient of $y_l(\boldsymbol{z})$ is zero if $y_l(\boldsymbol{z})$ is not an element of $\boldsymbol{y}_{(v)}$, i.e., $\beta(S,l) = 0$ for all $S \in C_k^- \cup C_k^+$.
- For any p in S or T it holds that $\varphi_p(\cdot)$ is a function of $\boldsymbol{z}_{(v)}$ only.

For $k = n_y$, i.e., the last eliminated variable, this implies the lower and upper bounds on $y_{n_y}()$ are independent of $\boldsymbol{z}_{(w)}$ for $w \neq v$, and any feasible decision rule can be written as a function of $\boldsymbol{z}_{(v)}$ only. Plugging any such decision rule in the lower and upper bounds for $k = n_y - 1$ yields the same result for $y_{n_y-1}()$. The final result follows from backward induction.

Let $\boldsymbol{y}(\boldsymbol{z})$ be the decision rule resulting from the above procedure. Because $\boldsymbol{x}$ is ARF to P_{block}, the resulting pair $(\boldsymbol{x}, \boldsymbol{y}(\boldsymbol{z}))$ is ARF to P_{block}.

5.A.5 Proof Lemma 5.22

We consider only adjustable robust feasibility and not optimality, so the objective of P_{simplex} can be ignored. According to Lemma 5.36, in the FME procedure the bounds on variable $y_k(\boldsymbol{z})$ are given by (5.A.1). It is sufficient to satisfy the bounds on $y_k(\boldsymbol{z})$ for all extreme points of uncertainty set U, so we can alternatively write:

$$\begin{aligned}\max_{S_k \in C_k^-} \Big\{ \sum_{p \in S_k} \alpha(S_k,p)\varphi_p(\boldsymbol{x},\boldsymbol{z}^j) - \sum_{l=k+1}^{n_y} \beta(S_k,l) y_l(\boldsymbol{z}^j) \Big\} \leq y_k(\boldsymbol{z}^j) \\ \leq \min_{T_k \in C_k^+} \Big\{ \sum_{q \in T} \alpha(T_k,q)\varphi_q(\boldsymbol{x},\boldsymbol{z}^j) - \sum_{l=k+1}^{n_y} \beta(T_k,l) y_l(\boldsymbol{z}^j) \Big\}, \quad \forall \boldsymbol{z}^j,\ j = 1,\ldots,L+1.\end{aligned} \tag{5.A.8}$$

For each $j = 1,\ldots,L+1$, let $l_k(\boldsymbol{z}^j)$ and $u_k(\boldsymbol{z}^j)$ denote the lower resp. upper bound on $y_k(\boldsymbol{z}^j)$ from (5.A.8). Affine independence of $\boldsymbol{z}^1,\ldots,\boldsymbol{z}^{L+1}$ implies linear independence of $(1,\boldsymbol{z}^1),\ldots,(1,\boldsymbol{z}^{L+1})$. Hence, by basic linear algebra, there exists exactly one $(a_0,\boldsymbol{a}) \in \mathbb{R} \times \mathbb{R}^L$ such that $a_0 + \boldsymbol{a}^\top \boldsymbol{z}^j = l(\boldsymbol{z}^j)$ for all $j = 1,\ldots,L+1$. Consider the LDR $y_k(\boldsymbol{z}) = a_0 + \boldsymbol{a}^\top \boldsymbol{z}$. Then

$l(\boldsymbol{z}^j) = y_k(\boldsymbol{z}^j) \leq u(\boldsymbol{z}^j)$ for all $j = 1, \ldots, L+1$. Hence, $y_k(\boldsymbol{z})$ is an LDR that satisfies bounds (5.A.8). Alternatively, one can construct an LDR that passes through points $(\boldsymbol{z}^j, u(\boldsymbol{z}^j))$ for all $j = 1, \ldots, L+1$, or any LDR that is a convex combination of the previous two LDRs.

Thus, we can construct a decision rule for $y_k(\boldsymbol{z})$ that is linear in $\boldsymbol{z}$. For all $k = 1, \ldots, n_y - 1$, this decision rule depends on $y_{k+1}(\boldsymbol{z}), \ldots, y_{n_y}(\boldsymbol{z})$. For variable $y_{n_y}(\cdot)$, the constructed decision rule is independent of other adjustable variables. Plugging this in the decision rule for $y_{n_y-1}(\cdot)$ yields a decision rule that is again independent of other adjustable variables, and still linear in $\boldsymbol{z}$ because the coefficient for $y_{n_y}(\boldsymbol{z})$ in $l_{n_y-1}(\boldsymbol{z})$ and $u_{n_y-1}(\boldsymbol{z})$ does not depend on $\boldsymbol{z}$ (fixed recourse). Continuing this procedure yields LDRs for all adjustable variables $y_1(\cdot), \ldots, y_{n_y}(\cdot)$.

Let $\boldsymbol{y}(\boldsymbol{z})$ be the decision rule resulting from the above procedure. Because $\boldsymbol{x}$ is ARF to P_{simplex}, the resulting pair $(\boldsymbol{x}, \boldsymbol{y}(\boldsymbol{z}))$ is ARF to P_{simplex}.

5.A.6 Proof Lemma 5.24

We first prove that the original problem (5.3) is equivalent to a convex PWL static RO problem; its proof uses Lemma 5.36.

Lemma 5.37. *If $(\boldsymbol{x}^*, \boldsymbol{y}^*(\cdot))$ is ARO to* (5.3)*, $\boldsymbol{y}^*(\cdot)$ satisfies*

$$\boldsymbol{d}^\top \boldsymbol{y}^*(\boldsymbol{z}) = \max_{(S,T)\in M} \{h_{S,T}(\boldsymbol{x}^*, \boldsymbol{z})\}, \quad \forall \boldsymbol{z} \in U, \tag{5.A.9}$$

and $\boldsymbol{x}^*$ is optimal to

$$\min_{\boldsymbol{x}\in\mathcal{X}_{FME}} \max_{\boldsymbol{z}\in U} \boldsymbol{c}(\boldsymbol{z})^\top \boldsymbol{x} + \max_{(S,T)\in M} \{h_{S,T}(\boldsymbol{x}, \boldsymbol{z})\}, \tag{5.A.10}$$

with

$$M = \{(S,T) \mid \exists k = 1, \ldots, n_y \text{ s.t. } S \in C_k^-, T \in C_k^+, \beta(S,l) = \beta(T,l),\ \forall l > k,\ 0 \in S \cup T\},$$

and linear functions

$$h_{S,T}(\boldsymbol{x}, \boldsymbol{z}) = \sum_{p\in S, p>0} \frac{\alpha(S,p)}{\alpha(T,0) - \alpha(S,0)} \varphi_p(\boldsymbol{x}, \boldsymbol{z}) - \sum_{q\in T, q>0} \frac{\alpha(T,q)}{\alpha(T,0) - \alpha(S,0)} \varphi_q(\boldsymbol{x}, \boldsymbol{z}),$$

and sets C^-, C^+, functions $\varphi(\cdot)$ and coefficients α and β defined as in Lemma 5.36. Conversely, if $\boldsymbol{x}^*$ is optimal to (5.A.10)*, there exists a $\boldsymbol{y}^*(\cdot)$ such that $(\boldsymbol{x}^*, \boldsymbol{y}^*(\cdot))$ is ARO to* (5.3)*, and any such $\boldsymbol{y}^*(\cdot)$ satisfies* (5.A.9)*.*

Proof of Lemma 5.37. Consider problem (5.3), with the objective moved to the constraints using epigraph variable $t \in \mathbb{R}$:

$$\min_{t, \boldsymbol{x}, \boldsymbol{y}(\cdot)} \quad t, \tag{5.A.11a}$$

$$\text{s.t.} \quad t \geq \boldsymbol{c}(\boldsymbol{z})^\top \boldsymbol{x} + \boldsymbol{d}^\top \boldsymbol{y}(\boldsymbol{z}), \quad \forall \boldsymbol{z} \in U, \tag{5.A.11b}$$

$$\boldsymbol{A}(\boldsymbol{z})\boldsymbol{x} + \boldsymbol{B}\boldsymbol{y}(\boldsymbol{z}) \leq \boldsymbol{r}(\boldsymbol{z}), \quad \forall \boldsymbol{z} \in U. \tag{5.A.11c}$$

Eliminate all adjustable variables in (5.A.11b)-(5.A.11c) via FME. Let $\varphi_0(\boldsymbol{x}, t, \boldsymbol{z}) = t - \boldsymbol{c}(\boldsymbol{z})^\top \boldsymbol{x}$. In notation of Lemma 5.36, FME is performed on

$$\boldsymbol{d}^\top \boldsymbol{y}(\boldsymbol{z}) \le \varphi_0(\boldsymbol{x}, t, \boldsymbol{z}), \tag{5.A.12a}$$
$$\boldsymbol{b}_i^\top \boldsymbol{y}(\boldsymbol{z}) \le \varphi_i(\boldsymbol{x}, t, \boldsymbol{z}), \ \forall i = 1, \dots, m, \tag{5.A.12b}$$

where the coefficient for t is zero in φ_i, $i = 1, \dots, m$. According to Lemma 5.36, after elimination of variable k, inequalities (5.A.1) hold. Suppose for some $S_k \in C_k^-$, $T_k \in C_k^+$ the upper and lower bounds on $y_k(\boldsymbol{z})$ do not depend on $y_{k+1}(\boldsymbol{z}), \dots, y_{n_y}(\boldsymbol{z})$. Then the following constraint is derived for the static robust optimization problem after completing the full FME procedure:

$$\sum_{p \in S_k} \alpha(S_k, p) \varphi_p(\boldsymbol{x}, t, \boldsymbol{z}) \le \sum_{q \in T_k} \alpha(T_k, q) \varphi_q(\boldsymbol{x}, t, \boldsymbol{z}), \ \ \forall \boldsymbol{z} \in U, \tag{5.A.13}$$

where $\varphi_p(\cdot)$ is a function of t only if $p = 0$. Constraints of the original system (5.A.11c) that are independent of adjustable variables can also be represented in form (5.A.13). Original constraints (5.A.11b) are part of a particular constraint in form (5.A.13) if and only if $0 \in S_k \cup T_k$ for some $S_k \in C_k^-$, $T_k \in C_k^+$, $k = 1, \dots, n_y$. Thus, problem (5.A.11) after FME can be written as

$$\min_{t, \boldsymbol{x}} \ t, \tag{5.A.14a}$$
$$\text{s.t.} \ \sum_{p \in S} \alpha(S, p) \varphi_p(\boldsymbol{x}, t, \boldsymbol{z}) \le \sum_{q \in T} \alpha(T, q) \varphi_q(\boldsymbol{x}, t, \boldsymbol{z}), \ \ \forall (S, T) \in M, \ \ \forall \boldsymbol{z} \in U, \tag{5.A.14b}$$
$$\sum_{p \in S} \alpha(S, p) \varphi_p(\boldsymbol{x}, t, \boldsymbol{z}) \le \sum_{q \in T} \alpha(T, q) \varphi_q(\boldsymbol{x}, t, \boldsymbol{z}), \ \ \forall (S, T) \in N, \ \ \forall \boldsymbol{z} \in U, \tag{5.A.14c}$$

with

$$M = \{(S, T) \mid \exists k = 1, \dots, n_y \text{ s.t. } S \in C_k^-, T \in C_k^+, \beta(S, l) = \beta(T, l), \ \forall l > k, \ 0 \in S \cup T\},$$
$$N = \{(S, T) \mid \exists k = 1, \dots, n_y \text{ s.t. } S \in C_k^-, T \in C_k^+, \beta(S, l) = \beta(T, l), \ \forall l > k, \ 0 \notin S \cup T\}.$$

In other words, we separated the constraints depending on t from the constraints not depending on t. From Lemma 5.36 one can see that (5.A.14c) is the result of performing FME on the set of constraints (5.A.12b), which are the constraints defining set $\mathcal{X}$. Thus, (5.A.14c) describes set $\mathcal{X}_{\text{FME}}$. Furthermore, if we define $\alpha(S, 0) = 0$ if $0 \notin S$ and $\gamma(T, 0) = 0$ if $0 \notin T$, constraint (5.A.14b) can be rewritten to

$$t \ge \boldsymbol{c}(\boldsymbol{z})^\top \boldsymbol{x} + \sum_{p \in S, p > 0} \frac{\alpha(S, p)}{\alpha(T, 0) - \alpha(S, 0)} \varphi_p(\boldsymbol{x}, t, \boldsymbol{z}) - \sum_{q \in T, q > 0} \frac{\alpha(T, q)}{\alpha(T, 0) - \alpha(S, 0)} \varphi_q(\boldsymbol{x}, t, \boldsymbol{z}) \quad \forall (S, T) \in M, \ \ \forall \boldsymbol{z} \in U, \tag{5.A.15}$$

because $\alpha(T, 0) > \alpha(S, 0)$ according to Lemma 5.36. Note that the coefficient for t is zero for all functions φ on the RHS. Thus, for fixed $\boldsymbol{z} \in U$, constraint (5.A.15) defines a lower bound

on epigraph variable t that is convex PWL in $\boldsymbol{x}$. Subsequently, we eliminate t and define

$$h_{S,T}(\boldsymbol{x},\boldsymbol{z}) := \sum_{p\in S, p>0} \frac{\alpha(S,p)}{\alpha(T,0)-\alpha(S,0)}\varphi_p(\boldsymbol{x},\boldsymbol{z}) - \sum_{q\in T, q>0} \frac{\alpha(T,q)}{\alpha(T,0)-\alpha(S,0)}\varphi_q(\boldsymbol{x},\boldsymbol{z}).$$

This yields the following problem equivalent to (5.A.14):

$$\min_{\boldsymbol{x}\in\mathcal{X}_{\text{FME}}} \max_{\boldsymbol{z}\in U} \boldsymbol{c}(\boldsymbol{z})^\top \boldsymbol{x} + \max_{(S,T)\in M} \{h_{S,T}(\boldsymbol{x},\boldsymbol{z})\}. \tag{5.A.16}$$

If $(\boldsymbol{x}^*, t^*, \boldsymbol{y}^*(\cdot))$ is optimal to (5.A.11), $\boldsymbol{x}^*$ is optimal to (5.A.16) with equal objective value. This implies that $\boldsymbol{y}^*(\cdot)$ satisfies

$$\boldsymbol{d}^\top \boldsymbol{y}^*(\boldsymbol{z}) = \max_{(S,T)\in M} \{h_{S,T}(\boldsymbol{x}^*,\boldsymbol{z})\}, \quad \forall \boldsymbol{z}\in U. \tag{5.A.17}$$

Conversely, if $\boldsymbol{x}^*$ is optimal to (5.A.16), there exists a $(t^*, \boldsymbol{y}^*(\cdot))$ such that $(\boldsymbol{x}^*, t^*, \boldsymbol{y}^*(\cdot))$ is optimal to (5.A.11) with equal objective value. This implies that any such $\boldsymbol{y}^*(\cdot)$ satisfies (5.A.17). Lastly, note that $\boldsymbol{x}^*$ is optimal to (5.3) if and only if there exists a $t^*\in\mathbb{R}$ such that $(t^*, \boldsymbol{x}^*)$ is optimal to (5.A.11). This completes the proof. □

The result of Lemma 5.37 is also illustrated in Example 5.10, where if auxiliary variable t is eliminated the resulting problem has a convex PWL objective. If the number of adjustable variables in (5.3) is small enough that full FME can be performed (order of magnitude: 20 adjustable variables (Zhen et al., 2018)), one can solve (5.10) via an epigraph formulation in order to obtain an ARO $\boldsymbol{x}$ to (5.3).

We are now in position to prove the result of Lemma 5.24.

Proof of Lemma 5.24. By Definition 5.8(i) a solution $\boldsymbol{x}^*$ is PARO to (5.3) if and only if

- There exists a $\boldsymbol{y}^*\in\mathcal{R}^{L,n_y}$ such that $(\boldsymbol{x}^*, \boldsymbol{y}^*(\cdot))$ is ARO to (5.3) and there does not exist a pair $(\bar{\boldsymbol{x}}, \bar{\boldsymbol{y}}(\cdot))$ that is ARO to (5.3) and the following conditions hold:

$$\begin{aligned} &\boldsymbol{c}(\boldsymbol{z})^\top \bar{\boldsymbol{x}} + \boldsymbol{d}^\top \bar{\boldsymbol{y}}(\boldsymbol{z}) \le \boldsymbol{c}(\boldsymbol{z})^\top \boldsymbol{x}^* + \boldsymbol{d}^\top \boldsymbol{y}^*(\boldsymbol{z}), \quad \forall \boldsymbol{z}\in U, \\ &\boldsymbol{c}(\tilde{\boldsymbol{z}})^\top \bar{\boldsymbol{x}} + \boldsymbol{d}^\top \bar{\boldsymbol{y}}(\tilde{\boldsymbol{z}}) < \boldsymbol{c}(\tilde{\boldsymbol{z}})^\top \boldsymbol{x}^* + \boldsymbol{d}^\top \boldsymbol{y}^*(\tilde{\boldsymbol{z}}), \quad \text{for some } \tilde{\boldsymbol{z}}\in U. \end{aligned} \tag{5.A.18}$$

By Lemma 5.37, this holds if and only if

- $\boldsymbol{x}^*$ is optimal to (5.10) and there exists a $\boldsymbol{y}^*\in\mathcal{R}^{L,n_y}$ such that

$$\boldsymbol{d}^\top \boldsymbol{y}^*(\boldsymbol{z}) = \max_{(S,T)\in M} \{h_{S,T}(\boldsymbol{x}^*,\boldsymbol{z})\} \quad \forall \boldsymbol{z}\in U, \tag{5.A.19}$$

  and there does not exist a $(\bar{\boldsymbol{x}}, \bar{\boldsymbol{y}})$ such that $\bar{\boldsymbol{x}}$ is optimal to (5.10) and $(\bar{\boldsymbol{x}}, \bar{\boldsymbol{y}}(\cdot))$ satisfies (5.A.19) and (5.A.18) holds.

Substituting (5.A.19) in (5.A.18) yields the following set of equivalent conditions:

- $\boldsymbol{x}^*$ is optimal to (5.10) and there does not exist another $\bar{\boldsymbol{x}}$ optimal to (5.10) such that

$$\boldsymbol{c}(\boldsymbol{z})^\top \bar{\boldsymbol{x}} + \max_{(S,T)\in M} \{h_{S,T}(\bar{\boldsymbol{x}}, \boldsymbol{z})\} \leq \boldsymbol{c}(\boldsymbol{z})^\top \boldsymbol{x}^* + \max_{(S,T)\in M} \{h_{S,T}(\boldsymbol{x}^*, \boldsymbol{z})\}, \quad \forall \boldsymbol{z} \in U,$$
$$\boldsymbol{c}(\bar{\boldsymbol{z}})^\top \bar{\boldsymbol{x}} + \max_{(S,T)\in M} \{h_{S,T}(\bar{\boldsymbol{x}}, \bar{\boldsymbol{z}})\} < \boldsymbol{c}(\bar{\boldsymbol{z}})^\top \boldsymbol{x}^* + \max_{(S,T)\in M} \{h_{S,T}(\boldsymbol{x}^*, \bar{\boldsymbol{z}})\}, \quad \text{for some } \bar{\boldsymbol{z}} \in U.$$

This statement holds if and only if $\boldsymbol{x}^*$ is PRO to (5.10), by Definition 5.2. □

5.A.7 Proof Theorem 5.26

First, we prove the existence of PRO solutions to a general class of static RO problems, with bounded feasible region $\mathcal{X}$.

Lemma 5.38. *Let $f : \mathbb{R}^n \times \mathbb{R}^L \mapsto \mathbb{R}$, with $f(\boldsymbol{x}, \boldsymbol{z})$ continuous in $\boldsymbol{z}$. Consider the static RO problem*

$$\min_{\boldsymbol{x}\in\mathcal{X}} \max_{\boldsymbol{z}\in U} f(\boldsymbol{x}, \boldsymbol{z}). \tag{5.A.20}$$

Let $U \subseteq \mathbb{R}^L$ be closed, convex with a nonempty relative interior. If (i) $\mathcal{X}$ is compact and $f(\boldsymbol{x}, \boldsymbol{z})$ continuous in $\boldsymbol{x}$ and/or (ii) $\mathcal{X}$ is a finite set, and additionally there exists an RO solution to (5.A.20)*, there also exists a PRO solution to* (5.A.20).

Proof of Lemma 5.38. Let $(\mathbb{R}^L, \mathcal{B}(\mathbb{R}^L))$ be a measurable space, with $\mathcal{B}(\mathbb{R}^L)$ the Borel σ-algebra. For fixed $\boldsymbol{x}$, function $f(\boldsymbol{x}, \boldsymbol{z})$ is continuous in $\boldsymbol{z}$, so it is measurable on closed subsets of $\mathbb{R}^L$, in particular set U. Define function $g : \mathbb{R}^n \mapsto \mathbb{R}$ with

$$g(\boldsymbol{x}) := \int_U f(\boldsymbol{x}, \boldsymbol{z}) dP(\boldsymbol{z}), \tag{5.A.21}$$

where P denotes a strictly positive probability measure on $\mathbb{R}^L$, such as the Gaussian measure. Because $0 \leq P(U) \leq P(\mathbb{R}^L) = 1$, the Lebesgue integral (5.A.21) assumes finite values for any $\boldsymbol{x}$. Hence, $f(\boldsymbol{x}, \boldsymbol{z})$ is Lebesgue-integrable in its second argument on measured space $(\mathbb{R}^L, \mathcal{B}(\mathbb{R}^L), P)$ for any $\boldsymbol{x}$ and g is well-defined.

We proceed by showing that an optimal solution to the following optimization problem is PRO to (5.A.20):

$$\min_{\boldsymbol{x}\in\mathcal{X}^{\text{RO}}} g(\boldsymbol{x}). \tag{5.A.22}$$

The remainder of the proof consists of two parts. First, we show that an optimal solution to (5.A.22) is always attained. Subsequently, we show that such an optimal solution is PRO to (5.A.20).

Part 1 (The optimum is attained):
We treat the two cases for $\mathcal{X}$ separately.

Case (i): Set $\mathcal{X}$ is compact and $f(\boldsymbol{x},\boldsymbol{z})$ continuous in $\boldsymbol{x}$. We show that g is continuous. Consider a sequence $\{\boldsymbol{x}_n\}_{n\in\mathbb{N}}$ converging to $\boldsymbol{x}$. By continuity of f in $\boldsymbol{x}$, $\lim_{n\to\infty} f(\boldsymbol{x}_n,\boldsymbol{z}) = f(\boldsymbol{x},\boldsymbol{z})$. Thus,

$$g(\boldsymbol{x}) = \int_U f(\boldsymbol{x},\boldsymbol{z})dP(\boldsymbol{z}) = \int_U \lim_{n\to\infty} f(\boldsymbol{x}_n,\boldsymbol{z})dP(\boldsymbol{z}). \tag{5.A.23}$$

Let $M > 0$ be such that $|f(\boldsymbol{x},\boldsymbol{z})| < M$, and define $h : \mathbb{R}^L \mapsto \mathbb{R}$ with $h(\boldsymbol{z}) = M$ for all $\boldsymbol{z}$. Then h is Lebesgue-integrable, and we can apply the dominated convergence theorem to switch the order of the limit and integration in (5.A.23) to obtain

$$g(\boldsymbol{x}) = \lim_{n\to\infty} \int_U f(\boldsymbol{x}_n,\boldsymbol{z})dP(\boldsymbol{z}) = \lim_{n\to\infty} g(\boldsymbol{x}_n),$$

Hence, $g(\boldsymbol{x})$ is continuous for each $\boldsymbol{x}\in\mathbb{R}^n$. Let $\mathcal{X}^{\mathrm{RO}}$ denote the set of robustly (worst-case) optimal solutions to (5.A.20). Then $\mathcal{X}^{\mathrm{RO}}$ is compact if $\mathcal{X}$ is compact. Problem (5.A.22) minimizes a continuous function over a compact domain, so, by the extreme value theorem, a minimum is always attained.

Case (ii): Set $\mathcal{X}$ is a finite set. Problem (5.A.22) minimizes $g(\boldsymbol{x})$ over a finite set, so the minimum is attained.

Part 2 (An optimal solution is PRO):
Let $\hat{\boldsymbol{x}}$ denote an optimal solution to (5.A.22). We proceed by showing via proof by contradiction that $\hat{\boldsymbol{x}}$ is PRO to (5.A.20). Suppose $\hat{\boldsymbol{x}}$ is not PRO to (5.A.20). Then there exists an $\bar{\boldsymbol{x}}\in\mathcal{X}^{\mathrm{RO}}$ such that

$$f(\bar{\boldsymbol{x}},\boldsymbol{z}) \le f(\hat{\boldsymbol{x}},\boldsymbol{z}), \quad \forall \boldsymbol{z}\in U,$$
$$f(\bar{\boldsymbol{x}},\tilde{\boldsymbol{z}}) < f(\hat{\boldsymbol{x}},\tilde{\boldsymbol{z}}), \quad \text{for some } \tilde{\boldsymbol{z}}\in U.$$

We proceed by showing that there must exist a ball contained in U with strictly positive measure where strict inequality holds. Let $\tilde{B}$ denote the ball with radius δ centered at $\tilde{\boldsymbol{z}}$:

$$\tilde{B} = \{\boldsymbol{z}\in\mathbb{R}^L : \|\boldsymbol{z}-\tilde{\boldsymbol{z}}\|_2 \le \delta\}.$$

By continuity of $f(\bar{\boldsymbol{x}},\boldsymbol{z}) - f(\hat{\boldsymbol{x}},\boldsymbol{z})$ w.r.t. $\boldsymbol{z}$, there exists a $\delta > 0$ such that for each $\boldsymbol{z}\in\tilde{B}$ it holds that $f(\bar{\boldsymbol{x}},\boldsymbol{z}) - f(\hat{\boldsymbol{x}},\boldsymbol{z}) < 0$. Note that $\tilde{\boldsymbol{z}}$ need not be in the relative interior of U. Hence, the ball $\tilde{B}$ need not be contained in U. Let $\tilde{\boldsymbol{z}}\in\mathrm{ri}(U)$. We construct a new scenario $\boldsymbol{z}^* = \theta\tilde{\boldsymbol{z}} + (1-\theta)\bar{\boldsymbol{z}}$. Because U is convex, $\boldsymbol{z}^*\in\mathrm{ri}(U)$ if $0\le\theta<1$ according to Rockafellar (1970, Theorem 6.1). Choosing $1-\delta\|\tilde{\boldsymbol{z}}-\bar{\boldsymbol{z}}\|_2^{-1} < \theta < 1$ ensures that $\boldsymbol{z}^*\in\mathrm{int}(\tilde{B})\cap\mathrm{ri}(U) = \mathrm{ri}(U\cap\tilde{B})$. Consider the ball B^* with radius $\epsilon > 0$ centered at $\boldsymbol{z}^*$:

$$B^* = \{\boldsymbol{z}\in\mathbb{R}^L : \|\boldsymbol{z}-\boldsymbol{z}^*\|_2 \le \epsilon\}.$$

For sufficiently small $\epsilon > 0$, it holds that $\boldsymbol{z} \in B^* \Rightarrow \boldsymbol{z} \in U \cap \bar{B}$. In other words, for such an ϵ, each point $\boldsymbol{z} \in B^*$ is in the uncertainty set U and is such that $f(\bar{\boldsymbol{x}}, \boldsymbol{z}) < f(\hat{\boldsymbol{x}}, \boldsymbol{z})$.

Finally, we consider the difference between $g(\bar{\boldsymbol{x}})$ and $g(\hat{\boldsymbol{x}})$ on U. Note that $|g(\boldsymbol{x})| < \infty$ for all $\boldsymbol{x}$. The following holds:

$$g(\bar{\boldsymbol{x}}) - g(\hat{\boldsymbol{x}}) = \int_{U \setminus B^*} f(\bar{\boldsymbol{x}}, \boldsymbol{z}) - f(\hat{\boldsymbol{x}}, \boldsymbol{z}) dP(\boldsymbol{z}) + \int_{B^*} f(\bar{\boldsymbol{x}}, \boldsymbol{z}) - f(\hat{\boldsymbol{x}}, \boldsymbol{z}) dP(\boldsymbol{z}).$$

The first integral is nonpositive since $f(\bar{\boldsymbol{x}}, \boldsymbol{z}) \leq f(\hat{\boldsymbol{z}}, \boldsymbol{z})$ for each $\boldsymbol{z} \in U \setminus B^*$. The second integral is strictly negative since $f(\bar{\boldsymbol{x}}, \boldsymbol{z}) < f(\hat{\boldsymbol{z}}, \boldsymbol{z})$ for $\boldsymbol{z} \in B^*$ and measure P is strictly positive, i.e., $P(B^*) > 0$. Hence, $g(\bar{\boldsymbol{x}}) < g(\hat{\boldsymbol{x}})$, contradicting the fact that $\hat{\boldsymbol{x}}$ is optimal to (5.A.22). □

The result of Theorem 5.26 immediately follows.

Proof of Theorem 5.26. By Lemma 5.24, it suffices to prove existence of a PRO solution to (5.10). Because $\mathcal{X} = \mathcal{X}_{\text{FME}}$, set $\mathcal{X}_{\text{FME}}$ is compact. By construction of (5.3), uncertainty set U is assumed to be convex, compact with a nonempty relative interior. Lastly, the objective function of (5.10) is continuous in $\boldsymbol{x}$ and $\boldsymbol{z}$. Hence, all conditions of Lemma 5.38 are satisfied, and existence of a PARO solution to (5.3) is guaranteed. □

5.A.8 Proof Lemma 5.28 via FME

Let $\boldsymbol{x}$ be ARF to (5.3). W.l.o.g., suppose in the FME procedure the adjustable variables are eliminated in the order $y_1, \ldots, y_{n_y}$, i.e., according to their index. Let $F_k(y_{k+1}(\boldsymbol{z}), \ldots, y_{n_y}(\boldsymbol{z}), \boldsymbol{z})$ denote the optimal decision rule for y_k as a function of the decision rules for the adjustable variables with higher index and the uncertain parameter $\boldsymbol{z}$. We prove by induction on $k = 1, \ldots, n_y$ that $F_k(y_{k+1}(\boldsymbol{z}), \ldots, y_{n_y}(\boldsymbol{z}), \boldsymbol{z})$ is jointly PWL in $y_{k+1}, \ldots, y_{n_y}$ and $\boldsymbol{z}$.

According to Lemma 5.36, we can write the bounds after elimination of variable $y_1(\boldsymbol{z})$ as

$$\begin{aligned}\max_{S \in C_1^-} \Big\{ \sum_{p \in S} \alpha(S,p) \varphi_p(\boldsymbol{z}) - \sum_{l=2}^{n_y} \beta(S,l) y_l(\boldsymbol{z}) \Big\} \leq y_1(\boldsymbol{z}) \\ \leq \min_{T \in C_1^+} \Big\{ \sum_{q \in T} \alpha(T,q) \varphi_q(\boldsymbol{z}) - \sum_{l=2}^{n_y} \beta(T,l) y_l(\boldsymbol{z}) \Big\}, \quad \forall \boldsymbol{z} \in U,\end{aligned}$$

for some coefficients α and β independent of $\boldsymbol{z}$. For fixed $y_2, \ldots, y_{n_y}$, $\boldsymbol{z}$ and $\boldsymbol{x}$, the highest possible contribution of y_1 to the objective value is achieved by setting y_1 equal to its upper bound if $d_1 < 0$, and equal to its lower bound if $d_1 > 0$. Thus, $F_1(y_2(\boldsymbol{z}), \ldots, y_{n_y}(\boldsymbol{z}), \boldsymbol{z})$ is equal to either the upper or the lower bound on y_1. Both the upper and lower bound are jointly PWL in y_i, $i = 2, \ldots, n_y$ and $\boldsymbol{z}$.

Now, suppose that for each $i = 1, \ldots, k-1$, after elimination of variable $y_i(\boldsymbol{z})$ the optimal decision rule $F_i(y_{i+1}(\boldsymbol{z}), \ldots, y_{n_y}(\boldsymbol{z}), \boldsymbol{z})$ is jointly PWL in $y_{i+1}, \ldots, y_{n_y}$.

After elimination of $y_k(\boldsymbol{z})$ we can again write the bounds according to Lemma 5.36. For fixed $y_{k+1},\dots,y_{n_y}$, $\boldsymbol{z}$ and $\boldsymbol{x}$, the highest possible contribution of y_k to the objective value is achieved by minimizing $\boldsymbol{d}^\top \boldsymbol{y}$, i.e., solving

$$\begin{aligned}\min_{y_k}\ & \sum_{i=1}^{k-1} d_i F_i(F_{i+1}(\dots),\dots,F_{k-1}(y_k(\boldsymbol{z}),\dots,y_{n_y}(\boldsymbol{z}),\boldsymbol{z}),y_k(\boldsymbol{z}),\dots,y_{n_y}(\boldsymbol{z}),\boldsymbol{z}) \\ & + d_k y_k(\boldsymbol{z}) + \sum_{i=k+1}^{n_y} d_i y_i(\boldsymbol{z}),\end{aligned} \tag{5.A.24a}$$

$$\text{s.t.}\ \max_{S\in C_k^-}\Big\{\sum_{p\in S}\alpha(S,p)\varphi_p(\boldsymbol{z}) - \sum_{l=k+1}^{n_y}\beta(S,l)y_l(\boldsymbol{z})\Big\} \le y_k(\boldsymbol{z}), \tag{5.A.24b}$$

$$\min_{T\in C_k^+}\Big\{\sum_{q\in T}\alpha(T,q)\varphi_q(\boldsymbol{z}) - \sum_{l=k+1}^{n_y}\beta(T,l)y_l(\boldsymbol{z})\Big\} \ge y_k(\boldsymbol{z}), \tag{5.A.24c}$$

where the last term in the objective (the last summation) may be dropped because it does not depend on y_k. In the objective each decision rule F_i, $i=1,\dots,k-1$, is a function of the decision rules $F_{i+1},\dots,F_{k-1}$, variables $y_k(\boldsymbol{z}),\dots,y_{n_y}(\boldsymbol{z})$ and $\boldsymbol{z}$. Plugging in a PWL argument in a PWL function retains the piecewise linear structure. Thus, (5.A.24) asks to minimize a univariate PWL function on a closed interval. The optimum is attained at either an interior point or a boundary point; we consider these cases separately.

- Problem (5.A.24) has a boundary minimum. The minimum is attained at either the lower or upper bounds provided by (5.A.24b) and (5.A.24c). In this case, the function $F_k(y_{k+1}(\boldsymbol{z}),\dots,y_{n_y}(\boldsymbol{z}),\boldsymbol{z})$ is clearly jointly PWL in $y_{k+1}(\boldsymbol{z}),\dots,y_{n_y}(\boldsymbol{z})$ and $\boldsymbol{z}$.
- Problem (5.A.24) has an interior minimum. The unrestricted minimum of (5.A.24a) is at the intersection of two functions that are jointly linear in $y_k,\dots,y_{n_y}$ and $\boldsymbol{z}$. Any intersection point can be expressed as

  $$s_0(\boldsymbol{z}) + \sum_{i=k}^{n_y} s_i y_i(\boldsymbol{z}) = t_0(\boldsymbol{z}) + \sum_{i=k}^{n_y} t_i y_i(\boldsymbol{z}),$$

  for some scalars $s_0(\boldsymbol{z})$ and $t_0(\boldsymbol{z})$ depending linearly on $\boldsymbol{z}$ and some vectors $\boldsymbol{s},\boldsymbol{t}\in\mathbb{R}^{n_y-k}$. This is equivalent to

  $$y_k(\boldsymbol{z}) = \frac{s_0(\boldsymbol{z}) - t_0(\boldsymbol{z}) + \sum_{i=k+1}^{n_y}(s_i-t_i)y_i(\boldsymbol{z})}{t_k - s_k},$$

  and this is jointly linear in $y_k,\dots,y_{n_y}$ and $\boldsymbol{z}$. The pair $\{(s_0(\boldsymbol{z}),\boldsymbol{s}),(t_0(\boldsymbol{z}),\boldsymbol{t})\}$ that defines the interior minimum intersection point depends on $y_k,\dots,y_{n_y}$ and $\boldsymbol{z}$. Thus, the optimal decision rule $F_k(y_{k+1}(\boldsymbol{z}),\dots,y_{n_y}(\boldsymbol{z}),\boldsymbol{z})$ is a PWL function of $y_{k+1},\dots,y_{n_y}$ and $\boldsymbol{z}$.

This completes the induction step. Lastly, note that $F_{n_y}(\boldsymbol{z})$ is PWL in $\boldsymbol{z}$ and that plugging in a PWL argument in a PWL function retains the piecewise linear structure. Thus, going from $k = n_y$ to $k = 1$ and for each k plugging in $F_k(y_{k+1}(\boldsymbol{z}), \ldots, y_{n_y}(\boldsymbol{z}), \boldsymbol{z})$ in $F_{k-1}(y_k(\boldsymbol{z}), \ldots, y_{n_y}(\boldsymbol{z}), \boldsymbol{z})$ yields decision rules that are PWL in $\boldsymbol{z}$ for all variables $y_1, \ldots, y_{n_y}$.

5.A.9 Proof Lemma 5.28 via linear optimization

Let $\boldsymbol{x}$ be ARF to (5.3). We make use of the concept of basic solutions in linear optimization (Bertsimas and Tsitsiklis, 1997). In standard form the remaining problem for $\boldsymbol{y}$ for fixed $\boldsymbol{z}$, reads:

$$\min_{\boldsymbol{y}^+, \boldsymbol{y}^-, \boldsymbol{s}} \quad \boldsymbol{d}^\top \big(\boldsymbol{y}^+ - \boldsymbol{y}^-\big), \tag{5.A.25a}$$

$$\text{s.t.} \quad \boldsymbol{B}\big(\boldsymbol{y}^+ - \boldsymbol{y}^-\big) + \boldsymbol{s} = \boldsymbol{r}(\boldsymbol{z}) - \boldsymbol{A}(\boldsymbol{z})\boldsymbol{x}, \tag{5.A.25b}$$

$$\boldsymbol{y}^+, \boldsymbol{y}^-, \boldsymbol{s} \geq \boldsymbol{0}, \tag{5.A.25c}$$

where $\boldsymbol{s}$ is a slack variable and $\boldsymbol{y}$ is represented by the difference of two nonnegative variables. Let $\boldsymbol{v} \in \mathbb{R}^{2n_y+m}$, $\boldsymbol{M} \in \mathbb{R}^{m \times (2n_y+m)}$ and $\boldsymbol{f} \in \mathbb{R}^{2n_y+m}$ denote the vector of decision variables, the equality constraint matrix and the objective vector of (5.A.25), respectively:

$$\boldsymbol{v} = [\boldsymbol{y}^+ \ \boldsymbol{y}^- \ \boldsymbol{s}]^\top, \ \boldsymbol{M} = [\boldsymbol{B} \ -\boldsymbol{B} \ \boldsymbol{I}], \ \boldsymbol{f} = [\boldsymbol{d} \ -\boldsymbol{d} \ \boldsymbol{0}]^\top.$$

Each basis is represented by m linearly independent columns of $\boldsymbol{M}$. Let $\boldsymbol{W} \in \mathbb{R}^{m \times m}$ denote a basis matrix, and let $\boldsymbol{v}_W$ and $\boldsymbol{f}_\mathrm{W}$ denote the components of $\boldsymbol{v}$ and $\boldsymbol{f}$ corresponding to the basic variables. For any basic solution $\boldsymbol{v}$ it holds that

$$\boldsymbol{v}_W = \boldsymbol{W}^{-1}\big(\boldsymbol{r}(\boldsymbol{z}) - \boldsymbol{A}(\boldsymbol{z})\boldsymbol{x}\big), \tag{5.A.26}$$

and the remaining non-basic components of $\boldsymbol{v}$ are equal to zero. Denote the basic solution by $(\boldsymbol{v}_W, \boldsymbol{0}_{\setminus W})$; it is a basic feasible solution (BFS) to (5.A.25) if and only if $\boldsymbol{v}_W \geq \boldsymbol{0}$. For optimality of $(\boldsymbol{v}_W, \boldsymbol{0}_{\setminus W})$ it is additionally required that the reduced costs are nonnegative. Nonnegativity of the reduced costs (i.e., optimality of $(\boldsymbol{v}_W, \boldsymbol{0}_{\setminus W})$) reads

$$\boldsymbol{f} - \boldsymbol{f}_\mathrm{W}^\top \boldsymbol{W}^{-1} \boldsymbol{M} \geq \boldsymbol{0}. \tag{5.A.27}$$

We restrict ourselves to those basic solutions for which optimality condition (5.A.27) holds, note that this condition is independent of $\boldsymbol{z}$. It follows that for each basis matrix $\boldsymbol{W}$ that satisfies (5.A.27), it associated basic solution $(\boldsymbol{v}_W, \boldsymbol{0}_{\setminus W})$ is feasible (and optimal) if and only if $\boldsymbol{z}$ is in the following subset of U:

$$U_W(\boldsymbol{x}) = \{\boldsymbol{z} \in U \ : \ \boldsymbol{W}^{-1}\big(\boldsymbol{r}(\boldsymbol{z}) - \boldsymbol{A}(\boldsymbol{z})\boldsymbol{x}\big) \geq \boldsymbol{0}\}.$$

Let $\boldsymbol{y}(\boldsymbol{x}, \boldsymbol{z}, \boldsymbol{W})$ denote the basic solution corresponding to $\boldsymbol{W}$ in terms of the original variables $\boldsymbol{y}$. From (5.A.26) it follows that $\boldsymbol{y}(\boldsymbol{x}, \boldsymbol{z}, \boldsymbol{W})$ is linear in $\boldsymbol{z}$.

Any basic solution to (5.A.25) corresponds with at least one basis, and each basis is represented by m linearly independent columns of $\boldsymbol{M}$. Thus, there are at most $\beta = \binom{2n_y+m}{m}$ bases (i.e., matrices $\boldsymbol{W}$) to (5.A.25) that satisfy (5.A.27), independent of $\boldsymbol{z}$. Number the matrices $\boldsymbol{W}_1, \ldots, \boldsymbol{W}_\beta$. Each of these matrices $\boldsymbol{W}_j$ has its own LDR $\boldsymbol{y}(\boldsymbol{x}, \boldsymbol{z}, \boldsymbol{W}_j)$ that is optimal for all $\boldsymbol{z} \in U_{\boldsymbol{W}_j}(\boldsymbol{x})$.

Because $\boldsymbol{x}$ is ARF to (5.3) and (5.3) has a finite optimal objective value, problem (5.A.25) is feasible and has a finite optimum for all $\boldsymbol{z} \in U$. Therefore, there exists an optimal basic feasible solution for all $\boldsymbol{z} \in U$, and the union of all $U_{\boldsymbol{W}_i}$ equals U itself. This implies that, for the given $\boldsymbol{x}$, the following PWL decision rule is optimal for each $\boldsymbol{z} \in U$:

$$\boldsymbol{y}(\boldsymbol{z}) = \boldsymbol{y}(\boldsymbol{x}, \boldsymbol{z}, \boldsymbol{W}_{i^*}) \text{ if } i^* = \min\{i : \boldsymbol{z} \in U_{\boldsymbol{W}_i}(\boldsymbol{x})\}.$$

Note that a different numbering of the matrices gives a (possibly) different optimal PWL decision rule. In essence, the proof performs sensitivity analysis on the right-hand side vectors of (5.A.25), which is the only term in (5.A.25) that depends on $\boldsymbol{z}$.

5.A.10 Proof Theorem 5.30

Let OPT denote the optimal (worst-case) objective value of P. By Definition 5.8(i), and using that $\boldsymbol{d} = \boldsymbol{0}$, a solution $\boldsymbol{x}^*$ is PARO to P if and only if the following statement holds:

- There exists a $\boldsymbol{y}^* \in \mathcal{R}^{L,n_y}$ such that $(\boldsymbol{x}^*, \boldsymbol{y}^*(\cdot))$ is ARO to P and there does not exist a pair $(\bar{\boldsymbol{x}}, \bar{\boldsymbol{y}}(\cdot))$ that is ARO to P and

$$\begin{aligned} &\boldsymbol{c}(\boldsymbol{z})^\top \bar{\boldsymbol{x}} \leq \boldsymbol{c}(\boldsymbol{z})^\top \boldsymbol{x}^*, \quad \forall \boldsymbol{z} \in U, \\ &\boldsymbol{c}(\tilde{\boldsymbol{z}})^\top \bar{\boldsymbol{x}} < \boldsymbol{c}(\tilde{\boldsymbol{z}})^\top \boldsymbol{x}^*, \quad \text{for some } \tilde{\boldsymbol{z}} \in U. \end{aligned} \tag{5.A.28}$$

By definition of set $\mathcal{X}$, this holds if and only if

- $\boldsymbol{x}^* \in \mathcal{X}$, $\text{OPT} = \max_{\boldsymbol{z} \in U} \boldsymbol{c}(\boldsymbol{z})^\top \boldsymbol{x}^*$ and there does not exist an $\bar{\boldsymbol{x}} \in \mathcal{X}$ such that $\text{OPT} = \max_{\boldsymbol{z} \in U} \boldsymbol{c}(\boldsymbol{z})^\top \bar{\boldsymbol{x}}$ and (5.A.28) holds.

Because for any ARF $\boldsymbol{x}$ there exists an ARF decision rule $\boldsymbol{y}(\cdot)$ such that $\boldsymbol{y}(\boldsymbol{z}) = f_{\boldsymbol{w}}(\boldsymbol{z})$ for some $\boldsymbol{w}$, it follows that $\mathcal{X}$ is equal to

$$\mathcal{X}_f = \{\boldsymbol{x} \in \mathbb{R}^{n_x} \mid \exists \boldsymbol{w} \in \mathbb{R}^p : \boldsymbol{A}(\boldsymbol{z})\boldsymbol{x} + \boldsymbol{B} f_{\boldsymbol{w}}(\boldsymbol{z}) \leq \boldsymbol{r}(\boldsymbol{z}), \quad \forall \boldsymbol{z} \in U\},$$

which is the set of feasible $\boldsymbol{x}$ when stage-2 decision rules are restricted to be of form $f_{\boldsymbol{w}}(\boldsymbol{z})$. Hence, the previous set of conditions holds if and only if

- $\boldsymbol{x}^* \in \mathcal{X}_f$, $\text{OPT} = \max_{\boldsymbol{z} \in U} \boldsymbol{c}(\boldsymbol{z})^\top \boldsymbol{x}^*$ and there does not exist an $\bar{\boldsymbol{x}} \in \mathcal{X}$ such that $\text{OPT} = \max_{\boldsymbol{z} \in U} \boldsymbol{c}(\boldsymbol{z})^\top \bar{\boldsymbol{x}}$ and (5.A.28) holds.

Parameters $\boldsymbol{w}$ are now stage-1 decision variables, so $\mathcal{X}_f$ does not contain adjustable variables. The set of conditions describes a PRO solution to the static robust optimization problem obtained after plugging in decision rule structure $f_{\boldsymbol{w}}(\cdot)$.

5.A.11 Proof Corollary 5.31

Corollary 5.31(i): For any vector of parameters $\boldsymbol{w} \in \mathbb{R}^p$, let $f_{\boldsymbol{w}}(\hat{\boldsymbol{z}})$ denote a decision rule that depends only on $\hat{\boldsymbol{z}} \in \hat{U}$, the non-constraintwise component of uncertain parameter $\boldsymbol{z}$. From Lemma 5.15 it follows that $\mathcal{X}$ is equal to

$$\mathcal{X}_{\text{hybrid}} = \{\boldsymbol{x} \in \mathbb{R}^{n_x} \mid \exists \boldsymbol{w} \in \mathbb{R}^p : \boldsymbol{A}(\boldsymbol{z})\boldsymbol{x} + \boldsymbol{B} f_{\boldsymbol{w}}(\hat{\boldsymbol{z}}) \leq \boldsymbol{r}(\boldsymbol{z}), \ \ \forall \boldsymbol{z} \in U\},$$

i.e., the feasible region for $\boldsymbol{x}$ remains unchanged if all adjustable variables are restricted to depend only on the non-constraintwise component of $\boldsymbol{z}$. Hence, setting $X_f = \mathcal{X}_{\text{hybrid}}$ in the proof of Theorem 5.30 yields the result.

Corollary 5.31(ii): For each block $v = 1, \ldots, V$, let $\boldsymbol{w}(v) \in \mathbb{R}^{p(v)}$ denote a vector of parameters and let $f^v_{\boldsymbol{w}(v)}(\boldsymbol{z}_{(v)})$ denote a decision rule that depends only on $\boldsymbol{z}_{(v)}$, the uncertain parameters in block v. From Lemma 5.19 it follows that $\mathcal{X}$ is equal to

$$\mathcal{X}_{\text{block}} = \Big\{\boldsymbol{x} \in \mathbb{R}^{n_x} \mid \forall v = 1, \ldots, V, \ \exists \boldsymbol{w}(v) \in \mathbb{R}^{p(v)} : \\ \boldsymbol{a}_i(\boldsymbol{z}_{(v)})^\top \boldsymbol{x} + \boldsymbol{b}_i^\top f^v_{\boldsymbol{w}(v)}(\boldsymbol{z}_{(v)}) \leq r_i(\boldsymbol{z}_{(v)}), \ \ \forall \boldsymbol{z} \in U^v, \ \forall i \in K(v)\Big\},$$

i.e., the feasible region for $\boldsymbol{x}$ remains unchanged if all adjustable variables are restricted to depend only on uncertain parameters in their own block. Hence, setting $X_f = \mathcal{X}_{\text{block}}$ in the proof of Theorem 5.30 yields the result.

Corollary 5.31(iii): From Lemma 5.22 it follows that for simplex uncertainty $\mathcal{X}$ is equal to

$$\mathcal{X}_{\text{simplex}} = \{\boldsymbol{x} \in \mathbb{R}^{n_x} \mid \exists \boldsymbol{u} \in \mathbb{R}^{n_y}, \ \boldsymbol{V} \in \mathbb{R}^{n_y \times L} : \boldsymbol{A}(\boldsymbol{z})\boldsymbol{x} + \boldsymbol{B}(\boldsymbol{u} + \boldsymbol{V}\boldsymbol{z}) \leq \boldsymbol{r}(\boldsymbol{z}), \ \ \forall \boldsymbol{z} \in U\},$$

i.e., the feasible region for $\boldsymbol{x}$ remains unchanged if all adjustable variables are restricted to depend affinely on $\boldsymbol{z}$. Hence, setting $X_f = \mathcal{X}_{\text{simplex}}$ in the proof of Theorem 5.30 yields the result.

5.A.12 Proof Lemma 5.32

The two cases are considered separately.

- *Optimal objective value is zero*: Proof by contradiction. Suppose $\tilde{\boldsymbol{y}}(\cdot)$ is not a PARO extension of $\tilde{\boldsymbol{x}}$. Then, by Definition 5.9, there exists a $\bar{\boldsymbol{y}}(\cdot)$ such that $(\tilde{\boldsymbol{x}}, \bar{\boldsymbol{y}}(\cdot))$ is ARO to (5.3) and for some $\bar{\boldsymbol{z}} \in U$ it holds that

  $$\boldsymbol{c}(\bar{\boldsymbol{z}})^\top \tilde{\boldsymbol{x}} + \boldsymbol{d}^\top \tilde{\boldsymbol{y}}(\bar{\boldsymbol{z}}) > \boldsymbol{c}(\bar{\boldsymbol{z}})^\top \tilde{\boldsymbol{x}} + \boldsymbol{d}^\top \bar{\boldsymbol{y}}(\bar{\boldsymbol{z}}).$$

  However, then $(\boldsymbol{z}, \boldsymbol{y}) = (\bar{\boldsymbol{z}}, \bar{\boldsymbol{y}}(\bar{\boldsymbol{z}}))$ is feasible to (5.13) with positive objective value. This is a contradiction.

- *Optimal objective value is positive*: Let (z^*, y^*) denote the optimal solution to (5.13) and let v^* denote the optimal objective value. The decision rule

$$y(z) = \begin{cases} \tilde{y}(z) & \text{if } z \neq z^* \\ y^* & \text{otherwise,} \end{cases}$$

dominates the decision rule $\tilde{y}(\cdot)$, so the latter is not PARO. We prove the last part of the lemma by contradiction. Suppose there exists a scenario $\bar{z}$ and a decision $\bar{y}$ such that

$$\begin{aligned} \left(c(\bar{z})^\top \tilde{x} + d^\top \tilde{y}(\bar{z})\right) - \left(c(\bar{z})^\top \tilde{x} + d^\top \bar{y}\right) > v^*, \\ A(\bar{z})\tilde{x} + B\bar{y} \leq r(\bar{z}), \end{aligned}$$

i.e., $\bar{y}$ is a feasible wait-and-see decision for scenario $\bar{z}$, and the resulting objective value of $\tilde{y}(\bar{z})$ exceeds that of $\bar{y}$ by more than v^*. Then $(\bar{z}, \bar{y})$ is feasible to (5.13) with a strictly better objective value than v^*. This is a contradiction.

5.A.13 Proof Lemma 5.34

Proof by contradiction, analogous to proof of Theorem 1 of Iancu and Trichakis (2014). Because U is the convex hull of $z^1, \ldots, z^N$, (5.16b) and (5.16c) ensure that $\bar{x}$ is ARO to (5.3) (with $d = 0$). Suppose $\bar{x}$ is not PARO to (5.3). According to Definition 5.8(i) there exists an $\hat{x}$ that is ARO to (5.3) and

$$\begin{aligned} &c(z)^\top \hat{x} \leq c(z)^\top \bar{x}, \quad \forall z \in U, \\ &c(\hat{z})^\top \hat{x} < c(\hat{z})^\top \bar{x}, \quad \text{for some } \hat{z} \in U. \end{aligned}$$

Because $\hat{x}$ is ARO to (5.3), there also exist $(\hat{y}^1, \ldots, \hat{y}^N)$ that, together with $\hat{x}$, are feasible to (5.16).

The linear optimization problem $\min_{z \in U} c(z)^\top (\hat{x} - \bar{x})$ attains the minimum in a vertex solution, so without loss of generality we can assume $\hat{z} \in \text{ext}(U)$. Any point $\bar{z} \in \text{ri}(U)$ can be written as a strict convex combination of the extreme points of U (Rockafellar, 1970), so $\bar{z} = \sum_{i=1}^N \alpha_i z^i$ for some $\alpha \in \mathbb{R}^N$ with $\sum_{i=1}^N \alpha_i = 1$, $\alpha_i > 0$ for all i. Then

$$c(\bar{z})^\top (\hat{x} - \bar{x}) = \sum_{\substack{i=1 \\ z^i \neq \hat{z}}}^{N} \alpha_i c(z^i)^\top (\hat{x} - \bar{x}) + \hat{\alpha} c(\hat{z})^\top (\hat{x} - \bar{x}),$$

where the first term of the RHS is nonpositive and the second term is strictly negative. This contradicts the fact that $(\bar{x}, \bar{y}^1, \ldots, \bar{y}^N)$ is optimal to (5.16).

5.A.14 Proof Lemma 5.35

First, we note that in problem $p(\hat{\boldsymbol{x}}, V)$, setting stage-1 decision $\bar{\boldsymbol{x}} = \hat{\boldsymbol{x}}$ is feasible, and in that case for any scenario the optimal recourse decision is the same for the original $\bar{\boldsymbol{x}}$ and the new $\bar{\boldsymbol{x}}$. Thus, $p(\hat{\boldsymbol{x}}, V)$ is always nonpositive.

Suppose Algorithm 5.1 terminates after k iterations with solution $\bar{\boldsymbol{x}}$. Then $\bar{\boldsymbol{x}}$ is part of the optimal solution to problem $p(\boldsymbol{x}^{\boldsymbol{k-1}}, V_k)$ which is solved in iteration k and yields objective value 0. Thus, due to (5.17c) and (5.17d) and the fact that the extreme points are in set V_k, we know that $\bar{\boldsymbol{x}}$ is ARO.

It remains to show that $\bar{\boldsymbol{x}}$ is PARO according to Definition 5.8(i). Proof by contradiction. Suppose $\bar{\boldsymbol{x}}$ is not PARO. Then there exists another $\boldsymbol{x}^*$ that is ARO to (5.3) that additionally satisfies the following two conditions:

1. For each $\boldsymbol{z} \in U$ there exists a $\boldsymbol{y}$ such that for all $\bar{\boldsymbol{y}}$ with $\boldsymbol{A}\bar{\boldsymbol{x}} + \boldsymbol{B}\bar{\boldsymbol{y}} \leq \boldsymbol{r}(\boldsymbol{z})$ we have
$$\begin{aligned} \boldsymbol{c}^\top \boldsymbol{x}^* + \boldsymbol{d}^\top \boldsymbol{y} &\leq \boldsymbol{c}^\top \bar{\boldsymbol{x}} + \boldsymbol{d}^\top \bar{\boldsymbol{y}}, \\ \boldsymbol{A}\boldsymbol{x}^* + \boldsymbol{B}\boldsymbol{y} &\leq \boldsymbol{r}(\boldsymbol{z}). \end{aligned}$$
2. There exists a $\boldsymbol{z}^* \in U$ and a $\boldsymbol{y}^*$ such that for all $\bar{\boldsymbol{y}}$ with $\boldsymbol{A}\bar{\boldsymbol{x}} + \boldsymbol{B}\bar{\boldsymbol{y}} \leq \boldsymbol{r}(\boldsymbol{z}^*)$ we have
$$\begin{aligned} \boldsymbol{c}^\top \boldsymbol{x}^* + \boldsymbol{d}^\top \boldsymbol{y}^* &< \boldsymbol{c}^\top \bar{\boldsymbol{x}} + \boldsymbol{d}^\top \bar{\boldsymbol{y}}, \\ \boldsymbol{A}\boldsymbol{x}^* + \boldsymbol{B}\boldsymbol{y}^* &\leq \boldsymbol{r}(\boldsymbol{z}^*). \end{aligned}$$

Because for every $(\boldsymbol{z}^i, v^i) \in V_k$ it holds that $\boldsymbol{z}^i \in U$, the first condition implies that for each $(\boldsymbol{z}^{\boldsymbol{i}}, v^i) \in V^k$ there exists a recourse decision $\boldsymbol{y}^{\boldsymbol{i}*}$ such that $(\boldsymbol{x}^*, \boldsymbol{y}^{\boldsymbol{i}*})$ satisfies constraints (5.17c) and (5.17d). The second condition is equivalent to the statement that there exists $\boldsymbol{z}^* \in U$ and a $\boldsymbol{y}^*$ such that

$$\begin{aligned} \max_{\bar{\boldsymbol{y}}: \boldsymbol{A}\bar{\boldsymbol{x}} + \boldsymbol{B}\bar{\boldsymbol{y}} \leq \boldsymbol{r}(\boldsymbol{z}^*)} (\boldsymbol{c}^\top \boldsymbol{x}^* + \boldsymbol{d}^\top \boldsymbol{y}^*) - (\boldsymbol{c}^\top \bar{\boldsymbol{x}} + \boldsymbol{d}^\top \bar{\boldsymbol{y}}) < 0, \\ \boldsymbol{A}\boldsymbol{x}^* + \boldsymbol{B}\boldsymbol{y}^* \leq \boldsymbol{r}(\boldsymbol{z}^*). \end{aligned}$$

Put together, this implies that $(\boldsymbol{z}^*, \boldsymbol{x}^*, \boldsymbol{y}^*, \boldsymbol{y}^{\boldsymbol{1}*}, \ldots, \boldsymbol{y}^{|V_k|*})$ is a feasible solution to (5.17) with strictly negative objective value. This contradicts with $p(\boldsymbol{x}^{\boldsymbol{k-1}}, V_k) = 0$. Thus, $\bar{\boldsymbol{x}}$ is PARO.

CHAPTER 6

Optimal combined proton-photon therapy schemes

6.1 Introduction

In external beam radiation therapy (EBRT), the goal is to kill the tumor cells using ionizing radiation, while sparing the normal (healthy) tissues as much as possible. In spatial optimization, the radiation beam directions and intensities are optimized such that the dose to the healthy tissues is minimal, while still delivering the prescribed dose to the tumor. On the other hand, temporal optimization aims to select the optimal number of fractions of the treatment. The concept of fractionation is based on the observation that healthy cells have the capability to tolerate a larger dose if it is delivered in smaller fractions over multiple days, since they can repair radiation damage between treatments (Fowler, 1989; Withers, 1985).

Regarding the spatial component, different beam types (modalities) have different healthy tissue sparing properties. The relevant modalities for this work are photon beams (X-rays) and proton beams. Photon therapy is a conventional method that is by far the most frequently used. Proton therapy is a more advanced method, which theoretically has superior healthy tissue sparing properties, but is more expensive. While protons can offer higher dose conformity due to the pronounced Bragg peak, in the current planning approach often larger margins are used for protons than for photons due to range uncertainties (Perkó et al., 2018). This is not a fundamental characteristic of proton therapy, but rather a consequence of limited image guidance and range control abilities in current proton therapy practice. Therefore, in present clinical setting using protons is not necessarily better for organs very close to the target (Perkó et al., 2018), and investigating combined proton-photon treatments can be of interest.

In the fractionation optimization literature we can distinguish between single and multiple normal tissues, and between single and combined modality models. The biologically effective dose (BED) model (Fowler, 1989, 2010) has been the basis of

most work on the topic. For the case with a single normal tissue and a single treatment modality, many numerical and analytical results have been derived. Mizuta et al. (2012) mathematically prove that in this case the decision between hypofractionation and hyperfractionation depends on the ratio between the normal tissue α/β-ratio and the tumor α/β-ratio, where the α/β-ratio is a tissue-specific parameter representing the sensitivity of the tissue to fractionation. In the work of Unkelbach et al. (2013a) this is generalized to the case where a spatially heterogeneous dose distribution is allowed via the introduction of dose sparing factors. Bortfeld et al. (2015) further extend this model by including a tumor repopulation term. Many other studies examine specific aspects of the problem, or applications to specific tumor sites (Bertuzzi et al., 2013; Yang and Xing, 2005a; Wein et al., 2000).

Recently there has been significant progress on the optimal fractionation problem with a single treatment modality and multiple normal tissues. Saberian et al. (2015) and Badri et al. (2016) independently formulate and solve the optimization problem via a reformulation to a two variable linear programming problem. Saberian et al. (2016a) derive several results for the general optimization problem with maximum point dose, mean dose and dose-volume histogram (DVH) constraints. Amongst others they derive sufficient conditions for optimality of equal-dosage (more than one fraction) or single-dosage solutions. Kim et al. (2015) apply the single modality optimal fractionation model with multiple normal tissues to phantom lung cases and find that, especially for cases with favorable geometry, nonconventional fractionation schemes may improve local tumor control while yielding shorter treatment courses. Perkó et al. (2016) apply the same method to liver patients cases, and it is demonstrated that an intermediate fractionation scheme is optimal in the case of competing normal tissues.

In Unkelbach et al. (2013b) and Unkelbach and Papp (2015) the spatiotemporal optimization problem is considered, where they simultaneously optimized the spatial dose distribution and the fractionation, in order to minimize a weighted sum of normal tissue doses and deviations from a prescribed tumor BED. Saberian et al. (2017) consider the spatiotemporal optimal fractionation problem where they maximize tumor BED subject to BED constraints on multiple normal tissues. O'Connor et al. (2018) solve the physical dose-based beam orientation optimization problem, allowing for different (non-coplanar) beam angles in different fractions.

Nill (2001, Chapter 4) concludes that combined proton-photon treatments do not improve over proton treatments. However, they do not take into account fractionation. An application of the BED model to combined modality treatments is discussed in Bodey et al. (2004), but this study combines photon therapy with targeted radionuclide therapy (a form of internal radiation therapy), instead of another EBRT modality.

This chapter investigates combined modality fractionated treatments where each fraction employs either photon or proton therapy. Our three main contributions are as follows:

- **Analytical and numerical demonstration of optimal combined modality treatments:** We formulate and solve simplified combined modality optimization problems, that prove they can outperform single modality proton treatments for two reasons. First, in situations with multiple constraints, one constraint may be more restrictive for one treatment modality, while the other more restrictive for the other modality, making combined treatments optimal. Second, in situations where proton plans are superior in terms of dose, using photon fractions can yield plans that are better in terms of BED, due to the fractionation effect.

- **Demonstration of improved patient treatment plans:** We formulate the multiple normal tissue combined proton-photon fractionation optimization problem and solve it using real data from 17 patients, showing that for 5 patients combined modality treatments are an improvement over single modality proton treatments. Out of these 5, for 2 also the single modality photon plan outperformed the proton plan.

- **Demonstration of better resource allocation:** For 3 patients we show that a combined modality treatment plan can be found that is only marginally worse than the optimal proton treatment, while it uses fewer proton fractions.

The literature on (fractionation) optimization for combined proton-photon treatments is limited. The recent paper Unkelbach et al. (2018b) studies a similar combined modality problem, using spatiotemporal optimization. In their paper, first a 30-fraction plan is optimized for photons only and protons only. They use these to generate a reference plan, which is a proportional combination of these single modality plans such that the total number of photon and proton fractions is 30. Finally they optimize the combined modality plan, restricted to 30 fractions and enforcing that several performance measures do not deteriorate with respect to the reference plan. Unlike their approach, our method does not fix the total number of fractions and within a single modality we allow for nonuniform fractionation. Furthermore, while the method of Unkelbach et al. (2018b) is demonstrated only for a single patient, our larger data set indicates that several types of patients can be distinguished with regard to the benefit of combined modality. Lastly, we provide theoretical results that demonstrate the conditions under which combined modality can outperform single modality treatments.

Nourollahi et al. (2019) also study BED-based combined modality fractionation optimization problems. However, they do not allow for a heterogeneous dose distribution via voxel-specific dose sparing factors, and consequently do not take DVH constraints into account either. Their approach and numerical results mainly focus on hypothetical cases with a single healthy tissue, whereas we find that one of the reasons for optimality of combined modality treatments is the interplay of multiple healthy tissues.

The outline of this chapter is as follows. Section 6.2.1 discusses two reasons why combined proton-photon treatments may outperform single modality treatments. Section 6.2.2 presents the full combined proton-photon fractionation optimization problem. In Section 6.3 this model is tested on a data set of liver patients treated at Massachusetts General Hospital (Boston, USA) and the results are presented. Section 6.4 discusses the results and their relevance to clinical practice. Last, Section 6.5 presents our conclusions.

6.2 Methods

Our approach is based on the standard biologically effective dose (BED) model. Tumor repopulation is not taken into account. The standard BED model states that the biological effect of a dose D given to a tissue in N fractions is given by

$$\text{BED} = D\Big(1 + \frac{1}{\alpha/\beta}\frac{D}{N}\Big), \tag{6.1}$$

where α/β is a parameter indicating the fractionation sensitivity of the tissue, and BED is measured in $\text{Gy}_{\alpha/\beta}$ instead of Gy. We generalize BED equation (6.1) to the situation with unequal dose per fraction and two treatment modalities. Due to additivity, the BED to an irradiated tissue equals the BED from a photon dose plus the BED from a proton dose. Let $D_i^T = \sum_{t_i=1}^{N_i} d_{i,t_i}$ be the total dose to the tumor of modality i, where d_{i,t_i} is the dose of modality i to the tumor in fraction t_i, and N_i is the number of fractions of modality i. Subscripts $i = \gamma$ and $i = p$ stand for photons and protons, respectively. Let $s_{i,j}$ denote the dose sparing factor of any voxel j in the tumor or in an OAR for treatment modality i. The BED to voxel j is given by

$$\text{BED}_j = \sum_{t_\gamma=1}^{N_\gamma} s_{\gamma,j} d_{\gamma,t_\gamma} + \rho \sum_{t_\gamma=1}^{N_\gamma} s_{\gamma,j}^2 d_{\gamma,t_\gamma}^2 + \sum_{t_p=1}^{N_p} s_{p,j} d_{p,t_p} + \rho \sum_{t_p=1}^{N_p} s_{p,j}^2 d_{p,t_p}^2,$$

where ρ denotes the inverse α/β ratio of the tissue containing voxel j.

In Section 6.2.1 we describe two reasons why combined proton-photon treatments may outperform single modality treatments. Section 6.2.2 presents the BED-based full combined proton-photon fractionation optimization problem.

6.2.1 Two reasons why combined proton-photon treatments can outperform single modality treatments

We consider a situation with two organs-at-risk (OARs). OAR 1 includes the tumor and OAR 2 is another organ close to the tumor, see Figure 6.1. The outer circle indicates OAR 1, the tumor is the black circle in the middle, and the blue circle indicates OAR 2. No other OARs play a significant role. Figure 6.1 is naturally a 2D representation of a 3D situation, with OAR 2 interpreted as an organ close to the tumor.

(a) The photon dose distribution causes 'high' damage inside the intersection of the beams (red) and 'low' damage everywhere else (green).

(b) The proton beam causes 'high' damage in the spread out Bragg Peak (red), 'low' damage at the entrance (green) and no damage anywhere else.

Figure 6.1: Schematic view of the simplified (2D) scenario with an OAR containing a tumor, and a second nearby OAR. The outer circle represents OAR 1 with the tumor in the middle (black), and the blue circle represents OAR 2.

For the photon dose distribution (Figure 6.1a) we assume that the gantry completes a full rotation around the patient shooting beams from all angles. These angles intersect in the area within the red circle, where the dose is high. Outside this area, we assume that photon beams do not intersect, so the dose is equally low everywhere (green area). Thus, the tumor and a small part of OAR 1 receive a uniform high dose, and the rest of OAR 1 and the entire volume of OAR 2 (blue area) receive a uniform low dose.

For the proton dose distribution (Figure 6.1b) there is a single beam. There is a high dose area (spread out Bragg Peak in red) and a low dose area (the beam entrance in green). Thus, the tumor, part of OAR 1 (around the tumor) and part of OAR 2 (intersection of red and blue area) receive a uniform high dose, part of OAR 1 receives

a uniform low dose, and the remaining parts of OAR 1 and OAR 2 receive no dose.

We need to determine how much dose should be given with each modality, i.e. how much the dose distributions described above should be scaled. The corresponding optimization problem can be formulated in terms of dose, or in terms of BED. In the latter case, it must also be determined how many fractions are needed for each modality. The objective is to maximize the dose or BED to the tumor, such that the dose or BED to the OARs remains below some tolerance level. If the optimal solution makes use of both photon and proton dose (and fractions), this implies that combined modality yields a better solution than single modality, and analyzing the underlying mathematical model can reveal the conditions under which this occurs. Below we identify two such reasons. Combined modality treatments can also be shown to be optimal (see Appendix 6.A.3) if one minimizes the dose or BED to one of the OARs, while one constrains the tumor dose or BED to a prescribed level and the dose or BED to the other OAR below a tolerance.

Optimality due to competing constraints, with protons and photons being better for different ones

The first reason why combined modality treatments may outperform single modality proton treatments is due to the different shape of the high dose regions of the photon and proton dose distributions, when there are multiple OARs in proximity to the tumor. As seen in Figure 6.1, part of OAR 2 falls in the proton high dose region, but not in the photon high dose region, meaning that a DVH or maximum point dose constraint may be more restrictive for protons than for photons. For example, consider a DVH constraint on OAR 2 where the restricted volume (the maximum volume for which the dose may exceed a given tolerance level) is smaller than the high dose region of OAR 2 for the proton dose distribution. This constraint is much more restrictive for protons than for photons. Hence, if we only set this constraint, the photon dose distribution is favorable. On the other hand, a mean dose constraint on OAR 1 is more restrictive for the photon dose distribution than for the proton dose distribution, due to the much larger photon low dose region. Hence, a mean dose constraint favors protons.

In essence, we have two competing constraints, both favoring a different treatment modality. A combined modality treatment that uses part photons and part protons is able to balance these two interests best. As mathematically derived in Appendix 6.A.1, a combined modality treatment can deliver a higher dose to the tumor than either modality alone, while it also satisfies the DVH and mean dose constraints on OAR 2 and OAR 1 respectively.

A similar conclusion can be reached if a DVH constraint is set such that the proton

entrance dose is constrained, or if more DVH constraints are added, and the example can naturally be generalized to allow more proton beams. While we supposed a larger high dose region for protons than for photons, this is not a necessary condition for our statements to hold, simple shape differences can also lead to similar conclusions (protons depositing high dose in OAR 2 while photons not). Moreover, proton plans in practice can indeed show larger high dose regions compared to photon plans due to larger planning margins (due to more uncertainty in range, e.g., for organs with significant internal motion) and worse lateral penumbra (Perkó et al., 2018). As shown in Section 6.3, this is truly the case for our patient data.

Optimality due to having more fractions, even if photons are somewhat worse

The second reason why combined modality may outperform single modality proton treatments is related to the fractionation effect. If the α/β-ratio of the OAR is smaller than that of the tumor, the benefit of fractionation is larger for the OAR than for the tumor. For simplicity, suppose the α/β-ratio of the tumor is sufficiently large so that we can neglect the fractionation effect and optimize for maximum tumor physical dose. Next, consider a mean dose constraint on OAR 1. For a fixed dose to (part of) OAR 1, the BED to (that part of) OAR 1 will be lower if this dose is administered over multiple fractions. As the number of fractions does not influence the damage to the tumor, once we are delivering a non-zero dose with a modality (photons or protons), it will always be optimal to use the maximum number of allowed fractions for this modality.

For the same tumor dose, the proton dose distribution has a lower mean dose in OAR 1 than the photon dose distribution. Therefore, when using equal dose per fraction to minimize BED, protons also deliver lower mean BED in OAR 1 than photons for a given number of fractions, and it is always optimal to set a non-zero dose per fraction to the proton fractions. In case we use only protons, the proton dose per fraction is increased until we reach the mean BED tolerance on OAR 1. Delivering part of the dose via photon fractions allows for a lower dose per fraction in the proton fractions. Adding these photon fractions naturally leads to slightly worse OAR sparing in terms of physical dose, however due to the higher total number of fractions, the BED in OAR 1 does not necessarily increase. Whether or not using the photon fractions is optimal depends on the trade-off between the worse OAR sparing in terms of physical dose and the benefit of fractionation. In Appendix 6.A.2 we demonstrate that this trade-off indeed occurs, and that combined proton-photon treatments outperform single modality proton treatments in terms of achievable tumor dose, if the BED tolerance level exceeds a threshold. That is, unless the BED tolerance of OAR 1 is very restrictive, the benefit of having more fractions outweighs the disadvantage of some of these fractions (the

photon fractions) having worse physical OAR sparing.

6.2.2 General combined modality fractionation model with multiple OARs

In this section the general optimization problem for the combined proton-photon optimal fractionation problem with multiple normal tissues is formulated. The model can take into account maximum point dose, mean dose and dose-volume constraints, accepts arbitrary proton and photon dose distributions as given inputs, and determines the optimal dose for each modality (i.e. how much the dose distributions need to be scaled) and the number of fractions these doses should be delivered. Note that the general model described in this section is completely separate from the simplified geometry of Section 6.2.1 and makes no assumptions regarding the dose distributions.

Similar to the approach of Saberian et al. (2015) for the single modality fractionation problem, we formulate our model not in terms of dose vectors $\boldsymbol{d}_\gamma$ and $\boldsymbol{d}_p$ (for photons and protons respectively), but instead in terms of four new variables. For photons, let x_γ and y_γ denote the total dose and the sum of squared doses. For protons, denote these quantities by x_p and y_p, respectively. Thus, we use the following substitutions:

$$x_\gamma = \sum_{t_\gamma=1}^{N_\gamma} d_{\gamma,t_\gamma}, \quad y_\gamma = \sum_{t_\gamma=1}^{N_\gamma} d_{\gamma,t_\gamma}^2, \quad x_p = \sum_{t_p=1}^{N_p} d_{p,t_p}, \quad y_p = \sum_{t_p=1}^{N_p} d_{p,t_p}^2. \tag{6.2}$$

First we consider the objective function. Let n^T be the number of voxels in the tumor, and ρ^T the inverse α/β-ratio of the tumor. Let $s_{i,j}^T$ be the dose sparing factor of tumor voxel j for treatment modality i. The objective is to maximize the mean target BED, which can be formulated as

$$\max_{x_\gamma,y_\gamma,x_p,y_p} \frac{1}{n^T} \sum_{j=1}^{n^T} \left(s_{\gamma,j}^T x_\gamma + \rho^T (s_{\gamma,j}^T)^2 y_\gamma + s_{p,j}^T x_p + \rho^T (s_{p,j}^T)^2 y_p \right).$$

Next, we consider the constraint types. Let $\mathcal{M}_1$, $\mathcal{M}_2$ and $\mathcal{M}_3$ denote the set of maximum point dose, DVH and mean dose constraints, respectively. For the OAR corresponding to constraint m, let n^m denote the number of voxels in the OAR, ρ^m denote the inverse α/β ratio for the OAR, and $s_{i,j}^m$ be the dose sparing factor of voxel j in the OAR for treatment modality i.

Maximum point dose constraints

A maximum point dose constraint on OAR m states that no voxel in the OAR may receive a dose higher than dose $D_{\max}^m$ if delivered in N^m fractions. This tolerance dose

corresponds with a BED of

$$\text{BED}^m_{\max} = D^m_{\max}\Big(1+\rho^m\frac{D^m_{\max}}{N^m}\Big).$$

Thus, the constraint reads

$$s^m_{\gamma,j}x_\gamma + \rho^m(s^m_{\gamma,j})^2 y_\gamma + s^m_{p,j}x_p + \rho^m(s^m_{p,j})^2 y_p \le \text{BED}^m_{\max},\ \forall j=1,\dots,n^m,\ \ m\in\mathcal{M}_1.$$

DVH constraints

For a DVH constraint on OAR m, no more than a fraction F^m of the OAR volume V^m may receive a dose higher than D^m_{dvh} if given in N^m fractions. This tolerance is equivalent to a BED of

$$\text{BED}^m_{\text{dvh}} = D^m_{\text{dvh}}\Big(1+\rho^m\frac{D^m_{\text{dvh}}}{N^m}\Big).$$

The constraint now reads

$$s^m_{\gamma,j}x_\gamma + \rho^m(s^m_{\gamma,j})^2 y_\gamma + s^m_{p,j}x_p + \rho^m(s^m_{p,j})^2 y_p \le \text{BED}^m_{\text{dvh}} + M(1-u^m_j),$$
$$\forall j=1,\dots,n^m,\ \ m\in\mathcal{M}_2,$$

where $M\in\mathbb{R}$ is a sufficiently large positive number, and u^m_j are binary decision variables for $\forall j=1,\dots,n^m$. Let $\boldsymbol{u}$ denote the stacked vector of all binary variables for $\forall m\in\mathcal{M}_2$. A value $u^m_j=1$ implies that voxel j in the OAR corresponding to constraint m receives a BED lower than or equal to $\text{BED}^m_{\text{dvh}}$ and $u^m_j=0$ implies that voxel j receives a BED higher than $\text{BED}^m_{\text{dvh}}$. Because volume V^m is discretized into n^m voxels, we add extra constraints that at least $n^m-\lfloor F^m n^m\rfloor$ voxels must receive a BED lower than $\text{BED}^m_{\text{dvh}}$:

$$\sum_{j=1}^{n^m} u^m_j \ge n^m - \lfloor F^m n^m\rfloor,\quad \forall m\in\mathcal{M}_2,$$
$$u^m_j\in\{0,1\},\ \ \forall j\in\mathcal{N}^m,\ \ \forall m\in\mathcal{M}_2.$$

Mean dose constraints

A mean dose constraint on OAR m states that a mean dose of D^m_{mean} over all voxels is tolerated if given in N^m fractions. This constraint can be formulated as

$$\frac{1}{n^m}\sum_{j=1}^{n^m}\Big(s^m_{\gamma,j}x_\gamma + \rho^m(s^m_{\gamma,j})^2 y_\gamma + s^m_{p,j}x_p + \rho^m(s^m_{p,j})^2 y_p\Big) \le \text{BED}^m_{\text{mean}}.$$

For the mean dose tolerance, we note that there is a difference between the BED of the mean dose and the mean BED, due to the influence of the spatial distribution of the dose. In Perkó et al. (2018) this effect is captured for a single modality by a parameter named the dose shape factor. The dose shape factor φ^m for the photon dose distribution in the OAR corresponding to constraint m is given by

$$\varphi^m = \frac{n^m \sum_{j=1}^{n^m} s_{\gamma,j}^2}{\left(\sum_{j=1}^{n^m} s_{\gamma,j}\right)^2},$$

and similar for the proton dose distribution. For more details, see Perkó et al. (2018).

Final optimization problem

All put together, the optimization problem reads:

$$\max_{x_\gamma, y_\gamma, x_p, y_p, u} \quad \frac{1}{n^T} \sum_{j=1}^{n^T} \left(s_{\gamma,j}^T x_\gamma + \rho^T (s_{\gamma,j}^T)^2 y + s_{p,j}^T x_p + \rho^T (s_{p,j}^T)^2 y_p \right), \tag{6.3a}$$

$$\text{s.t.} \quad s_{\gamma,j}^m x_\gamma + \rho^m (s_{\gamma,j}^m)^2 y_\gamma + s_{p,j}^m x_p + \rho^m (s_{p,j}^m)^2 y_p \le \text{BED}_{\max}^m, \quad \forall j = 1, \dots, n^m, \ \forall m \in \mathcal{M}_1, \tag{6.3b}$$

$$s_{\gamma,j}^m x_\gamma + \rho^m (s_{\gamma,j}^m)^2 y_\gamma + s_{p,j}^m x_p + \rho^m (s_{p,j}^m)^2 y_p \le \text{BED}_{\text{dvh}}^m + M(1 - u_j^m), \quad \forall j = 1, \dots, n^m, \ \forall m \in \mathcal{M}_2, \tag{6.3c}$$

$$\sum_{j=1}^{n^m} u_j^m \ge n^m - \lfloor F^m n^m \rfloor, \quad \forall m \in \mathcal{M}_2, \tag{6.3d}$$

$$u_j^m \in \{0, 1\}, \quad \forall j = 1, \dots, n^m, \quad \forall m \in \mathcal{M}_2, \tag{6.3e}$$

$$\frac{1}{n^m} \sum_{j=1}^{n^m} \left(s_{\gamma,j}^m x_\gamma + \rho^m (s_{\gamma,j}^m)^2 y_\gamma + s_{p,j}^m x_p + \rho^m (s_{p,j}^m)^2 y_p \right) \le \text{BED}_{\text{mean}}^m, \quad \forall m \in \mathcal{M}_3, \tag{6.3f}$$

$$\sqrt{y_\gamma} \le x_\gamma \le \sqrt{N_\gamma y_\gamma}, \tag{6.3g}$$

$$\sqrt{y_p} \le x_p \le \sqrt{N_p y_p}, \tag{6.3h}$$

$$x_\gamma \ge 0, \ y_\gamma \ge 0, \ x_p \ge 0, \ y_p \ge 0. \tag{6.3i}$$

Constraints (6.3g) and (6.3h) model the relations between decision variables x_γ and y_γ, and x_p and y_p, respectively. In Appendix 6.D it is shown that (6.3) is equivalent to (6.D.5), i.e., the optimization problem in terms of the original dose-per-fraction

vectors $\boldsymbol{d}_\gamma \in \mathbb{R}_+^{N_\gamma}$ and $\boldsymbol{d}_p \in \mathbb{R}_+^{N_p}$. Compared to the single modality model in Saberian et al. (2015) (also detailed in Appendix 6.B), the main difficulty is found in the DVH constraints, as there is no a-priori ordering of the voxels in terms of BED. To overcome this we developed the algorithm described below.

Optimization algorithm

To solve problem (6.3) we make use of the following variable transformation:

$$\theta = \frac{x_\gamma}{x_\gamma + x_p}, \quad v_\gamma = \frac{x_\gamma^2}{y_\gamma}, \quad v_p = \frac{x_p^2}{y_p}. \tag{6.4}$$

Variable θ can be interpreted as the fraction of photon dose to total dose. Variables v_γ and v_p are, when rounded up, equal to the number of used photon and proton fractions, respectively. The new set of variables is $\{x_\gamma, \boldsymbol{u}, \theta, v_\gamma, v_p\}$. Let f and $\mathcal{F}$ denote the objective function and feasible set of (6.3) in terms of the new variable set.

We split the new variables set into two sets: $\{x_\gamma, \boldsymbol{u}\}$ and $\{\theta, v_\gamma, v_p\}$. In Appendix 6.E.1 it is described how for fixed variables $\{\theta, v_\gamma, v_p\}$ we can (exactly) compute the optimal values of $\{x_\gamma, \boldsymbol{u}\}$. The described procedure eliminates the (large number of) binary variables $\boldsymbol{u}$ and requires only a sorting algorithm to compute the optimal value for x_γ. Hence, this procedure is very fast. Denote these optimal values by $x_\gamma^*(\theta, v_\gamma, v_p)$ and $\boldsymbol{u}^*(\theta, v_\gamma, v_p)$. Then we can concisely represent problem (6.3) as

$$\max_{\theta, v_\gamma, v_p} f(x_\gamma^*(\theta, v_\gamma, v_p), \boldsymbol{u}^*(\theta, v_\gamma, v_p), \theta, v_\gamma, v_p), \tag{6.5a}$$

$$\text{s.t. } \left\{x_\gamma^*(\theta, v_\gamma, v_p), \boldsymbol{u}^*(\theta, v_\gamma, v_p), \theta, v_\gamma, v_p\right\} \in \mathcal{F}, \tag{6.5b}$$

which is a problem of only three variables, as (θ, v_γ, v_p) are all scalar variables. We solve (6.5) via a Generalized Pattern Search (GPS) algorithm (Audet and Dennis Jr., 2003). GPS is an optimization algorithm that does not require a gradient, nor does it require the objective function to be continuous. To improve performance, we take a multi-start approach, details of which are provided in Appendix 6.E.2.

This separation into two variable sets also enables setting an additional constraint on the dose per fraction values. Specifically, it allows us to set a minimum dose per fraction value $d_{\min}$ and a maximum dose per fraction value $d_{\max}$. This may be clinically interesting, as it avoids treatments that could be considered unrealistic in current practice, with too high or negligibly small dose per fraction values.

Implementation

All computations were performed on a 2.6GHz Intel-Core i5 PC with 8GB RAM, using the software package MATLAB R2017b (Mathworks, Natick, MA, US). The MATLAB

toolbox CERR (Deasy et al., 2003) is used to visualize and analyze patient data, and to transfer the data to the MATLAB environment. For all patients we solve problem (6.3) using the MATLAB function `patternsearch` for all combinations of N_γ and N_p such that $N_\gamma + N_p = 15$, so the total number of allowed fractions is 15. The single modality proton optimal fractionation problem (see Appendix 6.B) is also solved. During the optimization procedure, we set a minimum and a maximum dose per fraction of $d_{\min} = 1$ Gy/fx and $d_{\max} = 10$ Gy/fx, respectively.

Patient data

The data set is a subset of the data set used in Perkó et al. (2018), consisting of actual patient data (in DICOM format) from 17 patients who were treated at Massachusetts General Hospital, and was provided by physicians collaborating with the physics research group. All patients in the data set are liver patients and were treated with passively scattered protons in practice, in 5 or 15 fractions. All proton plans incorporated compensator smearing and are adjusted for relative biological effectiveness (RBE) by setting $\text{RBE}_{\text{proton}} = 1.1$. Next to the clinically used proton plans, the treatment planners also derived photon plans for these patients, taking into account all proper clinical measures to deal with uncertainties. For the proton plans, a planning target volume (PTV) margin was added manually. For more details on patient selection and how uncertainties were handled we refer to Perkó et al. (2018).

Patients with liver tumors are interesting for combined modality treatments, due to the large number of neighboring healthy tissues, and the different constraints on the tissues that are in the paths of the beams. Our patient cohort well reflected that proton distributions are not necessarily superior in terms of the high dose area: due to larger motion uncertainty they typically used larger margins. Although the used proton plans are passive scattering plans, even in IMPT larger margins could be present than in their photon counterparts.

6.3 Results for patients for combined modality fractionation model with multiple OARs

The objective is to maximize the BED to the gross tumor volume (GTV). Throughout the results and discussion the terms GTV and tumor are used interchangeably. Table 6.1 presents the most important constraints for all patients in terms of dose and BED. In clinical practice, the dose tolerance levels for healthy liver mean dose are not hard constraints but are used as 'goals', meaning that for a given number of fractions a range of dose tolerances is acceptable. Correspondingly, in our optimization dose tolerance

values are picked such that the resulting GTV BED is between 50 and 200 Gy. This value is applied consistently in the optimization of the single modality photon and proton treatments and the combined modality treatment, to allow for a fair comparison. In clinical practice, the range of dose tolerances for the 5 and 15 fraction regimens are [13 Gy, 17 Gy] and [23 Gy, 27 Gy], respectively. However, for cases with very small tumors, the mean GTV BED can take very high values before these liver mean dose constraints are binding. Hence, we extend these dose tolerance ranges to [8 Gy, 17 Gy] for the 5 fraction regiment and [16 Gy, 27 Gy] for the 15 fraction regimen.

Constraints			
OAR	dose tolerance (Gy)	fractions	constraint type
Liver-CTV	15	5	DVH: sparing $> 700cc$
	10	5	DVH: sparing $> 30\%$
	[8, 17]	5	Mean dose (goal range)
	[16, 27]	15	Mean dose (goal range)
Stomach	{30, 40}	{5, 15}	DVH: violation $< 0.5cc$
	{25, 36}	{5, 15}	DVH: violation $< 5cc$
Duodenum	{30, 40}	{5, 15}	DVH: violation $< 0.5cc$
	{25, 36}	{5, 15}	DVH: violation $< 5cc$
Small bowel	{30, 40}	{5, 15}	DVH: violation $< 0.5cc$
	{25, 36}	{5, 15}	DVH: violation $< 5cc$
Large bowel	{32, 40}	{5, 15}	DVH: violation $< 0.5cc$
Cord	{25, 37.5}	{5, 15}	DVH: violation $< 0.5cc$

Table 6.1: Most important constraints for the patients in the numerical study. DVH constraints are formulated either in the largest volume (in *cc* or %) that may be violated or in the smallest volume that needs to be spared. Our cases did not have any maximum point dose constraints.

In clinical practice, the healthy liver (liver - clinical target volume (CTV)) constraints are either mean dose constraints or DVH constraints, where DVH constraints are used for cases with large tumors and mean dose constraints are used for cases with small tumors. In our numerical experiments we use both sets of constraints simultaneously, except that the 700cc healthy liver DVH constraint is omitted for those patients where it was violated clinically, to achieve an adequate tumor dose. Hence, for several cases more constraints are included than what was done clinically. We emphasize

that for every patient, the same set of constraints is used for the single and combined modality optimization.

To compare the combined modality results to the single modality results, the single modality proton fractionation scheme is taken as the baseline. For the photon and the combined modality treatment, we determine the physical dose that is required in the single modality proton fractionation scheme to obtain the same tumor BED. This physical dose value is named the *BED equivalent dose* the treatment, and is used as a performance measure for a fractionation scheme.

Results indicate that the potential for combined modality solutions is quite substantial. Out of 17 patients, for 5 patients there is a combined modality treatment that offers an improvement over the optimal single modality proton treatments. Out of these 5 patients, for 2 also the single modality photon plan outperformed the proton plan. This group is discussed in Section 6.3.1. For 3 patients a near-optimal combined modality solution exists that can reduce the number of required proton fractions; this is discussed in Section 6.3.2. For the remaining 9 patients combined modality treatments cannot offer any interesting alternative compared to the optimal single modality proton treatment, because the proton dose distribution is better than the photon dose distribution for all relevant OARs. This group is discussed in Section 6.3.3. There are no cases where the single modality photon plan performs better than the optimal combined modality plan.

6.3.1 Group 1: Combined modality treatment offers clear improvement

For five patients, results indicate that a combined modality treatment can give better results than the single modality proton treatment. Figure 6.2 compares the optimal single modality proton and photon treatments to the combined modality treatment that is found via solving (6.3). Above every bar the resulting BED equivalent physical tumor dose is given and the number of used fractions are reported as *(photon fx, proton fx)*.

For these five patients, the BED equivalent dose is between 7.2% and 14.8% higher in the combined modality treatment than in the single modality proton treatment. For patients P_2 and P_3 the combined modality optimum uses more proton fractions than the single modality proton optimum, but for the other three patients the number of used proton fractions is in fact lower. For patient P_1 the photon and proton treatments yield a similar BED equivalent dose. For patients P_2 and P_3 the BED equivalent dose of the proton treatment was higher than that of the photon treatment, and vice versa for patients P_4 and P_5.

Typically, for these patients the two modalities have different binding constraints. That is, there are competing constraints, which prefer different treatment modalities. In a combined modality treatment both of these constraints are binding. This will be discussed in more detail in Section 6.4.

As an additional analysis, we have made slight adaptations to the optimization algorithm, and minimized the mean liver BED under the restriction that the mean tumor BED should be at least the mean tumor BED of the optimal single modality proton treatment. For existence of a combined modality treatment with lower mean liver BED than the optimal proton treatment, it is necessary for a patient to be in group 1 (in other groups combined modality cannot attain the required tumor BED), but this is not sufficient. More details on this are provided in Section 6.4.5. Out of the five patients in group 1, for two patients (P_2 and P_3) combined modality can reduce mean liver BED (decrease of 8.0% and 10.2% in BED equivalent dose, respectively).

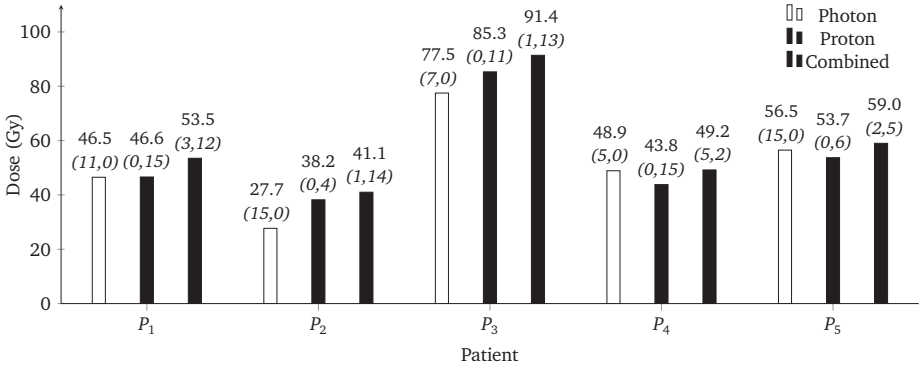

Figure 6.2: Results for group 1, with separate bars for the optimal photon (white), proton (black) and combined modality (dashed) results. Reported doses are in BED equivalent physical dose, to correct for different fractionation schemes. Above every bar the resulting BED equivalent dose and the number of used fractions is reported as *(photon fx, proton fx)*.

6.3.2 Group 2: Combined modality treatment offers alternative with fewer proton fractions

This group consists of three patients. For these patients the optimum is a single modality proton treatment, which clearly outperforms the single modality photon treatment. However, there are near-optimal combined modality solutions that use fewer proton fractions. If we force the use of a number of photon fractions in (6.3), we obtain alter-

native combined modality treatments. Figure 6.3 compares the optimal single modality photon and proton treatments to an alternative combined modality treatment.

We emphasize that the reported combined modality treatments in Figure 6.3 are an example of a combined modality treatment that is optimal if we force the use of a number of photon fractions (6.3), but this number may be varied. For example, for patient P_6 we forced the use of 8 photon fractions, but a smaller number is also possible. This yields a BED equivalent GTV dose between that of the *(0,15)* and the *(8,7)* treatment.

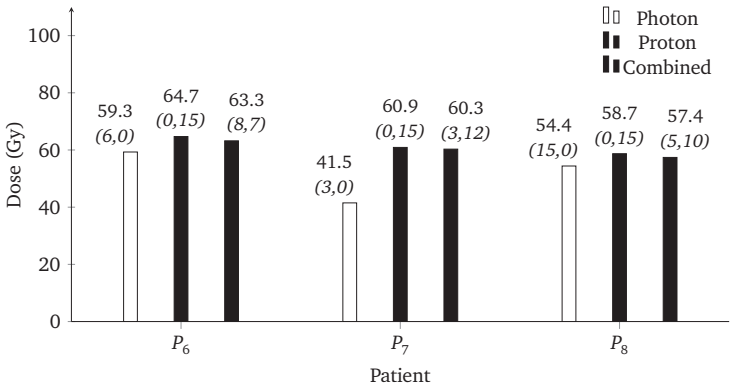

Figure 6.3: Results for group 2, with separate bars for the optimal photon (white) and proton (black) results and an example of a combined modality alternative treatment (dashed). Reported doses are in BED equivalent physical dose, to correct for different fractionation schemes. Above every bar the resulting BED equivalent dose and the number of used fractions is reported as *(photon fx, proton fx)*.

For each of these patients several proton fractions can be replaced by photon fractions without a large decrease in average GTV BED equivalent dose. For example, for patient P_6 going from the *(0,15)* treatment to the *(8,7)* treatment gives a decrease of 1.4 Gy in BED equivalent dose, which is on average −0.175 Gy per replaced fraction. Such an alternative combined modality treatment is interesting if only a limited number of proton fractions is available, and these must be allocated among a set of patients.

6.3.3 Group 3: Single modality proton therapy is superior

For the remaining nine patients, the proton plan is significantly better than the photon plan for all relevant OARs and a combined modality treatment is not very suitable. The

optimal single modality proton treatments are reported in Table 6.2. For most of these patients, it may only be optimal to combine proton fractions with photon fractions if the maximum number of proton fractions that can be allocated is very low. In that case, the added photon fractions provide the benefit of the fractionation effect. Typically, the dose distributions for these patients are such that there is only one OAR that restricts the dose that can be delivered, and the proton plan spares this OAR better than the photon plan. For illustration, columns 4 and 5 of Table 6.2 give the optimal treatment if we force the use of at least one photon fraction. For some patients the deterioration in BED equivalent GTV dose is not very large. However, in all these cases only one photon fraction with a dose between 1.0 and 1.2 Gy (the lower bound is 1.0 Gy) is used. Hence, for these patients enforcing the use of a single photon fraction has a visible negative effect even if the photon fraction uses only a low dose.

Patient	Photon optimum		Proton optimum		Combined modality alternative	
	Dose (Gy)	Fractions	Dose (Gy)	Fractions	Dose (Gy)	Fractions
P_9	43.0	(3,0)	55.0	(0,15)	54.6	(1,14)
P_{10}	35.0	(15,0)	71.0	(0,15)	70.2	(1,14)
P_{11}	57.6	(15,0)	72.4	(0,15)	71.9	(1,14)
P_{12}	55.7	(4,0)	78.8	(0,15)	78.4	(1,14)
P_{13}	44.3	(15,0)	74.4	(0,15)	73.7	(1,14)
P_{14}	45.0	(4,0)	87.2	(0,9)	86.5	(1,9)
P_{15}	37.8	(3,0)	63.2	(0,15)	62.8	(1,14)
P_{16}	54.4	(15,0)	66.9	(0,15)	66.5	(1,14)
P_{17}	60.8	(15,0)	92.5	(0,15)	91.8	(1,14)

Table 6.2: Results for group 3. The optimal single modality proton and photon solutions are reported, with doses in BED equivalent dose. The reported combined modality alternatives are the optimal treatments if we force the use of at least one photon fraction. The used photon fraction in the combined modality solutions has a dose between 1.0 and 1.2 Gy for all patients. The number of used fractions is reported as *(photon fx, proton fx)*.

6.4 Discussion

This section provides a detailed discussion of the results of Sections 6.3.1 and 6.3.2, by analyzing the results for two patients: patient P_1 (Section 6.4.1) and P_6 (Section 6.4.3). Additionally, Section 6.4.2 discusses the results for OAR sparing.

6.4.1 Illustration of Group 1

Patient P_1 was clinically treated with 15 proton fractions. The location of the GTV in the liver is indicated in Figure 6.4, which displays two computed tomography (CT) slices for both the photon and the proton dose distribution. For the most relevant constraints see Table 6.1. The clinical plan violated the 700cc constraint, which is omitted here as well.

For this patient the dose tolerances for the healthy liver mean constraints are 17 Gy in 5 fractions and 27 Gy in 15 fractions. Table 6.3 shows the results for the optimal combined modality treatment and the optimal single modality treatments. The optimal combined modality treatment delivers an average GTV BED of 72.5 Gy_{10}, and uses 3 photon fractions and 12 proton fraction. The corresponding BED equivalent GTV dose (in 15 fractions) is 53.5 Gy. The optimal single modality proton treatment delivers an average GTV BED of 61.0 Gy_{10} in 15 fractions; the corresponding BED equivalent dose is 46.6 Gy. Therefore, the combined modality treatment gives an improvement in BED equivalent dose of 14.8% compared to the optimal single modality proton treatment.

	Single modality photon	Single modality proton	Combined modality
GTV BED	61.0 Gy_{10}	61.0 Gy_{10}	72.5 Gy_{10}
BED equivalent dose	46.5 Gy	46.6 Gy	53.5 Gy
Photon fractions	10 fx (4.2 Gy/fx) 1 fx (1.0 Gy/fx)	-	3 fx (4.7 Gy/fx)
Proton fractions	-	15 fx (3.1 Gy/fx)	12 fx (3.2 Gy/fx)

Table 6.3: Results for patient P_1. The optimal combined modality treatment delivers a higher BED equivalent dose to the GTV than the single modality treatments. For this patient the optimal single modality photon and proton plans perform similarly.

In the single modality proton case the 0.5*cc* duodenum DVH constraint is binding, and in the single modality photon case the (17 Gy in 5 fractions) liver-CTV mean dose constraint is binding (technically, the 30% liver-CTV DVH constraint is also binding). Note that single modality photon is the only treatment that has non-constant dose per fraction. the optimal single modality proton treatment has constant dose per fraction, and the optimal combined modality treatment has constant dose per fraction within each modality. Restricting the single modality photon case to constant dose per fraction as well, the optimal treatment delivers an average GTV BED of 60.9 Gy_{10}, using 10 fractions of 4.3 Gy/fx. This is only marginally worse than the optimal non-constant dose per fraction single modality photon treatment.

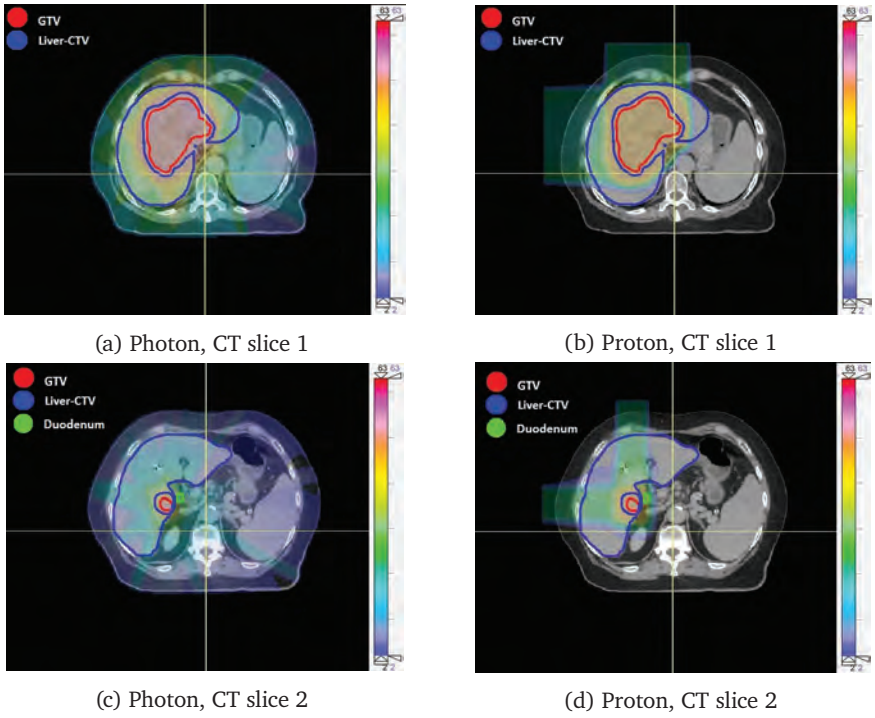

(a) Photon, CT slice 1

(b) Proton, CT slice 1

(c) Photon, CT slice 2

(d) Proton, CT slice 2

Figure 6.4: Spatial dose distribution in photon and proton plans of patient P_1 in two slices. The GTV, liver-CTV and duodenum are delineated.

If both photon and proton fractions are used, the GTV BED can be increased (compared to the single modality cases) such that both the liver mean dose constraint and the duodenum constraint are binding, while the 30% liver-CTV DVH constraint is also satisfied.

As seen on the CT slices in Figure 6.4b, a small portion of the duodenum volume extends to the center of the high dose region of the proton beam. The photon dose to this area is much lower. The only way for protons to protect the duodenum is to keep the dose per fraction relatively low, consequently the dose per fraction in the single modality proton plan is only 3.1 Gy/fx (see Table 6.3). In comparison, using photons allows mild hypofractionation, until the liver mean dose constraint becomes binding. The combined treatment allows us to deliver some of the proton dose using photons, which are less restrictive for the duodenum. Therefore, we can increase the GTV BED until the liver mean dose constraint also becomes binding. Essentially, some of the

proton fractions are omitted to give a hypofractionated photon dose boost.

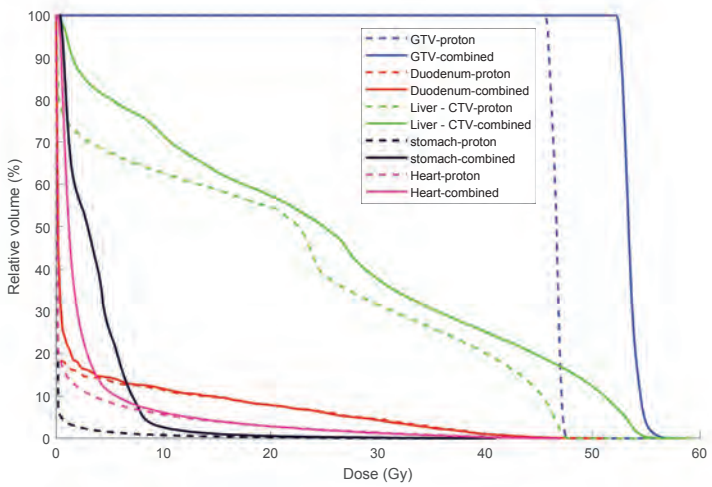

Figure 6.5: DVH for proton and combined modality plans for patient P_1. Dashed lines are the optimal single modality proton solution, solid lines the optimal combined modality solution. The combined modality solution attains a higher average GTV BED while satisfying all constraints, but at the cost of increased dose to several OARs, most notably the healthy liver.

Figure 6.5 shows the DVH of the combined modality optimal solution and the single modality proton optimal solution for the GTV and some relevant OARs, in terms of BED equivalent physical dose in 15 fx. Clearly, the GTV dose is significantly larger in the combined modality plan than in the single modality proton plan. This does come at the cost of a larger dose to several OARs: in particular, larger volumes of the liver and the stomach receive a low to medium dose instead of no dose, due to the photon dose distribution. However, all OAR constraints are naturally still satisfied.

6.4.2 Demonstration of OAR sparing

From Figure 6.5 it may seem that simply allowing higher OAR doses for a single modality proton plan could yield similarly large tumor BED values as the combined modality plan. This is in general not the case. To show this we performed additional analysis for patient P_1 by minimizing healthy liver BED for both single modality proton and combined proton-photon treatments, subject to the constraint that the tumor BED should be at least 72.5 Gy_{10} (the mean GTV BED value in the optimal combined plan when GTV BED was maximized). All other OAR constraints are omitted. The resulting DVH

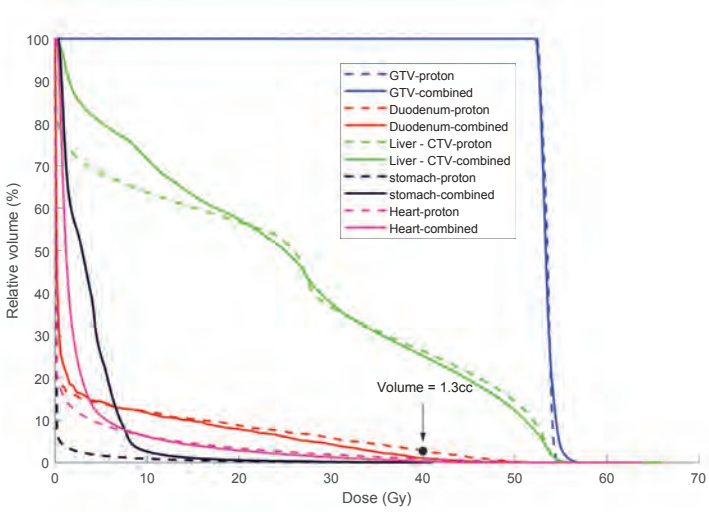

Figure 6.6: DVH for proton and combined modality plans for patient P_1 for mean liver BED minimization. Mean tumor BED is constrained to be at least 72.5 Gy_{10}. Dashed lines are the optimal single modality proton solution, solid lines the optimal combined modality solution. The healthy liver dose distribution is comparable, while the single modality proton solution violates the duodenum 0.5cc DVH constraint.

is displayed in Figure 6.6, where also the optimal combined modality plan is displayed. The resulting proton plan uses 15 fractions of 3.6 Gy. The resulting liver dose distributions are comparable, however by not using proton fractions alone combined modality is better able to spare the duodenum. As given in Table 6.1, at 15 fractions the duodenum volume that receives more than 40 Gy should be at most 0.5cc, but as indicated in Figure 6 this volume in the proton plan is in fact 1.3cc. This result indicates that, even if combined modality is not able to reduce mean liver BED compared to single modality proton (see Section 6.3.1), combined modality plans may still yield benefits in terms of OAR sparing for other OARs than healthy liver.

As mentioned in Section 6.3.1, for 2 patients (P_2 and P_3) combined modality treatment was found to be able to lower healthy liver mean dose. In case of mean tumor BED maximization, for patient P_2 the binding constraint in the single modality proton and photon treatments are the $0.5cc$ small bowel DVH constraint and the mean liver dose constraint, respectively. For P_3, the situation is similar, the only difference being that the binding constraint for single modality proton is the $0.5cc$ stomach DVH constraint. For the mean healthy liver BED minimization, the lower bound on the GTV

mean BED is set at the GTV BED of optimal single modality proton treatment. For patients P_2 and P_3 single modality proton attains the maximum GTV BED using fewer than the maximum of 15 fractions. For the combined modality treatment it is easier to get to this GTV BED, because it can better spare the second OAR (small bowel or stomach) than the single modality proton treatment. Hence, it can exploit the fractionation effect better for OAR sparing. Furthermore, although the photon dose distribution has a higher mean healthy liver dose than the proton dose distribution, the locations of their healthy liver high dose areas need not be the same. Hence, a combined treatment may deliver the healthy liver dose more homogeneously, leading to a lower dose shape factor (Perkó et al., 2018) and a lower healthy liver BED.

6.4.3 Illustration of Group 2

Patient P_6 was also clinically treated with 15 proton fractions. Two CT slices are displayed in Figure 6.7, visualizing the dose distributions for both photons and protons. The relevant organs are the liver, the stomach, and the cord (see Figures 6.7c and 6.7d showing the lower CT slice). The dose tolerances for the healthy liver mean dose constraint are 17 Gy in 5 fractions and 27 Gy in 15 fractions, for the other constraints see Table 6.1. The clinical plan violated the 700cc constraint, which is omitted here as well.

The optimal GTV BED is 92.6 Gy_{10} and is obtained at 15 proton fractions, see column 3 of Table 6.4. The corresponding physical dose to the GTV is 64.7 Gy. There are no combined modality treatments that yield a higher average GTV BED, the reason for this is shown in Figure 6.7. As seen in the CT slices of Figure 6.7a and Figure 6.7b, both the proton and the photon high dose region fall almost entirely inside the liver, so the healthy part of the liver gets a large average dose in both modalities. However, the tumor is very close to a small extension of the stomach, and protons spare this part slightly better than photons, making single modality proton treatments optimal.

In the single modality proton plan the binding constraint is the (17 Gy in 5 fractions) mean dose constraint on the liver, while the $0.5cc$ stomach DVH constraint is almost binding. In the single modality photon plan this is reversed; the stomach constraint is binding, while the liver mean dose constraint is almost binding. Similar to patient P_1, we check the influence of restricting the single modality photon case to constant dose per fraction: the optimal treatment delivers an average GTV BED of 82.7 Gy_{10}, using 6 fractions of 7.8 Gy/fx, again a negligible difference (compared to column 1 in Table 6.4).

Using the results reported in Table 6.4, let us compare the optimal single modality proton solution to the combined modality alternative that uses 7 proton fractions

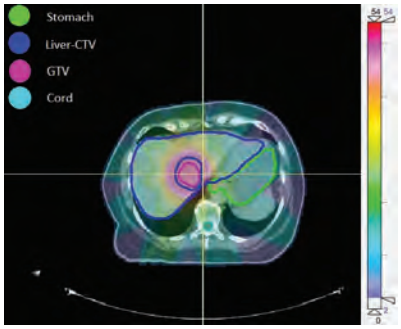

(a) Photon, CT slice 1

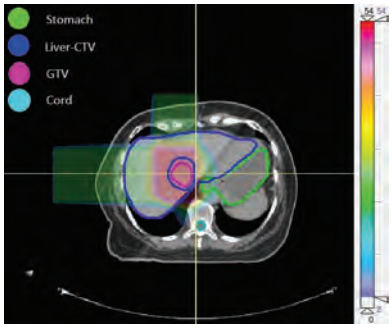

(b) Proton, CT slice 1

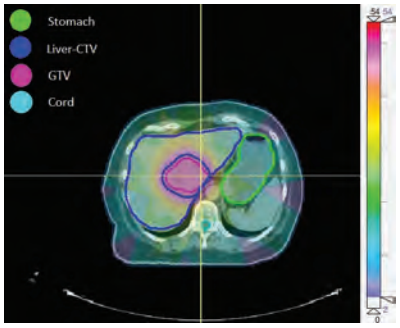

(c) Photon, CT slice 2

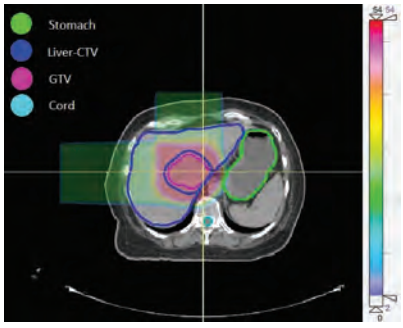

(d) Proton, CT slice 2

Figure 6.7: Spatial dose distribution in photon and proton plans of patient P_6 in two slices. The GTV, liver-CTV, stomach and cord are delineated. CT slice 1 is the higher of the two slices.

and 8 photon fractions. The average GTV BED of this combined modality solution is 90.1 Gy_{10}, and the corresponding BED equivalent physical GTV dose is 63.3 Gy. This is a decrease of 1.4 Gy in BED equivalent GTV dose for a substitution of 8 fractions.

When substituting some proton fractions in the single modality proton treatment with photon fractions, the remaining space in the 0.5*cc* stomach DVH constraint is used as well. This is because protons damage the part of the stomach that is close to the tumor slightly more than photons. Consequently, both the 0.5*cc* stomach DVH constraint and the liver mean dose constraint become binding. However, as protons spare the liver a bit better, the attainable average GTV BED decreases. The BED to the cord also increases significantly compared to the single modality proton plan, where it received almost no dose. Nevertheless, the tolerance level of the 0.5*cc* cord DVH constraint is not violated.

	Single modality photon	Single modality proton	Combined modality
GTV BED	82.8 Gy_{10}	92.6 Gy_{10}	90.1 Gy_{10}
BED equivalent dose	59.3 Gy	64.7 Gy	63.3 Gy
Photon fractions	5 fx (8.7 Gy/fx) 1 fx (1.0 Gy/fx)	-	8 fx (3.7 Gy/fx)
Proton fractions	-	15 fx (4.3 Gy/fx)	7 fx (4.8 Gy/fx)

Table 6.4: Results for patient P_6. The reported combined modality treatment is an alternative to the single modality proton treatment. It delivers a slightly lower BED equivalent dose to the GTV, but uses fewer proton fractions.

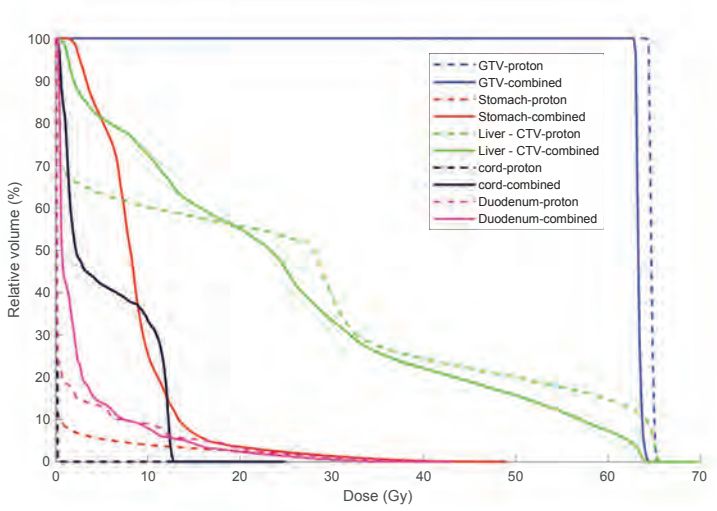

Figure 6.8: DVH for proton and combined modality plans for patient P_6. The dashed lines are the optimal single modality proton solution, the solid lines are the alternative combined modality solution. The combined modality solution yields a slightly lower average GTV BED, while using 8 fewer proton fractions.

Figure 6.8 shows the DVH for the GTV, healthy liver, stomach, cord and duodenum, in terms of BED equivalent dose. The dashed lines are the optimal single modality proton plan which uses 15 proton fractions, and the solid lines are the alternative combined modality plan which uses 7 proton fractions and 8 photon fractions. We see that indeed the BED equivalent average GTV dose is slightly higher for the single modality proton plan than for the combined modality plan. Furthermore, the low

dose volumes for the liver, stomach and cord increase. At the same time, the high dose volume for the liver decreases.

6.4.4 Connection to clinically used NTCP models

In the Netherlands a model based approach is used to determine proton therapy eligibility (Blanchard et al., 2016; Widder et al., 2016; Bijman et al., 2017). Patients are eligible for protons if normal tissue complication probability (NTCP) models show that protons offer a significant improvement over photons. As NTCP models are often BED distribution based models (Perkó et al., 2018), our work fits this procedure nicely. Our approach can show that when using a combined modality approach we can get a higher tumor BED for the same BED constraint, or alternatively for a given tumor dose we can decrease OAR BED. This takes the current Dutch approach to the next level, not only making binary decisions between photons or protons, but instead looking into the correct combination of proton and photon fractions for complication minimization.

6.4.5 Clinical aspects and limitations

We do not have a precise measure of the robustness of the combined proton-photon plans that are obtained via the approach of Section 6.2.2. However, any combined proton-photon plan that is obtained via our approach is essentially a weighted average of the input clinical proton and photon plans. As discussed in Section 6.2.2 and Perkó et al. (2018), for all used plans proper clinical measures were taken to handle uncertainties. Therefore, as in any fraction either (a scaled version of) the proton or photon plan is delivered, the combined proton-photon treatment is also robust against the same uncertainties.

As the approach of Section 6.2.2 takes the proton and photon dose distribution as an input, whether or not combined modality is optimal for a patient depends on these initial proton and photon plans. As such, different plans may yield different results. The proton and photon plans used in the numerical study in Section 6.3 were however either clinically used plans, or plans that were derived under clinical circumstances, as if they were to be delivered. This implies that under the same clinical circumstances, our results are representative of the realistic clinical benefit of combined modality treatments.

Our approach excludes spatiotemporal optimization, and simply scales the given proton and photon dose distributions. Since in spatiotemporal optimization of a combined proton-photon treatment the individual dose spatial distributions are also optimized, this may improve on our methodology. However, the results from spatiotemporal optimization can only yield a larger benefit for combined modality treatments

compared to what is presented in Section 6.3. That is, the presented results for individual patients should be seen as a 'lower bound' on the benefit of a combined modality treatment for the patient, reinforcing our main conclusions. Furthermore, although spatiotemporal optimization may yield better results, the presented approach has some practical advantages. Planning, reviewing and quality assurance procedures are well established for single modality treatment plans and these could be seamlessly used for our combined modality approach, as either modality can be separately dealt with. In fact, this is exactly how currently combined treatments are used in the clinic (e.g., in case of a proton machine breakdown when patients are redirected to photon treatments for the remainder of their treatment).

We have only tested our approach on liver patients, thus we cannot make any statements about the potential of combined proton-photon treatment schemes in other tumor sites. Nevertheless, the mathematical approach of Section 6.2.2 does not make any assumptions on the specific tumor site, and is applicable to any case where both a proton and photon dose distribution are available. The reasons why combined modality may be optimal, as demonstrated in Section 6.2.1, can also occur in other tumor sites, particularly those where there are multiple OARs in proximity to the tumor.

In our numerical experiments the objective is to maximize the mean BED to the GTV (a general recommendation for liver patients is to not expand the GTV to a larger CTV (Dawson et al., 2012)). However, we also performed experiments with maximizing mean CTV BED, indicating that the difference in results from maximizing mean GTV BED is very little. The protocol (Dawson et al., 2012) also recommends the mean liver dose to be calculated on the liver-GTV, whereas we considered liver-CTV (volume that is healthy with high likelihood). This difference is not expected to influence results either (as the CTV-GTV volume receives very similar doses from both protons and photons).

We also show that minimizing OAR BED can lead to optimal combined modality treatments for the same reasons. First, Appendix 6.A.3 discusses the simplistic analytical model to show why also for OAR dose sparing combined modality may be of use. Second, the numerical experiments have shown that, for the patients in Group 1 (Section 6.3.1), combined modality may also achieve lower healthy liver BED. Section 6.4.1 discusses these numerical results and additionally shows an example of lower duodenum dose due to difference in spatial dose distribution.

6.5 Conclusion

Proton therapy has several advantages over conventional photon therapy. However, in current clinical practice protons are not better for all organs in all cases, especially not when larger margins are needed for large motion uncertainty. Consequently, this work analyzed the benefit of combined modality treatments. It is demonstrated both via theoretical results and real patient case studies that combined modality treatments can result in superior dosimetric treatment plan quality. One reason for this is that in case of multiple constraints, one constraint may be more restrictive for one treatment modality, while the other is more restrictive for the other. A second reason is that even in situations where the proton plan is superior in terms of physical dose, using photon fractions can result in treatment plans that are better, due to the fractionation effect.

Results from the case study on real data from patients treated at Massachusetts General Hospital show that for 5 out of 17 patients indeed combined modality treatments outperform the single modality proton treatment, with improvements of up to 14.8% in BED equivalent physical dose. For these patients in our cohort the single modality photon and proton treatments have different binding constraints, while their combination is binding in the optimal combined modality solution, corresponding well with theoretical results. For 2 out of these 5 patients, also the single modality photon plan yields a higher BED equivalent physical dose than the proton plan.

For several other patients combined modality treatments are near-optimal while using fewer proton fractions. Especially because of the price tag and the limited availability of proton fractions, such alternatives that put less pressure on the proton machine of a certain treatment facility may be very interesting. In conclusion, the potential for combined modality treatments is considerable.

Acknowledgments

The authors thank Ted Hong and John Wolfgang (Massachusetts General Hospital and Harvard Medical School) for their valuable input during discussions.

6.A Mathematical derivation of optimality of combined modality treatments

This section discusses the simplified geometry of Figure 6.1 in Section 6.2.1, and formulates several mathematical models that demonstrate the benefit of combining photons with protons

instead of using only protons. The optimization is based on the BED model, which is introduced in Section 6.2, and in Section 6.2.1 the setting is described. For this demonstration we make two assumptions. Note that these assumptions are strictly only made for this analytical exercise highlighting why combined modality can be optimal, and not for the general methodology or any of the real patient cases in the chapter.

Assumption 6.1. *The protons dose distribution has a larger high dose but smaller low dose region than the photon dose distribution.*

Assumption 6.2. *For a fixed tumor dose, the proton dose distribution delivers lower mean dose to OAR 1 than the photon dose distribution.*

Parameters f_i^H and f_i^L denote the high and low dose volume fraction of OAR 1 for modality i, respectively, where $i = \gamma$ denotes photons and $i = p$ denotes protons. Let w denote the high dose volume fraction of OAR 2 for the proton beam. Assumption 6.1 mathematically implies that $f_\gamma^H < f_p^H$ and $f_\gamma^L > f_p^L$. Let D_γ^T, the mean tumor dose for photons, and D_p^T, the mean tumor dose for protons, be the decision variables (superscript T refers to the tumor). For the OARs, the low dose can be expressed as $D_i^{\text{low}} = s_i D_i^T$, where $s_i \in [0,1]$ is the dose sparing factor of modality i for the low dose region. The high dose areas are assumed to receive the full tumor dose, so $D_i^{\text{high}} = D_i^T$. The mean dose in OAR 1 due to modality i can be written as a function of mean tumor dose due to modality i:

$$D_i^{\text{OAR1}}(D_i^T) = s_i f_i^L D_i^T + f_i^H D_i^T = (s_i f_i^L + f_i^H) D_i^T.$$

Assumption 6.2 implies that for a fixed tumor dose the mean proton dose to OAR 1 is smaller than the mean photon dose to OAR 1, i.e., $s_\gamma f_\gamma^L + f_\gamma^H > s_p f_p^L + f_p^H$. For notational convenience, we introduce the parameters

$$r_\gamma = s_\gamma f_\gamma^L + f_\gamma^H, \quad q_\gamma = s_\gamma^2 f_\gamma^L + f_\gamma^H, \tag{6.A.1a}$$

$$r_p = s_p f_p^L + f_p^H, \quad q_p = s_p^2 f_p^L + f_p^H, \tag{6.A.1b}$$

which provide a linear and quadratic mapping from tumor dose to OAR dose. Using this notation, Assumption 6.2 implies $r_\gamma > r_p$.

The first model (related to reason 1 in Section 6.2.1) does not take into account fractionation, and sets a mean dose constraint on OAR 1 and a DVH constraint on OAR 2. In the second model (related to reason 2 in Section 6.2.1) we allow for a fractionation effect in OAR 1 but not in the tumor, and we set a mean BED constraint on OAR 1 (OAR 2 is not taken into account). In Appendix 6.C, a third model is discussed, which is an extension of the second model also allowing for fractionation effects in the tumor. In Appendix 6.A.3 we take an alternative approach, and minimize OAR BED subject to a prescribed tumor dose.

6.A.1 Reason 1 - Mathematical model

To maximize the dose delivered to the tumor, while satisfying all constraints set on the OARs, we rescale the dose distributions, increasing or decreasing the dose in the OARs and the tumor simultaneously. That is, D_γ^T and D_p^T are the decision variables.

We set a mean dose constraint on OAR 1 and a DVH constraint on OAR 2. Let $D_{\text{mean}}^{\text{tol}}$ denote the largest average dose that OAR 1 can tolerate, as determined by the physician. Suppose the DVH constraint states that no more than a fraction k of the volume of OAR 2 may receive a higher dose than $D_{\text{dvh}}^{\text{tol}}$. This constraint can potentially be more restrictive for the proton dose distribution than for the photon dose distribution. In the photon plan OAR 2 receives only low dose. If $k < w$, the total dose to the proton high dose volume w must not exceed the tolerance level $D_{\text{dvh}}^{\text{tol}}$. OAR 2 receives only photon low dose. Therefore, volume w receives a dose of $s_\gamma D_\gamma^T + D_p^T$ in the combined modality plan, which must be below the DVH tolerance dose $D_{\text{dvh}}^{\text{tol}}$. The optimization problem with both a mean dose constraint and a DVH constraint reads

$$\max_{D_\gamma^T,\, D_p^T} \; D_\gamma^T + D_p^T, \tag{6.A.2a}$$

$$\text{s.t.} \;\; r_\gamma D_\gamma^T + r_p D_p^T \le D_{\text{mean}}^{\text{tol}}, \tag{6.A.2b}$$

$$s_\gamma D_\gamma^T + D_p^T \le D_{\text{dvh}}^{\text{tol}}, \tag{6.A.2c}$$

$$D_\gamma^T \ge 0,\; D_p^T \ge 0. \tag{6.A.2d}$$

In the problem described by (6.A.2) it does not necessarily have to hold that using only photons or only protons is optimal. Problem (6.A.2) is a linear programming problem with two variables. The feasible region of (6.A.2b) is illustrated in Figure 6.A.1. It can easily be verified that the vertices of the feasible region are

$$C_1 = \big(0, 0\big), \qquad C_2 = \Big(\min\Big\{\frac{D_{\text{mean}}^{\text{tol}}}{r_\gamma},\; \frac{D_{\text{dvh}}^{\text{tol}}}{s_\gamma}\Big\}, 0\Big),$$

$$C_3 = \Big(0, \min\Big\{\frac{D_{\text{mean}}^{\text{tol}}}{r_p},\; D_{\text{dvh}}^{\text{tol}}\Big\}\Big), \qquad C_4 = \Big(\frac{D_{\text{mean}}^{\text{tol}} - D_{\text{dvh}}^{\text{tol}} r_p}{r_\gamma - s_\gamma r_p},\; \frac{r_\gamma D_{\text{dvh}}^{\text{tol}} - s_\gamma D_{\text{mean}}^{\text{tol}}}{r_\gamma - s_\gamma r_p}\Big).$$

Linear programming theory states that the optimal solution is attained in one (or more) of these vertices. Vertex C_1 is clearly not optimal because the corresponding objective value is 0. Vertices C_2 and C_3 comprise single modality solutions and C_4 is the combined modality solution. Vertex C_4 is only a feasible vertex if both coordinates are positive. It readily follows that this leads to the following condition:

$$r_p < \frac{D_{\text{mean}}^{\text{tol}}}{D_{\text{dvh}}^{\text{tol}}} < \frac{r_\gamma}{s_\gamma}. \tag{6.A.3}$$

In Figure 6.A.1a this condition holds, so all vertices C_1, C_2, C_3 and C_4 are feasible. In Figure 6.A.1b condition (6.A.3) does not hold, and the horizontal coordinate of C_4 is negative. In this situation, the mean dose constraint (6.A.2b) is binding at any feasible vertex. In case the vertical coordinate of C_4 is negative, DVH constraint (6.A.2c) is binding at any feasible vertex.

We are interested in conditions under which C_4 is optimal, in case it is feasible (the situation in Figure 6.A.1a), rather than the single modality solutions (vertices C_2 and C_3). In (6.A.2a) the coefficients for D_1^T and D_2^T are both 1, so the objective function is a straight line with slope -1. Due to Assumption 6.2 the mean dose to OAR 1 is lower for the proton dose distribution than for the photon dose distribution. Therefore, in the mean dose constraint (6.A.2b) the coefficient for proton dose is smaller than that for photon dose, implying that the slope for the mean dose constraint is smaller than -1. If the slope of the DVH constraint (6.A.2c) is larger than -1, combined modality is optimal. This reduces to $s_\gamma < 1$, which holds by definition. Hence, combined modality is always optimal as long as the solution candidate C_4 is feasible, which holds if the dose tolerances satisfy condition (6.A.3).

For example, let $f_\gamma^L = 0.82$, $f_\gamma^H = 0.18$, $s_\gamma = 0.32$ be the parameters for the photon dose distribution, and let $f_p^L = 0.37$, $f_p^H = 0.23$ and $s_p = 0.38$ be the parameters for the proton dose distribution. Then the proton high dose area is larger than the photon high dose area, while the photon mean dose to OAR 1 is larger than the proton mean dose to OAR 1. Condition (6.A.3) reads

$$0.37 < \frac{D_{\text{mean}}^{\text{tol}}}{D_{\text{dvh}}^{\text{tol}}} < 1.38,$$

which is satisfied by for example $D_{\text{mean}}^{\text{tol}} = 20$ Gy and $D_{\text{dvh}}^{\text{tol}} = 35$ Gy.

6.A.2 Reason 2 - Mathematical model

We extend the previous model to allow for a fractionation effect in OAR 1. For this model, OAR 2 is ignored to demonstrate that even with a single OAR combined modality treatments can be optimal. Let ρ denote the inverse α/β-ratio of OAR 1. With r_i and q_i defined by (6.A.1), one can verify that the mean BED to OAR 1 due to modality i is

$$\text{BED}_i^{\text{OAR1}}(d_i, N_i) = r_i \sum_{t_i=1}^{N_i} d_{i,t_i} + \rho q_i \sum_{t_i=1}^{N_i} d_{i,t_i}^2.$$

We assume that the α/β-ratio in the tumor is very large so that we can neglect the fractionation effect in the tumor. That is, we are interested in the physical tumor dose

$$D^T = D_\gamma^T + D_p^T = \sum_{t_\gamma=1}^{N_\gamma} d_{\gamma,t_\gamma} + \sum_{t_p=1}^{N_p} d_{p,t_p}.$$

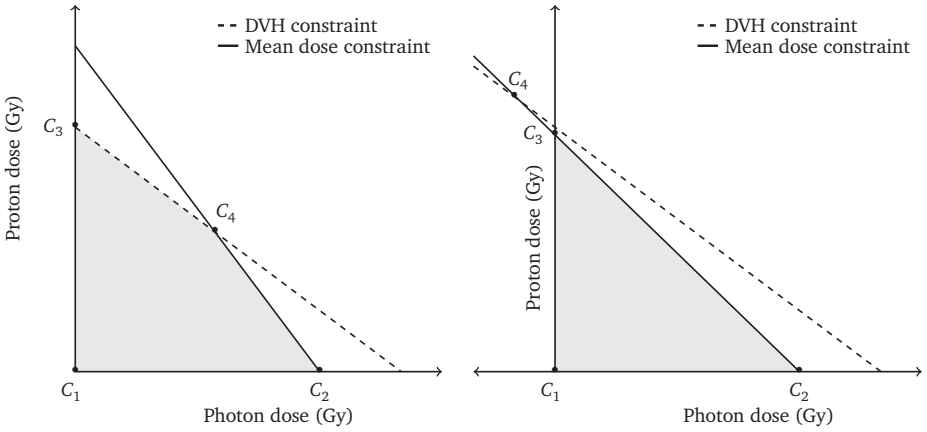

(a) Feasible region (in grey) for (6.A.2) if vertex C_4 is feasible.

(b) Feasible region (in grey) for (6.A.2) if vertex C_4 is infeasible because the horizontal coordinate is negative.

Figure 6.A.1: Feasible region (grey) of (6.A.2), which is the convex hull of (some of) the vertices $C_1 - C_4$. The feasible region is constrained by a DVH constraint (on OAR2) and a mean dose constraint (on OAR1).

We aim to maximize the total tumor dose while constraining mean OAR BED below a fixed value BED_{tol}. The optimization problem looks as follows:

$$\max_{\boldsymbol{d}_\gamma,\, \boldsymbol{d}_p} \quad \sum_{t_\gamma=1}^{N_\gamma} d_{\gamma,t_\gamma} + \sum_{t_p=1}^{N_p} d_{p,t_p}, \tag{6.A.4a}$$

$$\text{s.t.} \quad r_\gamma \sum_{t_\gamma=1}^{N_\gamma} d_{\gamma,t_\gamma} + \rho q_\gamma \sum_{t_\gamma=1}^{N_\gamma} d_{\gamma,t_\gamma}^2 + r_p \sum_{t_p=1}^{N_p} d_{p,t_p} + \rho q_p \sum_{t_p=1}^{N_p} d_{p,t_p}^2 \leq \text{BED}_{\text{tol}}, \tag{6.A.4b}$$

$$d_{\gamma,t_\gamma} \geq 0,\ t_\gamma = 1,\ldots,N_\gamma,\ d_{p,t_p} \geq 0,\ t_p = 1,\ldots,N_p. \tag{6.A.4c}$$

Our decision variables are $\boldsymbol{d}_\gamma \in \mathbb{R}_+^{N_\gamma}$ and $\boldsymbol{d}_p \in \mathbb{R}_+^{N_p}$. In (6.A.4), N_γ and N_p are considered fixed parameters, and treatment plans with fewer than N_γ photon or N_p proton fractions can be found by setting the corresponding elements of $\boldsymbol{d}_\gamma$ and $\boldsymbol{d}_p$ at zero. In other words, N_γ and N_p are parameters indicating an upper bound on the number of photon and proton fractions, respectively.

In Appendix 6.D it is shown that the following problem is equivalent to (6.A.4):

$$\max_{x_\gamma,\, y_\gamma,\, x_p,\, y_p} \quad x_\gamma + x_p, \tag{6.A.5a}$$

$$\text{s.t.} \quad r_\gamma x_\gamma + \rho q_\gamma y_\gamma + r_p x_p + \rho q_p y_p \leq \text{BED}_{\text{tol}}, \tag{6.A.5b}$$

$$\sqrt{y_\gamma} \leq x_\gamma \leq \sqrt{N_1 y_\gamma}, \tag{6.A.5c}$$

$$\sqrt{y_p} \leq x_p \leq \sqrt{N_2 y_p}, \tag{6.A.5d}$$

$$x_\gamma \geq 0,\ y_\gamma \geq 0,\ x_p \geq 0,\ y_p \geq 0. \tag{6.A.5e}$$

For a fixed dose to (part of) the OAR, the BED to (that part of) the OAR will be lower if this dose is administered over multiple fractions. Because in this problem the number of fractions does not influence the damage to the tumor (fractionation in the tumor is ignored), the optimal solution will always use the maximum number of allowed fractions. Therefore, it will always hold that $x_\gamma = \sqrt{N_\gamma y_\gamma}$ and $x_p = \sqrt{N_p y_p}$. Plugging this in (6.A.5b) gives an optimization problem with only decision variables x_γ and x_p. Furthermore, at optimality (6.A.5b) will hold with equality, because the total physical dose to the tumor is increased until the OAR BED tolerance is reached. Therefore, we can rewrite (6.A.5b) in terms of x_γ and eliminate variable x_p as well.

The resulting optimization problem reads

$$\max_{x_p} \ f(x_p),$$
$$\text{s.t. } 0 \leq x_p \leq x_p^U,$$

where

$$f(x_p) = x_p + \frac{N_\gamma}{2\rho q_\gamma}\Big(-r_\gamma + \big(r_\gamma^2 - 4\frac{\rho q_\gamma}{N_\gamma}(r_p z + \frac{\rho q_p}{N_p}x_p^2 - \text{BED}_{\text{tol}})\big)^{\frac{1}{2}}\Big),$$

$$x_p^U = \frac{N_p}{2\rho q_p}\Big(-r_p + \big(r_p^2 + 4\frac{\rho q_p}{N_p}\text{BED}_{\text{tol}}\big)^{\frac{1}{2}}\Big).$$

Function $f(x_p)$ is concave, because it is a composite function of a nondecreasing concave function and a concave function (Boyd and Vandenberghe, 2004). Hence, it follows that a single modality photon treatment is optimal if $f'(0) \leq 0$, a single modality proton treatment is optimal if $f'(x_p^U) \geq 0$, and combined modality is optimal otherwise. The derivative of the objective function is

$$f'(x_p) = 1 + \Big(-r_p - 2\frac{\rho q_p}{N_p}x_p\Big)\Big(4\frac{\rho q_\gamma}{N_\gamma}(\text{BED}_{\text{tol}} - x_p(r_p + \frac{\rho q_p}{N_p}x_p)) + r_\gamma^2\Big)^{-\frac{1}{2}}. \tag{6.A.6}$$

From (6.A.6) the following easily follows:

- Single modality photon is never optimal;
- Combined modality is optimal if $\text{BED}_{\text{tol}} > \dfrac{N_p(r_\gamma^2 - r_p^2)}{4\rho q_p}$;
- Single modality proton is optimal otherwise.

Thus, there is a threshold for BED_{tol} beyond which the benefit of fractionation outweighs the worse OAR sparing properties of the photons in terms of physical dose. Using basic algebra the optimal dose per fraction values can be calculated for both situations.

6.A.3 Minimization of OAR BED

To show that the optimality of combined modality treatments is not restricted to the previously presented models, we analyze a model where we do not maximize tumor dose but minimize OAR BED, while delivering a prescribed dose $\hat{D}$ to the tumor. We immediately apply the mapping from tumor dose to OAR dose defined by (6.A.1), and the reformulation provided in Appendix 6.D. The optimization problem looks as follows:

$$\begin{aligned}\min_{x_\gamma,\, y_\gamma,\, x_p,\, y_p} \quad & r_\gamma x_\gamma + \rho q_\gamma y_\gamma + r_p x_p + \rho q_p y_p, \\ \text{s.t.} \quad & x_\gamma + x_p = \hat{D}, \\ & \sqrt{y_\gamma} \le x_\gamma \le \sqrt{N_\gamma y_\gamma}, \\ & \sqrt{y_p} \le x_p \le \sqrt{N_p y_p}, \\ & x_\gamma \ge 0,\ y_\gamma \ge 0,\ x_p \ge 0,\ y_p \ge 0.\end{aligned}$$

Similar to Appendix 6.A.2 the optimal solution will always use the maximum number of allowed fractions. Therefore, it will always hold that $x_\gamma = \sqrt{N_\gamma y_\gamma}$ and $x_p = \sqrt{N_p y_p}$. This leads to a problem with four variables and three equality constraints, which can be simplified to a problem with one variable. Making the substitution $z = \sqrt{y_p}$ leads to

$$\min_z \ \Big(\rho q_\gamma \frac{N_\gamma}{N_p} + \rho q_p\Big) z^2 + \Big((r_p - r_\gamma)\sqrt{N_p} - 2\rho q_\gamma \hat{D}\frac{\sqrt{N_p}}{N_\gamma}\Big) z + \Big(p_\gamma \hat{D} + \rho \frac{q_\gamma}{N_\gamma}\hat{D}^2\Big), \tag{6.A.7a}$$

$$\text{s.t. } 0 \le z \le \frac{\hat{D}}{\sqrt{N_p}}. \tag{6.A.7b}$$

The first order condition, i.e., zero-derivative, gives

$$\hat{z} = \frac{(r_\gamma - r_p)N_\gamma\sqrt{N_p} + 2\rho q_\gamma \sqrt{N_p}\hat{D}}{2\rho(q_p N_\gamma + q_\gamma N_p)}.$$

Because $r_\gamma > r_p$, it holds that $\hat{z} > 0$, so a single modality solution using only photons cannot be optimal. It is easily verified that $\hat{z}$ satisfies (6.A.7b) if $\hat{D} \ge D^*$, where

$$D^* = \frac{(r_\gamma - r_p)N_p}{2q_p\rho}.$$

In this case, we can write $x_\gamma = \hat{D} - x_p = \hat{D} - \sqrt{N_p}\hat{z}$, from which it follows that if $\hat{D} > D^*$ holds we have $x_\gamma > 0$ (and thus $y_\gamma > 0$). This implies a combined proton-photon fractionation

scheme. On the other hand, if $\hat{D} \leq D^*$, then the optimal solution to (6.A.7) is

$$x_p = \frac{\hat{D}}{\sqrt{N_p}}.$$

Because $\sqrt{y_p} = x_p$, we obtain $x_p = \hat{D}$, $x_\gamma = 0$ and $y_\gamma = 0$. Summarizing, we find that two situations can be distinguished with regard to a single modality or combined modality solution:

$$\begin{cases} \hat{D} \leq D^* & \text{A single modality solution using only protons is optimal,} \\ \hat{D} > D^* & \text{A combined modality solution is optimal.} \end{cases}$$

Using basic algebra the optimal dose per fraction values can be calculated for both situations. Similar to Appendix 6.A.2, combined modality is optimal if a threshold is exceeded, although there the threshold is in terms of OAR BED tolerance while here it is in terms of the prescribed tumor dose. Nevertheless, the intuition for the current result is analogous to the intuition 'reason 2' presented in Section 6.2.1.

6.B Single modality optimal fractionation problem

Let ρ^T be the inverse α/β ratio for the tumor, let $\mathcal{M}$ denote the set of constraints and let ρ^m denote the inverse α/β ratio for constraint $m \in \mathcal{M}$. In Saberian et al. (2015) it is shown that the single modality optimal fractionation problem with maximum point dose constraints, DVH constraints and mean dose constraints can be formulated as

$$\max_{x,\, y} \; rx + \rho^T q y, \tag{6.B.1a}$$

$$\text{s.t.} \;\; \sigma^m x + \rho^m (\sigma^m)^2 y \leq B^m, \;\; \forall m \in \mathcal{M}, \tag{6.B.1b}$$

$$y \leq \gamma^* x, \tag{6.B.1c}$$

$$c^* x \leq y, \tag{6.B.1d}$$

$$x \geq 0, \; y \geq 0, \tag{6.B.1e}$$

where r, q, and σ^m, B^m, $\forall m$, are parameters. Furthermore,

$$\gamma^* = \min_{m \in \mathcal{M}} \frac{-1 + \sqrt{1 + 4\rho^m B^m}}{2\sigma^m \rho^m},$$

$$c^* = \min_{m \in \mathcal{M}} \frac{-1 + \sqrt{1 + 4\rho^m B^m / N}}{2\sigma^m \rho^m},$$

where N is the maximum allowed number of fractions. Variables x and y denote the dose and sum of squared doses. Problem (6.B.1) is a 2-variable linear programming problem and is easily solved.

6.C Optimality with full fractionation and sensitivity analysis

The model of Appendix 6.A.2 is extended to allow for a fractionation effect in the tumor as well. This will make the problem more interesting, as it is not immediately clear how many fractions of each modality should be used. The optimization problem will be formulated such that the objective is to maximize the average tumor BED, under a constraint on the mean BED in the OAR. In addition to the existing notation, let ρ^T denote the inverse α/β-ratio of the tumor. The optimization problem now reads

$$\max_{x_\gamma,\, y_\gamma,\, x_p,\, y_p} \quad x_\gamma + \rho^T y_\gamma + x_p + \rho^T y_p, \tag{6.C.1a}$$

$$\text{s.t.} \quad r_\gamma x_\gamma + \rho q_\gamma y_\gamma + r_p x_p + \rho q_p y_p \leq \text{BED}_{\text{tol}}, \tag{6.C.1b}$$

$$\sqrt{y_\gamma} \leq x_\gamma \leq \sqrt{N_\gamma y_\gamma}, \tag{6.C.1c}$$

$$\sqrt{y_p} \leq x_p \leq \sqrt{N_p y_p}, \tag{6.C.1d}$$

$$x_\gamma \geq 0,\ y_\gamma \geq 0,\ x_p \geq 0,\ y_p \geq 0. \tag{6.C.1e}$$

The objective and the BED tolerance constraint are linear, but the problem is nonconvex due to the constraints $\sqrt{y_\gamma} \leq x_\gamma$ and $\sqrt{y_p} \leq x_p$. Therefore, it is much harder to derive analytical solutions. However, due to the small scale of the problem good solutions can be obtained numerically using solvers such as the MATLAB `fmincon` function (MATLAB R2017b, Mathworks, Natick, MA, US).

Problem (6.C.1) is solved using realistic data from an example patient (Patient P_4 from our data set). The clinical photon and proton dose distributions were available, from which the mean OAR and mean tumor doses were obtained. For simplicity we assume that the liver, i.e., the OAR that contains the tumor, is the only relevant OAR. Let the high dose region be the region where the OAR receives more than 80% of the average tumor dose. From DVH statistics it is estimated that for the photon plan this is 18% of the OAR volume, and for the proton plan it is 23%. From these statistics the dose sparing factors s_γ and s_p can be computed. The 3D dose distribution, of which a slice is depicted in Figure 6.C.1, shows that the high dose region of the proton plan is indeed encapsulated in the high dose region of the photon plan. Therefore, the clinical plans indeed satisfy Assumption 6.1. Table 6.C.1 summarizes the most important statistics for both distributions.

The values for the maximum number of allowed proton fractions, N_p, the OAR fractionation sensitivity parameter ρ and the tolerance value of the mean dose constraint, BED_{tol}, are varied. For comparison, the single modality proton problem is solved as well via the linear programming formulation developed in Saberian et al. (2015), see also Appendix 6.B. The tumor fractionation sensitivity parameter ρ^T is set at $\frac{1}{10}$ and the number of allowed photon fractions N_γ is set at 10.

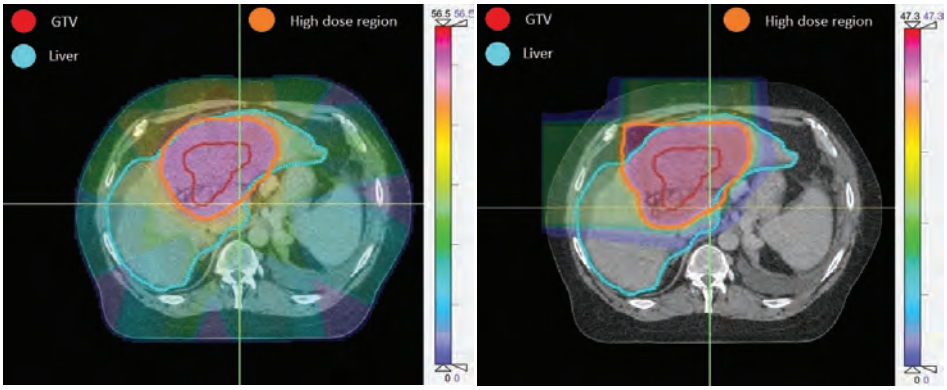

(a) Photon dose distribution (b) Proton dose distribution

Figure 6.C.1: 3D dose distribution of patient P_4. The high dose region of the photon dose distribution is encapsulated in the high dose region of the proton dose distribution.

	Photon	Proton
Dose sparing factor (s_i)	0.324	0.380
Volume fraction no dose	0%	40%
Volume fraction low dose (f_i^L)	82%	37%
Volume fraction high dose (f_i^H)	18%	23%

Table 6.C.1: Statistics on the photon dose distribution and the proton dose distribution and the reference plans for patient P_4.

Furthermore, the base values of the parameters are $N_p = 10$, $\rho = \frac{1}{4}$ and $\text{BED}_{\text{tol}} = 20\ \text{Gy}_{\alpha/\beta}$. In Figure 6.C.2a the value of ρ is varied, in Figure 6.C.2b the value of N_p is varied and in Figure 6.C.2c the value of BED_{tol} is varied. In each figure, the average tumor BED is measured on the left vertical axis and the number of used fraction is measured on the right axis. In every scenario, the number of used proton fractions is equal for both the single modality proton treatment (squares) and the combined modality treatment (circles). The used photon fractions, displayed with a grey circle, are used only in the combined modality treatment.

In Figure 6.C.2a parameter ρ is changed from $\frac{1}{4}$ to $\frac{1}{3}$, $\frac{1}{6}$, $\frac{1}{8}$ and $\frac{1}{12}$, respectively. A lower ρ value yields an optimal solution with less photon dose. At $\rho = \frac{1}{6}$ no photons are used anymore and the optimal solution uses 10 proton fractions. Decreasing ρ even further gives solutions that use hypofractionation instead of hyperfractionation. A lower ρ means that fractionation is less beneficial, so adding extra photon fractions mainly leads to worse OAR sparing.

In Figure 6.C.2b the maximum number of allowed proton fractions is varied. As expected,

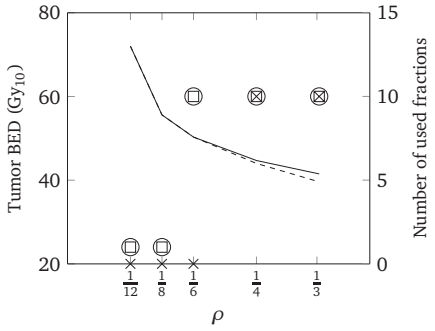

(a) Varying the value of ρ in problem (6.C.1) and the single modality proton LP. For higher values of ρ it is optimal to use a combined modality treatment, for lower values single modality proton treatments are optimal. The higher ρ, the more proton fractions are used.

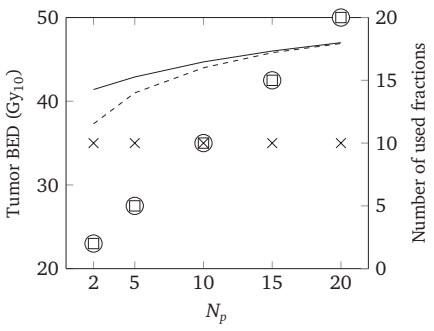

(b) Varying the value of N_p in problem (6.C.1) and the single modality proton LP. In all scenarios, all available fractions are used. The higher N_p, the smaller the difference in tumor BED between the combined modality treatment and the single modality proton treatment.

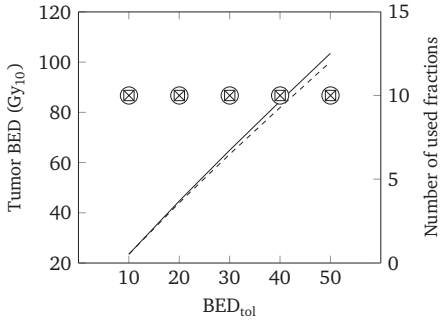

(c) Varying the value of BED_{tol} in problem (6.C.1) and the single modality proton LP. In all cases, all available fractions are used. The larger BED_{tol}, the larger the difference in tumor BED between the combined modality treatment and the single modality proton treatment.

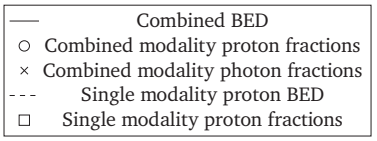

Figure 6.C.2: Results of solving problem (6.C.1) and the single modality LP as formulated in Saberian et al. (2015) for the data in Table 6.C.1. The average tumor BED is measured on the left vertical axis and the number of used fractions is measured on the right axis. In every scenario, the number of used proton fractions is equal for both the single modality proton treatment and the combined modality treatment. The displayed photon fractions for every scenario are used only in the combined modality treatment.

a higher number of allowed proton fractions means there is less need to use the extra photon fractions. Hence, the total physical dose delivered via photon fractions is lower. In the case with $N_p = 20$ the photon fractions deliver a dose of 1.5 Gy in 10 fractions. This is clinically not desirable, and in such a situation one would simply omit these fractions.

In Figure 6.C.2c the BED tolerance level of the mean dose constraint is varied. First of all, we note that an increase of 10 $\text{Gy}_{\alpha/\beta}$ results in an average tumor BED increase of 20 $\text{Gy}_{\alpha/\beta}$. Furthermore, we find that a higher BED_{tol} yields optimal solutions where more dose is delivered via photon fractions. This corresponds with the analytical results derived for the model of Appendix 6.A.2.

6.D 4-Variable reformulations

The following lemma extends the results of Saberian et al. (2015) for the single modality case to the combined modality case.

Lemma 6.3. *Let* $f : \mathbb{R}_+^{N_\gamma \times N_p} \mapsto \mathbb{R}$ *and* $g : \mathbb{R}^4 \mapsto \mathbb{R}$ *such that*

$$f(\boldsymbol{d}_\gamma, \boldsymbol{d}_p) = g(\boldsymbol{d}_\gamma^\top \boldsymbol{e},\ \boldsymbol{d}_\gamma^\top \boldsymbol{d}_\gamma,\ \boldsymbol{d}_p^\top \boldsymbol{e},\ \boldsymbol{d}_p^\top \boldsymbol{d}_p), \tag{6.D.1}$$

holds, where $\boldsymbol{e}$ *denotes the all-ones vector. Furthermore, let* $\boldsymbol{u} \in \mathbb{R}^r$*, and* $X \subseteq \mathbb{R}^{4+r}$*, such that* $X \neq \emptyset$*. Then the optimization problem*

$$\min_{\boldsymbol{d}_\gamma,\, \boldsymbol{d}_p,\, \boldsymbol{u}} \quad f(\boldsymbol{d}_\gamma, \boldsymbol{d}_p), \tag{6.D.2a}$$

$$s.t. \quad \left(\boldsymbol{d}_\gamma^\top \boldsymbol{e},\ \boldsymbol{d}_\gamma^\top \boldsymbol{d}_\gamma,\ \boldsymbol{d}_p^\top \boldsymbol{e},\ \boldsymbol{d}_p^\top \boldsymbol{d}_p,\ \boldsymbol{u}\right) \in X, \tag{6.D.2b}$$

$$\boldsymbol{d}_\gamma \geq \boldsymbol{0},\ \boldsymbol{d}_p \geq \boldsymbol{0}, \tag{6.D.2c}$$

is equivalent to

$$\min_{x_\gamma,\, y_\gamma,\, x_p,\, y_p,\, \boldsymbol{u}} \quad g(x_\gamma, y_\gamma, x_p, y_p), \tag{6.D.3a}$$

$$s.t. \quad (x_\gamma, y_\gamma, x_p, y_p, \boldsymbol{u}) \in X, \tag{6.D.3b}$$

$$\sqrt{y_\gamma} \leq x_\gamma \leq \sqrt{N_\gamma y_\gamma}, \tag{6.D.3c}$$

$$\sqrt{y_p} \leq x_p \leq \sqrt{N_p w}, \tag{6.D.3d}$$

$$x_\gamma \geq 0,\ y_\gamma \geq 0,\ x_p \geq 0,\ y_p \geq 0. \tag{6.D.3e}$$

Proof. First, we show that from any feasible solution to (6.D.2) a feasible solution to (6.D.3) can be obtained. Then we show the reverse statement.

1. Let $(\boldsymbol{d}_\gamma, \boldsymbol{d}_p, \boldsymbol{u})$ be a feasible solution to (6.D.2). Define

$$x_\gamma = \boldsymbol{d}_\gamma^\top \boldsymbol{e}, \;\; y_\gamma = \boldsymbol{d}_\gamma^\top \boldsymbol{d}_\gamma, \;\; x_p = \boldsymbol{d}_p^\top \boldsymbol{e}, \;\; y_p = \boldsymbol{d}_p^\top \boldsymbol{d}_p. \tag{6.D.4}$$

   Due to (6.D.2c), it holds that $(x_\gamma, y_\gamma, x_p, y_p)$ satisfies (6.D.3e). Due to (6.D.2b) it holds that $(x_\gamma, y_\gamma, x_p, y_p, \boldsymbol{u})$ satisfies (6.D.3b). Also, due to the Cauchy-Schwartz inequality:

$$\begin{aligned} y_\gamma = \boldsymbol{d}_\gamma^\top \boldsymbol{d}_\gamma \leq (\boldsymbol{d}_\gamma^\top \boldsymbol{e})^2 = x_\gamma^2, \\ x_\gamma^2 = (\boldsymbol{d}_\gamma^\top \boldsymbol{e})^2 \leq N_\gamma \boldsymbol{d}_\gamma^\top \boldsymbol{d}_\gamma = N_\gamma y_\gamma, \end{aligned}$$

   so x_γ and y_γ satisfy (6.D.3c). Similarly it can be shown that x_p and y_p satisfy (6.D.3d). Therefore, $(x_\gamma, y_\gamma, x_p, y_p, \boldsymbol{u})$ is feasible for (6.D.3). Due to (6.D.1) and (6.D.4), it holds that $f(d_\gamma, d_p) = g(x_\gamma, y_\gamma, x_p, y_p)$.

2. Let $(x_\gamma, y_\gamma, x_p, y_p, \boldsymbol{u})$ be a feasible solution to (6.D.3). Then $\sqrt{y_\gamma} \leq x_\gamma \leq \sqrt{N_\gamma y_\gamma}$. There is an integer value $\hat{N}_\gamma = 1, \ldots, N_\gamma$ such that $\sqrt{(\hat{N}_\gamma - 1) y_\gamma} \leq x_\gamma \leq \sqrt{\hat{N}_\gamma y_\gamma}$. Define

$$\begin{aligned} d_\gamma^{\text{low}} &= \frac{x_\gamma - \sqrt{(\hat{N}_\gamma - 1)(\hat{N}_\gamma y_\gamma - x_\gamma^2)}}{\hat{N}_\gamma}, \\ d_\gamma^{\text{high}} &= \frac{x_\gamma + \sqrt{(\hat{N}_\gamma - 1)^{-1}(\hat{N}_\gamma y_\gamma - x_\gamma^2)}}{\hat{N}_\gamma}. \end{aligned}$$

   Note that $d_\gamma^{\text{low}} \geq 0$ and $d_\gamma^{\text{high}} \geq 0$. Let $\boldsymbol{d}_\gamma$ be a vector with one entry d_γ^{low}, $(\hat{N}_\gamma - 1)$ entries d_γ^{high} and $(N_\gamma - \hat{N}_\gamma)$ zeros. Then $\boldsymbol{d}_\gamma \in \mathbb{R}_+^{N_\gamma}$, and we find

$$\boldsymbol{d}_\gamma^\top \boldsymbol{e} = d_\gamma^{\text{low}} + (\hat{N} - 1) d_\gamma^{\text{high}} = x_\gamma,$$

   where the last equality follows from elementary calculus. Similarly it can be shown that $\boldsymbol{d}_\gamma^\top \boldsymbol{d}_\gamma = y$. Using the same method we can construct a vector $\boldsymbol{d}_p \in \mathbb{R}_+^{N_2}$ for which it holds that $\boldsymbol{d}_p^\top \boldsymbol{e} = x_p$ and $\boldsymbol{d}_p^\top \boldsymbol{d}_p = y_p$. Therefore,

$$\left(\boldsymbol{d}_\gamma^\top \boldsymbol{e}, \; \boldsymbol{d}_\gamma^\top \boldsymbol{d}_\gamma, \; \boldsymbol{d}_p^\top \boldsymbol{e}, \; \boldsymbol{d}_p^\top \boldsymbol{d}_p, \; \boldsymbol{u}\right) \in X,$$

   so $(\boldsymbol{d}_\gamma, \boldsymbol{d}_p, \boldsymbol{u})$ is feasible for (6.D.2). Due to (6.D.1) and $x_\gamma = \boldsymbol{d}_\gamma^\top \boldsymbol{e}$, $y_\gamma = \boldsymbol{d}_\gamma^\top \boldsymbol{d}_\gamma$, $x_p = \boldsymbol{d}_p^\top \boldsymbol{e}$, $y_p = \boldsymbol{d}_p^\top \boldsymbol{d}_p$, it holds that $f(\boldsymbol{d}_\gamma, \boldsymbol{d}_p) = g(x_\gamma, y_\gamma, x_p, y_p)$.

It remains to show that an optimal solution to (6.D.2) defines an optimal solution to (6.D.3) and vice versa. This is trivial. The procedures (i) and (ii) provide feasible solutions that have equal objective value. Therefore, procedures (i) and (ii) map optimal solutions of one problem to optimal solutions of the other problem, and (6.D.2) and (6.D.3) are equivalent. □

This result covers the equivalence of (6.A.4) and (6.A.5) in Appendix 6.A.2. Furthermore, it implies that problem (6.3) in Section 6.2.2 is equivalent to the following:

$$\max_{\boldsymbol{d}_\gamma,\boldsymbol{d}_p,\boldsymbol{u}} \ \frac{1}{n^T}\sum_{j=1}^{n^T}\Big(s^T_{\gamma,j}\sum_{t_\gamma=1}^{N_\gamma} d_{\gamma,t_\gamma}+\rho^T(s^T_{\gamma,j})^2\sum_{t_\gamma=1}^{N_\gamma} d^2_{\gamma,t_\gamma}+s^T_{p,j}\sum_{t_p=1}^{N_p} d_{p,t_p}+\rho^T(s^T_{p,j})^2\sum_{t_p=1}^{N_p} d^2_{p,t_p}\Big), \tag{6.D.5a}$$

$$\text{s.t. } s^m_{\gamma,j}\sum_{t_\gamma=1}^{N_\gamma} d_{\gamma,t_\gamma}+\rho^m(s^m_{\gamma,j})^2\sum_{t_\gamma=1}^{N_\gamma} d^2_{\gamma,t_\gamma}+s^m_{p,j}\sum_{t_p=1}^{N_p} d_{p,t_p}+\rho^m(s^m_{p,j})^2\sum_{t_p=1}^{N_p} d^2_{p,t_p} \le \mathrm{BED}^m_{\max},\ \forall j=1,\dots,n^m,\ \forall m\in\mathcal{M}_1, \tag{6.D.5b}$$

$$s^m_{\gamma,j}\sum_{t_\gamma=1}^{N_\gamma} d_{\gamma,t_\gamma}+\rho^m(s^m_{\gamma,j})^2\sum_{t_\gamma=1}^{N_\gamma} d^2_{\gamma,t_\gamma}+s^m_{p,j}\sum_{t_p=1}^{N_p} d_{p,t_p}+\rho^m(s^m_{p,j})^2\sum_{t_p=1}^{N_p} d^2_{p,t_p} \le \mathrm{BED}^m_{\mathrm{dvh}}+M(1-u^m_j),\ \forall j=1,\dots,n^m,\ \forall m\in\mathcal{M}_2, \tag{6.D.5c}$$

$$\sum_{j=1}^{n^m} u^m_j \ge n^m-\lfloor F^m n^m\rfloor,\quad \forall m\in\mathcal{M}_2, \tag{6.D.5d}$$

$$u^m_j\in\{0,1\},\quad \forall j=1,\dots,n^m,\quad \forall m\in\mathcal{M}_2, \tag{6.D.5e}$$

$$\frac{1}{n^m}\sum_{j=1}^{n^m}\Big(s^m_{\gamma,j}\sum_{t_1=1}^{N_\gamma} d_{\gamma,t_\gamma}+\rho^m(s^m_{\gamma,j})^2\sum_{t_\gamma=1}^{N_\gamma} d^2_{\gamma,t_\gamma}+s^m_{p,j}\sum_{t_p=1}^{N_p} d_{p,t_p}+\rho^m(s^m_{p,j})^2\sum_{t_p=1}^{N_p} d^2_{p,t_p}\Big) \le \mathrm{BED}^m_{\mathrm{mean}},\ \forall m\in\mathcal{M}_3, \tag{6.D.5f}$$

$$d_{\gamma,t_\gamma}\ge 0,\ t_\gamma=1,\dots,N_\gamma,\ d_{p,t_p}\ge 0,\ t_p=1,\dots,N_p. \tag{6.D.5g}$$

6.E Details on optimization algorithm of Section 6.2.2

6.E.1 Solve for fixed $\{\theta, v_\gamma, v_p\}$

Using the transformation (6.4) we reformulate model (6.3) in terms of $\{x_\gamma, u, \theta, v_\gamma, v_p\}$. It turns out that, for given $\{\theta, v_\gamma, v_p\}$ the resulting problem is easy to solve. It is given by

$$\max_{x_\gamma,\boldsymbol{u}} \ \frac{1}{n^T}\sum_{j=1}^{n^{\mathrm{GTV}}}\Big(s^T_{\gamma,j}+s^T_{p,j}\frac{1-\theta}{\theta}\Big)x_\gamma+\Big(\rho^T\frac{(s^T_{\gamma,j})^2}{v_\gamma}+\rho^T\Big(\frac{1-\theta}{\theta}\Big)^2\frac{(s^{GTV}_{p,j})^2}{v_p}\Big)x^2_\gamma, \tag{6.E.1a}$$

$$\text{s.t. } \Big(s^m_{\gamma,j}+s^m_{p,j}\frac{1-\theta}{\theta}\Big)x_\gamma+\Big(\rho^m\frac{(s^m_{\gamma,j})^2}{v_\gamma}+\rho^m\Big(\frac{1-\theta}{\theta}\Big)^2\frac{(s^m_{p,j})^2}{v_p}\Big)x^2_\gamma \le \mathrm{BED}^m_{\max},\quad \forall j\in n^m, \forall m\in\mathcal{M}_1, \tag{6.E.1b}$$

$$\Big(s^m_{\gamma,j}+s^m_{p,j}\frac{1-\theta}{\theta}\Big)x_\gamma+\Big(\rho^m\frac{(s^m_{\gamma,j})^2}{v_\gamma}+\rho^m\big(\frac{1-\theta}{\theta}\big)^2\frac{(s^m_{p,j})^2}{v_p}\Big)x_\gamma^2 \leq \mathrm{BED}^m_{\mathrm{dv}}+M(1-u^m_j),\quad \forall j\in\mathcal{N}^m,\quad m\in\mathcal{M}_2, \tag{6.E.1c}$$

$$\sum_{j=1}^{n^m}u^m_j\geq n^m-\lfloor F^m n^m\rfloor,\quad \forall m\in\mathcal{M}_2, \tag{6.E.1d}$$

$$u^m_j\in\{0,1\},\quad \forall j\in\mathcal{N}^m,\quad \forall m\in\mathcal{M}_2, \tag{6.E.1e}$$

$$\frac{1}{n^m}\sum_{j=1}^{n^m}\Big(s^m_{\gamma,j}+s^m_{p,j}\frac{1-\theta}{\theta}\Big)x_\gamma+\Big(\rho^m\frac{(s^m_{\gamma,j})^2}{v_\gamma}+\rho^m(\frac{1-\theta}{\theta})^2\frac{(s^m_{p,j})^2}{v_p}\Big)x_\gamma^2 \leq \mathrm{BED}^m_{\mathrm{mean}},\quad \forall m\in\mathcal{M}_3, \tag{6.E.1f}$$

$$x_\gamma\geq 0. \tag{6.E.1g}$$

Next to the binary variables $\boldsymbol{u}^m\in\{0,1\}^{n^m}$ for the DVH constraints, this problem has a single variable $x_\gamma\in\mathbb{R}$. In the remainder of this section we demonstrate that for fixed $\{\theta,v_\gamma,v_p\}$ we can remove the binary variables $\boldsymbol{u}^m$ and that the resulting problem is easily solved. We consider a single DVH constraint m. For a single voxel $j\in\mathcal{N}^m$, define

$$a^m_j(\theta,v_\gamma,v_p)=\rho^m\frac{(s^m_{\gamma,j})^2}{v_\gamma}+\rho^m\big(\frac{1-\theta}{\theta}\big)^2\frac{(s^m_{p,j})^2}{v_p},\quad b^m_j(\theta)=s^m_{\gamma,j}+s^m_{p,j}\frac{1-\theta}{\theta}.$$

Then the BED in voxel j is given by

$$\mathrm{BED}^m_j(x_\gamma;\theta,v_\gamma,v_p)=a^m_j(\theta,v_\gamma,v_p)x_\gamma^2+b^m_j(\theta)x_\gamma. \tag{6.E.2}$$

The DVH constraint on voxel j reads $\mathrm{BED}^m_j(x_\gamma;\theta,v_\gamma,v_p)\leq\mathrm{BED}^m_{\mathrm{dv}}$. For at least $n^m-\lfloor F^m n^m\rfloor$ voxels this constraint has to be satisfied. Figure 6.E.1 illustrates (6.E.2) for a couple of voxels.

For the single modality case, the ordering of voxels in terms of received BED depends purely on their dose sparing factors, and not on the dose and/or fractionation scheme. However, for the combined modality case the BED depends on both the proton and photon dose sparing factor, and the ordering depends on the dose and fractionation of both modalities. Hence, there is no ordering in the BED^m_j values that holds for every x_γ, and for given (θ,v_γ,v_p) we cannot easily see which voxels will receive a low dose and which voxels will receive a high dose. For example, for two voxels j and k it may be the case that $a^m_j>a^m_k$ but $b^m_j<b^m_k$. Consequently, which of these voxels j and k receives the highest dose depends on the value of x_γ. In other words, the lines in Figure 6.E.1 may intersect.

Because the BED tolerance BED^m_{dv} is known, we can calculate the highest value of x_γ for which the constraint on voxel j is not violated. We can rewrite $\mathrm{BED}^m_j(x_\gamma;\theta,v_\gamma,v_p)\leq\mathrm{BED}^m_{\mathrm{dv}}$

to

$$x_\gamma \leq \frac{-b_j(\theta)+\sqrt{b_j^2(\theta)+4a_j(\theta,\nu_\gamma,\nu_p)\text{BED}^m_{dv}}}{2a_j(\theta,\nu_\gamma,\nu_p)} =: \tau^m_j(\theta,\nu_\gamma,\nu_p).$$

In Figure 6.E.1, the values τ^m_j are the horizontal coordinates of the intersection of the functions BED^m_j with the horizontal line BED^m_{dv}. Let $\{\tau^m_j(\theta,\nu_\gamma,\nu_p)\}^\uparrow$ denote the increasing sequence of $\tau^m_j(\theta,\nu_\gamma,\nu_p)$ values. If we consider only DVH constraint m, the highest attainable value of x_γ is the $n^m - \lfloor F^m n^m \rfloor$-th entry of the sequence $\{\tau^m_j(\theta,\nu_\gamma,\nu_p)\}^\uparrow$. Denote this value by $\tau^m_F(\theta,\nu_\gamma,\nu_p)$. Then, instead of setting constraints (6.E.1c)-(6.E.1e), we can set the constraints

$$x_\gamma \leq \tau^m_F(\theta,\nu_\gamma,\nu_p), \quad \forall m \in \mathcal{M}_2.$$

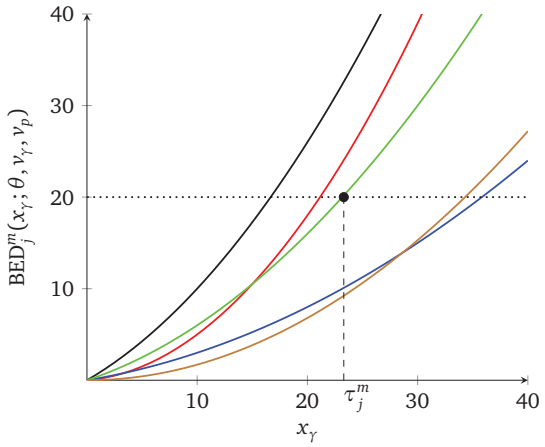

Figure 6.E.1: BED to voxels $j \in \mathcal{N}^m$ for a given DVH constraint m. Each line represents the BED to a voxel as function of the total tumor photon dose x_γ, for given variable set $(\theta,\nu_\gamma,\nu_p)$. Although the ordering of the voxels in terms of BED depends on x_γ, we do know what the ordering will be when the BED is equal to the tolerance BED^m_{dv}. The voxels $j \in \mathcal{N}^m$ can be ordered according to the x_γ value where $\text{BED}^m_j(x_\gamma;\theta,\nu_\gamma,\nu_p)$ crosses the dotted line with value BED^m_{dv}.

In terms of (s_γ, s_p) the idea is visualized in Figure 6.E.2. Every voxel j is represented by the coordinate $(s^m_{\gamma,j}, s^m_{p,j})$ in the 2D-plane. For a fixed value of x_γ the BED to every voxel j is known. Therefore, we can draw the line through all pairs $(s^m_{\gamma,j}, s^m_{p,j})$ that receive exactly the tolerated BED. In other words, we determine all $(s^m_{\gamma,j}, s^m_{p,j})$ that solve $\text{BED}^m_j(x_\gamma;\theta,\nu_\gamma,\nu_p) = \text{BED}^m_{\text{dv}}$. This line is drawn in black in Figure 6.E.2. Voxels above the line receive a BED higher than the tolerated dose, voxels below the line receive a lower BED. The goal is to pick the

value of x_γ such that exactly the required number of voxels is below the line, this value is denoted by $\tau_F^m(\theta, v_\gamma, v_p)$. Therefore, the DVH constraint is equivalent to setting the constraint $x_\gamma \leq \tau_F^m(\theta, v_\gamma, v_p)$. The values for variables u_j^m are obtained by setting $u_j^m = 1$ for all voxels j below the line, and $u_j^m = 0$ otherwise. Furthermore, note that because (6.E.1a) is an increasing function of x_γ, we can simply maximize x_γ instead.

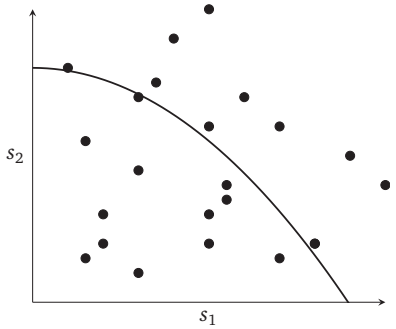

Figure 6.E.2: Visualization of a DVH constraint for fixed variables (θ, v_γ, v_p). Every voxel j is represented by a coordinate $(s_{\gamma,j}^m, s_{p,j}^m)$. For a given value of x_γ, all voxels j for which $\text{BED}_j(x_\gamma; \theta, v_\gamma, v_p) = \text{BED}_{\text{dv}}^m$ receive the maximum tolerated BED. Voxels above this curve receive a higher BED, voxels below the curve receive a lower BED. Increasing or decreasing the value of x_γ scales the curve downward or upward, respectively. The DVH voxel tolerance is reached if we pick x_γ such that exactly the required number of voxels receives at most BED tolerance level. This is done by setting $x_\gamma = \tau_F^m(\theta, v_\gamma, v_p)$.

In clinical practice very high or very low dose per fraction is undesirable. Therefore, we set a minimum and maximum dose per fraction. Due to our reformulation the dose per fraction is not a variable anymore. Instead, we can enforce that d_{γ,t_γ} and d_{p,t_p} are within pre-specified bounds $d_{\min}$ and $d_{\max}$ by setting the constraints

$$\max\left\{\text{lb}(d_{\min}, v_\gamma), \frac{\theta}{1-\theta}\text{lb}(d_{\min}, v_p)\right\} \leq x_\gamma \leq \min\left\{\text{ub}(d_{\max}, v_\gamma), \frac{\theta}{1-\theta}\text{ub}(d_{\max}, v_p)\right\},$$

where the upper and lower bounds $\text{lb}(\cdot)$ and $\text{ub}(\cdot)$ are obtained as follows. In the definitions of d^{low} and d^{high} from the methodology of Appendix 6.D, we apply the variable transformations (6.4), i.e., we replace $y = x^2/v$. Moreover, we note that $N = \lceil v \rceil$. Subsequently, we solve $d^{\text{low}} \geq d_{\min}$ and $d^{\text{high}} \leq d_{\max}$. This yields:

$$\text{lb}(d_{\min}, v) = \lceil v \rceil d_{\min} \frac{-1 - \sqrt{(\lceil v \rceil - 1)(\frac{\lceil v \rceil}{v} - 1)}}{\frac{\lceil v \rceil}{v}(\lceil v \rceil - v - 1)},$$

$$\text{ub}(d_{\max}, v) = \lceil v \rceil d_{\max} \frac{-1 + \sqrt{(\lceil v \rceil - 1)^{-1}(\frac{\lceil v \rceil}{v} - 1)}}{\frac{\lceil v \rceil}{v}(1 - v)(\lceil v \rceil - 1)^{-1}}.$$

Combining all of the above, the resulting optimization problem for x_γ reads

$$\max_{x_\gamma} \; x_\gamma, \tag{6.E.3a}$$

$$\text{s.t.} \; \Big(s^m_{\gamma,j} + s^m_{p,j}\frac{1-\theta}{\theta}\Big)x_\gamma + \Big(\rho^m \frac{(s^m_{\gamma,j})^2}{\nu_\gamma} + \rho^m\big(\frac{1-\theta}{\theta}\big)^2\frac{(s^m_{p,j})^2}{\nu_p}\Big)x_\gamma^2 \leq \text{BED}^m_{\max}, \quad \forall j \in n^m, \quad \forall m \in \mathcal{M}_1, \tag{6.E.3b}$$

$$x_\gamma \leq \tau^m_F(\theta, \nu_\gamma, \nu_p), \quad \forall m \in \mathcal{M}_2, \tag{6.E.3c}$$

$$\frac{1}{n^m}\sum_{j=1}^{n^m}\Big(s^m_{\gamma,j} + s^m_{p,j}\frac{1-\theta}{\theta}\Big)x_\gamma + \Big(\rho^m \frac{(s^m_{\gamma,j})^2}{\nu_\gamma} + \rho^m\big(\frac{1-\theta}{\theta}\big)^2\frac{(s^m_{p,j})^2}{\nu_p}\Big)x_\gamma^2 \leq \text{BED}^m_{\text{mean}}, \quad \forall m \in \mathcal{M}_3, \tag{6.E.3d}$$

$$x_\gamma \leq \min\Big\{\text{ub}(d_{\max}, \nu_\gamma), \frac{\theta}{1-\theta}\text{ub}(d_{\max}, \nu_p)\Big\}, \tag{6.E.3e}$$

$$x_\gamma \geq \max\Big\{\text{lb}(d_{\min}, \nu_\gamma), \frac{\theta}{1-\theta}\text{lb}(d_{\min}, \nu_p)\Big\}, \tag{6.E.3f}$$

$$x_\gamma \geq 0. \tag{6.E.3g}$$

Also constraints (6.E.3b) and (6.E.3d) can be reformulated to an upper bound on x_γ via the quadratic formula. This means that problem (6.E.3) can be solved analytically. Computationally, solving problem (6.E.3) requires computing τ^m_j values for all $j \in \mathcal{N}^m$ and sorting these to obtain the sequence $\{\tau^m_j(\theta, \nu_\gamma, \nu_p)\}^\uparrow$.

6.E.2 Multi-start pattern search

In Appendix 6.E.1 it is described how for fixed $\{\theta, \nu_\gamma, \nu_p\}$ the optimal values $x^*(\theta, \nu_\gamma, \nu_p)$ and $u^*(\theta, \nu_\gamma, \nu_p)$ are computed. As described in Section 6.2.2, the original problem (6.3) can be written as (6.5). It is easily verified that this reduces to

$$\max_{\theta, \nu_\gamma, \nu_p} \; f\big(x^*_\gamma(\theta, \nu_\gamma, \nu_p), u^*(\theta, \nu_\gamma, \nu_p), \theta, \nu_\gamma, \nu_p\big), \tag{6.E.4a}$$

$$\text{s.t.} \; 0 < \theta \leq 1, \tag{6.E.4b}$$

$$1 \leq \nu_\gamma \leq N_\gamma, \tag{6.E.4c}$$

$$1 \leq \nu_p \leq N_p. \tag{6.E.4d}$$

Problem (6.E.4) is solved via a multi-start GPS algorithm. That is, instead of directly applying the GPS algorithm on (6.E.5), we apply GPS to

$$\max_{\theta, v_\gamma, v_p} f\left(x_\gamma^*(\theta, v_\gamma, v_p), u^*(\theta, v_\gamma, v_p), \theta, v_\gamma, v_p\right), \tag{6.E.5a}$$

$$\text{s.t. } 0 < \theta \leq 1, \tag{6.E.5b}$$

$$\tilde{N}_\gamma - 1 \leq v_\gamma \leq \tilde{N}_\gamma, \tag{6.E.5c}$$

$$\tilde{N}_p - 1 \leq v_p \leq \tilde{N}_p, \tag{6.E.5d}$$

for all feasible $(\tilde{N}_\gamma, \tilde{N}_p)$ pairs. Although GPS provides only a local maximum, numerical experiments have shown that the multi-start approach generally gives good solutions.

Bibliography

Ahnesjö, A., Saxner, M., and Trepp, A. (1992). A pencil beam model for photon dose calculation. *Med. Phys.*, 19(2):263–273.

Ajdari, A. and Ghate, A. (2016). Robust fractionation in cancer radiotherapy. Preprint arXiv:2108.03209.

Ajdari, A., Ghate, A., and Kim, M. (2018). Adaptive treatment-length optimization in spatiobiologically integrated radiotherapy. *Phys. Med. Biol.*, 63(7):075009.

Ajdari, A., Niyazi, M., Nicolay, N., Thieke, C., Jeraj, R., and Bortfeld, T. (2019). Towards optimal stopping in radiation therapy. *Radiother. Oncol.*, 134:96–100.

Alber, M. and Nüsslin, F. (2001). A representation of an NTCP function for local complication mechanisms. *Phys. Med. Biol.*, 46(2):439–447.

Alber, M., Paulsen, F., Eschmann, S. M., and Machulla, H. J. (2003). On biologically conformal boost dose optimization. *Phys. Med. Biol.*, 48(2):N31–N35.

Alber, M. and Reemtsen, R. (2007). Intensity modulated radiotherapy treatment planning by use of a barrier-penalty multiplier method. *Optim. Method. Softw.*, 22(3):391–411.

Aleman, D. M. (2018). Fluence map optimization in intensity-modulated radiation therapy treatment planning. In Kong, N. and Zhang, S., editors, *Decision analytics and optimization in disease prevention and treatment*. John Wiley & Sons, Inc.

Aleman, D. M., Glaser, D., Romeijn, H. E., and Dempsey, J. F. (2010). Interior point algorithms: guaranteed optimality for fluence map optimization in IMRT. *Phys. Med. Biol.*, 55(18):5467–5482.

Audet, C. and Dennis Jr., J. E. (2003). Analysis of generalized pattern searches. *SIAM J. Optim.*, 13(3):889–903.

Badenbroek, R. and Dahl, J. (2021). An algorithm for nonsymmetric conic optimization inspired by MOSEK. *Optim. Method Softw.* Online ahead of print.

Badri, H., Salari, E., Watanabe, Y., and Leder, K. (2018). Optimization chemoradiotherapy to target metastatic disease and tumor growth. *INFORMS J. Comput.*, 30(2):259–277.

Badri, H., Watanabe, Y., and Leder, K. (2016). Optimal radiotherapy dose schedules under parametric uncertainty. *Phys. Med. Biol.*, 61(1):338–364.

Barendsen, G. W. (1982). Dose fractionation, dose rate and iso-effect relationships for normal tissue responses. *Int. J. Radiat. Oncol. Biol. Phys.*, 8(11):1981–1997.

Barker, C. A. and Powell, S. N. (2010). Enhancing radiotherapy through a greater understanding of homologous recombination. *Semin. Radiat. Oncol.*, 20(4):267–273.

Barry, M. A., Hussein, M., and Schettino, G. (2020). Evaluating the propagation of uncertainties in biologically based treatment planning parameters. *Front. Oncol.*, 10:1058.

Baumann, M., Krause, M., Overgaard, J., Debus, J., Bentzen, S. M., Daartz, J., ..., and Bortfeld, T. (2016). Radiation oncology in the era of precision medicine. *Nat. Rev. Cancer*, 16(4):234–249.

Been, L. B., Elsinga, P. H., de Vries, J., Cobben, D. C., Jager, P. L., Hoekstra, H. J., and Suurmeijer, A. J. (2006). Positron emission tomography in patients with breast cancer using (18)F-3'-deoxy-3'-fluoro-l-thymidine ((18)F-FLT)-a pilot study. *Eur. J. Surg. Oncol.*, 32(1):39–43.

Bemporad, A., Borrelli, F., and Morari, M. (2003). Min–max control of constrained uncertain discrete-time linear systems. *IEEE Trans. Automat. Contr.*, 48(9):1600–1606.

Ben-Tal, A., den Hertog, D., and Vial, J. P. (2015). Deriving robust counterparts of nonlinear uncertain inequalities. *Math. Program.*, 149:265–299.

Ben-Tal, A., El Housni, O., and Goyal, V. (2020). A tractable approach for designing piecewise affine policies in two-stage adjustable robust optimization. *Math. Program.*, 182:57–102.

Ben-Tal, A., Goryashko, A., Guslitzer, E., and Nemirovski, A. (2004). Adjustable robust solutions of uncertain linear programs. *Math. Program.*, 99:351–376.

Ben-Tal, A. and Nemirovski, A. (1998). Robust convex optimization. *Math. Oper. Res.*, 23(4):769–805.

Ben-Tal, A. and Nemirovski, A. (1999). Robust solutions of uncertain linear programs. *Oper. Res. Lett.*, 25:1–13.

Ben-Tal, A. and Nemirovski, A. (2001). *Lectures on Modern Convex Optimization - Analysis, Algorithms and Engineering Applications*. Society for Industrial and Applied Mathematics. MPS-SIAM Series on Optimization.

Bertsimas, D., Bidkhori, H., and Dunning, I. (2015). The price of flexibility. Available at `https://dbertsim.mit.edu/pdfs/papers/2015-the-price-of-flexibility.pdf`. Accessed 11-08-2021.

Bertsimas, D., Brown, D. B., and Caramanis, C. (2011). Theory and applications of robust optimization. *SIAM Rev.*, 53(3):464–501.

Bertsimas, D., Cacchiani, V., Craft, D., and Nohadini, O. (2013). A hybrid approach to beam angle optimization in intensity-modulated radiation therapy. *Comput. Oper. Res.*, 40:2187–2197.

Bertsimas, D. and Goyal, V. (2012). On the power and limitations of affine policies in two-stage adaptive optimization. *Math. Program.*, 134:491–531.

Bertsimas, D. and Sim, M. (2004). The price of robustness. *Oper. Res.*, 52(1):35–53.

Bertsimas, D., ten Eikelder, S. C. M., den Hertog, D., and Trichakis, N. (2021). Pareto adaptive robust optimality via a Fourier-Motzkin elimination lens. Preprint arXiv:2012.04419.

Bertsimas, D. and Tsitsiklis, J. N. (1997). *Introduction to linear optimization*. Athena Scientific.

Bertuzzi, A., Bruni, C., Papa, F., and Sinisgalli, C. (2013). Optimal solution for a cancer radiotherapy problem. *J. Math. Biol.*, 66(1-2):311–349.

Bijman, R. G., Breedveld, S., Arts, T., Astreinidou, E., de Jong, M. A., Granton, P. V., ..., and Hoogeman, M. S. (2017). Impact of model and dose uncertainty on model-based selection of oropharyngeal cancer patients for proton therapy. *Acta Oncol.*, 56(11):1444–1450.

Bindra, R. S., Goglia, A. G., Jasin, M., and Powell, S. N. (2013). Development of an assay to measure mutagenic non-homologous end-joining repair activity in mammalian cells. *Nucleic Acids Res.*, 41(11):e115.

Blanchard, P., Wong, A. J., Gunn, G. B., Garden, A. S., Mohamed, A. S. R., Rosenthal, D. I., ..., and Frank, S. J. (2016). Toward a model-based patient selection strategy for proton therapy: External validation of photon-derived normal tissue complication probability models in a head and neck proton therapy cohort. *Radiother. Oncol.*, 121(3):381–386.

Böck, M., Eriksson, K., and Forsgren, A. (2019). On the interplay between robustness and dynamic planning for adaptive radiation therapy. *Biomed. Phys. Eng. Express*, 5(4):045004.

Böck, M., Eriksson, K., Forsgren, A., and Hårdemark, B. (2017). Toward robust adaptive radiation therapy strategies. *Med Phys.*, 44(6):2054–2065.

Bodey, R., Evans, P., and Flux, G. (2004). Application of the linear-quadratic model to combined modality radiotherapy. *Int. J. Radiat. Oncol. Biol. Phys.*, 59:228–241.

Bokrantz, R. and Forsgren, A. (2013). An algorithm for approximating convex Pareto surfaces based on dual techniques. *INFORMS J. Comput*, 25(2):377–393.

Bortfeld, T. (2006). IMRT: a review and preview. *Phys. Med. Biol.*, 51:R363–R379.

Bortfeld, T. (2010). The number of beams in IMRT - theoretical investigations and implications for single-arc IMRT. *Phys. Med. Biol.*, 55:83–97.

Bortfeld, T., Bürkelbach, J., Boesecke, R., and Schlegel, W. (1990). Methods of image reconstruction from projections applied to conformation radiotherapy. *Phys. Med. Biol.*, 35(10):1423–1434.

Bortfeld, T., Ramakrishnan, J., Tsitsiklis, J. N., and Unkelbach, J. (2015). Optimization of radiation therapy fractionation schedules in the presence of tumor repopulation. *INFORMS J. Comput.*, 27(4):788–803.

Bortfeld, T., Stein, J., and Preiser, K. (1997). Clinically relevant intensity modulation optimization using physical criteria. In *XII International Conference on the Use of Computers in Radiation Therapy*, pages 1–4. Medical Physics Publishing.

Boyd, S. and Vandenberghe, L. (2004). *Convex Optimization*. Cambridge University Press.

Bradshaw, T. J., Bowen, S. R., Deveau, M. A., Kubicek, L., White, P., Bentzen, S. M., ..., and Jeraj, R. (2015). Molecular imaging biomarkers of resistance to radiation therapy for spontaneous nasal tumors in canines. *Int. J. Radiat. Oncol. Biol. Phys.*, 91:787–795.

Bradshaw, T. J., Bowen, S. R., Jallow, N., Forrest, L. J., and Jeraj, R. (2013). Heterogeneity in intratumor correlations of 18F-FDG, 18F-FLT, and 61Cu-ATSM PET in canine sinonasal tumors. *J. Nucl. Med.*, 54(11):1931–1938.

Brahme, A. and Argren, A. K. (1987). Optimal dose distribution for eradication of heterogeneous tumors. *Acta. Oncol.*, 26(5):377–385.

Breedveld, S., Craft, D., van Haveren, R., and Heijmen, B. (2019). Multi-criteria optimization and decision-making in radiotherapy. *Eur. J. Oper. Res.*, 277:1–19.

Breedveld, S. and Heijmen, B. (2017). Data for TROTS - the radiotherapy optimisation test set. *Data Brief*, 12:143–149.

Breedveld, S., Storchi, P. R. M., Keijzer, M., and Heijmen, B. J. M. (2006). Fast, multiple optimizations of quadratic dose objective functions in IMRT. *Phys. Med. Biol.*, 51(14):3569–3579.

Breedveld, S., Storchi, P. R. M., Voet, P. W. J., and Heijmen, B. J. M. (2012). iCycle: integrated, multicriterial beam angle, and profile optimization for generation of coplanar and noncoplanar IMRT plans. *Med. Phys.*, 39(2):951–963.

Breedveld, S., van den Berg, B., and Heijmen, B. (2017). An interior-point implementation developed and tuned for radiation therapy treatment planning. *Comput. Optim. Appl.*, 68:209–242.

Burman, C., Kutcher, G. J., Emami, B., and Goitein, M. (1991). Fitting of normal tissue tolerance data to an analytic function. *Int. J. Radiat. Oncol. Biol. Phys.*, 21:123–135.

Casares-Magaz, O., Raidou, R. G., Rørvik, J., Vilanova, A., and Muren, L. P. (2018). Uncertainty evaluation of image-based tumour control probability models in radiotherapy of prostate cancer using a visual analytic tool. *Phys. Imag. Radiat. Oncol.*, 5:5–8.

Censor, Y., Bortfeld, T., Martin, B., and Trofimov, A. (2006). A unified approach for inversion problems in intensity-modulated radiation therapy. *Phys. Med. Biol.*, 51:2353–2365.

Chan, T. C. Y. and Mišić, V. V. (2013). Adaptive and robust radiation therapy optimization for lung cancer. *Eur. J. Oper. Res*, 231:745–756.

Chapman, J. D. and Nahum, A. (2015). *Radiotherapy treatment planning: linear-quadratic radiobiology*. CRC Press, Taylor & Francis Group.

Chen, W., Craft, D., Madden, T. M., Zhang, K., Kooy, H. M., and Herman, G. T. (2010). A fast optimization algorithm for multicriteria intensity modulated proton therapy planning. *Med. Phys.*, 37:4938–4945.

Cheng, F., Su, L., and Qian, C. (2016). Circulating tumor DNA: a promising biomarker in the liquid biopsy of cancer. *Oncotarget*, 7(30):48832–48841.

Choi, B. and Deasy, J. O. (2002). The generalized equivalent uniform dose function as a basis for intensity-modulated treatment planning. *Phys. Med. Biol.*, 47(20):3579–3589.

Choi, S. J., Kim, J. S., Kim, J. H., Oh, S. J., Lee, J. G., Kim, C. J., ..., and Moon, D. H. (2005). [18F]3'-deoxy-3'-fluorothymidine PET for the diagnosis and grading of brain tumors. *Eur. J. Nucl. Med. Mol. Imaging*, 32(6):653–659.

Chu, M., Zinchenko, Y., Henderson, S. G., and Sharpe, M. B. (2005). Robust optimization for intensity modulated radiation therapy treatment planning under uncertainty. *Phys. Med. Biol.*, 50:5463–5477.

Clausen, M. M., Hansen, A. E., Lundemann, M., Hollensen, C., Pommer, T., Munck Af Rosenschöld, P., ..., and Engelholm, S. A. (2014). Dose painting based on tumor uptake of Cu-ATSM and FDG: a comparative study. *Radiat. Oncol.*, 9:228.

Cobben, D. C., Elsinga, P. H., Hoekstra, H. J., Suurmeijer, A. J., Vaalburg, W., Maas, B., ..., and Groen, H. M. (2004a). Is 18F-3'-fluoro-3'-deoxy-L-thymidine useful for the staging and restaging of non-small cell lung cancer? *J. Nucl. Med.*, 45(10):1677–1682.

Cobben, D. C., van der Laan, B. F., Maas, B., Vaalburg, W., Suurmeijer, A. J., Hoekstra, H. J., ..., and Elsinga, P. H. (2004b). 18F-FLT PET for visualization of laryngeal cancer: comparison with 18F-FDG PET. *J. Nucl. Med.*, 45(2):226–231.

Coey, C., Kapelevich, L., and Vielma, J. P. (2021). Solving natural conic formulations with Hypatia.jl. Preprint arXiv:2005.01136.

Corless, R. M., Gonnet, G. H., Hare, D. E. G., Jeffrey, D. J., and Knuth, D. E. (1996). On the Lambert W function. *Adv. Comput. Math.*, 5:329–359.

Cox, J. D. (1986). Presidential address: Fractionation: A paradigm for clinical research in radiation oncology. *Int. J. Radiat. Oncol. Biol. Phys.*, 13:1271–1281.

Craft, D., Halabi, T., Shih, H., and Bortfeld, T. (2006). Approximating convex Pareto surfaces in multiobjective radiotherapy planning. *Med. Phys.*, 33:3399 – 3407.

Craft, D., McQuaid, D., Wala, J., Chen, W., Salari, E., and Bortfeld, T. (2012). Multicriteria VMAT optimization. *Med. Phys.*, 39(2):686–696.

Currie, J. and Wilson, D. I. (2012). OPTI: Lowering the barrier between open source optimizers and the industrial MATLAB user. In Sahinidis, N. and Pinto, J., editors, *Foundations of computer-aided process operations*, Savannah, Georgia, USA.

Dabadghao, S. and Roy, A. (2020). Optimal interventions for adaptive robust optimization under time-dependent uncertainty with application to radiotherapy. Available at SSRN.

Dahl, J. and Andersen, E. D. (2021). A primal-dual interior-point algorithm for nonsymmetric exponential-cone optimization. *Math. Program.* Online ahead of print.

Das, I. J., Sanfilippo, N. J., Fogliata, A., and Cozzi, L. (2020). *Intensity modulated radiation therapy - a clinical overview*. IPEM–IOP series in physics and engineering in medicine and biology, IOP Publishing, Bristol, UK.

Das, S. K., Miften, M. M., Zhou, S., Bell, M., Munley, M. T., Whiddon, C. S., ..., and Marks, L. B. (2004). Feasibility of optimizing the dose distribution in lung tumors using fluorine-18-fluorodeoxyglucose positron emission tomography and single photon emission computed tomography guided dose prescriptions. *Med. Phys.*, 31(6):1452–1461.

Dawson, L. A. et al. (2012). RTOG 1112: Randomized Phase III study of sorafenib versus stereotactic body radiation therapy followed by sorafenib in hepatocellular carcinoma. Technical Report, Radiation Therapy Oncology Group, Philadelpia, PA.

De Ruiter, F. J. C. T., Ben-Tal, A., Brekelmans, R. C. M., and den Hertog, D. (2017). Robust optimization of uncertain multistage inventory systems with inexact data in decision rules. *Comput. Manag. Sci.*, 14(1):45–77.

De Ruiter, F. J. C. T., Brekelmans, R. C. M., and den Hertog, D. (2016). The impact of the existence of multiple adjustable robust solutions. *Math. Program.*, 160:531–545.

Deasy, J. O. (1997). Multiple local minima in radiotherapy optimization problems with dose–volume constraints. *Med. Phys.*, 24(7):1157–1161.

Deasy, J. O., Blanco, A. I., and Clark, V. H. (2003). CERR: a computational environment for radiotherapy research. *Med. Phys.*, 30(5):979–985.

Delaney, G., Jacob, S., Featherstone, C., and Barton, M. (2005). The role of radiotherapy in cancer treatment: Estimating optimal utilization from a review of evidence-based clinical guidelines. *Cancer*, 104(6):1129–1137.

Domahidi, A., Chu, E., and Boyd, S. (2013). ECOS: An SOCP solver for embedded systems. In *European Control Conference (ECC)*, pages 3071–3076.

Doolan, P. J., Alshaikhi, J., Rosenberg, I., Ainsley, C. G., Gibson, A., D'Souza, D., ..., and Royle, G. (2014). A comparison of the dose distributions from three proton treatment planning systems in the planning of meningioma patients with single-field uniform dose pencil beam scanning. *J. Appl. Clin. Med. Phys.*, 16(1):86–99.

Ehrgott, M. (2005). *Multicriteria Optimization*. Lecture Notes in Economics and Mathematical Systems. Springer.

Ehrgott, M., Güler, Ç., Hamacher, H. W., and Shao, L. (2008). Mathematical optimization in intensity modulated radiation therapy. *4OR-Q. J. Oper. Res.*, 6:199–262.

El Ghaoui, L. and Lebret, H. (1997). Robust solutions to least-squares problems with uncertain data. *SIAM J. Matrix. Anal. Appl.*, 18(4):1035–1064.

Engberg, L., Forsgren, A., Eriksson, K., and Hårdemark, B. (2017). Explicit optimization of plan quality measures in intensity-modulated radiation therapy treatment planning. *Med. Phys.*, 44(6):2045–2053.

Farkas, J. (1902). Theorie der einfachen Ungleichungen. *J. Reine Angew. Math.*, 124:1–27.

Ferlay, J., Laversanne, M., Ervik, M., Lam, F., Colombet, M., Mery, L., ..., and Bray, F. (2020). Global Cancer Observatory: Cancer tomorrow. Available from: `https://gco.iarc.fr/tomorrow`, accessed 11-08-2021.

Flynn, R. (2007). *A comparison of intensity modulated X-ray therapy to intensity modulated proton therapy for the delivery of non-uniform dose distributions*. PhD thesis, University of Wisconsin - Madison.

Fourier, J. (1827). Reported in: Analyse des travaux de l'Académie, Royale des Sciences, pendant l'année 1824, Partie mathématique. In *Mémoires de l'Académie des sciences de l'Institut de France*, volume 7. Académie des sciences.

Fowler, J. F. (1989). The linear-quadratic formula and progress in fractionated radiotherapy. *Brit. J. Radiol.*, 62(740):679–694.

Fowler, J. F. (2009). Sensitivity analysis of parameters in linear-quadratic radiobiologic modeling. *Int. J. Radiat. Oncol. Biol. Phys.*, 73(5):1532–1537.

Fowler, J. F. (2010). 21 Years of biologically effective dose. *Brit. J. Radiol.*, 83:554–568.

Fowler, J. F., Harari, P. M., Leborgne, F., and Leborgne, J. H. (2003). Acute radiation reactions in oral and pharyngeal mucosa: tolerable levels in altered fractionation schedules. *Radiother. Oncol.*, 69:161–168.

Fu, A., Ungun, B., Xing, L., and Boyd, S. (2019). A convex optimization approach to radiation treatment planning with dose constraints. *Optim. Eng.*, 20(1):277–300.

Gabrel, V., Murat, C., and Thiele, A. (2014). Recent advances in robust optimization: an overview. *Eur. J. Oper. Res.*, 235:471–483.

Gaddy, M. R. (2019). *Optimization of radiotherapy treatments with spatiotemporal fractionation schemes*. PhD thesis, North Caroline State University.

Gao, H. (2016). Robust fluence map optimization via alternating direction method of multipliers with empirical parameter optimization. *Phys. Med. Biol.*, 61(7):2838–2850.

Ghate, A. (2011). Dynamic optimization in radiotherapy. In Geunes, J., Gray, P., and Greenberg, H., editors, *Tutorials in Operations Research: transforming research into action*, chapter 4. INFORMS.

Gorissen, B. L. (2019). Guaranteed ε-optimal solutions with the linear optimizer ART3+O. *Phys. Med. Biol.*, 64(7):075017.

Gorissen, B. L. (2021). Nymph: the fastest exact inverse planning algorithm for radiation therapy. `https://3142.nl/nymph/`. Accessed 11-08-2021.

Gorissen, B. L., Yanıkoğlu, İ., and den Hertog, D. (2015). A practical guide to robust optimization. *Omega*, 53:124–137.

Gotein, M. (2008). *Radiation oncology: A physicist's-eye view*. Biological and Medical Physics, Biomedical Engineering, Springer.

Gurobi Optimization LLC (2020). Gurobi optimizer reference manual.

Guslitser, E. (2002). Uncertainty-immunized solutions in linear programming. `http://citeseerx.ist.psu.edu/viewdoc/download?doi=10.1.1.623.2382&rep=rep1&type=pdf`. Master's thesis, Technion - Israel Institute of Technology.

Gutiérrez, A. N., Deveau, M., Forrest, L. J., Tomé, W. A., and Mackie, T. R. (2007). Radiobiological and treatment planning study of a simultaneously integrated boost for canine nasal tumors using helical tomotherapy. *Vet. Radiol. Ultrasound*, 48(6):594–602.

Hadjiyiannis, M. J., Goulart, P. J., and Kuhn, D. (2011). A scenario approach for estimating the suboptimality of linear decision rules in two-stage robust optimization. In *50th IEEE Conference on Decision and Control and European Control Conference*, pages 7386–7391.

Hall, E. J. and Giaccia, A. J. (2012). *Radiobiology for the radiologist*. Lippincott Williams & Wilkins. Philadelphia, Pennsylvania, USA.

Hoffmann, A. L., den Hertog, D., Siem, A. Y. D., Kaanders, J. H. A. M., and Huizenga, H. (2008). Convex reformulation of biologically-based multi-criteria intensity-modulated radiation therapy optimization including fractionation effects. *Phys. Med. Biol.*, 53(22):6345–6362.

Iancu, D. A. and Trichakis, N. (2014). Pareto efficiency in robust optimization. *Manag. Sci.*,

60(1):130–147.

Iancu, D. A., Trichakis, N., and Yoon, D. Y. (2021). Monitoring with limited information. *Manag. Sci.*, 67(7):4233–4251.

Jabr, R. A. (2013). Adjustable robust OPF with renewable energy sources. *IEEE T. Power Syst.*, 28(4):4742–4751.

Joiner, M. and van der Kogel, A., editors (2009). *Basic clinical radiobiology*. London, Hodder Arnold.

Källman, P., Agren, A., and Brahme, A. (1992). Tumour and normal tissue responses to fractionated non-uniform dose delivery. *Int. J. Radiat. Biol.*, 62(2):249–262.

Kang, J., Schwartz, R., Flickinger, J., and Beriwal, S. (2015). Machine learning approaches for predicting radiation therapy outcomes: a clinician's perspective. *Int. J. Radiat. Oncol. Biol. Phys.*, 93(5):1127–1135.

Kehwar, T. S. (2005). Analytical approach to estimate normal tissue complication probability using best fit of normal tissue tolerance doses into the NTCP equation of the linear quadratic model. *J. Canc. Res. Ther.*, 1(3):168–179.

Kenny, L. M., Vigushin, D. M., Al-Nahhas, A., Osman, S., Luthra, S. K., Shousha, S., ..., and Aboagye, E. O. (2005). Quantification of cellular proliferation in tumor and normal tissues of patients with breast cancer by [18F]fluorothymidine-positron emission tomography imaging: evaluation of analytical methods. *Cancer Res.*, 65(21):10104–10112.

Khanh Hien, L. T. (2015). Differential properties of Euclidean projection onto power cone. *Math. Meth. Oper. Res.*, 82:265–284.

Kim, H., Suh, T.-S., Lee, R., Xing, L., and Li, R. (2012a). Efficient IMRT inverse planning with a new L1-solver: template for first-order conic solver. *Phys. Med. Biol.*, 57:4139–4153.

Kim, M., Ghate, A., and Phillips, M. H. (2009). A markov decision process approach to temporal modulation of dose fractions in radiation therapy planning. *Phys. Med. Biol.*, 54(14):4455–4476.

Kim, M., Ghate, A., and Phillips, M. H. (2012b). A stochastic control formalism for dynamic biologically conformal radiation therapy. *Eur. J. Oper. Res.*, 219:541–556.

Kim, M., Stewart, R., and Philips, M. (2015). A feasibility study: Selection of a personalized radiotherapy fractionation schedule using spatiotemporal optimization. *Med. Phys.*, 42(11):6671–6678.

Kishimoto, S. and Yamashita, M. (2018). A successive LP approach with C-VaR type constraints for IMRT optimization. *Oper. Res. Health Care*, 17:55–64.

Klement, R. J. (2017). Radiobiological parameters of liver and lung metastases derived from tumor control data of 3719 metastases. *Radiother. Oncol.*, 123:218–226.

Kong, F.-M., Ten Haken, R. K., Schipper, M., Frey, K. A., Hayman, J., Gross, M., ..., and Kalemkerian, G. P. (2017). Effect of midtreatment PET/CT-adapted radiation therapy with concurrent chemotherapy in patients with locally advanced non–small-cell lung cancer: A phase 2 clinical trial. *JAMA Oncol.*, 3(10):1358–1365.

Konno, H. (1976). A cutting plane algorithm for solving bilinear programs. *Math. Program.*, 11:14–27.

Küfer, K.-H., Monz, M., Scherrer, A., Süss, P., Alonso, F., Sultan, A. S. A., Bortfeld, T., Craft, D., and Thieke, C. (2005). Multicriteria optimization in intensity modulated radiotherapy planning. *Berichte des Fraunhofer ITWM*, Nr 77, Kaiserslautern.

Küfer, K.-H., Scherrer, A., Monz, M., Alonso, F., Trinkaus, H., Bortfeld, T., and Thieke, C. (2003). Intensity-modulated radiotherapy - a large scale multi-criteria programming problem. *OR Spectrum*, 25:223–249.

Kuhn, D., Wiesemann, W., and Georghiou, A. (2009). Primal and dual linear decision rules in stochastic and robust optimization. *Math. Program.*, 130:177–209.

Kutcher, G. J. and Burman, C. (1989). Calculation of complication probability factors for non-uniform normal tissue irradiation: the effective volume method. *Int. J. Radiat. Oncol. Biol. Phys.*, 16:1623–1630.

Levegrün, S., Jackson, A., Zelefsky, M. J., Skwarchuk, M. W., Venkatraman, E. S., Schlegel, W., ..., and Ling, C. C. (2001). Fitting tumor control probability models to biopsy outcome after three-dimensional conformal radiation therapy of prostate cancer: pitfalls in deducing radiobiologic parameters for tumors from clinical data. *Int. J. Radiat. Oncol. Biol. Phys.*, 51(4):1064–1080.

Li, X. A., Alber, M., Deasy, J. O., Jackson, A., Ken Jee, K. W., Marks, L. B., ..., and Yorke, E. D. (2012). The use and QA of biologically related models for treatment planning: short report of the TG-166 of the therapy physics committee of the AAPM. *Med Phys.*, 39(3):1386–1409. AAPM Report No. 166.

Lim, G. J., Kardar, L., Ebrahimi, S., and Cao, W. (2020). A risk-based modeling approach for radiation therapy treatment planning under tumor shrinkage uncertainty. *Eur. J. Oper. Res.*, 280(1):266–278.

Lim-Reinders, S., Keller, B. M., Al-Ward, S., Sahgal, A., and Kim, A. (2017). Online adaptive radiation therapy. *Int. J. Radiat. Oncol. Biol. Phys.*, 99(4):994–1003.

Ling, C. C., Li, X. A., and Hendee, W. R. (2005). Over the next decade the success of radiation treatment planning will be judged by the immediate biological response of tumor cells rather than by surrogate measures such as dose maximization and uniformity. *Med. Phys.*, 32(7):2189–2192.

Liu, H., Chen, Y., and Lu, B. (2018). A new inverse planning formalism with explicit DVH constraints and kurtosis-based dosimetric criteria. *Phys. Med. Biol.*, 63(18):185015.

Liu, X., Pelizzari, C., Belcher, A. H., Grelewicz, Z., and Wiersma, R. D. (2017). Use of proximal operator graph solver for radiation therapy inverse treatment planning. *Med. Phys.*, 44(4):1246–1256.

Long, T. (2015). *Optimization problems in radiation therapy treatment planning*. PhD thesis, University of Michigan. Chapter 5: Adaptive treatment planning for lung cancer.

Lubin, M., Yamangil, E., Bent, R., and Vielma., J. P. (2016). Extended formulations in mixed-

integer convex programming. In Louveaux, Q. and Skutella, M., editors, *Integer programming and combinatorial optimization. IPCO 2016. Lecture notes in computer science,*, volume 9682, pages 102–113. Springer, Cham.

Lyman, J. T. (1985). Complication probability as assessed from dose–volume histograms. *Radiat. Res. Suppl.*, 8:S13–S19.

Mahmoudzadeh, H. (2015). *Robust optimization methods for breast cancer radiation therapy*. PhD thesis, University of Toronto. Chapter 4: Pareto robust optimization in breast cancer RT.

Mar, P. A. and Chan, T. C. Y. (2015). Adaptive and robust radiation therapy in the presence of drift. *Phys. Med. Biol.*, 60(9):3599–3615.

Marandi, A. and den Hertog, D. (2018). When are static and adjustable robust optimization problems with constraint-wise uncertainty equivalent? *Math. Program.*, 170(2):555–568.

Marcu, L. G., Reid, P., and Bezak, E. (2018). The promise of novel biomarkers for head and neck cancer from an imaging perspective. *Int. J. Mol. Sci.*, 19(9):2511.

McGary, J. E., Grant, W., and Woo, S. Y. (2000). Applying the equivalent uniform dose formulation based on the linear-quadratic model to inhomogeneous tumor dose distributions: Caution for analyzing and reporting. *J. Appl. Clin. Med. Phys.*, 1(4):126–137.

McMahon, S. J. (2019). The linear quadratic model: usage, interpretation and challenges. *Phys. Med. Biol.*, 64:01TR01.

Miettinen, K. (1999). *Nonlinear multiobjective optimization*. Kluwer Academic Publishers. International Series in Operations Research & Management Science.

Mizuta, M., Takao, S., Date, H., Kishimoto, N., Sutherland, K. L., Onimaru, R., and Shirato, H. (2012). A mathematical study to select fractionation regimen based on physical dose distribution and the linear-quadratic model. *Int. J. Radiat. Oncol. Biol. Phys.*, 84(3):829–833.

Mohan, R., Mageras, G. S., Baldwin, B., Brewster, L. J., Kutcher, G. J., Leibel, S., ..., and Fuks, Z. (1992). Clinically relevant optimization of 3D conformal treatments. *Med. Phys.*, 19(4):933–944.

MOSEK ApS (2018). MOSEK modeling cookbook. Release 3.1.

MOSEK ApS (2020). Mosek version 9.2. `https://www.mosek.com/documentation/`.

Motzkin, T. (1936). *Beiträge zur Theorie der linearen Ungleichungen*. Azriel, Jerusalem, Israel.

Muzi, M., Vesselle, H., Grierson, J. R., Mankoff, D. A., Schmidt, R. A., Peterson, L., ..., and Krohn, K. A. (2005). Kinetic analysis of 3'-deoxy-3'-fluorothymidine PET studies: validation studies in patients with lung cancer. *J. Nucl. Med.*, 46(2):274–282.

Nahapetyan, A. H. (2009). Bilinear programming. In Floudas, C. A. and Pardalos, P. M., editors, *Encyclopedia of optimization*, pages 279–288. Springer.

Nemirovski, A. (2007). Advances in convex optimization: conic programming. In *Proceedings of International Congress of Mathematicians*, pages 413–444.

Nesterov, Y. (2006). Constructing self-concordant barriers for convex cones. CORE discussion

paper 2006/30, Center for Operations Research and Econometrics, Catholic University of Louvain.

Nesterov, Y. and Nemirovski, A. (1994). *Interior-point polynomial algorithms in convex programming*. Society for Industrial and Applied Mathematics. Studies in Applied and Numerical Mathematics.

Nesterov, Y. and Todd, M. J. (1997). Self-scaled barriers and interior-point methods for convex programming. *Math. Oper. Res.*, 22(1):1–42.

Nesterov, Y. and Todd, M. J. (1998). Primal-dual interior-point methods for self-scaled cones. *SIAM J. Optimiz.*, 8(2):324–364.

Niemierko, A. (1997). Reporting and analyzing dose distributions: a concept of equivalent uniform dose. *Med. Phys.*, 24(1):103–110.

Niemierko, A. (1999). A generalized concept of equivalent uniform dose. *Med. Phys.*, 26:1100. (abstract).

Niemierko, A. (2006). Biological optimization. In Bortfeld, T., Schmidt-Ullrich, R., De Neve, W., and Wazer, D. E., editors, *Image-guided IMRT*. Springer.

Nill, S. (2001). *Development and application of a multi-modality inverse treatment planning system*. PhD thesis, University of Heidelberg.

Niyazi, M., Niemierko, A., Paganetti, H., Söhn, M., Schapira, E., Goldberg, S., ..., and Shih, H. A. (2020). Volumetric and actuarial analysis of brain necrosis in proton therapy using a novel mixture cure model. *Radiother. Oncol.*, 142:154–161.

Nobel Media AB (2018). The Nobel Prize in Physiology or Medicine 2018. `https://www.nobelprize.org/prizes/medicine/2018/summary/`, accessed 11-08-2021.

Nohadani, O. and Roy, A. (2017). Robust optimization with time-dependent uncertainty in radiation therapy. *IISE Trans. Healthc. Syst. Eng.*, 7(2):81–92.

Nourollahi, S., Ghate, A., and Kim, M. (2019). Optimal modality selection in external beam radiotherapy. *Math. Med. Biol.*, pages 361–380.

O'Connor, D., Yu, V., Nguyen, D., Ruan, D., and Sheng, K. (2018). Fraction-variant beam orientation optimization for non-coplanar IMRT. *Phys. Med. Biol.*, 63(4):045015.

O'Donoghue, B., Chu, E., Parikh, N., and Boyd, S. (2016). Conic optimization via operator splitting and homogeneous self-dual embedding. *J. Optim. Theory Appl.*, 169:1042–1068.

O'Donoghue, B., Chu, E., Parikh, N., and Boyd, S. (2019). SCS: Splitting conic solver, version 2.1.2. `https://github.com/cvxgrp/scs`.

Otto, K. (2008). Volumetric modulated arc therapy: IMRT in a single gantry arc. *Med. Phys.*, 35(1):310–317.

Paganetti, H., editor (2019). *Proton Therapy Physics*. Second edition, CRC Press.

Parikh, N. and Boyd, S. (2014). Proximal algorithms. *Found. Trends Optim.*, 1(3):123–231.

Park, C. S., Kim, Y., Lee, N., Bucci, K. M., Quivey, J. M., Verhey, L. J., and Xia, P. (2005). Method to account for dose fractionation in analysis of IMRT plans: modified equivalent uniform dose. *Int. J. Radiat. Oncol. Biol. Phys.*, 62(3):925–932.

Perkó, Z., Bortfeld, T., Hong, T., Wolfgang, J., and Unkelbach, J. (2016). Optimal fractionation schemes for liver SBRT based on BED. In *18th International Conference on the Use of Computers in Radiation Therapy*.

Perkó, Z., Bortfeld, T., Hong, T., Wolfgang, J., and Unkelbach, J. (2018). Derivation of mean dose tolerances for new fractionation schemes and treatment modalities. *Phys. Med. Biol.*, 63(3):035038.

Perumal, V., Corica, T., Dharmarajan, A. M., Sun, Z., Dhaliwal, S. S., Dass, C. R., and Dass, J. (2019). Circulating tumour cells (CTC), head and neck cancer and radiotherapy; future perspectives. *Cancers*, 11(3):367.

Petit, S. F., Breedveld, S., Unkelbach, J., den Hertog, D., and Balvert, M. (2021). Robust dose-painting-by-numbers vs. non-selective dose escalation for non-small cell lung cancer patients. *Med. Phys.*, 48(6):3096–3108.

Pflugfelder, D., Wilkens, J. J., Nill, S., and Oelfke, U. (2008). A comparison of three optimization algorithms for intensity modulated radiation therapy. *Z. Med. Phys.*, 18:111–119.

Philips (2019). Improving performance with proprietary optimization. White paper.

Polinder, G. J., Breugem, T., Dollevoet, T., and Maróti, G. (2019). An adjustable robust optimization approach for periodic timetabling. *Transport. Res. B-Meth.*, 128:50–68.

RaySearch Laboratories AB (2017a). Biological optimization and evaluation in raystation. Version 2017-04-20.

RaySearch Laboratories AB (2017b). RayStation product configurations overview. Version 2017-05-12.

RaySearch Laboratories AB (2020). Multi-critera optimization in RayStation. White paper, Version 2020-06-08.

Renegar, J. (2001). *A mathematical view of interior-point methods in convex optimization*. MPS-SIAM Series on Optimization.

Rockafellar, T. R. (1970). *Convex analysis*. Princeton University Press, Princeton, NJ.

Romeijn, H. E., Ahuja, R. K., and Dempsey, J. F. (2003). A novel linear programming approach to fluence map optimization for intensity modulated radiation therapy treatment planning. *Phys. Med. Biol*, 48(21):3521–3542.

Romeijn, H. E., Ahuja, R. K., Dempsey, J. F., and Kumar, A. (2006). A new linear programming approach to radiation therapy treatment planning problems. *Oper. Res.*, 54(2):201–216.

Romeijn, H. E. and Dempsey, J. F. (2008). Intensity modulated radiation therapy treatment plan optimization. *TOP*, 16:215–243.

Romeijn, H. E., Dempsey, J. F., and Li, J. G. (2004). A unifying framework for multi-criteria fluence map optimization models. *Phys. Med. Biol.*, 49(10):1991–2013.

Saberian, F., Ghate, A., and Kim, M. (2015). A two-variable linear program solves the standard linear–quadratic formulation of the fractionation problem in cancer radiotherapy. *Oper. Res. Lett.*, 43:254–258.

Saberian, F., Ghate, A., and Kim, M. (2016a). Optimal fractionation in radiotherapy with

multiple normal tissues. *Math. Med. Biol.*, 33(2):211–252.

Saberian, F., Ghate, A., and Kim, M. (2016b). A theoretical stochastic control framework for adapting radiotherapy to hypoxia. *Phys. Med. Biol.*, 61(19):7136–7161.

Saberian, F., Ghate, A., and Kim, M. (2017). Spatiotemporally optimal fractionation in radiotherapy. *INFORMS J. Comput.*, 29(3):422–437.

Saka, B., Rardin, R. L., and Langer, M. P. (2014). Biologically guided intensity modulated radiation therapy planning optimization with fraction-size dose constraints. *J. Oper. Res. Soc.*, 65:557–571.

Salari, E., Unkelbach, J., and Bortfeld, T. (2015). A mathematical programming approach to the fractionation problem in chemoradiotherapy. *IISE Trans. Healthc. Syst. Eng.*, 5:55–73.

Santiago, A., Barczyk, S., Jelen, U., Engenhart-Cabillic, R., and Wittig, A. (2016). Challenges in radiobiological modeling: can we decide between LQ and LQ-L models based on reviewed clinical NSCLC treatment outcome data. *Radiat. Oncol.*, 11:67.

Scott, J. G., Berglund, A., Schell, M. J., Mihaylov, I., Fulp, W. J., Yue, B., ..., and Torres-Roca, J. F. (2017). A genome-based model for adjusting radiotherapy dose (GARD): a retrospective, cohort-based study. *Lancet Oncol.*, 18(2):202–211.

Seco, J. and Verhaegen, F., editors (2013). *Monte Carlo techniques in radiation therapy*. Imaging in Medical Diagnosis and Therapy, CRC Press.

Serrano, S. A. (2015). *Algorithms for unsymmetric cone optimization and an implementation for problems with the exponential cone*. PhD thesis, Stanford University.

Serre, R., Benzekry, S., Padovani, L., Meille, C., André, N., Ciccolini, J., ..., and ... Barbolosi, D. (2016). Mathematical modeling of cancer immunotherapy and its synergy with radiotherapy. *Cancer Res.*, 76(17):4931–4940.

Shapiro, A., Dentcheva, D., and Ruszczyński, A. (2014). *Lectures on stochastic programming: modeling and theory*. SIAM, Philadelphia. Second edition.

Shepard, D. M., Ferris, M. C., Olivera, G. H., and Mackie, T. R. (1999). Optimizing the delivery of radiation therapy to cancer patients. *SIAM Rev.*, 41(4):721–744.

Shields, A. F., Briston, D. A., Chandupatla, S., Douglas, K. A., Lawhorn-Crews, J., Collins, J. M., ..., and Muzik, O. (2005). A simplified analysis of [18F]3'-deoxy-3'-fluorothymidine metabolism and retention. *Eur. J. Nucl. Med. Mol. Imaging*, 32(11):1269–1275.

Somaiah, N., Rothkamm, K., and Yarnold, J. (2015). Where do we look for markers of radiotherapy fraction size sensitivity? *Clin. Oncol.*, 27:570–578.

South, C. P., Partridge, M., and Evans, P. M. (2008). A theoretical framework for prescribing radiotherapy dose distributions using patient-specific biological information. *Med. Phys.*, 35(10):4599–4611.

Søvik, Å., Malinen, E., Skogmo, H. K., Bentzen, S. M., Bruland, Ø. S., and Olsen, D. R. (2007). Radiotherapy adapted to spatial and temporal variability in tumor hypoxia. *Int. J. Radiat. Oncol. Biol. Phys.*, 68(5):1496–1504.

Stavrev, P., Hristov, D., Warkentin, B., Sham, E., Stavreva, N., and Fallone, B. G. (2003). Inverse

treatment planning by physically constrained minimization of a biological objective function. *Med Phys.*, 30(11):2948–2958.

Sung, H., Ferlay, J., Siegel, R. L., Laversanne, M., Soerjomataram, I., Jemal, A., and Bray, F. (2021). Global cancer statistics 2020: GLOBOCAN estimates of incidence and mortality worldwide for 36 cancers in 185 countries. *CA Cancer J. Clin.*, 71(3):209–249.

Sung, W., Grassberger, C., McNamara, A. L., Basler, L., Ehrbar, S., Tanadini-Lang, S., ..., and Paganetti, H. (2020). A tumor-immune interaction model for hepatocellular carcinoma based on measured lymphocyte counts in patients undergoing radiotherapy. *Radiother. Oncol.*, 151:73–81.

Tai, A., Erickson, B., Khater, K. A., and Li, X. A. (2008). Estimate of radiobiologic parameters from clinical data for biologically based treatment planning for liver irradiation. *Int. J. Radiat. Oncol. Biol. Phys.*, 70(3):900–907.

Ten Eikelder, S. C. M., Ajdari, A., Bortfeld, T., and den Hertog, D. (2021a). Adjustable robust treatment-length optimization in radiation therapy. Preprint arXiv:1906.12116.

Ten Eikelder, S. C. M., Ajdari, A., Bortfeld, T., and den Hertog, D. (2021b). Conic formulation of fluence map optimization problems. Unpublished manuscript.

Ten Eikelder, S. C. M., den Hertog, D., Bortfeld, T., and Perkó, Z. (2019). Optimal combined proton-photon therapy schemes based on the standard BED model. *Phys. Med. Biol.*, 64(6):065011.

Ten Eikelder, S. C. M., Ferjančič, P., Ajdari, A., Bortfeld, T., den Hertog, D., and Jeraj, R. (2020). Optimal treatment plan adaptation using mid-treatment imaging biomarkers. *Phys. Med. Biol.*, 65:245011.

Toyohara, J., Waki, A., Takamatsu, S., Yonekura, Y., Magata, Y., and Fujibayashi, Y. (2002). Basis of FLT as a cell proliferation marker: comparative uptake studies with [3H]thymidine and [3H]arabinothymidine, and cell-analysis in 22 asynchronously growing tumor cell lines. *Nucl. Med. Biol.*, 29(3):281–287.

Unkelbach, J., Alber, M., Bangert, M., Bokrantz, R., Chan, T. C. Y., Deasy, J. O., ..., and Huijun, X. (2018a). Robust radiotherapy planning. *Phys. Med. Biol.*, 63:22TR02.

Unkelbach, J., Bangert, M., Bernstein, K., Andratschke, N., and Guckenberger, M. (2018b). Optimization of combined proton – photon treatments. *Radiother. Oncol.*, 128(1):133–138.

Unkelbach, J., Craft, D., Salari, E., Ramakrishnan, J., and Bortfeld, T. (2013a). The dependence of optimal fractionation schemes on the spatial dose distribution. *Phys. Med. Biol.*, 58(1):159–167.

Unkelbach, J. and Papp, D. (2015). The emergence of nonuniform spatiotemporal fractionation schemes within the standard BED model. *Med. Phys.*, 42(5):2234–2241.

Unkelbach, J., Zeng, C., and Engelsman, M. (2013b). Simultaneous optimization of dose distributions and fractionation schemes in particle radiotherapy. *Med. Phys.*, 40(9):091702.

Van Haveren, R. and Breedveld, S. (2019). Fast and exact hessian computation for a class of nonlinear functions used in radiation therapy treatment planning. *Phys. Med. Biol.*,

64(16):16NT01.

Van Herk, M. (2004). Errors and margins in radiotherapy. *Semin. Radiat. Oncol.*, 14(1):52–64.

Van Leeuwen, C. M., Oei, A., Crezee, J., Bel, A., Franken, N. A. P., Stalpers, L. J. A., and Kok, H. P. (2018). The alpha and beta of tumours: a review of parameters of the linear-quadratic model, derived from clinical radiotherapy studies. *Radiation. Oncol.*, 13:96.

Vanderstraeten, B., Duthoy, W., De Gersem, W., De Neve, W., and Thierens, H. (2006). [18F]fluoro-deoxy-glucose positron emission tomography ([18F]FDG-PET) voxel intensity-based intensity-modulated radiation therapy (IMRT) for head and neck cancer. *Radiother. Oncol.*, 79:249–258.

Vesselle, H., Grierson, J., Muzi, M., Pugsley, J. M., Schmidt, R. A., Rabinowitz, P., ..., and Wood, D. E. (2002). In vivo validation of 3'deoxy-3'-[(18)F]fluorothymidine ([(18)F]FLT) as a proliferation imaging tracer in humans: correlation of [(18)F]FLT uptake by positron emission tomography with Ki-67 immunohistochemistry and flow cytometry in human lung tumors. *Clin. Cancer Res.*, 8(11):3315–3323.

Vigerske, S. (2021). MINLPLIB2 library. `http://www.gamsworld.org/minlp/minlplib2/html/`. Accessed 11-08-2021.

Voet, P. W. J., Dirkx, M. L. P., Breedveld, S., Al-Mamgani, A., Incrocci, L., and Heijmen, B. J. M. (2014). Fully automated volumetric modulated arc therapy plan generation for prostate cancer patients. *Int. J. Radiat. Oncol. Biol. Phys.*, 88(5):1175–1179.

Wächter, A. and Biegler, L. T. (2006). On the implementation of an interior-point filter line-search algorithm for large-scale nonlinear programming. *Math. Program.*, 106(1):25–57.

Webb, S., Convery, D. J., and Evans, P. M. (1998). Inverse planning with constraints to generate smoothed intensity-modulated beams. *Phys. Med. Biol.*, 43(10):2785–2794.

Webb, S. and Lomax, T. (2001). There is no IMRT. *Phys. Med. Biol.*, 46:L7–L8.

Webb, S. and Nahum, A. E. (1993). A model for calculating tumour control probability in radiotherapy including the effects of inhomogeneous distributions of dose and clonogenic cell density. *Phys. Med. Biol.*, 38(6):653–666.

Wein, L. M., Cohen, J. E., and Wu, J. T. (2000). Dynamic optimization of a linear-quadratic model with incomplete repair and volume-dependent sensitivity and repopulation. *Int. J. Radiat. Oncol. Biol. Phys.*, 47(4):1073–1083.

Widder, J., van der Schaaf, A., Lambin, P., Marijnen, C. A. M., Pignol, J. P., Rasch, C. R., ..., and Langendijk, J. A. (2016). The quest for evidence for proton therapy: model-based approach and precision medicine. *Int. J. Radiat. Oncol. Biol. Phys.*, 95(1):30–36.

Wiesemann, W., Kuhn, D., and Sim, M. (2014). Distributionally robust convex optimization. *Oper. Res.*, 62(6):1358–1376.

Wieser, H. P., Cisternas, E., Wahl, N., Ulrich, S., Stadler, A., Mescher, H., ..., and Bangert, M. (2017). Development of the open-source dose calculation and optimization toolkit matRad. *Med. Phys.*, 44(6):2556–2568.

Withers, H. R. (1985). Biological basis for altered fractionation schemes. *Cancer*, 55:2086–

2095.

World Health Organization (2020). Global Health Estimates 2020: Deaths by Cause, Age, Sex, by Country and by Region, 2000-2019. Geneva.

Wright, S. J. (1997). *Primal-dual interior-point methods*. Society for Industrial and Applied Mathematics, Philadelphia.

Wu, Q. and Mohan, R. (2000). Algorithms and functionality of an intensity modulated radiotherapy optimization system. *Med. Phys.*, 27(4):701–711.

Wu, Q., Mohan, R., Niemierko, A., and Schmidt-Ullrich, R. (2002). Optimization of intensity-modulated radiotherapy plans based on the equivalent uniform dose. *Int. J. Radiat. Oncol. Biol. Phys.*, 52(1):224–235.

Yan, D., Vicini, F., Wong, J., and Martinez, A. (1997). Adaptive radiation therapy. *Phys. Med. Biol.*, 42(1):123–132.

Yang, Y. and Xing, L. (2005a). Optimization of radiotherapy dose-time fractionation with consideration of tumor specific biology. *Med. Phys.*, 32(12):3666–3677.

Yang, Y. and Xing, L. (2005b). Towards biologically conformal radiation therapy (BCRT): selective IMRT dose escalation under the guidance of spatial biology distribution. *Med. Phys.*, 32(6):1473–1484.

Yanıkoğlu, İ., Gorissen, B. L., and den Hertog, D. (2019). A survey of adjustable robust optimization. *Eur. J. Oper. Res.*, 277:799–813.

Yu, C. X. (1995). Intensity-modulated arc therapy with dynamic multileaf collimation: an alternative to tomotherapy. *Phys. Med. Biol.*, 40:1435–1449.

Zeng, B. and Zhao, L. (2013). Solving two-stage robust optimization problems using a column-and-constraint generation method. *Oper. Res. Lett.*, 41(5):457–461.

Zhang, L., Hub, M., Thieke, C., Floca, R. O., and Karger, C. P. (2013). A method to visualize the uncertainty of the prediction of radiobiological models. *Phys. Medica*, 29:556–561.

Zhang, X., Liu, H., Wang, X., Dong, L., Wu, Q., and Mohan, R. (2004). Speed and convergence properties of gradient algorithms for optimization of IMRT. *Med. Phys.*, 31(5):1141–1152.

Zhen, J. and den Hertog, D. (2018). Computing the maximum volume inscribed ellipsoid of a polytopic projection. *INFORMS J. Comput.*, 30(1):31–42.

Zhen, J., den Hertog, D., and Sim, M. (2018). Adjustable robust optimization via Fourier-Motzkin elimination. *Oper. Res.*, 66(4):1086–1100.

Zhen, J., Marandi, A., de Moor, D., den Hertog, D., and Vandenberghe, L. (2021). Disjoint bilinear programming: A two-stage robust optimization perspective. Available at Optimization Online.

Zinchenko, Y., Craig, T., Keller, H., Terlay, T., and Sharpe, M. (2008). Controlling the dose distribution with gEUD-type constraints within the convex radiotherapy optimization framework. *Phys. Med. Biol.*, 53:3231–3250.

CENTER DISSERTATION SERIES

CentER for Economic Research, Tilburg University, the Netherlands

No.	Author	Title	ISBN	Published
617	Matjaz Maletic	Essays on international finance and empirical asset pricing	978 90 5668 618 5	January 2020
618	Zilong Niu	Essays on Asset Pricing and International Finance	978 90 5668 619 2	January 2020
619	Bjorn Lous	On free markets, income inequality, happiness and trust	978 90 5668 620 8	January 2020
620	Clemens Fiedler	Innovation in the Digital Age: Competition, Cooperation, and Standardization	978 90 5668 621 5	October 2020
621	Andreea Popescu	Essays in Asset Pricing and Auctions	978 90 5668 622 2	June 2020
622	Miranda Stienstra	The Determinants and Performance Implications of Alliance Partner Acquisition	978 90 5668 623 9	June 2020
623	Lei Lei	Essays on Labor and Family Economics in China	978 90 5668 624 6	May 2020
624	Farah Arshad	Performance Management Systems in Modern Organizations	978 90 5668 625 3	June 2020
625	Yi Zhang	Topics in Economics of Labor, Health, and Education	978 90 5668 626 0	June 2020
626	Emiel Jerphanion	Essays in Economic and Financial decisions of Households	978 90 5668 627 7	July 2020
627	Richard Heuver	Applications of liquidity risk discovery using financial market infrastructures transaction archives	978 90 5668 628 4	September 2020
628	Mohammad Nasir Nasiri	Essays on the Impact of Different Forms of Collaborative R&D on Innovation and Technological Change	978 90 5668 629 1	August 2020
629	Dorothee Hillrichs	On inequality and international trade	978 90 5668 630 7	September 2020
630	Roland van de Kerkhof	It's about time: Managing implementation dynamics of condition-based maintenance	978 90 5668 631 4	October 2020

No.	Author	Title	ISBN	Published
631	Constant Pieters	Process Analysis for Marketing Research	978 90 5668 632 1	December 2020
632	Richard Jaimes	Essays in Macroeconomic Theory and Natural Resources	978 90 5668 633 8	November 2020
633	Olivier David Armand Zerbib	Asset pricing and impact investing with pro-environmental preferences	978 90 5668 634 5	November 2020
634	Laura Capera Romero	Essays on Competition, Regulation and Innovation in the Banking Industry	978 90 5668 635 2	December 2020
635	Elisabeth Beusch	Essays on the Self-Employed in the Netherlands and Europe	978 90 5668 636 9	December 2020
636	Sophie Zhou	Innovation and the Macroeconomy	978 90 5668 637 6	November 2020
637	Vincent Peters	Turning modularity upside down: Patient-centered Down syndrome care from a service modularity perspective	978 90 5668 638 3	December 2020
638	Pranav Desai	Essays in Corporate Finance and Innovation	978 90 5668 639 0	January 2021
639	Kristy Jansen	Essays on Institutional Investors, Asset Allocation Decisions, and Asset Prices	978 90 5668 640 6	January 2021
640	Riley Badenbroek	Interior Point Methods and Simulated Annealing for Nonsymmetric Conic Optimization	978 90 5668 641 3	February 2021
641	Stephanie Koornneef	It's about time: Essays on temporal anchoring devices	978 90 5668 642 0	February 2021
642	Vilma Chila	Knowledge Dynamics in Employee Entrepreneurship: Implications for parents and offspring	978 90 5668 643 7	March 2021
643	Minke Remmerswaal	Essays on Financial Incentives in the Dutch Healthcare System	978 90 5668 644 4	July 2021
644	Tse-Min Wang	Voluntary Contributions to Public Goods: A multi-disciplinary examination of prosocial behavior and its antecedents	978 90 5668 645 1	March 2021

No.	Author	Title	ISBN	Published
645	Manwei Liu	Interdependent individuals: how aggregation, observation, and persuasion affect economic behavior and judgment	978 90 5668 646 8	March 2021
646	Nick Bombaij	Effectiveness of Loyalty Programs	978 90 5668 647 5	April 2021
647	Xiaoyu Wang	Essays in Microeconomics Theory	978 90 5668 648 2	April 2021
648	Thijs Brouwer	Essays on Behavioral Responses to Dishonest and Anti-Social Decision-Making	978 90 5668 649 9	May 2021
649	Yadi Yang	Experiments on hold-up problem and delegation	978 90 5668 650 5	May 2021
650	Tao Han	Imperfect information in firm growth strategy: Three essays on M&A and FDI activities	978 90 5668 651 2	June 2021
651	Johan Bonekamp	Studies on labour supply, spending and saving before and after retirement	978 90 5668 652 9	June 2021
652	Hugo van Buggenum	Banks and Financial Markets in Microfounded Models of Money	978 90 5668 653 6	August 2021
653	Arthur Beddock	Asset Pricing with Heterogeneous Agents and Non-normal Return Distributions	978 90 5668 654 3	September 2021
654	Mirron Adriana Boomsma	On the transition to a sustainable economy: Field experimental evidence on behavioral interventions	978 90 5668 655 0	September 2021
655	Roweno Heijmans	On Environmental Externalities and Global Games	978 90 5668 656 7	August 2021
656	Lenka Fiala	Essays in the economics of education	978 90 5668 657 4	September 2021
657	Yuexin Li	Pricing Art: Returns, Trust, and Crises	978 90 5668 658 1	September 2021
658	Ernst Roos	Robust Approaches for Optimization Problems with Convex Uncertainty	978 90 5668 659 8	September 2021
659	Joren Koëter	Essays on asset pricing, investor preferences and derivative markets	978 90 5668 660 4	September 2021

No.	Author	Title	ISBN	Published
660	Stefan ten Eikelder	Biologically-based radiation therapy planning and adjustable robust optimization	978 90 5668 662 8	October 2021

Stefan ten Eikelder (Eindhoven, the Netherlands, 1994) received his Bachelor's degree in Econometrics and Operations Research from Tilburg University in 2015, followed by a Master's degree (2017) and a Research Master degree (2018), both in Operations Research, from the same university. In September 2018, he became a PhD candidate in Operations Research at Tilburg University. Stefan carried out his research in collaboration with researchers at Massachusetts General Hospital / Harvard Medical School (Boston, USA), which he has visited several times.

Radiation therapy is one of the main treatment modalities for various different cancer types. One of the core components of personalized treatment planning is the inclusion of patient-specific biological information in the treatment planning process. Using biological response models, treatment parameters such as the treatment length and dose distribution can be tailored, and mid-treatment biomarker information can be used to adapt the treatment during its course. These additional degrees of freedom in treatment planning lead to new mathematical optimization problems. This thesis studies various optimization aspects of biologically-based treatment planning, and focuses on the influence of uncertainty. Adjustable robust optimization is the main technique used to study these problems, and is also studied independently of radiation therapy applications.

ISBN: 978 90 5668 662 8
DOI: 10.26116/center-lis-2120

TILBURG SCHOOL OF ECONOMICS AND MANAGEMENT

CentER Dissertation Series